Contribution au développement d'une station d'observation de l'Atmosphère à la Réunion et à l'étude de l'ozone troposphérique en région tropicale

Jean-Luc Baray

Mémoire d'HABILITATION A DIRIGER DES RECHERCHES

Contribution au développement d'une station d'observation de l'Atmosphère à la Réunion et à l'étude de l'ozone troposphérique en région tropicale

Jean-Luc BARAY

Soutenance le 9 Avril 2009

Composition du jury :

Rapporteurs :	Dr Jean-Pierre CAMMAS	Physicien, LA, Toulouse
	Dr Alain HAUCHECORNE	DR CNRS, LATMOS, Paris
	Dr Philippe KECKHUT	Physicien, LATMOS, Paris
Examinateurs :	Dr Martine DE MAZIERE	DR, IASB, Bruxelles
	Pr Robert DELMAS	Professeur, LACY, la Réunion,
	Pr Jean LEVEAU	Professeur, LACY, la Réunion

Table des matières

Préambule

Nous étions au début de l'année 1995, je terminai mon parcours d'étudiant en DEA de physique atmosphérique de Clermont Ferrand. Il s'agissait de choisir un stage, qui, dans mon esprit, devrait déboucher sur une thèse. Un professeur, Serge Baldy, et un maître de Conférence, Miloud Bessafi, membre du jeune laboratoire LPA[1] de l'université de la Réunion, avaient proposé un sujet sur les échanges stratosphère-troposphère. Intéressé par la dynamique atmosphérique et volontaire pour un peu de mobilité après un parcours scolaire et universitaire totalement passé en Auvergne, je choisissais ce stage et, un jour d'avril 1995, je découvrais l'île de la Réunion. Treize ans après, je ne l'ai pas quitté et je rédige ce mémoire d'HDR. En effet, de ce stage a débouché une thèse, puis, un recrutement sur un poste de physicien adjoint. Ce document constitue donc une synthèse de ma dizaine d'années d'activité scientifique passées sous les tropiques, en tant que physicien adjoint affecté à l'IPSL[2] et détaché à la Réunion, au LPA qui devint LACY[3] en s'associant à Météo-France.

Un physicien adjoint est un enseignant-chercheur universitaire chargé de plusieurs missions:

1- Une mission de recherche ainsi que de valorisation de ses résultats en science de la planète.

2- Une mission de collecte des données d'observation, de leur conservation sur le long terme et de leur exploitation scientifique.

3- Des missions d'intérêt général, national ou international

4- Une mission de gestion des moyens de recherche.

5- Une mission de coopération internationale.

6- Une mission de formation, d'enseignement à et par la recherche et de diffusion de la culture et de l'information scientifique et technique.

Ma mission de service d'observation a consisté à assurer le suivi et participer au développement de la station d'observation de l'atmosphère de l'île de la Réunion. Ma tâche de

[1] Laboratoire de Physique de l'Atmosphère
[2] Institut Pierre Simon Laplace

service a inclus la responsabilité scientifique d'instruments tels que les lidars ozone troposphérique et stratosphérique, de leur installation, du suivi de leur fonctionnement, du traitement des données produites et de leur mise à disposition. J'ai donc eu une activité importante pour que la station de la Réunion ait une bonne visibilité et une activité importante dans le cadre des réseaux internationaux.

Dans le cadre de ma mission de formation et d'enseignement, j'ai développé et donné des cours sur l'instrumentation géophysique et les réseaux de recherche et d'observation dans le cadre du master géosphère de l'université de la Réunion, lorsque celui-ci a été ouvert. Je prends en charge également la présentation de l'instrumentation de l'OPAR[4] lorsque des visites de laboratoire sont organisées, souvent dans le cadre de l'accueil de lycéens et de collégiens par la faculté des sciences.

Mon activité de recherche scientifique proprement dite s'est organisée autour du bilan de l'ozone troposphérique tropical. En effet, cette dizaine d'années d'observation de l'ozone troposphérique par lidar nous a permis d'approfondir des cas d'études pour détailler les mécanismes source de l'ozone troposphérique à la Réunion, d'établir la climatologie de l'ozone et de la tropopause et de dégager les premières estimations de tendances de l'ozone troposphérique.

L'essor instrumental de la station de mesure et mon activité scientifique sont donc très liées. J'ai donc décidé d'organiser ce document en deux chapitres :
Le premier chapitre est une présentation de l'essor instrumental de la station de l'OPAR et sa place dans les réseaux de recherche internationaux. Il reflète mon activité dans le cadre de ma mission de participation aux services d'observation.
Le second chapitre est une synthèse des principaux résultats obtenus par rapport au bilan de l'ozone troposphérique tropical. Il synthétise d'avantage mon activité de recherche scientifique.

Ces deux chapitres seront suivis d'une partie de conclusion et de prospective, et d'une série d'annexes présentant mes activités d'enseignement, l'encadrement de stagiaires et d'étudiants

[3] Laboratoire de l'Atmosphère et des CYclones
[4] Observatoire de Physique de l'Atmosphère de la Réunion

en thèse, une synthèse de mes responsabilités administratives et la liste de mes publications et présentations.

Je ne peux conclure ce préambule sans avoir une pensée amicale et reconnaissante pour les professeurs Serge Baldy et Jean Leveau qui sont à l'origine, à la fois de ma venue à la Réunion, de l'essor instrumental de l'OPAR et scientifique du LACY, et également de beaucoup d'études présentées dans ce mémoire.

Je suis également très reconnaissant au professeur Robert Delmas qui a pris leur succession à la direction du LACY et de l'OPAR, et qui a réussi à me donner l'impulsion nécessaire pour concrétiser la rédaction et la présentation de mon H.D.R

Je remercie plus largement toutes les personnes, de la Réunion, de Paris, de Toulouse ou d'ailleurs, qui ont pris part, de manière directe ou indirecte, aux activités d'observation et de recherche à la Réunion, enseignants-chercheurs, administratifs, techniciens opérateurs lidar et ingénieurs, étudiants en thèse et post-doctorants, avec une pensée spéciale pour les valeureux thésards avec qui j'ai eu la chance de travailler, Jimmy, Gaëlle et Valentin.

Chapitre 1

Une station d'observation atmosphérique à la Réunion : l'OPAR

1.1 Contexte géophysique et historique des mesures atmosphériques à la Réunion

De part sa situation géographique à la position 21° Sud, 55° Est, le site de l'île de la Réunion bénéficie d'une situation exceptionnelle pour les études atmosphériques. Dans la troposphère, du fait de sa latitude, en hiver austral, le site de la Réunion est situé près de la zone d'influence du courant-jet subtropical susceptible d'induire des échanges de masses d'air entre la stratosphère et la troposphère (foliations subtropicales, gouttes froides). En été austral elle est soumise à l'influence de la convection tropicale et au printemps, étant à l'est de l'Afrique et de Madagascar, dans la partie sud-ouest de l'Océan Indien, elle subit l'influence des contaminations des brûlages de biomasse, suivant un mécanisme différent des contaminations observées en basse couche en Afrique de l'Ouest, au-dessus de l'océan Atlantique.

Pour les études stratosphériques, ce site présente également un intérêt particulier de part sa localisation en bordure sud de la zone tropicale, il constitue un point privilégié d'observation et d'analyse des mécanismes de confinement et d'échanges entre cette zone et les latitudes moyennes. Cette articulation clé pour la dynamique atmosphérique et la répartition des constituants traces est vulnérable vis-à-vis des sollicitations dynamiques externes, les ondes notamment, qui dépendent du forçage climatique via les évolutions différentielles dans les différents compartiments atmosphériques.

La situation privilégiée de ce site explique l'initiation de mesures atmosphériques au début des années 1990, sous l'impulsion de deux professeurs en activité à l'université de la Réunion à l'époque, Serge Baldy et Jean Leveau, et grâce à l'appui politique au niveau national de responsables scientifiques tels que Gérard Mégie et le soutien technique du Service d'Aéronomie.

Lorsque je suis arrivé à la Réunion pour la première fois en 1995, dans le cadre de mon stage de DEA, un certain nombre d'activités d'observations étaient en cours de développement dans le cadre du laboratoire de recherche, le LPA[1]. La situation instrumentale de la station était la suivante :

Les mesures lidar Rayleigh de température stratosphérique venaient d'être installées et étaient exploitées dans le cadre de la thèse de Hassan Bencherif. Les études troposphériques étaient basées

[1] Laboratoire de Physique de l'Atmosphère

principalement sur les radiosondages, et étaient menées dans le cadre de la thèse de Fabienne Taupin et de celle de Tantely Randriambelo.

Un instrument de type SAOZ était également en fonctionnement mais relativement peu exploité scientifiquement localement, en dehors de la calibration des sondes.

Par la suite, l'activité instrumentale du LPA a connu un essor exponentiel, avec principalement l'implémentation de nouvelles voies lidar sur le système existant, ainsi que l'acquisition d'un autre système lidar en 2000 dédié à la mesure de l'ozone stratosphérique. Le 4 Février 2003 est une date importante, puis qu'elle a vu la création officielle de l'OPAR[2], sous l'égide de la région Réunion, de l'université de la Réunion, du CNRS et de l'université Versailles St Quentin (IPSL), dans le but d'installer dans la durée une structure dédiée à l'observation de l'atmosphère à l'île de la Réunion.

Figure 1.1 Signature de la convention de l'OPAR le mardi 4 Février 2003. De gauche à droite : Jean Jouzel (directeur de l'IPSL), Gérard Mégie (président du CNRS), Paul Vergès (président du conseil régional de la Réunion) et Frédéric Cadet (président de l'université de la Réunion).

Le développement de la station a connu un nouvel essor à partir 2006-2007, date de l'arrivée de Robert Delmas à la direction de l'OPAR et du laboratoire (le LPA devenu LACy[3] avec le statut

[2] Observatoire de Physique de l'Atmosphère de la Réunion, http://opar.univ-reunion.fr/
[3] Laboratoire de l'Atmosphère et des Cyclones, http://lacy.univ-reunion.fr/

d'unité mixte de recherche associé au CNRS et à Météo-France), ainsi qu'un renforcement important du staff technique avec l'arrivée de trois ingénieurs (Hélène Ferré, Yann Courcoux et Franck Gabarrot) et d'un technicien (Patrick Hernandez).

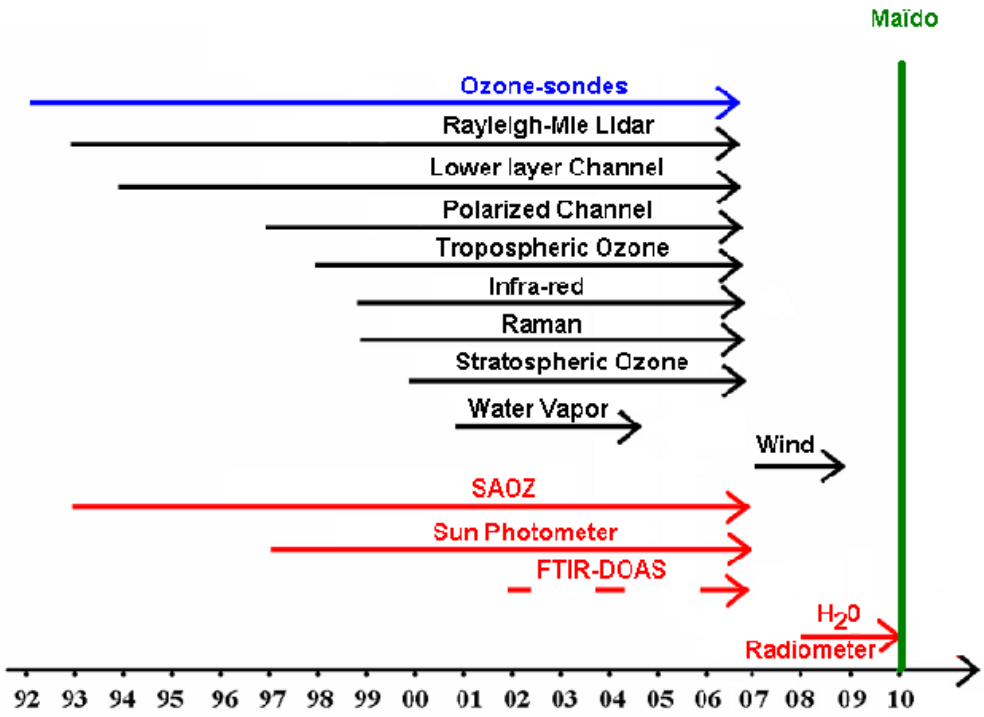

Figure 1.2 Evolution du parc instrumental à la Réunion, avec en bleu les sondes, en noir les mesures lidar et en rouge les radiomètres et spectromètres.

Ma tâche de physicien adjoint a été de m'impliquer au maximum dans les développements instrumentaux, et de favoriser à la fois leur visibilité dans les réseaux de recherche internationaux et donc leur utilisation leur exploitation scientifique. Cette implication se traduit par une participation active au comité de pilotage de l'OPAR (depuis 2003, date de sa création) et au bureau NDACC-France (depuis 2006, date de sa création). Les développements instrumentaux dans lequel j'ai été impliqué sont présentés dans la section 1.2, et les réseaux de recherche internationaux dans la section 1.3. La section 1.4 présente les projets instrumentaux incluant le projet de construction de la station d'altitude au Maïdo dans l'ouest de l'île, un projet de longue date qui va se concrétiser à l'horizon 2010.

1.2 Le développement instrumental de l'OPAR

1.2.1 Introduction

En 2006, le parc instrumental de l'OPAR qui s'était développé au fil des années était composé :
- D'un système lidar pour la mesure de la température et des aérosols troposphériques et stratosphériques, par méthode Rayleigh et Raman, de l'ozone troposphérique, de la vapeur d'eau troposphérique et des cirrus (voie dépolarisation)
- D'un autre système lidar pour la mesure de l'ozone stratosphérique
- De deux photomètres CIMEL
- D'un spectromètre SAOZ (Système d'Analyse par Observation Zénithale)
- D'un système de mesures par radiosondages

De plus, l'OPAR accueille fréquemment d'autres instruments tels que les spectromètres FTIR et MAX-DOAS dans le cadre de campagnes de mesure spécifiques.

Il m'avait donc paru opportun de soumettre à un journal de rang A une présentation de ce parc instrumental, et des objectifs scientifiques associés à ce développement instrumental pour améliorer la visibilité de la station. Cet article est présenté dans la section 1.2.2.

Certains instruments présentent une originalité instrumentale. C'est le cas des voies lidar ozone troposphérique, implémentées sur le lidar Rayleigh-Mie en 1998, avec le système de double fibres développé pour ces voies lidar. L'utilisation des fibres de 0,4 mm diamètre utilisées pour le système Rayleigh-température n'était pas possible car les mesures d'ozone troposphérique nécessitent un champ de vue plus grand pour obtenir un recouvrement optimal dans la gamme d'altitude prévue. Un système de fixation mécanique à double fibre a donc été mis en place, le diamètre des fibres pour l'ozone étant de 1,5 mm. Les deux fibres sont liées mécaniquement et maintenues au point focal pour chaque faisceau, la distance entre les deux fibres correspondant à la distance angulaire entre les deux faisceaux. La mise en phase des champs de vue des télescopes se fait par un mouvement global des fibres aux foyers, l'intérêt de ce mécanisme étant d'utiliser facilement la partie optique d'un autre mode de fonctionnement indépendant, tout en bénéficiant de l'alignement d'un mode sur l'autre. Cette originalité optique nous a permis de publier leur description technique et leur validation dans l'article présenté dans la section 1.2.3.

Après son installation en juin 1998, je me suis attaché à faire fonctionner cet instrument aussi

régulièrement que possible, la régularité des mesures ayant été amélioré avec le recrutement d'opérateurs lidar.

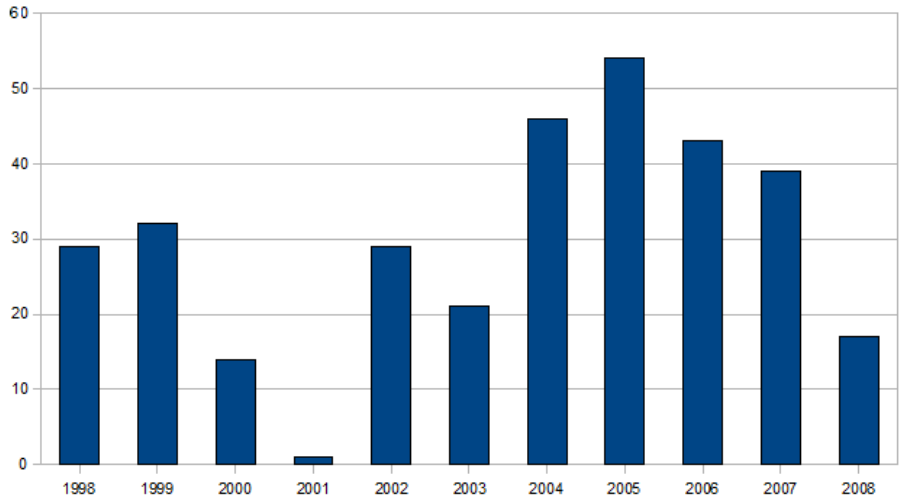

Figure 1.3 Nombre de nuits de mesures acquises par an avec le système lidar ozone troposphérique.

L'intérêt scientifique évident de cet instrument, tant pour l'étude des différentes sources d'ozone troposphériques que pour la surveillance climatologique est illustrée par le nombre d'études exploitant ces données[4,5,6,7] et dont certaines sont présentées en détail dans le chapitre 2 du présent document.

Après mon recrutement et suite au départ en mission longue durée en coopération à Madagascar du responsable scientifique Franck Molinaro, je me suis impliqué également sur cet instrument qui est présenté dans la section 1.2.4

Certains radiomètres complexes de type DOAS et FTIR ont fonctionné dans le cadre de campagnes de mesure à la Réunion en collaboration avec l'IASB, l'institut d'Aéronomie Spatiale de Belgique et avec l'Université libre de Bruxelles. Le multi-axis DOAS est un radiomètre qui permet des mesures spectrales de BrO troposphériques et stratosphériques. Il a fonctionné dans le cadre d'une campagne longue durée d'Août 2004 à Juin 2005. Les méthodes d'inversion et les résultats de cette campagne figurent dans l'article présenté dans la section 1.2.5.

[4] Baray J.L. et al., Planetary-scale tropopause folds in the southern subtropics, *Geophys. Res. Lett.*, 27, 353-356, 2000.
[5] Randriambelo T., et al., Investigation of the short-time variability of tropical tropospheric ozone, *Ann. Geophys.*, 21, 9, 2095-2106, 2003.
[6] Leclair De Bellevue, J., et al., Signatures of stratosphere to troposphere, transport near deep convective events in the southern subtropics, *J. Geophys. Res.*, 111, D24107, doi:10.1029/2005JD006947, 2006.
[7] Clain G. , et al., Tropospheric ozone climatology at two southern subtropical sites, (Reunion Island and Irene, South Africa) from ozone sondes, LIDAR, aircraft and in situ measurements, *Atmos. Chem. and Phys.*, en révision, 2008

Egalement en collaboration avec les équipes belges, des campagnes de mesure par FTIR ont été élaborées en 2002, 2004 et 2007. Le FTIR est un radiomètre à haute résolution spectrale fonctionnant dans le domaine de l'infrarouge, et dont l'inversion des spectres permet d'obtenir des profils et des colonnes intégrées d'un grand nombre d'espèces trace telles que l'ozone, le monoxyde de carbone ainsi qu'un grand nombre d'espèces traces détaillées dans l'article présentant les observations lors des campagnes 2002 et 2004 et constituant la section 1.2.6. Je dois souligner que je ne me suis pas impliqué de manière égale dans tous les développements instrumentaux présentés dans ce chapitre. Mon implication dans les expériences lidar ozone troposphérique et stratosphérique a couvert l'acquisition des données, et particulièrement aux périodes ou le LACY ne comptait pas beaucoup d'opérateurs lidar, une participation au travail de maintenance en étroite collaboration avec les équipes techniques du service d'aéronomie et de la Réunion, le traitement, le formatage et l'exploitation des données en co-responsabilité avec Gérard Ancellet pour l'ozone troposphérique et Sophie Godin-Beekmann pour l'ozone stratosphérique. Mon implication dans les expériences FTIR et multi-axis DOAS n'a pas été aussi importante puisque je me suis contenté d'accompagner et d'aider les équipes belges dans la mise en place et l'opération de ces expériences. Pour ce qui concerne les expériences FTIR, je me suis également impliqué dans l'exploitation scientifique des données au travers du co- encadrement avec Martine de Mazière du stage de Valentin Duflot. Les différentes campagnes de mesure ont montré que cet instrument produit des profils de constituants dont l'intérêt scientifique est très important par rapport aux thématiques scientifiques du LACY, il est donc important à mon sens de travailler à l'acquisition d'un minimum d'expertise technique et scientifique ce qui a été initié avec le stage de Valentin Duflot.

1.2.2 Présentation de l'OPAR en 2006

PAPER www.rsc.org/jem | Journal of Environmental Monitoring

An instrumented station for the survey of ozone and climate change in the southern tropics†

J.-L. Baray,*[ab] J. Leveau,[b] S. Baldy,[b] J. Jouzel,[a] P. Keckhut,[ac] G. Bergametti,[d] G. Ancellet,[e] H. Bencherif,[b] B. Cadet,[bc] M. Carleer,[f] C. David,[ae] M. De Mazière,[g] D. Faduilhe,[b] S. Godin Beekmann,[ae] P. Goloub,[h] F. Goutail,[ac] J. M. Metzger,[b] B. Morel,[b] J. P. Pommereau,[c] J. Porteneuve,[c] T. Portafaix,[b] F. Posny,[b] L. Robert[b] and M. Van Roozendael[g]

Received 1st June 2006, Accepted 24th July 2006
First published as an Advance Article on the web 9th August 2006
DOI: 10.1039/b607762e

The assessment of changes induced by human activities on Earth atmospheric composition and thus on global climate requires a long-term and regular survey of the stratospheric and tropospheric atmospheric layers. The objective of this paper is to describe the atmospheric observations performed continuously at Reunion Island (55.5° east, 20.8° south) for 15 years. The various instruments contributing to the systematic observations are described as well as the measured parameters, the accuracy and the database. The LiDAR systems give profiles of temperature, aerosols and ozone in the troposphere and stratosphere, probes give profiles of temperature, ozone and relative humidity, radiometers and spectrometers give stratospheric and tropospheric integrated columns of a variety of atmospheric trace gases. Data are included in international networks, and used for satellite validation. Moreover, some scientific activities for which this station offers exceptional opportunities are highlighted, especially air mass exchanges nearby dynamical barriers: (1) On the vertical scale through the tropical tropopause layer (stratosphere–troposphere exchange). (2) On the quasi-horizontal scale across the southern subtropical barrier separating the tropical stratospheric reservoir from mid- and high latitudes.

Introduction

In the last 25 years, research in atmospheric chemistry and physics has been marked by the destruction of the stratospheric ozone layer in Antarctica[1] and the impact of increasing levels of carbon dioxide and other greenhouse gases on global climate.[2,3] The discovery of the sensitivity of the global atmosphere to growing emissions of anthropogenic substances put in evidence the lack of adequate observations for understanding and thus possibly predicting the global evolution of the composition of the atmosphere (Fig. 1). The NDSC (Network for Detection of Stratospheric Change) was set up rapidly at the end of the eighties based on the use of the most recent research instruments which could be deployed at stations distributed in latitude for starting the mandatory long term monitoring of the composition of the stratosphere.[4] Largely based on already existing stations at mid- and high latitudes of the Northern Hemisphere, the challenge was to extend the network to other latitudes, particularly to the Southern Hemisphere and the tropics where almost nothing was available. In 2006, to better reflect the free tropospheric and stratospheric coverage of NDSC, measurement, analyses, and modeling activities, as well as to convey the linkage to climate change, the steering committee voted to change the name of the network to NDACC (Network for the Detection of Atmospheric Composition Change). It is indeed now well-known that the UTLS (Upper Troposphere–Lower Stratosphere) is the atmospheric layer where the effects of the climate changes should be particularly marked. For example, climate models predict a cooling in the stratosphere up to 7 K, and a warming in the troposphere of about 2 K.[5] Thus, it is of primary importance to be able to detect and quantify such changes and to connect these changes into the different atmospheric compartments, to identify the dynamical links and the strength of their exchanges.

[a] *Pierre-Simon Laplace (IPSL), Université Versailles Saint Quentin, 5 Boulevard d'Alembert, 78280 Guyancourt, France*
[b] *Laboratoire de L'Atmosphère et des Cyclones (LACy), UMR-CNRS 8105, 15, av. René Cassin, BP 7151, 97715 St-Denis Cedex 9, La Réunion, France. E-mail: baray@univ-reunion.fr; Fax: 262 93 86 65; Tel: 262 93 86 64*
[c] *Service d'Aéronomie (SA), UMR-CNRS 7620 Verrières le Buisson, 91371, France*
[d] *Laboratoire Inter-Universitaire des Systèmes Atmosphériques (LISA), UMR-CNRS 7583, 61 avenue du Général de Gaulle, F-94010 Créteil, France*
[e] *Service d'Aéronomie (SA), UMR-CNRS 7620 Université Pierre et Marie Curie, 4 place Jussieu, 75252 Paris Cédex 05, France*
[f] *Université Libre de Bruxelles(ULB), Chimie Quantique et Photophysique, CP 160/09, Avenue F.D. Roosevelt 50, 1050 Bruxelles, Belgium*
[g] *Institut d'Aéronomie Spatiale de Belgique (IASB-BIRA), 3 Av. Circulaire, B-1180 Bruxelles, Belgium*
[h] *Laboratoire d'Optique Atmospherique (LOA), Université des sciences et technologies Lille 1, UMR-CNRS 8518, 59655 Villemenuve d'asq, France*
† The HTML version of this article has been enhanced with colour images.

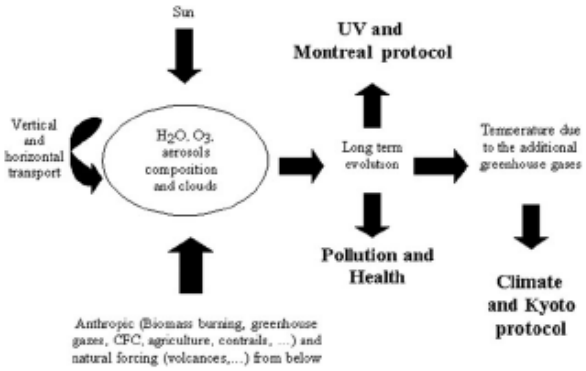

Fig. 1 The primary objective of the NDSC, the survey of the stratosphere, is complementary to the other scientific environmental issues, like pollution, climate change, or atmospheric ozone balance.

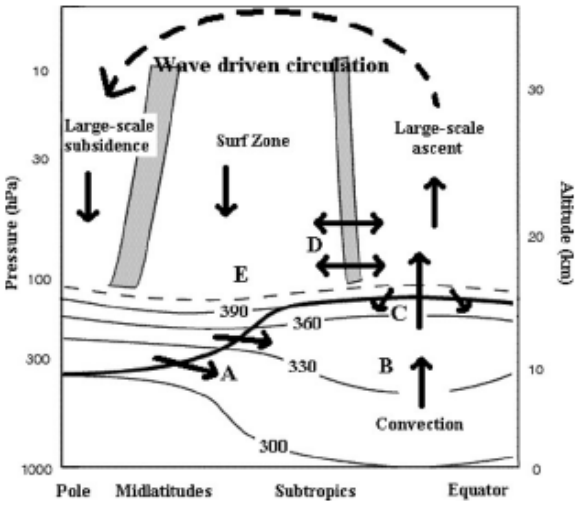

Fig. 2 Latitude–altitude cross-section schematic representation showing the different compartments of the atmosphere. The letters represent the mechanisms studied in Section 3. A: Tropopause folds, cut-off lows, Rossby wave breaking and filamentation of the tropopause induced by the subtropical jet stream. B: Mesoscale modeling of the tropical convection (cyclone, convective depressions), gravity waves induced by the convection. C: Stratosphere–troposphere induced by convection, variability of ozone and water vapor in the tropical UTLS region. D: Stratospheric ozone lamina, meridian exchanges, gravity and Kelvin waves in the tropical stratosphere. As function of the season, Reunion Island can be affected by these mechanisms.

Especially, tropical latitude bands are of special interest since, in these regions, the upper troposphere is affected by specific dynamical processes like the subtropical jet stream and the tropical convection. A program like SHADOZ (Southern Hemisphere ADditional OZonesondes) focuses on the tropospheric ozone balance in these regions.[6] In the stratosphere, tropical waves, meridional transfers of air masses and tidal perturbations of the middle atmosphere are the main drivers of the dynamics. Reunion Island is a tropical island located in the south-western part of the Indian Ocean at 20.8° S and 55.5° E. Due to its location, Reunion Island is seasonally submitted to biomass burning plumes transported from the subcontinent of Southern Africa, which can significantly affect the free tropospheric concentrations of ozone and other pollutants like CO. Moreover, it is affected by the dynamical influence of the subtropical jet stream and the tropical convection. In the stratosphere, the island is located near the subtropical barrier and special patterns of stratospheric ozone transport can be observed.

The understanding of the barrier effect and dynamical exchanges between the tropical reservoir and midlatitudes, and vertically between the troposphere and the stratosphere is of great interest to document climate change and Reunion Island is ideally located to make measurements in order to document these themes (Fig. 2). Hence, in response to the request of the network NDACC, the Service d'Aéronomie and the University of Reunion Island decided in 1991 to start building a stratospheric observing capacity in the southern tropics in the Indian Ocean.

The paper is organized as follow: firstly an overview of the instruments and facilities currently available at Reunion Island is presented. Then some important scientific results already achieved based on these measurements are given, and finally the plans for further improving and developing the station are displayed.

Instrumentation

The instrumentation operating presently at Reunion Island has been developed gradually. In collaboration with the Service d'Aéronomie (SA/CNRS) and the Institut Pierre Simon Laplace (IPSL), measurements of ozone, temperature and humidity profiles by radio soundings started in 1992 (Fig. 3). A SAOZ UV-visible spectrometer was installed nearly one year later, in 1993 (SAOZ, Système d'Analyse par Observation Zénitale). Based on the Rayleigh–Mie techniques to retrieve temperature and aerosol profiles, the first LiDAR (Light Detection And Ranging) experiments started by early 1994, thanks to the established expertise of the SA/CNRS at the Observatoire de Haute Provence and Dumont D'Urville. Then, in parallel to the continuous improvement of the existing instruments, several other instruments have been developed and implemented at Reunion station, as a set of complementary instruments, in order to: (1) provide high quality datasets that meet the NDACC quality standard, (2) contribute to validation of a number of global atmospheric experiments on space shuttles or satellites (*e.g.*, TOMS, GOME, ENVISAT, AURA and CALIPSO), (3) survey and report on original geophysical events, such as sudden stratospheric warming, total ozone reduction, biomass burning and stratosphere–troposphere exchanges, (4) improve and assess models outputs at various scales.

In the light of these developments and requirements, the Observatoire de Physique de l'Atmosphère de la Réunion (OPAR) was officially formed in February 2003. It is a French consortium based on four partners: (1) University of Reunion Island, (2) University of Versailles-Saint-Quentin, (3) Reunion Regional Council (Conseil Régional de La Réunion), and (4) CNRS, the French national research centre.

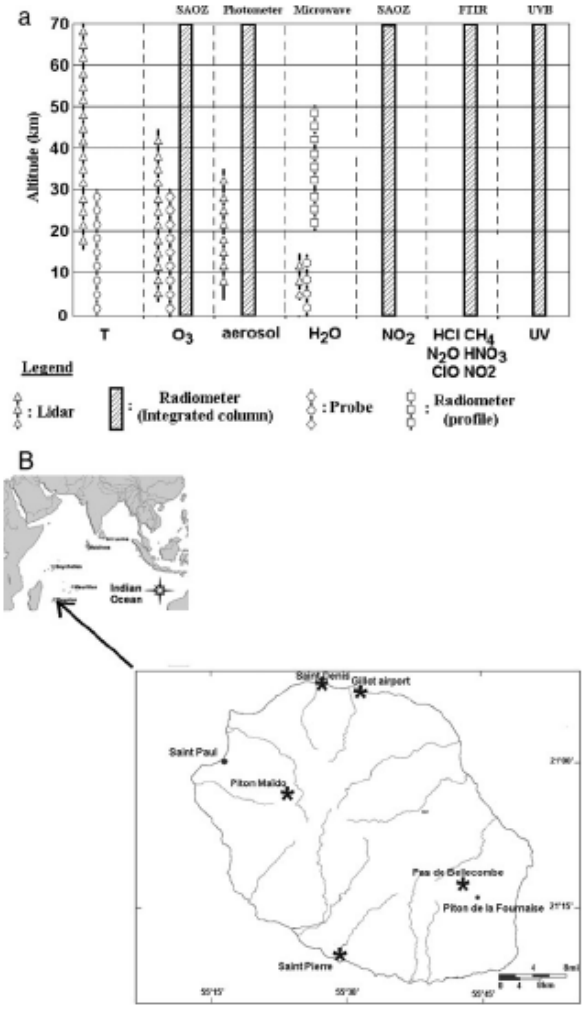

Fig. 3 (a) Parameters (bottom x axis) measured by the instrumental set (top of x axis) developed at Reunion Island, or at the planning stage. (b) Map showing the locations of the instruments on Reunion Island: The university is located at Saint Denis, radio soundings are performed from Gillot airport, and the future altitude station will be located at Piton Maïdo.

The description of the instruments is organized as follow: ozone and water vapor probes, and SAOZ and MAXDOAS UV-visible spectrometers, sun-photometer, FTIR, and finally LiDAR systems. The pictures of each instrument are given in Fig. 4. In order to show how routinely each instrument operates, the annual frequency of measurements is given in Table 1.

Ozone probes

The ozone probe program started in 1992 using ECC (Electro-Chemical Cells) and Vaisala RS80 radio probes providing temperature, pressure and humidity every 7 s during the ascent of the balloon at 5 m s^{-1} up to the burst altitude at 30–35 km. In 2006, the interface change led to a measurement rate of 2 s which had improved the resolution, which is about 50 m. The precision of the ozone concentration is estimated to 5% in the stratosphere and 10% in the troposphere.[6] According to the manufacturer, the precision of the temperature of the RS80 is 0.5 °C, while humidity readings are accurate only in the lower troposphere, up to 5–8 km, but less significant above.

The ozone probe program began with bi-monthly measurements from September 1992 to December 1998, further enhanced to weekly probes in January 1999 when the station became part of the SHADOZ network.[6] The objective of this network is to document the tropospheric ozone concentrations to better assess the estimation of tropical tropospheric ozone budget and to participate in satellite validation. To fulfill these objectives, an ozone probe is launched every week from 12 stations of the southern subtropics. Within this framework, the Reunion Island ozone probe system was involved in the JOSIE 2000 project, where the ECC probes and the methods of preparation used at SHADOZ sites were tested and qualified.[7]

In addition to the routine program, some radiosounding specific campaigns are organized, for studying mesoscale dynamical events in the troposphere and stratosphere–troposphere exchange induced by the subtropical jet stream (15 additional soundings in July 1998),[8] or by the tropical convection (8 additional soundings in February 2002) or for validating remote sensing measurements from long duration balloons passing close to the station (2 soundings in February 2001 and 2 in February 2004).[9]

In order to assess the water vapor distribution in the tropical UTLS and in the framework of the validation of satellites AQUA and AURA, some specific radiosoundings have been performed using a dedicated sensor developed by NOAA at the University of Colorado[10] allowing water vapor measurements in the local UTLS. Two specific campaigns were performed in March 2004 and February 2005.

SAOZ UV-visible spectrometer

The SAOZ (Système d'Analyse par Observation Zénitale) is an automated UV-visible spectrometer developed by the Service d'Aéronomie at the end of the eighties for studying the polar stratosphere.[11] It is a UV-visible spectrometer of 1 nm resolution looking at the sunlight scattered at zenith in the 300–630 nm spectral range. The spectrometer, housed in a waterproof container with a quartz window to enable measurements at zenith within a 10° conical field of view, is installed on the roof of the laboratory building. Total ozone and NO_2 columns are measured twice a day at sunrise and sunset between 86°–91° solar zenith angle with an accuracy of, respectively, 3 and 5%.

The first SAOZ equipped with a 512 pixel detector was installed at Reunion Island in 1993. The detector was replaced by one with 1024 pixels in 1997 after a detector failure. The SAOZ instrument has been further updated from the Hewlett-Packard to a PC version in 2002. Between 250 and 350 days of measurements are available every year archived in the NDSC database.

Fig. 5 shows the series of data retrieved since 1993. Both ozone and NO_2 show a seasonal cycle of, respectively 24 DU (Dobson units) and 1.17×10^{15} mol cm^{-2} average amplitude,

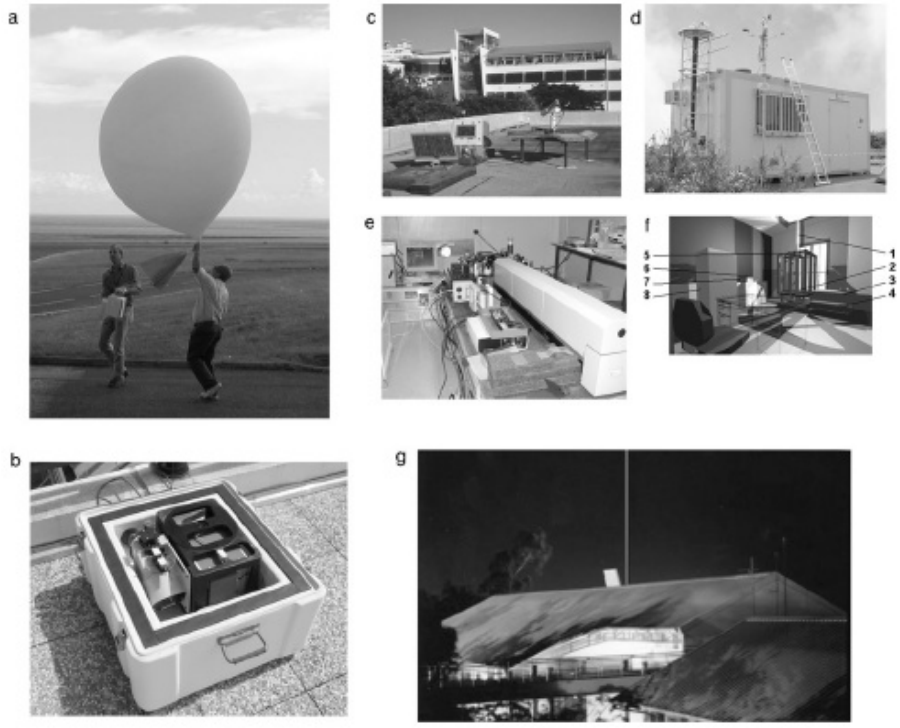

Fig. 4 Photos of the instruments: (a) ozone probe; (b) SAOZ; (c) Sun-photometer; (d) FTIR container at Piton Maïdo; (e) FTIR instrument at the university; (f) image of the stratospheric ozone LiDAR with the different component labelled (1: laser beam, 2: parabolic mirrors, 3: excimer laser, 4: Nd:YAG laser, 5: optical fibers, 6: spectrometer bloc and photomultiplier tubes, 7: mechanical chopper, 8: electronic chain); (g) laser beam emitted by the Rayleigh–Mie–Raman LiDAR.

with a late autumn-winter minimum and a spring maximum. Additional noise can be seen on NO_2: it is due to urban pollution since the instrument is located in the city of Saint Denis. A multi-regression analysis has been performed on these data showing a significant quasi-biennial oscillation modulation of 17 DU for ozone as well as some influence of magnetic activity of 8 DU, while the largest modulation on NO_2 after the seasonal cycle is the ENSO with an average reduction of 0.45×10^{15} mol cm^{-2} during the El Nino event of 1998–99. After removing those contributions no significant trend could be observed since 1993. Together with those of the other SAOZ stations, the Reunion Island data are being extensively used for the validation of TOMS, GOME and more recently SCIAMACHY and OMI ozone and NO_2 space instruments, for which very limited observations from the southern tropics are available.[12]

Table 1 Number of times each routine instrument was operated per year

	T-aerosol LiDAR	Strato-O_3 DIAL[a]	Tropo-O_3 DIAL[a]	SAOZ	O_3 probes
1992					13
1993				94	22
1994	54			341	16
1995	90			321	18
1996	130			181	17
1997	102			116	25
1998	54		36	304	35
1999	99		32	320	49
2000	83	28	17	314	39
2001	59	8	4	217	28
2002	88	8	30	111	30
2003	93	0	24	326	21
2004	115	14	52	255	41
2005	121	10	61	261	43

[a] DIAL = Differential Absorption Lidar.

MAXDOAS UV-visible spectrometer

The Multi-AXis DOAS (MAXDOAS) instrument is another UV-visible spectrometer designed to measure stratospheric and/or tropospheric columns of a variety of atmospheric trace

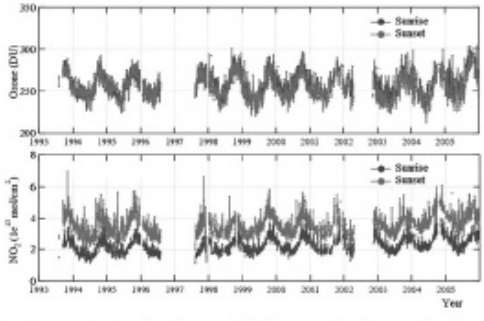

Fig. 5 Ozone (top) and nitrogen dioxide total columns obtained from 1993 to 2005 by the SAOZ spectrometer installed at Reunion Island.

gases (NO_2, BrO, HCHO, O_3, SO_2, IO, O_4).[13] Assembled at BIRA-IASB (Institut d'Aéronomie Spatiale de Belgique), the instrument has been installed at the University of Saint-Denis in July 2004 during the second campaign of the FTIR instrument (described in the following section), and after that continuously operated during one full year except for the period from March 25 until April 28, 2005, when it had to been dismantled due to a storm. Longer-term operation is foreseen from 2007 onwards.

In its current configuration, the MAXDOAS instrument consists of a grating spectrometer from ARC (Acton Research Corporation SpectraPro 275) equipped with a grating of 600 grooves mm^{-1} that covers the spectral range from 300 to 450 nm with a resolution of approximately 0.75 nm FWHM. The detector is a two-dimensional back-illuminated CCD array from Roper Scientific (NTE/CCD-400EB) operated at the nominal temperature of −40 °C. A fiber optic bundle mounted on a telescope and coupled to a rotating mirror is used to collect the skylight scattered from a series of elevation angles (typically 3°, 6°, 10°, 18° and zenith) within a field of view of approximately one degree. The whole system is placed inside a thermally regulated container that is directed towards the north. The data acquisition is controlled automatically *via* a computer and an internet connection allows for remote processing of the recorded spectra.

The MAXDOAS observations are intended to be complementary to the SAOZ total ozone and NO_2 measurements already conducted on the site since 1993 by allowing the detection of more trace gases as well as enabling a more accurate separation of their tropospheric and stratospheric contents. In the current stage of the data evaluation, the capability of the system to detect spectral absorption features of all primary target gases (NO_2, O_3, HCHO, SO_2 and BrO) has been demonstrated. More specifically the analysis of BrO data has received a special attention. A new retrieval scheme has been designed to infer the tropospheric and stratospheric BrO columns based on an analysis of the complete diurnal evolution of the measured column. The evaluation makes uses of a multiple-scattering radiative transfer code coupled to a chemical box model that properly accounts for the large gradients in the stratospheric BrO field at twilight.[12] Results confirm the presence of a free-tropospheric BrO background of approximately 1×10^{13} mol cm^{-2} corresponding to approximately 1–2 pptv at 6 km altitude. The inferred total columns are consistent with simultaneous observations from the SCIAMACHY instrument on board ENVISAT.

FTIR spectrometer

The FTIR (Fourier transform infra-red) instrument is a high spectral resolution Fourier transform spectrometer able to provide quasi simultaneously total column and/or vertical profiles of about 20 atmospheric species among which are ozone, CO, N_2O, OCS, HF, HCl and HNO_3.

Up to now, FTIR solar absorption measurements have been made using commercially available Bruker 120 M spectrometers. The observations are not running in routine mode but are performed on a campaign basis in the framework of a collaboration between the Université de la Réunion and the Belgian institutes, ULB (Université Libre de Bruxelles) and BIRA-IASB. Two FTIR measurement campaigns have been performed. A first campaign was organized in September-October 2002 during which measurements have been performed from two sites at very different altitudes (Universityof Saint Denis, 50 m asl and Piton Maïdo, 2200 m asl, Fig. 3b). The data obtained at Piton Maïdo at 2200 m were of very good quality. At the sea level site (University of Saint Denis), because of too high H_2O vapor absorptions, a few species could not be observed, like NO, or showed larger uncertainties, like is the case for HF. But the overall quality of the data was good and reliable data retrievals could be performed. For logistical reasons, the second campaign (July to end of October 2004) took place at the university site. These campaigns have demonstrated the feasibility of a long-term monitoring of the atmospheric composition based on FTIR solar absorption observations, especially if they are performed at a high altitude station.

During these campaigns, the following observations have been made. In 2002, the differential column of tropospheric species such as N_2O and C_2H_2 in the 2150 m thick layer between the altitudes of both observation sites has been observed. In 2004, the seasonal variation of CO in the local spring period has been in good agreement with correlative MOPITT data. The comparisons between the FTIR retrieved profiles for HNO_3 and O_3 and overpass data of the ACE/SciSat-1 satellite instrument and local O_3 probe measurements showed a good agreement confirming the reliability of the FTIR data.

Further data analysis of the 2004 campaign is still ongoing. Among others, we are investigating the information content of the FTIR spectra regarding water vapor in the upper troposphere/lower stratosphere. The FTIR experiment has been run using BARCOS, the Bruker Automation and Remote Control System, developed at IASB-BIRA for enabling the operation of the FTIR instrument in an automatic or remotely-controlled way.[14,15] We intend to use this system in any future campaign as well as for the permanent operations in the future NDACC infrastructure.

Sun-photometer

A CE 318 automatic sun tracking photometer designed and realized by CIMEL has been installed in 1997, in collaboration with the LOA (Laboratoire d'Optique Atmosphérique) and NASA. This instrument is the standard instrument used in the AERONET (AErosol RObotic NETwork) international network which provides most of aerosol optical measurements used to characterize the aerosol properties and to validate satellite data.[16] The CIMEL 318 measures the solar radiance in 6 spectral bands: 440, 670, 870, 936, and 1020 nm. The spectral band of 870 nm is measured from 3 polarized channels of 120 degrees. This instrument gives the integrated optical thickness of atmospheric aerosols, the volume size distribution, and the Angstrõm coefficient.

Two measurement campaigns have first been organized: the first one was performed at Pas de Bellecombe (June 1997–June 1998), near the volcano Piton de la Fournaise, while the second campaign (March 1999–May 2000) took place at

St Pierre, in the south west of Reunion Island (Fig. 3b). The instrument works again routinely since January 2004 at the University (Saint Denis). In addition, a second instrument (type CE 312) has been installed since January 2006 in order to provide measurements in the infra-red spectral band simultaneously with LiDAR measurements of clouds and aerosols. Data are treated by PHOTONS-AERONET and are available on internet (web links in appendix).

LiDAR measurements

The principle of the LiDAR is based on the active emission of laser pulses in the atmosphere.[17] Backscattered photons by atmospheric layers result from an elastic or inelastic diffusion. Depending on the emission/detection characteristics, the return signals are processed in order to derive accordingly, on a daily basis, atmospheric parameters. Two LiDAR systems are operating, one for aerosol, temperature, water vapor and tropospheric ozone profiles, and a second for stratospheric ozone profiles.

Temperature and aerosol profiles

The first LiDAR operating at Reunion observatory was a Rayleigh–Mie one. It has been devoted to retrieve temperature and aerosol profiles by the use of two channels in the 30–75 km and 12–35 km height ranges, respectively. The initial laser was a Nd:YAG laser, doubled by a KDP crystal, in order to emit at 532 nm, with a repetition rate of 10 pulses per second, and delivering 300 mJ per pulse. In 1996, the laser source was changed. The operating laser is a Nd:YAG emitting with a higher repetition rate (30 Hz) and delivering 500 mJ $pulse^{-1}$. The reception system is composed by a mosaic of 4 parabolic mirrors, with a diameter of 500 mm each; the backscattered signal is transmitted using optical fibers to photomultiplier tubes (Hamamatsu R1477S). The electronic chain is similar to that operating at the Observatoire de Haute Provence in the South of France.[18,19]

Due to the aerosol distribution, temperature retrieval from a Rayleigh–Mie LiDAR is possible only for altitudes higher than 30 km (where aerosol contribution to the LiDAR signals is negligible). In order to extend temperature measurements by the LiDAR downward, a Raman-N_2 setup has been implemented in 1999.[20] The Raman-N_2 method is based on the Raman shift induced by the nitrogen molecules.

Clouds, aerosol and water vapor profiles

Aerosol profiles obtained from the Rayleigh–Mie channels do not cover all tropospheric heights. Those channels are also dedicated to detect and characterize the seasonal and vertical distribution of the tropical cirrus clouds over the Reunion site. In November 1995, the LiDAR was improved by adding new channels using a smaller telescope (diameter 200 mm), to extend the aerosol altitude range downwards. The installation of a dioptric afocal optical system allows the reduction of the emitted laser beam divergence. Polarized channels have also been implemented, especially to study cirrus clouds. In 1997, six simultaneous counting channels were installed, using the infra-red fundamental Nd:YAG emission. Raman channels allow to retrieve tropospheric temperature[20] and water vapor concentration.[21] The technology used is presented by Whiteman *et al.*[22] The detection of Raman signals is obtained by a Czerny–Turner spectrometer using a holographic grating. The water vapor mixing ratio is deduced from the ratio between the shifted Raman backscattered photons and the Raman nitrogen backscattered photons. This second signal is used as a reference and allows to derive directly the water vapor mixing ratio with a limited sensitivity to instrumental parameters. However, modifications of the filtering devices and detectors are specific to each channel. Today some calibrations of water vapor measurements remain to be realized and hence this channel is still in a validation phase.

Tropospheric ozone profiles

In 1998, a differential LiDAR system has been implemented in order to measure tropospheric ozone. The method is based on the differential absorption between two UV wavelengths (289 nm and 316 nm), generated in a high pressure deuterium cell. Because of difference in beam emission divergence (between visible and UV beams) and in expected vertical ranges (troposphere for ozone, stratosphere for temperature), the use of the fibers of the temperature-aerosol system was not appropriate and an original system of double fibers has been developed, constituting the originality of this system.[23] The spectral separation of both wavelength of the ozone system is obtained by a Czerny–Turner spectrometer using a holographic grating. The reception system is common with the temperature Rayleigh/Raman system.

Stratospheric ozone profiles

Another LiDAR system, built by Geneva University (Switzerland) in collaboration with the Service d'Aéronomie has been implemented at Reunion Island in June 2000. The principle is the same as for the LiDAR used for tropospheric ozone measurements. However, to observe the stratosphere, it is necessary to use wavelengths less absorbed by ozone and the emitted wavelengths are shifted towards the near UV.[24] Thus, the technical choices for the beam generation are different: two lasers are used, one Nd:YAG tripled producing the 355 nm wavelength at 30 Hz and 150 mJ per pulse and one Excimer laser producing the 308 nm wavelength at 40 Hz and 200 mJ per pulse.

The reception system is similar to the other LiDAR system (same mosaic of 4 parabolic mirrors and transmission of signal by optical fibers). To avoid the saturation of the photomultiplier tubes, a mechanical chopper rotating in vacuum at 800 Hz is used. A separation lens after the spectrometer block is also used to separate the return signal in two channels in the proportions of 8% for the lower stratospheric channel and of 92% for the upper stratospheric channel. In addition, electronic gating is used for upper stratospheric channels.

With a time integration of two hours, the statistical error linked to the signal ãÑ noise ratio is less than 10% between 18 and 38 km, and less than 5% between 20 and 35 km. This instrument is well adapted to the survey of stratospheric ozone over Reunion Island. On 20 July 2000, both tropospheric and stratospheric ozone DIAL systems operated simultaneously, and an ozone probe was launched. As depicted on Fig. 6,

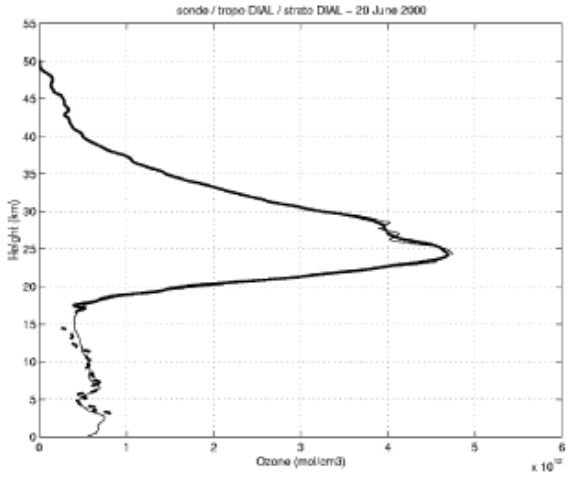

Fig. 6 Ozone profiles by stratospheric DIAL (bold), tropospheric DIAL (dotted) and ozone probe (thin) on 20 June 2000.

corresponding ozone profiles show a good agreement. When the conditions of observations are good, ozone measurements combining the tropospheric and stratospheric systems are available from 3 to 45 km.

Scientific studies

Some examples of scientific studies at Reunion Island are now given, to illustrate how continuous data can be used to improve our knowledge of atmospheric processes.

Aerosols and tropospheric ozone balance

Measurements provided by ozone soundings have allowed the characterization of the seasonal variability of tropospheric ozone. It has been shown that this variability results from the coupling between photochemical and dynamical processes:[25] the photochemical influence of biomass burning from South Africa and Madagascar,[26,27] the ozone diurnal cycle in the boundary layer[28] and the ozone loss due to cirrus clouds.[29,30] Moreover, at the end of the biomass burning season, the daily variability of the dynamical context can induce an important daily variability of the tropospheric ozone profile.[31]

Troposphere–stratosphere transport, dynamics of tropical cyclones

The exchanges between stratosphere and troposphere have been especially examined and the relative roles of processes like tropopause fold,[8] Rossby wave breaking and tropical cut-off lows[32] or tropical convection[33] have been quantified. The localization of Reunion Island makes it ideal for the observation of cyclones during the austral summer. Therefore tropical cyclones have been the subject of many studies such as Doppler radar observations of tropical cyclone Dina,[34] mesoscale modelisation of gravity waves generated by cyclone Hudah,[35] and of stratosphere–troposphere exchange generated by cyclone Marlene[36] or the effects of Rossby wave breaking on cyclogenesis, intensity and trajectories of cyclones.

Presently, we are working mainly on the use of dynamical tools such as Reverse Domain Filling techniques, Flexpart and mesoscale models (meso-nh and MM5) to obtain more insight to these processes.

Atmospheric dynamics

It is well established that the subtropical barrier, a dynamical border that separates the tropical stratospheric reservoir from mid-latitudes, as for the polar vortex, controls and limits the meridional exchanges. Indeed, the efficiency of the confinement of the tropical stratospheric reservoir depends on the strength of the subtropical barriers and on their variability.[37] Recent studies conducted at Reunion University, combining ground-based and satellite measurements together with global modeling, showed that developments of laminae nearby the southern subtropical barrier might be associated with the anomalous growth and break of gravity waves and planetary waves that propagate from the troposphere into the stratosphere during winter.[38,39] In fact, with regard to its geographical position in the southern tropics, the Reunion site might be under influences of several transient and/or seasonal dynamical processes, such as ITCZ, convective and cyclone developments, jet-streams, or subtropical barriers.

Up to now, the number of ground-based instruments running in the Tropics has still been limited. We thus have taken the advantage of the variety of qualified atmospheric datasets offered at Reunion Island, to contribute to several topics related to dynamical processes in the stratosphere—upper troposphere region:

(1) Atmospheric tides and gravity waves characteristics by the use of daily LiDAR temperature profiles;[40–42]

(2) Survey and variability of isentropic transport and planetary waves propagation nearby the southern subtropical barrier, by the use of ozone profiles obtained by LiDAR and radio probes and daily ozone columns recorded by SAOZ;[37]

(3) Stratospheric ozone trend estimation using satellite (SAGE II, HALOE) and radio probe data;

(4) Tropical tropopause characteristics;[43]

(5) Climatology and variability of stratospheric parameters: temperature, ozone and aerosols.[18,20,44]

In fact the LiDAR technique, as well as radiosounding, are well adapted to study the dynamic and variability of the stratosphere—upper troposphere region at different timescales, through regular measurements of atmospheric key parameters: temperature, ozone, water vapour, and aerosol contents.

Conclusion and future plans

In order to provide significant improvement of our understanding of the dynamic of the tropical troposphere and stratosphere, scientific studies have to be based on the complementarity of several different instruments, and of multiple approaches (ground based observations, satellite data, and models). These studies contribute to the support of the decisions taken in international agreements like the Montreal protocol, relative to the production of CFCs and halogenated

species, or like the Kyoto protocol, relative to emissions of greenhouse gases.

The atmospheric survey is, then, important all over the globe, and especially in the tropical region, which is a key region for many mechanisms playing a role in climate change. Reunion Island is an exceptional site for the study of atmospheric dynamics, and participates in this international effort. The instrumentation of this station uses recent technologies, and studies based on the recorded data are of a special interest for understanding processes, climatologies and trends.

However, measurement techniques are still lacking, especially for dynamical observations and the measurement of water vapor in the UTLS is an actual instrumental challenge. Then, in the near future, in order to improve the contribution of Reunion Island in this regard, some additional instruments will be implemented:

-A Doppler LiDAR giving horizontal components of the wind from 5 to 50 km, for the study of gravity wave activity.[45]

A micro-wave radiometer with one large (8–13 m) and three thick (8.2–9.2 m/10.3–11.3 m/11.5–12.5 m) spectral bands in the infrared in order to assess the tropical cirrus cloud microphysics, such as the size of the crystals.

A radiometer giving the water vapor profile from 15 to 60 km, with a vertical resolution of 5–15 km, for the survey of the tropical UTLS variability.

The last plan for the future of this site is to build an altitude station at Piton Maïdo, located in the western part of the island, 2200 m asl (Fig. 3b). The building of the altitude station is expected by 2010. The functioning of many instruments (LiDAR, FTIR and radiometers especially) will be improved, avoiding the perturbation by the humidity contained in the lower layer of the tropical troposphere. This new altitude station will be a platform to receive other instruments on a temporary basis for international campaigns. Moreover, in the future, the station could be included in the OARA structure (Observatoire Atmosphérique des terres australes) grouping the activities of all the southern hemisphere French atmospheric stations (Reunion, Crozet, Saint Paul, Kerguelen and Amsterdam islands) and new instrumentation onboard the research vessel Marion Dufresne.

Appendix

Web links of data networks

AERONET, http://aeronet.gsfc.nasa.gov/; PHOTONS, http://www-loa.univ-lille1.fr/photons/; NDSC (NDACC), http://www.ndsc.ws/; SHADOZ, http://croc.gsfc.nasa.gov/shadoz/.

Acknowledgements

Gérard Mégie (1946–2004) was an internationally recognized scientist and played a leading role in setting up the Network for the Detection of Stratospheric Changes. The development of an atmospheric station at Reunion Island has been made possible thanks to his action at the *Service d'Aéronomie*, then at CNRS. We acknowledge the work of the technical staff of Reunion Island and of the collaborating laboratories, with a special attention to Guy Bain and Stéphane Richard. The MAXDOAS and FTIR campaigns (IASB-BIRA and ULB) are funded by the Belgian Science Policy through the IASI and ACE ESA-Prodex arrangements and the national project ESACII. The station is supported by French regional, national (PNCA, INSU, CNRS), and international (EQUAL, NASA/GFSC) fundings.

References

1 WMO, *Scientific assessment of ozone depletion: 1991 (WMO Global ozone research and monitoring project, report no 25)*, World Meteorological Organization, Geneva, 1991.
2 IPCC, *Climate change: the IPCC scientific assessment*, Cambridge University Press, Cambridge, UK, 1990.
3 D. J. Wuebbles, A. Jain, J. Edmonds, D. Harvey and K. Hayhoe, Global change: state of the science, *Environ. Pollut.*, 1999, **100**, 57–86.
4 M. J. Kurylo and S. Solomon, *Network for the Detection of Stratospheric Change: a status and implementation report, NASA Upper Atmosphere Research Program and NOAA Climate and Global Change Program (NASA)*, NASA, Washington, DC, 1990.
5 J. F. Royer, D. Cariolle, F. Chauvin, M. Déqué, H. Douville, R. M. Hu, S. Planton, A. Rascol, J. L. Ricard, D. Salas, Y. Melia, F. Sevault, P. Simon, S. Somot, S. Tyteca, L. Terray and S. Valcke, Simulation des changements climatiques au cours du XXI^{ème} siècle incluant l'ozone stratosphérique, *C. R. Geosci.*, 2002, **334**, 147–154.
6 A. M. Thompson *et al.*, The 1998–2000 SHADOZ (Southern Hemisphere ADditional OZonesondes) tropical ozone climatology. 1. Comparisons with TOMS and ground-based measurements, *J. Geophys. Res.*, 2003, **108**, 8238.
7 H. G. J. Smit, W. Straeter, B. Johnson, S. Oltmans, J. Davies, D. W. Tarasick, B. Hoegger, R. Stubi, F. Schmidlin, T. Northam, A. Thompson, J. Witte, I. Boyd and F. Posny, Assessment of the performance of ECC-ozonesondes under quasi-flight conditions in the environmental simulation chamber: Insights from the Jülich Ozone Sonde Intercomparison Experiment (JOSIE), *J. Geophys. Res.*, 2006, submitted.
8 J. L. Baray, V. Daniel, G. Ancellet and B. Legras, Planetary-scale tropopause folds in the southern subtropics, *Geophys. Res. Lett.*, 2000, **27**(3), 353–356.
9 F. Borchi, J. P. Pommereau, A. Garnier and M. Pinharanda, Evaluation of SHADOZ sondes, HALOE and SAGE II ozone profiles at the tropics from SAOZ UV-Vis remote measurements onboard long duration balloons, *Atm. Chem. Phys.*, 2005, **5**, 1381–1397.
10 H. Vömel, S. J. Oltmans, D. J. Hofmann, T. Deshler and J. M. Rosen, The evolution of the dehydration in the Antarctic stratospheric vortex, *J. Geophys. Res.*, 1995, **100**(13), 919-13–926.
11 J. P. Pommereau and F. Goutail, O_3 and NO_2 ground-based measurements by visible spectrometry during Arctic winter and spring 1988, *Geophys. Res. Lett.*, 1988, **15**, 891–894.
12 J. C. Lambert *et al.*, Combined characterisation of GOME and TOMS total ozone measurements from space using ground-based observations from the NDSC, *Adv. Space Res.*, 2000, **26**, 1931–1940.
13 N. Theys *et al.*, Determination of tropical stratospheric and tropospheric BrO columns from multi-axis DOAS measurements at Reunion Island, *Atmos. Chem. Phys. Discuss.*, 2006, paper in preparation.
14 E. Neefs *et al.*, The BARCOS system for automatic and remote control of a Bruker FTS for solar absorption measurements from ground, *OSA, Quebec*, 2003.
15 E. Neefs *et al.*, BARCOS: a system for making atmospheric observations with a Bruker FTS in an automatic or remotely controlled way, *Rev. Sci. Instrum.*, 2006, submitted.
16 B. N. Holben, T. F. Eck, I. Slutsker, D. Tanre, J. P. Buis, A. Setzer, E. Vermote, J. A. Reagan, Y. Kaufman, T. Nakajima, F. Lavenu, I. Jankowiak and A. Smirnov, AERONET—A federated instrument network and data archive for aerosol characterization, *Remote Sens. Environ.*, 1998, **66**, 1–16.
17 A. Hauchecorne and M. L. Chanin, Density and temperature profiles obtained by lidar between 35 and 70 km, *Geophys. Res. Lett.*, 1980, 565–568.

18 H. Bencherif, J. Leveau, J. Porteneuve, P. Keckhut, A. Hauchecorne, G. Mégie, F. Fassina and M. Bessafi, *LiDAR Developments and Observations over Reunion Island (20.8° S, 55.5° E)*, *proceedings of the 18th International Laser Radar Conference*, ed. A. Ansmann, R. Neuber, P Rairoux and U. Wandinger, Springer Verlag, Berlin, 1996, pp. 553–556.

19 A. Hauchecorne, M. L. Chanin, P. Keckhut and D. Nedeljkovic, LiDAR monitoring of the temperature in the middle and lower atmosphere, *Appl. Phys. B*, 1992, **55**, 29–34.

20 D. Faduilhe, P. Keckhut, H. Bencherif, L. Robert and S. Baldy, Stratospheric temperature monitoring using a vibrational Raman LiDAR. Part 1: Aerosols and ozone interferences, *J. Environ. Monit.*, 2005, **7**, 357–364.

21 L. Robert, P. Keckhut, L. Leveau, F. Chane-Ming and J. Porteneuve, Development of Raman water-vapor LiDAR at a NDSC complementary station in the southern tropics, *Proceedings of ILRC 22, Matera, Italy, 12th–16th July 2004*, 2004, vol. 1, pp. 111–114.

22 D. Whiteman, *et al.*, Raman LiDAR system for the measurement of water vapour and aerosols in the earth atmosphere, *Appl. Opt.*, 1992, **3**, 3068–3082.

23 J. L. Baray, J. Leveau, J. Porteneuve, G. Ancellet, P. Keckhut, F. Posny and S. Baldy, Description and evaluation of a tropospheric ozone lidar implemented on an existing lidar in the southern subtropics, *Appl. Opt.*, 1999, **38**, 6808–6817.

24 S. Godin-Beekmann, J. Porteneuve and A. Garnier, Systematic DIAL ozone measurements at Observatoire de Haute-Provence, *J. Environ. Monit.*, 2003, **5**, 57–67.

25 S. Baldy, G. Ancellet, M. Bessafi, A. Badr and D. Lan-Sun-Luk, Field observations of the vertical distribution of tropospheric ozone at the Island of La Reunion, *J. Geophys. Res.*, 1996, **101**, 23835–23849.

26 T. Randriambelo, S. Baldy, M. Bessafi, M. Petit and M. Despinoy, An improved detection and characterization of active fires and smoke plumes in Southeastern Africa and Madagascar, *Int. J. Remote Sens.*, 1998, **19**, 2623–2638.

27 F. G. Taupin, M. Beekmann, P. J. Bremaud and T. Randriambelo, Ozone generation over the Indian Ocean during the South African biomass-burning period: case study of October 1992, *Ann. Geophys.*, 2001, **19**, 1–11.

28 P. J. Bremaud, F. Taupin, A. M. Thompson and N. Chaumerliac, Ozone nighttime recovery in the marine boundary layer: Measurement and simulation of the ozone diurnal cycle at Reunion Island, *J. Geophys. Res.*, 1998, **103**, 3463–3473.

29 S. Roumeau, P. Bremaud, E. Riviere, S. Baldy and J. L. Baray, Tropical cirrus clouds: a possible sink for ozone, *Geophys. Res. Lett.*, 2000, **27**, 2233–2236.

30 B. Cadet, L. Goldfarb, D. Faduilhe, S. Baldy, V. Giraud, P. Keckhut and A. Rechou, A sub-tropical cirrus clouds climatology from Reunion Island (21°S, 55°E) lidar data set, *Geophys. Res. Lett.*, 2003, **30**, 1130–1133.

31 T. Randriambelo, J. L. Baray, S. Baldy, A. M. Thompson, S. Oltmans and P. Keckhut, Investigation of the short-time variability of tropical tropospheric ozone, *Ann. Geophys.*, 2003, **21**, 2095–2106.

32 J. L. Baray, S. Baldy, R. D. Diab and J. P. Cammas, Dynamical study of a tropical cut-off low over South Africa and its impact on tropospheric ozone, *Atmos. Environ.*, 2003, **37**, 1475–1488.

33 J. L. Baray, G. Ancellet, T. Randriambelo and S. Baldy, Tropical cyclone Marlene and stratosphere–troposphere exchange, *J. Geophys. Res.*, 1999, **104**, 13953–13970.

34 F. Roux, F. Chane Ming and A. Lasserre-Bigorry, Doppler radar observations of tropical cyclone Dina as it passed near La Réunion on 22 January 2002, *Proceedings of the Second European Conference on Radar Meteorology (ERAD), Delft, 18th–22nd November, 2002*, 2002, p. 6.

35 F. Chane Ming, G. Roff, L. Robert and J. Leveau, Gravity wave characteristics over Tromelin Island during the passage of cyclone Hudah, *Geophys. Res. Lett.*, 2002, **29**, 1094.

36 J. Leclair de Bellevue, J. L. Baray, S. Baldy and G. Ancellet, Stratosphere–troposphere exchange near tropical convection: observations, mesoscale and global analyses, *SPARC 3rd General Assembly, Victoria, BC, Canada, 1st–6th August, 2004*, 2004.

37 T. Portafaix, B. Morel, H. Bencherif, S. Godin-Beekmann, S. Baldy and A. Hauchecorne, Fine scale study of a thick stratospheric ozone lamina at the edge of the southern subtropical barrier, *J. Geophys. Res.*, 2003, **108**, 4196–4205.

38 H. Bencherif, T. Portafaix, J. L. Baray, B. Morel, S. Baldy, J. Leveau, A. Hauchecorne, P. Keckhut, A. Moorgawa, M. Michaelis and R. Diab, Lidar observations of lower stratospheric aerosols over South Africa linked to large scale transport across the southern subtropical barrier, *J. Atmos. Terr. Phys.*, 2003, **65**, 707–715.

39 B. Morel, H. Bencherif, P. Keckhut, T. Portafaix, A. Hauchecorne and S. Baldy, Fine-scale study of a thick stratospheric ozone lamina at the edge of the southern subtropical barrier. Part II: Numerical simulations with coupled dynamics models, *J. Geophys. Res.*, 2005, **110**, D17101.

40 B. Morel, H. Bencherif, P. Keckhut, S. Baldy and A. Hauchecorne, Evidence of tidal perturbations in the middle atmosphere over Southern Tropics as observed by Rayleigh Lidar, *J. Atmos. Terr. Phys.*, 2002, **64**, 1979–1988.

41 B. Morel, P. Keckhut, H. Bencherif, A. Hauchecorne, G. Mégie and S. Baldy, Investigation of the tidal variations in a 3-D dynamics-chemistry-transport model of the middle atmosphere, *J. Atmos. Terr. Phys.*, 2004, **66**, 251–265.

42 F. Chane Ming, F. Molinaro, J. Leveau, P. Keckhut, A. Hauchecorne and S. Godin, Vertical short-scale structures in the upper tropospheric-lower stratospheric temperature and ozone at La Réunion island (20.8° S, 55.3° E), *J. Geophys. Res.*, 2000, **105**, 26857–26870.

43 V. Sivakumar, J. L. Baray, S. Baldy and H. Bencherif, Tropopause characteristics over a southern sub-tropical site: Reunion Island (21° S, 55° E): using Radiosonde/Ozonesonde data, *J. Geophys. Res.*, 2006, in press.

44 V. Sivakumar, P. B. Rao and H. Bencherif, Lidar observations of middle atmospheric gravity wave activity over a low latitude, *Ann. Geophys.*, 2006, AG/2005160, in press.

45 Souprayen, C. A. Garnier, A. Hertzog, A. Hauchecorne and J. Porteneuve, Rayleigh–Mie Doppler wind LiDAR for atmospheric measurements. I. Instrumental setup validation and first climatological results, *Appl. Opt.*, 1999, **3**, 2410–2421.

1.2.3 Description du lidar ozone troposphérique

Description and evaluation of a tropospheric ozone lidar implemented on an existing lidar in the southern subtropics

Jean-Luc Baray, Jean Leveau, Jacques Porteneuve, Gérard Ancellet, Philippe Keckhut, Françoise Posny, and Serge Baldy

Rayleigh–Mie lidar measurements of stratospheric temperature and aerosol profiles have been carried out at Reunion Island (southern tropics) since 1993. Since June 1998, an operational extension of the system is permitting additional measurements of tropospheric ozone to be made by differential absorption lidar. The emission wavelengths (289 and 316 nm) are obtained by stimulated Raman shifting of the fourth harmonic of a Nd:YAG laser in a high-pressure deuterium cell. A mosaic of four parabolic mirrors collects the backscattered signal, and the transmission is processed by the multiple fiber collector method. The altitude range of ozone profiles obtained with this system is 3–17 km. Technical details of this lidar system working in the southern tropics, comparisons of ozone lidar profiles with radiosondes, and scientific perspectives are presented. The significant lack of tropospheric ozone measurements in the tropical and equatorial regions, the particular scientific interest in these regions, and the altitude range of the ozone measurements to 16–17 km make this lidar supplement useful and its adaptation technically conceivable at many Rayleigh–Mie lidar stations.

OCIS codes: 010.0010, 010.3640, 280.1910.

1. Introduction

Atmospheric chemistry is dominated by cycles of ozone and water vapor. It is known that photochemical formation is one important source of tropospheric ozone.[1] In the southern tropics, ozone precursors result mostly from episodic events such as biomass burning and are causing a significant increase in tropospheric ozone.[2] Moreover, recent numerical studies have pointed out the role of acetone and peroxides in ozone production in the upper tropical troposphere.[3] However, the stratosphere and the troposphere are dynamically coupled, and the global climate is highly dependent on ozone changes in the upper troposphere and on exchanges between the stratosphere and the troposphere. This makes the upper troposphere a key zone, especially in the tropics, where many complex and interconnected chemical and dynamic mechanisms occur. From a dynamic point of view, stratospheric inputs into the troposphere linked to the subtropical jet stream could be important.[4–6] The role of deep tropical convection has been studied with MOZAIC (Measurement of OZone and water vapor by Airbus In service airCraft[7]) data and with radiosounding and model data.[8] For many years, observing and understanding the physical and chemical states of the stratosphere have been important objectives of the scientific community. Since 1993, in the framework of the network of detection of stratospheric changes,[9] Rayleigh–Mie lidar measurements of stratospheric aerosols and temperature have been carried out in the southern tropics at the University of Reunion.[10]

Yet, despite this scientific interest in both tropical stratosphere and troposphere, there is a significant lack of tropospheric ozone measurements in the tropical and equatorial regions. Ozonosonde stations are confined mostly to the midlatitude Northern Hemisphere.[11,12] The development of ground-based lidar stations whose research would include making ozone measurements could improve this situation. The technique of tropospheric ozone lidar measure-

J.-L. Baray, J. Leveau, F. Posny, and S. Baldy are with the Laboratoire de Physique de l'Atmosphere, Reunion University, 15 avenue R. Cassin, 97715 St. Denis Cedex, Reunion Island, France. The e-mail address for J.-L. Baray is barray@univ-reunion.fr. J. Porteneuve, G. Ancellet, and P. Keckhut are with Service d'Aeronomie, B. P. 3 91371 Verriere-le-Buisson Cedex, France.

Received 1 March 1999; revised manuscript received 2 August 1999.

0003-6935/99/336808-10$15.00/0

ments by differential absorption between two wavelengths has been known for a long time and is well developed.[13] Many lidar stations throughout the world operate in a routine mode, mainly in the midlatitudes.[14–22] A ground-based lidar station is well suited for monitoring the troposphere with good continuity of measurement and for studying short-time-scale events such as tropopause folds and stratosphere–troposphere exchange induced by the tropical convective activity, i.e., for long-term climatological survey and flux studies. To meet these scientific objectives, it should be quite valuable to develop a differential absorption lidar to measure the troposphe at Reunion Island. Most tropospheric ozone lidars are currently operating within the framework of urban pollution studies and are located at midlatitudes where the tropopause is rather low. The range of the existing tropospheric ozone lidar thus does not exceed 12–13 km. For example, an installation such as the Observatoire de Haute Provence station, with only one mirror of reception, would probably not be sufficient for use in achieving our measurement goal, that of the tropical high troposphere, which is higher than at average latitudes (16–17 km). At Reunion University, a lidar devoted to atmospheric monitoring already exists. This Rayleigh lidar measures aerosols and temperature in the stratosphere and the mesosphere, using a mosaic of four telescopes with a total area of 0.78 m^2.[10] It would be interesting to imagine a system that would allow the same reception component to be used for two modes, stratospheric Rayleigh and tropospheric ozone. Moreover, having a single instrument for several measurements would provide a great opportunity to reduce the human and financial resources needed for its operation. However, stratospheric and tropospheric lidars have different requirements for laser power and wavelength, field of view, noise, etc. In this paper we present an integration solution, developed and tested at Reunion Island, for tropospheric ozone lidar implementation with a Rayleigh–Mie system. The setup of the Rayleigh–Mie lidar at Reunion Station is described in Section 2. Integration and technical choice justifications, performance evaluation, experimental arrangement, data processing, and error analysis are described in Section 3. First results and comparisons with electrochemical cell (ECC) soundings are presented and discussed in Section 4.

2. Lidar Chronological Setup at the Reunion Station

A schematic of the optical part of the Rayleigh–Mie lidar at Reunion Station is shown in Fig. 1. This station was installed in 1993 to monitor stratospheric and mesospheric aerosols in the southern tropics.[10] The first laser emission was made by the second harmonic of a Nd:YAG pulsed laser at 532 nm with a 10-Hz repetition rate and an energy of 300 mJ per pulse. In this first version, the optical receiving system was a parabolic telescope (diameter, 530 mm). After prospecting and validation, routine measurements began in 1994. Evolution of the system has

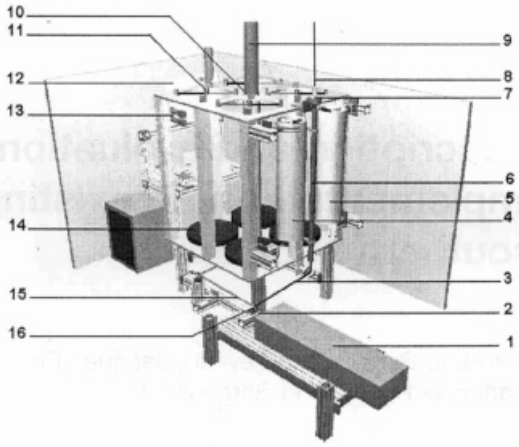

Fig. 1. Schematic representation of the Reunion lidar system: 1, laser; 2, KDP crystals; 3, 266-nm beam; 4, polarized channel telescope; 5, B channel telescope; 6, Raman cell; 7, divergence optimizer; 8, 289–316-nm beam; 9, 532–1064-nm beam; 10, Rayleigh afocal dioptric; 11, location of optical fiber fixation; 12, spectrometer; 13, PMT's; 14, B channel telescope; 15, 532–1064-nm beam; 16, 266-nm removable mirror. For ozone measurements the removable mirror (16) deflects the 266-nm beam, which is then deflected upward in the Raman cell. For Rayleigh measurements, mirror 16 is turned off and the 532–1064-nm beam is deflected upward at the middle of the four parabolic mirrors (14).

improved the system's performance. The reception system was upgraded to four receiving telescopes (diameter, 500 mm; point 14 in Fig. 1). In November 1995 this system was further upgraded by installation of a second optical channel of lower sensitivity with a smaller-diameter telescope (200 mm; point 4 in Fig. 1). The use of smaller telescopes allows the signal intensity to be reduced and the range of altitude probed during routine measurements to be extended downward. This solution was preferred to the use of a dichroic mirror as at other French stations.[23] In March 1996 the laser source was replaced by a new Nd:YAG laser emitting with a power of 500 mJ per pulse and a 30-Hz repetition rate (point 1 in Fig. 1). In November 1996 the installation of dioptric afocal optics (point 10 in Fig. 1) that comprises one concave lens (diameter, 25 mm) and one output double lens (diameter, 160 mm) allowed the 532- and 1064-nm beam divergence to be reduced by a factor of 12. Polarized channels have also been added (point 5 in Fig. 1). In November 1997 six simultaneous counting channels began operating, including the infrared fundamental Nd:YAG emission. The combination of these wavelength emissions and polarized channels permits a better characterization of aerosols in the upper troposphere and stratosphere.[24] The station has now been running in routine mode for four years. The numbers of nighttime measurements made during this period are listed in Table 1. Finally, in June 1998 the tropospheric ozone extension was installed.

Table 1. Nighttime Measurements of the Reunion Lidar Station from 1994 to 1999

Year	Number of Nights
1994	74
1995	93
1996	150
1997	127
1998	120[a]
1999	65[b]

[a]With 31 O_3 measurements
[b]Until April, with 16 O_3 measurements.

3. Description of the Tropospheric Ozone Measurement System

The ozone measurement technique is based on the principle of differential absorption by ozone of an ultraviolet beam.[25] Electronic and computing processing permit retrieval of the ozone profile. Considering the technical constraints that are linked to the actual Rayleigh lidar, use of the Nd:YAG laser of the NDSC (Network for the Detection of Stratospheric Change) Station was imperative. Many useful wavelengths for tropospheric ozone measurements can be generated by stimulated Raman scattering of the fourth harmonic of the Nd:YAG laser in hydrogen and deuterium (Table 2). Inasmuch as our scientific objectives include upper-tropospheric measurements, the lidar range should reach the tropopause, which is quite high in the tropics (near 17 km). As indicated in Table 2, the 266-nm wavelength is obtained directly with the fourth harmonic of the Nd:YAG laser and is generally used as the absorbed wavelength for the lowest kilometers of the atmosphere (the boundary layer). It is not possible to use it for the upper troposphere because this wavelength is absorbed too much by ozone. Molina and Molina[28] have determined the ozone absorption coefficient for a mixing ratio near the ground of 38 parts in 10^9 by volume (ppbv): 947×10^{-3} km^{-1} for a 266-nm beam, 159×10^{-3} km^{-1} for a 289-nm beam, and 4.6×10^{-3} km^{-1} for a 316-nm beam. Wavelengths longer than 340 nm are not absorbed sufficiently to have sufficient sensitivity in the troposphere and are useful only for stratospheric measurements. Some previous studies[15,26] showed that the choice of an excimer laser was not necessarily optimum for tropospheric ozone measurements. Hence, considering on one hand the technical and financial constraints and on the other hand our scientific objective to reach near the tropical tropopause, the most feasible choice, and the one that was made, was to consider the wavelength coupling (289–316 nm) obtained by stimulated Raman scattering shifting in a single deuterium Raman cell. Moreover, using a unique cell to provide both wavelengths is a great advantage for reducing any differential misalignment between emission and collectors. It is useful to evaluate the performance of the theoretical signal by using the optical coefficients and quantum efficiencies of the existing system to gain a theoretical appreciation of the utility of this system for ozone measurement.

Table 2. Available Wavelengths with a Nd:YAG Laser and Typical Efficiencies of Stimulated Raman Scattering in Hydrogen and Deuterium

		Maximal efficiency (%)	
Wavelength (nm)	Type of Stimulated Raman Scattering	Papayannis[a]	Ancellet and Ravetta[b]
266	None (×4)	–	–
289	$S1$, D_2	30	38
299	$S1$, H_2	30	36
316	$S2$, D_2	15	18
341	$S2$, H_2	20	35
349	$S3$, D_2	4	–
355	None (×3)	–	–
397	$S3$, H_2	4	–

[a]Ref. 26.
[b]Ref. 27.

A. Performance Evaluation

For a single pulse, the strength of return signal S depends on the distance r from the telescope to the scattering event and on the wavelength λ. This dependence is given by the formula

$$S(r, \lambda) = \frac{A(\lambda)}{r^2}\,\beta(r, \lambda)\exp\left[-2\int_0^r \alpha(r', \lambda)\mathrm{d}r'\right], \quad (1)$$

where $A(\lambda)$ is a system constant that includes the level of laser pulse energy, the telescope area, the optical detector efficiency, and the photomultiplier tube (PMT) quantum efficiency; β is the atmospheric volume backscatter radiation (Rayleigh and Mie); and α is the atmospheric volume extinction coefficient (Rayleigh, Mie, and ozone). Because Reunion Station is located at sea level in a tropical oceanic environment, strong humidity and marine aerosols are expected in the marine boundary layer. Hence the optical thickness for the lowest layer is set to 1.6.[29,30] By using optical and electronic constants of the lidar system and by imposing ozone and density profiles obtained from radiosounding climatology at the Reunion site,[8] we can evaluate the strength of the return signal as a function of wavelength (Fig. 2). Our simulations permit only an evaluation of the magnitude order, because it is difficult to take account the following operating conditions:

(1) We consider that the fields of view of the receiver completely overlap that of the transmitter.
(2) We neglect the effects of multiple scattering events.
(3) We assume that the counting system works in a perfectly linear way (which is not the case for upper-tropospheric measurements). The linearity of the counting is limited by the bandpass of the system. The comparison of two similar systems that are receiving a backscattered signal from the same portion

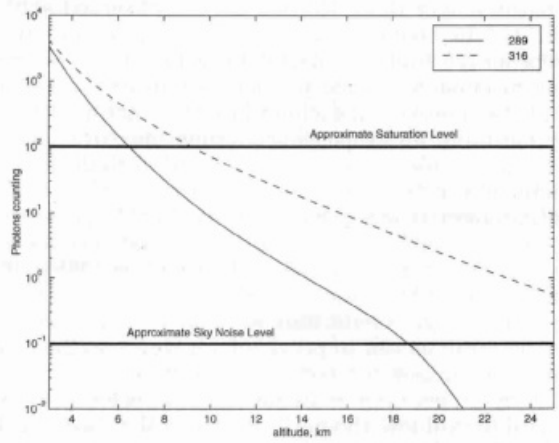

Fig. 2. Modeled wintertime backscatter return photon counting, for the 289–316-nm wavelength couple, compared with typical counting saturation and sky noise levels.

of the sky with one attenuated because it uses a glass splitter allows us to verify that our system is linear (uncertainty, <0.1%) as soon as less than one photon per shot per microsecond arrives on the photocathode.

Despite the use of the approximations mentioned above, these simulations are useful in evaluation of the potentiality of the lidar system and of the wavelength coupling within a tropical context (strong humidity in the lowest layers; tropopause level, 17 km). As was seen by Proffitt and Langford,[21] the return signal increases with wavelength and decreases by a factor of 10^4 between the lowest layers and the upper troposphere. The results of this simulation emphasize two points:

(1) The lowest sounded layers are likely saturated by the photon-counting system. Hence the use of an analog processing mode, alone or in combination with the photocounting mode, should be necessary for processing the signal from the lower troposphere.

(2) The upper-range limit of the system is close to the altitude of the tropical tropopause. Below 18 km, the simulated signal is significantly superior to the typical night sky noise level observed at these wavelengths by a typical ground-based lidar station (Fig. 2).

B. Technical Description of the Emission System

The fourth-harmonic Nd:YAG (266 nm) is obtained by the nonlinear effects of two successive passages in potassium dihydrogen phosphate (KDP) crystals located at the output of the laser. The two emitted wavelengths, 289 nm (absorbed by ozone, ON channel) and 316 nm (nonabsorbed, OFF channel), are generated by stimulated Raman scattering in a deuterium high-pressure cell in which the 266-nm beam is focused by a lens that comprises silica windows. The characteristics of the emission system are listed in Table 3. These two wavelengths correspond to the first and second Stokes lines for deuterium. The energy-conversion efficiency depends mainly on the active gas pressure in the Raman cell,[31] on the focal distance of the window lenses, and on the quality and the power of the beam that is entering the cell.[32] In the present system the 266-nm beam is deflected 90° by two UV mirrors, one of which is removable to permit switching between two operating modes. It then enters the Raman cell, which is placed in a vertical position (point 6 in Fig. 1). The Raman cell is equipped with two silica window lenses that have diameters adapted to the beam and a focal distance of 75 cm to focus the beam as closely as possible to the center of the cell for optimal stimulated Raman scattering. Generation of an UV beam by the Raman diffusion principle is not without consequences for the quality of the emitted beam. Indeed, disruptions by nonlinear phenomena and chromatic aberrations take place in the high-pressure Raman cell and degrade the quality of the emitted beam. To minimize the deleterious consequences of this effect, we place an optical system at the output of the Raman cell to reduce the emitted beam divergence to 0.25 mrad (Table 3). This value corresponds to one quarter of the field of view of the telescope. This system comprises three lenses, whose disposition and composition are shown in Fig. 3.

Table 3. Emission Characteristics

Subsystem	Parameter	Value
Laser	Energy at 255 nm	40 mJ/pulse
	Frequency	30 Hz
	Beam diameter	10 mm
	Divergence of 266-nm beam	0.70 mrad
Raman cell	Length	1500 mm
	Diameter (in/out)	20/55 mm
	D_2 pressure/purity	10 bars/99.7%
	He pressure/purity	24 bars/99.999%
Optical system to reduce divergence	Beam expander for 289–316-nm magnification	3.2
	Output diameter of beams	30 mm
	Divergence of emitted beam	0.25 mrad

C. Technical Description of the Reception System

For measurements of stratospheric temperature and aerosols the 532-nm backscattered beam is collected by an optical fiber system. One 0.4-mm fiber is located at the focal point of each telescope and is used to transport the collected signal to the electronic detection units. This collection method allows the collecting area to be increased without the need for using a unique, costly mirror. In the integration of the new ozone lidar system, the same telescopes as for the stratospheric measurements at 532 nm are

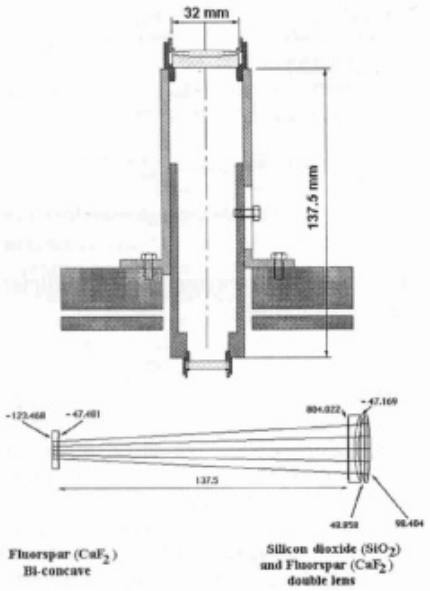

Fig. 3. Optical system used to minimize the divergence of the UV emitted beams (289 and 316 nm).

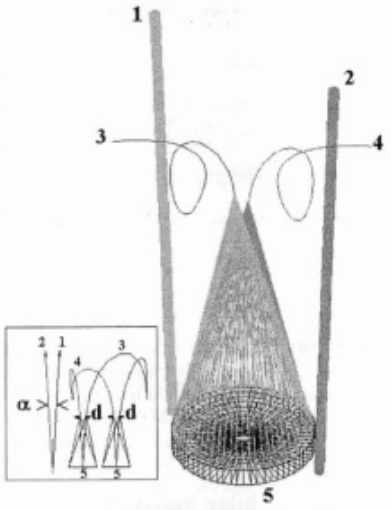

Fig. 4. MFC system: 1, UV emitted beam; 2, visible emitted beam (for stratospheric temperature and aerosol measurements); 3, UV fiber; 4, visible fiber; 5, receiving telescopes. For each telescope the linear distance d = 3.3 mm between the two fibers corresponds to the angular distance α between the two beams.

used. For stratospheric temperature and aerosol measurements the choice of a small field of view permits a compromise between the noise level and the vertical range; hence the use of 0.4-mm fibers. However, because of differences in beam emission divergences and in expected vertical measurement ranges, the use of these existing optical fibers is not possible for the differential absorbing lidar configuration. The ozone channels require a larger field of view for the telescopes to obtain full beam recovery in the expected altitude range (mid and upper tropical troposphere); hence larger-diameter optical fibers (1.5 mm) are required. Their diameter is inferred from the calculation of the spot size in the focal plane where the optical fiber is implemented and results from a larger beam divergence and from the defocusing effect for short vertical ranges. (The image of a scattering volume not strictly located at infinity is not found exactly at the focus of the receiver.[33]) Above 2 km, the 1.5-mm fiber diameter is closer to the defocalization distance, as indicated in Table 4. This configuration provides the full collection of backscattered UV signals in the required vertical range. To permit both measurements (stratospheric temperature and aerosols, and tropospheric ozone) to be made with the same collecting set, a mechanical system that holds a couple of fibers was thus developed: the multiple fiber collector (MFC; Fig. 4 and point 11 in Fig. 1). For each telescope, the linear distance d between the two fibers corresponds to the angular distance α between the UV (for tropospheric ozone measurements) and the visible (for stratospheric temperature and aerosols) beams (Fig. 5 and point 12 in Fig. 1). Both fiber positions can be adjusted at the focal point to keep the fields of view of the telescopes in phase. The advantage of using the MFC is the possibility of being able to use the same optical col-

Table 4. Calculation as a Function of Height *Z* of Defocalization Distance *Df*, Parallax *P*, Spot Size *Tz*, and Spot Size in the Focal Plane *Tf* for the Optical Fiber Dedicated for Ozone Measurements and of Geometrical Factor *Fg* for the Optical Fiber Dedicated for Rayleigh Measurements[a]

Z (km)	*Df* (mm)	*P* (mm)	*Tz* (mm)	*Tf* (mm)	*Fg* (%)
2	1.13	0.75	0.821	1.383	34.3
4	0.56	0.38	0.623	0.904	61.1
6	0.38	0.25	0.557	0.744	77.4
8	0.28	0.19	0.524	0.664	87.3
10	0.23	0.15	0.504	0.617	93.4
12	0.19	0.13	0.491	0.585	97.1
14	0.16	0.11	0.481	0.562	99.3
16	0.14	0.09	0.474	0.545	100
18	0.13	0.08	0.469	0.531	100

[a]The geometrical factor for the optical fiber dedicated for ozone measurements is 100% over 2 km, and the ozone system permits a large latitude for alignment.

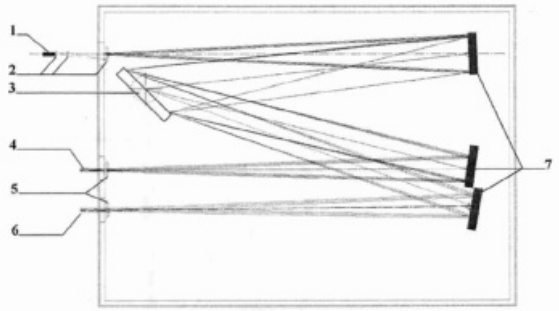

Fig. 5. Spectrometer formed by a holographic grating and two spherical mirrors: 1, four-fiber terminal transmitting the 289–316-nm beam; 2, adaptive lens; 3, 3600-line/mm grating; 4,289-nm PMT; 5, adaptive lens; 6, 316-nm PMT; 7, spherical mirror.

lectors for different lidar measurements. The optical system allows an image quality (pulse response of a star image located at infinity) associated with the atmospheric turbulence of 0.8 mrad to be obtained. With reference to the part associated with the quality of the receiving telescopes, 90% of the energy is included in 0.6 mrad.

Spectral separation of 289- and 316-nm beams is obtained with a spectrometer that includes a Czerny–Turner holographic grating (Fig. 4). After a system of three lenses used to reduce the divergence of the beam by a factor of 3 and to adapt the numerical aperture of the fibers to that of the grating, the backscattered beam is separated by a high-performance grating (3600 lines/mm). Then each beam is redirected toward PMT's by concave mirrors. The noncooled bialkali Hamamatsu R1527P PMT's used for the ozone channels are preamplified. These PMT's provide good sensitivity in the near-UV spectral range. Typical voltage operation is less than 900 V to limit the signal-induced bias associated with the PMT response to an intense luminous pulse.[34] The electronic system includes analog channels (of 15-m resolution) for the lower layers and photon-counting channels (of 150-m resolution) for the high layers, for each wavelength 289 and 316 nm. The signal-processing electronic chain is rather similar to those used for the OHP ozone lidar station at the Observatoire de Haute Provence[15] and for the Airborne Lidar for Tropospheric Ozone (ALTO).[27]

D. Data Processing: Signal Inversion and Error Analysis

The ozone concentration (in molecules per cubic meter) is deduced from the lidar backscattered signal by use of the following equation:

$$c_{O_3} = \frac{1}{2\Delta\sigma}\frac{\mathrm{d}}{\mathrm{d}r}\ln\left(\frac{p^{\mathrm{off}}}{p^{\mathrm{on}}}\right). \quad (2)$$

To take account of the Rayleigh scattering by the atmospheric molecules, using the Rayleigh molecular extinction (α) and backscattering (β) coefficients, we modify Eq. (2) as follows[35]:

$$c_{O_3} = \frac{1}{2\Delta\sigma}\frac{\mathrm{d}}{\mathrm{d}r}\ln\left(\frac{p^{\mathrm{off}}}{p^{\mathrm{on}}}\right) - \frac{1}{2\Delta\sigma}\frac{\mathrm{d}}{\mathrm{d}r}\ln\left(\frac{\beta^{\mathrm{off}}}{\beta^{\mathrm{on}}}\right) - \frac{\Delta\alpha}{\Delta\sigma}. \quad (3)$$

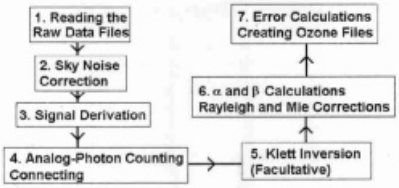

Fig. 6. Algorithm to calculate ozone profiles from raw data.

Data processing is then based on differential absorption of two wavelengths by ozone and on the assumption that the two wavelengths are close enough that the backscattering coefficients are practically identical for the two beams. [The dependence law is $\alpha = \alpha_0(\lambda)^{-k}$, with k varying from 0, in the presence of cirrus clouds, to 2. For typical values at the wavelengths 289 and 316 nm, the differential extinction that is due to aerosol background is smaller by 1 or 2 orders of magnitude than the Rayleigh extinction, as measurements are performed only for cloud-free conditions or with cirrus.] The calculation of ozone concentration is based on Eq. (3) with the algorithm described in Fig. 6. After it reads the raw data, the lidar signal is normalized and corrected for the inverse square range dependence. The signal is corrected for the sky noise component by polynomial or exponential interpolation, separately on each channel, between two levels at the end of the signal. The correction for possible radio-frequency interference of the laser can also be applied in our algorithm by generation of a noise file obtained by blocking the laser. The range-corrected signal is smoothed after numerical low-pass digital filtering, which corresponds to a second-order polynomial fit over a number of points that increases with altitude. We then obtain the terms p^{off} and p^{on} of Eq. (3). The analog and photon-counting slope signals are then combined by use of an analog signal in the low layer and a photon-counting signal in the upper layer. The connection between the two is made by linear mixing in a layer whose height and thickness are chosen as functions of the lidar signal (generally 1 km, near 6-km height). The correction for the influence of strong aerosol layers by the method of Klett[36,37] can be applied in our processing algorithm if necessary. However, this correction does not significantly improve the ozone profiles in the free troposphere and is not used for our lidar system. The aerosol backscatter coefficient is calculated at 316 nm, where ozone absorption is negligible, by a backward integration scheme in which the Rayleigh backscatter is taken into account.[38,39] If the aerosol layer is significant (cloud), data are removed from the profile at the cloud altitude. The numerical filter applied to calculate

the signal derivative is also used to differentiate the aerosol backscatter profiles. In the Eq. (3), coefficients α and β depend on the atmospheric density profile calculated by means of an atmospheric standard-atmosphere model whose main characteristics (vertical temperature gradient, ground temperature, tropopause height) are adjustable. Knowing the difference of absorption $\Delta\sigma$ between ON and OFF channels calculated by Bass and Paur,[40] we are able to have access to the vertical ozone concentration.

Lidar ozone measurement is subject to errors, which are either systematic or statistical. Systematic errors originate from the contribution on the signal of chemical species other than ozone. The influence of nitrogen dioxide (NO_2) absorption[41] and sulfur dioxide (SO_2) absorption[42] was evaluated. At a 38-ppbv mixing ratio, the absorption coefficients at 289 and 316 nm, respectively, are 9×10^{-3} and 7×10^{-3} km^{-1} for SO_2 and 8.6×10^{-3} and 24×10^{-3} km^{-1} for NO_2. The influences of SO_2 and NO_2 are then relevant only in the boundary layer, where the concentration of these pollutants can be potentially high, and are negligible in the free troposphere.[27]

Another type of error comprises statistical errors associated with the signal and sky noise fluctuations. For the analog mode one calculates the statistical error from the root mean square of the signal in the noise region. For the photon-counting mode one calculates the error by assuming that the signal's standard deviation is equal to that which is expected for a Poisson statistical distribution of detected photons. The error is thus estimated directly from the signal intensity. Donovan *et al.* found that a pure Poisson statistic overestimates the error compared with that which they derive in their method in which error depends on sampling time, width of pulse, and observed count rate.[43] However, when the PMT is saturated, the counting is no longer Poissonian. Even when the counting is not saturated, it is slightly different from Poissonian counting according to the position of the discriminator that separates the noise pulse from the signal pulse. The discriminator disturbs the statistic: if it is too low, it counts the noise pulse; if it is too high it does not count all the signal pulse and the count is less than expected.[44] The discriminator is adjusted to provide the best compromise, and the counting distribution does not vary more than 10% from theory. Other recent studies showed that the Poissonian method underestimates the statistical signal and then cannot be applied successfully for an analog signal in the lower troposphere.[45] However, Poisson's law remains a good estimation of the statistical error, especially for an upper-tropospheric photon-counting signal. In Section 4, error bars attached to ozone profiles are evaluated from these considerations.

4. Results and Comparisons

In this section we present results obtained in austral winter 1998 from the Reunion ozone lidar. One of the first ozone measurement obtained by lidar at Reunion Island was made on 26 June 1998. Slopes of

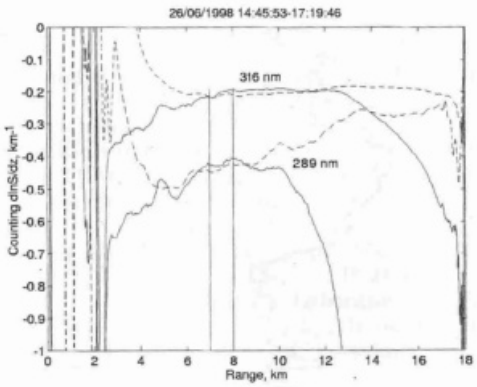

Fig. 7. Range derivative of the logarithm of the range-corrected lidar signal corresponding to photocounting (dashed curves) and analog (solid curves) detection of the two wavelengths 289 and 316 nm on 26 June 1998. We computed the range-corrected profiles by exponentially correcting the sky noise signal over 21 km for the 289-nm channel and over 31 km for the 316-nm channel. The connection between analog and photocounting channels was made between 7 and 8 km. In this and the following figures the data on which the measurements were made are given in day–month–year order, followed by the local time (hours–minutes-seconds) during which the measurements were made.

the channels are shown in Fig. 7. For that profile, 289- and 316-nm photocounting channels are saturated below 5 and 6 km, respectively, and reach 16 km. Hence the use of analog channels makes available ozone measurements between 3 and 7 km. Below 3 km the recovery between reception and emission fields is not sufficient to provide useful data. Above 10 km (289-nm signal) and 14 km (316-nm signal) the analog signal is too weak and there is too much sky noise relative to the signal. Thus the connection between analog and photocounting channels is made between 7 and 8 km (Fig. 7). The corresponding ozone profile is presented in Fig. 8. For the

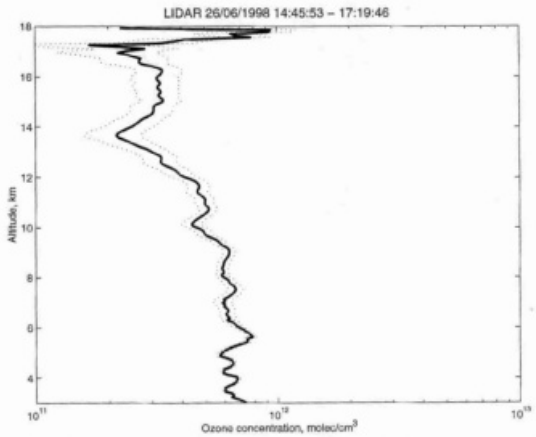

Fig. 8. Corresponding ozone profile (see Fig. 7) for 26 June 1998.

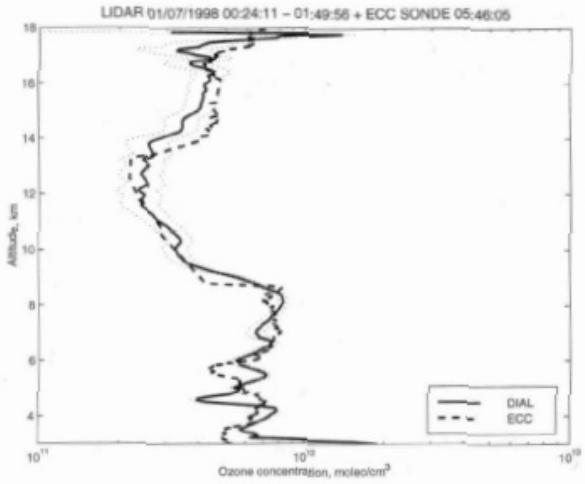

Fig. 9. Ozone concentrations obtained by lidar on 1 July 1998 (acquisition time, 1 h and 25 min) compared with the profile obtained by an ECC sonde 5 h later. Solid curve, lidar profiles; dotted curves, statistical error intervals for lidar measurements; dashed curves, ECC profiles.

measurements on 26 June the upper-range limit is ~14 km. Results from 14 to 18 km are uncertain because the signal is weak and noisy. The upper limit depends on clear sky conditions, on alignment of the reception system, and on measurement integration time and reaches the tropical tropopause (17 km) for clear sky conditions.

After the first profiles were obtained during June 1998, the lidar operated almost daily during July 1998, in the framework of the European campaign TRACAS (TRAnsport of Chemical species Across the Subtropical tropopause). Two measurement comparisons between lidar and radiosounding were made, on 1 July (Fig. 9) and on 29 July (Fig. 10).

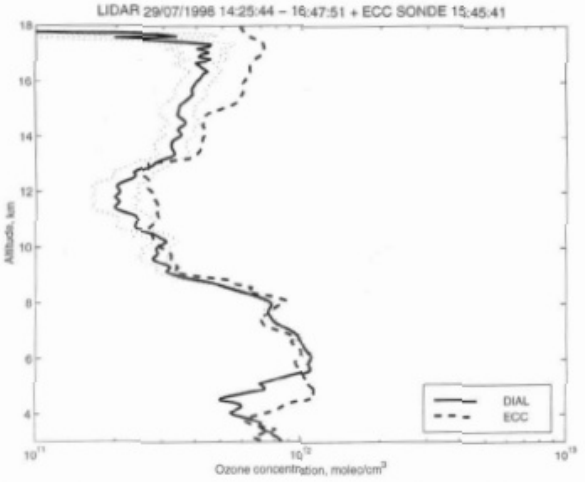

Fig. 10. Ozone concentrations obtained by lidar on 29 July 1998 (acquisition time, 2 h and 20 min) compared with the profile obtained nearly simultaneously by electrochemical sonde.

Ozone radiosounding profiles are obtained with the ECC standard processing calculator, used with a T_{max} interface and coupled with a Vaisala RS80 radiosonde.[2] The relative precision of ECC ozone measurements in the troposphere was found to be by field tests 10%.[46] Comparisons with ECC sounding (Figs. 9 and 10) globally show good agreement between the two techniques. After ozone concentration was converted to mixing ratio by use of temperature and pressure profiles obtained with radiosondes, the average difference between the two profiles was calculated from 4 to 14 km and is less than 7.5 ppbv for the 1 July profile and less than 6.5 ppbv for the 29 July profile. These values have less than the precision of the two measurement techniques. However, one can note some difference between the ECC sonde and lidar profiles, mainly in the lower layers on 1 July (Fig. 9) and in the upper troposphere on 29 July (Fig. 10). For the first comparison (Fig. 9) the measurements were not obtained simultaneously (nearly a 5-h interval). For the second comparison (Fig. 10), even when measurements were obtained simultaneously, a simple advection calculation that used horizontal wind data obtained with the European global model data [ECMWF (European Center for Medium Range Weather Forecast)] and the vertical advection measured by the radiosonde indicates a displacement of the balloon of more than 65 km between the launch and the tropopause level measure. Hence, ECMWF data indicate the presence of the subtropical jet stream over Reunion Island on 1 July and 29 July, with wind speed greater than 30 m s^{-1} over 300 hPa. The lidar provides vertical measurements and then not exactly the same measurements as an ECC sonde, which are advected by the wind.

We further note that this lidar system can follow the tropospheric ozone evolution on short time scales. For example, Fig. 11 shows the evolution, in increments of 20 min, of the tropospheric ozone mixing ratio profile observed on 29 July. One can indeed notice the interesting ozone maximum observed by lidar from 6 to 8 km, which is associated with tropopause folding under the subtropical jet stream. The time of integration used to build each elementary profile is sufficient to trace ozone short-time variability up to 13–14 km. Above that level the analysis of ozone values must be done with great care because the measurement uncertainty becomes significant. Figure 11 shows that the tropospheric ozone above Reunion Island has a short-term variability (in time and space) that is consistent with differences between ECC sonde and lidar observed on comparison (Figs. 9 and 10). The results presented in this section clearly illustrate the capability of this instrument to provide experimental data for the study of stratosphere–troposphere mass exchanges in the tropics.

5. Concluding Remarks

Our scientific objectives are to measure ozone in the high tropical troposphere. To limit the cost and maintenance of the lidar system we integrated it with

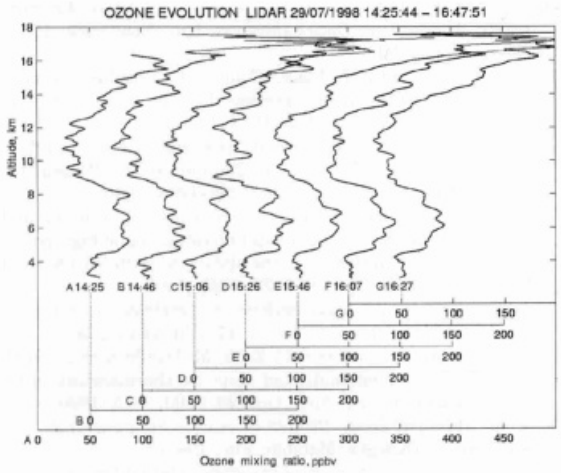

Fig. 11. Ozone mixing ratio evolution during the time from 14:25:44 (profile A) to 16:47:51 (profile G) universal time as observed by lidar at Reunion on 29 July 1998. The temporal file summation is 20 min (36,000 shots). The profiles have been offset successively by 50 ppbv.

an existing Rayleigh–Mie lidar system. Using the same laser source as the Rayleigh–Mie system, the unique Raman cell reduces problems of misalignment, and the emission afocally reduces the field of view and noise. For the reception, the use of optical fibers permits thermal and mechanical separation of the reception part and the analysis part of the system. The MFC system allows sharing of collecting surfaces for different fields of view. The spectrometer was studied for optimum spectral separation in the UV. The electronic system (PMT and analog mode) allows a large altitude range to be covered.

When the requisite conditions are achieved (clear sky and optimal alignment of the reception system), the lidar system permits ozone measurement from 3 to 17 km, the altitude of the tropical tropopause. Comparisons with ECC ozone soundings show good agreement between the two techniques. The average difference in the troposphere observed on several joined soundings does not exceed 8 ppbv. We have also shown the capability of the lidar to study tropospheric ozone evolution in tropics. The significant lack of tropospheric ozone measurements in the tropical and equatorial regions makes this lidar implementation useful and technically conceivable for many Rayleigh–Mie lidar stations. At a site such as Reunion Island, where we wish to conduct various studies (stratosphere–troposphere exchange linked to the subtropical jet stream, study of tropical convection and influence of biomass burning), scientific interest in this extension of the Reunion lidar system is substantial. It will permit an increase in the database of ozone profiles that have been obtained by semimonthly radiosoundings launched from Reunion since 1992 (Ref. 2) and in particular offers the possibility of studying ozone evolution on a shorter temporal scale than those permitted by radiosounding.

The Reunion lidar development has been supported by the French Centre National de la Recherche Scientifique/Institut National des Sciences de l'Univers and Conseil Régional de la Réunion. The July 1998 TRACAS campaign (radiosondes and lidar data) was supported by European Community grant ENV4-CT97-0520. We gratefully acknowledge the assistance of the Service d'Aéronomie technical staff (J. L. Conrad, F. Fassina, C. Laqui, J. P. Marcovici, A. Théodon, and P. Weill) and the Laboratoire de Physique de l'Atmosphère radiosounding team (G. Bain, D. Faduilhe, J. M. Metzger, T. Portafaix, and S. Roumeau).

References

1. World Meteorological Organization, "Scientific assessment on ozone depletion," Tech. Rep. 37, Global Ozone Research Monitoring Project (World Health Organization, Geneva, 1994).
2. S. Baldy, G. Ancellet, M. Bessafi, A. Badr, and D. Lan Sun Luk, "Field observation of the vertical distribution of tropospheric ozone at the island of Reunion (southern tropics)," J. Geophys. Res. **96,** 23,835–23,849 (1996).
3. I. Folkins, R. Chatfield, H. Singh, Y. Chen, and B. Heikes, "Ozone production efficiencies of acetone and peroxides in the upper troposphere," Geophys. Res. Lett. **25,** 1305–1308 (1998).
4. H. Gouget, J. P. Cammas, A. Marenco, R. Rosset, and I. Jonquières, "Ozone peaks associated with a subtropical tropopause fold and with the trade wind inversion: a case study from the airborne campaign TROPOZ II over the Caribbean in winter," J. Geophys. Res. **101,** 25,979–25,993 (1996).
5. J. L. Baray, G. Ancellet, F. G. Taupin, M. Bessafi, S. Baldy, and P. Keckhut, "Subtropical tropopause break as a possible stratospheric source of ozone in the tropical troposphere," J. Atmos. Terr. Phys. **60,** 27–36 (1998).
6. J. P. Cammas, S. Jacobi-Koaly, K. Suhre, R. Rosset, and A. Marenco, "Atlantic subtropical potential vorticity barrier as seen by Measurements of Ozone by Airbus In Service Aircraft (MOZAIC) flights," J. Geophys. Res. **103,** 25,681–25,693 (1998).
7. K. Suhre, J. P. Cammas, P. Nédelec, R. Rosset, A. Marenco, and H. G. J. Smit, "Ozone-rich transients in the upper equatorial Atlantic troposphere," Nature **388,** 661–663 (1997).
8. J. L. Baray, G. Ancellet, T. Randriambelo, and S. Baldy, "Tropical Marlene cyclone and stratosphere–troposphere exchange," J. Geophys. Res. **104,** 13,953–13,970 (1999).
9. M. J. Kurylo and S. Solomon, "Network for the detection of stratospheric change: a status and implementation report," NASA and NOAA Special Rep. (NASA, Washington, D.C., 1990).
10. H. Bencherif, J. Leveau, J. Porteneuve, P. Keckhut, A. Hauchecorne, G. Mégie, F. Fassina, and M. Bessafi, "Lidar development and observations over Reunion Island (20.8 °S, 55.5 °E)," in *Proceedings of the 18th International Laser Radar Conference*, A. Ansmann, R. Neuber, P. Rairoux, and U. Wandinger (Springer-Verlag, Berlin, 1996), pp. 553–556.
11. J. A. Logan, "Trends in the vertical distribution of ozone: an analysis of ozonesonde data," J. Geophys. Res. **99,** 25,535–25,585 (1994).
12. G. Ancellet and M. Beekmann, "Evidence for changes in the ozone concentrations in the free troposphere over southern France from 1976 to 1995," Atmos. Environ. **31,** 2835–2851 (1997).
13. J. Pelon and G. Mégie, "Ozone monitoring in the troposphere and lower stratosphere: evaluation and operation of a

ground-based lidar station," J. Geophys. Res. **87,** 4947–4955 (1982).
14. O. Uchino, M. Tokunaga, M. Maeda, and Y. Miyazoe, "Differential absorption lidar measurements of tropospheric ozone with an excimer–Raman hybrid laser," Opt. Lett. **8,** 347–349 (1983).
15. G. Ancellet, A. Papayannis, J. Pelon, and G. Mégie, "DIAL tropospheric measurement, using a Nd:YAG laser and the Raman shifting technique," J. Atmos. Ocean. Technol. **6,** 832–839 (1989).
16. L. Stefanutti, F. Castagnoli, M. Del Guasta, M. Morandi, V. M. Sacco, L. Zuccagnoli, S. Godin, G. Mégie, and J. Porteneuve, "The Antarctic ozone LIDAR system," Appl. Phys. B **55,** 3–12 (1992).
17. U. Kempfer, W. Carnuth, R. Lotz, and T. Trickl, "A wide-range ultraviolet lidar system for tropospheric ozone measurements: development and application," Rev. Sci. Instrum. **65,** 3145–3164 (1994).
18. J. A. Sunesson, A. Apituley, and D. P. J. Swart, "Differential absorption lidar system for routine monitoring of tropospheric ozone," Appl. Opt. **33,** 7045–7058 (1994).
19. J. Reichardt, U. Wandinger, M. Serwazi, and C. Weitkamp, "Combined Raman lidar for aerosol, ozone, and moisture measurements," Opt. Eng. **35,** 1457–1465 (1996).
20. Z. Wang, J. Zhou, H. Hu, and Z. Gong, "Evaluation of dual differential absorption lidar based on Raman-shifted Nd:YAG or KrF laser for tropospheric ozone measurements," Appl. Phys. B. **62,** 143–147 (1996).
21. M. H. Proffitt and A. O. Langford, "Ground-based differential absorption lidar system for day or night measurements of ozone throughout the free troposphere," Appl. Opt. **36,** 2568–2585 (1997).
22. L. Fiorani, B. Calpini, L. Jaquet, H. Van Den Bergh, and E. Durieux, "A combined determination of wind velocities and ozone concentrations for a first measurement of ozone fluxes with a DIAL instrument during the medcaphot-trace campaign," Atmos. Environ. **32,** 2151–2159 (1998).
23. P. Keckhut, A. Hauchecorne, and M. L. Chanin, "A critical review of the database acquired for the long term surveillance of the middle atmosphere by the French Rayleigh lidar," J. Atmos. Ocean. Technol. **10,** 850–867 (1993).
24. K. Sassen, "Advances in polarization diversity lidar for cloud remote sensing," Proc. IEEE **82,** 1907–1914 (1994).
25. G. Mégie and R. T. Menzies, "Complementarity of UV and IR differential absorption lidar for global measurements of atmospheric species," Appl. Opt. **19,** 1173–1183 (1980).
26. A. Papayannis, G. Ancellet, J. Pelon, and G. Mégie, "Multiwavelength lidar for ozone measurements in the troposphere and the lower stratosphere," Appl. Opt. **29,** 467–476 (1990).
27. G. Ancellet and F. Ravetta, "Compact airborne lidar for tropospheric ozone: description and field measurements," Appl. Opt. **37,** 5509–5521 (1998).
28. L. T. Molina and M. J. Molina, Absolute "Absorption cross sections of ozone in the 185 to 350 nm wavelength range," J. Geophys. Res. **91,** 14,501–14,508 (1986).
29. S. L. Valley, *Handbook of Geophysics and Space Environments, Atmospheric Optics* (McGraw-Hill, New York, 1965), Chap. 7, pp. 1–36.
30. D. B. Rensch and R. K. Long, "Comparative studies of extinction and backscattering by aerosols, fog, and rain at 10.6 and 0.63 μm," Appl. Opt. **9,** 1563–1573 (1970).
31. D. A. Haner and I. S. Mc Dermid, "Stimulated Raman shifting of the Nd:YAG fourth harmonic (266 nm) in H_2, HD and D_2," IEEE J. Quantum Electron. **26,** 1292–1298 (1990).
32. L. De Schoulepnikoff, V. Mitev, V. Simeonov, B. Calpini, and H. Van den Bergh, "Experimental investigation of high-power single pass Raman shifters in the ultraviolet with Nd:YAG and KrF lasers," Appl. Opt. **36,** 5026–5043 (1997).
33. T. Halldorsson and J. Langerholc, "Geometrical form factors for the lidar function," Appl. Opt. **17,** 240–244 (1978).
34. H. S. Lee, G. Schwemmer, C. Korb, M. Dombrowski, and C. Prasad, "Gated photomultiplier response characterization for DIAL measurements," Appl. Opt. **29,** 3303–3315 (1990).
35. R. M. Measure, *Laser Remote Sensing: Fundamentals and Applications* (Krieger, Malabar, Fla., 1992).
36. J. D. Klett, "Stable analytical inversion solution for processing lidar returns," Appl. Opt. **20,** 211–220 (1981).
37. J. D. Klett, "Lidar inversion with variable backscatter/extinction ratios," Appl. Opt. **24,** 1638–1643 (1985).
38. E. Browell, S. Ismail, and S. Shipley, "Ultraviolet DIAL measurements of O_3 profiles in regions of spatially inhomogeneous aerosols," Appl. Opt. **24,** 2827–2836 (1985).
39. V. A. Kovalev and J. L. McElroy, "Differential absorption lidar measurement of vertical ozone profiles in the troposphere that contains aerosol layers with strong backscattering gradients: a simplified version," Appl. Opt. **33,** 8393–8401 (1994).
40. A. M. Bass and R. J. Paur, "Ultraviolet absorption cross-section of ozone: measurements, results and error analysis," in *Proceedings, Quadriennal Ozone Symposium, Halkidiki, Greece* (Reidel, Hingham, Mass., 1984), p. 606.
41. A. M. Bass, A. E. Ledford, Jr., and A. H. Laufer, "Extinction coefficients of NO_2 and N_2O_4," J. Res. Natl. Bur. Stand. Sect. A **80,** 143–166 (1976).
42. S. L. Manatt and A. L. Lane, "A compilation of the absorption cross section of SO_2 from 106 to 403 nm," J. Quant. Spectrosc. Radiat. Transfer **50,** 267–276 (1993).
43. D. P. Donovan, J. A. Whiteway, and A. I. Carswell, "Correction for non-linear photon-counting effects in lidar systems," Appl. Opt. **32,** 6742–6753 (1993).
44. J. P. Thayer, N. B. Nielsen, R. E. Warren, C. J. Heinselman, and J. Sohn, "Rayleigh lidar system for middle atmosphere research in the Arctic," Opt. Eng. **36,** 2045–2061 (1997).
45. L. Fiorani, B. Calpini, L. Jaquet, H. Van den Bergh, and E. Dirieux, "Correction scheme for experimental biases in differential absorption lidar tropospheric ozone measurements based on the analysis of shot per shot data samples," Appl. Opt. **36,** 6857–6863 (1997).
46. R. A. Barnes, A. R. Bandy, and A. L. Torres, "Electrochemical concentration cell ozonesonde accuracy and precision," J. Geophys. Res. **90,** 7881–7888 (1985).

1.2.4 Description du lidar ozone stratosphérique

Un autre système lidar, dédié à l'ozone stratosphérique, a été mis en place à la Réunion en juin 2000 dans le cadre de la thèse de Thierry Portafaix. Ce lidar avait été construit à l Université de Genève par Christian Hirt, sous la direction technique de Jacques Porteneuve et des équipes techniques du Service d Aéronomie (CNRS- Paris). La responsabilité scientifique était assurée par Sophie Godin-Beekmann et Franck Molinaro. J'ai pris la suite de Franck Molinaro suite à son détachement à Madagascar en 2002.

Ce lidar est basé sur le même principe que le lidar ozone troposphérique décrit dans la section 1.2.3, à savoir l'absorption différentielle entre 2 longueurs d'onde. Pour décaler la gamme de mesure de la troposphère à la stratosphère, il est nécessaire de choisir des longueurs d'onde moins absorbées par l'ozone, pour s'adapter aux quantités d'ozone stratosphériques qui sont beaucoup plus importantes que dans la troposphère. Le choix des longueurs d ondes retenu pour l installation de la Réunion a donc été 308 nm pour la voie absorbée et 355 nm pour la voie non absorbée.

Pour générer ces longueurs d'onde, le système utilise deux sources laser : Pour la longueur d'onde 355nm, un laser Nd/Yag (Neodyme-Yag) triplé et cadencé à 30 Hz, qui fournit une énergie maximale d environ 150 mJ par pulse et pour la voie 308 nm, un laser exciplexe, qui fournit une énergie d'environ 200 mJ par pulse. Ce laser appartient à la classe des lasers à impulsions à gaz haute pression. Le milieu amplificateur est un mélange de gaz rares (néon -xénon) et de gaz halogène (chlorure d hydrogène).

Le système de réception est similaire à celui du système ozone troposphérique, avec une mosaïque de quatre miroirs de 500 mm de diamètre. Le signal rétrodiffusé est détecté au point focal des miroirs par 4 fibres optiques, puis dirigé à l entrée d un spectromètre où est effectuée la séparation spectrale. La dispersion du signal en deux faisceaux de 308 et 355 nm, est réalisée par un réseau holographique (Jobin Yvon) à l intérieur du bloc spectromètre. Chacun des faisceaux est ensuite séparé de nouveau en deux parties (8%-92% de l énergie) par une lame séparatrice de verre non traitée, puis détecté par des tubes photomultiplicateurs et enfin envoyé vers un système d analyse. Ce système est un système de comptage rapide (bande passante 400 MHz) de 1024 canaux qui fait l analyse temporelle du signal avec une résolution temporelle de 1µs (soit une résolution spatiale initiale de 150 m). Un micro ordinateur PC pilote les tirs, ainsi que l enregistrement et le traitement en temps réel des données.

Un obturateur mécanique (ou chopper) est utilisé. Il est constitué d un disque métallique plein ajouré de 2 fenêtres symétriques, en rotation à 2400 tours/min. Son utilité est double. Il permet d une part de cadencer le tir des lasers. Il sert d autre part à obturer la partie du signal rétrodiffusé par les basses couches dont l intensité trop importante saturerait les systèmes de comptage. Son défaut est d obturer simultanément les voies hautes et basses, sans permettre de particulariser les voies.

La séparation 8%-92% des 2 voies 308 et 355 nm est rendue nécessaire en raison de la saturation du système de comptage aux altitudes inférieures à 25 km. Le système effectue donc simultanément 4 mesures correspondant à 4 voies d acquisition: 2 voies à 355 nm, basse et haute et 2 voies à 308 nm, basse et haute. Ces 4 voies conduiront, après traitement, à 2 profils distincts bas (17-25 km) et haut (25 km haut du profil).

Une obturation électronique a été installée sur les voies hautes en 2002, ainsi que 2 voies Raman pour vérifier la linéarité des voies Rayleigh pour les basses altitudes.

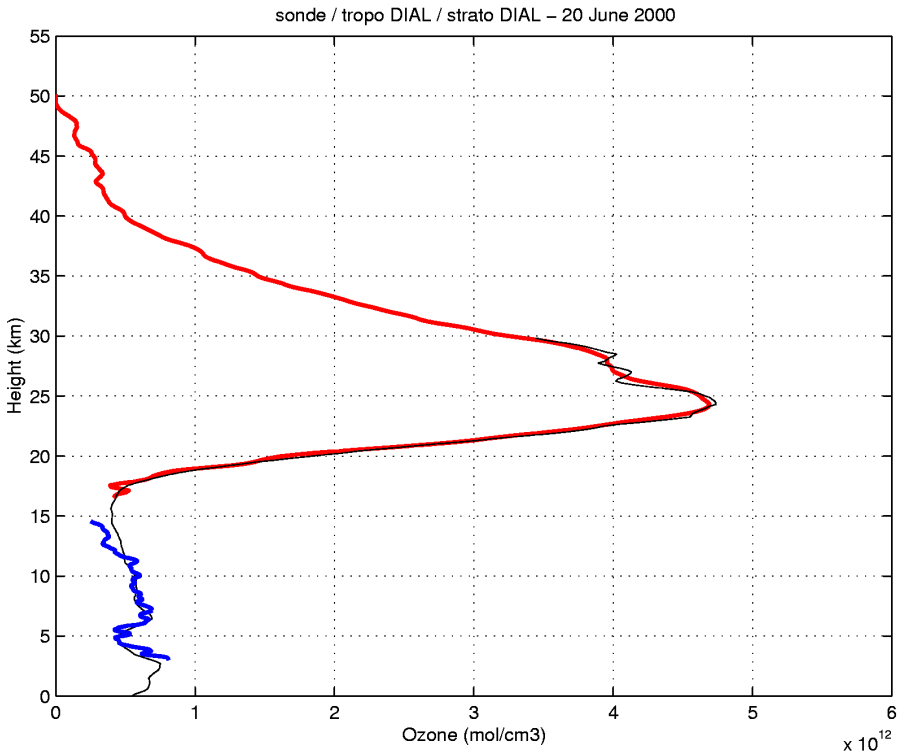

Figure 1.4 Inter-comparaison effectuée le 20 juin 2000 entre les deux systèmes lidar ozone troposphérique et stratosphérique, et un radiosondage.

L'inter-comparaison présentée dans la figure 1.4 montre que lorsque le système est dans un bon état

de fonctionnement, sa configuration permet d obtenir des profils de concentration d ozone entre 18 et 45 km d altitude environ.

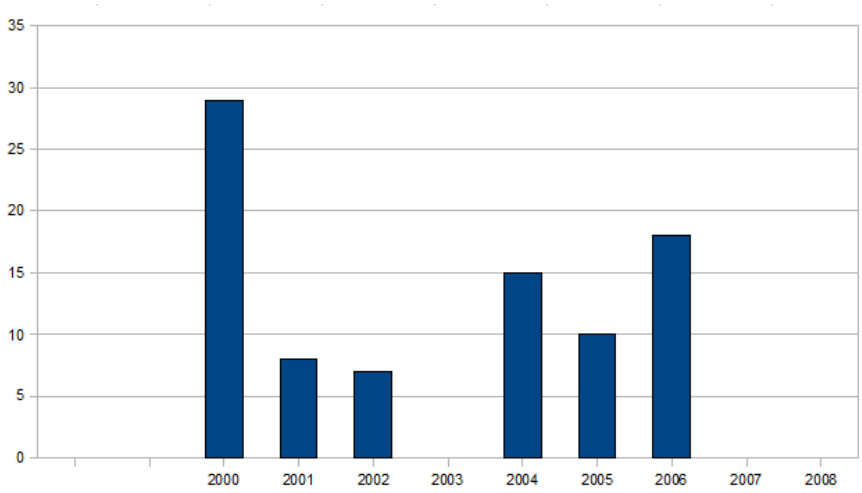

Figure 1.5 Nombre de nuits de mesures acquises par an avec le système lidar ozone stratosphérique.

Cet instrument est central pour les études stratosphériques du LACy, et également très important pour l'OPAR car c'est l'instrument le mieux adapté de part sa résolution verticale pour la surveillance de la stratosphère. Pourtant, lorsque l'on observe l'activité de mesure sur l'histogramme présenté en figure 1.5, force est de constater que s'il a été possible de le faire fonctionner de manière intensive dans le cadre de la campagne de l'hiver 2000, une suite de problèmes techniques s'est succédé sur cet instrument, touchant principalement le laser excimer, le chopper et la partie électronique. Il a donc été impossible, malgré des efforts importants, sur le plan financier comme sur le plan humain, de ma part ainsi que du staff technique (Jean Marc Metzger jusqu'en 2006, puis Yann Courcoux) de faire fonctionner cet instrument en routine à une fréquence satisfaisante.

L'exploitation scientifique de cet instrument s'est donc, pour le moment limité à la campagne de juillet 2000[8], faute de jeu de donnée suffisant pour être exploité. Toutefois, les données qui ont pu être obtenues ont été traitées et formatées pour la mise à disposition dans les réseaux NDACC et EQUAL, et ont été utilisées pour une inter-comparaison dans le cadre du réseau NDACC (section 1.3.2) et pour la validation du satellite ENVISAT (section 1.3.3)

En 2008, la responsabilité de l'instrument a été transmise à Jimmy Leclair de Bellevue, nouvellement recruté comme maître de conférences dans l'équipe stratosphère du LACy. Avec la succession de changements de composants, l'implantation d'une nouvelle chaîne de traitement

[8] Portafaix, T.; et al., Fine-scale study of a thick stratospheric ozone lamina at the edge of the southern subtropical barrier, *J. Geophys. Res*. **108** No. D6, 10.1029/2002JD002741, 2003

électronique LICEL et la planification du changement des laser, on pourra quasiment considérer que la remise à neuf de l'instrument sera quasiment totale. On peut donc espérer que la remise en route du lidar ozone stratosphérique sera enfin couronnée de succès pour 2009.

1.2.5 Présentation et validation du radiomètre MAX-DOAS

Atmos. Chem. Phys., 7, 4733–4749, 2007
www.atmos-chem-phys.net/7/4733/2007/

Atmospheric Chemistry and Physics

Retrieval of stratospheric and tropospheric BrO columns from multi-axis DOAS measurements at Reunion Island (21° S, 56° E)

N. Theys[1], M. Van Roozendael[1], F. Hendrick[1], C. Fayt[1], C. Hermans[1], J.-L. Baray[2], F. Goutail[3], J.-P. Pommereau[3], and M. De Mazière[1]

[1]Belgium Institute for Space Aeronomy (IASB-BIRA), Brussels, Belgium
[2]Laboratoire de L'Atmosphère et des Cyclones (LACy), UMR-CNRS, St-Denis, La Réunion, France
[3]Service d'Aéronomie, Verrières-le-Buisson, France

Received: 16 May 2007 – Published in Atmos. Chem. Phys. Discuss.: 14 June 2007
Revised: 3 September 2007 – Accepted: 13 September 2007 – Published: 18 September 2007

Abstract. Spectral measurements of BrO using zenith-sky and off-axis viewing geometries are combined in a linear multiple regression retrieval algorithm to provide stratospheric and tropospheric BrO vertical columns. One year of measurement data are investigated over Reunion-Island (20.9° S, 55.5° E), from August 2004 to June 2005. A comparison between the stratospheric columns retrieved at 45°, 80°, 85°, 87.5° and 92.5° solar zenith angles and photochemical simulations initialized by chemical fields from the 3-D-CTM SLIMCAT and further constrained by observed NO_2 profiles shows a good agreement only by considering a contribution from the very short-lived organic bromine substances to the stratospheric inorganic bromine budget, of 6 to 8 pptv. Furthermore, stratospheric BrO profiles retrieved from late twilight zenith-sky observations are consistent with a total inorganic bromine (Br_y) loading of approximately 23 pptv. This represents 6 to 7 pptv more than can be supplied by long-lived organic bromine sources, and therefore supports an added contribution from very short-lived organic bromine substances as recently suggested in several other studies. Moreover strong evidences are presented for the existence of a substantial amount of BrO in the tropical free-troposphere, around 6 km altitude, possibly supplied by the decomposition of short-lived biogenic bromine organic compounds. Tropospheric BrO vertical columns of $1.1\pm0.45\times10^{13}$ molec/cm^2 are derived for the entire observation period. Comparisons between ground-based BrO vertical columns and total BrO columns derived from SCIAMACHY (onboard the ENVISAT satellite) nadir observations in a latitudinal band centered around 21° S present a good level of consistency, which further strengthens the conclusions of our study.

Correspondence to: N. Theys
(theys@aeronomie.be)

1 Introduction

Inorganic bromine (Br_y=Br, BrO, $BrONO_2$, HBr, HOBr, BrCl) is the second most important halogen that affects stratospheric ozone. Although much less abundant than chlorine, stratospheric bromine presently contributes to the global ozone loss by about 25%, owing to its much larger ozone depletion potential relative to chlorine (e.g. WMO, 2003, and references therein). During daytime the most abundant inorganic bromine species is BrO, which represents 30 to 70% of total Br_y. BrO is also the only compound within the Br_y family to be measured routinely (e.g. Wagner et al., 1998; Richter et al., 1998; Van Roozendael et al., 1999; Hausmann et al., 1994; Schofield et al., 2004a; Pundt et al., 2002; Dorf et al., 2006a, Sinnhuber et al., 2002, 2005; Sioris et al., 2006). The sources of inorganic bromine in the stratosphere originate from naturally and anthropogenically emitted bromine-containing organic gases. Long-lived organic species are transported into the stratosphere with a time delay of approximately 3 to 4 years, before being converted into inorganic forms by photolysis or reaction with OH radicals. Until recently, the Br_y mixing ratio was generally assumed to be negligibly small below and at the tropopause while rapidly increasing with altitude up to about 25 km where full conversion into inorganic forms is achieved. Based on a budget of the long-lived natural (CH_3Br) and anthropogenic (CH_3Br, $CBrClF_2$, $CBrF_3$, $CBrF_2CBrF_2$, CBr_2F_2) organic bromine source gases observed over the last decade (Wamsley et al., 1998), the stratospheric Br_y loading is currently estimated to be about 16–17 pptv. However, several recent studies (Pundt et al., 2002; Salawitch et al., 2005; Sioris et al., 2006; Sinnhuber et al., 2002, 2005; Schofield et al., 2004a; Dorf et al., 2006a, b) have suggested that an additional contribution of about 5.6±2 pptv must be considered, due to bromine release from short-lived biogenic organic compounds (such as $CHBr_3$, CH_2Br_2, CH_2BrCl, $CHBr_2Cl$,

Published by Copernicus Publications on behalf of the European Geosciences Union.

$CHBrCl_2$, CH_2BrCH_2Br) or even the direct intrusion of inorganic bromine from tropospheric origin into the lower stratosphere. Inorganic bromine compounds may be produced and sustained in the free troposphere due to the decomposition of short-lived organic bromine compounds under the action of heterogeneous and/or gas-phase photochemical reactions. This is supported by recent observations from space (Pundt et al., 2000; Van Roozendael et al., 2002; Richter et al., 2002), the ground (Hendrick et al., 2007) and balloons (Fitzenberger et al., 2000), all suggesting although with large uncertainties the widespread presence of BrO in the troposphere, with mixing ratios in the range from 0.5 to 2 pptv if uniformly mixed. Elaborating on these observations, recent modeling results (von Glasow et al., 2004; Lary, 2005; Yang et al., 2005) have highlighted the possible role of tropospheric halogens (in particular bromine) as an additional sink for ozone, a process so far largely ignored. These studies suggest that bromine might be responsible for a reduction in the zonal mean O_3 mixing ratio of up to 18% and locally even up to 40%. In Polar Regions, additional amounts of inorganic bromine are seasonally released in large quantities in the boundary layer during spring due to the so-called Polar-bromine explosion phenomenon (Hausmann and Platt, 1994; Kreher et al., 1997; Hönninger and Platt, 2002; Frieß et al., 2004). These emissions are responsible of complete ozone depletion events (ODEs) in the polar boundary layer. A comprehensive review of the role of bromine species in the polar ODEs can be found in Simpson et al. (2007). Although in smaller quantities, boundary layer BrO emissions have also been identified over salt lakes (Hebestreit et al., 1999), as well as in the marine boundary layer (Leser et al., 2003) and in volcanic plumes (Bobrowski et al., 2003).

Here we present an advanced retrieval method enabling the simultaneous determination of both tropospheric and stratospheric BrO vertical columns, based on multi-axis DOAS (MAXDOAS) UV-visible observations. By combining in a retrieval scheme measurements of the scattered sky light acquired from noon to twilight in different viewing elevations (from the horizon to the zenith) and making use of the change in sensitivities associated to the different observations geometries, the vertical distribution of the BrO concentration can be inferred. The analysis explicitly takes into account the effect of the BrO photochemical variations, in particular for the simulation of the radiative transfer at twilight when photochemical gradients along the slant stratospheric photon path are important. The retrieval algorithm has been applied to observations performed from August 2004 to June 2005 at Reunion Island (20.9° S, 55.5° E, Indian Ocean), a latitude where currently available BrO observations are very sparse. It has been recently argued that biogenic short-lived organic compounds (e.g. $CHBr_3$) that are mainly released by oceans could be rapidly transported in the UT/LS region under the action of the strong tropical convection. This highlights the importance of tropics in determining the stratospheric bromine budget as pointed out by several authors (Salawitch 2006; Carpenter et al., 2000; Yang et al., 2005; Sinnhuber et al., 2005).

The paper is organized in four parts. After a short description of the instrumental setup in Sect. 2, the methodology applied to retrieve stratospheric and tropospheric BrO vertical columns is detailed in Sect. 3. This section also includes a quantitative discussion of the information content of the retrieval according to Rodgers (2000) as well as a comprehensive error budget. This is followed in Sect. 4 by a presentation of the results and their discussion in the light of our current understanding of bromine photochemistry in the atmosphere. Conclusions are given in Sect. 5.

2 Instrument

Measurements have been performed using a multi-axis DOAS (MAXDOAS) spectrometer designed and assembled at IASB-BIRA. This instrument was continuously operated on the roof of the LPA (Laboratory of Atmospheric Physics) building of the University of Saint-Denis, La Réunion (20.9° S, 55.5° E) from August 2004 to June 2005, except from 25 March to 28 April when the container had to be dismantled due to a strong tropical storm event. The instrument consists of a grating spectrometer from Acton Research Corporation (ARC SpectraPro 275) installed inside a watertight thermoregulated case and connected through a fiber optic bundle to an entrance telescope having a field of view of approximately 1° full angle. The telescope is itself connected to a rotating mirror allowing viewing elevation angles to be scanned from 3° above the horizon up to the vertical at zenith. The optical head faces the sea towards the North direction. The control of the acquisition cycle including the positioning of the pointing mirror, the optimization of the exposure time to ensure adequate photon filling of the CCD detector and the spectral acquisition is fully automated, one complete scan of all elevation angles (3°, 6°, 10°, 18°, zenith) requiring approximately 15 min. The spectrometer has a focal length of 275 mm and is mounted with a ruled grating of 600 grooves/mm covering a spectral window from 300 nm to 450 nm. It is equipped with a 1340×400 back-illuminated CCD detector from Roper Scientific (NTE/CCD-400EB), cooled to −40°C using a triple stage Pelletier system. Recorded scattered light spectra have a resolution of 0.75 nm FWHM and a sampling ratio of 7 pixels/ FWHM. At twilight, the instrument switches from the full multi-axis viewing mode to a dedicated stratospheric mode where only zenith-sky measurements are taken. In this mode, the time sampling and the signal to noise ratio of the twilight zenith-sky observations are optimized in view of the inversion of stratospheric columns and profiles (see Hendrick et al., 2004).

3 Data analysis

The data analysis involves two main steps. First, the total slant column amount of BrO is determined for each viewing direction according to the DOAS technique. Second, model simulations of the BrO slant column obtained from coupled radiative transfer and photochemical model calculations are adjusted to the observations until a consistent stratospheric and tropospheric BrO vertical column solution is obtained that matches all viewing directions.

3.1 DOAS slant column retrieval

The measured spectra are analysed using the Differential Optical Absorption Spectroscopy technique (Platt, 1994). This method relies on the assumption that one effective photon path can be defined, which represents in average over the fitting interval the complex path of scattered photons in the atmosphere. For optically thin conditions in the UV-visible region this assumption is largely verified, which implies that the absorption by atmospheric trace gases along the effective slant path of measured photons can be treated in a simple way using the Beer-Lambert law. In practice, atmospheric absorbers (in particular BrO) are separated using the characteristic differential structures of their absorption cross-sections determined from laboratory measurements. Since in most cases several absorbers display absorption structures in the same wavelength interval, the inversion process requires that all relevant interfering absorption features be taken into account. In the case of BrO, the spectral interval that optimizes the sensitivity to the target differential absorption structures while minimizing interferences with other absorbers is in the range from 345 to 359 nm. Further details on the optimization of this fitting interval are given below. The spectral evaluation consists in a least-squares fit procedure where cross-sections of BrO (228 K) (Wilmouth et al., 1999), ozone (223 K and 243 K) (Bogumil et al., 2003), NO_2 (220 K) (Vandaele et al., 1997), HCHO (293 K) (Meller and Moortgat, 2000), and the collision pair of oxygen molecules O_4 (Greenblatt et al., 1990) are adjusted to the log-ratio of a measured and a reference spectrum usually taken at noon in zenith-sky geometry. The quantity retrieved with this method is a so-called differential slant column density (DSCD), which is the difference of the column amount of the absorber along the light path and the absorber amount in the reference spectrum. The residual broadband features due to Rayleigh and Mie scattering are removed using a third order closure polynomial. To match the spectral resolution of the instrument, the laboratory absorption cross-sections are convolved using the measured slit function at 346.6 nm. In the case of the strongest absorbers ozone and NO_2, a correction for the so-called solar I_0 effect (Aliwell et al., 2002; P. V. Johnston, unpublished results) is further applied. The wavelength calibration of the measured spectra is accurately determined by reference to the high-resolution solar atlas of Kurucz et al. (1984), according to the procedure described in Van Roozendael et al. (1999). To correct for the Ring effect (Grainger and Ring, 1962) a pseudo absorption cross-section generated after Vountas et al. (1998) using the SCIATRAN radiative transfer model (Rozanov et al., 2001) is included in the fit. Similar settings are used for the retrieval of O_4 DSCDs except for the fitting interval, which is slightly shifted towards longer wavelengths (338.5–364.5 nm) in order to capture the strong O_4 absorption band centered at 360 nm.

Due to the faintness of the BrO differential absorption features (typically smaller than 0.1% of absorbance) and the presence of much stronger interfering absorption bands from ozone in the same wavelength region, the retrieval of BrO DSCDs is generally difficult and requires careful treatment. Main sources of uncertainties including those related to instrumental parameters (wavelength calibration, spectral stray light, slit function, etc.), the temperature dependence of the ozone absorption cross-sections or the impact of the solar I_0 effect have been addressed in the literature leading to a set of recommended BrO retrieval settings (see e.g. Arpag et al., 1994; Richter et al., 1999; Aliwell et al., 2002). In the present work, the problem of the optimization of the wavelength interval used for BrO retrieval has been revisited. As already mentioned the fitting interval is usually determined empirically in an attempt to maximize the sensitivity to the target gas and at the same time minimize interferences with other absorbers. In the case of BrO, the main difficulty comes from the unavoidable presence of strong interfering ozone absorption bands. At twilight, the ozone absorption becomes so large that the optically thin approximation used in the DOAS technique may not be fully satisfied, leading to systematic misfit effects that may introduce biases in the retrieved BrO DSCDs.

In order to assess the importance of such effects, simulations of the zenith-sky radiance have been performed using the SCIATRAN model (Rozanov et al., 2001) and used to test different choices of fitting intervals. Radiative transfer calculations were performed in the 340–360 nm interval for a range of solar zenith angle values (50–92 degrees) and considering absorption by all relevant trace gases. Rotational Raman scattering by molecular oxygen and nitrogen (i.e. the main source of the Ring effect) was also explicitly included (Vountas et al., 1998). In order to simulate the impact of the solar I_0 effect, calculations were realized at the resolution of 0.1 nm, further convolved to the instrumental bandpass (0.7 nm FWHM) and finally resampled on the wavelength grid of the field instrument. Based on this set of synthetic spectra, test retrievals were conducted in various wavelength intervals and the resulting BrO DSCDs were compared to the reference DSCDs calculated from the radiative transfer model at the wavelength of 352 nm (reference wavelength used for BrO air mass factor calculations, see Sect. 3.2). Results from these sensitivity tests are displayed in Fig. 1a for three typical intervals recommended in the literature. As can

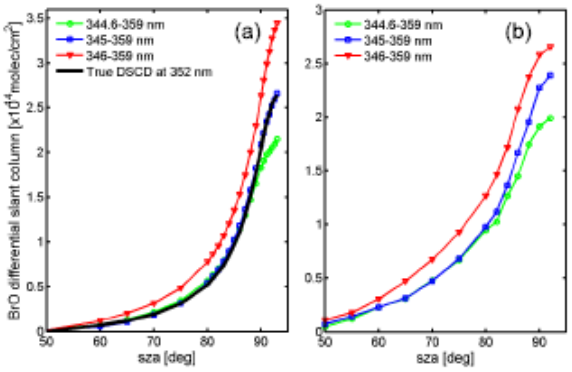

Fig. 1. BrO differential slant columns (DSCDs) retrieved in different wavelength intervals from **(a)** simulated radiances generated using the SCIATRAN model, and **(b)** actual zenith-sky observations performed at Reunion Island. Reference DSCDs calculated at 352 nm from the model are plotted with a thick black line.

be seen, differences as small as a few tenths of a nm in the selection of the shorter wavelength of the interval (where ozone absorption is strongest) can have a very significant impact on the BrO DSCD. Our simulations strongly suggest that the 345–359 nm interval efficiently minimizes the bias on the retrieved BrO columns in the full range of solar zenith angles. This interval has therefore been selected as a baseline for the present study. As an additional verification, the test fitting windows have also been applied to actual BrO measurements (see Fig. 1b). Although the shape of the observed BrO DSCD variation cannot be precisely captured by the simulations due to the non-inclusion of BrO photochemical effects in the SCIATRAN version used here (version 1.2), one can see that both synthetic and actual retrievals display similar dependences on the fitting interval, which reinforces our confidence in the reliability of the simulations.

3.2 Inversion of stratospheric and tropospheric columns

As already mentioned, the quantity retrieved by the DOAS technique is the differential slant column density, which corresponds to the trace gas concentration integrated along the effective light path of scattered photons. Since the light that reaches the instrument travels through the entire atmosphere from top to bottom, the measured BrO DSCD will contain absorption originating from both stratospheric and tropospheric altitudes (provided of course that sizeable amounts of BrO do exist in both regions). In order to separate the stratospheric and tropospheric contributions, it is necessary to combine observations displaying different sensitivities to the various atmospheric layers. In this work, we first exploit the geometrical path enhancement characteristic of scattered light measurements at twilight to get information on the stratospheric part of the BrO profile in a way similar to that used in vertical profiling studies (e.g. Preston et al., 1997; Schofield et al., 2004a, b; Hendrick et al., 2004). Second MAXDOAS observations performed at 3°, 6°, 10° and 18° of elevation above the horizon are combined with zenith-sky measurements to infer additional information on the tropospheric part of the BrO profile. The geometrical light path enhancement at low viewing angle elevation is such that the sensitivity to trace gas absorptions occurring in the atmospheric boundary layer can be increased by an order of magnitude (see e.g. Wagner et al., 2004; Wittrock et al., 2004).

The inversion method applied here is based on an analysis of the diurnal evolution of the measured BrO differential slant column, which is assumed to be well represented by the following equation:

$$\begin{aligned}&\mathrm{DSCD}(\theta(t),\varphi(t),\phi)+\mathrm{RSCD}\\&\quad=\mathrm{VCD}_{\mathrm{strato}}(\theta(t))\mathrm{AMF}_{\mathrm{strato}}(\theta(t),\varphi(t))\\&\quad+\mathrm{VCD}_{\mathrm{tropo}}(\theta(t))\mathrm{AMF}_{\mathrm{tropo}}(\theta(t),\varphi(t),\phi)\end{aligned}\quad(1)$$

Where VCD is the vertical column, AMF the air mass factor, θ the solar zenith angle (SZA), φ the relative azimuth angle between the sun and the viewing direction and ϕ the viewing elevation angle. RSCD represents the residual slant column density in the reference spectrum, derived as explained in Sect. 4.2. As a result of the photochemically induced diurnal variation of BrO, the stratospheric and tropospheric VCDs depend on the SZA, while the AMFs depend on both viewing and solar zenith angles. Note that the stratospheric AMF can be considered with a good level of approximation as independent of the viewing angle. Photochemical effects, mostly important at twilight, are explicitly treated in the inversion process, as further explained below.

The air mass factors $\mathbf{AMF}_{\mathrm{tropo}}$ and $\mathbf{AMF}_{\mathrm{strato}}$ represent the enhancement of the absorption along the light path with respect to the vertical path, in the troposphere and the stratosphere respectively. In the present analysis, a tropopause height of 16 km characteristic of tropical regions has been considered, in agreement with temperature profiles from the European Centre for Medium-Range Weather Forecasts (ECMWF). The AMFs can be determined through appropriate calculation of the transfer of the solar radiation in a multiple scattering atmosphere. In addition photochemical effects that introduce spatial and temporal gradients in the BrO concentration field must be taken into account, especially for twilight conditions. In this work, forward model calculations of the BrO absolute slant columns (SCD) and corresponding AMFs have been obtained using the pseudo-spherical radiative transfer model (RTM) UVSpec/DISORT (Mayer and Kylling, 2005) coupled to the stacked photochemical box model PSCBOX (Errera and Fonteyn, 2001; Hendrick et al., 2004). The PSCBOX model includes 48 variable species, 141 gas-phase photochemical reactions and is initialized at 20 independent altitude levels with 00:00 UT pressure, temperature and chemical species profiles from the 3-D chemical transport model (CTM) SLIMCAT (Chipperfield, 1999,

2006; see also Sect. 4.3). A stratospheric inorganic bromine total loading of 21.2 pptv, accounting for long-lived sources (CH_3Br and halons, WMO 2003) and an additional contribution of 6 pptv from short-lived bromine compounds, has been assumed within the SLIMCAT model. Updated kinetic and photochemical data are taken from the JPL 2006 compilation (Sander et al., 2006). As investigated in Fietkau et al. (2007), the reaction $BrONO_2+O(^3P)$ can play an important role in the tropical stratosphere and has thus, been included in the model simulations. The results of the photochemical model are given at chemical time steps of 6 min.

Model BrO profiles are supplied to the RTM code, and used to compute the AMFs. The UVSpec/DISORT model has the capability to ingest two-dimensional arrays (altitude and SZA) of BrO concentration fields so that the impact of photochemical changes along the incident light path can be accounted for in the calculations (see e.g. Fish et al., 1995). This particular feature of the model has been recently validated as part of a dedicated RTM intercomparison (Hendrick et al., 2006). As already mentioned, BrO AMFs have been calculated at the wavelength of 352 nm (center wavelength of the applied DOAS fitting interval), for a fixed albedo of 6% which has been found to be typical for sea-surface conditions (Koelemeijer et al., 2003).

Following Schofield et al. (2004a, b) and in order to limit the number of retrieval parameters, we have assumed that six profiles given, respectively, at 45°, 80°, 85°, 87.5° and 92.5° of SZA describe adequately the diurnal variation of BrO in the stratosphere. The stratospheric VCDs can be determined at other SZAs using simple linear interpolations. The vertical distribution of BrO being largely unknown in the troposphere, our baseline for the retrieval has been to assume a free-tropospheric profile consistent with the observed profile of Fitzenberger et al. (2000). This assumption will be further tested in Sect. 4.4, where attempts to derive the vertical distribution of BrO in the troposphere from multi-axis DOAS observations are presented. Since no measurements of the diurnal variation of BrO in the troposphere are currently available, we have adopted the approach introduced in Schofield et al. (2004a, b). This consists in assuming a tropospheric BrO diurnal variation similar to the one modeled in the lowest levels of the stratosphere. It will be shown later that inversion results are weakly dependent on this assumption.

The inversion for the stratospheric and tropospheric BrO VCDs is obtained by fitting Eq. (1) to a set of measurements recorded from noon to twilight at various elevation viewing angles and solar zenith angles. Morning and afternoon measurements are treated separately. For the stratosphere-troposphere separation, the technique takes benefit of the different evolution of the stratospheric and tropospheric AMFs as a function of SZA. This is illustrated in Fig. 2 for typical conditions in the zenith-sky geometry. In the inversion process, the stratospheric BrO VCDs are simultaneously (and independently) retrieved at five values of the SZA (45°, 80°, 85°, 87.5° and 92.5°) meaning that the diurnal variation of the stratospheric BrO column is actually retrieved from the observations and not forced a priori from photochemical model calculations. Note that photochemical calculations are in fact only used to ensure proper calculation of the late twilight AMFs when two-dimensional gradients of the BrO concentration are important.

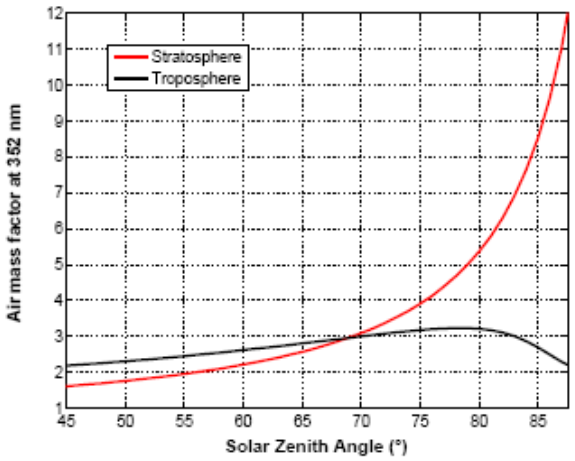

Fig. 2. Stratospheric and tropospheric BrO air mass factors calculated at 352 nm in the zenith-sky viewing geometry. The enhancement of the sensitivity to stratospheric BrO at twilight is obvious.

Since the introduction of an extra retrieval parameter for the slant column in the reference spectrum (**RSCD** in Eq. 1) can lead to unwanted uncertainties and retrieval instabilities, **RSCD** has been determined prior to the inversion as described in more details in Sect. 4.2.

3.3 Averaging kernels

In this section the capacity of the inversion method to separate adequately the stratospheric and tropospheric signals from the observations is addressed, based on the concept of the averaging kernels as developed in (Rodgers, 2000). The averaging kernel represents the sensitivity of the retrieval to the true state:

$$A = \frac{\partial \hat{x}}{\partial x} \tag{2}$$

where $\hat{x}$ is the retrieved state vector (i.e. here the tropospheric and stratospheric VCDs) and x represents the true BrO vertical profiles. Equation (2) can also be written:

$$A = \frac{\partial \hat{x}}{\partial y}\frac{\partial y}{\partial x} = G\frac{\partial y}{\partial x} \tag{3}$$

where y is the measurement vector, and G is the contribution matrix expressing the sensitivity of the retrieval to the measurement. The derivative of the measurement vector (the

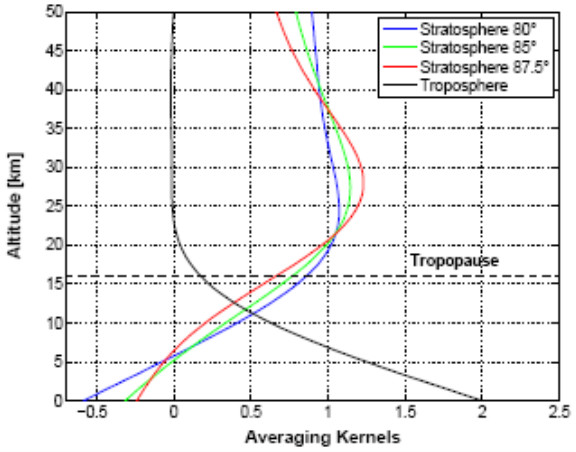

Fig. 3. Typical examples of ground-based averaging kernels for stratospheric BrO columns (at 80°, 85° and 87.5° SZA) and for tropospheric BrO columns (see text).

slant column densities) with respect to the BrO vertical profiles have been determined by a perturbation method using the radiative transfer model.

Figure 3 shows the tropospheric and stratospheric VCDs averaging kernels (AK) calculated according to Eq. (3) for three representative values of the SZA (80°, 85° and 87.5°). The AK values represent the way the retrieval smooths the respective partial column profiles (for a 1 km layer around the altitude given in the y-axis). It can be deduced from Fig. 3 that the inverted tropospheric columns are largely independent from the simultaneously inverted stratospheric columns. The high value of the tropospheric AK nearby the surface is related to the enhanced sensitivity of the off-axis observations in this altitude region. On the contrary, the stratospheric averaging kernels peak in the stratosphere around the maximum of BrO concentration profiles.

3.4 Error analysis

The contributions to the total retrieval uncertainty are divided into three categories: (1) random errors caused by measurement noise and BrO variability (2) errors affecting the slant column density in a systematic way, and (3) errors due to remaining uncertainties in the modeling and representation of the atmosphere, affecting the air mass factors.

We investigate the errors affecting the SCDs and the AMFs. A careful estimate of the uncertainties is especially crucial at high SZA. Indeed, a large part of the information used to separate the stratospheric and tropospheric BrO columns comes from measurements at high SZA. The uncertainties affecting the SCDs (random and systematic errors) as well as the AMFs are largest at low sun.

Measurement and modeling uncertainties have been estimated by means of sensitivity studies. As an example, the results for zenith-sky observations are displayed in Table 1 for typical low, medium and high solar zenith angles (respectively 70°, 85° and 90° SZA). The scatter of the measured DSCDs has been found to be relatively constant from month to month. Hence average values of 1.2, 1.9 and 3.4×10^{13} molec/cm^2 have been attributed to random error sources, respectively, for the three representative SZAs. These values are also consistent with the one-sigma uncertainties derived from the DOAS fitting procedure. DSCDs systematic errors are mainly introduced by uncertainties on the absorption cross-sections of the molecules included in the analysis, leading to mutually correlated DOAS results.

In order to estimate the errors due to absorption cross-sections and their cross-correlations, one approach is to consider the cross-sections as forward model parameters of the DOAS retrieval. Following the formalism introduced by Rodgers (2000), the forward model parameter error of the retrieval can be derived from the quoted uncertainties on the cross-sections used in the DOAS analysis. Based on literature data and sensitivity tests using various data sources, the following uncertainty figures have been adopted for BrO: 8%, NO_2: 3%, O_3: 3%, O_4: 5%, HCHO: 5% and Ring effect interferences: 5%. In addition to cross-sections, other sources of systematic errors can be identified, like the errors linked to calibration or other additional instrumental uncertainties. As already pointed out in Sect. 3.1, the use of the DOAS approximation by which slant columns are assumed to be constant within the spectral fitting window, can also be a significant source of systematic uncertainty. Using the optimal fitting window derived in Sect. 3.1, sensitivity studies suggest that these sources of uncertainties do not contribute more than 5% to the total SCD error. Considering absolute slant columns (i.e. corrected for the BrO residual amount in the reference spectrum), a constant additional error of ±0.5 10^{13} molec/cm^2 has been introduced, following estimates described in Sect. 4.2. From Table 1, it must be emphasized that SCDs errors are largely dominated at twilight by systematic biases mainly introduced by uncertainties on the absorption cross-sections.

In addition to the error analysis described above, an alternative study has been performed to estimate systematic errors due to absorption cross-sections uncertainties. It consisted in running test retrievals using different sources of cross-sections available from the literature and investigating the resulting variability of the retrieved BrO slant columns. Uncertainties empirically estimated in this way were found to be in good agreement with the values (see Table 1) deduced from the approach based on the Rodgers (2000) formalism.

Once the total uncertainties on the measurements has been estimated for each elevation angle and for all solar zenith angles, the resulting uncertainties on the retrieved stratospheric and tropospheric BrO vertical columns are given by simple error propagation (see Table 2). The next step is to evaluate the errors on the AMFs. For small SZA (<85°), the stratospheric AMF can be satisfactorily approached by a

Table 1. Summary error budget for BrO slant column densities (random, systematic and RSCD error sources) and air mass factors in zenith-sky geometry, for three representative solar zenith angles.

Slant column density error ($\times 10^{13}$ molec/cm^2)	Solar zenith angle 70°	85°	90°
Random	1.2	1.9	3.4
Systematic bias	0.7	4	6.8
Residual slant column density (RSCD)	0.5	0.5	0.5
Total ($\times 10^{13}$ molec/cm^2)	1.5	4.5	7.6
Total (%)	13	23	24
Air mass factor error (%)	**Solar zenith angle 70°**	**85°**	**90°**
Stratosphere: AM	1.5	1.5	3.5
Stratosphere: PM	1.5	1.5	2.5
Troposphere	5	15	5

geometrical calculation. The error on the stratospheric AMF is therefore negligible. In contrast at high SZA, the stratospheric AMF is highly dependent on the BrO concentration at the bulk altitude for Rayleigh scattering, the latter increasing with the SZA (see e.g. Sinnhuber et al., 2002). Hence accurate modeling of the photochemistry is needed to evaluate correctly the stratospheric AMFs. To a large extent, the stratospheric BrO concentration is controlled by NO_2 through the termolecular reaction BrO+NO_2+M. In order to minimize errors due to the interplay between BrO and NO_2, the photochemical simulations have been constrained using NO_2 profiles derived from simultaneous zenith-sky observations in the visible region (Hendrick et al., 2004). Nevertheless remaining uncertainties in other aspects of the photochemical model calculations may have a substantial impact on the results. Hence sensitivity studies have been carried out in order to estimate the impact of the uncertainties on main reaction rate constants, following the work presented in Sinnhuber et al. (2002). The stratospheric AMF errors have been estimated by the standard deviation of the ensemble of AMFs generated by varying independently the reaction rate constants. Results from this analysis are summarized in Table 1.

The estimation of the errors on the tropospheric AMFs is difficult, mainly due to the following two reasons: (1) the treatment of the radiative transfer down to the surface strongly depends on the aerosol loading as well as the (unknown) BrO vertical distribution, and (2) the diurnal variation of the tropospheric BrO content might have to be taken into account. Since substantial uncertainties accompany these parameters, several hypotheses have been made here. Some of these will be justified later on in the discussion (see Sect. 4). As a baseline for our retrievals, we have assumed that the aerosol content was small (justified in Sect. 4.1) and that the bulk of the tropospheric BrO concentration was mainly located in the free-troposphere (justified in Sect. 4.4).

A rough estimate of the tropospheric AMF error has been obtained by varying input BrO profiles in the RTM calculations. Gaussian profiles of various heights [5–8 km] and widths [1–4 km] have been used to this purpose. Corresponding tropospheric BrO AMFs show a root mean square deviation of less than 15% as indicated in Table 1. For the diurnal variation, we assume that the known photochemistry of BrO in the lower stratosphere constitutes a reasonable proxi for the free troposphere (Schofield et al., 2004a, b). In reality, one may expect the tropospheric BrO amount to vary in response to e.g. emissions from the oceans, meteorological conditions, changes in photolysis rates (e.g. due to clouds), and other physical and chemical processes. It is difficult to comprehensively account for all these effects in a realistic way. However, in order to roughly estimate the order of magnitude of errors related to diurnal variation effects, we have considered two extreme cases: (1) the baseline tropospheric BrO diurnal variation, where basically the BrO concentration drops to zero from noon to late twilight and (2) the case where tropospheric BrO has no diurnal variation at all (which is very unlikely). We assume that in reality the tropospheric BrO diurnal variation lies somewhere in between these two cases. Test retrievals considering these two scenarios resulted in minor differences on the inverted BrO columns (approximately 1×10^{12} molec/cm^2).

The main sources of uncertainties on the inverted BrO VCDs (obtained by propagation of the error discussed above) are summarized in Table 2 for morning conditions. Although not reported here, similar results have been derived for afternoon observations. As can be seen, stratospheric VCDs have largest uncertainties (>30%) at low sun and at very high sun, while errors are kept in the range of 20% for intermediate values of the SZA. The absolute error on the tropospheric

Table 2. Summary error budget for morning stratospheric BrO and tropospheric BrO columns.

	Stratospheric VCD error ($\times 10^{13}$ molec/cm^2) Solar zenith angle (°)					Tropospheric VCD error
Error source	45	80	85	87.5	92.5	
Slant column densities	0.5	0.3	0.3	0.3	0.1	0.3
Stratospheric AMFs	<0.1	<0.1	<0.1	<0.1	<0.1	<0.1
Tropospheric AMFs	0.6	0.4	0.3	0.2	0.1	0.4
Total VCD error ($\times 10^{13}$ molec/cm^2)	0.8	0.5	0.4	0.4	0.1	0.5
Total VCD error (%)	30	21	17	17	33	46

BrO VCD, mainly dominated by uncertainties on the tropospheric AMFs and on the measured SCDs, is estimated to be about 45%.

4 Results and discussion

To simplify the discussion, we first restrict the analysis to clear-sky measurement days when the transfer of the scattered radiation can be simulated with best accuracy. We focus on the determination of three key parameters that control the accuracy of the target BrO VCD products; namely the aerosol extinction, the residual BrO slant column density in the reference spectrum and the shape of the tropospheric BrO profile. Results are then discussed with regard to our current understanding of the bromine chemistry in both the stratosphere and the troposphere. In a second step, a simplified version of the inversion algorithm is applied to the whole series of measurements from from August 2004 until June 2005, and the consistency of the retrieved BrO columns is investigated in comparison with coincident satellite observations from SCIAMACHY.

4.1 Determination of the aerosol settings

The light path of photons scattered in the lower atmosphere is strongly dependent on the aerosol loading, especially nearby the surface. A good estimate of the aerosol extinction profile is thus needed for the calculation of the tropospheric BrO AMFs. This is especially true for small elevation angles, which in principle have the longest light paths. As suggested by Wagner et al. (2004) and Frieß et al. (2006), multi-axis observations of the oxygen dimmer O_4 can be used to deduce the aerosol extinction profile. The analysis of aerosol properties has to be limited to measurements without significant cloud influence, since O_4 absorptions are greatly affected by clouds. Out of the complete 2004 data set (i.e. approximately six months of measurements), seven days could be selected as fully clear sky days (day numbers 242, 246, 253, 271, 272, 326, 346), based on an analysis of the diurnal variation of the measured O_4 absorptions at all elevation angles. For all these days, O_4 absorptions were found to follow the same smooth diurnal evolution, indicating similar aerosols scenarios. In Fig. 4., the O_4 DSCDs averaged on the selected days (and on a 2.5° SZA bin grid) are represented as a function of SZA for morning and afternoon observations. In order to reproduce the O_4 observations, a set of O_4 AMFs were computed for each elevation angle and for different aerosol extinction profiles. Radiative transfer calculations were initialized using vertical profiles of O_4, pressure, temperature and O_3 characteristic of tropical regions, according to the AFGL atmospheric constituent profiles data base (Anderson et al., 1986). The aerosol extinction profile was then varied until good agreement was found for the O_4 verticals columns derived from all viewing elevations. This procedure is similar to the one proposed and applied in Heckel et al. (2005). As demonstrated in Fig. 5, the optimal aerosol extinction profile corresponds to an aerosol visibility (Middleton, 1952) of 80 km with an enhanced maritime aerosol load (extinction $\sim$0.2 km^{-1}) introduced into a 100 m thick layer above the surface. O_4 VCDs retrieved assuming an aerosol visibility of 40 km are also shown for comparison purpose.

4.2 Determination of the residual slant column density

In this work, the zenith-sky and off-axis measurements have been processed using a fixed zenith reference spectrum selected at minimum solar zenith angle (28.7° SZA) on 2 September 2004. As mentioned earlier, the introduction of an extra fitting parameter for the residual slant column (RSCD in Eq. 1) can be a source of uncertainty for the retrieved stratospheric and tropospheric BrO VCDs. In order to minimize this error and stabilize the retrieval process, the residual slant column density is therefore determined prior to the inversion process so that absolute slant columns (rather than differential SCDs) can be fitted.

The residual slant column density has been estimated from an average of clear days measurements (selected in Sect. 4.1), assuming that the BrO field is stable enough to allow meaningful interpretation of the resulting averaged SCDs. This assumption will be further verified in Sect. 4.5.

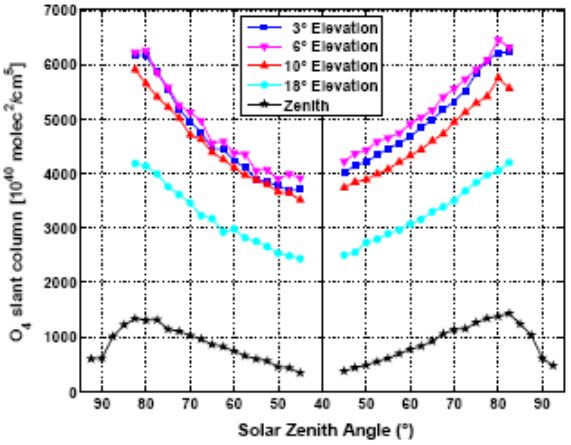

Fig. 4. Differential slant columns of O_4 measured for different elevation angles as a function of the SZA. Morning and afternoon measurements are displayed together. The O_4 DSCDs have been averaged from a selection of 7 clear-sky days and binned on a grid of 2.5° SZA.

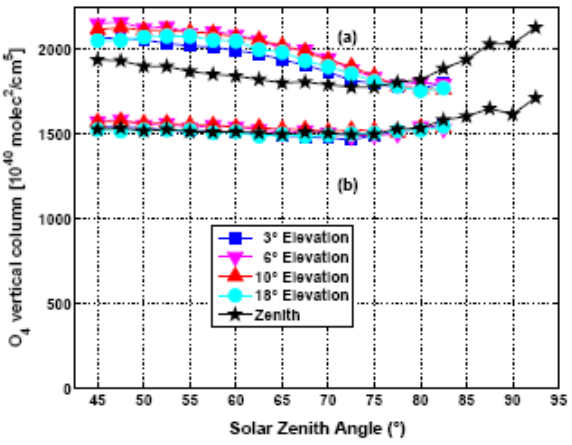

Fig. 5. Vertical columns of O_4 calculated for all viewing directions based on AMFs for two aerosols scenarios, as a function of SZA: aerosol extinction profiles corresponding to **(a)** a visibility of 40 km and **(b)** a visibility of 80 km with a higher aerosol load (extinction: $\sim 0.2\,km^{-1}$) added in a thin layer close to the surface (0–100 m).

Based on Eq. (1), the RSCD is treated as an additional parameter in the BrO VCDs retrieval. In order to minimize the impact of uncertainties related to the diurnal variation, systematic measurement errors or AMFs modeling errors (all becoming important at twilight), only the measurements corresponding to solar zenith angles lower than 85° are considered. This also reduces the number of fitted parameters and therefore stabilizes the inversion for the RSCD. Using this approach, residual slant column densities of 6.42×10^{13} and 6.37×10^{13} molec/cm^2 are retrieved, respectively from morning and afternoon measurements. The (small) differences in the retrieved RSCDs can be attributed to a large extend to the propagation of the measurement errors into the BrO VCDs retrieval. An error analysis according to Sect. 3.3., leads to a best estimate of $6.4\pm0.5\times10^{13}$ molec/cm^2. Furthermore, this value is found to be consistent with the re-calculated RSCD based on the retrieved VCDs evaluated at the time of the reference spectrum.

4.3 Clear-sky results

The inversion technique described in Sect. 3.2 has been applied to the restricted data set of clear sky measurements, also used for the aerosol and residual BrO column determination. The resulting retrieval fit results are displayed in Fig. 6. For the sake of clarity, only afternoon results are represented for a limited number of viewing directions. As can be seen, the modeled SCDs are consistent with the observations, for all SZA and viewing angles. In Fig. 7, the differences between the measured and the modeled slant column densities are shown as a function of the SZA, for the various elevation angles. A comparison with the results of the algorithm assuming that BrO would only be present in the stratosphere clearly demonstrates the need to include both a stratospheric and a tropospheric BrO contribution in the inversion process. The level of agreement between the elevation directions observations strongly depends on the hypothesis made for the tropospheric BrO profile as part of the tropospheric AMFs calculations. This will be addressed in the next section, where the relevance of using a free-tropospheric profile as derived in Fitzenberger et al. (2000) is tested and discussed.

The retrieved BrO vertical columns and their respective retrieval uncertainties (based on the error analysis developed in Sect. 3.4) are displayed in Fig. 8, for both morning and afternoon conditions.

4.3.1 Tropospheric BrO

Tropospheric BrO vertical columns (at 80° of SZA) of about 1.1 and 1.2×10^{13} molec/cm^2 are retrieved independently from morning and afternoon measurements separately, with a mean uncertainty of about 0.5×10^{13} molec/cm^2. This represents approximately one third of the total BrO column retrieved at the same SZA and therefore supports the existence of significant sources of inorganic bromine in the tropical troposphere.

Such results are roughly consistent with mid-latitude tropospheric BrO background values of $1–3\times10^{13}$ molec/cm^2 obtained from GOME, ground-based and balloon measurements (e.g. Van Roozendael et al., 2002). Similarly GOME measurements over the equatorial pacific using a technique contrasting cloudy and clear-sky scenes conclude to a background tropospheric BrO column of $1–4\times10^{13}$ molec/cm^2 (Richter et al., 2002). The combined use of SCIAMACHY

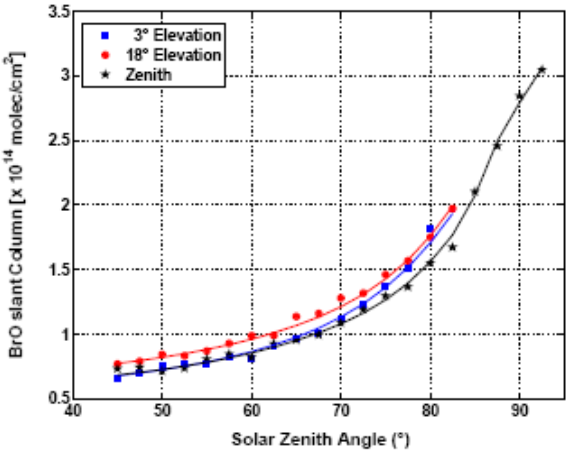

Fig. 6. Measured and modeled afternoon BrO slant column densities, as a function of the SZA for 3 elevation viewing angles (3°, 18° and zenith).

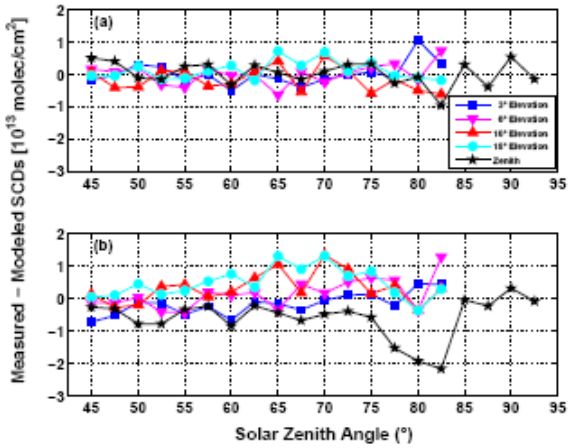

Fig. 7. Retrieval residuals for averaged clear-sky data (see text), as a function of the SZA. The modeled SCDs are subtracted from the measured SCDs, for all viewing directions. Two different assumptions are made for the BrO vertical repartition: **(a)** BrO is present in both stratosphere and troposphere, **(b)** BrO is entirely located in the stratosphere.

(onboard the ENVISAT satellite) nadir and limb observations also suggests an average global tropospheric BrO column below 15 km of about $2–4\times10^{13}$ molec/cm^2 (Sinnhuber et al., 2005). On the other hand, significantly smaller tropospheric BrO columns in the range of $0.2\pm0.4\times10^{13}$ molec/cm^2 are derived from the combined use of direct sun and zenith sky measurements at the Southern mid-latitude site of Lauder (Schofield et al., 2004a).

More specifically, BrO measurements in the tropical troposphere have been very sparse and in fact limited to few

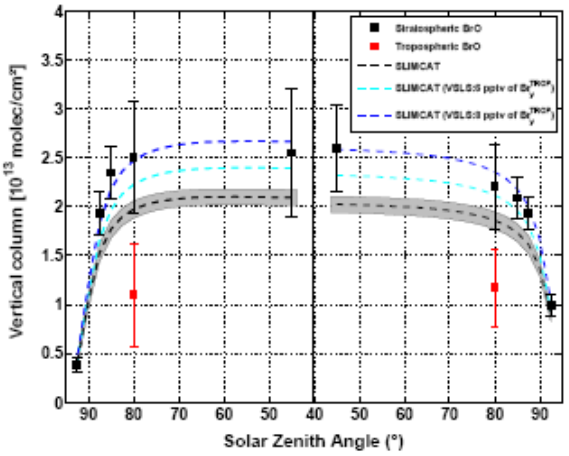

Fig. 8. Morning and afternoon stratospheric and tropospheric BrO vertical columns retrieved from averaged clear-sky data. The dashed lines correspond to stratospheric columns obtained from photochemical model simulations initialized with SLIMCAT fields having different contributions from the very short-lived bromine species (VSLS): (black) 6 pptv, (cyan) 6 pptv and (blue) 8 pptv directly injected at the tropopause. The shaded area corresponds to the range of uncertainties associated to reaction rate constants.

studies. More recently at Nairobi, measurements similar to those reported here (Fietkau et al., 2007) conclude to tropospheric BrO columns in the range from 4 to 7.5×10^{12} molecules/cm^2 in closer agreement with Reunion Island results although still slightly smaller. The difference could possibly be explained by the fact that the profile inversion used at Nairobi loses sensitivity above 6 km of altitude, while the different stratosphere-troposphere approach used in our study maintain better sensitivity higher up in the troposphere (see averaging kernels in Fig. 3). Beyond retrieval issues, the possibility of an added tropospheric BrO content at Reunion Island due to influx from sea salt aerosol might also be considered (Fietkau et al., 2007).

4.3.2 Stratospheric BrO

The retrieved stratospheric BrO vertical columns and their respective error estimates (at the chosen SZAs of 45°, 80°, 85°, 87.5° and 92.5°) are displayed in Fig. 8. A strong diurnal variation is observed as a result of the photochemically evolving interplay between BrO and its nighttime reservoirs (HOBr, $BrONO_2$) (e.g. Lary et al., 1996a, b). From Fig. 8., higher stratospheric BrO columns are found at sunrise than at sunset, for the reference SZAs of 80° and 85°. The rapid increase of BrO at sunrise is due to the fast photolysis of HOBr, which is produced during the night due to heterogeneous conversion of bromine nitrate by hydrolysis on sulfate aerosols. The decrease of BrO during the day is related to the increase of stratospheric NO_2, which in turn influences

the bromine partitioning through the termolecular reaction $BrO+NO_2+M$.

The stratospheric column results of the photochemical model (initialized with the chemical fields from the SLIMCAT model) are also shown in Fig. 8 (black dashed line). The diurnal evolution of the measured columns is properly captured by the model, providing strong evidence that the stratospheric bromine photochemistry is well understood and represented. It can also be seen however that modeled vertical columns are substantially smaller than the retrieved stratospheric columns. The shaded region around the modeled vertical columns indicates the impact (at the 1 σ level) of the uncertainties of the rate constants for the most important reactions. One possible explanation for the underestimation of the BrO columns by the model run can be found in the way bromine sources (including the short-lived species) have been treated in the relatively old SLIMCAT version used for the present work (run D in Feng et al., 2007). These are represented using a single effective source of CH_3Br (with a mixing ratio of 21.2 pptv at the surface). Since in reality the short-lived source gases are decomposed faster than methyl bromide, the Br_y mixing ratio could be substantially underestimated by the model, especially in the lower stratosphere, which might have an important impact on the integrated BrO vertical column. In order to investigate this effect, we considered the extreme case where the short-lived species are totally converted in Br_y at the tropopause. This was achieved by applying a simple offset to the SLIMCAT Br_ymixing ratio profile (scaled for the contribution of the long-lived bromine sources only). The stratospheric BrO columns resulting from this test scenario are displayed in Fig. 8 for contributions of 6 pptv (cyan dashed line) and 8 pptv (blue dashed line) from the decomposition of the short-lived bromine species. The value of 8 pptv can be considered as a plausible upper limit for the contribution of the bromine short-lived species, in agreement with recent studies (Pfeilsticker et al., 2000; Salawitch et al., 2005; Schofield et al., 2006; Dorf et al., 2006a, b; Sioris et al., 2006). This also confirms the findings of Feng et al. (2007), who have tested different methods of implementing the bromine source gases in the SLIMCAT model and found that the agreement between model and balloon data is significantly improved when having explicitly the short-lived source gases.

In order to gain better insight into the consistency between our retrieved stratospheric BrO content and data from the literature, the stratospheric BrO profiling algorithm of Hendrick et al. (2004, 2007) based on the optimal estimation technique (Rodgers, 2000), has been applied to the zenith-sky clear-sky observations performed at Reunion Island. Figure 9a displays a comparison of the resulting BrO profile with those obtained from the balloon-borne SAOZ instrument during the late afternoon ascent of the balloon at 75°–80° SZA at the same latitude (22.4° S, 49° W) in Brazil in November 1997 (Pundt et al., 2002), and January–February 2004 during the Hibiscus campaign (F. Goutail et al., personal communication). Since SAOZ balloon measurements are performed during evening twilight in ascent mode (typically around 86–87° SZA) the ground-based BrO profile was retrieved from afternoon observations at the appropriate SZA. Although significant changes can be observed in the stratosphere from one flight to another a reasonable agreement is found between ground-based and balloon profiles at the same latitude. This is especially true for the flight in November 1997.

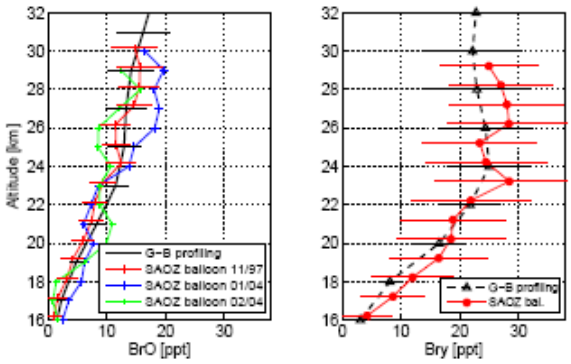

Fig. 9. Retrieved stratospheric BrO profile compared to tropical SAOZ balloon BrO profiles (left plot). Profile of Br_y inferred from ground-based BrO profile compared to the SAOZ balloon Br_y profile at 22° S, November 1997 (right plot).

From the stratospheric BrO profile, it is also possible to derive a stratospheric inorganic bromine profile based on estimates of the BrO/Br_y ratio given by the photochemical model. Figure 9b shows the Br_y profile deduced from our retrieved tropical BrO profile. A good agreement is found with the Br_y vertical distribution derived by Salawitch et al. (2005) based on SAOZ observations.

From these results, one concludes to a total inorganic bromine content of about 23 pptv, which suggests a contribution from several short-lived organic bromine sources to the stratospheric inorganic bromine budget, in agreement with studies from Pfeilsticker et al. (2000) and Salawitch et al. (2005).

4.4 Determination of the tropospheric BrO vertical distribution

Since the light path through the troposphere strongly depends on both SZA and viewing elevation angle, only an appropriate tropospheric BrO vertical profile in the AMFs calculation will lead to a good agreement between the modeled SCDs and the measured SCDs, for all viewing angles. An illustration of the sensitivity of the multi-axis DOAS observations for an absorber located at different altitudes is given in Fig. 10, in the form of air mass factor (AMF) curves represented for two different values of the SZA (60° and 80°). By comparing Figs. 6 and 10, it can be easily deduced that our observations do not show evidence for large amounts

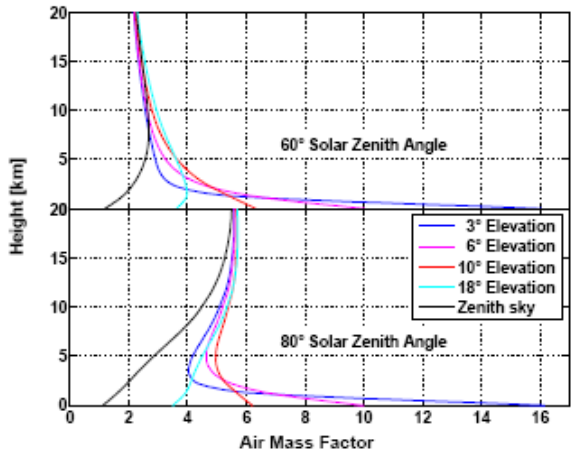

Fig. 10. Height dependence of the sensitivity to BrO for the different viewing directions at 60° SZA (upper plot) and at 80° SZA (lower plot). The value on the x-axis is the air mass factor for a 1 km layer positioned around the height given on the y-axis.

of BrO in the boundary layer. Indeed this would require a systematic and pronounced increase of the measured BrO SCDs towards low elevation angles, which is definitely not observed. Based on the error budget of the retrieved BrO slant column densities (summarized in Table 1), one cannot exclude a possible enhancement in the range of approximately 1×10^{13} molec/cm^2, which translate to an upper limit of 0.5 pptv for BrO being possibly present in the oceanic boundary layer at Reunion Island.

If one assumes a BrO profile peaking higher up in the troposphere around 6–7 km, Fig. 10 indicates that at low SZA (60°) the AMF is almost the same at 3° elevation and at zenith, a sizeable enhancement of the sensitivity being only obtained at 18° of elevation. On the contrary at larger SZA (80°), larger AMF values are found at both 3° and 18° elevation. This characteristic behavior of the elevation angles sensitivities for a free-tropospheric profile is consistently observed in the measured slant columns in Fig. 6. In order to gain information on the vertical distribution of BrO in the troposphere, sensitivity tests have been made on the average of the 7 clear days of measurements (selected in Sect. 4.3) and have consisted in varying bulk altitudes and full widths at half maximum (FWHM) of Gaussian tropospheric profiles used to calculate tropospheric AMFs. The best residuals were obtained for a concentration profile peaking at 6 km altitude with a FWHM of 2 km, for both morning and afternoon observations. A maximum of 2 to 5 pptv in the free troposphere is deduced from our estimate of the tropospheric BrO column ($1.1\pm0.5\times10^{13}$ molec/cm^2). These results are roughly in agreement with the tropospheric BrO profile measurements reported in Fitzenberger et al. (2000), based on balloon borne DOAS observations performed at Kiruna, Sweden. In contrast MAXDOAS profile inversion results recently obtained above Nairobi, Kenya (Fietkau et al., 2007) suggest a bulk tropospheric BrO layer located between 2 and 3 km altitude, hence slightly lower than found at Reunion Island.

This apparent discrepancy might be related to the fact that the inversion technique used in the Fietkau et al. (2007) study was essentially limited to the lowest 6.5 km. In addition, Nairobi is a continental station located at relatively high altitude (1600 m) likely not influenced by bromine emission from oceanic origin.

4.5 Seasonal variation

Since clear-sky observations do not show evidence for sizeable amounts of BrO being present in the lowest troposphere, one can safely expect that slant column measurements will generally be weakly affected by the presence of low altitude clouds and/or particles. Hence we decided to apply our inversion technique on a daily basis in order to derive information of the seasonal cycle of the retrieved stratospheric and tropospheric BrO vertical columns.

In order to somehow stabilize the inversion and allow its application to day-to-day observations inherently noisier than averages considered so far, the algorithm has been slightly simplified with respect to the scheme presented in Sect. 3.2. Instead of retrieving the diurnal variation of the stratospheric VCD for each day, it was decided to fix this variation based on the clear-sky analysis obtained in Sect. 4.3. Accordingly a single stratospheric BrO vertical column is derived from the inversion process, for a given reference SZA (80° was selected here), together with the tropospheric BrO column. This approach applied separately to morning and evening observations was found to represent the best compromise between information content and retrieval noise on a daily basis.

The resulting time-series of stratospheric and tropospheric BrO columns (hence retrieved at 80° SZA at both sunrise and sunset) are displayed in Fig. 11, for the entire observation period. Only vertical columns corresponding to retrieval residuals lower than 2×10^{13} molec/cm^2 were considered in this analysis. This threshold has been chosen in order to reject unrealistic measurements, contaminated by thick clouds or affected by spectral artifact due e.g. to anomalously large O_4 absorption. The retrieved stratospheric and tropospheric BrO columns are on average in excellent agreement with the values derived from the averaged clear-sky observations (Sect. 4.3) and show no noticeable seasonal variation. This result is somewhat in contradiction with expectations based on photochemical considerations valid for tropical latitudes. Model simulations of the noon or near twilight (SZA$<$80°) stratospheric BrO column at Reunion-Island indeed show a small seasonality, with an amplitude smaller than 10%. Such an effect however lies within the uncertainties of our retrieved stratospheric BrO columns, which moreover do not

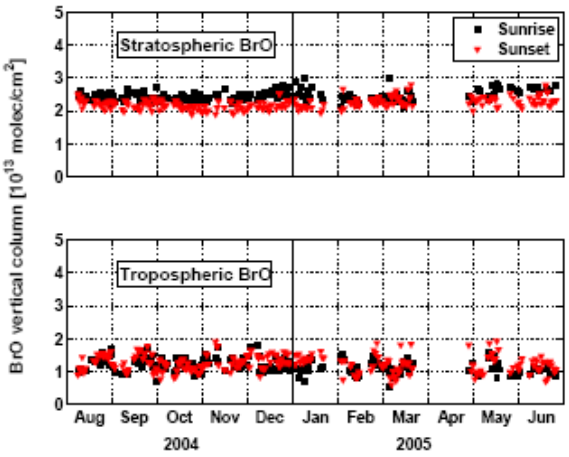

Fig. 11. Time-series of stratospheric (top) and tropospheric (bottom) BrO columns retrieved for 80° SZA, displayed separately for sunrise (squares) and sunset (triangles).

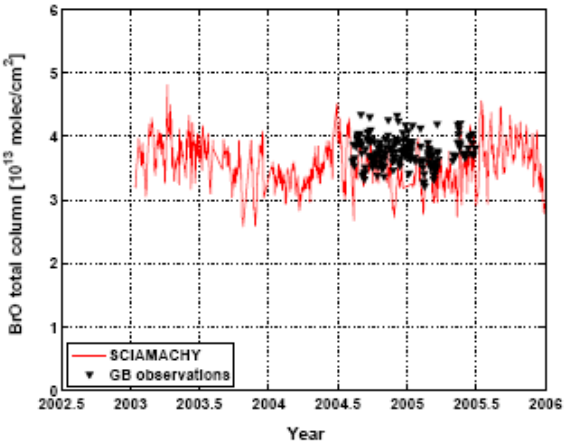

Fig. 12. Total BrO columns retrieved from ground-based DOAS observations at Reunion-Island and from SCIAMACHY nadir observations averaged in a zonal band of 10 degrees centered at the latitude of the ground-based station.

cover a complete annual cycle. Longer observational time series would certainly help characterizing better the seasonal variations.

The seasonal photochemical response of stratospheric BrO to changes in NO_2 concentration can in fact be studied with larger sensitivity when considering twilight observations above 80° SZA. To this aim, comparisons of modeled and measured BrO 90–80° differential slant columns were performed. Under these conditions, results show that both simulations and measurements present a significant seasonal cycle which follows the expected anti-correlation with NO_2, i.e. a minimum in summer and a maximum in winter. The observations also reproduces the diurnal cycle well, with PM values larger than AM ones, as reported in other studies (Sinnhuber et al., 2002; Fietkau et al., 2007).

4.6 Comparison with SCIAMACHY total column BrO observations

Onboard the ENVISAT platform, the SCanning Imaging Absorption spectroMeter for Atmospheric CHartographY (SCIAMACHY) measures the sunlight reflected, backscattered or transmitted by the Earth's atmosphere in the ultraviolet, visible and near-infrared spectral regions (Bovensmann et al., 1999). Among other geophysical data products, the vertical column of BrO can be derived from SCIAMACHY nadir measurements, using DOAS algorithms similar to those applied to ground-based measurements reported here. Prior to SCIAMACHY, BrO columns were also measured by the GOME instrument onboard ERS-2. However the diffuser plate used for irradiance measurements on the GOME instrument exhibits a time dependent interference pattern, which correlates with BrO and prevents reliable independent BrO column measurements to be obtained with this instrument, therefore making it unsuitable for an assessment of the tropical BrO content (e.g. Richter et al., 2002). To overcome this problem, SCIAMACHY was equipped with a quasi-volume diffuser plate on the back of its azimuth scan mirror (ASM) with the aim to provide irradiance measurements suitable for minor trace gases retrievals. SCIAMACHY BrO columns used in this work were analysed using daily sun irradiance from the ASM diffuser plate, according to retrieval settings described in Van Roozendael et al. (2004). To optimize the consistency with ground-based retrieval, SCIAMACHY BrO vertical columns were evaluated using AMFs calculated according to the BrO vertical distribution retrieved at Reunion Island.

Figure 12 presents the comparison between SCIAMACHY BrO vertical columns extracted from daily fields in a latitude zone of +/− 5 degrees around Reunion Island and the ground-based BrO total vertical columns, photochemically adjusted at the time of the satellite overpass using the BrO diurnal variation determined in Sect. 4.3. Considering the uncertainties on both satellite and ground-based BrO measurements, the agreement obtained is highly satisfying. Since the ground-based and satellite total column analysis are essentially independent from each other (the dependency of the satellite nadir AMF on the shape of the BrO profile being in practice very small), these results consolidate our confidence in both ground-based and satellite estimates of the tropical BrO column. They also indirectly consolidate our estimate of the tropospheric BrO column, which as already stated represents a significant part (one third) of the total BrO column.

5 Conclusions

Tropospheric and stratospheric BrO columns were derived using a new double-column inversion method, accounting for the transfer of the radiation in the atmosphere and the BrO diurnal variation. This was applied to combined zenith-sky and off-axis ground-based UV-visible spectroscopic measurements at Reunion Island. Tropospheric BrO columns of $1.1\pm0.5\times10^{13}$ molec/cm^2 were retrieved, generally in agreement with estimations sparsely available from the literature. Sensitivity tests demonstrate a substantial contribution from the free-troposphere (around 6 km altitude) to the tropospheric BrO vertical column, however our observations do not support the existence of significant amounts of BrO in the tropical boundary layer. These results are in agreement with recent studies suggesting that tropical biogenic sources of short-lived organic bromine species might be converted into active bromine in the free-troposphere by mechanisms involving heterogeneous reactions possibly on ice crystals and water droplets (Fitzenberger et al., 2000).

The retrieved stratospheric columns show a diurnal variation coherent with photochemical model calculations based on recently updated rates. From a comparison between the retrieved stratospheric BrO columns and results from the 3-D chemical-transport model SLIMCAT, one concludes that a satisfactory agreement can only be achieved by assuming an important delivery of Br_y (of about 6–8 pptv) in the stratosphere possibly produced by short-lived bromine organic compounds, rapidly converted into inorganic forms at the tropical tropopause. Based on the inversion of the stratospheric BrO profile according to Hendrick et al. (2007), a total stratospheric inorganic bromine content of about 23 pptv is inferred, which further strengthens the likely importance of short-lived bromine species as an important contribution to the Br_y budget. Total BrO columns are found to be in agreement with SCIAMACHY observations in a latitudinal band centered around Reunion Island. These results consolidate our confidence in both ground-based and satellite estimates of the tropical BrO columns.

Acknowledgements. The authors wish to thank J.-P. Decuyper (technical support at BIRA), J.-M. Metzger (technical support at Reunion Island), M. Chipperfield (for providing us with SLIMCAT data), A. Richter and F. Wittrock (for providing us with a Windows version of SCIATRAN). The balloon flights in 2004 in Brazil were part of the EC FP5 HIBISCUS project (EVK2-2001-000111). This research was financially supported by the EC FP6 SCOUT-O3 (505390-GOCE-CT-2004), AGACC projects and the Belgium Prodex NOy-Bry projects.

Edited by: T. Wagner

References

Aliwell, S. R., Van Roozendael, M., Johnston, P. V., Richter, A., Wagner, T., et al.: Analysis for BrO in zenith-sky spectra: An intercomparison exercise for analysis improvement, J. Geophys. Res., 107, D140, doi:10.1029/2001JD000329, 2002.

Anderson, G. P., Clough, S. A., Kneizys, F. X., Chetwynd, J. H., and Shettle, E. P.: AFGL atmospheric constituent profiles (0–120 km), Tech. Rep. AFGL-TR-86-0110, Air Force Geophys. Lab., Hascom Air Force Base, Mass., 1986.

Arpag, K. H., Johnston, P. V., Miller, H. L., Sander, R. W., and Solomon, S.: Observations of stratospheric BrO column over Colorado, 40° N, J. Geophys. Res., 99, 8175–8181, 1994.

Bobrowski, N., Höninger, G., Galle, B., and Platt, U.: Detection of bromine monoxide in a volcanic plume, Nature, 423, 273–276, 2003.

Bogumil, K., Orphal, J., Homann, T., Voigt, S., Spietz, P., Fleischmann, O. C., Vogel, A., Hartmann, M., Bovensmann, H., Frerik, J., and Burrows, J. P.: Measurements of molecular absorption spectra with the SCIAMACHY Pre-Flight Model: Instrument characterization and reference spectra for atmospheric remote sensing in the 230–2380 nm region, J. Photochem. Photobiol. A, 157, 167–184, 2003.

Bovensmann, H., Burrows, J. P., Buchwitz, M., Frerick, J., Noël, S., Rozanov, V. V., Chance, K. V., and Goede, A. P. H.: SCIAMACHY: Mission objectives and Measurement Modes, J. Atmos. Sci., 56, 127–150, 1999.

Carpenter, L. J. and Liss, P. S.: On temperature sources of bromoform and other reactive organic bromine gases, J. Geophys. Res. D., 105(D16), 20 539–20 547, 2000.

Chipperfield, M. P.: Multiannual simulations with a three-dimensional chemical transport model, J. Geophys. Res., 104(D1), 1781–1805, 1999.

Chipperfield, M. P.: New Version of the TOMCAT/SLIMCAT Off-Line Chemical Transport Model: Intercomparison of Stratospheric Tracer Experiments, Q. J. Roy. Meteor. Soc., 132, 1179–1203, doi:10.1256/qj.05.51, 2006.

Dorf, M., Bösch, H., Butz, A., Camy-Peyret, C., Chipperfield, M., Engel, A., Goutail,F., Grunow, K., Hendrick, F., Hrechanyy, S., Naujokat, B., Pommereau, J.-P., Van Roozendael, M., Sioris, C., Stroh, F., Weidner, F., and Pfeilsticker, K.: Balloon-borne stratospheric BrO measurements: Intercomparisons with ENVISAT/SCIAMACHY BrO limb profiles, Atmos. Chem. Phys., 6, 2483–2501, 2006a.

Dorf, M., Butler, J. H., Butz, A., Camy-Peyret, C., Chipperfield, M. P., Kritten, L., Montzka, S. A., Simmes, B., Weidner, F., and Pfeilsticker, K.: Long-term observations of stratospheric bromine reveal slow down in growth, Geophys. Res. Lett., 33, L24803, doi:10.1029/2006GL027714, 2006b.

Errera, Q. and Fonteyn, D.: Four-dimensional variational chemical assimilation of CRISTA stratospheric measurements, J. Geophys. Res., 106(D11), 12 253–12 265, 2001.

Feng, W., Chipperfield, M. P., Dorf, M., Pfeilsticker, K., and Ricaud, P.: Mid-latitude ozone changes: studies with a 3-D CTM forced by ERA-40 analyses, Atmos. Chem. Phys., 7, 2357–2369, 2007, http://www.atmos-chem-phys.net/7/2357/2007/.

Fietkau, S., Medeke, T., Richter, A., Sheode, N., Simnhuber, B.-M., Wittrock, F., Theys, N., Van Roozendael, M., and Burrows, J. P.: Ground-based measurements of tropospheric and stratospheric

bromine monoxide above Nairobi (1° S, 36° E), Atmos. Chem. Phys. Discuss., 7, 6527–6555, 2007, http://www.atmos-chem-phys-discuss.net/7/6527/2007/.

Fish, D. J., Jones, R. L., and Strong, E. K.: Mid-latitude observations of the diurnal variation of stratospheric BrO, J. Geophys. Res., 100, 18 863–18 871, 1995.

Fitzenberger, R., Bösch, R., Camy-Peyret, C., Chipperfiel, M. P., Harder, H., Platt, U., Sinnhuber, B.-M., Wagner, T., and Pfeilsticker, K.: First profile measurements of tropospheric BrO, Geophys. Res. Lett., 27, 2921–2924, 2000.

Frieß, U., Hollwedel, J., König-Langlo, G., Wagner, T., and Platt, U.: Dynamics and chemistry of tropospheric bromine explosion events in the Antarctic coastal region, J. Geophys. Res., 109, D06305, doi:10.1029/2003JD004133, 2004.

Frieß, U., Monks, P. S., Remedios, J. J., Rozanov, A., Sinreich, R., Wagner, T., and Platt, U.: MAX-DOAS O_4 measurements: A new technique to derive information on atmospheric aerosols: 2. Modeling studies, J. Geophys. Res., 111, D14203, doi:10.1029/2005JD006618, 2006.

Grainger, J. F. and Ring, J.: Anomalous Fraunhofer line profiles, Nature, 193, 762, 1962.

Greenblatt, G. D., Orlando, J. J., Burkholder, J. B., and Ravishankara, A. R.: Absorption measurements of oxygen between 330 and 1140 nm, J. Geophys. Res., 95, 18 577–18 582, 1990.

Hausmann, M. and Platt, U.: Spectroscopic measurement of bromine oxide and ozone in the high Arctic during Polar Sunrise Experiment 1992, J. Geophys. Res., 99, 25 399–25 414, 1994.

Hebestreit, K., Stutz, J., Rosen, D., Matveiv, V., Peleg, M., Luria, M., and Platt, U.: DOAS measurements of tropospheric bromine oxide in mid-latitudes, Science, 283, 55–57, 1999.

Heckel, A., Richter, A., Tarsu, T., Wittrock, F., Hak, C., Pundt, I., Junkermann, and Burrows, J. P.: MAX-DOAS measurements of formaldehyde in the Po-Valley, Atmos. Chem. Phys., 5, 909–918, 2005, http://www.atmos-chem-phys.net/5/909/2005/.

Hendrick, F., Barret, B., Van Roozendael, M., Boesch, H., Butz, A., De Mazière, M., Goutail, F., Hermans, C., Lambert, J.-C., Pfeilsticker, K., and Pommereau, J.-P.: Retrieval of nitrogen dioxide stratospheric profiles from ground-based zenith-sky UV-visible observations: validation of the technique through correlative comparisons, Atmos. Chem. Phys., 4, 2091–2106, 2004, http://www.atmos-chem-phys.net/4/2091/2004/.

Hendrick, F., Van Roozendael, M., Kylling, A., Petritoli, A., Rozanov, A., Sanghavi, S., Schofield, R., von Friedeburg, C., Wagner, T., Wittrock, F., Fonteyn. D., and De Mazière, M.: Intercomparison exercise between different radiative transfer models used for the interpretation of ground-based zenith-sky and multi-axis DOAS observations, Atmos. Chem. Phys., 6, 93–108, 2006, http://www.atmos-chem-phys.net/6/93/2006/.

Hendrick, F., Van Roozendael, M., Chipperfield, M. P., Dorf, M., Goutail, F., Yang, X., Fayt, C., Hermans, C., Pfeilsticker, K., Pommereau, J.-P., Pyle, J. A., Theys, N., and De Mazière, M.: Retrieval of stratospheric and tropospheric BrO profiles and columns using ground-based zenith-sky DOAS observations at Harestua, 60° N, Atmos. Chem. Phys. Discuss., 7, 8663–8708, 2007, http://www.atmos-chem-phys-discuss.net/7/8663/2007/.

Hönninger, G. and Platt, U.: Observations of BrO and its vertical distribution during surface ozone depletion at Alert, Atmos. Environ., 36, 2481–2489, 2002.

Koelemeijer, R. B. A., de Haan, J. F., and Stammes, P.: A database of spectral surface reflectivity in the range 335–772 nm derived from 5.5 years of GOME observations, J. Geophys. Res.-Atm., 108(D2), 4070, doi:10.1029/2002JD002429, 2003.

Kreher, K., Johnston, P. V., Wood, S. W., Nardi, B., and Platt, U.: Ground-based measurements of tropospheric and stratospheric BrO at Arrival Heights, Antartica, Geophys. Res. Lett., 24, 3021–3024, 1997.

Kurucz, R. L., Furenlid, I., Brault, J., and Testerman, L.: Solar flux atlas from 296 nm to 1300 nm, National Solar Observatory Atlas No. 1, 1984.

Lary, D. J.: Gas phase atmospheric bromine photochemistry, J. Geophys. Res., 101, 1505–1516, 1996a.

Lary, D. J., Chipperfield, M. P., Toumi, R., and Lenton, T.: Heterogeneous atmospheric bromine photochemistry, J. Geophys. Res., 101, 1489–1504, 1996b.

Lary, D. J.: Halogens and the chemistry of the free troposphere, Atmos. Chem. Phys., 5, 227–237, 2005, http://www.atmos-chem-phys.net/5/227/2005/.

Leser, H., Höninger, G., and Platt, U.: Max-DOAS measurements of BrO and NO_2 in the marine boundary layer, Geophys. Res. Lett., 30, 1537, doi:10.1029/2002GL015811, 2003.

Mayer, B. and Kylling, A.: Technical note: The libRadtran software package for radiative transfer calculations – description and examples of use, Atmos. Chem. Phys., 5, 1855–1877, 2005, http://www.atmos-chem-phys.net/5/1855/2005/.

Meller, R. and Moortgat, G. K.: Temperature dependence of the absorption cross-sections of formaldehyde between 223 and 323 K in the wavelength range 225–375 nm, J. Geophys. Res., 105, 7089–7101, 2000.

Middleton, W. E. K.: Vision through the Atmosphere, Univ. of Toronto Press, Toronto, 1952.

Platt, U.: Differential optical absorption spectroscopy (DOAS), Air Monit. By Spectr. Techniques, edited by: Sigrist, M. W., Chemical Analysis Series, 127, 27–84, John Wiley & Sons, Inc., 1994.

Pfeilsticker, K., Sturges, W. T., Bösch, H., Camy-Peyret, C., Chipperfield, M. P., Engel, A., Fitzenberger, R., Müller, M., Payan, S., and Sinnhuber, B.-M.: Lower stratospheric organic and inorganic bromine budget for the arctic winter 1998/99, Geophys. Res. Lett., 27, 3305–3308, 2000.

Preston, K. E., Jones, R. L., and Roscoe, H. K.: Retrieval of NO_2 profiles from ground-based UV-visible measurements – method and validation, J. Geophys. Res., 102, 19 089–19 097, 1997.

Pundt, I., Van Roozendael, M., Wagner, T., Richter, A., Chipperfield, M., Burrows, J. P., Fayt, C., Hendrick, F., Pfeilsticker, K., Platt, U., and Pommereau, J.-P.: Simultaneous UV-vis measurementsof BrO from balloon, satellite and ground: implications for tropospheric BrO, in Proc. Fifth European Symp. on polar stratospheric ozone 1999, Air Poll. Res. Report 73, EUR 19340, European Commission, Brussels, Belgium, edited by: Harris, N. R. P., Guirlet, M., and Amanatidis, G. T., p. 316–319, 2000.

Pundt, I., Pommereau, J.-P., Chipperfield, M. P., Van Roozendael, M., and Goutail, F.: Climatology of the stratospheric BrO vertical distribution by balloon-borne UV-visible spectrometry, J. Geophys. Res., 107(D24), 4806, doi:10.1029/2002JD002230, 2002.

Richter, A., Wittrock, F., Eisinger, M., and Burrows, J. P.: GOME observations of tropospheric BrO in Northern Hemi-

spheric spring and summer 1997, Geophys. Res. Lett., 25, 2683–2686, 1998.
Richter, A., Eisinger, M., Ladstätter-Weissenmayer, A., and Burrows, J. P.: DOAS zenith-sky observations, 2, seasonal variation of BrO over Bremen (53° N) 1994–1995, J. Atmos. Chem., 32, 83–99, 1999.
Richter, A., Wittrock, F., Ladstätter-Weissenmayer, A., and Burrows, J. P.: GOME measurements of stratospheric and tropospheric BrO, Adv. Space Res., 29, 1667–1672, 2002.
Rodgers, C. D.: Inverse Methods for Atmospheric Sounding, Theory and Practice, World Scientific Publishing, Singapore-New-Jersey-London-Hong Kong, 2000.
Rozanov, A., Rozanov, V., and Burrows, J. P.: A numerical radiative transfer model for a spherical planetary atmosphere: Combined differential integral approach involving the Piccard iterative approximation, J. Quant. Spectrosc. Radiat. Trans., 69, 491–512, 2001.
Salawitch, R. J., Weisenstein, D. K., Kovalenko, L. J., Sioris, C. E., Wennberg, P. O., Chance, K., Ko, M. K. W., and McLinden, C. A.: Sensitivity of ozone to bromine in the lower stratosphere, Geophys. Res. Lett., 32, L05811, doi:10.1029/2004GL021504, 2005.
Salawitch, R. J.: Atmospheric chemistry: biogenic bromine, Nature, 439, 275–277, 2006.
Sander, S. P., Friedl, R. R., Ravishankara, A. R., et al.: Chemical Kinetics and Photochemical Data for Use in Atmospheric Studies, Evaluation no. 15, NASA JPL Publication no. 06-2, 2006.
Schofield, R., Kreher, K., Connor, B. J., Johnston, P. V., Thomas, A., Shooter, D., Chipperfield, M. P., Rodgers, C. D., and Mount, G. H.: Retrieved tropospheric and stratospheric BrO columns over Lauder, New Zealand., J. Geophys. Res., 109, D14304, doi:10.1029/2003JD004463, 2004a.
Schofield, R., Connor, B. J., R., Kreher, K., Johnston, P. V., and Rodgers, C. D.: The retrieval of profile and chemical information from ground-based UV-visible spectroscopic measurements, J. Quant. Spectrosc. Radiat. Trans., 86, 115–131, 2004b.
Schofield, R., Johnston, P. V., Thomas, A., Kreher, K., Connor, B. J., Wood, S., Shooter, D., Chipperfield, M. P., Richter, A., von Glasow, R., and Rodgers, C. D.: Tropospheric and stratospheric BrO columns over Arrival Heights, Antartica, 2002, J. Geophys. Res., 111, D22310, doi:10.1029/2005JD007022, 2006.
Simpson, W. R., von Glasow, R., Riedel, K., Anderson, P., Ariya, P., Bottenheim, J., Burrows, J., Carpenter, L., Frieß, U., Goodsite, M. E., Heard, D., Hutterli, M., Jacobi, H.-W., Kaleschke, L., Neff, B., Plane, J., Platt, U., Richter, A., Roscoe, H., Sander, R., Shepson, P., Sodeau, J., Steffen, A., Wagner, T., and Wolff, E.: Halogens and their role in polar boundary-layer ozone depletion, Atmos. Chem. Phys., 7, 4375–4418, 2007, http://www.atmos-chem-phys.net/7/4375/2007/.
Sinnhuber, B.-M., Arlander, D. W., Bovensmann, H., et al.: Comparison of measurements and model calculations of stratospheric bromine monoxide, J. Geophys. Res., 107(D19), 4398, doi:10.1029//2001JD000940, 2002.
Sinnhuber, B.-M., Rozanov, A., Sheode, N., Afe, O. T., Richter, A., Sinnhuber, M., Wittrock, F., and Burrows, J. P.: Global observations of stratospheric bromine monoxide from SCIAMACHY, Geophys. Res. Lett., 32, L20810, doi:10.1029/2005GL023839, 2005.
Sioris, C. E., Kovalenko, L. J., McLinden, C. A., Salawitch, R. J., Van Roozendael, M., Goutail, F., Dorf, M., Pfeilsticker, K., Chance, K., von Savigny, C., Liu, X., Kurosu, T. P., Pommereau, J.-P., Bösch, H., and Frerick, J.: Latitudinal and vertical distribution of bromine monoxide in the lower stratosphere from Scanning Imaging Absorption Spectrometer for Atomspheric Chartography limb scattering measurements, J. Geophys. Res., 111, D14301, doi:10.1029/2005JD006479, 2006.
Vandaele, A.-C., Hermans, C., Simon, P. C., Carleer, M., Colin, R., Fally, S., Mérienne, M.-F., Jenouvrier, A., and Coquart, B.: Measurements of the NO2 absorption cross-section from 42 000 cm^{-1} to 10 000 cm^{-1} (238–1000 nm) at 220 K and 294 K, J. Quant. Spectrosc. Radiat. Trans., 59, 171–184, 1997.
Van Roozendael, M., Fayt, C., Lambert, J.-C., Pundt, I., Wagner, T., Richter, A., and Chance, K.: Development of a bromine oxide product from GOME, European Symposium on Atmosph. Measurements from Space, ESA WPP-161, 543–547, 1999.
Van Roozendael, M., Wagner, T., Richter, A., Pundt, I., Arlander, D., Burrows, J. P., Chipperfield, M., Fayt, C., Johnston, P. V., Lambert, J.-C., Kreher, K., Pfeilsticker, K., Platt, U., Pommereau, J.-P., Sinnhuber, B.-M., Tornkvist, K. K., and Wittrock, F.: Intercomparison of BrO measurements from ERS-2 GOME, ground-based and balloon platforms, Adv. Space Res., 29, 1661–1666, 2002.
Van Roozendael, M., De Smedt, I., Fayt, C., Wittrock, F., Richter, A., and Afe, O.: First validation of SCIAMACHY BrO columns, in Proc. Second Workshop on the Atmospheric Chemistry Validation of ENVISAT (ACVE-2), Frascati, Italy, 3–7 May 2004.
von Glasow, R., von Kuhlmann, R., Lawrence, M. G., Platt, U., and Crutzen, P. J.: Impact of reactive bromine chemistry in the troposphere, Atmos. Chem. Phys., 4, 2481–2497, 2004, http://www.atmos-chem-phys.net/4/2481/2004/.
Vountas, M., Rozanov, V. V., and Burrows, J. P.: Ring effect: Impact of rotational raman scattering on radiative transfer in earth's atmosphere, J. Quant. Spectrosc. Radiat. Trans., 60, 943–961, 1998.
Wagner, T. and Platt, U.: Satellite mapping of enhanced BrO concentrations in the troposphere, Nature, 395, 486–490, 1998.
Wagner, T., Dix, D., von Friedeburg, C., Friess, U., Sanghavi, S., Sinreich, R., and Platt, U.: MAX-DOAS O_4 measurements: A new technique to derive information an atmospheric aerosols-Principles and information content, J. Geophys. Res., 109, D22205, doi:10.1029/2004JD004904, 2004.
Wamsley, P. R., Elkins, J. W., Fahey, D. W., Dutton, G. S., Volk, C. M., Myers, R. C., Montzka, S. A., Butler, J. H., Clarke, A. D., Fraser, P. J., Steele, L. P., Lucarelli, M. P., Atlas, E. L., Schauffler, S. M., Blake, D. R., Rowland, F. S., Sturges, W. T., Lee, J. M., Penkett, S. A., Engel, A., Stimpfle, R. M., Chan, K. R., Weisenstein, D. K., Ko, M. K. W., and Salawitch, R. J.: Distribution of halon-1211 in the upper troposphere and lower stratosphere and the 1994 total bromine budget, J. Geophys. Res., 103(D1), 1513–1526, 1998.
WMO: Global ozone research and monitoring project, in: Scientific Assessment of Ozone Depletion: 1998, Rep. 44, Geneva, 1998.
WMO: Global ozone research and monitoring project, in: Scientific Assessment of Ozone Depletion: 2002, Rep. 47, Geneva, 2003.
Wilmouth, D. M., Hanisco, T. F., Donahue, N. M., and Anderson, J. G.: Fourier transform ultraviolet spectroscopy of the $A^2\Pi_{3/2} \leftarrow X^2\Pi_{3/2}$ transition of BrO, J. Phys. Chem. A., 103, 8935–8945, 1999.

Wittrock, F., Oetjen, H., Richter, A., Fietkau, S., Medeke, T., Rozanov, A., and Burrows, J. P.: Max-DOAS measurements of atmospheric trace gases in Ny-Ålesund – Radiative transfer studies and their application, Atmos. Chem. Phys., 4, 955–966, 2004, http://www.atmos-chem-phys.net/4/955/2004/.

Yang, X., Cox, R. A., Warwick, N. J., Pyle, J. A., Carver, G. D., O'Connor, F. M., and Savage, N. H.: Tropospheric bromine chemistry and its impact on ozone: A model study, J., Geophys. Res., 110, D23311, doi:10.1029/2005JD006244, 2005.

1.2.6 Observations FTIR à la Réunion : campagnes 2002 et 2004

Atmos. Chem. Phys., 8, 3483–3508, 2008
www.atmos-chem-phys.net/8/3483/2008/

Atmospheric Chemistry and Physics

Technical Note: New ground-based FTIR measurements at Ile de La Réunion: observations, error analysis, and comparisons with independent data

C. Senten[1], M. De Mazière[1], B. Dils[1], C. Hermans[1], M. Kruglanski[1], E. Neefs[1], F. Scolas[1], A. C. Vandaele[1], G. Vanhaelewyn[1], C. Vigouroux[1], M. Carleer[2], P. F. Coheur[2], S. Fally[2], B. Barret[3,*], J. L. Baray[4], R. Delmas[4], J. Leveau[4], J. M. Metzger[4], E. Mahieu[5], C. Boone[6], K. A. Walker[6,7], P. F. Bernath[6,8], and K. Strong[7]

[1]Belgian Institute for Space Aeronomy (BIRA-IASB), Brussels, Belgium
[2]Service de Chimie Quantique et Photophysique (SCQP), Université Libre de Bruxelles (ULB), Brussels, Belgium
[3]formerly at: BIRA-IASB and SCQP/ULB
[4]Laboratoire de l'Atmosphère et des Cyclones (LACy), Université de La Réunion, France
[5]Institute of Astrophysics and Geophysics, University of Liège, Liège, Belgium
[6]Department of Chemistry, University of Waterloo, Waterloo, Ontario, Canada
[7]Department of Physics, University of Toronto, Toronto, Ontario, Canada
[8]Department of Chemistry, University of York, Heslington, York, UK
[*]now at: Institut d'Aérologie, Toulouse, France

Received: 1 November 2007 – Published in Atmos. Chem. Phys. Discuss.: 17 January 2008
Revised: 23 April 2008 – Accepted: 20 May 2008 – Published: 2 July 2008

Abstract. Ground-based high spectral resolution Fourier-transform infrared (FTIR) solar absorption spectroscopy is a powerful remote sensing technique to obtain information on the total column abundances and on the vertical distribution of various constituents in the atmosphere. This work presents results from two FTIR measurement campaigns in 2002 and 2004, held at Ile de La Réunion (21° S, 55° E). These campaigns represent the first FTIR observations carried out at a southern (sub)tropical site. They serve the initiation of regular, long-term FTIR monitoring at this site in the near future. To demonstrate the capabilities of the FTIR measurements at this location for tropospheric and stratospheric monitoring, a detailed report is given on the retrieval strategy, information content and corresponding full error budget evaluation for ozone (O_3), methane (CH_4), nitrous oxide (N_2O), carbon monoxide (CO), ethane (C_2H_6), hydrogen chloride (HCl), hydrogen fluoride (HF) and nitric acid (HNO_3) total and partial column retrievals. Moreover, we have made a thorough comparison of the capabilities at sea level altitude (St.-Denis) and at 2200 m a.s.l. (Maïdo). It is proved that the performances of the technique are such that the atmospheric variability can be observed, at both locations and in distinct altitude layers. Comparisons with literature and with correlative data from ozone sonde and satellite (i.e., ACE-FTS, HALOE and MOPITT) measurements are given to confirm the results. Despite the short time series available at present, we have been able to detect the seasonal variation of CO in the biomass burning season, as well as the impact of particular biomass burning events in Africa and Madagascar on the atmospheric composition above Ile de La Réunion. We also show that differential measurements between St.-Denis and Maïdo provide useful information about the concentrations in the boundary layer.

Correspondence to: C. Senten
(cindy.senten@aeronomie.be)

1 Introduction

The Network for the Detection of Atmospheric Composition Change[1] (NDACC, http://www.ndacc.org/) is a worldwide network of observatories, for which primary objectives are to monitor the evolution of the atmospheric composition and structure, and to provide independent data for the validation of numerical models of the atmosphere and of satellite data. NDACC also supports field campaigns focusing on specific processes at various latitudes and seasons. Only

[1]This was formerly called the Network for the Detection of Stratospheric Change or NDSC.

Published by Copernicus Publications on behalf of the European Geosciences Union.

a few stations in NDACC are situated in the tropical and subtropical belts. In particular, there are not yet any long-term Fourier transform infrared (FTIR) measurements in the Southern Hemisphere tropics. The only tropical NDACC stations at which FTIR measurements are performed are Mauna Loa (19.54° N, 155.6° W) and Paramaribo (5.8° N, 55.2° W), both in the Northern Hemisphere. The former one is at high altitude (3459 m a.s.l.), and at the latter one, the measurements are performed on a campaign basis, since September 2004 only (Petersen et al., 2008). Therefore, we have chosen the Observatoire de Physique de l'Atmosphère de La Réunion (OPAR) to initiate such measurements. The OPAR is located at 21° S, 55° E, in the Indian Ocean, East of Madagascar, at the edge between the southern tropics and subtropics. It is a measurement station led by the Laboratoire de l'Atmosphère et des Cyclones (LACy) of the Université de La Réunion, that performs radio sonde observations since 1992, SAOZ measurements since 1993 and lidar measurements since 1994 (Baray et al., 2006). The implementation of FTIR solar absorption measurements at this site, providing information about the total column abundances and vertical distributions of a large number of atmospheric constituents (e.g., Brown et al., 1992), will therefore be a useful complement to the station's observations, and will fill the gap in the Southern Hemisphere tropical region.

In this paper, we present results from the first two FTIR campaigns that we performed at Ile de La Réunion, in 2002 and 2004, to verify the feasibility of FTIR measurements at a tropical site and to start the long-term monitoring. Knowing that water vapour is a strong absorber in the infrared and that there is a larger humidity at tropical sites than at mid- and high-latitude sites, especially at low altitude, it is important to characterize the capabilities of FTIR monitoring at a tropical location. During the first campaign we have made simultaneous measurements at two locations with an altitude difference of about 2.2 km, to compare the observation characteristics at these two altitudes. This campaign has also allowed us to make some differential measurements, characterizing the boundary layer. The second campaign was made at the lowest altitude site, to initiate the long-term measurements and to contribute to satellite validation, in particular of the Atmospheric Chemistry Experiment – Fourier Transform Spectrometer (ACE-FTS), onboard the Canadian satellite SCISAT-1 (http://www.ace.uwaterloo.ca).

The results presented here concern a number of species that have been selected for three main reasons: their important roles in tropospheric or stratospheric chemistry, their link to current environmental problems like climate change or stratospheric ozone depletion, and the fact that they are needed for satellite validation. More specifically, our analyses focus on the primary greenhouse gases CH_4, N_2O and O_3, on the secondary greenhouse gases CO and C_2H_6, and on HCl, HF and HNO_3. Apart from their indirect effect on climate change, CO and C_2H_6 play a central role in tropospheric chemistry through their reactions with the hydroxyl radical OH (Brasseur and Solomon, 1984). They are emitted primarily by anthropogenic sources, and they can be used as tracers of tropospheric pollution and transport (e.g., transport of emissions from biomass burning), because they have relatively high tropospheric abundances and long tropospheric lifetimes.

In the stratosphere, HCl has a non-negligible impact on the ozone budget, acting as a reservoir species for chlorine. HF is a useful tracer of vertical transport, and of the anthropogenic emissions of fluorinated compounds.

HNO_3 is formed in the reaction of OH with NO_2 and plays an essential role as a reservoir molecule for both the NO_x (nitrogen oxides) and HO_x (hydrogen oxides) radicals, which are potentially active contributors to the ozone destruction in the stratosphere through catalytic reactions.

The results cover only short time periods, but their comparison with literature data and with correlative measurements shown in the paper, demonstrate the potential of these measurements at Ile de La Réunion. In particular, we show that the location of the site East of Africa and Madagascar offers interesting opportunities to observe transport of biomass burning emissions.

Sections 2, 3 and 4 describe the campaign characteristics, the retrieval method and the optimal retrieval parameters for every selected molecule individually. Section 5 presents the associated error budget calculations, together with a discussion of the resulting error estimations. Section 6 discusses the FTIR data as well as comparisons with correlative data. Conclusions and future plans are given in Sect. 7.

2 Specifications of the FTIR measurement campaigns

During the first FTIR solar absorption measurement campaign at Ile de La Réunion, in October 2002, two almost identical instruments, i.e., mobile Bruker 120M Fourier transform spectrometers, were operated in parallel at two different locations. The one belonging to the Belgian Institute for Space Aeronomy (BIRA-IASB) was installed on the summit of the mount Maïdo (2203 m a.s.l., 21° 04′S and 55° 23′E), and the one from the Université Libre de Bruxelles (ULB) at the nearby St.-Denis University campus (50 m a.s.l., 20° 54′S and 55° 29′E).

The BIRA-IASB instrument was placed in an air-conditioned container, and the electricity was provided with a power generator located south of the container. The solar tracker (purchased from Bruker) was mounted on a mast attached to the wall of the container, and the solar beam entered the container through a hole in that wall. The ULB instrument was installed in a laboratory of the university. Its solar tracker (also purchased from Bruker) was attached to the edge of the roof of the laboratory and the solar beam entered the room through a side-window.

During the second campaign, from August to October 2004, we limited ourselves to one instrument from

BIRA-IASB at St.-Denis only. The instrument was installed in the same container as in 2002, now put on the roof of a university building, with electricity provided by the university network. A different solar tracker was used, built at the University of Denver and modified at BIRA-IASB (Hawat et al., 2003; Neefs et al., 2007). In 2002 as well as in 2004, a second mast was used to carry a small meteorological station that belongs to the BARCOS system. BARCOS is the Bruker Automation and Remote COntrol System developed at BIRA-IASB to operate the FTIR experiment in an automatic or remotely controlled way (Neefs et al., 2007). It has successfully been used during both campaigns with the BIRA-IASB instrument. The BARCOS system includes a meteorological station and a data logger to continuously monitor and log the local weather conditions as well as other housekeeping parameters, i.e., instrument and environment status. BARCOS executes a daily script that schedules and runs the measurements. It interrupts the observation schedule when the solar tracker is not capable of tracking the sun because of the presence of clouds, and it resumes the schedule once the sun re-appears. BARCOS automatically closes or opens the suntracker hatch when it starts or stops raining, respectively. Unfortunately, at the time of the campaigns, the automatic filling of the detector dewars with liquid nitrogen was not implemented yet, and hence it was not possible to operate the FTIR instrument without a person on site.

Both spectrometers allowed a maximum optical path difference (MOPD) of 250 cm, providing a maximum spectral resolution, defined as 0.9/MOPD, of 0.0036 cm^{-1}. Nevertheless, to record the solar absorption FTIR spectra, we have not always used the maximum spectral resolution. The actual resolution has been selected on the basis of the Doppler broadening of the lines and it has been lowered at high solar zenith angles, in order to reduce the measurement time. More specific information is given in Sect. 4. For all spectra, we have used a KBr beamsplitter in the interferometer, and one of six different optical bandpass filters in front of the detector, which is a nitrogen-cooled InSb (indium antimonide) or MCT (mercury cadmium telluride or HgCdTe) detector, according to the target spectral range. The optical filters are the ones used generally in the NDACC FTIR community. In particular, during the first campaign in 2002 we have used filters 1, 2, 3, 5 and 6, while during the second campaign in 2004 we have used filters 1, 2, 3, 4 and 6. So during the 2002 campaign the spectral region between 1400 and 2400 cm^{-1} has been covered using the MCT detector with the NDSC-5 filter (range 1350–2250 cm^{-1}). To improve the signal-to-noise ratio (SNR) in this spectral domain, during the 2004 campaign this region has been recorded with the InSb detector and the NDSC-4 filter (range 1850–2750 cm^{-1}). This change in measurement configuration has an impact on the quality of the CO data, as will be seen in Sect. 5.2.

The total spectral domain thus covered by our measurements spans the wavenumber range from 600 to 4300 cm^{-1}, in which it is possible to detect, among many other gases,

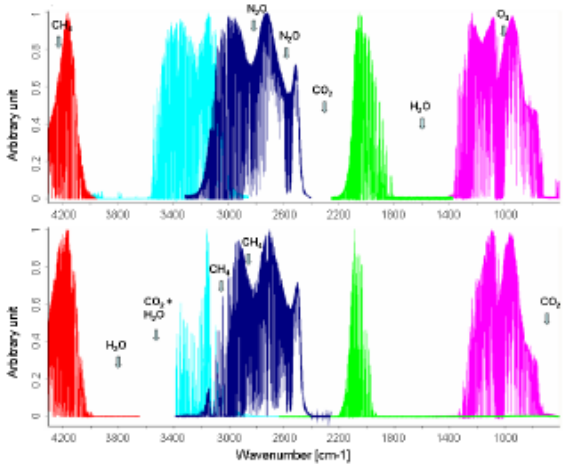

Fig. 1. Composite spectra for different bandpass filters (NDSC-1: red, NDSC-2: blue, NDSC-3: dark blue, NDSC-5: green, and NDSC-6: pink), taken at Maïdo (upper plot) and at St.-Denis (bottom plot) in 2002, for solar zenith angles between 40 and 50°.

the target species O_3, CH_4, N_2O, CO, C_2H_6, HCl, HF and HNO_3. Figure 1 shows composite spectra from the first campaign in 2002, at Maïdo and at St.-Denis, including the different optical bandpasses (shown in different colours). For this figure, we selected spectra that were recorded on corresponding days for both locations and at solar zenith angles between 40 and 50°. All spectra have been standardized to improve the visibility of the figure. Note that some of the main absorbers are marked. One clearly observes the reduced absorptions by water vapour at the high-altitude site Maïdo. For example, the spectral range between 3000 and 3550 cm^{-1}, that is completely opaque at St.-Denis, can be exploited at Maïdo.

Whenever the sky was clear at local noon, a reference HBr cell spectrum was recorded using the NDSC-4 filter. For this purpose, a cell containing hydrogen bromide (HBr) at low pressure (2 mbar) was placed in the interferometer output beam in front of the InSb detector, and a spectrum was recorded using the sun as light source. When this was not possible on several consecutive days because of the noon-time weather situation, the reference HBr cell spectrum was taken the same way, but using a tungsten lamp source. The cell spectra have been analysed using Linefit version 8 (Hase et al., 1999), to monitor the alignment of the instrument. For the ULB instrument at St.-Denis, a cell spectrum was taken only once during the first campaign; it confirmed the correct alignment of the instrument.

Because reliable solar absorption measurements require clear sky conditions, the number of observation days was limited: in total, we had about 24 days with observations during the first campaign and about 60 days during the second

campaign. Also, during the first campaign, it was often not possible to perform the measurements simultaneously at both sites, because the local weather conditions were not necessarily the same. It is worth mentioning that most of the measurements have been carried out before noon, because most often clouds appeared in the afternoon. Sometimes additional late evening measurements have been possible at Maïdo.

3 General description of the retrieval method

As already mentioned, we have focused on the retrieval of ozone (O_3), methane (CH_4), nitrous oxide (N_2O), carbon monoxide (CO), ethane (C_2H_6), hydrogen chloride (HCl), hydrogen fluoride (HF) and nitric acid (HNO_3). In addition to the total column abundances of these molecules, we have extracted information – whenever feasible – about their vertical distribution in the altitude range where the pressure broadening of the absorption lines can be resolved.

For these retrievals, we have used the inversion algorithm SFIT2 (v3.92), jointly developed at the NASA Langley Research Center, the National Center for Atmospheric Research (NCAR) and the National Institute of Water and Atmosphere Research (NIWA) at Lauder, New Zealand (Rinsland et al., 1998). This algorithm uses a semi-empirical implementation of the Optimal Estimation Method (OEM) of Rodgers (2000). Further details on the SFIT2 program can be found in the paper by Hase et al. (2004).

All retrievals are executed on a 44 layer altitude grid, starting at 50 m a.s.l. for St.-Denis and at 2200 m a.s.l. for Maïdo, with layer thicknesses of about 1.2 km in the troposphere and lower stratosphere up to 33.4 km altitude, then growing steadily to about 4 km around 50 km altitude and to about 8 km for the higher atmospheric layers up to 100 km. This choice was made to take into account the local atmospheric pressure and temperature variabilities. Daily pressure and temperature profiles were taken from the National Centre for Environmental Prediction (NCEP).

For the error analysis (see Sect. 5.1.4) we also used temperature profiles from the European Center for Medium range Weather Forecasting (ECMWF).

3.1 Forward model parameters

The forward model in SFIT2 is a multi-layer multi-species line-by-line radiative transfer model. The instrument parameters in the forward model include a wavenumber scale multiplier and background curve parameters, as well as the actual optical path difference (OPD) and field of view (FOV) of the instrument. The background slope and curvature are determined by fitting a polynomial of degree 2, and the wavelength shift is also fitted in every spectral micro-window independently.

To account for deviations from the ideal instrument line shape function (ILS) due to small instrument misalignments or imperfections, apodization and phase error functions are included. These functions can either be acquired from the Linefit analyses of the measured HBr cell spectra, or they can be approximated by a polynomial or a Fourier series of a user specified order. Our retrievals have been carried out using the second approach, i.e., fitted empirical apodization and phase error functions, because in all our retrievals this approach resulted in the smallest spectral residuals and the least oscillations in the retrieved profiles. In particular, we approximated the empirical apodization by a polynomial of degree 2 and, if beneficial, the empirical phase error by a polynomial of degree 1.

3.2 Inverse model

The inverse problem consists of determining the state of the atmosphere, in particular the vertical distributions of the target molecules, from the observed absorption spectra. In order to solve this ill-posed problem, the SFIT2 retrievals request ad hoc covariance matrices for the uncertainties associated with the a priori vertical profiles of the target gases and with the measurements. The retrieved profiles and total column amounts of the target species are the ones that provide the best representation of the truth, given the measurements and the a priori information, and their respective uncertainties.

3.2.1 A priori profile and associated covariance matrix

The used a priori profile $\mathbf{x}_a$ and its covariance matrix S_a should well represent a first guess of the 'true' state, in order to reasonably constrain the retrieval solution, in particular at those altitudes where one can hardly get information out of the measurements. For each target gas we have decided to use one single a priori profile and associated covariance matrix for both campaigns, to avoid any biases between the results and to make sure that the results are directly comparable. The diagonal and off-diagonal elements of each S_a have been chosen such as to yield the best compromise between the spectral residuals, the number of oscillations in the retrieved profiles, and the number of degrees of freedom for signal (DOFS; see Sect. 3.3). We have assumed that the correlations between the layers decay according to a Gaussian-shaped function. Details about the choice of the a priori vertical profiles and the associated covariance matrices are provided for each molecule individually in Sect. 4.2.

While we used constant values on the diagonal of S_a for the retrievals of all molecules, except CH_4, we used more realistic uncertainties in the error calculations. Nevertheless, the S_a matrices used in the error analysis still have a Gaussian shape because of the limited knowledge about their full structure.

3.2.2 Measurement noise covariance matrix

The retrieval covariance matrix associated with the measurements, S_ε, is considered to be diagonal, containing an ad hoc estimation of the squared reciprocals of the SNR of the observed spectra as diagonal elements.

Together with the a priori covariance matrix of the profiles, the measurement noise covariance matrix has a great influence on the retrieval characterization and error analysis.

3.2.3 Selection of spectral micro-windows

Deriving information about the vertical distribution of trace gases out of high resolution FTIR spectra is possible because of the pressure broadening of the absorption lines, leading to an altitude dependence of the line shapes. While the line centers provide information about the higher altitudes of the distribution, the wings of a line provide information about the lower altitudes. Therefore the information content of the retrieval will strongly depend on the choice of the absorption lines. For all species, the absorption line parameters were taken from the HITRAN 2004 spectral database (Rothman et al., 2005). In addition, updates for H_2O, N_2O, HNO_3 and C_2H_6 line parameters that are available on the HITRAN site (http://www.hitran.com) have been included. We have verified that they give similar or slightly better spectral fits than the original HITRAN 2004 values.

The retrieval spectral micro-windows are selected such that they contain unsaturated well-isolated absorption features of the target species with a minimal number of interfering absorption lines. One also aims at maximizing the amount of information present in the spectra, represented by the DOFS.

For the present retrievals, we adopted spectral micro-windows used by other FTIR research groups and we verified slight modifications of those micro-windows, in order to improve our retrievals.

Further details about the micro-window selections and characteristics are discussed in Sect. 4.1.

3.3 Information content and sensitivity

The retrieved state vector $\mathbf{x}_r$ is related to the a priori and the true state vectors $\mathbf{x}_a$ and $\mathbf{x}$, respectively, by the equation

$$\mathbf{x}_r = \mathbf{x}_a + \mathbf{A}\,(\mathbf{x} - \mathbf{x}_a) \quad (1)$$

(Rodgers, 2000).

The rows of the matrix $\mathbf{A}$ are called the averaging kernels and the trace of $\mathbf{A}$ equals the DOFS. For each of the 44 layers the full width at half maximum of the averaging kernels provides an estimate of the vertical resolution of the profile retrieval at the corresponding altitude, while the area of the averaging kernel represents the sensitivity of the retrieval at the corresponding altitude to the true state. The DOFS together with the averaging kernel shapes will define the partial columns that best represent the retrieval results. The error analysis (Sect. 5) has been carried out for these partial columns.

4 Retrieval strategy and spectral fits

In this section, we give an overview of our retrieval approach for all target molecules.

Table 1 gives a summary of the selected retrieval micro-windows (fitted simultaneously), the spectral resolution, the effective SNR, and the associated interfering molecules, together with our choice of the diagonal elements and the half-widths at half-maximum (HWHM) defining the Gaussian inter-layer correlation length of S_a adopted in the retrieval, and finally also the achieved mean DOFS for each target species, at Maïdo in 2002, and at St.-Denis in 2002 and 2004.

4.1 Spectral micro-window selections

The micro-windows in which O_3, CH_4, N_2O, CO and C_2H_6 are retrieved, as well as the interfering absorbers whose total columns are fitted simultaneously with the target species, have been adopted from the EC project UFTIR (http://www.nilu.no/uftir; De Mazière et al., 2004). Our tests have shown that these windows are still appropriate for the Maïdo and St.-Denis sites at Ile de La Réunion, despite the prevailing high humidity.

The UFTIR project also provided us with corrected spectral line parameters for ozone in the 2960–2980 cm^{-1} region (D. Mondelain and A. Barbe, private communication), which improve the spectral fits for C_2H_6. For HF and HCl the fitted micro-windows and interfering species were adopted from Reisinger et al. (1994) and from Rinsland et al. (2003), respectively. For the HCl retrievals, Rinsland et al. (2003) propose to fit two other micro-windows around 2727.78 and 2775.78 cm^{-1}, in addition to the two windows we use. But since they contain strong interfering water vapour lines, fitting them appeared to be problematic at our (sub)tropical site. We therefore restricted our spectral fits to the two micro-windows defined in Table 1. The HNO_3 micro-window selection is based on the discussions by Flaud et al. (2006) and Perrin et al. (2004).

4.2 Construction of a priori information and retrieval results

4.2.1 Ozone (O_3)

For the O_3 retrievals, we adopted a single mean a priori profile from the UGAMP (UK Universities Global Atmospheric Modelling Programme, http://ugamp.nerc.ac.uk/) climatology, calculated for a square of 2.5°×2.5° enclosing St.-Denis (http://badc.nerc.ac.uk/data/ugamp-o3-climatology/), which provides a global 4-D

Table 1. Summary of the retrieval characteristics for each target species, for the FTIR campaigns at Ile de La Réunion. Variab. represents the diagonal elements of S_a and HWHM the inter-layer correlation length in S_a The fourth, fifth and seventh columns list the spectral micro-windows that are fitted simultaneously, the associated spectral resolution, and the main interfering species. SNR is the ad hoc signal-to-noise ratio adopted in the retrievals. The last column provides the mean DOFS achieved at Maïdo, 2002, and at St.-Denis, 2002 and 2004.

Molecule	Variab. [%]	HWHM [km]	Micro-window(s) [cm^{-1}]	Spectral resolution [cm^{-1}]	SNR	Interfering species	DOFS Maïdo / St.-Denis
O_3	20	6	1000.00–1005.00	0.0072	150	H_2O	4.9 / 5.1
CH_4	variable	5	2613.70–2615.40 2650.60–2651.30 2835.50–2835.80 2903.60–2904.03 2921.00–2921.60	0.00513	250	HDO, H_2O (fitted first), CO_2	2.2 / 2.4
N_2O	10	5	2481.30–2482.60 2526.40–2528.20 2537.85–2538.80 2540.10–2540.70	0.00513	150	CO_2, CH_4, O_3, H_2O, HDO	3.0 / 3.2
CO	20	4	2057.70–2057.91 2069.55–2069.72 2157.40–2159.35	0.0036	150	O_3, OCS, CO_2, N_2O, H_2O, solar CO lines	2.6 / 2.8
C_2H_6	40	5	2976.50–2977.20	0.00513	250	H_2O, CH_4, O_3	1.5 / 1.7
HCl	20	5	2843.30–2843.80 2925.70–2926.60	0.00513	150	H_2O, CH_4, HDO	1.2 / 1.4
HF	20	3	4038.70–4039.05	0.0072	300	H_2O	1.4 / 1.5
HNO_3	20	5	872.25–874.80	0.01098	200	OCS, C_2H_6, H_2O	1.0 / 1.2

climatological distribution of ozone covering the years 1985 to 1989 and the altitude range 0 to 100 km.

Figure 2 shows the single micro-window fit of O_3 from a single spectrum on 13 October 2002 and 15 October 2004 at Maïdo and St.-Denis, respectively, together with the residuals, computed as measured minus simulated transmission. In the spectral fits for St.-Denis we observe systematic residuals around 1001.10 and 1003.70 cm^{-1}, which are due to water vapour lines. However, fitting H_2O profiles first to use the resulting daily a priori profiles in the O_3 retrieval, or excluding the two small regions from our micro-window, did not affect the retrievals significantly.

We obtain about 5 degrees of freedom for O_3 at both sites. It is therefore possible to distinguish 5 independent layers with good sensitivity, namely 2 layers in the troposphere (2.2 / 0.1 to 8.2 and 8.2 to 17.8 km), and 3 layers in the stratosphere (17.8 to 23.8, 23.8 to 31.0 and 31.0 to 100 km).

4.2.2 Methane (CH_4)

The CH_4 a priori profile was based on available data from the Halogen Occultation Experiment (HALOE), onboard the Upper Atmosphere Research Satellite (UARS), launched in September 1991 (http://haloedata.larc.nasa.gov/home). CH_4 retrievals from HALOE have been validated by Park et al. (1996). We took a six year weighted mean of all HALOE (version 19) vertical profiles from 2000 to 2005 within the 15° longitude and 10° latitude rectangle around Ile de La Réunion, with weights defined by the errors that are provided together with the HALOE profiles.

The resulting weighted mean profile covers the range 14 to 80 km, so below and above these altitudes we have extrapolated the profile by repeating the values at 14 and 80 km, respectively. In contrast to all other retrieved molecules we have used non constant diagonal elements to construct S_a. This is done, because it significantly reduces the large oscillations in the retrieved profiles that emerge when using constant uncertainties. The values are calculated out of the same HALOE profiles as used to determine the a priori profile. The obtained variabilities (in percentage) from 14.2 to 78.4 km are then extrapolated to the complete altitude range by repeating the first and last value. The off-diagonal elements are defined by a Gaussian distribution having a HWHM of 5 km and finally the matrix is transformed into squared volume mixing ratio units.

Figure 3 shows the multiple micro-window fit of CH_4 from a single spectrum on 16 October 2002 and 12 October 2004 at Maïdo and St.-Denis, respectively, together with the residuals, computed as measured minus simulated transmission. Note that the retrieved profiles slightly oscillate near the surface.

As the number of degrees of freedom is about 2 at both sites, we manage to resolve two independent partial columns of CH_4, namely 2.2 to 11.8 km and 11.8 to 100 km for Maïdo and 0.1 to 8.2 and 8.2 to 100 km for St.-Denis.

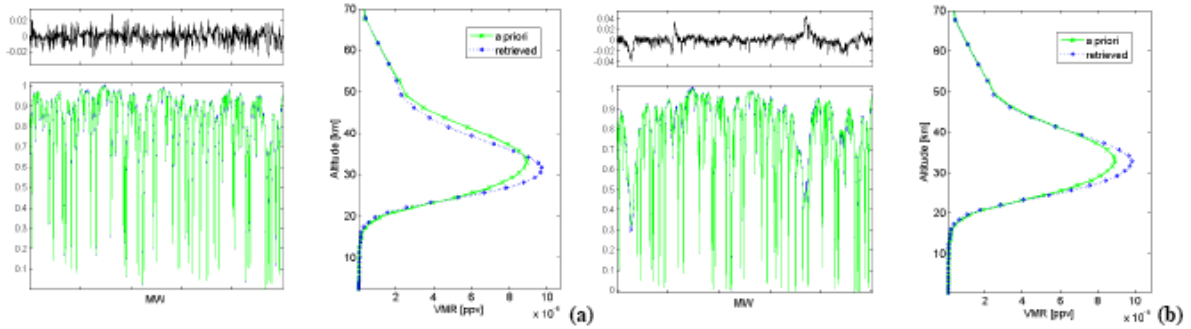

Fig. 2. Single micro-window (1000.00–1005.00 cm^{-1}) fit of O_3 plus interfering species from a single spectrum on **(a)** 13 October 2002 at Maïdo and on **(b)** 15 October 2004 at St.-Denis. Measured (blue) and simulated spectra (green) are shown (left lower plot), together with the residuals (left upper plot), computed as measured minus simulated. The right plot shows the a priori (green crosses) and retrieved (blue diamonds) profile.

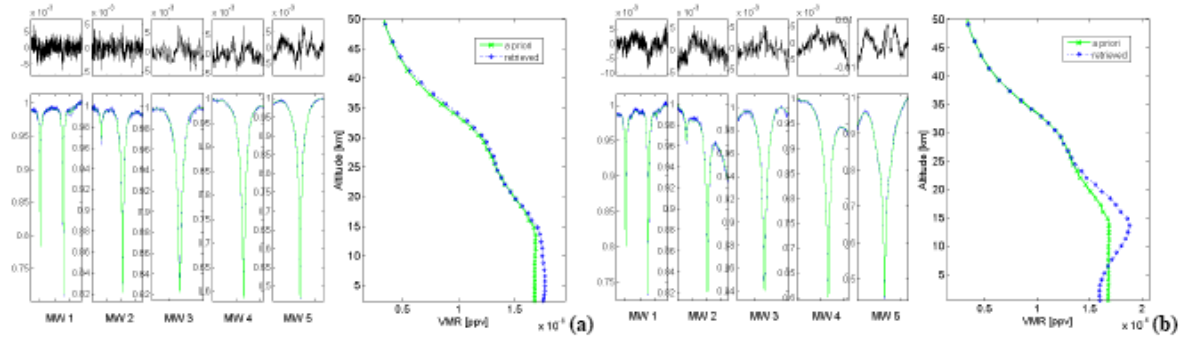

Fig. 3. Multiple micro-window (MW1: 2613.70–2615.40, MW2: 2650.60–2651.30, MW3: 2835.50–2835.80, MW4: 2903.60–2904.03, and MW5: 2921.00–2921.60 cm^{-1}) fit of CH_4 plus interfering species from a single spectrum on **(a)** 16 October 2002 at Maïdo and on **(b)** 12 October 2004 at St.-Denis. Measured (blue) and simulated spectra (green) are shown (left lower plot), together with the residuals (left upper plot), computed as measured minus simulated. The right plot shows the a priori (green crosses) and retrieved (blue diamonds) profile.

4.2.3 Nitrous oxide (N_2O)

For the N_2O a priori profile we used the 1976 U.S. Standard profile (U.S. NOAA, 1976) scaled with a yearly factor of 0.25%, to account for the slight yearly N_2O increase observed by Zander et al. (2005).

Figure 4 shows the multiple micro-window fit of N_2O from a single spectrum on 16 October 2002 and 12 October 2004 at Maïdo and St.-Denis, respectively, together with the residuals, computed as measured minus simulated transmission.

As the number of degrees of freedom for N_2O is about 3 for Maïdo as well as for St.-Denis, three independent partial columns can be distinguished, in particular from 2.2 / 0.1 to 4.6, from 4.6 to 15.4 and from 15.4 to 100 km.

4.2.4 Carbon monoxide (CO)

The CO a priori profile has been based on available data from the MOPITT space-borne instrument onboard the EOS-TERRA satellite, which was launched in December 1999 (http://terra.nasa.gov/About/MOPITT/index.php). CO retrievals from MOPITT have been validated by Emmons et al. (2004). Our CO a priori profile is a five year mean of all MOPITT vertical profiles (version L2V5) from 2000 to 2004 within 15° longitude and 10° latitude around the location of our observations. We only used daytime measurements for which the solar zenith angle was smaller than 80°. The thus obtained mean a priori profile from 0 to 14 km was then completed with the U.S. Standard Atmosphere (1976) values from 16 to 100 km.

Figure 5 shows the multiple micro-window fit of CO from a single spectrum on 19 October 2002 and 12 October 2004 at Maïdo and St.-Denis, respectively, together with the residuals, computed as measured minus simulated transmission.

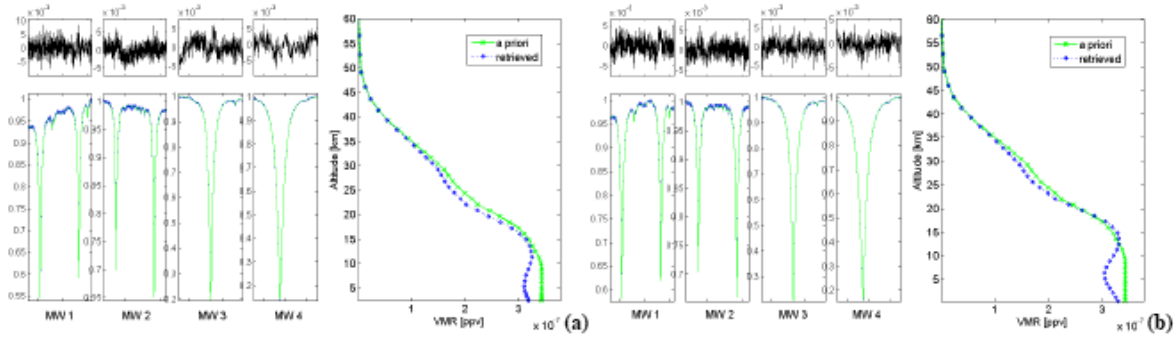

Fig. 4. Multiple micro-window (MW1: 2481.30–2482.60, MW2: 2526.40–2528.20, MW3: 2537.85–2538.80, and MW4: 2540.10–2540.70 cm^{-1}) fit of N_2O plus interfering species from a single spectrum on **(a)** 16 October 2002 at Maïdo and on **(b)** 12 October 2004 at St.-Denis. Measured (blue) and simulated spectra (green) are shown (left lower plot), together with the residuals (left upper plot), computed as measured minus simulated. The right plot shows the a priori (green crosses) and retrieved (blue diamonds) profile.

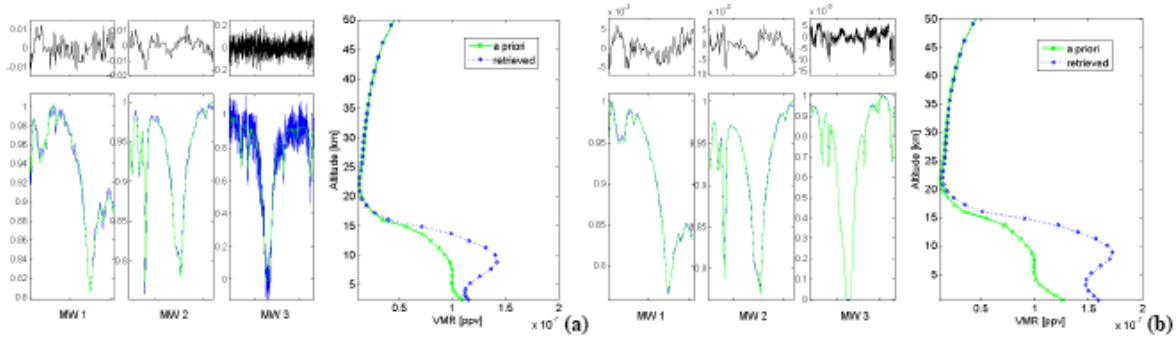

Fig. 5. Multiple micro-window (MW1: 2057.70–2057.91, MW2: 2069.55–2069.72, and MW3: 2157.40–2159.35 cm^{-1}) fit of CO plus interfering species from a single spectrum on **(a)** 19 October 2002 at Maïdo and on **(b)** 12 October 2004 at St.-Denis. Measured (blue) and simulated spectra (green) are shown (left lower plot), together with the residuals (left upper plot), computed as measured minus simulated. The right plot shows the a priori (green crosses) and retrieved (blue diamonds) profile.

From the first figure it is clear that for the 2002 spectra the CO micro-windows are contaminated by noise, due to the bad filters choice.

The DOFS for CO in our measurements is about 2.7, providing us with just 2 independent layers, namely 2.2 to 10.6 km and 10.6 to 100 km for Maïdo and 0.1 to 9.4 and 9.4 to 100 km for St.-Denis.

4.2.5 Ethane (C_2H_6)

Between 12 and 30 km, the a priori profile for C_2H_6 was adopted from Cronn and Robinson (1979) and above 30 km from Rudolph and Ehhalt (1981). Below 12 km the a priori volume mixing ratio was set constant at 7×10^{-10} ppv.

Figure 6 shows the single micro-window fit of C_2H_6 from a single spectrum on 14 October 2002 and 9 October 2004 at Maïdo and St.-Denis, respectively, together with the residuals, computed as measured minus simulated.

Since we obtain about 1.6 degrees of freedom, we consider only total column amounts of C_2H_6.

4.2.6 Hydrogen chloride (HCl)

The HCl a priori profile between 16 and 60 km was created from HALOE (version 19) observations, following the same approach as for CH_4. HCl retrievals from HALOE have been validated by Russell et al. (1996a). Below 16 km the profile was completed with values from Smith (1982) and above 60 km a constant mixing ratio was adopted, which was equal to the upper value of the weighted mean HALOE profile.

Figure 7 shows the multiple micro-window fit of HCl from a single spectrum on 16 October 2002 and 15 October 2004 at Maïdo and St.-Denis, respectively, together with the residuals, computed as measured minus simulated transmission. Note that around 25 km the retrieved profile differs strongly from the a priori profile. Such deviations are observed for all our HCl measurements, but up to now we did not manage to find the origin of this structure.

Again, we can only derive total column amounts, because the number of degrees of freedom for HCl is about 1.3 at both sites.

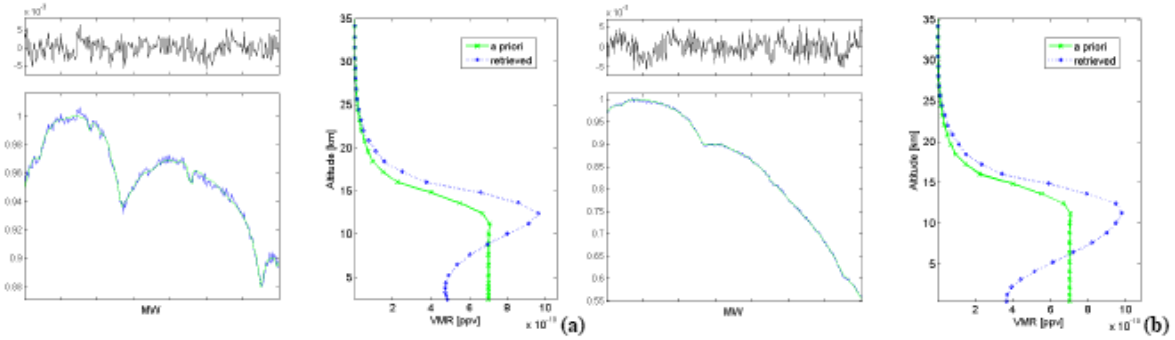

Fig. 6. Single micro-window (2976.50–2977.20 cm^{-1}) fit of C_2H_6 plus interfering species from a single spectrum on **(a)** 14 October 2002 at Maïdo and on **(b)** 9 October 2004 at St.-Denis. Measured (blue) and simulated spectra (green) are shown (left lower plot), together with the residuals (left upper plot), computed as measured minus simulated. The right plot shows the a priori (green crosses) and retrieved (blue diamonds) profile.

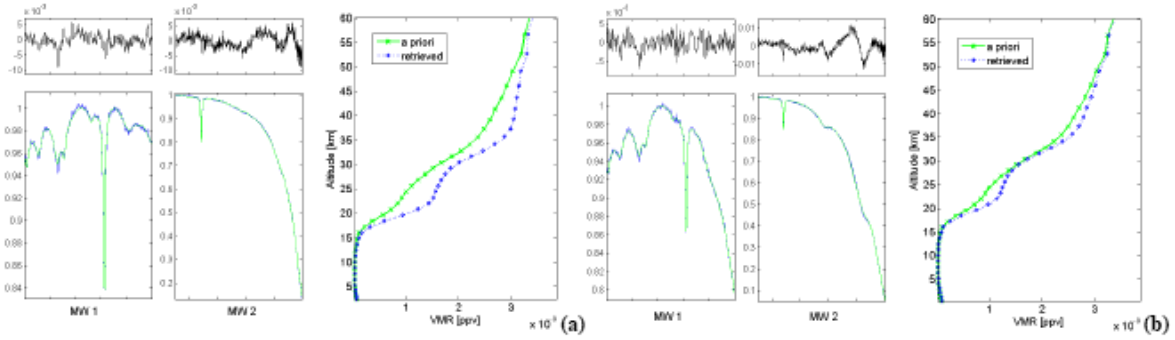

Fig. 7. Multiple micro-window (MW1: 2843.30–2843.80 and MW2: 2925.70–2926.60 cm^{-1}) fit of HCl plus interfering species from a single spectrum on **(a)** 16 October 2002 at Maïdo and on **(b)** 15 October 2004 at St.-Denis. Measured (blue) and simulated spectra (green) are shown (left lower plot), together with the residuals (left upper plot), computed as measured minus simulated. The right plot shows the a priori (green crosses) and retrieved (blue diamonds) profile.

4.2.7 Hydrogen fluoride (HF)

The HF a priori profile between 14 and 60 km was derived from HALOE (version 19) observations, as was done for HCl. HF retrievals from HALOE have been validated by Russell et al. (1996b). The profile was extrapolated with constant values above and below that altitude range, by repeating the volume mixing ratio at 60 and 14 km, respectively.

Figure 8 shows the single micro-window fit of HF from a single spectrum on 13 October 2002 and 11 October 2004 at Maïdo and St.-Denis, respectively, together with the residuals, computed as measured minus simulated transmission.

The 1.5 degrees of freedom tell us that we can only determine the total columns of HF.

4.2.8 Nitric acid (HNO_3)

For the creation of an HNO_3 reference profile, we used data from the SMR instrument, onboard the satellite Odin, launched in February 2001 (http://diamond.rss.chalmers.se/Odin). HNO_3 retrievals from Odin have been validated by Urban et al. (2005). In particular, we calculated a five year weighted mean, from 2001 to 2005, of all Odin/SMR profiles (version 2.0) within a 1500 km radius around St.-Denis, with weights defined by the errors on the Odin profiles. This gave us representative a priori values between 16 and 36 km. Below and above these altitudes we completed the profile with a seasonal mean climatology for the 0°–20° S latitude band in the period September–November 2002 from the Michelson Interferometer for Passive Atmospheric Sounding (MIPAS) onboard ESA's Envisat satellite, launched in March 2002 (http://envisat.esa.int/instruments/mipas/index.html). HNO_3 retrievals from MIPAS have been validated by Oelhaf et al. (2004) and Wang et al. (2007).

Figure 9 shows the single micro-window fit of HNO_3 from a single spectrum on 16 October 2002 and 21 October 2004 at Maïdo and St.-Denis, respectively, together with the residuals, computed as measured minus simulated transmission.

For HNO_3 we get about 1 degree of freedom, so again only total column amounts can be obtained.

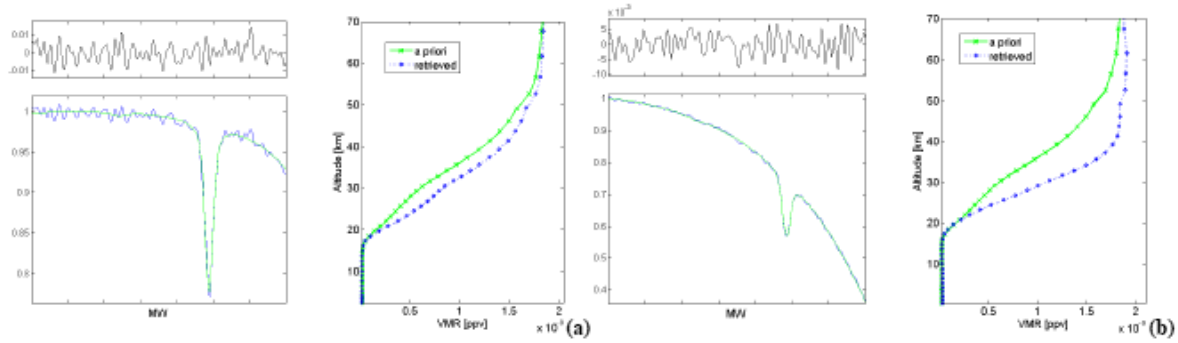

Fig. 8. Single micro-window (4038.70–4039.05 cm^{-1}) fit of HF plus interfering species from a single spectrum on **(a)** 13 October 2002 at Maïdo and on **(b)** 11 October 2004 at St.-Denis. Measured (blue) and simulated spectra (green) are shown (left lower plot), together with the residuals (left upper plot), computed as measured minus simulated. The right plot shows the a priori (green crosses) and retrieved (blue diamonds) profile.

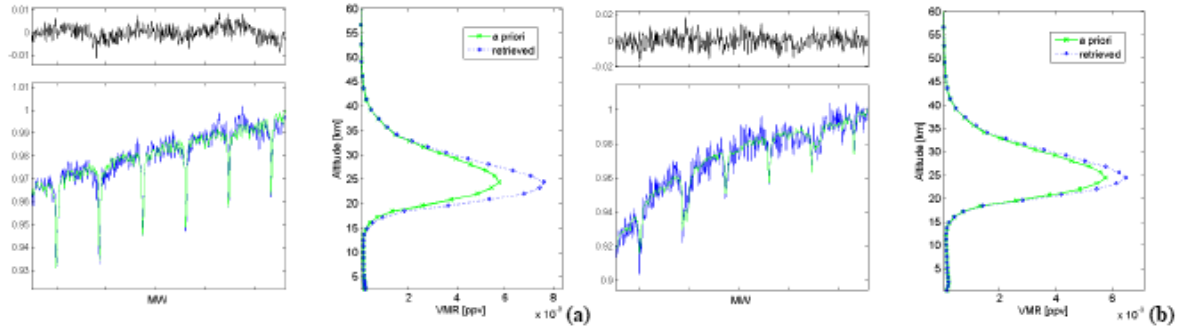

Fig. 9. Single micro-window (872.25–874.80 cm^{-1}) fit of HNO_3 plus interfering species from a single spectrum on **(a)** 16 October 2002 at Maïdo and on **(b)** 21 October 2004 at St.-Denis. Measured (blue) and simulated spectra (green) are shown (left lower plot), together with the residuals (left upper plot), computed as measured minus simulated. The right plot shows the a priori (green crosses) and retrieved (blue diamonds) profile.

5 Error budget evaluations

5.1 Adopted approach

Using the formalism described in Rodgers (2000) – assuming a linearization of the forward and inverse model about some reference state and spectrum, respectively – the difference between the retrieved and the real state of the atmosphere can be written as

$$\mathbf{x}_r - \mathbf{x} = (\mathbf{A}-\mathbf{I})(\mathbf{x}-\mathbf{x}_a) + \mathbf{G}_y \mathbf{K}_b (\mathbf{b}-\mathbf{b}_r) + \mathbf{G}_y (\mathbf{y}-\mathbf{y}_r), \quad (2)$$

where $\mathbf{A}$ is the averaging kernel matrix as defined in Sect. 3.3, $\mathbf{I}$ the identity matrix, $\mathbf{G}_y$ the gain matrix representing the sensitivity of the retrieved parameters to the measurement, $\mathbf{K}_b$ the sensitivity matrix of the spectrum to the forward model parameters $\mathbf{b}$, $\mathbf{b}_r$ the estimated model parameters, $\mathbf{y}$ the observed spectrum, and $\mathbf{y}_r$ the calculated spectrum corresponding to the retrieved state vector. The equation above splits the total error in the retrieved profile into three different error sources, i.e., the smoothing error, the forward model parameter error and the measurement error. In addition, we have determined the temperature and interfering species error as individual contributions to the total random error. Besides the random errors we must also consider the systematic errors due to uncertainties in the spectroscopic line parameters. More details about the evaluation of the individual contributions to the error budget are provided in the next sections.

5.1.1 Smoothing error

The smoothing error covariance is calculated as $(\mathbf{I}-\mathbf{A})\,\mathbf{S}_a\,(\mathbf{I}-\mathbf{A})^t$, where $\mathbf{S}_a$ is the a priori covariance matrix (see Sect. 3.2.1). In order to construct a realistic $\mathbf{S}_a$ matrix, we need information about the variability and covariances of an ensemble of real profiles. However, this information is not always available at all altitudes, obliging us to replace $\mathbf{S}_a$ with a Gaussian covariance matrix for example, for which we still have to estimate the natural variabilities and the inter-layer

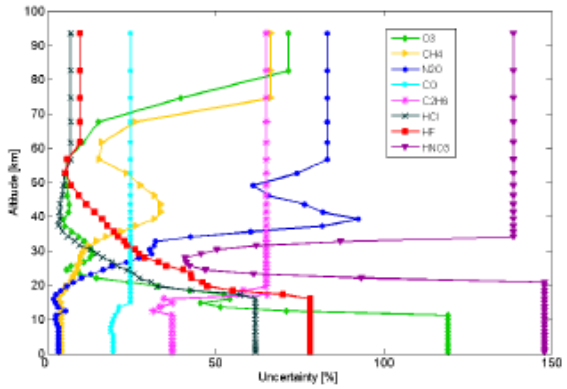

Fig. 10. A priori uncertainties (in %) in the volume mixing ratios of each retrieved trace gas as a function of altitude, used for estimating the smoothing errors.

correlations based on real data. We have chosen these values such that S_a approaches the covariance matrix derived from satellite measurements within the available altitude range. For each species we calculated the weighted covariance matrix of all available vertical profiles measured by the specified satellite within the 15° longitude and 10° latitude rectangle around Ile de La Réunion, and used the resulting diagonal elements to create S_a. The thus obtained variabilities that are reliable within a certain altitude range are then extrapolated to the complete altitude range (0–100 km) by repeating the lower- and uppermost values in percentage. The off-diagonal elements of S_a are defined by a Gaussian distribution having a HWHM which can be different for each molecule. The resulting matrix is then transformed into squared volume mixing ratio units. Table 2 summarizes which satellite data have been used for every trace gas, the altitude range in which they provide reliable values and the HWHM used to calculate the Gaussian off-diagonal elements of the S_a matrix. For more information about the satellite data used, we refer to Sect. 6.1. Figure 10 shows the resulting uncertainties in the a priori volume mixing ratios of each species as a function of altitude.

5.1.2 Forward model parameter error

We considered the random uncertainties in the forward model parameters, described in Sect. 3.1, to be mutually independent; hence we used a matrix S_b that is diagonal. For the wavenumber shift, background curve parameters, and ILS parameters, we adopted uncertainties of 10%, 10%, and 20%, respectively. The resulting errors on the retrieved target profile are then calculated as $(\mathbf{G}_y\,\mathbf{K}_b)\,S_b\,(\mathbf{G}_y\,\mathbf{K}_b)^t$.

Table 2. Source information, altitude range of the obtained a priori variability vector and HWHM of the Gaussian off-diagonal elements of S_a for each molecule.

Molecule	Source	Altitude range [km]	HWHM [km]
O_3	HALOE	10.6–86.8	5
CH_4	HALOE	14.2–78.4	6
N_2O	ACE	7.0–58.8	6
CO	MOPITT	4.6–16.6	5
C_2H_6	ACE	10.6–20.2	3
HCl	HALOE	15.4–58.8	7
HF	HALOE	15.4–64.4	6
HNO_3	Odin	20.2–34.8	4

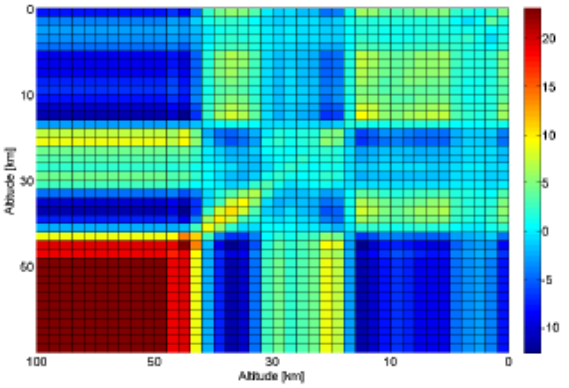

Fig. 11. Temperature covariance matrix (in K^2) from NCEP and ECMWF temperature profiles at Ile de La Réunion in October 2004, used for estimating the temperature errors.

5.1.3 Measurement error

The uncertainties coming from the measurement noise are calculated as $\mathbf{G}_y S_\varepsilon \mathbf{G}_y^t$, where S_ε is the measurement noise covariance matrix, defined as a diagonal matrix consisting of the squared noise in the observed spectra. These noise values have been determined for every fitted micro-window independently, as the root mean squared value (rms) of the differences between the observed and calculated spectrum within each bandpass.

5.1.4 Temperature error

The atmospheric temperature profile is a forward model parameter that is not fitted. Nevertheless, the associated uncertainties must be considered as well, because they influence the retrieved profiles via the temperature dependence of the absorption lines. The temperature error covariance matrix is calculated as $(\mathbf{G}_y\mathbf{K}_T)\,S_T\,(\mathbf{G}_y\mathbf{K}_T)^t$, in which S_T is a realistic covariance matrix of the temperature profile uncertainties.

Table 3. Summary of the error budgets (in %) on the total (2.2–100 km) and partial columns (altitude ranges specified in km) for each target species retrieved from the Ile de La Réunion campaign data, for Maïdo 2002. The total and partial column amounts (in molecules/cm^2) and corresponding natural variabilities (in %) are listed in the second and third columns, respectively.

Molecule	Column amount [molec/cm^2]	Natural variab. [%]	Temp. error [%]	Interf. species error [%]	FM param. error [%]	Meas. error [%]	Smooth. error [%]	Total random error [%]	Line intens. error [%]	Air broad. error [%]	Total syst. error [%]
O_3											
2.2–100	7.57×10^{18}	15.41	0.47	0.01	0.02	0.41	1.29	**1.43**	4.71	0.49	**4.74**
2.2–8.2	5.71×10^{17}	111.27	0.10	0.39	0.04	4.37	16.06	**16.64**	4.97	6.20	**7.95**
8.2–17.8	7.66×10^{17}	67.00	1.38	0.78	0.10	5.87	22.25	**23.06**	6.81	6.84	**9.65**
17.8–23.8	1.67×10^{18}	19.02	1.26	0.53	0.02	3.36	13.14	**13.63**	6.10	8.86	**10.75**
23.8–31.0	3.10×10^{18}	9.35	1.91	0.34	0.10	2.63	10.78	**11.26**	5.10	2.22	**5.57**
31.0–100	1.47×10^{18}	7.48	1.97	0.34	0.07	1.68	8.72	**9.10**	4.96	3.88	**6.30**
CH_4											
2.2–100	2.86×10^{19}	3.15	0.87	0.01	0.09	0.16	0.58	**1.06**	19.61	3.44	**19.91**
2.2–11.8	2.14×10^{19}	3.67	0.49	0.05	0.23	0.32	0.54	**0.82**	20.15	1.66	**20.21**
11.8–100	7.16×10^{18}	3.75	2.04	0.10	0.75	0.62	0.82	**2.41**	18.01	17.73	**25.28**
N_2O											
2.2–100	5.05×10^{18}	2.51	0.12	0.02	0.13	0.09	0.17	**0.26**	4.61	0.84	**4.69**
2.2–4.6	1.34×10^{18}	3.24	0.99	0.20	0.06	0.69	2.08	**2.41**	4.41	8.73	**9.78**
4.6–15.4	3.12×10^{18}	2.76	0.10	0.06	0.04	0.37	1.28	**1.34**	4.65	4.03	**6.15**
15.4–100	5.86×10^{17}	5.49	0.83	0.08	1.43	1.06	1.38	**2.40**	5.05	5.80	**7.69**
CO											
2.2–100	1.76×10^{18}	15.57	0.94	0.01	0.16	6.37	0.32	**6.45**	4.73	0.37	**4.74**
2.2–10.6	1.39×10^{18}	17.13	1.29	0.01	0.12	9.68	0.98	**9.82**	4.89	1.85	**5.22**
10.6–100	3.75×10^{17}	19.03	0.36	0.02	0.33	12.10	3.58	**12.63**	4.30	5.19	**6.74**
C_2H_6											
2.2–100	9.14×10^{15}	23.11	0.62	0.67	0.32	1.02	0.88	**1.66**	19.96	7.27	**21.24**
HCl											
2.2–100	3.15×10^{15}	20.95	0.28	0.03	0.49	0.91	7.11	**7.19**	1.32	3.04	**3.32**
HF											
2.2–100	1.04×10^{15}	24.48	0.22	0.01	0.33	1.61	5.81	**6.04**	4.86	0.98	**4.96**
HNO_3											
2.2–100	1.03×10^{16}	64.50	0.74	0.01	0.72	1.21	21.13	**21.19**	14.70	2.22	**14.87**

The factor $(\mathbf{G}_y\mathbf{K}_T)$, containing the partial derivatives of the retrieval to the temperatures, has been determined by repeating the retrieval with temperature profiles that are slightly perturbed at all altitudes separately. Our estimation of S_T is based on the differences between the NCEP and ECMWF temperature profiles for Ile de La Réunion in the period August–October 2004. Its elements are calculated as

$$S_T(i,j) = E[(T_{NCEP}(i) - T_{ECMWF}(i)) * (T_{NCEP}(j) - T_{ECMWF}(j))]. \quad (3)$$

This matrix is visualized in Fig. 11. The 41 profile layers from high to low altitude are defined as follows: from 100 to 50 km by steps of 5 km, from 50 to 10 km by steps of 2 km and from 10 km to the surface by steps of 1 km. As the NCEP profiles do not reach higher than about 54 km, we have repeated the covariances at 50 km for all altitudes above.

5.1.5 Interfering species error

The error on the retrieval of a target gas coming from the uncertainties in the vertical distributions of the interfering species has been calculated by performing retrievals using an ensemble of vertical profiles of every significant interferer separately, representing the uncertainties in its a priori profile (Sussmann and Borsdorff, 2007; Connor et al., 2008). Consequently we derive an error covariance matrix based on the thus obtained set of retrieved target profile differences relative to the reference profile, which represents the contribution of the interfering species uncertainties to the random error.

We have observed that when considering only the total column uncertainties of the interfering species, this error component is clearly underestimated in some cases.

Table 4. Summary of the error budgets (in %) on the total (0.05–100 km) and partial columns (altitude ranges specified in km) for each target species retrieved from the Ile de La Réunion campaign data, for St.-Denis 2004. The total and partial column amounts (in molecules/cm^2) and corresponding natural variabilities (in %) are listed in the second and third columns, respectively.

Molecule	Column amount [molec/cm^2]	Natural variab. [%]	Temp. error [%]	Interf. species error [%]	FM param. error [%]	Meas. error [%]	Smooth. error [%]	Total random error [%]	Line intens. error [%]	Air broad. error [%]	Total syst. error [%]
O_3											
0.05–100	7.78×10^{18}	14.43	0.50	0.12	0.01	0.31	0.57	**0.82**	4.68	0.38	**4.69**
0.05–8.2	6.46×10^{17}	106.23	0.09	1.02	0.02	3.84	10.71	**11.42**	5.60	4.51	**7.19**
8.2–17.8	6.80×10^{17}	61.72	1.86	1.38	0.09	4.75	13.53	**14.53**	5.04	4.68	**6.87**
17.8–23.8	1.82×10^{18}	19.38	1.59	1.65	0.04	3.23	8.88	**9.73**	5.20	7.49	**9.12**
23.8–31.0	3.05×10^{18}	9.31	2.37	1.48	0.10	2.50	5.97	**7.05**	4.31	1.74	**4.65**
31.0–100	1.59×10^{18}	7.32	1.89	0.92	0.10	2.39	6.60	**7.33**	5.18	3.91	**6.49**
CH_4											
0.05–100	3.58×10^{19}	3.06	1.08	0.48	0.01	0.25	0.18	**1.22**	19.94	3.17	**20.19**
0.05–8.2	2.23×10^{19}	3.78	1.17	0.76	0.21	0.70	0.58	**1.68**	20.69	6.19	**21.60**
8.2–100	1.35×10^{19}	3.43	0.94	0.94	0.39	0.68	0.60	**1.66**	18.69	18.49	**26.29**
N_2O											
0.05–100	6.63×10^{18}	2.44	0.18	0.02	0.09	0.08	0.15	**0.27**	4.59	0.79	**4.66**
0.05–4.6	2.89×10^{18}	3.17	0.80	0.16	0.14	0.32	0.89	**1.25**	4.64	6.88	**8.30**
4.6–15.4	3.11×10^{18}	2.75	0.34	0.13	0.14	0.25	0.91	**1.02**	4.62	7.17	**8.53**
15.4–100	6.26×10^{17}	5.34	0.20	0.13	1.04	0.53	1.20	**1.69**	4.36	4.82	**6.50**
CO											
0.05–100	2.96×10^{18}	14.95	0.69	0.05	0.17	0.46	0.37	**0.93**	3.05	0.16	**3.06**
0.05–9.4	2.32×10^{18}	16.80	0.73	0.04	0.14	0.65	1.06	**1.45**	2.92	1.02	**3.09**
9.4–100	6.38×10^{17}	18.51	0.54	0.15	0.38	2.09	3.79	**4.38**	3.57	2.97	**4.65**
C_2H_6											
0.05–100	1.20×10^{16}	22.46	0.78	2.16	0.72	1.92	1.47	**3.41**	14.67	3.04	**14.98**
HCl											
0.05–100	3.16×10^{15}	22.63	0.17	0.67	0.41	2.27	10.95	**11.21**	2.50	4.00	**4.72**
HF											
0.05–100	1.32×10^{15}	26.51	0.15	0.12	0.19	1.96	13.57	**13.71**	3.53	0.20	**3.54**
HNO_3											
0.05–100	9.58×10^{15}	60.40	1.28	0.27	0.87	2.71	25.61	**25.80**	33.32	7.00	**34.05**

5.1.6 Line intensity and pressure broadening error

In addition to the random error budget, we determined the systematic error in the retrievals originating from the uncertainties in the spectroscopic line intensities and in the pressure broadening coefficients. We therefore performed retrievals with perturbed spectroscopic line intensities and broadening coefficients of the target lines within our microwindows. The perturbation of these line parameters is based on their maximum uncertainties as given by Rothman et al. (2005). While for all molecules, except for CH_4 and HNO_3, these uncertainties are specified within certain limits, for CH_4 and HNO_3 we assumed the uncertainties on the line intensities to be 20 and 25%, respectively, as they are only specified to be larger than or equal to 20%. The corresponding systematic error covariance matrices are then calculated based on the differences between the thus retrieved vertical profiles and the originally retrieved profiles.

5.2 Discussion

The estimated error values for representative Maïdo and St.-Denis spectra, recorded at solar zenith angles between 40 and 65°, are summarized in Table 3 and Table 4, respectively. Note that we only show the error values for the 2004 campaign at St.-Denis, because the 2002 campaign at this location yields similar values.

The systematic errors are generally dominated by the uncertainties in the line intensities. For all species, they are very similar at both locations. This is a logical consequence of the fact that we use the same spectroscopic database and the same retrieval strategy for both sites.

In particular, the systematic errors are especially high for CH_4, HNO_3 and C_2H_6, because of strong uncertainties in their spectroscopic line parameters.

It can also be seen in Tables 3 and 4 that the uncertainties on the air broadening coefficients significantly affect the errors on the profile retrieval, or the partial column errors, but that they have a smaller impact on the total column errors, as one might expect. Only in the case of HCl, the error on the total column due to air broadening coefficient uncertainties is larger than the one due to line intensity uncertainties.

Regarding the total column smoothing error, we observe that it is larger for the stratospheric species than for the tropospheric species, at both sites. Generally it becomes larger with decreasing DOFS, and when the true profile has more vertical structure. For most molecules, we see slightly larger PC smoothing errors at Maïdo, where the DOFS is slightly smaller. If the DOFS exceeds one, the smoothing error is larger for the independent partial columns than it is for the total column. The smoothing error is highest for the partial columns in which the species' profile has more vertical structure. For the stratospheric species, the smoothing error is the dominant contribution to the random error. For the other species, the main error source may vary.

Only in the case of CO and C_2H_6 at Maïdo the measurement noise is the dominant random error contribution. C_2H_6 is a very weak signature, making the SNR very small. As to CO, we remind the reader (see Sect. 2) that in 2002 at Maïdo, we made a less appropriate choice of optical filter and detector for the observation of the spectral range in which the CO micro-windows are located, causing a lower SNR and therefore a larger measurement error. The measurement error listed in Table 4 for CO at St.-Denis represents the nominal case.

The temperature error is more important when the lower state energies of the absorbing lines in the micro-windows become higher, which is the case for example for some CH_4 and O_3 lines. It is quite similar at Maïdo and St.-Denis.

The error due to interfering species uncertainties is dominated by the uncertainties on the HDO and H_2O profiles. That explains why it is an important error source for species with strong H_2O and/or HDO interfering lines, like O_3, CH_4, HCl and C_2H_6. As all other interfering species uncertainties have a negligible impact on the target species, we only included the error budgets due to uncertainties on H_2O and/or HDO in Tables 3 and 4.

We see that in all cases this error is larger at the near sea level site St.-Denis than at the high-altitude site Maïdo, confirming the fact that the mountain site is much less affected by the high humidity in the (sub)tropics. Actually the mean H_2O column amount observed above Maïdo during our first campaign is about 1.5×10^{22} molecules/cm^2, while above St.-Denis it is about 7×10^{22} molecules/cm^2, respectively! The interfering species error on the total columns is below 0.7% for all cases at Maïdo, whereas it rises to about 2.2% for C_2H_6 at St.-Denis.

The forward model parameter error never is the dominant error source, except for the partial column of N_2O above Maïdo, above 15.4 km. This error source is similar at both measurement stations.

It is important to note that in all cases the total random errors are smaller than the species' natural variability, except for the upper two partial columns of O_3 at Maïdo. This implies that we can effectively extract useful information from the obtained partial and total column time series.

6 Discussion of the retrieval results and comparison with correlative data

Figure 12 shows the time series of the retrieved total column amounts (in molecules/cm^2) of all species observed during the St.-Denis campaigns in 2002 and 2004.

The only reported ground-based measurements of total column abundances in the same latitude belt that we have found to compare our data with, are measurements with a Bruker 120M FTIR spectrometer during a ship cruise across the Atlantic Ocean onboard the German research vessel Polarstern, in October 1996 (Notholt et al., 2000). Our mean total column amounts of O_3, CH_4, N_2O, CO, and C_2H_6 measured at St.-Denis, being 7.6×10^{18}, 3.6×10^{19}, 6.6×10^{18}, 1.9×10^{18}, and 1.1×10^{16} molecules/cm^2, respectively, agree well with the average values reported for this cruise between 15 and 20° S for CO and between 20 and 25° S for the other gases, namely 6.9×10^{18}, 3.5×10^{19}, 6.4×10^{18}, 2.0×10^{18}, and 1.0×10^{16} molecules/cm^2, respectively.

For HCl and HF, our total column amounts at Maïdo of 2.8×10^{15} and 1.0×10^{15} molecules/cm^2, respectively, agree quite well with the values found by long-term FTIR measurements performed at the Northern Hemisphere subtropical site Izaña (28° N, 16° W, 2370 m a.s.l.) from 1999 to 2003 (Schneider et al., 2005), namely 2.4×10^{15} and 0.8×10^{15} molecules/cm^2, respectively. The same conclusion can be drawn for the O_3, N_2O and CH_4 stratospheric columns. Finally, our HCl total column amounts also agree well with the values found at Mauna Loa (19° N, 156° W, 3400 m a.s.l.) by Rinsland et al. (2003), measured with a Bruker 120HR FTIR spectrometer from 1995 to 2001.

The fact that we find almost no data at latitudes around 21° S to compare with, demonstrates the importance of performing measurements at Ile de La Réunion.

Because of the limited time periods of the measurement campaigns up to now, we can not clearly distinguish any seasonal variations. Nevertheless, we have observed some interesting short-term variations (Sect. 6.3), we have made differential observations between Maïdo and St.-Denis (Sect. 6.2), and we have performed comparisons with correlative data (Sect. 6.1).

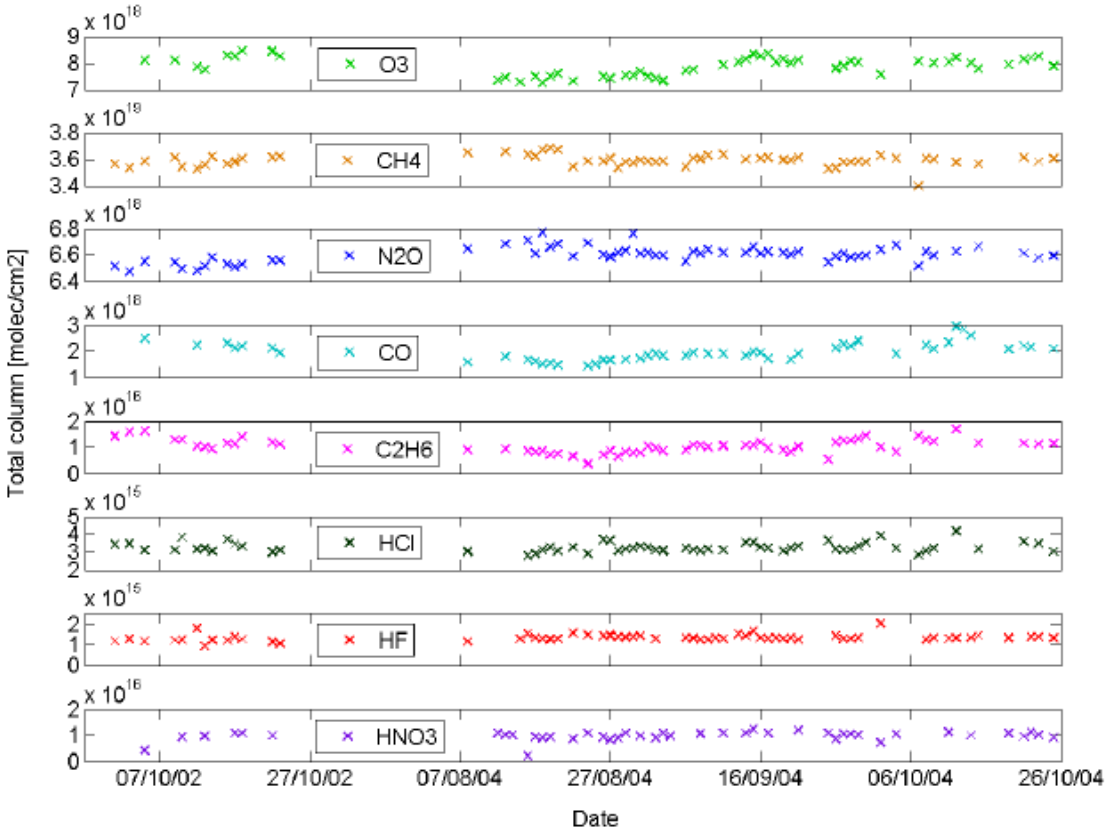

Fig. 12. Time series of the total column amounts (in molecules/cm^2) for all retrieved species during the FTIR campaigns at St.-Denis in 2002 and 2004.

6.1 Comparisons with correlative data

6.1.1 Methodology

The retrieval results obtained from our ground-based FTIR measurements have been compared with correlative vertical profile or partial column data from complementary ground-based observations at the site or from satellites. If the correlative data have a higher vertical resolution than the FTIR data, they are smoothed with the FTIR averaging kernels, using the formula

$$\mathbf{x'} = \mathbf{x}_a + \mathbf{A}(\mathbf{x} - \mathbf{x}_a) \quad (4)$$

(Rodgers and Connor, 2003).

For all comparisons with satellite data, we used coincidence criteria of maximum 15 degrees difference in longitude, 10 degrees in latitude, and maximum 24 h time difference. Besides the comparisons with ACE-FTS data as part of the ACE validation project, we have compared our FTIR observations with validated data from the HALOE satellite instrument. We have not found any other space-borne correlative data to compare with, knowing that MIPAS has stopped operating in nominal mode in March 2004.

In addition to the comparisons with satellite observations, sonde measurements performed at Ile de La Réunion in the frame of the SHADOZ network (http://croc.gsfc.nasa.gov/shadoz/) are used to evaluate our FTIR data. Unfortunately, there are no correlative O_3 profiles available from the lidar instrument at Ile de La Réunion, because the lidar was not operational during our measurement campaigns.

The numerical comparisons between the ground-based FTIR and the correlative data are limited to comparisons between their respective partial columns (PCs) defined by the altitude ranges in which the DOFS is about one. In any case, the comparisons are restricted to the altitude ranges within which the sensitivity of the FTIR measurement, as defined in Sect. 3.3, is equal to or greater than 50%. We therefore define the relative difference between the ground-based FTIR and correlative smoothed sonde or satellite data as 2 * (PC_{COR} − PC_{FTIR}) / (PC_{COR} + PC_{FTIR}) * 100. Note that this definition implies that none of the data is considered as

Table 5. Relative differences (in %) between O_3 partial columns from sonde and FTIR measurements at Ile de La Réunion on coincident days. DOFS gives the number of degrees of freedom for the partial column in the high sensitivity altitude range of both instruments. The last column provides the random errors (in %) on the relative differences, calculated as $4 * [PC_{Sonde} * PC_{FTIR} / (PC_{Sonde} + PC_{FTIR})^2] * \text{sqrt}\,(\sigma^2_{Sonde} + \sigma^2_{FTIR})$.

Date	Altitude range [km]	DOFS	Rel. diff. [%]	Error [%]
18/08/04	0.05–28.6	3.67	−0.47	**2.22**
01/09/04	0.05–32.2	4.11	−4.63	**2.03**
16/09/04	0.05–31.0	3.78	−7.77	**1.94**
04/10/04	0.05–33.4	4.46	−4.32	**2.02**

a reference. To support the interpretation of the observed differences between the FTIR and correlative partial column data, we have evaluated the random errors associated with the relative differences, from a combination of the random errors on the FTIR and sonde or satellite partial columns. This combined error is calculated as $4 * [PC_{COR} * PC_{FTIR} / (PC_{COR} + PC_{FTIR})^2] * \text{sqrt}\,(\sigma^2_{COR} + \sigma^2_{FTIR})$, where σ_{COR} and σ_{FTIR} are the relative random errors on the correlative sonde or satellite and on the FTIR partial column, respectively. Note that the smoothing error contribution can be neglected in this evaluation, because we have first smoothed the higher vertical resolution profiles from the sonde or satellite measurements (Rodgers and Connor, 2003).

6.1.2 Ground-based FTIR versus ozone sonde

There are only four days during the second campaign on which O_3 soundings and FTIR measurements have both been carried out at Ile de La Réunion. These are 18 August, 1 and 16 September, and 4 October 2004. The vertical profiles agree well in the high sensitivity altitude range. As an example, Fig. 13 shows the comparison of the O_3 profiles on 16 September 2004. The relative differences (in %) between the high sensitivity partial columns for all four days are summarized in Table 5, together with the number of DOFS for the partial column in the considered altitude range, and the percentage random errors on the relative differences (as defined in Sect. 6.1.1), from the combined sonde and FTIR random errors. Since the random error budget for the ozone sondes was not given in the NDACC database, we used typical values from the JOSIE-2000 report (Smit and Straeter, 2004): 5% in every layer from the ground up to 20 km, and 7% in the layers above. From Table 5, we deduce that the ground-based FTIR retrievals overestimate the amount of O_3 between the surface and about 30 km by 0 to 8%. Of course, this conclusion is based on 4 coincidences only. For all days the combined error is slightly dominated by the sonde errors.

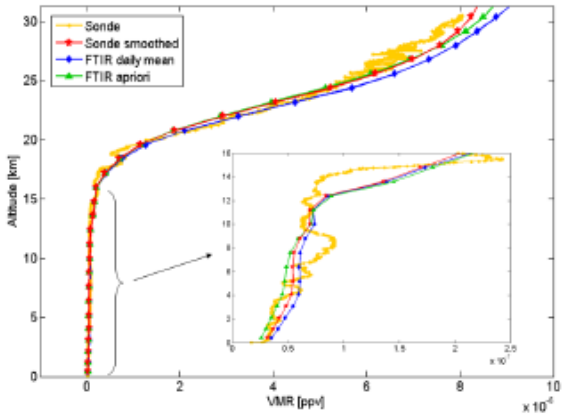

Fig. 13. Comparison of O_3 vertical profiles at St.-Denis on 16 September 2004 obtained from ground-based FTIR (blue diamonds) and O_3 sonde (yellow dots). Green triangles indicate the a priori FTIR profile and red stars the sonde profile smoothed by the FTIR averaging kernels.

6.1.3 Ground-based FTIR versus ACE-FTS

During the 2004 campaign, there have been five overpasses of ACE above Ile de La Réunion: occultation sr5497 on 20 August, occultation ss6153 on 3 October, occultation ss6168 on 4 October, occultation ss6197 on 6 October, and occultation sr6485 on 26 October. For each of these occultations we have compared the ACE-FTS profiles (version v2.2) with our ground-based FTIR data. Note that the profiles measured by the ACE-FTS occultation on October 26 do not reach altitudes below 16.6 km. Therefore the resulting comparisons for that day are not very valuable, but we do include them for completeness.

We have calculated the relative differences between the FTIR and smoothed ACE-FTS partial column amounts of each measured target gas, defined as $2 * (PC_{ACE} - PC_{FTIR}) / (PC_{ACE} + PC_{FTIR}) * 100$, in the altitude range where both FTIR and ACE-FTS are sensitive.

Figure 14 shows examples of profile comparisons for CH_4, HF, and HNO_3 on 20 August, for O_3, N_2O, CO and HCl on 4 October, and for C_2H_6 on 6 October. The horizontal red lines indicate the altitude ranges of high sensitivity. Within these ranges the smoothed ACE-FTS profiles agree quite well with the FTIR profiles.

Table 6 lists all comparison results, for each species and each coincident occultation. The above defined relative partial column differences are given (in %), together with the combined random errors (in %) on these differences, calculated as $4 * [PC_{ACE} * PC_{FTIR} / (PC_{ACE} + PC_{FTIR})^2] * \text{sqrt}\,(\sigma^2_{ACE} + \sigma^2_{FTIR})$.

In the discussion of the comparisons with the ACE-FTS data we will not take into account the results on 26 October, because of their limited reliability.

Table 6. Relative differences (in %) between ACE-FTS and FTIR high sensitivity partial columns at Ile de La Réunion in 2004 for each common measured species, together with the combined random errors, defined as 4 * [PC_{ACE} * PC_{FTIR} / (PC_{ACE} + PC_{FTIR})^2] * sqrt ($\sigma^2_{ACE} + \sigma^2_{FTIR}$) (in %).

Molecule	Date	Altitude range [km]	DOFS	Rel. diff. [%]	Error [%]
O_3	20/08/04	5.8–47.4	4.18	−3.82	**0.95**
	03/10/04	5.8–47.4	4.33	11.11	**0.86**
	04/10/04	8.2–47.4	4.08	6.36	**0.84**
	06/10/04	5.8–36.4	3.46	−13.34	**1.25**
	26/10/04	16.6–47.4	3.19	−2.83	**0.90**
CH_4	20/08/04	7.0–28.6	1.35	−6.16	**1.40**
	03/10/04	5.8–28.6	1.42	−5.08	**1.37**
	04/10/04	8.2–28.6	1.20	−6.53	**1.64**
	06/10/04	5.8–28.6	1.60	−0.22	**1.34**
	26/10/04	16.6–28.6	0.56	2.03	**11.16**
N_2O	20/08/04	5.8–25.0	1.75	−7.42	**0.59**
	03/10/04	5.8–31.0	2.02	−3.14	**0.72**
	04/10/04	8.2–31.0	1.70	−4.50	**0.74**
	06/10/04	5.8–28.6	6.57	15.03	**0.73**
	26/10/04	16.6–25.0	0.70	12.36	**1.45**
CO	20/08/04	7.0–19.0	1.19	−18.80	**3.33**
	03/10/04	5.8–19.0	1.31	25.02	**3.49**
	04/10/04	8.2–19.0	0.96	−17.82	**3.27**
	26/10/04	16.6–20.2	0.10	−2.44	**3.57**
C_2H_6	20/08/04	8.2–20.2	0.88	−14.15	**8.94**
	03/10/04	7.0–20.2	1.24	25.27	**6.16**
	04/10/04	8.2–20.2	1.16	−37.19	**7.08**
	06/10/04	7.0–19.0	0.78	−39.02	**12.98**
	26/10/04	17.8–20.2	0.09	−47.75	**19.22**
HCl	20/08/04	8.2–47.4	1.38	10.16	**4.10**
	03/10/04	9.4–42.4	1.28	30.31	**3.37**
	04/10/04	9.4–42.4	1.28	15.08	**3.41**
	06/10/04	8.2–47.4	1.25	−8.24	**4.32**
	26/10/04	16.6–44.8	1.07	−22.73	**2.58**
HF	20/08/04	14.2–40.2	1.14	−3.41	**3.12**
	26/10/04	17.8–38.2	1.07	−47.65	**2.48**
HNO_3	20/08/04	16.6–32.2	0.93	3.41	**4.67**
	03/10/04	16.6–28.6	1.09	25.93	**4.73**
	04/10/04	16.6–28.6	1.09	5.59	**4.80**
	06/10/04	16.6–32.2	1.03	−30.89	**4.59**
	26/10/04	16.6–28.6	0.97	−49.62	**4.05**

For O_3, the relative differences between ACE-FTS and ground-based FTIR vary between −14 and +12%, in the middle troposphere (~6 km) up to the stratopause (~47 km). For CH_4 and N_2O, the relative differences between ACE-FTS and ground-based FTIR range from −7 to 0% and from −8 to +15%, respectively, in the middle troposphere up to about 30 km. For CO and C_2H_6, the upper altitude limit for the comparison is restricted to 20 km; the differences between ACE-FTS and ground-based FTIR vary between −19 and +25% for CO, and between −39 and +26% for C_2H_6. The altitude range for the comparison of HCl goes from the middle troposphere to about the stratopause; the observed differences range from −9 to +31%.

For HF, we have only one reliable comparison, namely on 20 August, for which the relative difference between the ACE-FTS and the ground-based FTIR partial column in the range 14 to 40 km is about −4%. Comparisons for HNO_3 in the range 17 to 30 km, show differences between −31 and +26%.

In all mentioned comparisons, the variations in the observed differences are larger than what we expect on the basis of the random errors on the relative differences. For all species we see that the FTIR errors are equivalent to or slightly bigger than the ACE-FTS errors.

Table 7. Relative differences (in %) between HALOE and FTIR high sensitivity partial columns at Ile de La Réunion in 2004 for each common measured species, together with the combined random error, defined as 4 * [PC_{HALOE} * PC_{FTIR} / (PC_{HALOE} + PC_{FTIR})^2] * sqrt ($\sigma^2_{HALOE} + \sigma^2_{FTIR}$) (in %).

Molecule	Date	Altitude range [km]	DOFS	Rel. diff. [%]	Error [%]
O_3	29/08/04	10.6–47.4	3.66	−12.34	**1.64**
	30/08/04	10.6–47.4	3.54	−9.03	**0.89**
	31/08/04	10.6–50.8	3.61	−14.82	**0.92**
	14/09/04	10.6–42.4	3.32	−56.51	**16.30**
	15/09/04	10.6–50.8	3.63	−13.09	**0.90**
	16/09/04	10.6–47.4	3.46	−16.31	**0.87**
CH_4	29/08/04	14.2–28.6	0.71	−6.86	**10.71**
	30/08/04	14.2–28.6	0.70	−8.47	**5.26**
	31/08/04	14.2–28.6	0.70	−5.22	**5.37**
	14/09/04	14.2–28.6	0.69	−4.76	**5.34**
	15/09/04	14.2–28.6	0.69	−5.57	**7.97**
	16/09/04	14.2–28.6	0.72	−4.67	**5.44**
HCl	29/08/04	15.4–44.8	1.09	2.13	**13.94**
	30/08/04	15.4–44.8	1.00	−7.86	**8.87**
	31/08/04	15.4–23.8	1.91	−15.24	**11.13**
	14/09/04	15.4–44.8	1.20	−47.09	**1.94**
	15/09/04	16.6–47.4	0.74	−15.51	**2.87**
	16/09/04	15.4–44.8	1.51	2.04	**2.14**
HF	29/08/04	15.4–40.2	1.15	−0.10	**8.57**
	30/08/04	15.4–40.2	1.18	−8.30	**2.97**
	31/08/04	15.4–40.2	1.17	−13.59	**3.91**
	14/09/04	15.4–40.2	1.13	−45.44	**4.80**
	15/09/04	15.4–38.2	1.11	−19.25	**2.73**
	16/09/04	15.4–38.2	1.10	−1.06	**4.36**

6.1.4 Ground-based FTIR versus HALOE

In the same way as we did for ACE-FTS, we have compared our ground-based FTIR data with correlative data from HALOE. Conform to the ACE comparisons in this paper, we have calculated the relative differences between the FTIR and smoothed HALOE partial column amounts as 2 * ($PC_{HALOE} - PC_{FTIR}$) / ($PC_{HALOE} + PC_{FTIR}$) * 100, in the altitude range where both FTIR and HALOE are sensitive for the target species.

Figure 15 shows examples of comparisons between retrieved FTIR and the original and smoothed HALOE profiles of O_3, CH_4, HCl, and HF on 16 September 2004. The horizontal red lines indicate the altitude ranges of high sensitivity. Analogue to the ACE-FTS comparisons, the smoothed HALOE profiles agree fairly well with the FTIR profiles within these ranges. Table 7 gives an overview of all comparisons, for each species and each coincident occultation. The relative differences on the relevant partial column are given (in %), together with the associated DOFS and random error (in %), defined as 4 * [PC_{HALOE} * PC_{FTIR} / (PC_{HALOE} + PC_{FTIR})^2] * sqrt ($\sigma^2_{HALOE} + \sigma^2_{FTIR}$). It appears in Table 7 that the discrepancies between HALOE and ground-based FTIR partial columns are always larger on 14 September 2004 than on the other days. We have verified the HALOE and ground-based FTIR data for that particular day and up to now, we haven't found any good explanation for the large inconsistencies. We therefore don't take into account that day in the current discussion.

For HCl and HF, in general, the HALOE partial columns in the range 15 to 45 km and 15 to 40 km, respectively, are smaller than the corresponding FTIR partial columns, by about 7 to 16% and 1 to 20%, respectively. This agrees to some extent with previous findings by Russell et al. (1996a, 1996b) saying that HALOE slightly underestimates the HCl and HF vmr profiles. In particular, they found that the mean difference between HALOE and correlative balloon measurements is better than 7% for HF and ranges from 8 to 19% for HCl, throughout most of the stratosphere. Following Russell et al. there appears to be a systematic offset between HALOE and ATMOS measurements ranging from 10 to 20% both for HF and HCl, and even reaching 40% for HF in the lower stratosphere. The differences between the HALOE and ground-based FTIR O_3 partial columns in the range 10 to 47 km vary between 9 and 17%, with the HALOE profiles being smaller than the ground-based FTIR profiles. For CH_4, the HALOE partial columns in the lower stratosphere (15 to 28 km) are smaller than the ground-based FTIR columns by about 4 to 9%.

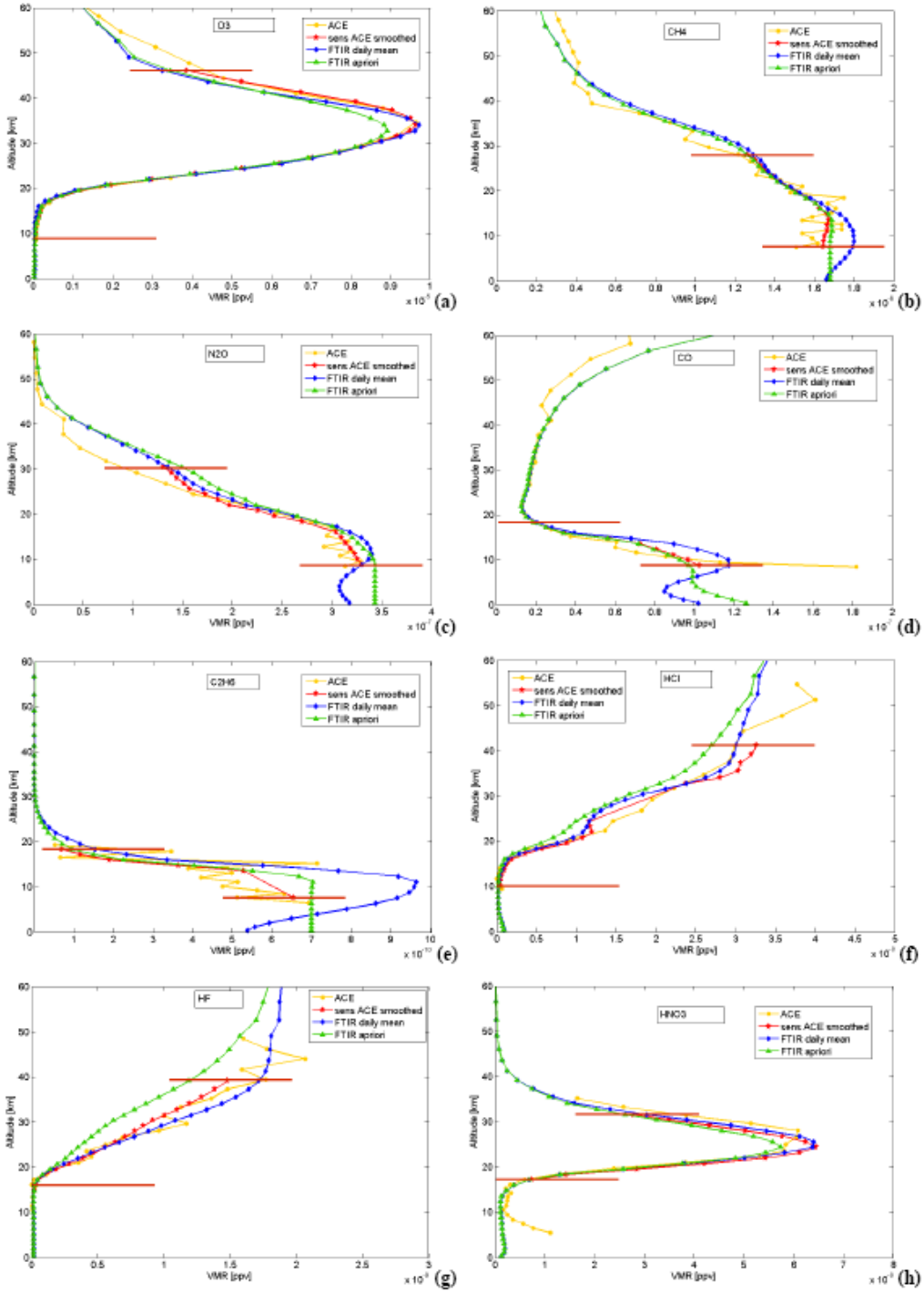

Fig. 14. Vertical vmr profiles from 0 to 60 km of **(a)** O_3 on 4 October, **(b)** CH_4 on 20 August, **(c)** N_2O on 4 October, **(d)** CO on 4 October, **(e)** C_2H_6 on 6 October, **(f)** HCl on 4 October, **(g)** HF on 20 August, and **(h)** HNO_3 on 20 August, measured at St.-Denis in 2004 by ground-based FTIR (blue diamonds) and by ACE-FTS (raw: yellow circles; smoothed: red stars). The FTIR a priori profile is indicated by the green triangles.

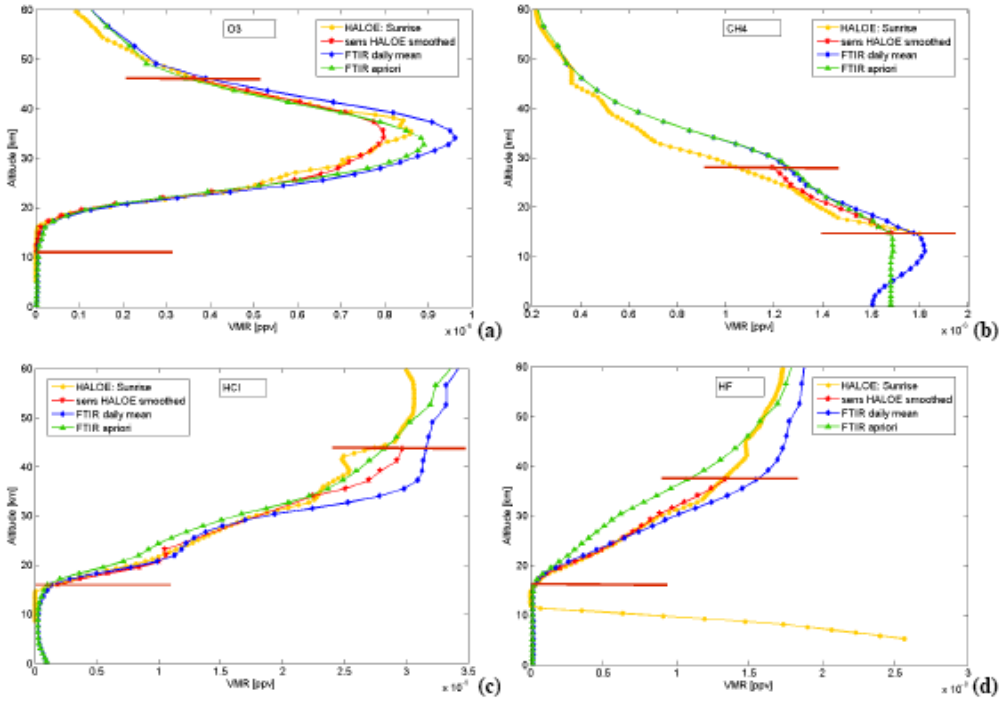

Fig. 15. Vertical vmr profiles form 0 to 60 km of **(a)** O_3, **(b)** CH_4, **(c)** HCl and **(d)** HF, measured at St.-Denis by ground-based FTIR (blue diamonds) and by HALOE (raw: yellow circles; smoothed: red stars) on 16 September 2004. The green triangles indicate the a priori FTIR profile.

For O_3 and CH_4 the combined error is dominated by the FTIR errors, whereas for HCl and HF it is dominated by the HALOE errors.

6.2 Differential observations between Maïdo and St.-Denis

The campaign in 2002 has allowed us to look at the species' abundances in the about 2.15 km thick atmospheric bottom layer between St.-Denis and Maïdo. Unfortunately, only very few measurements could be made on exactly the same day at both sites, because of meteorological conditions.

Figure 16 shows the total column amounts (TC) of O_3, CH_4, N_2O, CO, C_2H_6, HCl, HF, and HNO_3, retrieved at Maïdo and at St.-Denis in 2002, together with their respective absolute differences, $TC_{StDenis} - TC_{Maido}$, and the combined random error on those differences, defined as sqrt ($\sigma^2_{StDenis} * TC^2_{StDenis} + \sigma^2_{Maido} * TC^2_{Maido}$), where $\sigma_{StDenis}$ and σ_{Maido} are the relative random error on the total columns at St.-Denis and Maïdo, respectively.

As expected, the total column amounts measured on the same day at both sites coincide within the error bars for the stratospheric species HCl, HF and HNO_3. For the tropospheric species CH_4, N_2O, CO, and C_2H_6 there is a significant offset in their total columns, corresponding to their abundances in the atmospheric layer in between both observatories. For O_3, there is also a small offset, confirming its non-zero concentration in the boundary layer.

Based on these differences between the column values at Maïdo and at St.-Denis, we can derive an estimate of the surface volume mixing ratios of the target species, assuming a constant vmr between 0.05 and 2.2 km. This is a good assumption for the well-mixed long-lived gases CH_4 and N_2O, and a reasonable approximation for the other ones. Our thus obtained estimates are 1324 ppbv for CH_4, 86 ppbv for CO, 265 ppbv for N_2O, and 139 pptv for C_2H_6.

For CH_4 and CO the values agree well (i.e., within the error bars) with the ones from the NOAA ESRL Globalview database (http://www.esrl.noaa.gov/gmd/ccgg/globalview/co/co_intro.html), namely about 1750 and 80 ppbv, respectively, at 20° S in October, if we take into account the total uncertainties on the total column values, including the systematic uncertainties. Analogously, our estimate of the N_2O surface concentration agrees reasonably well with the value of 316 ppbv at the Southern Hemisphere station of Cape Matatula (14° S, 171° W) in 2002, reported by Jiang et al. (2007).

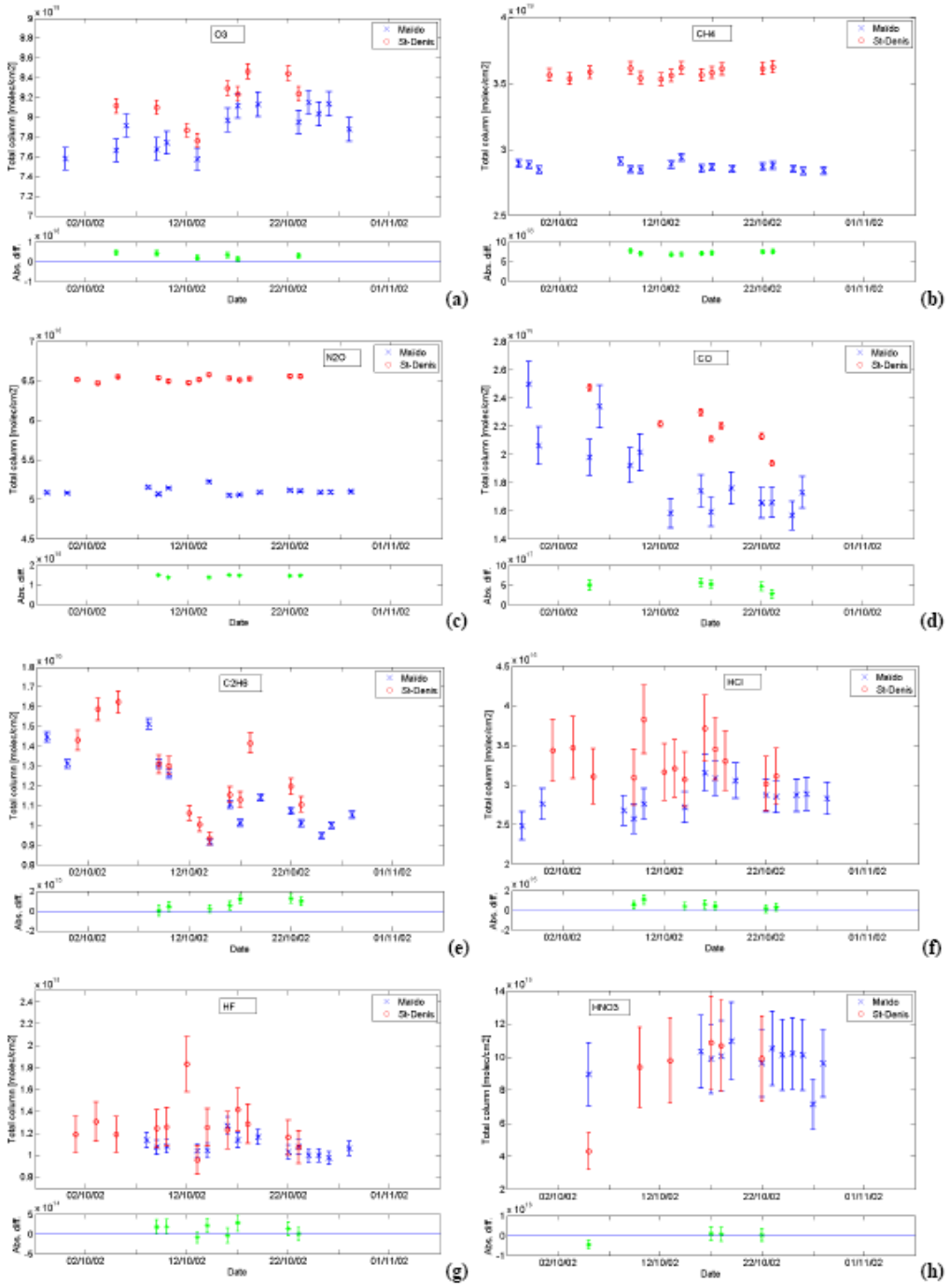

Fig. 16. Upper plots: total column amounts (in molecules/cm^2) together with random error bars of **(a)** O_3, **(b)** CH_4, **(c)** N_2O, **(d)** CO, **(e)** C_2H_6, **(f)** HCl, **(g)** HF, and **(h)** HNO_3, measured at Maïdo (blue crosses) and at St.-Denis (red circles) in 2002 by ground-based FTIR. Lower plots: absolute differences (in molecules/cm^2) of the total column amounts, calculated as the St.-Denis column value minus the Maïdo one, together with their random error bars.

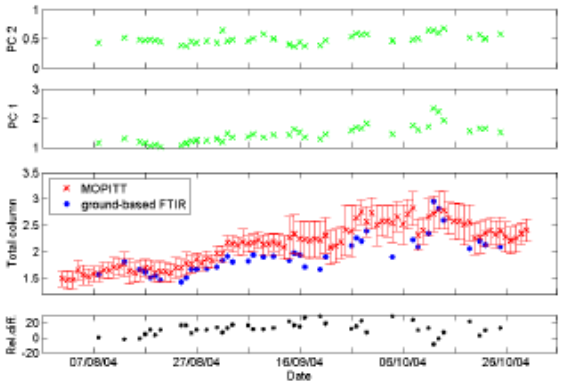

Fig. 17. From top to bottom: Time series from the period August–October 2004 of daily mean CO abundances (in 10^{18} molecules/cm^2) measured by the ground-based FTIR instrument at St.-Denis, in the 9.4–100 km layer (PC2), in the surface to 9.4 km layer (PC1), and in the total column (blue circles). The latter plot also includes the daily mean CO total column amounts and associated standard deviations measured by MOPITT (red crosses). The lowest plot shows the relative differences (in %) between the MOPITT and ground-based FTIR data for the CO total columns, on coincident days.

6.3 Impact of biomass burning emissions on CO and C_2H_6 abundances

6.3.1 CO total columns from ground-based FTIR compared to MOPITT

We compared the retrieved CO total columns with data from the MOPITT instrument.

Figure 17 shows the CO partial and total columns above Ile de La Réunion obtained from our ground-based FTIR measurements during the campaign in 2004, together with the correlative total columns from MOPITT. It also includes the relative differences between both data sets for coinciding dates, defined as 2 * (TC_{MOPITT} − TC_{FTIR}) / (TC_{MOPITT} + TC_{FTIR}) * 100. We observe a very good agreement between the time series, both showing the seasonal trend of CO – although MOPITT seems to slightly overestimate the CO concentrations – and an additional increase around 12 October. The mean relative difference between the corresponding FTIR and MOPITT total column values is 11.9%. A similar bias was also noticed by Barret et al. (2003) and Emmons et al. (2004).

6.3.2 Transport of biomass burning pollutants

The observed rise of the CO tropospheric concentrations by the end of October 2004 agrees with the known seasonal cycle of CO in the southern tropical and subtropical regions, which is attributed to the effect of enhanced mean biomass burning and cross-equatorial transport of CO from the Northern Hemisphere (WMO WDCGG, 2006). We have been able to verify that the additional increase for a few days around 12 October takes place in the (lower) troposphere (see also Fig. 17) and that it originates from fire emissions in Southern Africa and Madagascar. In order to establish a clear source-receptor relationship between the FTIR site at St.-Denis and potential gas emitting locations, we calculated retroplumes using the Lagrangian particle dispersion model FLEXPART, version 6.2 (Stohl et al., 1998, 2005). This model simulates the transport and dispersion of linear tracers, by calculating the trajectories of a chosen ensemble of particles. Not only do the retroplumes trace the origin of a particular air mass, they also give an estimate on the amount of time the air mass has spent in close proximity to the Earth's surface. Knowledge of this residence time delivers insight into the ratio of the emitted to detected trace gas. The FLEXPART model was driven by global wind field data from ECMWF, with a spatial resolution of 1° × 1° and 60 vertical levels and a temporal resolution of 3 h. The fire emissions used are 8 day averages taken from the Global Fire Emissions Database (GFED), version 2 (Van der Werf et al., 2006), using MODIS fire hot spots (Giglio et al., 2003). The emissions were distributed as follows: 20% between 0–100 m altitude, 40% between 100–500 m and 40% between 500–1000 m. Anthropogenic CO emissions, which have a small contribution, were taken from the EDGAR 3.2 Fast Track 2000 database (http://www.mnp.nl/edgar). Background CO was fixed at 85 ppb, since this is the lowest CO amount between 1 and 13 km, observed by FTIR in the period September–October, 2004. Note that this could well be an underestimation, as background CO levels are increasing in this period. For our calculations we released 200 000 particles between 0 and 13 km over St.-Denis for each corresponding FTIR measurement. Each release lasted for 602 s and each CO retroplume was traced back in time for 20 days. For each retroplume, its residence time near the surface has been calculated (in s m^3 kg^{-1}). If this response function is folded with the 3-D field of emission flux data (in kg m^{-3} s^{-1}) into this grid box, a mass mixing ratio at the receptor point is obtained. Figure 18 shows a comparison of time series of CO abundances between 0 and 13 km altitude at Ile de La Réunion in October 2004, measured by ground-based FTIR and calculated by FLEXPART. One can clearly see an enhancement in the CO amounts around 12 October, although much more obvious in the FTIR time series than in the FLEXPART series. This increase can be attributed to the transport of CO amounts originating from biomass burning events in Madagascar and Southern Africa the days before, as confirmed by Fig. 19, showing the total CO amounts emitted and transported to Ile de La Réunion on 12 October.

In order to obtain in the FLEXPART simulations the same CO levels as the observed ones, we had to increase the GFED emissions by a factor of 4; the corresponding time series are also shown in Fig. 18. One must not forget however that there are quite some uncertainties in the fire emissions due to

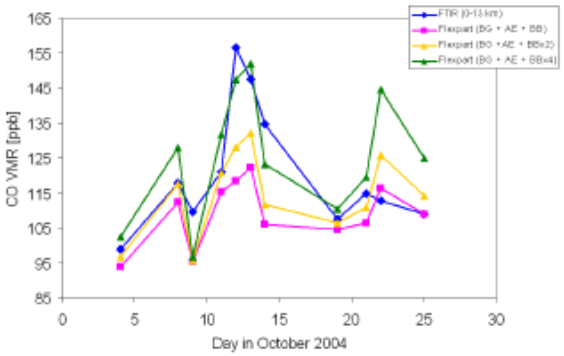

Fig. 18. Time series of CO abundances at St.-Denis between 0 and 13 km, in October 2004, calculated by ground-based FTIR (blue diamonds) and FLEXPART with (1) GFED emissions (pink squares), (2) GFED emissions x 2 (yellow triangles), and (3) GFED emissions x 4 (green triangles).

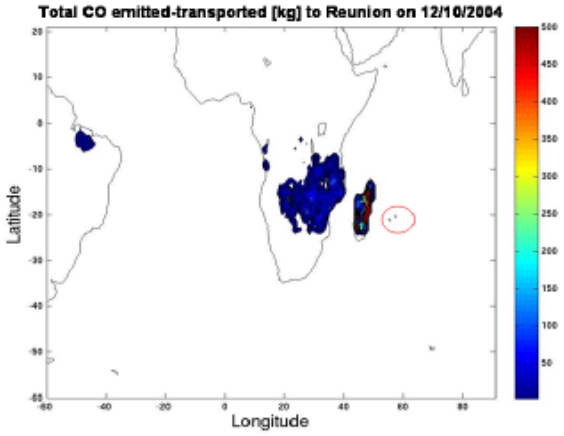

Fig. 19. Total amount of CO emitted and transported (in kg) to Ile de La Réunion (located within the red circle) on 12 October 2004, calculated by FLEXPART.

their high variability. Other factors that could lead to the observed differences between the FLEXPART simulations and the ground-based FTIR observations are: (1) we have traced back the emissions to 20 days, while the lifetime of CO permits contributions from larger time frames, (2) there are still non negligible errors in the wind fields, especially in their vertical component, (3) the temporal emission resolution (8 day averages) is not very accurate, and (4) the choice of the vertical distribution of the emissions up to 1 km is rather arbitrary since in reality the altitude dependence of the emissions is strongly influenced by the size, temperature, and type of fire (e.g., Hyer et al., 2007).

Rinsland et al. (1998) and Zhao et al. (2002) have shown that CO enhancements originating in biomass burning are

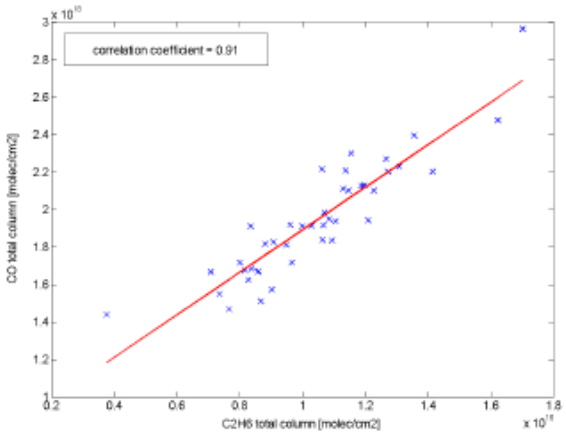

Fig. 20. Correlation plot (n = 42) of CO versus C_2H_6 total column amounts (in molecules/cm^2) during the FTIR campaigns at St.-Denis in 2002 and 2004.

strongly correlated with enhancements in C_2H_6. Such correlation has indeed been observed in our data sets: the time series of the total column values of C_2H_6 at St.-Denis in 2004 shows an increase by the end of October, in line with the observed increase of the tropospheric CO amount (Fig. 17). This is even better seen in Fig. 20 that shows the correlation plot of CO total columns versus C_2H_6 total columns during the 2002 and 2004 campaigns at St.-Denis. The correlation coefficient equals 0.91 (number of points is 42), confirming that the observed increases have the same origin, namely tropical biomass burning in Madagascar and on the African continent.

7 Conclusions and perspectives

Ground-based FTIR spectroscopy is a very useful technique to derive total column abundances and low-resolution vertical profiles of many important trace gases in the atmosphere. The technique is being used at many stations worldwide, mostly in the frame of NDACC, but rarely at low-altitude tropical or subtropical stations. Up to now, there are no regular FTIR measurements in the southern tropics.

In this technical note, we have reported the first two FTIR measurement campaigns at Ile de La Réunion, located at 21° S and 55° E, in the southern (sub)tropics. The first measurement campaign in 2002 included observations from a low- and high-altitude site simultaneously. The second campaign was performed at the low-altitude site St.-Denis only.

We have demonstrated the feasibility of these observations, at both sites, including a full error budget evaluation. Our results show that we can derive total column amounts and some vertical profile information for many of the atmospheric species of interest in tropospheric and strato-

spheric chemistry, with a precision that allows the detection of atmospheric variability. We also show that the capabilities at the high-altitude site are better than at sea level, but that it is nevertheless possible to also obtain useful data at the low-altitude site, even if water vapour causes significant interfering absorptions in the spectra. The error due to interfering species is the dominant random error source for the retrieval of C_2H_6 at St.-Denis; for all other species, other sources of error are more important. In particular, we have shown that we obtain between 1 and 5 independent pieces of information, depending on the species. This allowed us to retrieve partial column abundances for O_3, CH_4, N_2O and CO and total column values for HF, HCl, HNO_3 and C_2H_6. We have verified our data by comparisons with correlative data from satellite or sonde, and with literature values.

From the differential measurements performed during the first campaign, we have retrieved valid boundary layer information for the tropospheric species. The shortness of the campaign has prohibited investigation of the variability in the boundary layer.

It is known that the Southern Hemisphere troposphere is affected by biomass burning emissions in the dry season (September–November), which explains part of the observed variation for species like CO and C_2H_6. Here, we have confirmed that the chemical composition of the troposphere above Ile de La Réunion can suffer significant impacts from biomass burning emission events in Africa and Madagascar. Such an event was investigated in local spring 2004, supported by FLEXPART simulations.

It is planned to continue this type of measurements, first on a campaign basis and in the future on a permanent basis, and to retrieve additional species of interest, e.g., for the characterization of biomass burning emissions and transport.

A third campaign has been held in 2007, lasting from May until the end of October; the data will be used for the validation of IASI onboard METOP-1. A new campaign is planned for end of 2008 to 2009. From 2010 onward, we will be able to operate a Bruker 125HR instrument at the new NDACC infrastructure at the Maïdo: this experiment will enable regular high-quality ground-based FTIR measurements from this complementary NDACC site. The measurements will contribute to the NDACC database and further support satellite and model validation in the tropics where ground-based data are highly needed. As the dataset grows, it will provide useful information to studies of atmospheric processes in the southern (sub)tropics.

Acknowledgements. Thanks for financial support for the campaigns at Ile de La Réunion and associated research are due to the Belgian Federal Science Policy (Ministerial Order MO/35/020, ESAC II and AGACC contracts), to the PRODEX Office, and to the EU SCOUT-O3, GEOmon and HYMN projects. The former two are also supported by the Belgian Federal Science Policy.

Edited by: A. Richter

References

Anderson, G. P., Chetwynd, J. H., Clough, S. A., Kneizys, F. X., and Shettle, E. P.: AFGL atmospheric constituent profiles (0–120 km), Env. Res. Papers, AFGL-TR-86-0110, 1986.

Baray, J. L., Leveau, J., Baldy, S., Jouzel, J., Keckhut, P., Bergametti, G., Ancellet, G., Bencherif, H., Cadet, B., Carleer, M., David, C., De Mazière, M., Faduilhe, D., Beekmann, S. G., Goloub, P., Goutail, F., Metzger, J. M., Morel, B., Pommereau, J. P., Porteneuve, J., Portafaix, T., Posny, F., Robert, L., and Van Roozendael, M.: An instrumented station for the survey of ozone and climate change in the southern tropics: Scientific motivation, technical description and future plans, J. Environ. Monit., 8, 10, 1020-8, doi:10.1039/b607762e, 2006.

Barret, B., De Mazière, M., and Demoulin, P.: Retrieval and characterisation of ozone profiles from solar infrared spectra at the Jungfraujoch, J. Geophys. Res., 107, D24, 4788, doi:10.1029/2001JD001298, 2002.

Barret, B., De Mazière, M., and Mahieu, E.: Ground-based FTIR measurements of CO from the Jungfraujoch: characterisation and comparison with in-situ surface and MOPITT data, Atmos. Chem. Phys., 3, 2217–2223, 2003, http://www.atmos-chem-phys.net/3/2217/2003/.

Bernath, P. F., McElroy, C. T., Abrams, M. C., et al.: Atmospheric Chemistry Experiment (ACE): Mission overview, Geophys. Res. Lett., 32, L15S01, doi:10.1029/2005GL022386, 2005.

Boone, C. D., Nassar, R., Walker, K. A., Rochon, Y., McLeod, S. D., Rinsland, C. P., and Bernath, P. F.: Retrievals for the atmospheric chemistry experiment Fourier-transform spectrometer, Appl. Optics, 44, 33, 7218–7231, 2005.

Brasseur, G. and Solomon, S.: Aeronomy of the Middle Atmosphere: Chemistry and Physics of the Stratosphere and Mesosphere, D. Reidel Publishing Company, 1984.

Brown, L. R., Farmer, C. B., Rinsland, C. P., and Zander, R.: Remote Sensing of the Atmosphere by High Resolution Infrared Absorption Spectroscopy, in: Spectroscopy of the Earth's Atmosphere and Interstellar Medium, edited by: Rao, K. N. and Weber, A., Academic Press, 1992.

Connor, B. J., Boesch, H., Toon, G., Sen, B., Miller, C., and Crisp, D.: Orbiting Carbon Observatory: Inverse method and prospective error analysis, J. Geophys. Res., 113, D05305, doi:10.1029/2006JD008336, 2008.

Cronn, D. and Robinson, E.: Tropospheric and Lower Stratospheric Vertical Profiles of Ethane and Acetylene, Geophys. Res. Lett., 6, 8, 641–644, 1979.

De Mazière, M., Barret, B., Vigouroux, C., Blumenstock, T., Hase, F., Kramer, I., Camy-Peyret, C., Chelin, P., Gardiner, T., Coleman, M., Woods, P., Ellingsen, K., Gauss, M., Isaksen, I., Mahieu, E., Demoulin, P., Duchatelet, P., Mellqvist, J., Strandberg, A., Velazco, V., Schulz, A., Notholt, J., Sussmann, R., Stremme, W., and Rockmann, A.: Ground-based FTIR measurements of O_3- and climate-related gases in the free troposphere and lower stratosphere, Proceedings of the Quadrennial Ozone Symposium QOS 2004 (Kos, Greece, June 1–8, 2004), P211, 2004.

Emmons, L. K., Deeter, M. N., Gille, J. C., Edwards, D. P., Attié, J.-L., Warner, J., Ziskin, D., Francis, G., Khattatov, B., Yudin, V., Lamarque, J.-F., Ho, S.P., Mao, D., Chen, J. S., Drummond, J., Novelli, P., Sachse, G., Coffey, M. T., Hannigan, J. W., Gerbig, C., Kawakami, S., Kondo, Y., Takegawa,

N., Schlager, H., Baehr, J., and Ziereis, H.: Validation of Measurements of Pollution in the Troposphere (MOPITT) CO retrievals with aircraft in situ profiles, J. Geophys. Res., 109, D03309, doi:10.1029/2003JD004101, 2004.

Flaud, J.-M., Brizzi, G., Carlotti, M., Perrin, A., and Ridolfi, M.: MIPAS database: Validation of HNO_3 line parameters using MIPAS satellite measurements, Atmos. Chem. Phys., 6, 5037–5048, 2006, http://www.atmos-chem-phys.net/6/5037/2006/.

Giglio, L., Descloitres, J., Justice, C. O., and Kaufman, Y. J.: An enhanced contextual fire detection algorithm for MODIS, Remote Sens. Environ., 87, 2–3, 273–282, 2003.

Hase, F., Blumenstock, T., and Paton-Walsh, C.: Analysis of the instrumental lineshape of high-resolution Fourier transform IR spectrometers with gas cell measurements and new retrieval software, Appl. Optics, 38, 15, 3417–3422, 1999.

Hase, F., Hannigan, J. W., Coffey, M. T., Goldman, A., Höpfner, M., Jones, N. B., Rinsland, C. P., and Wood, S. W.: Intercomparison of retrieval codes used for the analysis of high-resolution ground-based FTIR measurements, J. Quant. Spectrosc. Ra., 87, 25–52, 2004.

Hawat, T., Stephen, T. M., De Mazière, M., and Neefs, E.: Proceedings SPIE, Acquisition, Tracking and Pointing XVII, edited by: M. K. Masten, L. A. Stockum, 5082, 13–20, 2003.

Hyer, E. J., Allen, D. J., and Kasischke, E. S.: Examining injection properties of boreal forest fires using surface and satellite measurements of CO transport, J. Geophys. Res., 112, D18307, doi:10.1029/2006JD008232, 2007.

Jiang, X., Ku, W. L., Shia, R.-L., Li, Q., Elkins, J. W., Prinn, R. G., and Yung, Y. L.: Seasonal cycle of N_2O: Analysis of data, Global Biogeochem. Cyc., 21, GB1006, doi: 10.1029/2006GB002691, 2007.

Meier, A., Toon, G. C., Rinsland, C. P., Goldman, A., and Hase, F.: Spectroscopic atlas of atmospheric micro-windows in the middle infrared, 2nd edition, IRF Technical Report 048, IRF Institute for Rymdfysik, Kiruna, 2004.

Neefs, E., De Mazière, M., Scolas, F., Hermans, C., and Hawat, T.: BARCOS, an automation and remote control system for atmospheric observations with a Bruker interferometer, Review of Scientific Instruments, 78, 3, 035109, doi:10.1063/1.2437144, 2007.

Notholt, J., Toon, G. C., Rinsland, C. P., Pougatchev, N. S., Jones, N. B., Connor, B. J., Weller, R., Gautrois, M., and Schrems, O.: Latitudinal variations of trace gas concentrations in the free troposphere measured by solar absorption spectroscopy during a ship cruise, J. Geophys. Res., 105, D1, 1337–1349, 2000.

Oelhaf, H., Blumenstock, T., De Mazière, M., Mikuteit, S., Vigouroux, C., Wood, S., Bianchini, G., Baumann, R., Blom, C., Cortesi, U., Liu, G. Y., Schlager, H., Camy-Peyret, C., Catoire, V., Pirre, M., Strong, K., and Wetzel, G.: Validation of MIPAS-ENVISAT version 4.61 HNO_3 operational data by stratospheric balloon, aircraft and ground-based measurements, Proceedings of ACVE-2, ESA-ESRIN, Italy, 2004.

Park, J. H., Russel, J. M., III, Gordley, L. L., Drayson, S. R., Benner, D. C., McInerney, J. M., Gunson, M. R., Toon, G. C., Sen, B., Blavier, J.-F., Webster, C. R., Zipf, E. C., Erdman, P., Schmidt, U., and Schiller, C.: Validation of Halogen Occultation Experiment CH_4 measurements from the UARS, J. Geophys. Res., 101, D6, 10 183–10 204, doi:10.1029/95JD02736, 1996.

Perrin, A., Orphal, J., Flaud, J.-M., Klee, S., Mellau, G., Mäder, H., Walbrodt, D., and Winnewisser, M.: New analysis of the ν_5 and $2\nu_9$ bands of HNO_3 by infrared and millimeter wave techniques: line positions and intensities, J. Mol. Spectrosc., 228, 375–391, 2004.

Petersen, A.K., Warneke, T., Lawrence, M. G., Notholt, J., and Schrems, O.: First ground-based FTIR observations of the seasonal variation of carbon monoxide in the tropics, Geophys. Res. Lett., 35, L03813, doi:10.1029/2007GL031393, 2008.

Randriambelo, T., Baray, J. L., and Baldy, S.: Effect of biomass burning, convective venting, and transport on tropospheric ozone over the Indian Ocean: Reunion Island field observations, J. Geophys. Res., 105, D9, 11 813–11 832, 2000.

Reisinger, A. R., Jones, N. B., Matthews, W. A., and Rinsland, C. P.: Southern hemisphere ground based measurements of Carbonyl Fluoride (COF_2) and Hydrogen Fluoride (HF): Partitioning between flouride reservoir species, Geophys. Res. Lett., 21, 9, 797–800, doi:10.1029/94GL00693, 1994.

Rinsland, C. P., Nicholas, B. J., Connor, B. J., Logan, J. A., Pougatchev, N. S., Goldman, A., Murcray, F. J., Stephen, T. M., Pine, A. S., Zander, R., Mahieu, E., and Demoulin, P.: Northern and southern hemisphere ground-based infrared spectroscopic measurements of tropospheric carbon monoxide and ethane, J. Geophys. Res., 103, D21, 28 197–28 218, doi:10.1029/98JD02515, 1998.

Rinsland, C. P., Mahieu, E., Zander, R., Jones, N. B., Chipperfield, M. P., Goldman, A., Anderson, J., Russel, J. M., III, Demoulin, P., Notholt, J., Toon, G. C., Blavier, J.-F., Sen, B., Sussmann, R., Wood, S. W., Meier, A., Griffith, D. W. T., Chiou, L. S., Murcray, F. J., Stephen, T. M., Hase, F., Mikuteit, S., Schultz, A., and Blumenstock, T.: Long-term trends of organic chlorine from ground-based infrared solar spectra: Past increases and evidence for stabilization, J. Geophys. Res., 108, D8, 4252, doi:10.1029/2002JD003001, 2003.

Rodgers, C. D.: Inverse Methods for Atmospheric Sounding: Theory and Practice, Series on Atmospheric, Oceanic and Planetary Physics, Vol. 2, World Scientific, Singapore, 2000.

Rodgers, C. D. and Connor, B. J.: Intercomparison of remote sounding instruments, J. Geophys. Res., 108, D3, 4116, doi:10.1029/2002JD002299, 2003.

Rothman, L. S. Jacquemart, D., Barbe, A., Benner, D. C., Birk, M., Brown, L. R., Carleer, M. R. Chackerian, Jr. C., Chance, K., Coudert, L. H., Dana, V., Devi, V. M., Flaud, J. M., Gamache, R.,R., Goldman, A., Hartmann, J.,M., Jucks, K.,W., Maki, A.,G., Mandin, J.,Y., Massie, S.,T., Orphal, J., Perrin, A., Rinsland, C. P., Smith, M. A. H., Tennyson, J., Tolchenov, R. N., Toth, R. A., Vander, J., Varanasi, P., and Wagner, G.: The Hitran 2004 molecular spectroscopic database, J. Quant. Spectrosc. Ra., 96, 139–204, 2005.

Rudolph, J. and Ehhalt, D. H.: Measurements of C2-C5 hydrocarbons over the North Atlantic, J. Geophys. Res., 86, C12, 11 959–11 964, 1981.

Russell, J. M., III, Deaver, L. E., Luo, M., Park, J. H., Gordley, L. L., Tuck, A. F., Toon, G. C., Gunson, M. R., Traub, W. A., Johnson, D. G., Jucks, K. W., Murcray, D. G., Zander, R., Nolt, I. G., and Webster, C. R.: Validation of hydrogen chloride measurements made by the Halogen Occultation Experiment from the UARS platform, J. Geophys. Res., 101, D6, 10 151–10 162, doi:10.1029/95JD01696, 1996a.

Russell, J. M., III, Deaver, L. E., Luo, M., Cicerone, R. J., Park, J.

H., Gordley, L. L., Toon, G. C., Gunson, M. R., Traub, W. A., Johnson, D. G., Jucks, K. W., Zander, R., and Nolt, I. G.: Validation of hydrogen fluoride measurements made by the Halogen Occultation Experiment from the UARS platform, J. Geophys. Res., 101, D6, 10 163–10 174, doi:10.1029/95JD01705, 1996b.

Schneider, M., Blumenstock, T., Chipperfield, M. P., Hase, F., Kouker, W., Reddmann, T., Ruhnke, R., Cuevas, E., and Fischer, H.: Subtropical trace gas profiles determined by ground-based FTIR spectroscopy at Izaña (28° N, 16° W): Five-year record, error analysis, and comparison with 3-D CTMs, Atmos. Chem. Phys., 5, 153–167, 2005, http://www.atmos-chem-phys.net/5/153/2005/.

Smit, H. G. J. and Straeter, W.: JOSIE-2000, Jülich Ozone Sonde Intercomparison Experiment 2000, The 2000 WMO international intercomparison of operating procedures for ECC-ozone sondes at the environmental simulation facility at Jülich, WMO Global Atmosphere Watch report series, No. 158, World Meteorological Organization, Geneva, 2004.

Smith, M. A. H.: Compilation of atmospheric gas concentration profiles from 0 to 50 km, NASA TM 83289, 1982.

Stohl, A., Hittenberger, M., and Wotawa, G.: Validation of the Lagrangian particle dispersion model FLEXPART against large scale tracer experiment data, Atmos. Environ., 24, 4245–4264, 1998.

Stohl, A., Forster, C., Frank, A., Seibert, P., and Wotawa, G.: Technical Note: The Lagrangian particle dispersion model FLEXPART version 6.2., Atmos. Chem. Phys., 5, 2461–2474, 2005, http://www.atmos-chem-phys.net/5/2461/2005/.

Sussmann, R. and Borsdorff, T.: Technical Note: Interference errors in infrared remote sounding of the atmosphere, Atmos. Chem. Phys. 7, 3537–3557, 2007.

Urban, J., Lautié, N., Le Flochmoën, E., Jiménez, C., Eriksson, P., de La Noë, J., Dupuy, E., Ekström, M., El Amraoui, L., Frisk, U., Murtagh, D., Olberg, M., and Ricaud, P.: Odin/SMR limb observations of stratospheric trace gases: Level 2 processing of ClO, N_2O, HNO_3, and O_3, J. Geophys. Res., 110, D14307, doi: 10.1029/2004JD005741, 2005.

U.S. National Oceanic and Atmospheric Administration: U.S. Standard Atmosphere: 1976 published by the U.S. Government Printing Office, Washington, D.C., 1976.

Van der Werf, G. R., Randerson, J. T., Giglio, L., Collatz, G. J., and Kasibhatla, P. S.: Interannual variability in global biomass burning emission from 1997 to 2004, Atmos. Chem. Phys., 6, 3423–3441, 2006, http://www.atmos-chem-phys.net/6/3423/2006/.

Wang, D. Y., Höpfner, M., Blom, C. E., Ward, W. E., Fischer, H., Blumenstock, T., Hase, F., Keim, C., Liu, G. Y., Mikuteit, S., Oelhaf, H., Wetzel, G., Cortesi, U., Mencaraglia, F., Bianchini, G., Redaelli, G., Pirre, M., Catoire, V., Huret, N., Vigouroux, C., De Mazière, M., Mahieu, E., Demoulin, P., Wood, S., Smale, D., Jones, N., Nakajima, H., Sugita, T., Urban, J., Murtagh, D., Boone, C. D., Bernath, P. F., Walker, K. A., Kuttippurath, J., Kleinböhl, A., Toon, G., and Piccolo, C.: Validation of MIPAS HNO_3 operational data, Atmos. Chem. Phys., 7, 4905–4934, 2007, http://www.atmos-chem-phys.net/7/4905/2007/.

WMO WDCGG Data Summary. WDCGG No. 30, GAW Data, Volume IV Greenhouse Gases and Other Atmospheric Gases, published by Japan Meteorological Agency, in co-Operation with the World Meteorological Organization, March 2006.

Zander, R., Mahieu, E., Demoulin, P., Duchatelet, P., Servais, C., Roland, G., Delbouille, L., De Mazière, M., and Rinsland, C. P.: Evolution of a dozen non-CO_2 greenhouse gases above Central Europe since the mid-1980s, Environ. Sci., (Special Issue: Non-CO_2 Greenhouse Gases), 2, 2–3, 295–303, 2005.

Zhao, Y., Strong, K., Kondo, Y., Koike, M., Matsumi, Y., Irie, H., Rinsland, C. P., Jones, N. B., Suzuki, K., Nakajima, H., Nakane, H., and Murata, I.: Spectroscopic measurements of tropospheric CO, C_2H_6,C_2H_2, and HCN in northern Japan, J. Geophys. Res., 107, D18, 4343, doi:10.1029/2001JD000748, 2002.

1.3 Les données de la Réunion dans les réseaux de recherche et de surveillance internationaux

1.3.1 Introduction

Pour une station de mesure, intégrer des mesures atmosphériques dans des réseaux de recherche et de surveillance nationaux et internationaux est particulièrement important. Cela permet :

- D'assurer la qualité des données grâce aux dispositifs d'inter-comparaison et le contrôle de la qualité des données associés à ces réseaux.
- De favoriser les contacts scientifiques avec les autres groupes participant aux réseaux
- D'assurer une bonne visibilité et une utilisation plus étendue de ses données et d'avoir un accès aux données des autres stations.
- D'obtenir des financements pour le développement, la maintenance et le fonctionnement de la station.

Aussi, dès les premières mesures à la Réunion, celles-ci ont été intégrées au réseau mondial de surveillance de la stratosphère NDSC[9] en tant que station complémentaire. Soutenu par les agences scientifiques nationales et internationales, ce réseau s'est développé à partir de 1991 pour favoriser à l'échelle globale l'implantation de stations de mesures sol destinées à mesurer conjointement les paramètres atmosphériques ayant une influence sur l'évolution à long terme de l'ozone stratosphérique. En 2006, le NDSC devient NDACC[10] pour prendre en compte les couplages dynamiques et physico-chimiques entre la haute troposphère et la basse stratosphère, dans le contexte du changement climatique.

Le réseau comprend un certain nombre de stations, dont la répartition mondiale est indiquée sur la figure 1.6. Historiquement, le réseau distinguait des stations primaires disposant d'un ensemble complet d'instruments destinés à mesurer plusieurs paramètres ou composants stratosphériques et de stations complémentaires disposant d'un ensemble d'instruments plus limité mais soumises aux mêmes critères de qualité que les stations primaires.

[9] Network for the Detection of Stratospheric Changes
[10] Network for the Detection of Atmospheric Composition Change, http://www.ndacc.org/

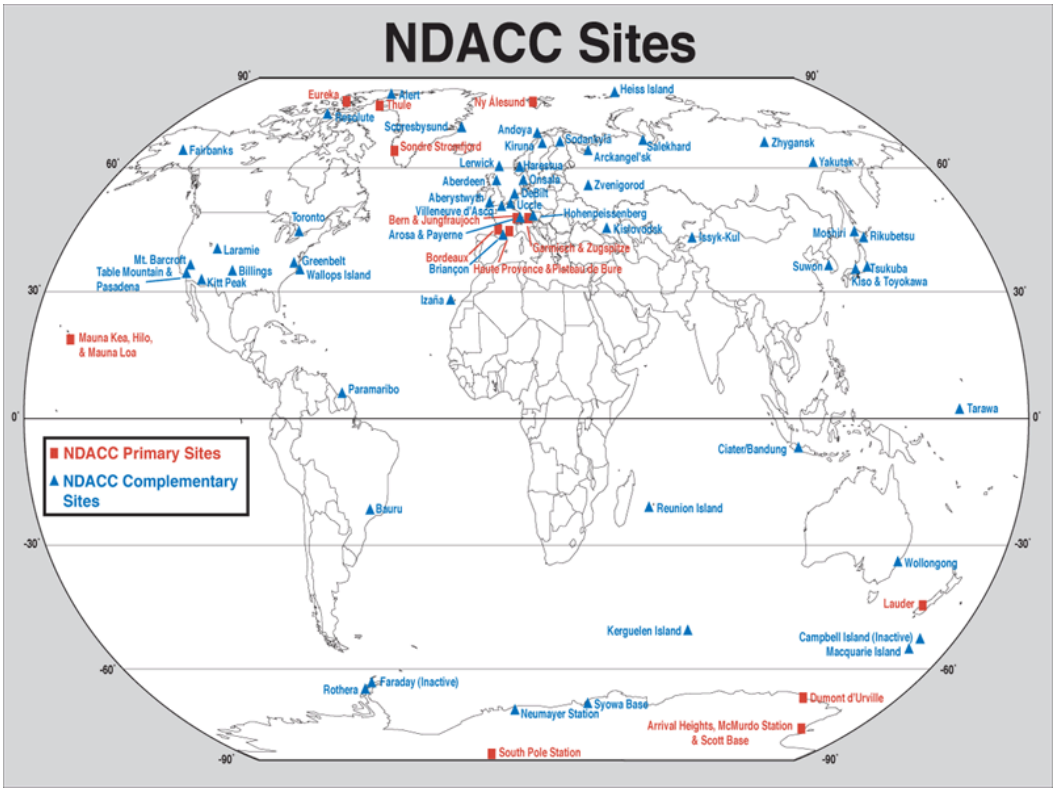

Figure 1.6 Répartition des stations NDACC dans le monde

L'origine de l'idée des stations primaires était d'en disposer d'une par tranche de latitude qui serait, si possible, équipée de l'ensemble des instruments NDACC. Pour différentes raisons, ceci ne s'est réalisé qu'exceptionnellement, pour laisser la place à des groupements régionaux de stations. Dès lors cette séparation entre stations primaires et complémentaires perdait son sens, et lors de la dernière réunion des responsables du NDACC en 2008, il a été décidé de supprimer cette séparation, et de considérer uniquement des stations NDACC dans une liste unique. Comme on peut le constater sur figure 1.6, si les régions polaires et les latitudes moyennes sont bien couvertes en station NDACC, il n'en est pas de même pour les régions tropicales. La Réunion a donc vocation à devenir une station référence de ce réseau pour la bande tropicale de l'hémisphère sud.

La participation à ce réseau implique un certain nombre d'obligations telles que la livraison régulière des données obtenues dans la base de données NDACC, la participation à différents exercices d'inter-comparaison instrumentales, comparaisons d'algorithme, calibration des instruments embarqués sur satellites. Ces exercices peuvent déboucher sur la publication d'articles techniques,.tels que celui présenté dans la section 1.3.2.

Depuis 1999, la Réunion est également impliquée dans le réseau SHADOZ[11], la répartition des stations dans le monde étant indiquée dans la figure 1.7. Ce réseau vise à constituer une base de données de sondages ozone dans la bande tropicale de l'hémisphère sud. Au départ, l'objectif de ce réseau était de valider les méthodes d'estimation du résidu troposphérique de l'ozone en régions tropicales à partir des satellites avec un jeu de données indépendant. Par le biais de ce réseau, la NASA finance 50% des sondages effectués à la Réunion, ce qui a permis de faire passer la fréquence des mesures de 1 toutes les deux semaines à un par semaine.

Figure 1.7 Répartition des stations SHADOZ dans le monde

La Réunion est également impliquée dans le projet EQUAL[12], qui vise à valider les données satellitales ENVISAT avec des données lidar. Les données lidar température et ozone sont donc fournies dans cette base de données, la partie ozone de ce projet ayant fait l'objet d'un article publié dans la session spéciale sur le protocole de Montréal du journal *Int. J. Remote. Sensing*. (section 1.3.3).

Comme indiqué dans la section 1.2.2 et sur la figure 1.2, l'OPAR est doté d'un photomètre CIMEL dans le cadre du réseau PHOTONS/AERONET[13], un réseau d'observations en quasi-temps réel de paramètres optiques visant à la caractérisation des aérosols atmosphériques par radiométrie[14], la répartition des stations AERONET étant indiquée sur la figure 1.8.

[11] Southern Hemisphere Additional Ozonesondes, http://croc.gsfc.nasa.gov/shadoz/
[12] Envisat Quality Assessment with Lidar
[13] AEosol RObotic NETwork, http://loaphotons.univ-lille1.fr/photons/index.php
[14] Holben B.N., et al., AERONET - A federated instrument network and data archive for aerosol characterization, *Rem. Sens. Environ*., **66**, 1-16, 1998.

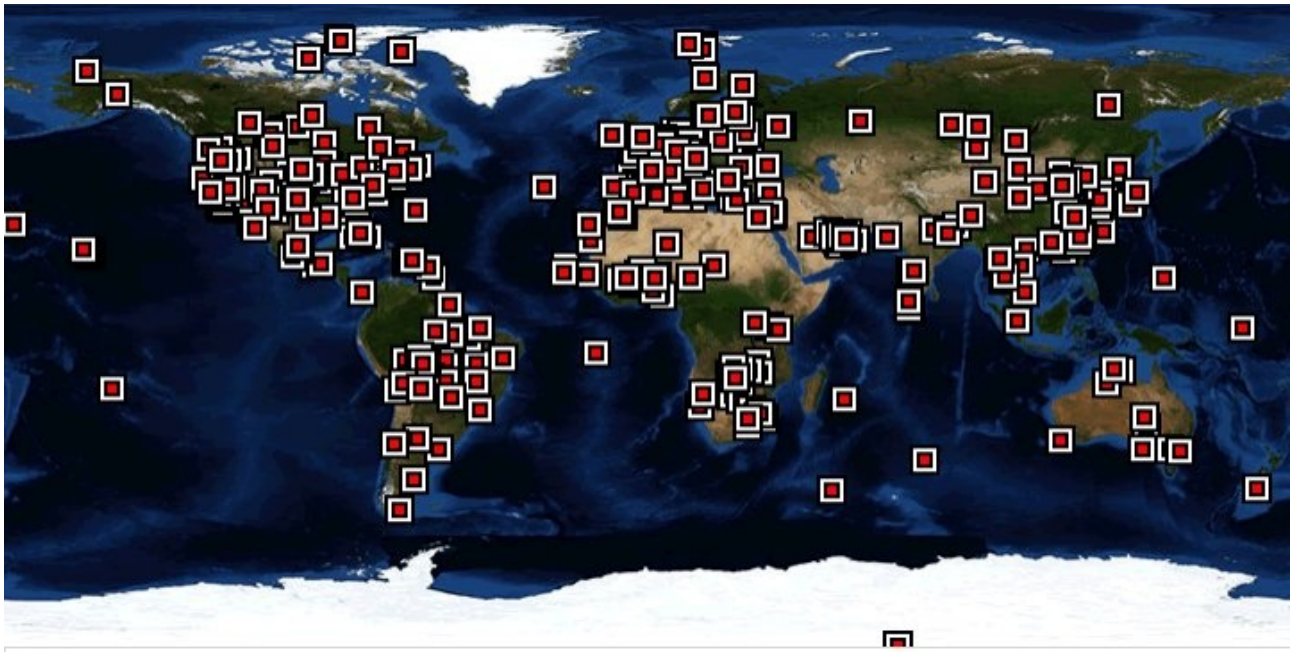

Figure 1.8 Répartition des stations AERONET dans le monde

La Réunion est également associée au réseau GEOMON[15], dont la mission est de structurer un système d'observation global des gaz à effet de serre, des gaz réactifs, aérosols et ozone stratosphérique, pour comprendre et identifier le rôle du changement climatique sur la composition de l'atmosphère.

Enfin, le réseau GAW[16] est le réseau de surveillance des gaz à effet de serre du système d'observation du climat global de l'OMM[17]. Au titre de la mise à disposition des radiosondages dans ce réseau via Météo-France, la Réunion participe à ce programme, dédié à la surveillance de la pollution de fond de l'atmosphère, est basé sur la mesure in situ et la télédétection des principaux polluants atmosphériques (composition chimique de l'atmosphère et paramètres physiques qui y sont liés), sans pour le moment développer concrètement les thématiques scientifiques du réseau GAW. Cependant, comme il le sera précisé dans la section 1.4, la mise en place de mesures in-situ spécialement dans le cadre de la future station d'altitude nous permettra de développer l'instrumentation nécessaire pour réellement contribuer à la surveillance de la pollution de fond atmosphérique.

Le fait de participer à de tels réseaux de recherche implique une lourde tache de validation des données et de mise à disposition dans les meilleurs délais, à laquelle je me suis consacré de manière importante. Pour améliorer à la fois la visibilité de l'OPAR et des données qui y sont produites,

[15] Global Earth Observation and Monitoring of the Atmosphere, http://www.geomon.eu/
[16] Global Atmosphere Watch, http://www.wmo.int/pages/prog/arep/gaw/gaw_home_en.html
[17] Organisation Météorologique Mondiale, http://www.wmo.ch/pages/index_fr.html

mais également pour optimiser le travail de mise à disposition des données pour les réseaux internationaux, un site internet-base de données de l'OPAR a été développé par Hélène Ferré et Franck Gabarrot (figure 1.9). J'ai fait en sorte de leur faciliter la tâche et de contribuer au maximum à ce projet important pour l'OPAR en communiquant un maximum d'informations (textes, photos) et toutes les données pour documenter les différentes rubriques du site et en répondant au mieux à leurs sollicitations.

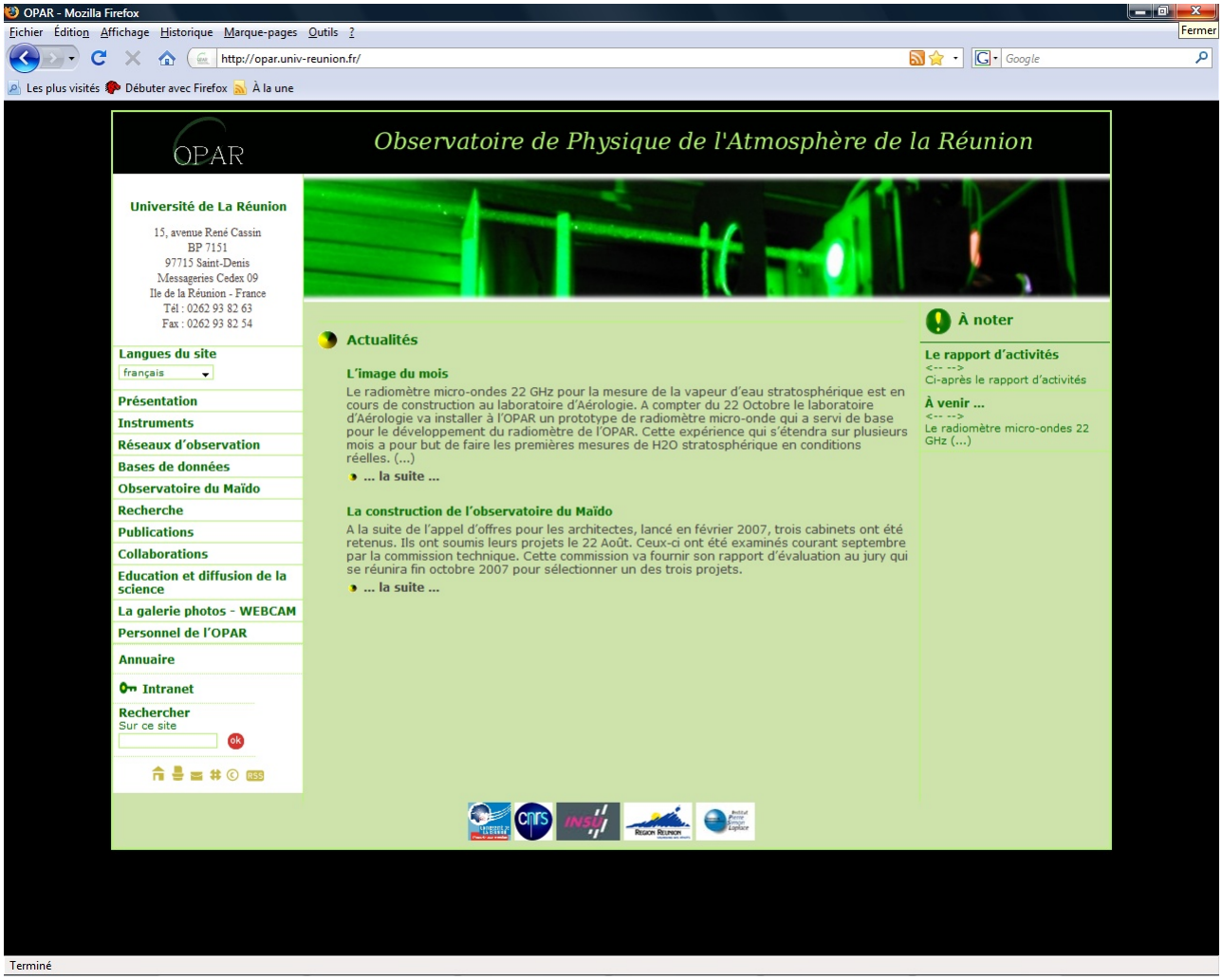

Figure 1.9 Site internet de l'OPAR contenant, via des menus à gauche, une présentation générale de l'OPAR, des instruments, des réseaux d'observation, une base de données, la liste des publications, du personnel de l'OPAR et des collaborations, et une galerie de photos.

1.3.2 Validation des lidar ozone et température dans le cadre du réseau NDSC/NDACC

CRITICAL REVIEW

JEM www.rsc.org/jem

Review of ozone and temperature lidar validations performed within the framework of the Network for the Detection of Stratospheric Change

Philippe Keckhut,[a] Stuart McDermid,[b] Daan Swart,[c] Thomas McGee,[d] Sophie Godin-Beekmann,[a] Alberto Adriani,[e] John Barnes,[f] Jean-Luc Baray,[g] Hassan Bencherif,[g] Hans Claude,[h] Aleide G. di Sarra,[i] Georgio Fiocco,[i] Georg Hansen,[j] Alain Hauchecorne,[a] Thierry Leblanc,[b] Choo Hie Lee,[k] Shiv Pal,[l] Gerard Megie,[a] Hideaki Nakane,[m] Roland Neuber,[n] Wolfgang Steinbrecht[h] and Jeffrey Thayer[o]

[a]*Service d'Aéronomie/IPSL, Verrière-le-Buisson, France*
[b]*Table Mountain Facility, Jet Propulsion Laboratory, Wrightwood, CA, USA*
[c]*National Institute for Public Health and the Environment, Bilthoven, The Netherlands*
[d]*Laboratory for Atmospheres, Goddard Space Flight Center, Greenbelt, MD, USA*
[e]*Istituto Fisica dell'Atmosfera, CNR, Rome, Italy*
[f]*National Oceanic and Atmospheric Administration, Mauna Loa Observatory, Hilo, HI, USA*
[g]*Laboratoire de Physique de l'Atmosphère, Université de La Réunion, St-Denis, France*
[h]*Meteorologisches Observatorium Hohenpeissenberg, Hohenpeissenberg, Germany*
[i]*Universita La Sapienza, Dipartemento di Fissica, Roma, Italy*
[j]*Norwegian Institute for Air Research, Kjeller, Norway*
[k]*Lidar Center of Kyung Hee University, Gyeonggi-Do, South Korea*
[l]*Science And Art Innovation Inc., Ontario, Canada*
[m]*National Institute for Environmental Studies, Tsukuba, Japan*
[n]*Alfred Wegener Institute, Potsdam, Germany*
[o]*SRI International Center for Geospace Studies, Menlo Park, CA, USA*

Received 15th April 2004, Accepted 1st June 2004
First published as an Advance Article on the web 26th July 2004

The use of assimilation tools for satellite validation requires true estimates of the accuracy of the reference data. Since its inception, the Network for Detection of Stratospheric Change (NDSC) has provided systematic lidar measurements of ozone and temperature at several places around the world that are well adapted for satellite validations. Regular exercises have been organised to ensure the data quality at each individual site. These exercises can be separated into three categories: large scale intercomparisons using multiple instruments, including a mobile lidar; using satellite observations as a geographic transfer standards to compare measurements at different sites; and comparative investigations of the analysis software. NDSC is a research network, so each system has its own history, design, and analysis, and has participated differently in validation campaigns. There are still some technological differences that may explain different accuracies. However, the comparison campaigns performed over the last decade have always proved to be very helpful in improving the measurements. To date, more efforts have been devoted to characterising ozone measurements than to temperature observations. The synthesis of the published works shows that the network can potentially be considered as homogeneous within $\pm 2\%$ between 20–35 km for ozone and ± 1 K between 35–60 km for temperature. Outside this altitude range, larger biases are reported and more efforts are required. In the lower stratosphere, Raman channels seem to improve comparisons but such capabilities were not systematically compared. At the top of the profiles, more investigations on analysis methodologies are still probably needed. SAGE II and GOMOS appear to be excellent tools for future ozone lidar validations but need to be better coordinated and take more advantage of assimilation tools. Also, temperature validations face major difficulties caused by atmospheric tides and therefore require intercomparisons with the mobile systems, at all sites.

1. Introduction

The idea to establish a network of high-quality remote-sounding research stations to observe and understand anthropogenic changes in the stratosphere was first discussed at a workshop in 1986. The result was the development of the international Network for the Detection of Stratospheric Change (NDSC). The initial goals of the network[1] were to make the earliest possible identification of changes in the stratospheric ozone layer and related parameters, to study the variability of the stratosphere, to provide an independent calibration and validation of satellite sensors, and to provide data to test and improve multi-dimensional atmospheric chemical and dynamical models. These goals were subsequently expanded to include establishing the links between changes in stratospheric ozone, UV radiation at the ground, tropospheric chemistry, and climate. To meet such objectives, the quality of the data is one of the key issues and a major challenge the NDSC had to face.

While traditional methods such as balloon soundings and Dobson observations that have so far provided the longest data series were included in the NDSC, new instruments were qualified on the basis of being remote sensors, capable of continuous long-term field operation with the best accuracies.

DOI: 10.1039/b404256e

Lidar methods, having the required precision and range resolution, were proposed to be used for ozone, temperature and aerosol profile measurements. Lidar systems are also good candidates for atmospheric monitoring because they have low manpower requirements and modest maintenance costs. To provide the optimum latitude coverage within the obvious constraints of quality, funds and resources, it was proposed that the network would consist of 5–7 primary stations fully equipped with all the NDSC-defined instruments: polar, mid-latitude, and tropical stations in both hemispheres, plus an equatorial station. Depending on specific site characteristics such as geography, orography or meteorology, a composite station may be formed with individual or a limited group of instruments at different sites within a given latitudinal or regional zone. Some complementary sites and mobile instruments are also associated with this network to expand the geographic coverage.

Considering the aims of this network, homogeneity of the data quality is required on both the temporal scale, for individual instruments, and on the horizontal scale over all the instruments involved in the network measuring the same geophysical quantity. The main limitations for trend detection, in addition to the natural variability, are temporal discontinuities.[2] An instrumental bias that remains unchanged is not in theory a limitation for trend quantification. However, instrumental changes cannot be avoided with ground-based instruments running on a quasi-daily basis spanning decades. So instrumental drifts are always possible and are in fact a severe limitation for the investigations of long-term change. It also appears that the altitude locations of bias and instrumental drifts are often correlated.

For satellite validation, horizontal homogeneity of the correlative measurements is required in order to be able to quantify possible latitudinal bias of the instrument in space. The NDSC instruments are all research prototypes and have some differences in their design and final capabilities. Systematic differences that are of particular relevance for data quality must be detected, critically analyzed, and ruled out. The Steering Committee of the NDSC has therefore proposed to use, when and wherever possible, a mobile system alternately visiting the different stations of the network.[1] Since ozone and temperature trends are expected to be small compared to the natural variability (around 10% and 1 K per decade respectively), the investigation of potential bias is more crucial than for stratospheric aerosol lidar measurements, where variability is mainly dominated by huge events such as volcanic eruptions or ice clouds in polar regions. For this reason, up to now, more effort has been expended on intercomparison campaigns for ozone and temperature profiles. Since the official inception of the network in 1991, several campaigns have been organized employing the NASA/Goddard Space Flight Center (GSFC) mobile lidar. However, comparisons with the mobile lidar are not the only way to determine the quality of the data and other techniques have been investigated simultaneously in some campaigns, or more routinely at some sites. Comparisons with co-located radiosondes, or microwave radiometers are often performed, and also with close-by satellite measurements. There is no absolute reference instrument and the individual capabilities, and the network homogeneity, cannot be assured or quantified without undertaking all the NDSC validation exercises. Instruments launched into space are continually improving and their capabilities are close to what is obtainable from the ground in terms of sensitivity. Validation using ground-based instruments is therefore pushed to the limit. The use of assimilation allows, in theory, freedom from most of the possible discrepancies induced by geophysical causes and non-perfect spatio-temporal coincidences. However, some weighting of the data input to the model needs to be decided. The use of the reference data requires provision of standard values for bias and noise. After 10 years of operation, a first review of the validation exercises using NDSC ozone and temperature lidar is presented.

Philippe Keckhut was born in 1964 in Paris (France). He graduated in Optics and obtained his Doctorate at Paris in 1991. He was a National Research Council visiting scientist at NOAA-NCEP in 1994. He has pursued his research at Service d'Aéronomie (France) on inter-annual variability and trends in the middle atmosphere using lidar, rocket, radiosonde and satellite data series. He is co-responsible for two lidars involved in the NDSC network. He is also working on the upper troposphere climatology. He coordinates the 'Observation Services' of the Institut Pierre Simon Laplace. He has published 43 peer-reviewed papers in atmospheric sciences.

Philippe Keckhut

2. Description of the instruments

Atmospheric ozone profiles up to 45–50 km can be measured using the DIfferential Absorption Lidar (DIAL) technique, which requires two laser beams in the UV spectral region.[3] The basic principle is to transmit two short laser pulses vertically into the atmosphere, one having a wavelength in an absorption band of ozone and the other not absorbed (or not so strongly absorbed) by ozone that can be used as reference. The ozone number density can then be retrieved from the difference in slope between the absorbed and non-absorbed lidar returns. Following major volcanic eruptions, it is necessary to avoid corruption of the backscattered signal caused by enhanced aerosols, and nitrogen Raman scattering can be used with the DIAL principle to derive ozone in the lower stratosphere under these conditions.[4] On average, the ozone measurement precision achieved by NDSC lidars is around 1% up to 30 km 2–5% at 40 km and 5–25% at 50 km.

Temperature profiles can be derived from Rayleigh scattering[5] by assuming the atmosphere follows the ideal gas law and is in hydrostatic equilibrium. Temperatures are typically measured from 30 to around 80 km where atmosphere is not polluted by the presence of aerosols. Temperature profiles can be derived with better than 1 K precision from 30 to 70 km. Above 70 km, the temperature uncertainty increases rapidly with altitude due to photon counting uncertainties.

Basically, two type of lidar can be found.

(1) DIAL systems designed primarily for ozone density profiles operating at UV wavelengths and which can also measure temperature using the non-absorbed channel(s).

(2) Backscatter lidars that use a single wavelength are specifically used for temperature retrieval and can be based on visible or UV wavelengths. While the efficiency compared to DIAL is not entirely obvious, some groups using a temperature specific lidar system have chosen to use the second harmonic of the Nd:YAG laser, probably because the visible wavelength is somewhat easier to manage compared to UV, although tripled Nd:YAG and XeF lasers are also used.

In the presence of aerosols, Raman techniques can be used to extend the temperature profile downward.[6] However, the lidar signal is directly affected by the aerosol attenuation and so can only be used for low to moderate aerosol loading. Alternative

techniques, using the temperature dependence of the rotational–vibrational Raman spectrum, have also been investigated. However, the need for calibration limits the application of such a method for long-term monitoring. No specific actions have been planned within the NDSC on this issue and the lidar community continues to perform further investigations.

The main differences between the lidars involved in the NDSC are the size of their receiver telescope and their laser power, *i.e.*, power–aperture product. However, these differences do not significantly affect the derivation methodology and their main effect is on the level of the counting noise that only restricts the altitude range of the measurement or the integration time for a given accuracy. Many variations in the actual lidar implementations can be noted, which can explain the differences observed between the various lidars involved in the NDSC. One difference is in the methods used to increase the dynamic range of the measurements. Usually, several channels with different sensitivity are set up and used simultaneously. To achieve this goal several technical solutions can be found and different signal processing methods have been reported to combine signals to provide a single profile through the entire stratosphere. The signal background levels also tend to be specific to a particular instrument design as is the way this is treated in the data analysis. The background noise level and the signal-induced-noise (SIN), which is due to the large initial burst of laser energy and the noise memory of the photomultiplier, can be mitigated with specific designs and analyses. The initialization of the temperature profile is strongly dependent on the lidar power and the methodology. The presence of aerosols, the filtering, or the alignment between the laser and the receiver field-of-view, are also some issues that have been resolved or at least investigated differently by each group.

It is difficult *a priori* to design an ideal lidar system for a long-term observations, accuracy, and reliability. In theory, most of the NDSC systems provide adequate designs and analyses to take care of all the well-known limitations mentioned previously. Ultimately, cross-validations or intercomparisons appear to be the only way to determine the quality of the different lidar systems. All the ozone and temperature lidars participating in the NDSC are listed in Table 1. However, in this section only lidars that have participated in NDSC sanctioned validation exercises are reported. Technical details can be found in specific publications referenced later. The locations of the NDSC sites extend all over the latitudes from 80°N to 78°S. Teams directly involved, reveal the large international community that concerns many countries all around the world (Canada, France, Germany, Italy, Japan, Norway, South Korea, The Netherlands, USA).

The GSFC stratospheric ozone lidar was developed by McGee *et al.*[7] as a mobile system to serve as a geographical transfer reference from one site to another. This instrument began development with funding from the NASA Upper Atmosphere Program in 1985 and has been a participant in the NDSC since its inception. This lidar is housed in a 45′ trailer allowing for transport around the world. The absorbed wavelength is provided by a XeCl excimer laser at 308 nm and the non-absorbed wavelength at 351 nm from a XeF excimer laser (more recently changed to 355 nm from Nd:YAG third harmonic). Spectral separation is accomplished using beamsplitters and interference filters. Each of the elastically scattered signals is further split to improve the dynamic range; roughly 2–5% is used to retrieve data in the lower stratosphere.[8] The two nitrogen Raman channels were added in late 1991 and tested at the first inter-comparison campaign at the Observatory of Haute-Provence (OHP) in summer 1992 just after the eruption of Mount Pinatubo. This permits DIAL ozone retrieval in the presence of enhanced particle concentrations.[9] The temperature profile is computed from the Rayleigh backscattering from the non-absorbed wavelength down to 28 km and using the Raman return down to ~15 km when the atmosphere is relatively clean of aerosols and described by Gross *et al.*[10] This instrument was used as the mobile reference and visits to many NDSC sites for collocated comparisons (Table 2).

One of the longest ozone and temperature series using lidar is available for OHP (43.9°N, 5.7°E). These two measurements are performed with two distinct instruments located at OHP that is part of the first NDSC site in the mid-northern hemisphere: The Alpine station. The ozone DIAL system operated by the Centre National de la Recherche Scientifique (CNRS) used a XeCl excimer laser at 308 nm and the third harmonic of a Nd:YAG laser at 355 nm, respectively, for the

Table 1 List of ozone and temperature lidars in operation in the framework of NDSC[a]

Site	Location	Measured parameters/PI	Team and laboratory	NDSC operation since	Station
Mobile lidar	—	O3, T/T. J. McGee	GSFC/NASA	1991	Mobile
Eureka	80.05°N, 86.42°W	O3/S. Pal	York University	1993	Arctic
Ny-Ålesund	78.92°N, 11.93°E	O3, T/R. Neuber, O. Schrems	AWI	1991	Arctic
Thule	76.53°N, 68.74°W	T/ G. Fiocco	Rome University	1991	Arctic
Sondrestrom	67.0°N, 50.9°W	T/ J. Thayer	SRI	2002	Complementary
ALOMAR DIAL	69.3°N, 16.0°E	O3/G. Hansen	NILU	1995	Complementary
ALOMAR Backsc.		T/Hauchecorne	CNRS/SA	1993	Complementary
Hohenpeissenberg	47.80°N, 11.02°E	O3, T/H. Claude	MOH	1987	Complementary
OHP/DIAL	43.94°N, 5.71°E	O3/S. Godin	CNRS/SA	1991	Alpine
OHP Backscatter		T/A. Hauchecorne	CNRS/SA	1991	Alpine
Toronto	43.8°N, 79.5°W	O3, T/S. Pal	York University	1990	Complementary
Suwon DIAL	37.2°N, 127.6°E	O3/C. H. Lee	Kyung Hee University	1992	Complementary
Suwon Backscatter		T/C. H. Lee	Kyung Hee University	1995	Complementary
Tsukuba	36.05°N, 140.13°E	O3/H. Nakane	NIES	1991	Complementary
TMF	34.4°N, 117.7°W	O3, T/I. S. McDermid	JPL	1991	Complementary
MLO DIAL	19.54°N, 155.58°W	O3, T/I. S. McDermid	JPL	1993	Hawaii
MLO Backscatter		T/ J. Barnes	NOAA-CMDL	1994	Hawaii
La Reunion	21.8°N, 55.5°E	T/H. Bencherif	La Reunion University	1994	Complementary
		O3/ J. L. Baray	La Reunion University	2000	Complementary
Lauder	45.05°S, 169.68°E	O3, T/D. Swart	RIVM	1994	New Zealand
		T/ Stefanutti	CNR/IROE	1994	New Zealand
DDU	66.67°S, 140.01°E	O3/S. Godin	CNRS/SA	1991	Antarctic
McMurdo	77.85°S, 166.70°E	T/A. Adriani	CNR/IFA	1991	Not NDSC

[a] Instruments in bold have been compared with the mobile system. O3 and T refer respectively to ozone and temperature while PI mean principal investigator or the person responsible for the scientific data quality. See the acronym list for "Team and laboratory".

Table 2 Intercomparison campaigns with the mobile GSFC lidar involved

Campaign name	Location	Date
Informal	TMF California	Oct–Nov 1988
STOIC	TMF California	Jul–Aug 1989
OHP 92	OHP France	Jul–Aug 1992
OPAL	Lauder New Zealand	Apr 1995
MLO3	MLO Hawaii	Aug 1995–Feb 1996
STRAT	TMF California	Feb–Mar 1997
OTOIC	OHP France	Jun–Jul 1997
NAOMI	Ny-Ålesund Svalbard	Jan–Feb 1998

absorbed and the non-absorbed wavelengths. A multi-channel monochromator separates the received wavelengths including (as the GSFC system) Raman channels and low sensitivity elastic channels. This instrument, redesigned in December 1993, follows a previous prototype that was in operation since 1986. This first instrument described by Godin *et al.*,[11] had only two channels, and two measurement sequences had to be made sequentially with, respectively, the full and a reduced laser power in order to cover the full 18–45 km altitude range. The temperature is obtained with an independent instrument, operating since 1984, using the second harmonic of a Nd:YAG laser at 532 nm using a method described by Hauchecorne and Chanin.[5] Since its inception, this instrument has undergone several modifications.[12] Prior to 1991, the low sensitivity channel was constructed similarly to the GSFC lidar system; now a second independent smaller telescope is used to collect the light from the lower altitudes. This configuration, described by Keckhut *et al.*,[12] has been preferred to check alignments between the emitted beam and the receiver field-of-view. This lidar was redesigned in September 1994 to increase the receiving area and the vertical resolution, and to change the computer and the analysis software. The signals from low and high channels are first merged together before computing the temperature profile. This method differs from most of the DIAL users who derive temperature first and then merge the geophysical quantities.

A complementary ozone DIAL lidar is located at Hohenpeissenberg (47.8°N, 11.0°E) and is closely associated with the Alpine Station. This lidar system, in operation since the end of 1987, uses a setup very similar to that described by *Werner et al.*,[13] and *Steinbrecht et al.*[14] One of the main differences to the previous systems mentioned here is the use of a single XeCl excimer laser to generate the absorbed wavelength at 308 nm and a hydrogen Raman shifter for the reference wavelength at 353 nm. To extend the altitude range, the lidar is operated successively in two modes. The first one dedicated to low altitude inserts a neutral density filter, with a transmission of 5%, in front of the receiver. No filter is applied in the second mode but raises the cut off altitude of the chopper to limit the maximum count rate. Before the derivation of ozone and temperature, both signals are merged with appropriate weights to provide a continuous return signal similar to the OHP temperature lidar analysis. The interactive determination of the ratio between both the channels also provides a check for counter linearity. The DIAL ozone data series has been measured consistently without any changes in the instrument parameters.

A similar wavelength generation, with a hydrogen Raman cell, was used for the DIAL ozone system in operation at Suwon in South Korea (37.2°N, 127.6°E). In addition to the stratospheric system, a deuterium Raman cell, providing the 291 and 319 nm wavelengths, was also implemented for extending ozone measurements throughout the whole troposphere by Park *et al.*[15]

The Jet Propulsion Laboratory (JPL) Table Mountain Facility (TMF) in California (34.4°N, 117.7°W) acts as an intercomparison and test research site for many of the NDSC primary instruments. For reasons of not duplicating a northern mid-latitude primary site it was decided that this would also be a complementary station. A DIAL system measuring both ozone and temperature has been in routine operation since 1988 by McDermid *et al.*[16] This is a very large power-aperture lidar system (100 W/1 m) at a high altitude location (2300 m) and measures ozone profiles to >50 km and temperature to >90 km. It also uses an a XeCl excimer laser at 308 nm and originally generated the reference wavelength at 353 nm by stimulated Raman shifting in a hydrogen cell although this was replaced by a tripled Nd:YAG laser at 355 nm in 2000. It was also supplemented with a tropospheric ozone DIAL operating at 289/299 nm by Raman shifting of a quadrupled Nd:YAG laser in deuterium and hydrogen. This now allows ozone profiles to be measured from 4 km to >50 km altitude. The stratospheric ozone DIAL instrument has participated in many ozone inter-comparisons and was the first prototype used by JPL to design the system implemented at Hawaii. The GSFC mobile lidar has, and continues, to undergo extensive testing and intercomparison at TMF. In 1999 the entire TMF dataset was reanalyzed by Leblanc *et al.*,[17] using a new, improved version of the analysis software.

An ozone DIAL system was also accepted as a complementary instrument at the National Institute for Environmental Studies (NIES) in Tsukuba, Japan (36.1°N, 140.1°W) for ozone and temperature measurements. The system is similar to the GSFC lidar and operates 6 channels simultaneously.

The JPL team also operates a DIAL system at Mauna Loa Observatory (19.5°N, 155.6°W) in Hawaii, since 1993. This instrument is part of the northern tropical primary NDSC site. Temperature, ozone, and aerosol profiles are derived with this lidar using similar hardware and software to those used at TMF. Two Raman channels have been implemented on this system to avoid contamination by stratospheric aerosols. Simultaneously with the relocation from a trailer to the NDSC building, a new Nd:YAG laser was implemented in April 2001. Also at MLO (Mauna Loa Observatory), the longest aerosol lidar series has been obtained with the National Oceanic and Atmospheric Administration (NOAA) backscatter lidar. Recently these data have also been used to derive temperature profiles.

At Lauder, New Zealand (45.0°S, 169.7°E), the southern hemisphere mid-latitude primary station of the NDSC, a DIAL lidar was implemented and measurements started in 1994 by the National Institute of Public Health and the Environment (RIVM) of The Netherlands. Several changes in both its design and software have been made by Brinksma *et al.*[18] since its inception. Altitude range and resolution were adjusted to better take into account signal-induced-noise. Effects related to the field-of-view and altitude offset, were also investigated. In the analysis, improvements were made relating to the temperature dependence of the Rayleigh extinction correction, and filtering.

In the southern hemisphere, CNRS and the University of La Réunion (Laboratoire de Physique de l'Atmosphere) implemented a Rayleigh lidar for temperature measurements at La Réunion Island (21.8°S, 55.5°W) in 1993. This instrument is very similar to the OHP system and uses the same algorithm. This instrument has also been enhanced with complementary channels for tropospheric ozone, cirrus, temperature, and water vapor measurements as described by Baray *et al.*[19] A new DIAL ozone lidar in a trailer built in collaboration between CNRS and the university of Geneva was also installed in 2000. The design of this lidar is also very close to the new OHP instrument.

There are several instruments operating in polar regions and in the northern hemisphere, the primary site is called the Arctic Station. Several sites located in the Arctic region compose this station. An ozone DIAL system was in operation at Eureka, Canada (80.1°N, 86.4°W) from 1993 to 2000. The design and data analyses are similar to the system at Toronto, which was operated by the same group. However, due to the high latitude

location, ozone and temperature measurements were only possible during the polar night period from November to March. A DIAL system providing ozone density and temperature profiles was installed in 1990 in Toronto, Canada (43.7°N, 79.4°W)) by CRESTech and York University. Raman channels were added in 1995. This system is similar to the Eureka system mentioned above. Signals from three altitude ranges are first merged to produce a single raw data profile, as done for the temperature lidar at OHP and as opposed to the other teams who first derive the ozone density and then merge the 3 density profiles.[20] The ozone profile is computed from the single composite signal. Temperature profiles are also derived from the 353 nm signals with a very similar procedure to the other groups.

A lidar installed in Thule, Greenland (76.5°N, 68.7°W) by the University of Rome, described by Marenco *et al.*,[21] provides temperature using the second harmonic of a Nd:YAG laser, similar to OHP. Measurements have been carried out at this location since 1993, mostly during night-times but occasionally in daylight, and on a schedule depending on weather conditions. This lidar was originally set up for lower stratospheric aerosol measurements. The transmitter is based on a two-stage Nd:YAG laser with a second harmonic generator emitting at 532 nm, a repetition rate of 40 Hz, and an energy of 300 mJ per pulse. The receiver includes a 0.8 m diameter telescope. A rotating disk (chopper) protects the photomultiplier from over loading due to intense signal from the lowest levels.

Since the winter of 1993, a Rayleigh/Mie lidar has been in operation at the ARCtic LIdar TEchnology (ARCLITE) facility located at the National Science Foundation's (NSF) Sondrestrom upper atmospheric research site near the town of Kangerlussuaq, Greenland (67.0N, 309.1E). This lidar system is capable of night and day operations and was described by Thayer *et al.*[22] Recently (2002), the Sondrestrom ARCLITE facility was designated as a primary instrument in the NDSC Arctic Station. While the GSFC mobile system has not yet visited this site, the temperature data derived there have been intensively compared with several other sources as National Centers for Environmental Prediction (NCEP) fields,[23] satellite temperature profiles from NASA's Cryogenic Limb Array Etalon Spectrometer (CLAES) and Microwave Limb Sounder (MLS) instruments onboard the Upper Atmosphere Research Satellite (UARS), Polar Ozone and Aerosol Measurement satellite (POAM III), Japan's Improved Limb Atmospheric Spectrometer (ILAS) instruments and NASA's Sounding of the Atmosphere using Broadband Emission Radiometry (SABER) instrument onboard the Thermosphere, Ionosphere, Mesosphere, Energetics and Dynamics spacecraft (TIMED).

Another polar lidar has been in operation at Ny-Ålesund, Spitsbergen (78.9°N, 11.9°E) since 1988. It is a DIAL system providing ozone density and temperature profiles. During winter 1993–1994 this system was equipped with Raman channels, and daylight channels were added in spring 1997 to enable year-round operations. The Artic Lidar Observatory for Middle Atmosphere Research (ALOMAR) described by Thrane and van Zahn,[24] was established in 1993, and is located on the North-Norwegian island of Andoya (69.3°N, 16.0°E). The DIAL ozone lidar follows the standard design, with a XeCl excimer laser as an emitter (308 nm), a hydrogen-filed Raman cell converting about 15% of the laser emission to 353 nm, and a 1 m Newtonian telescope as a receiver (Hoppe *et al.*[25]). A Rayleigh-Mie-Raman lidar system emitting at the 3 wavelengths corresponding to the harmonics of the Nd:YAG laser is also in operation at the same site.

There are several lidars operating in the Antarctic. At Dumont D'Urville (DDU, 66.7°S, 140.0°E) the DIAL ozone lidar should, in theory, be able to measure temperature profiles. However, the signal return was too low for temperature profiles to reach an altitude higher than 50–60 km and the measurement frequency too small to catch the main dynamic features. So it was decided not to archive them. A lidar dedicated to aerosol and temperature measurements was installed at McMurdo Station on Ross Island (78°S, 167°E) during the 1990 spring by Gobbi *et al.*[26] in support of a balloon-borne campaign. Since the 1991 campaign, this system has operated every winter to study the temperature variability and polar stratospheric cloud occurrence (Adriani *et al.*[27]). The basic design of this lidar system is similar to the other Italian instrument operating at Thule.

3. Comparison campaigns with the GSFC mobile lidar

The mobile lidar developed by GSFC has participated in a number of inter-comparison campaigns at NDSC sites where lidars are operated (Table 2). While the Table Mountain site in California was chosen for the first comparisons, other primary sites easy to access (such as Observatory of Haute-Provence, Lauder and Hawaii) and where lidars are already running in a routine mode for a long time, followed closely. Then the other sites located at higher latitudes have been proposed. While the mobile lidar cannot be considered as an absolute reference, the comparisons have been found to be very helpful to better understand the reliability of the lidars, and to reveal and aid in mitigating various problems.

3.1 Ozone comparisons

A first lidar inter-comparison campaign between the fixed JPL stratospheric lidar and the GSFC lidar was organized in October–November 1988, by McDermid *et al.*[28,29] The two lidars used the same wavelength and so, to reduce the possible interferences, both instruments were operated alternatively for several hours each. While a global agreement of $\pm 5\%$ was obtained from 30 to 40 km, outside this altitude range, the campaign revealed some instrumental problems associated with algorithm errors and signal-induced-noise effects. A second campaign called STOIC (STratospheric Ozone Intercomparison Campaign), which also represented the first formal NDSC intercomparison[30–32] following the established protocol, was organized during the following summer (July–August 1989). A $\pm 5\%$ agreement region was obtained from 26 to 35 km and some bias of up to 10–15% between the both lidars, remains outside this height range. Other instruments measuring ozone were used during this campaign including microwave radiometers, ROCOZ rocket sondes, balloon ozonesondes, and Stratospheric Aerosol and Gas Experiment (SAGE) satellite measurements. The comparison between the mobile lidar, the JPL lidar, and the few coincident ozonesondes showed an agreement of $\pm 2\%$ from 18 to 36 km. Above this altitude, the JPL lidar revealed a similar agreement with SAGE up to 42 km.

The next inter-comparison was organized at OHP in July–August 1992. The conditions of these inter-comparisons between the fixed CNRS lidar and the GSFC mobile were difficult because this campaign just came after the eruption of Mount Pinatubo and most of the stratosphere was strongly affected by volcanic aerosol particles.[9] A second comparison campaign at OHP took place from 1–18 July 1997. Braathen *et al.*[33] have reported that two ozone lidars agreed very well in the 30–40 km range (2%). In the 20 to 30 km range there was a discrepancy of 5%. Below 20 km the difference varies between $\pm 7\%$, but this can be explained by the larger variability at this height range together with the fact that the two instruments could not measure at exactly the same time. Above 40 km the differences increased rapidly. Comparison with ozonesondes gave a better agreement with the CNRS lidar in the 20–30 km range.

Analysis of the blind OPAL (Ozone Profiler Assessment at Lauder) comparison showed that the GSFC mobile lidar was in quite good agreement with SAGE II from 20 to 40 km.[34]

Conversely, large differences were observed with sondes and the RIVM lidar (10%). Using information gleaned from the blind intercomparison, the investigators were able to refine and improve their analysis algorithms. For example, the pulse-pile up effect (saturation) was reduced and signal-induced-noise corrections were implemented in the RIVM analysis tool. Microwave radiometer and ozonesonde results were also improved. The GSFC team discovered an altitude shift of 187 m and corrected it. These changes resulted in a new 'refined' dataset for the intercomparison. The subsequent reanalysis using the refined data revealed a better agreement between the lidars of 5% from 20 to 45 km.[35] Comparisons with ozonesondes were also improved and a mean difference of 5% was observed by Boyd *et al.*,[36] but with a lot of structures that differed up to 10%. Both lidars differed by 10% with the microwave measurements. Above 45 km, the measurements do not agree well but filtering and background effects in the lidar analysis are suspected.

Subsequent to the OPAL Campaign, lidar results were improved with better Rayleigh attenuation corrections and by including the temperature dependence of the ozone absorption cross-section in the analysis. Ozonesonde measurements were also improved with respect to altitude shifts, and the solutions in the electrochemical concentration cells (ECC) were modified. A constant correction with altitude was applied to SAGE results with the approval of SAGE team. The microwave retrieval algorithm was improved further. A new inter-comparison was done using 3 years of data obtained with the different permanent instruments at Lauder, plus SAGE. The RIVM lidar did not show any significant bias, between 20 and 35 km, larger than 1.5 $\pm$ 2% compared to the ozonesondes (75 pairs) and 2.5 $\pm$ 2.5% compared to SAGE (28 pairs). Below 20 km, the 4.96 version of SAGE data are definitively biased as are the lidar above 45 km. Below 20 km lidar and sondes still present significant differences of 9% with a noise from 2–4%. Microwave results compare better with lidar (140 pairs) but still show significant differences (4 $\pm$ 2%) above 45 km and confirm significantly that lidar is biased in this region by 5 $\pm$ 5%.

The MLO3 campaign was carried out at the Mauna Loa Observatory in August–September 1996 and studied by McDermid *et al.*,[37] and McPeters *et al.*[38] Almost all the instruments (Fig. 1) agreed to within $\pm$10%, and most agreed within $\pm$5%. The two lidars, the microwave instrument, and SAGE II agreed within $\pm$5% between 22 and 43 km, providing strong evidence that the lidars and the microwave instrument are making good accurate measurements in this range. The JPL lidar, microwave instrument and SAGE II continue to agree within 5% up to 50 km. The Goddard lidar, ozonesonde, and SAGE II agree within 5% down to 18 km. The SAGE II disagreement with the balloon profile below 18 km is due to some known algorithm problems.

The GSFC lidar was compared with the permanent lidar of the Alfred Wegner Institute (AWI) located at Ny-Ålesund, Spitzbergen, during a campaign called NAOMI (Ny-Ålesund Ozone Measurements Intercomparison, January–February 1998). In the 20 to 30 km altitude range, $\pm$2% agreement is observed while a larger bias of 5–10% is observed by Steinbrecht *et al.*[39] above and below. Below 20 km, the comparison of the AWI lidar and the co-located ECC sondes show $\pm$2% agreement, suggesting a possible bias in the GSFC profiles. However, between 30 and 40 km, the simultaneous microwave measurement seems to suggest that AWI lidar is affected by bias, probably associated with noise processing.

3.2 Temperature comparisons

During the first OHP inter-comparison (summer 1992), temperature profiles deduced from the GSFC lidar and from the fixed OHP lidar dedicated for temperature were compared by Singh *et al.*[40] Mean differences (Fig. 2), less than 1%, were obtained from 35 to 75 km. Below 35 km larger bias (2%) was observed due to the presence of aerosols; Raman channels were only implemented on the GSFC system. Despite the agreement

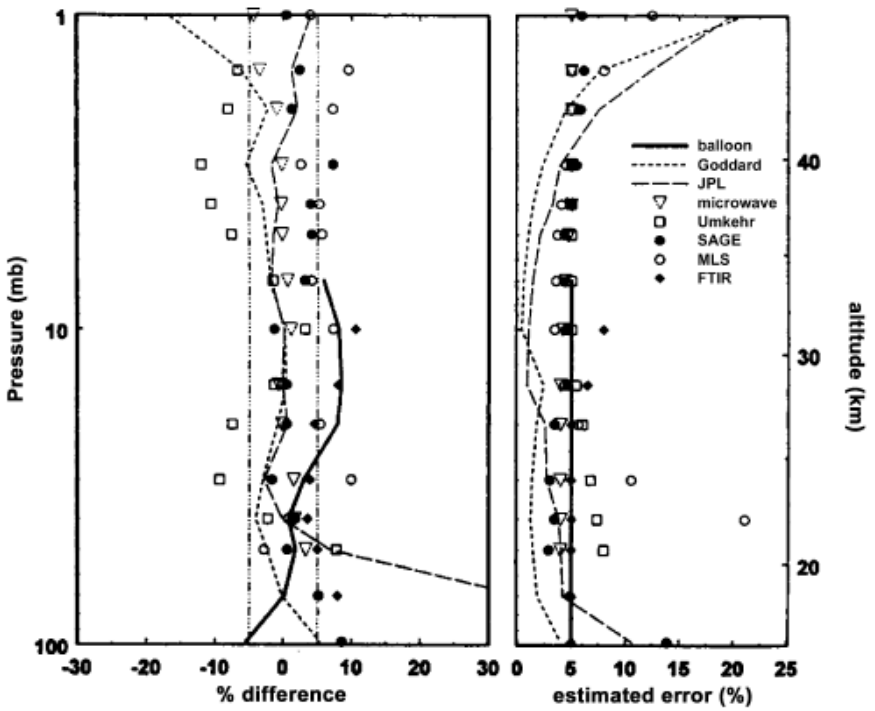

Fig. 1 Percent deviation of the comparison average for several instruments measuring ozone profiles from a "consensus" reference (left). The estimated percent error for each measurement (right) from McPeters *et al.*[38] (Copyright 1999, *Journal of Geophysical Research*).

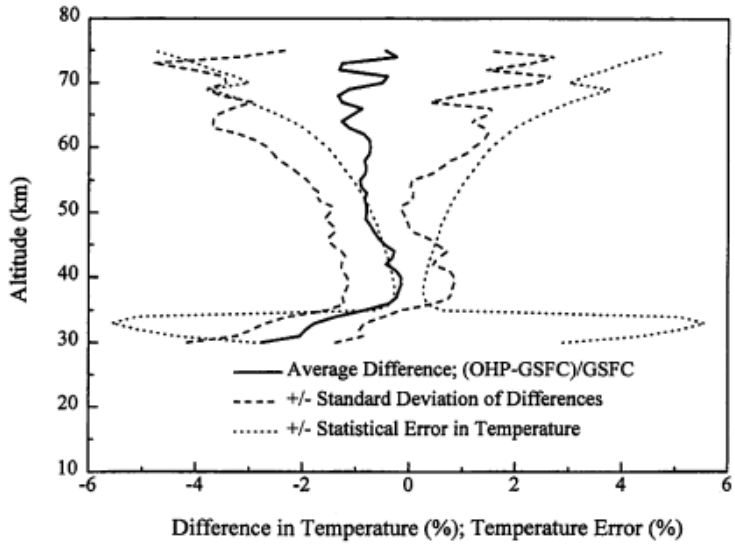

Fig. 2 Mean statistical difference of 18 coincident temperature profiles obtained by two independent lidars operating at OHP (from Singh *et al.*[40], Copyright 1996, *Journal of Geophysical Research*).

is not so good for trend estimates compared to the theoretical accuracy (< a few tenths of a Kelvin), this first inter-comparison was very promising. The second inter-comparison[32] was carried out in summer 1997 after the Rayleigh lidar system underwent a major change to the counting system in September 1994. The difference between the two lidars was within 1.5%, depending on the altitude. Since the maximum differences were associated with the maximum temperature gradients, this could suggest that an altitude difference exists between the two systems. However, 7 cases showed a constant 1.5% change according to altitude. This may suggest an additional problem in initialization or background estimation on one of the systems superimposed on the possible altitude bias. A comparison[41] of the OHP lidar with a very similar Rayleigh lidar located 500 km away and operating simultaneously reveals a mean difference smaller than 1 K with variability equal to 2 K from 3 to 65 km.

Temperature comparisons made at TMF in the spring 1992 campaign showed differences less than 1 K at 40 km, increasing up to 3 K at 50 km. The lidars were not operated simultaneously and investigations using NCEP analyses revealed an important role of atmospheric tides[42] that should be taken into account. A larger difference, as large as 5 K, that could not be attributed to tides was noted at 30 km. However at that time there were a lot of aerosols due to the Mount Pinatubo eruption.

4. Inter-comparison with satellites

4.1 Ozone comparisons

SAGE II provided a very important tool for evaluating ozone lidars and it was used extensively because of its availability over a long time period. The TMF lidar, which was compared in several successive studies,[43,44] showed agreement within 6% between 30 and 40 km with an increasing bias with altitude up to 13% above 40 km. A typical lidar-SAGE difference vertical profile can be found in Fig. 3. The good accuracy of the SAGE II profile in the mid stratosphere range permits the use of these global data to evaluate other ozone lidars that have not been compared with the GSFC mobile instrument. Such was the case for the NIES system operating at Tsukuba by Nakane *et al.*[45] Comparisons with SAGE II were conducted and revealed average mean differences smaller than 10% between 15 and 50 km. None of them were significant. Between 22 and 36 km the mean difference is smaller than 2%. An increasing bias with altitude can be observed above 37 km of 10%. Most of the DIAL lidars, deployed within the NDSC, have been compared with SAGE II. Three zones can be identified. The best agreement, of 5–10%, can be found between 25 and 40 km. Outside this range larger mean differences are reported at all sites, mainly due to the lidar methods. Also, in the lower stratosphere SAGE II exhibits a larger uncertainty. In addition, the spatio-temporal ozone variability is larger in the lower stratosphere due to horizontal transport and because the SAGE II-lidar coincidences are not perfect it may induce larger discrepancies.

UARS also provided a good opportunity for evaluating lidars since a number of them took part in the validation of the ozone profiles derived by several experiments onboard the satellite. Bruhl *et al.*[46] have reported a bias of 5–10% in the 10–20 hPa region (≈25–30 km) and differences of ±5% above in the comparison of Halogen Occultation Experiment (HALOE) ozone measurements with all the other correlative measurements. Most of the NDSC lidars (TMF, Hohenpeissenberg,

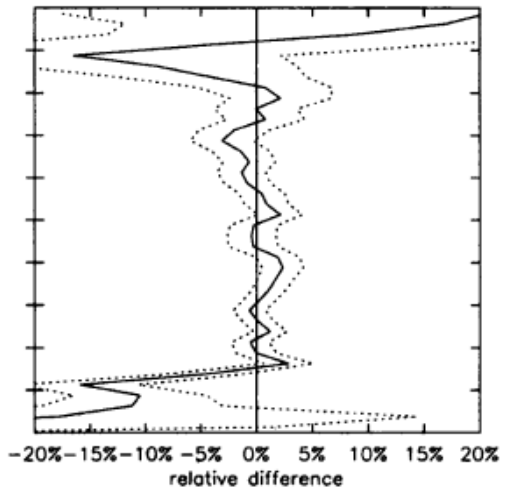

Fig. 3 Averages of the paired SAGE II Lauder ozone lidar between March 96 to January 98 (from *Brinskma et al.*[18], Copyright 2000, *Journal of Geophysical Research*).

GSFC) agreed within 10% between 20–2 hPa (≈25–45 km). DDU and OHP provided insufficient coincidences. Above 2 hPa (≈45 km), the differences increase, reaching 15–25% at 1 hPa (≈50 km). CLAES measurements were also compared with GSFC and TMF by Baily *et al.*[47] Ozone profiles agreed within 10% except below 100 hPa (≈15 km) for GSFC system, where the mean differences increased up to 30%, and around 1 hPa (≈50 km) with the TMF lidar where a bias of 25% appeared. The overall comparison made by Froidevaux *et al.*[48] between the TMF lidar and CLAES data between 10 and 2 hPa (≈25–30 km) were within 5%. MLS was only compared with the TMF lidar and showed a similar agreement as CLAES.

Some comparisons were performed between the Global Ozone Monitoring Experiment (GOME) onboard the European Remote Sensing Satellite (ERS-2) by Burrows *et al.*,[49] and the lidar located at Lauder, New Zealand. Mean differences were within ±10% from 10 to 45 km as reported by Meijer *et al.*[50] Such experiments can be used for long-term comparisons because instruments, using a very similar method, are expected to be launched successively in the future. However, the satellite product includes *a priori* information, and spectral calibration can introduce significant bias. Also, strong biases related to the Solar Zenith Angle (SZA) have been reported.

4.2 Temperature comparisons

Several lidars located at mid-latitude sites have been compared by Wild *et al.*[42] using NCEP data as a geographical transfer reference. This study included the NDSC lidars at TMF and OHP. At first glance the dispersion between the lidars appears quite large, from 4 to 6 K. However, adjustments related to the time of the day of the measurements reduce the dispersion to 4 K at 1 hPa (≈50 km, where stratospheric tides are the largest) with most of the measurements within less than 2 K. Comparisons with MLS/UARS (Fig. 4) report also large differences around 1–2 hPa (≈40–50 km). The geophysical nature of such disagreement is obvious in Fig. 4, as the same lidar have been compared with MLS at different locations (and so different time of measurements with MLS) and gave different bias. Comparisons of OHP lidar and NCEP analyses have continued and confirm the impact of tides not only in data comparisons but also in NCEP continuity. As well as SAGE, NCEP analyses can provide a preliminary comparison for temperature lidars. However, due to the problem of tides, it cannot provide validation accuracy better than several Kelvin. Temperatures retrieved by NIES during winter 1995–1996 were compared with NCEP, with a rocket climatology over Ryori, Japan, and with the CIRA model by Namboothiri *et al.*[51] The maximum deviation was up to 15 K. Comparisons with rockets launched the same day showed differences less than 10 K, no systematic differences, and most of the differences within ±5 K.

The lidar data obtained in 1994 at La Reunion were also compared with NCEP analyses. Mean differences of less than 2 K were obtained except near the stratopause where the mean differences increased to 4 K. These differences were in good agreement with other lidar comparisons mentioned previously[41] and were probably related to tidal effects. At 10 hPa (≈30 km), colder temperatures (4 K) were observed by the lidar but were probably associated with the interfering presence of aerosols.

Again, UARS provided many opportunities to compare simultaneous temperature measurements from the ground and space. TMF, OHP and the GSFC lidar (at Lauder in 1992 and 1994) were compared with HALOE by Hervig *et al.*[52] While the GSFC and the OHP comparisons show a similar bias in the profiles with an alternating pattern of 5–10 K, the GSFC at Lauder in 1994 showed a positive bias of 5 K, in agreement with TMF comparisons. The time window used for data selection was quite large and some tidal interference is therefore expected. Comparisons of these three lidars with CLAES performed by Gille *et al.*[53] were conclusive and in good agreement revealing a negative bias of 1–2 K around 5 hPa (≈38 km) and a positive bias at 1 hPa (≈50 km) increasing up to 3–4 K at 0.1 hPa (≈80 km). The comparisons by Fishbein *et al.*[54] with MLS show a dispersion of 4 K. However, GSFC and TMF on one side, and GSFC and OHP on the other, agreed within 1 K during comparisons at the same sites and a difference of 4 K between the two sites was probably due again to atmospheric tides. The comparison of the OHP lidar and the Improved Stratospheric and Mesospheric Sounder (ISAMS) temperature experiment revealed bias profiles of ±2 K with the same lidar data mentioned before. The selection of lidar measurements[55] where the integration period matched better the ISAMS observation time reduces this bias to less than 0.5 K from 5 to 0.2 hPa (≈38–70 km) showing the importance of temporal coincidence in the intercomparisons and reflecting the influence of tides.

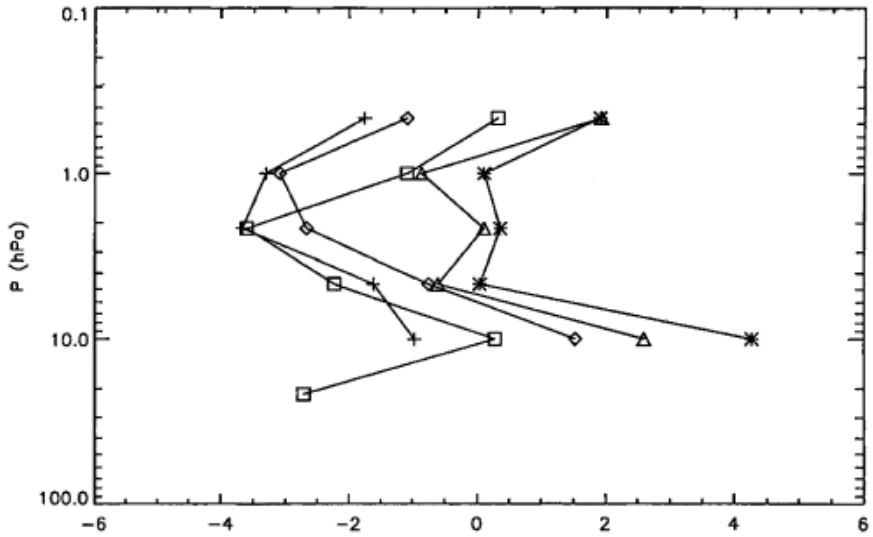

Fig. 4 Average differences between the closest MLS profile and the JPL lidar at TMF (plusses); the CNRS lidar at OHP (asterisks); the GSFC lidar at GSFC (diamonds), at TMF (triangles), and at OHP (squares) from *Fishbein et al.*[54] (Copyright 1996, *Journal of Geophysical Research*).

5. Algorithm inter-comparisons

Some instrument-related effects such as aerosol interferences, signal-induced-noise, and saturation of the data-acquisition system can degrade the quality of the lidar measurements. Several teams have addressed these problems and the expertise gained has been shared within the NDSC Lidar Working Group (LWG) and during inter-comparison exercises. Another possible instrumental effect not yet addressed was the filtering effects for ozone DIAL technique. All the teams involved in the NDSC use various low-pass filters, with variable cut-off frequencies with altitude, to account for the rapid decrease in the signal-to-noise ratio in the high altitude range. An inter-comparison of the ozone DIAL lidar algorithms based on artificial signals was performed in 1996 (Fig. 5) within the framework of the NDSC lidar-working group.[56] The results of the simulations showed that below 30 km all the retrieval algorithms observed the correct behavior with biases of less than 1%. Above this altitude the bias increased, especially above 40 km where 10% biases were reported. This result questions the ability of the DIAL technique to retrieve the correct ozone profile at these altitudes. However, if the biases are constant over time they might be irrelevant for trend studies. This limit is due to the signal-to-noise ratio available. This comparison was an important contribution because it explained some differences observed in the upper stratosphere during the previous comparisons between lidar itself or with satellites.

The CNRS and GSFC algorithms used to retrieve temperature were compared using the same raw data file. This study revealed differences smaller than the noise (<1.5 K) up to 70 km. Above this altitude the differences were larger and were probably related to the difference in methods for estimating and correcting for noise. Since then, the CNRS temperature software was recoded. The underlying physics remained unchanged but many functionalities were automated. At this time, the JPL algorithm was also evaluated and improved. The new CNRS version was tested and compared with the JPL version;[17] showing no bias below 70 km. The JPL and CNRS temperature algorithms have been tested using an alternative method that used artificial signals by Leblanc *et al.*[17] It reveals errors smaller than 1 K below 60 km and 5% around 80 km. Noise mainly due to counting uncertainties is expected to be smaller than 1 K below 60 km and around 5–20 K at 80 km depending on the filtering effects and resolution. If Raman scattering is used, then the profile can be obtained downward with a larger noise of several Kelvin. Investigation about the temperature retrieval based on Nitrogen Raman signals have been performed by Fadhuile *et al.*[57] showing the importance of estimating ozone and aerosol attenuations with simultaneous ancillary measurements.

6. Discussion and conclusions

Many intercomparisons of ozone and temperature profiles have been performed under the framework of the NDSC. Since the instruments were designed independently, it offers a good opportunity to evaluate the overall capability of such instruments for atmospheric monitoring. While the use of a mobile instrument travelling from one station to another is the preferred method for comparisons, satellites can also provide a good spatial transfer for a quasi-simultaneous comparison of several lidars. This is particularly true for ozone in the mid and upper stratosphere where the atmosphere is in photochemical equilibrium. In the lower stratosphere the horizontal and temporal variability is mainly driven by the transport and large fluctuations can be observed for non-simultaneous and non-collocated comparisons. For temperature in the upper stratosphere and mesosphere, tidal effects cause systematic changes and can induce bias in the data comparisons when they are not performed simultaneously. Also for temperature, summertime is more appropriate for comparisons as the variability has a strong seasonal component at mid and high latitudes. Variability is smaller in the tropics and does not exhibit a strong seasonal cycle. During winter, at high latitude the permanent daylight restricts the use of lidars. Few systems have been designed for daylight operations. In the lower stratosphere the presence of aerosols required the development of more sophisticated methods to provide non-biased data for both ozone and temperature. However, these techniques have been developed more recently and the quality of the data provided in this altitude range has been investigated less. The comparisons conducted with the mobile lidar, as well as algorithm inter-comparisons, allow improvements to individual systems by sharing the knowledge of the different groups involved in the NDSC. While not all the instruments have participated in intercomparison campaigns, conclusions can be drawn from this review with respect to two important issues: (1) the overall quality and homogeneity of the NDSC lidar

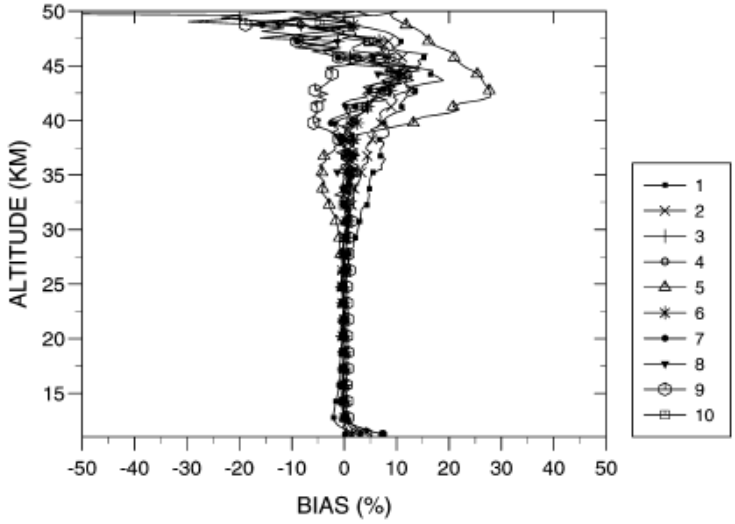

Fig. 5 Comparison of 10 analysis ozone retrieval softwares within NDSC from *Godin et al.*[56] (Copyright 1999, *Applied Optics*).

measurements, and (2) the capabilities of lidars to monitor long-term changes.

Through selection of the latest and/or best comparisons with the mobile lidar, the overall capabilities of the NDSC lidars have been determined (Table 3). For ozone, the standard deviations of the individual differences are comparable to the individual noise estimates. However, differences remain that are never smaller than 2% and are often around 5% in the altitude range from 25 to 35 km. These types of differences were obtained for most of the sites where comparison campaigns with the mobile system were performed. Also, the best comparisons between lidars and SAGE II exhibit similar agreements. Larger biases are often observed at the top of the profile that are probably due to the effects of signal-induced noise and the different numerical filters used in the ozone analysis. In the lower stratosphere, filamentary structures, due to horizontal motions, induce a large spatio-temporal variability that requires perfect coincidences or a large number of individual comparisons.

For temperature, fewer comparison campaigns have been performed under conditions where tides have not masked instrumental differences. While the standard deviations of the individual differences were close to the estimated noise, biases of 1 K are reported. Larger biases are reported below 30–35 km, due to stratospheric aerosols and around the top of the profile 75–85 km probably due to initialization and noise extraction. The use of satellite data is difficult for assessing temperature lidar measurements because tidal effects bias comparisons. To avoid such effects, solar occultation experiments would be preferred. However the number of coincidences would then be drastically reduced.

7. Recommendations and future plans

In conclusion, most of the lidars compared in the framework of NDSC can be now considered as operational and the lidar technique is quite mature for monitoring and satellite validation. For satellite validations, the network can, in principle, be considered as homogeneous within $\pm 2\%$ between 20–35 km for ozone and ± 1 K between 35–60 km for temperature. However, more efforts are required for temperature comparisons. The valid altitude range, for a nominal accuracy associated to trend detection, is given below. In the lower stratosphere, Raman channels seem to improve comparisons, but such capabilities were not systematically compared, probably because they have been implemented only more recently. For both ozone and temperature systems this issue needs to be addressed. The top profiles need also to be considered with caution as bias increases quickly with altitude. For ozone, microwave spectrometers, already involved within NDSC, are ideal candidates to extend above around 40 km, ozone measurements. For temperature powerful systems are required to push upward the initialization altitude, however signal-induced-noise can in turn bias the measurements. Special care is required. Tests and comparisons are likely to be performed but instrumental design is probably the most crucial part if covering the whole mesosphere is required.

Table 3 Errors (systematic and random) expected within ozone and temperature lidar within the NDSC

Parameter	Altitude	Bias	Variance
Ozone	<20 km	5–10% without Raman channels	5%
	<20 km	5% with Raman channels	5%
	20–35 km	2%	2%
	>40 km	5–10%	5–10%
Temperature	30 km	5–10 K without a Raman channel	2 K
	30 km	Expected 1 K with a Raman channel	4 K
	35–65 km	1 K	2 K
	75 km	5–10 K	5–10 K

For trend detection, better accuracy can be expected as the bias in a single instrument can remain unchanged and therefore the derived trends are significant despite possible systematic differences with other instruments. However, temporal discontinuities of this order can be expected on decadal timescale and need to be tracked by any means because they may induce spurious trends larger than those expected; 5–10% per decade for ozone, and several Kelvin per decade for temperature. Only two sites were visited twice by the mobile lidar system. Conditions of comparisons and instrumental improvements performed on all the systems do not provide information about the temporal stability. In principle, satellite experiments cannot offer such temporal reference because of their lifetime or their potential drift. This last decade, space measurements have been tremendously improved. For ozone, SAGE II was a quite good reference and served as a good horizontal geographical transfer among the different lidar sites. Also, the long-term, continuous nature of SAGE II results allowed such comparisons to be made at many different times and locations. However, such exercises were never synchronized and may involve different retrieval versions of SAGE II or different periods that are not truly comparable (drift or malfunctioning). In the future such exercises may be planned, as it will allow every DIAL lidar to be compared at the same time. GOMOS onboard ENVISAT utilizes an auto-calibrated technique based on stellar occultations. This technique is very promising to ensure long term monitoring. Despite the fact that the quality of the measurements may differ depending on the star observed, it will provide a lot more data than the solar occultation technique (potentially better coincidences) and a quasi-constant time-of-day period for the spatial measurements. Most of the NDSC ozone lidars are involved in GOMOS validation[58] and this will also offer a good opportunity to evaluate simultaneously the different lidars, despite the possible latitudinal bias or the start dependence. Assimilation efforts will also help to ensure the lidar network coherence and then will probably be considered as one of the best future solutions for frequent quality checks. This will be tested with the validation of experiments aboard ENVISAT. The use of satellites permits comparisons to be made with all the stations including those with difficult access such the Antarctic site.

For temperature, global measurements with GPS (Global Positioning Systems) will probably provide accurate measurements. However it will not cover the upper stratosphere and mesosphere. In this region tides cause some interferences that are not easy to handle since the amplitudes of the tides are also subject to strong variability.[59] Satellite measurements based on solar occultation will provide good references. However, few good coincidences will be available at lower latitudes and comparisons of results will not be sufficiently accurate compared to the dynamical variability of the temperature at different timescales. Comparisons taking into account tides are not straightforward because tidal characteristics are not well known or measured. The attempts using some tidal climatology made in previous studies[41,54] show some improvements but do not guarantee good representation of tides. Also, tide amplitudes can be modified in a complex manner[59] related to changes in several atmospheric parameters (ozone content, water vapour content, temperature, wind) preventing the use of tide climatologies.

Since the temperature assimilation is a more difficult task, up to now, collocated intercomparison lidar campaigns and analysis methods are still needed in the near future. A special emphasis on the top part is required. Up to now, such campaigns, focused on temperature, were not sufficient to have a good view of the homogeneity of the network for the temperature. This is probably one of the main priorities in the next decade. Also, specific efforts on quality data evaluation obtained in the lower stratosphere domain need to be planned.

To be useful as a whole every lidar needs to be compared with a common reference in order to check if all their data quality fit the standard requirements that are expected from

this study (Table 3). Also global validation plans need to be known to let every team, even outside the NDSC, to benefit the leadership provided by the network that could provide guidelines. The validation is proving difficult because differences can come both from the design and the analysis software. A common code will probably permit the raising of this issue and, at the same time, permit every team to reach the same degree of accuracy. About the design, this goal is virtually impossible to be predicted as lidar systems are sophisticated instruments that are often assembled through different phases. Also if the main body of the analysis is very similar within all the teams involved, the lidar technology itself is still improving. The analysis is not independent of the instrument itself and so is unique. However, one suggestion that can be made is the use of common software for all the analyses performed after signal corrections. This part of the analysis is not supposed to change much during the next decades. Then the design investigations can be shared to keep a certain degree of homogeneity in the network. However, this is not always easy to ensure as it strongly depends upon important resources.

Appendix

List of acronyms

ALOMAR	Artic Lidar Observatory for Middle Atmosphere Research
ARCLITE	ARCtic LIdar TEchnology
AWI	Alfred Wegener Institute
CLAES	Cryogenic Limb Array Etalon Spectrometer
CMDL	Climate Monitoring and Diagnostic Laboratory
CNR	Consiglio Nazionale delle Ricerche
CNRS	Centre National de la Recherche Scientifique
DDU	Dumont D'Urville
DIAL	DIfferential Absorption Lidar
ECC	Electrochemical Concentration Cells
ENVISAT	ENVIronmental SATellite
ERS-2	European Remote Sensing Satellite
GOME	Global Ozone Monitoring Experiment
GOMOS	Global Ozone Monitoring by Occultation of Stars
GPS	Global Positioning System
GSFC	Goddard Space Flight Center
HALOE	Halogen Occultation Experiment
IFA	Istituto Fisica dell'Atmosfera
ILAS	Improved Limb Atmospheric Spectrometer
IROE	Istituto Recerche Onde Electromagnetica
ISAMS	Improved Stratospheric and Mesospheric Sounder
JPL	Jet Propulsion Laboratory
MLO	Mauna Loa Observatory
MLS	Microwave Limb Sounder
MOHH	Meteorologisches Observatorium Hohenpeissenberg
NAOMI	Ny-Ålesund Ozone Measurements Intercomparison
NASA	National Administration and Space Agency
NCEP	National Centers for Environmental Prediction
NDSC	Network for Detection of Stratospheric Changes
NIES	National Institute for Environmental Studies
NILU	Norwegian Institue for Air Research
NOAA	National Oceanic and Atmospheric Administration
OHP	Observatory of Haute-Provence
OPAL	Ozone Profiler Assessment at Lauder
OTOIC	OHP temperature and Ozone Inter-Comparison
POAM	Polar Ozone and Aerosol Measurement
RIVM	Environmental Risks and External Safety Division
ROCOZ	Rocket sondes, balloon ozonesondes
SA	Service d'Aéronomie
SABER	Sounding of the Atmosphere using Broadband Emission Radiometry
SAGE	Stratospheric Aerosol and Gas Experiment
SRI	
STOIC	STratospheric Ozone Intercomparison Campaign
STRAT	STRatosphere Aerosol comparisons at TMF
SZA	Solar Zenith Angle
TIMED	Thermosphere, Ionosphere, Mesosphere, Energetics and Dynamics spacecraft
TMF	Table Mountain Facility
UARS	Upper Atmosphere Research Satellite

References

1 M. J. Kurylo and S. Solomon, Network for the Detection of Stratospheric Change, *NASA Report, Code EEU*, 1990.
2 T. R. Karl, R. Q. Quayle and P. Y. Groisman, Detecting climate variations and change: New challenges for observing and data management systems, *J. Clim.*, 1993, **6**, 1481–1494.
3 G. Megie, J. Y. Allain, M. L. Chanin and J. E. Blamont, Vertical profile of stratospheric ozone (18-28 km) by lidar sounding from the ground, *Nature*, 1977, **270**, 329.
4 T. J. McGee, M. R. Cross, R. Ferrare, W. Heaps and U. N. Singh, Raman DIAL measurements of stratospheric ozone in the presence of volcanic aerosols, *Geophys. Res. Lett.*, 1993, **20**, 955–958.
5 A. Hauchecorne and M.-L. Chanin, Density and temperature profiles obtained by lidar between 35 and 70 km, *Geophys. Res. Lett.*, 1980, **7**, 565–568.
6 P. Keckhut, M. L. Chanin and A. Hauchecorne, Stratosphere temperature measurement using Raman lidar, *Appl. Opt.*, 1990, **29**, 5182–5186.
7 T. J. McGee, D. Witheman, R. Ferrare, J. J. Butler and J. Burris, STROZ LITE: Stratospheric Ozone Lidar Trailer Experiment, *Opt. Eng.*, 1991, **30**, 31–39.
8 T. J. McGee, M. R. Cross, U. N. Singh, J. J. Butler and P. E. Kimvilakani, Improved stratospheric ozone lidar, *Opt. Eng.*, 1995, **34**, 1421–1430.
9 T. J. McGee, P. Newman, M. Gross, U. Singh, S. Godin, S. Lacoste and G. Megie, Correlation of ozone loss with the presence of volcanic aerosols, *Geophys. Res. Lett.*, 1994, **21**, 2,801–2,801.
10 M. R. Gross, T. J. McGee, R. A. Ferrare, U. Singh and P. Kimvilikani, Temperature Measurements Made with a Combined Rayleigh-Mie/Raman Lidar, *Appl. Opt.*, 1997, **24**, 5987–5995.
11 S. Godin, G. Megie and J. Pelon, Systematic lidar measurements of the stratospheric ozone vertical distribution, *Geophys. Res. Lett.*, 1989, **16**, 547–550.
12 P. Keckhut, A. Hauchecorne and M. L. Chanin, A critical review of the data base acquired for the long term surveillance of the middle atmosphere by the French Rayleigh lidars, *J. Atmos. Ocean. Technol.*, 1993, **10**, 850–867.
13 J. Werner, K. W. Rothe and H. Walther, Monitoring of the stratospheric ozone layer by laser radar, *Appl. Phys.*, 1983, **B32**, 113–118.
14 W. Steinbrecht, K. W. Rothe and H. Walther, Lidar setup for daytime and nighttime probing of stratospheric ozone and measurements in polar and equatorial regions, *Appl. Opt.*, 1989, **28**, 3616–3624.
15 C. B. Park, K. H. Park and C. H. Lee, Lidar observation of ozone and aerosol in the stratosphere and troposphere over Suwon, Korea, Advances in Atmospheric Remote Sensing with Lidar, Springer, New York-Berlin-Heidelberg, pp. 545–548, 1996.
16 I. S. McDermid, S. Godin and L. O. Lindquist, Ground-based laser DIAL system for long-term measurements of stratospheric ozone, *Appl. Opt.*, 1990, **29**, 3603–3612.
17 T. Leblanc, I. S. McDermid, A. Hauchecorne and P. Keckhut, Evaluation of optimization of lidar temperature analysis algorithms using simulated data, *J. Geophys. Res.*, 1998, **103**, 6177–6187.
18 E. J. Brinksma, Validation of 3 years of ozone measurements over Network for the Detection of Stratospheric Change station Lauder, New Zealand, *J. Geophys. Res.*, 2000, **105**, 17291–17306.
19 J-L. Baray, J. Leveau, J. Porteneuve, G. Ancellet, P. Keckhut, F. Posny and S. Baldy, Description and evaluation of a tropospheric ozone lidar implemented on an existing lidar in the southern subtropics, *Appl. Opt.*, 1999, **38**, 6808–6817.
20 D. P. Donovan, J. C. Bird, J. A. Whiteway, T. J. Duck, S. R. Pal and A. I. Carswell, Lidar observations of stratospheric ozone and aerosol, *Geophys. Res. Lett.*, 1995, **22**, 3489–3492.
21 F. Marenco, A. di Sarra, M. Cacciani, G. Fiocco and D. Fua, Thermal structure of the winter middle atmosphere observed by lidar at Thule, Greenland, during 1993–1994, *J. Atmos. Sol. Terr. Phys.*, 1997, **59**, 151–158.
22 J. P. Thayer, N. B. Nielsen, R. Warren, C. J. Heinselman and J. Sohn, Rayleigh lidar system for middle atmosphere research in the arctic, *Opt. Eng.*, 1997, **36**, 2045–2061.
23 A. J. Gerrard, T. J. Kane, J. P. Thayer, T. J. Duck and J. Whiteway, Synoptic-scale study of the arctic polar vortex's influence on the middle atmosphere, *J. Geophys. Res.*, 2002, **107**, pp. ACL1 1–15.
24 E. V. Thrane and U. von Zahn, ALOMAR – A new facility for

middle atmosphere research at Arctic latitudes, *J. Geomagn. Geoelectr.*, 1995, **47**, 921–928.
25 U.-P. Hoppe, G. Hansen and D. Opsvik, *Differential absorption lidar measurements of stratospheric ozone at ALOMAR: First results, ESA SP-370*, 1995, 335–344.
26 G. P. Gobbi, T. Deshler, A. Adriani and D. J. Hofmann, Evidence of denitrification in the 1990 Antarctic spring stratosphere 1. lidar and temperature measurements, *Geophys. Res. Lett.*, 1991, **18**, 1995–1998.
27 A. Adriani, T. Deshler, G. Gobbi, B. Johnson and G. Di Donfrancesco, Polar stratospheric clouds over McMurdo, Antarctica, during the 1991 spring: lidar and particle counter measurements, *Geophys. Res. Lett.*, 1991, **19**, 1755–1758.
28 I. S. McDermid, S. M. Godin, L. O. Lindquist, T. D. Walsh, J. Burris, J. Butler, R. Ferrare, D. Whiteman and T. J. McGee, Measurement Inter-Comparison of the JPL and GSFC Stratospheric Ozone Lidar Systems, *Appl. Opt.*, 1990, **29**, 4671–4676.
29 I. S. McDermid, S. M. Godin and T. D. Walsh, Lidar Measurements of Stratospheric Ozone and Inter-Comparisons and Validation, *Appl. Opt.*, 1990, **29**, 4914–4923.
30 W. D. Komhyr, B. J. Connor, I. S. McDermid, T. J. McGee, A. D. Parrish and J. J. Margitan, Comparison of STOIC 1989 Ground-Based Lidar, Microwave Radiometer, and Dobson Spectrophotometer Umkehr Ozone Profiles With Ozone Profiles from Balloon-Borne ECC Ozonesondes, *J. Geophys. Res.*, 1995, **100**, 9273–9282.
31 J. J. Margitan, R. A. Barnes, G. B. Brothers, J. Butler, J. Burris, B. J. Connor, R. A. Ferrare, J. B. Kerr, W. D. Komhyr, M. P. McCormick, I. S. McDermid, C. T. McElroy, T. J. McGee, A. J. Miller, M. Owens, A. D. Parrish, C. L. Parsons, A. L. Torres, J. J. Tsou, T. D. Walsh and D. Whiteman, Stratospheric Ozone Intercomparison Campaign (STOIC) 1989: Overview, *J. Geophys. Res.*, 1995, **100**, 9193–9208.
32 I. S. McDermid, S. M. Godin and T. D. Walsh, Results from the JPL Stratospheric Ozone Lidar During STOIC 1989, *J. Geophys. Res.*, 1995, **100**, 9263–9272.
33 G. O. Braathen, T. J. McGee, M. R. Gross, S. Godin, P. Keckhut, C. Vialle and A. Hauchecorne, Intercomparaison of stratospheric ozone and temperature measurements at the Observatoire de Haute Provence during an NDSC validation campaign from 1–18 July 1997, *Geophys. Res. Lett.*, 2002, submitted.
34 I. S. McDermid, J. B. Bergwerff, G. Bodeker, I. S. Boyd, E. J. Brinksma, B. J. Connor, R. Farmer, M. R. Gross, P. Kimvilakani, W. A. Matthews, T. J. McGee, F. T. Ormel, A. Parrish, U. Singh, D. P. J. Swart, J. J. Tsou, P-H. Wang and J. Zawodny, OPAL: Network for the Detection of Stratospheric Change Ozone Profiler Assessment at Lauder, New Zealand. I. Blind Intercomparisons, *J. Geophys. Res.*, 1998, **103**, 28,683–28,692.
35 I. S. McDermid, J. B. Bergwerff, G. Bodeker, I. S. Boyd, E. J. Brinksma, B. J. Connor, R. Farmer, M. R. Gross, P. Kimvilakani, W. A. Matthews, T. J. McGee, F. T. Ormel, A. Parrish, U. Singh, D. P. J. Swart and J. J. Tsou, OPAL: Network for the Detection of Stratospheric Change Ozone Profiler Assessment at Lauder, New Zealand. II. Intercomparison of Revised Results, *J. Geophys. Res.*, 1998, **103**, 28,693–28,699.
36 I. S. Boyd, G. E. Bodeker, B. J. Connor, D. P. J. Swart and E. J. Brinksma, An assessment of ECC ozonesondes operated using 1% and 0.5% KI cathode solutions at Lauder, New Zealand, *Geophys. Res. Lett.*, 1998, **25**, 2409–2412.
37 I. S. McDermid, T. J. McGee, D. P. J. Swart, NDSC Lidar Intercomparisons and Validation: OPAL and MLO3 Campaigns in 1995, *Advances in Atmospheric Remote Sensing with Lidar*, Springer, New York-Berlin-Heidelberg, 1996, pp. 525–528.
38 R. D. McPeters, D. J. Hofmann, M. Clark, L. Flynn, L. Froidevaux, M. Gross, B. Johnson, G. Koenig, X. Liu, I. S. McDermid, T. J. McGee, F. Murcray, M. J. Newchurch, S. Oltmans, A. Parrish, R. Schnell, U. Singh, J. J. Tsou, T. D. Walsh and J. M. Zawodny, Results from the 1995 Stratospheric Ozone Profile Intercomparison at Mauna Loa, *J. Geophys. Res.*, 1999, **104**, 30,505–30,514.
39 W. Steinbrecht, M. R. Gross, T. J. McGee, R. Neuber, P. von der Gathen, P. Wahl, U. Klein and J. Langer, Results of the 1998 Ny-Ålesund Ozone Measurements Intercomparison NAOMI, *J. Geophys. Res.*, 1999, **104**, 30,515–30,523.
40 U. N. Singh, P. Keckhut, T. J. McGee, M. R. Gross, A. Hauchecorne, E. F. Fishbein, J. W. Waters, J. C. Gille, A. E. Roche and J. M. Russell III, Stratospheric temperature measurements by two collocated NDSC lidars at OHP during UARS validation campaign, *J. Geophys. Res.*, 1996, **101**, 10287–10297.
41 P. Keckhut, J. Wild, M. Gelman, A. J. Miller and A. Hauchecorne, Investigations on long-term temperature changes in the upper stratosphere using lidar data and NCEP analyses, *J. Geophys. Res.*, 2001, **106**, 7937–7944.
42 J. D. Wild, M. E. Gelman, A. J. Miller, M. L. Chanin, A. Hauchecorne, P. Keckhut, R. Farley, P. D. Dao, J. W. Meriwether, G. P. Gobbi, F. Congeduti, A. Adriani, I. S. McDermid, T. J. McGee and E. F. Fishbein, Comparison of stratospheric temperatures from several lidars, using National Meteorological Center and microwave limb sounder data as transfer references, *J. Geophys. Res.*, 1995, **100**, 11,105–11,111.
43 I. S. McDermid, S. M. Godin, P-H. Wang and M. P. McCormick, Comparison of Stratospheric Ozone Profiles and Their Seasonal Variations as Measured by LIDAR and SAGE II During 1988, *J. Geophys. Res.*, 1990, **95**, 5605–5612.
44 J. J. Tsou, B. J. Connor, A. Parrish, I. S. McDermid and W. P. Chu, Ground-Based Microwave Monitoring of Middle Atmosphere Ozone: Comparison to Lidar and SAGE II Satellite Observations, *J. Geophys. Res.*, 1995, **100**, 3005–3016.
45 H. Nakane, Y. Sasano, S. S. Hayashida, N. Sugimoto, I. Matsui, A. Minato and M. P. McCormick, Comparison of ozone profiles obtained with NIES DIAL and SAGE II measurements, *J. Meteorol. Soc. Jpn*, 1993, **71**, 153–159.
46 C. Bruhl, S. R. Drayson, J. M. Russell, P. J. Crutzen, J. M. McInerney, P. N. Purcell, H. Claude, H. Gernandt, T. J. McGee and I. S. McDermid, Halogen Occultation Experiment ozone channel validation, *J. Geophys. Res.*, 1996, **101**, 10,217–10,240.
47 P. L. Baily, D. P. Edwards, J. C. Gille, L. V. Lyjak, S. T. Massie, A. E. Roche, J. B. Kumer, J. L. Mergenthaler, B. J. Connor, M. R. Gunson, J. J. Margitan, I. S. McDermid and T. J. McGee, Comparison of cryogenic limb array etalon spectrometer (CLAES) ozone observations with correlative measurements, *J. Geophys. Res.*, 1996, **101**, 9737–9756.
48 L. Froidevaux, W. G. Read, T. A. Lungu, R. E. Cofield, E. F. Fishbein, D. A. Flower, R. F. Jarnot, B. P. Ridenoure, Z. Shippony, J. W. Waters, J. J. Margitan, I. S. McDermid, R. A. Stachnik, G. E. Peckham, G. Braathen, T. Deshler, J. Fishman, D. J. Hofmann and S. J. Oltmans, Validation of UARS Microwave Limb Sounder ozone measurements, *J. Geophys. Res.*, 1996, **101**, 10,017–10,060.
49 J. P. Burrows, M. Weber, M. Buchwitz, V. Romanov, A. Ladstätter-Weißenmayer, A. Richter, R. Debeek, R. Hoogen, K. Bramstedt, K.-U. Eichmann, M. Eisinger and D. Perner, The Global Ozone Monitoring Experiment (GOME): Mission concept and first scientific results, *J. Atmos. Sci.*, 1999, **56**, 151–175.
50 Y. J. Meijer, R. J. van der A, R. F. van Oss, D. P. J. Swart, H. M. Kelder and P. V. Johnston, GOME ozone profile characterization using interpretation tools and lidar measurements for intercomparison, *J. Geophys. Res.*, 2003, submitted.
51 S. P. Namboothiri, N. Sugimoto, H. Nakane, I. Matsui and Y. Murayama, Rayleigh lidar observation of temperature over Tsukuba: winter thermal structure and comparison studies, *Earth Planets and Space*, 1999, **51**, 825–832.
52 M. E. Hervig, J. M. Russell III, L. L. Gordley, S. R. Drayson, K. Stone, R. E. Thompson, M. E. Gelman, I. S. McDermid, A. Hauchecorne, P. Keckhut, T. J. McGee, U. N. Singh and M. R. Gross, Validation of temperature measurements from the Halogen Occultation Experiment, *J. Geophys. Res.*, 1996, **101**, 10277–10285.
53 J. C. Gille, P. L. Bailey, S. T. Massie, L. V. Lyjak, D. P. Edwards, A. E. Roche, J. B. Kumer, J. L. Mergenthaler, M. R. Gross, A. Hauchecorne, P. Keckhut, T. J. McGee, I. S. McDermid, A. J. Miller and U. Singh, Accuracy and precision of Cryogenic Limb Array Etalon Spectrometer (CLAES) temperature retrievals, *J. Geophys. Res.*, 1996, **101**, 9583–9601.
54 E. F. Fishbein, R. E. Cofield, L. Froidevaux, R. F. Jarnot, T. Lungu, W. G. Read, Z. Shippony, J. W. Waters, I. S. McDermid, T. J. McGee, U. N. Singh, M. Gross, A. Hauchecorne, P. Keckhut, M. E. Gelman and R. M. Nagatani, Validation of UARS Microwave Limb Sounder temperature and pressure measurements, *J. Geophys. Res.*, 1996, **101**, 9983–10016.
55 P. Keckhut, M. E. Gelman, J. D. Wild, F. Tissot, A. J. Miller, A. Hauchecorne, M. L. Chanin, E. F. Fishbein, J. Gille, J. M. Russell III and F. W. Taylor, Semidiurnal and diurnal temperature tides (30–55 km): climatology and effect on UARS-LIDAR data comparisons, *J. Geophys. Res.*, 1996, **101**, 10299–10310.
56 S. Godin, A. I. Carswell, D. P. Donovan, H. Claude, W. Steinbrecht, I. S. McDermid, T. J. McGee, M. R. Gross, H. Nakane, D. P. J. Swart, H. B. Bergwerff, O. Uchino, P. von der

Gathen and R. Neuber, Ozone differential absorption lidar algorithm intercomparison, *Appl. Opt.*, 1999, **38**, 6225–6236.
57 D. Faduilhe, P. Keckhut, H. Bencherif, B. Cadet and S. Baldy, personal communication.
58 P. Keckhut, S. Marchand, A. Hauchecorne, S. Godin-Beekmann, F. Pinsard, I. S. McDermid, T. Leblanc, G. Hansen, J.-L. Baray, H. Bencherif, D. Swart, Y. Meijer, S. Pal, M. Guirlet, C. Vialle, F. Posny and F. Goutail, Validation of GOMOS ozone profiles using NDSC lidar: statistical comparisons, *Proceedings of ENVISAT Validation Workshop, ESA Publications Division, SP-531*, ed. H. Lacoste, 2003.
59 B. Morel, P. Keckhut, H. Bencherif, A. Hauchecorne, G. Megie and S. Baldy, Investigation of the tidal variations in a 3-d dynamics-chemistry-transport model of the middle atmosphere, *J. Atmos. Sol. Terr. Phys.*, 2004, **66**, 251–265.

1.3.3 Article de présentation du réseau EQUAL, accepté pour publication par *Int. J. Remote Sens.*

Global validation of ENVISAT ozone profiles using lidar measurements

J.A.E. VAN GIJSEL*☺, D.P.J. SWART☺, J.-L. BARAY‡, H. CLAUDE§, T. FEHR☼, P. VON DER GATHEN◊, S. GODIN-BEEKMANN◙, G.H. HANSEN ♣, T. LEBLANC♪, I.S. MCDERMID♪, Y.M. MEIJER☼, H. NAKANE¥, E.J. QUELΨ, W. STEINBRECHT§, K.B. STRAWBRIDGE∴, B. TATAROV◘ and E.A. WOLFRAMΨ

☺National Institute for Public Health and the Environment (RIVM), Laboratory for Environmental Monitoring, P.O. Box 1, 3720 BA, Bilthoven, The Netherlands
‡ Université de la Reunión, Laboratoire de l'Atmosphère et des Cyclones (LACy), UMR CNRS 8105, 15 avenue René Cassin, BP 7151, 97715 Saint Denis Messag Cedex 9, France
§German weather service (DWD), Ozone Research Unit, Meteorological Observatory Hohenpeissenberg, Albin-Schwaiger-Weg 10, 82383, Hohenpeissenberg, Germany
☼European space agency (ESA-ESRIN), Via Galileo Galilei, 00044, Frascati (RM), Italy
◊Alfred Wegener Institute (AWI), Polar and Marine Research, Telegrafenberg A43, 14473, Potsdam, Germany
◙CNRS/UPMC/UVSQ, Service d'Aeronomie/IPSL, UPMC - Boite 102, 4 Place Jussieu, 75252 Paris Cedex 05, France
♣Norwegian Air Research Institute (NILU), Polar Environmental Centre, 9296, Tromsø, Norway
♪NASA, JPL, Table Mountain Facility, P.O. Box 367, Wrightwood, CA 92397, United States
¥National Institute for Environmental Studies (NIES), Asian Environment Research Group, 16-2, Onogawa, Tsukuba, Ibaraki 305-8506, Japan
◘National Institute for Environmental Studies (NIES), Atmospheric Environment Division, 16-2 Onogawa, Tsukuba, Ibaraki 305-8506, Japan
ΨCEILAP (CITEFA-CONICET), Juan B. de La Salle 4397, B1603ALO Villa Martelli, Argentina
∴Environment Canada, Science and Technology Branch, Centre for Atmospheric Research Experiments (CARE), 6248 Eight Line, R.R. #1, Egbert (ON), LOL 1N0, Canada

Correspondence *J.A.E. van Gijsel. Email: Anne.van.Gijsel@rivm.nl

Abstract:
Satellite sensors provide global measurements of ozone concentration which can be used to study the effects of the implementation of the Montreal Protocol. However, a key issue in deriving long-term ozone trends from successive satellite instruments is inter-comparability. Ground-based measurements offer continuous time series but only at few locations. The combination of ground-based measurements with satellite data is therefore an effective means to evaluate satellite instrument inter-comparability.
In this study we present validation results of ozone profiles from three atmospheric sensors onboard ENVISAT by comparison with lidar measurements. Results for SCIAMACHY ozone profiles (version 3.01) show a reasonable agreement with ground-based measurements (0 - -20%). MIPAS full resolution (version 4.61) datasets have a good agreement with lidar (0 - 10%), whereas a small positive bias (up to 20%) was

found for MIPAS reduced resolution prototype data. GOMOS dark limb data (version 5.00) agree very well (0 ± 5%) with the correlative data, but underestimate the ozone concentration at the Polar Regions.

Keywords: GOMOS; MIPAS; SCIAMACHY; lidar; ozone; validation

1 Introduction

In order to assess the effectivity of the measures taken in the framework of the Montreal Protocol, accurate and reliable measurements of atmospheric properties such as ozone and temperature are essential. In addition, coordinated in-situ measurements provide and have provided a valuable contribution to our understanding of stratospheric processes. For instance, studies with ozone sondes have shown that ozone loss is not only related to enhanced chlorine levels, but it also has a strong dependence on stratospheric temperature (Schulz et al., 2000, Schulz et al., 2001). Lidar measurements have, for example, been used to characterise polar stratospheric clouds (Massoli et al., 2006) and to study geographic differences in observed stratospheric temperature and waves (Blum et al., 2004). Nevertheless, ground-based and balloon-borne measurements are only available at a few locations.

Satellite instruments are in this respect an excellent source of information as they can provide cost effective and timely global coverage. However, one of the key issues when using different satellite instruments to derive long-term ozone trends is the degree to which the measurements of these instruments properly correlate. This is especially of concern when no simultaneous measurements are available due to coverage gaps in successive missions. A second major issue is the trade-off between the geographic coverage (i.e. temporal and spatial resolutions) and the obtained accuracy for satellite retrievals (Meijer et al., 2004).

The establishment of a long-term time series of ground-based measurements with known quality and the comparison with satellite measurements is therefore a prerequisite to assess the quality of satellite data and to ensure both a good performance of individual sensors as well as an appropriate combination of multi-sensor datasets. Ground-based and balloon-borne measurements have already proven to be essential in the validation of various models (Reid et al., 1998) and satellite retrievals (Cortesi et al., 2007, Jiang et al., 2007, Meijer et al., 2003, Ridolfi et al., 2007, Witte et al., 2008).

In this study we evaluate the ozone profiles derived from the measurements of the three atmospheric instruments onboard ENVISAT: SCIAMACHY, MIPAS and GOMOS. More precisely, four ozone profile products derived from measurements by these instruments are compared with ground-based lidar measurements.

2 Datasets and methodology

In this study we have investigated the differences between lidar and satellite-based measurements of stratospheric ozone. The lidar measurements of stratospheric ozone were taken at eleven sites (see Table 1) ranging from Lauder, New Zealand (-45.04 °S) to Eureka, Canada (80.05 °N). All of these lidar systems are DIfferential Absorption Lidars (DIAL) which make use of two wavelengths. Since the absorption by ozone is wavelength dependent, comparison of the return signals allows the derivation of the ozone concentration as a function of altitude.

Insert table 1 about here

The validation approach followed in this study is similar to that of Meijer et al. (2004). Both satellite and lidar data were first interpolated using a linear spline to a common altitude grid and then compared in a quality assessment. The selected datasets were subsequently compared in terms of mean, median and standard

deviation of the differences for various subsets, such as the geographical region, measurement conditions and collocation criteria. Here, a lower confidence altitude limit was set for all lidar data to 18 km and the upper altitude limit was set to 45 km.

One prototype and three operational ESA satellite products from three atmospheric sensors have been compared with lidar:

- SCanning Imaging Absorption spectroMeter for Atmospheric CHartographY (SCIAMACHY) level 2 processor version 3.01. SCIAMACHY observes the solar radiation transmitted or reflected by the atmosphere during sunrise and sunset from 240 to 2380 nm. From these observations, vertical columns and profiles are retrieved for various atmospheric constituents. See Bovensmann et al (1999) for an overview of the measurement techniques of this instrument
- Michelson Interferometer for Passive Atmosphere Sounding (MIPAS) full resolution (FR) level 2 processor version 4.61. MIPAS provides profiles of temperature and atmospheric constituents from limb-viewing midinfrared emission measurements by a high resolution Fourier transform spectrometer. The high resolution observations cover the upper troposphere/lower stratosphere (UTLS) to the mesosphere. Fischer et al. (2008) provides a more detailed description of this sensor
- MIPAS reduced resolution (RR) prototype data
- Global Ozone Monitoring by Occultation of Stars (GOMOS) processor version 5.00. GOMOS utilises the stellar occultation technique to detect atmospheric trace gasses (with a focus on ozone), as well as temperature. The transmitted radiation of the star setting in the atmosphere is analysed by spectrometers covering the UV-visible (250 nm to 675 nm, 756 nm to 773 nm) and near infrared bands (926 nm to 952 nm) with a spectral resolution of 1.2 and 0.2 nm, respectively. Geophysical variables are retrieved over the altitude range from 15 to 100 km with an approximate height resolution of 1.7 km. See Kyrölä et al (2004) for a review of this sensor

Over 12 000 collocations (maximum of 800 km and 20 hours difference between measurements) of SCIAMACHY profiles with lidar were found for the period 2002-2007. The upper altitude limit for the comparison interval is restricted to 40 km as recommended in the SCIAMACHY data disclaimer.

The MIPAS instrument encountered an anomaly in March 2004. It was able to continue measurements in January 2005, but with a reduced spectral resolution. There are therefore two different MIPAS products available. For the comparison with operational MIPAS FR version 4.61 data, the collocations were restricted to a maximum of 10 hours and a maximum distance of 400 km (> 600 collocations). The reduced resolution data are not operationally produced and only a very limited dataset was available for verification activities. The collocation criteria have therefore been extended to a maximum of 20 hours and a distance of 500 km (only 28 collocations).

For GOMOS processor version 5.00, a maximum time lapse of 20 hours and a maximum distance of 800 km were chosen. The solar zenith angle was further restricted to 108° or larger to ensure that only star occultations in dark limb conditions are considered. The maximum error that was allowed for both the GOMOS data as well as the lidar data was set to 30%. More than 1600 collocations fulfilled these criteria. The analysis results for these collocated datasets are shown in section 3.

3 Results

3.1 SCIAMACHY processor version 3.01

Figure 1 displays the comparison results for SCIAMACHY processor version 3.01. The left panel shows the mean ozone number densities of the lidar (thick blue line) and SCIAMACHY (thick red line) measurements together with the standard deviations (thin lines) as a function of altitude. It is clear that SCIAMACHY is underestimating the ozone concentrations. We can quantify the underestimation using the middle panel which

shows the mean and median of the differences with respect to lidar. The underestimation of ozone is ranging between about 5% at the bottom of the profile (18 km) increasing to 25% at an altitude of 40 km. These results supported the SCIAMACHY processor development and the verification of the new prototype has shown significant improvements. This new dataset will be available beginning of 2009.

Insert Figure 1 about here

3.2 MIPAS FR processor version 4.61 and RR prototype data

In Figure 2 we present the comparison results for the completed MIPAS full spectral resolution dataset based on processor version 4.61. Differences with lidar are varying between 0 to 5% over the range 18-40 km with MIPAS overestimating the ozone concentrations. For MIPAS reduced resolution data processed with the prototype processor the differences are larger (up to 20%), but the available dataset is very limited (the number of collocations is less than 30). This product has a higher vertical resolution and it is anticipated that the operational processor version 5.00 will become available in the second half of 2008, thus increasing the size of the dataset for comparison soon.

Insert Figure 2 about here

3.3 GOMOS processor version 5.00

Figure 3 presents the validation results for GOMOS operational processor version 5.00. The three panels show the Polar Regions, mid-latitudes and tropics (from left to right respectively). We can observe that the GOMOS version 5.00 dataset has an excellent agreement with lidar in the mid-latitudes over the compared range (18-45 km). In the tropics, where the ozone maximum can be generally found at higher altitudes, we see the effects of decreasing signals when continuing to descent below the ozone maximum: GOMOS increasingly deviates from the lidar signals. For the mid-latitudes we can expect a similar behaviour at altitudes below the analysed minimum (18 km). In the Polar Regions GOMOS shows a constant underestimation of the ozone concentration, ranging from -5% at 18 km to 5-10% at 40 km and then rapidly increasing to about 30% at 45 km. We can see that some outlier profiles exist from the deviation between the mean and median profiles. Straylight may be playing a role in the origin of the differences between GOMOS and lidar.

Insert Figure 3 about here

4 Conclusions

In this study we have presented the validation results of the ozone profiles delivered by ESA from three atmospheric sensors onboard ENVISAT: GOMOS, MIPAS and SCIAMACHY. Intercomparisons with lidar measurements have been performed at 11 stations worldwide belonging to the Network for the Detection of Atmospheric Composition Change (NDACC). We have compared these collocated profiles and analyzed the results for dependence on several geophysical (e.g., latitude) and instrument observational (e.g., GOMOS star characteristics) parameters and looked at the instruments' performance in time.
The SCIAMACHY ozone profiles (version 3.01) have been more precisely corrected for the altitude shift present in previous data versions and showed a reasonable agreement with lidar. Ozone profile validation results showed a good agreement of MIPAS (version 4.61) full resolution and a small positive bias was found for MIPAS reduced resolution data throughout the stratosphere ranging from 0 to 20%. Nevertheless,

individual comparisons showed a very good agreement in the high vertical structures in the profiles. GOMOS data (version 5.00) from measurements in dark limb conditions agreed very well with the correlative data and no significant systematic errors are observed, except for the northern Polar Regions where GOMOS seems to slightly underestimate the ozone number densities.
The continuous monitoring of the quality of satellite-based products through validation with long-term ground-based measurements provides the means to instrument intercomparison and algorithm development. Despite data gaps in between satellite missions, the ozone layer can be globally monitored in a consistent way ensuring that the trends in ozone will be properly identified.

Acknowledgements

These studies have been performed in the framework of the Envisat quality assessment with lidar (EQUAL) project that was financed by the European Space Agency. The authors would also like to kindly thank the members of the GOMOS, MIPAS and SCIAMACHY quality working groups for their inputs and discussions. We also acknowledge the feedback from the anonymous reviewer which has provided valuable improvements to this manuscript.

References

BLUM, U., FRICKE, K. H., BAUMGARTEN, G. & SCHÖCH, A., 2004, Simultaneous lidar observations of temperatures and waves in the polar middle atmosphere on the east and west side of the Scandinavian mountains: a case study on 19/20 January 2003. *Atmospheric Chemistry and Physics,* 4, **3,** 809-816.

BOVENSMANN, H., BURROWS, J. P., BUCHWITZ, M., FRERICK, J., NOËL, S., ROZANOV, V. V., CHANCE, K. V. & GOEDE, A. P. H., 1999, SCIAMACHY: Mission objectives and measurement modes. *Journal of the Atmospheric Sciences,* 56, **2,** 127-150.

CORTESI, U., LAMBERT, J. C., DE CLERCQ, C., BIANCHINI, G., BLUMENSTOCK, T., BRACHER, A., CASTELLI, E., CATOIRE, V., CHANCE, K. V., DE MAZIE?RE, M., DEMOULIN, P., GODIN-BEEKMANN, S., JONES, N., JUCKS, K., KEIM, C., KERZENMACHER, T., KUELLMANN, H., KUTTIPPURATH, J., IARLORI, M., LIU, G. Y., LIU, Y., MCDERMID, I. S., MEIJER, Y. J., MENCARAGLIA, F., MIKUTEIT, S., OELHAF, H., PICCOLO, C., PIRRE, M., RASPOLLINI, P., RAVEGNANI, F., REBURN, W. J., REDAELLI, G., REMEDIOS, J. J., SEMBHI, H., SMALE, D., STECK, T., TADDEI, A., VAROTSOS, C., VIGOUROUX, C., WATERFALL, A., WETZEL, G. & WOOD, S., 2007, Geophysical validation of MIPAS-ENVISAT operational ozone data. *Atmospheric Chemistry and Physics,* 7, **18,** 4807-4867.

FISCHER, H., BIRK, M., BLOM, C., CARLI, B., CARLOTTI, M., VON CLARMANN, T., DELBOUILLE, L., DUDHIA, A., EHHALT, D., ENDEMANN, M., FLAUD, J. M., GESSNER, R., KLEINERT, A., KOOPMAN, R., LANGEN, J., LÓPEZ-PUERTAS, M., MOSNER, P., NETT, H., OELHAF, H., PERRON, G., REMEDIOS, J., RIDOLFI, M., STILLER, G. & ZANDER, R., 2008, MIPAS: An instrument for atmospheric and climate research. *Atmospheric Chemistry and Physics,* 8, **8,** 2151-2188.

JIANG, Y. B., FROIDEVAUX, L., LAMBERT, A., LIVESEY, N. J., READ, W. G., WATERS, J. W., BOJKOV, B., LEBLANC, T., MCDERMID, I. S., GODIN-BEEKMANN, S., FILIPIAK, M. J., HARWOOD, R. S., FULLER, R. A., DAFFER, W. H., DROUIN, B. J., COFIELD, R. E., CUDDY, D. T., JARNOT, R. F., KNOSP, B. W., PERUN, V. S., SCHWARTZ, M. J., SNYDER, W. V., STEK, P. C., THURSTANS, R. P., WAGNER, P. A., ALLAART, M., ANDERSEN, S. B., BODEKER, G., CALPINI, B., CLAUDE, H., COETZEE, G., DAVIES, J., DE BACKER, H., DIER, H., FUJIWARA, M., JOHNSON, B., KELDER, H., LEME, N. P., KÖNIG-LANGLO, G., KYRÖ, E., LANEVE, G., FOOK, L. S., MERRILL, J., MORRIS, G., NEWCHURCH, M., OLTMANS, S., PARRONDOS, M. C., POSNY, F., SCHMIDLIN, F., SKRIVANKOVA, P., STUBI, R., TARASICK, D., THOMPSON, A., THOURET, V., VIATTE, P., VÖMEL, H., VON DER GATHEN, P., YELA, M. & ZABLOCKI, G., 2007, Validation of Aura Microwave Limb Sounder Ozone by ozonesonde and lidar measurements. *Journal of Geophysical Research,* 112, **D24S34,** doi:10.1029/2007JD008776.

KYRÖLÄ, E., TAMMINEN, J., LEPPELMEIER, G. W., SOFIEVA, V. F., HASSINEN, S., BERTAUX, J.-L., HAUCHECORNE, A., DALAUDIER, F., COT, C., KORABLEV, O., FANTON D'ANDON, O., BARROT, G., MANGIN, A., THÉODORE, B., GUIRLET, M., ETANCHAUD, F., SNOEIJ, P., KOOPMAN, R. M., SAAVEDRA, L., FRAISSE, R., FUSSEN, D. & VANHELLEMONT, F., 2004, GOMOS on Envisat: An overview. *Advances in Space Research,* 33, **7,** 1020-1028.

MASSOLI, P., MATURILLI, M. & NEUBER, R., 2006, Climatology of Arctic polar stratospheric clouds as measured by lidar in Ny-Ålesund, Spitsbergen (79°N, 12°E). *Journal of Geophysical Research,* 111, **D09206,** doi:10.1029/2005JD005840.

MEIJER, Y. J., SWART, D. P. J., ALLAART, M., ANDERSEN, S. B., BODEKER, G., BOYD, I., BRAATHEN, G., CALISESI, Y., CLAUDE, H., DOROKHOV, V., VON DER GATHEN, P., GIL, M., GODIN-BEEKMANN, S., GOUTAIL, F., HANSEN, G., KARPETCHKO, A., KECKHUT, P., KELDER, H. M., KOELEMEIJER, R., KOIS, B., KOOPMAN, R. M., KOPP, G., LAMBERT, J.-C., LEBLANC, T., MCDERMID, I. S., PAL, S., SCHETS, H., STUBI, R., SUORTTI, T., VISCONTI, G. & YELA, M., 2004, Pole-to-pole validation of Envisat GOMOS ozone profiles using data from ground-based and balloon sonde measurements. *Journal of Geophysical Research,* 109, **D23305,** doi:10.1029/2004JD004834.

MEIJER, Y. J., VAN DER A, R. J., VAN OSS, R. F., SWART, D. P. J., KELDER, H. M. & JOHNSTON, P. V., 2003, Global Ozone Monitoring Experiment ozone profile characterization using interpretation tools and lidar measurements for intercomparison. *Journal of Geophysical Research,* 108, **D23,** doi:10.1029/2003JD003498.

REID, S. J., REX, M., VON DER GATHEN, P., FLØISAND, I., STORDAL, F., CARVER, G. D., BECK, A., REIMER, E., KRÜGER-CASTENSEN, K., DE HAAN, L. L., BRAATHEN, G., DOROKHOV, V., FAST, H., KYRÖ, E., GIL, M., LITYNSKA, Z., MOLYNEUX, M., MURPHY, G., O'CONNOR, F., RAVEGNANI, F., VAROTSOS, C., WENGER, J. & ZEREFOS, C., 1998, A study of ozone laminae using diabatic trajectories, contour advection and photochemical trajectory model simulations. *Journal of Atmospheric Chemistry,* 30, **1,** 187-207.

RIDOLFI, M., BLUM, U., CARLI, B., CATOIRE, V., CECCHERINI, S., CLAUDE, H., DE CLERCQ, C., FRICKE, K. H., FRIEDL-VALLON, F., IARLORI, M., KECKHUT, P., KERRIDGE, B., LAMBERT, J. C., MEYER, Y. J., MONA, L., OELHAF, H., PAPPALARDO, G., PIRRE, M., RIZI, V., ROBERT, C., SWART, D., VON CLARMANN, T., WATERFALL, A. & WETZEL, G., 2007, Geophysical validation of temperature retrieved by the ESA processor from MIPAS/ENVISAT atmospheric limb-emission measurements. *Atmospheric Chemistry and Physics,* 7, **16,** 4459-4487.

SCHULZ, A., REX, M., HARRIS, N. R. P., BRAATHEN, G. O., REIMER, E., ALFIER, R., KILBANE-DAWE, I., ECKERMANN, S., ALLAART, M., ALPERS, M., BOJKOV, B., CISNEROS, J., CLAUDE, H., CUEVAS, E., DAVIES, J., DE BACKER, H., DIER, H., DOROKHOV, V., FAST, H., GODIN, S., JOHNSON, B., KOIS, B., KONDO, Y., KOSMIDIS, E., KYRÖ, E., LITYNSKA, Z., MIKKELSEN, I. S., MOLYNEUX, M. J., MURPHY, G., NAGAI, T., NAKANE, H., O'CONNOR, F., PARRONDO, C., SCHMIDLIN, F. J., SKRIVANKOVA, P., VAROTSOS, C., VIALLE, C., VIATTE, P., YUSHKOV, V., ZEREFOS, C. & VON DER GATHEN, P., 2001, Arctic ozone loss in threshold conditions: Match observations in 1997/1998 and 1998/1999. *Journal of Geophysical Research,* 106, **D7,** 7495-7503.

SCHULZ, A., REX, M., STEGER, J., HARRIS, N. R. P., BRAATHEN, G. O., REIMER, E., ALFIER, R., BECK, A., ALPERS, M., CISNEROS, J., CLAUDE, H., DE BACKER, H., DIER, H., DOROKHOV, V., FAST, H., GODIN, S., HANSEN, G., KANZAWA, H., KOIS, B., KONDO, Y., KOSMIDIS, E., KYRÖ, E., LITYNSKA, Z., MOLYNEUX, M. J., MURPHY, G., NAKANE, H., PARRONDO, C., RAVEGNANI, F., VAROTSOS, C., VIALLE, C., VIATTE, P., YUSHKOV, V., ZEREFOS, C. & VON DER GATHEN, P., 2000, Match observations in the Arctic winter 1996/97: High stratospheric ozone loss rates correlate with low temperatures deep inside the polar vortex. *Geophysical Research Letters,* 27, **2,** 205-208.

WITTE, J. C., SCHOEBERL, M. R., DOUGLASS, A. R. & THOMPSON, A. M., 2008, The Quasi-biennial Oscillation and annual variations in tropical ozone from SHADOZ and HALOE. *Atmospheric Chemistry and Physics,* 8, **14,** 3929-3936.

Table 1. Overview of used lidar sites

Site	Latitude (°)	Longitude (°)
Alomar	69.3	16.0
Eureka	80.1	-86.4
Hohenpeissenberg	47.8	11.0
La Reunion	-20.8	55.5
Lauder	-45.0	169.7
Mauna Loa	19.5	-155.6
Ny Ålesund	78.9	11.9
Observatoire Haute Provence	43.9	5.7
Rio Gallegos	-51.6	-69.3
Table Mountain	34.4	-117.7
Tsukuba	36.1	140.1

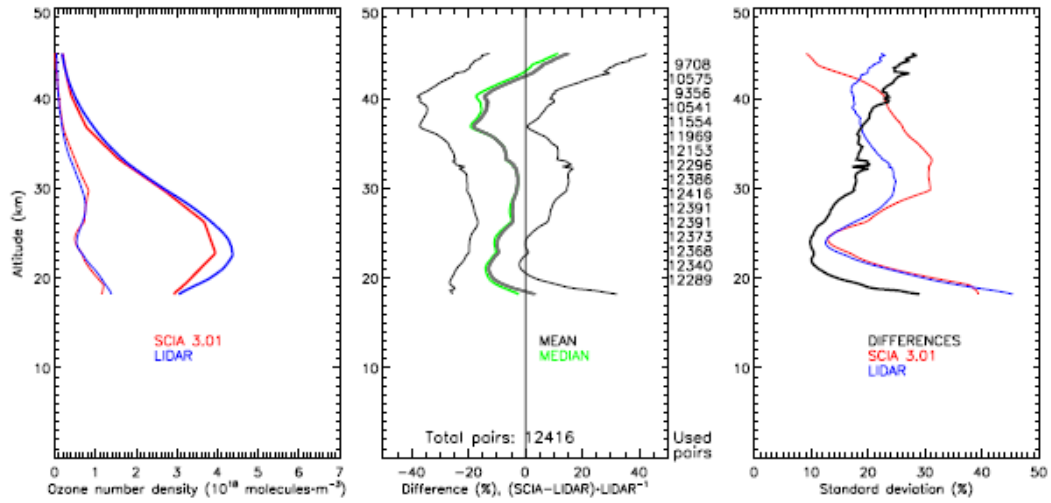

Figure 1. Validation results for SCIAMACHY operational processor version 3.01 in comparison with lidar measurements. Left panel: Mean SCIAMACHY (thick red line) and mean lidar (thick blue lines) ozone concentrations with their respective standard deviations (thin lines) as a function of altitude. Middle panel: Mean (thick black line) plus/minus one standard deviation (thin black lines) of all individual difference profiles from the mean difference profile and mean difference plus/minus two standard errors (thin grey lines) and median (green line) percentage difference (SCIAMACHY minus lidar divided by lidar) as a function of altitude. On the right side of the middle panel is listed the number of collocations for each altitude. The right panel shows the standard deviations of SCIAMACHY (red), lidar (blue) and the standard deviation of the differences between SCIAMACHY and lidar (black line) as a function of altitude.

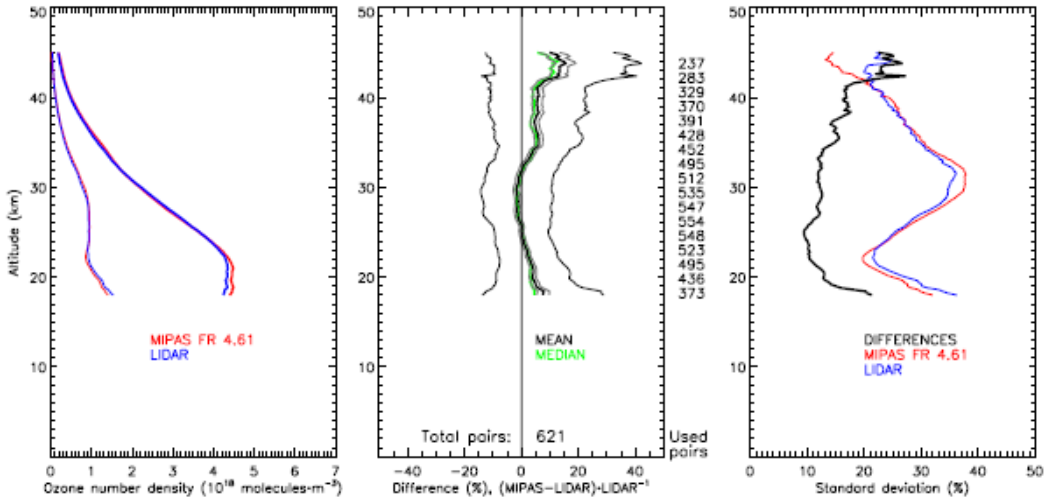

Figure 2. Validation results for MIPAS FR processor version 4.61 in comparison with lidar measurements. Same as Figure 1 except for MIPAS FR version 4.61.

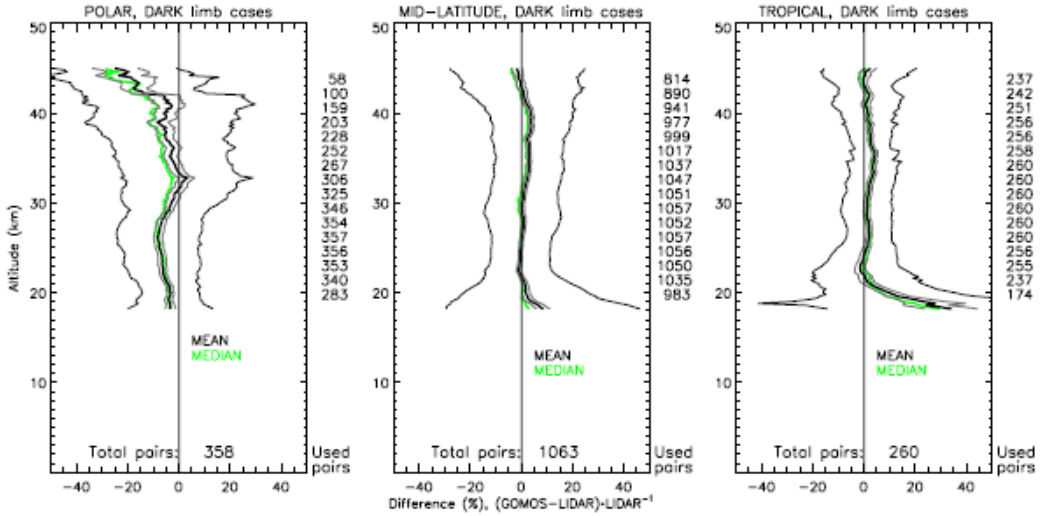

Figure 3. Validation results for GOMOS IPF 5.00 ozone profiles in comparison with lidar measurements. Mean (thick black lines) plus/minus one standard deviation (thin black lines), mean plus/minus two standard errors (thin grey lines) and median (thick green lines) of the percentage differences between GOMOS and lidar ozone concentrations as a function of altitude. On the right side of each panel is listed the number of collocations for each altitude. Left panel: Polar Regions. Middle panel: Mid-latitudes. Right panel: Tropics.

1.4 Perspectives instrumentales, station d'altitude au Maïdo

Comme il est indiqué dans la conclusion de l'article sur l'OPAR en 2006 (section 1.2.2), un certain nombre d'instruments étaient, à ce moment la, en projet à court terme.

Un radiomètre micro-onde centré à 22 GHz[18] et permettant des mesures de vapeur d'eau stratosphérique développé au Laboratoire d'Aérologie a été implanté à La Réunion pour une campagne-test de longue durée en 2007 (Figure 1.10).

Figure 1.10 Radiomètre micro-ondes pour la mesure de la vapeur d'eau stratosphérique

Cette campagne ayant produit des résultats satisfaisants (Figure 1.11), un nouveau prototype est en cours de développement et sera installé prochainement et de manière pérenne à la Réunion. Ce jeu de données original dans l'hémisphère sud permettra d'étudier, outre l'évolution à long terme de la vapeur d'eau, les processus de transports horizontaux à large échelle à travers la barrière tropicale, ainsi que les processus de transport verticaux lors de phénomènes convectifs intenses. Cet instrument sera complémentaire du radiomètre profileur troposphérique, développé par la société américaine Radiometrics, que nous projetons également d'acquérir.

[18] Motte, E., et al., A 22 GHz Mobile Microwave Radiometer (MobRa) for the study of stratospheric water vapor, IEEE Transactions on Geoscience and Remote Sensing, DOI 10.1109/TGRS.2008.2000626, pp. 3104-3114, 2008

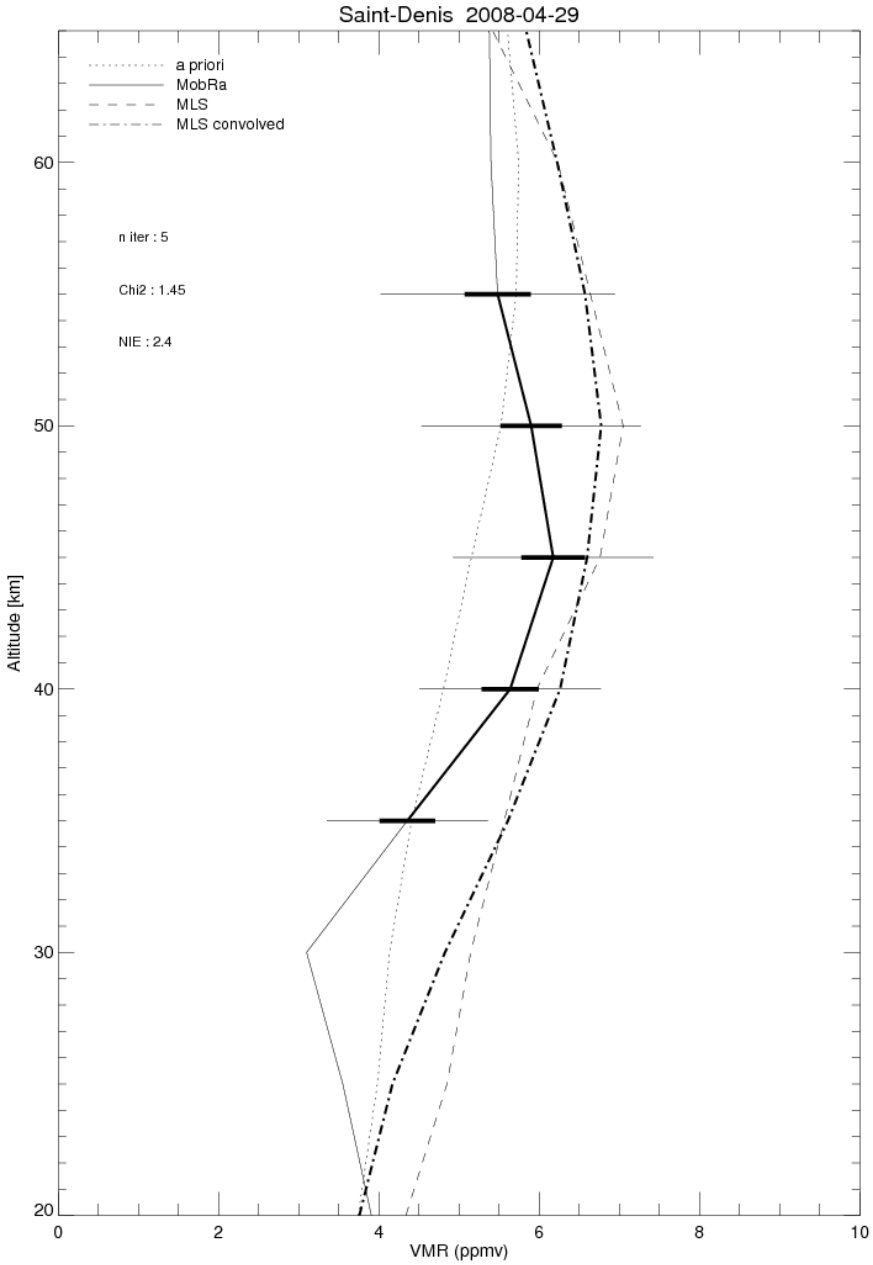

Figure 1.11 Profil de rapport de mélange de vapeur stratosphérique obtenue par radiomètre le 29 Avril 2008 (communication Philippe Ricaud, Laboratoire d'Aérologie)

Un lidar doppler destiner à la mesure de profils du vent horizontal dans la haute troposphère et dans la stratosphère est phase de mise au point finale et de tests. L'émission est produite par un Laser Nd :Yag hautement stabilisé en fréquence sur deux visées inclinées à 45°. Le principe de mesure est basé sur la mesure du décalage spectral subi par la raie rétrodiffusée au moyen d'un interféromètre de Fabry-Pérot, et qui permet d'obtenir la vitesse des particules diffusantes (molécules ou aérosols). Le principe de l'instrument est le même du système développé à l'Observatoire de Haute Provence[19],

[19] Souprayen, C., et al., Rayleigh-Mie Doppler wind lidar for atmospheric measurement. I. Instrumental setup,

mais le design optique est nouveau, l'instrument en développement à la Réunion étant d'une taille beaucoup plus réduite pour qu'il puisse être installé dans un container. Cet instrument permettra à l'OPAR de participer à la validation du satellite ADM-AEOLUS[20], de constituer une base de données du vent horizontal, en complément des mesures GPS par radiosondages effectuées depuis 2007, et de documenter les études des ondes de gravité et, me concernant plus particulièrement, du courant-jet subtropical.

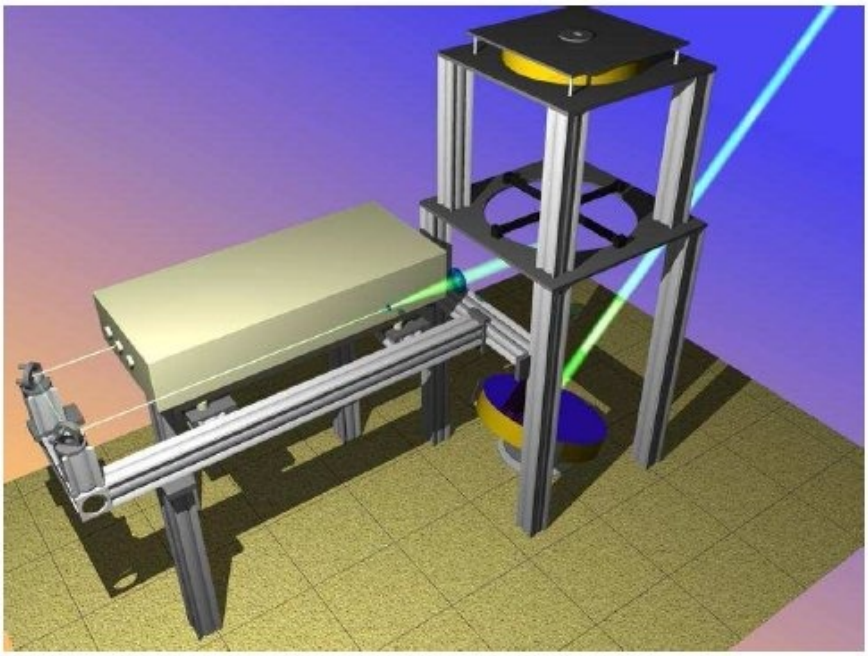

Figure 1.12 Image de synthèse du lidar Doppler pour la mesure des profils de vent en cours d'installation à l'OPAR (Communication : Jacques Porteneuve)

L'acquisition d'un radar profileur de vent UHF, complémentaire des autres systèmes de mesure du vent de l'OPAR (lidar et sondes GPS), notamment pour la caractérisation du vent entre 0 et 7 km d'altitude a été également programmée au titre du CPER 2007-2013. Un radar profileur de vent et de température UHF/RASS permet de faire des sondages de la dynamique et de la thermodynamique en continu avec une cadence d'un profil toutes les 5 minutes dans des conditions d'air clair ou précipitant. La couverture verticale s'étend de 100 mètres à 5-6 kilomètres et la résolution verticale est de 75 mètres. C'est donc un outil adapté à l'étude et la surveillance de la couche limite atmosphérique, qui permettra de documenter les études dynamiques troposphériques tels que l'inversion d'alizés, qui conditionne la répartition des composés atmosphériques tels que l'ozone ou le monoxyde de carbone.

validation and first climatological results, Appl. Opt., 38, 2410-2421, 1999.

[20] Earth Explorer Atmospheric Dynamics Mission, http://www.esa.int/esaLP/LPadmaeolus.html

Nous avons acquis dernièrement un lidar mobile leosphere ALS450[21], fonctionnant à la longueur d'onde 355 nm, pour l'observation des nuages et des aérosols dans les basses couches. Des comparaisons et un fonctionnement complémentaire avec un autre lidar mobile développé par le laboratoire LSCE[22] a eu lieu dans le cadre de l'expérience ECLAIR[23] et de la thèse de Dorothée Lesouef.

Figure 1.13 Photographie prise le 13 Novembre 2008, montrant en premier plan le lidar leosphere ALS 450, et en second plan, le faisceau incliné à 45 degrés du lidar doppler.

D'autre part, en collaboration avec le LOA, un spectroradiomètre UV sera prochainement installé à la Réunion. Cet instrument effectue des mesures en routine de l'éclairement spectral solaire au sol afin d'étudier sa variabilité et l'impact à la surface de l'évolution de l'atmosphère. Ses mesures d'éclairement global et diffus sont analysées à l'aide de codes de transfert radiatif pour comprendre le rôle des divers composants (ozone, aérosols, nuages) et des paramètres environnementaux (albédo de surface, topographie) qui modulent le rayonnement UV. La présence sur le site de l'OPAR d'un photomètre du réseau AERONET permettra des confrontations entre les mesures afin

[21] http://www.leosphere.com/
[22] Laboratoire des Sciences du Climat et de l'Environment, http://www.lsce.ipsl.fr/
[23] Expérience sur la Couche Limite Atmosphérique à l'Ile de la Réunion

de s'assurer de leur qualité. Le projet d'installer un spectroradiomètre à la Réunion n'est pas récent, puisque j'en avais personnellement discuté avec Colette Brogniez, Jacqueline Lenoble et Arnaud de la Casinère, et visité leur station de mesure à Briançon en avril 2002. Malheureusement, pour diverses raisons, ce projet n'avait pas pu se concrétiser, et je considère donc comme une très bonne chose la concrétisation future de ce projet.

Enfin, comme indiqué dans la section 1.3.1, il est envisagé de faire de l'OPAR, après son installation dans le bâtiment du Maïdo, une station globale du programme GAW. L'OPAR dispose actuellement d'un certain nombre de capteurs (sondes ozone, spectromètre SAOZ, photomètre Cimel, LiDAR aérosols) qui fournissent depuis plusieurs années certaines des données requises par GAW, mais il doit impérativement développer les mesures in situ pour pouvoir satisfaire davantage aux exigences de ce programme. Il est donc envisagé d'acquérir certains équipements de base, dont le choix, l'exploitation et la calibration se feront en liaison avec des laboratoires spécialisés et reconnus dans leur domaine, notamment le LSCE pour les gaz à effet de serre et certains radionucléides, le LA pour la chimie de précipitation, le LaMP et le LA pour les aérosols, le LOA pour les radiations UV. Le programme GAW accorde beaucoup d'importance à la qualité des mesures et des données. Les appareils devront être périodiquement calibrés, et les données validées avant d'être mises à disposition des bases de données. Les calibrations se feront en collaboration avec des laboratoires labellisés : localement l'ORA pourra participer à la calibration des instruments de mesure des gaz. Bien évidemment, les mesures in-situ dans le cadre du projet GAW sont destinées à établir le niveau de pollution de fond d'un site donné, et ne doit pas être perturbé par des sources de pollution locales. Ces mesures doivent êtres donc être idéalement être installées dans un site d'altitude.

Actuellement tous les instruments de mesure de l'OPAR sont en fonctionnement sur le site de l'université de St Denis, au niveau de la mer. Or, le fonctionnement de la plupart des instruments de télédétection (FTIR, radiomètres, lidar) est perturbé par les effets négatifs de la couche limite tropicale (humidité, pollution, lumière etc.)

Cet inconvénient sera résolu par la construction de la station d'altitude qui sera implantée au piton Maïdo, à 2200 mètres d'altitude, dans l'Ouest de l'île de la Réunion. Ce site présente un intérêt tout aussi important pour l'étude et le suivi de la composition chimique de la troposphère, dans le cadre de la station GAW. Cette construction sera destinée à recevoir la majorité des instruments décrits précédemment. Elle comprendra un espace lidars, un espace laboratoire, un espace pour accueillir des expériences lors de campagnes des équipes extérieures et un espace hébergement (Figure 1.14).

Le début des travaux est prévu mi 2009 pour une livraison du bâtiment avant fin 2010. L'installation des systèmes lidar dans ce bâtiment permettra une restructuration des systèmes avec la séparation des voies vapeur d'eau des mesures Rayleigh stratosphériques et ozone troposphérique. En effet, ce bâtiment va héberger un télescope de 120 centimètres de diamètre avec émission coaxiale. Ce nouveau système de réception devrait nous permettre d'améliorer la portée des profils de vapeur d'eau jusqu'à la basse stratosphère.

Figure 1.14 Plans d'architecture et images de synthèse de la future station d'altitude du Maïdo

Chapitre 2

L'ozone troposphérique tropical : Dynamique et physico-chimie ; mécanismes, climatologies et tendances

2.1 Introduction

L'ozone est un composant gazeux minoritaire de l'atmosphère, qui se trouve à 90% dans la stratosphère, où il a une action bénéfique de filtrage des rayons ultra-violets du soleil. L'étude de la partie troposphérique de l'ozone est toutefois importante, de part son rôle de gaz à effet de serre et également de part son caractère oxydant, qui en fait un polluant nocif. C'est dans ce cadre, pour documenter le bilan de l'ozone troposphérique dans les régions tropicales, qu'ont été initiées les premières mesures d'ozone par radiosondage qui, comme indiqué dans le chapitre 1, ont débuté en 1992.

A l'époque, les feux de végétation d'Afrique avaient été mis en évidence et étudiés dans le cadre de la campagne SAFARI/TRACE A, avec une issue spéciale du *Journal of Geophysical Research* consacrée à cette campagne parue en 1996. Compte tenu de la dynamique troposphérique particulière en Afrique du Sud, les feux de végétation sont, en fonction des situations dynamiques et des conditions de stabilité des masses d'air, à l'origine d'une augmentation de l'ozone troposphérique dans les régions africaines proches des feux de biomasse, et dans l'océan Atlantique Sud[1].

L'analyse des mécanismes d'influence des feux de végétation africains et malgaches sur l'ozone à la Réunion fut donc l'un des premiers thèmes de recherches du laboratoire. L'étude exploitant les premiers radiosondages-ozone effectués à la Réunion a mis en évidence le rôle des feux de végétation d'Afrique de l'Est et de Madagascar[2], lorsque les précurseurs d'ozone sont injectés dans la troposphère libre pour advectés vers l'Océan Indien sous l'influence des flux d'ouest dominants. Deux thèses ont été consacrées à ce sujet, celle de Fabienne Taupin qui quantifia par modélisation lagrangienne la production photochimique d'ozone pendant le transport[3], et celle de Tantely Randriambelo dont l'approche par analyse des observations satellitales permit de préciser les périodes et les occurrences des feux de végétation, et le rôle de la convection[4].

[1] Barsby J. and R. D. Diab, Total ozone and synoptic weather relationships over southern Africa and surrounding oceans, *J. Geophys. Res*., **100**, 3023-3032, 1995.
[2] Baldy S. et al., Field observation of the vertical distribution of tropospheric ozone at the island of Reunion (Southern Tropics), *J. Geophys. Res*., **96**, 23835-23849, 1996.
[3] Taupin F., Analyse et modélisation de la variabilité de l'ozone troposphérique en zone tropicale - Influence du brûlage de biomasse. Thèse de doctorat de l'université Clermont II, 1997.
[4] Randriambelo T., Détection satellitaire des feux de végétation et des zones de convection en zone tropicale: Application à l'étude climatologique de l'ozone troposphérique. Thèse de doctorat de l'université de la Réunion, 1998.

Dans le contexte de l'ozone troposphérique, les échanges stratosphère-troposphère étaient, de longue date, une source identifiée aux latitudes moyennes. En effet, dès 1948, Palmen et Newton[5] avaient mis en évidence la coïncidence entre le courant-jet de la haute troposphère polaire et les discontinuités de la tropopause, ouvrant la voie à de multiples approches de l'étude des échanges stratosphère-troposphère lié au courant-jet polaire dans le courant du XXe siècle (mesures par avion, radiosondages, mesures par télédétection), et étudié dans sa structure fine[6,7].

Pour les latitudes subtropicales, lorsque j'ai commencé à étudier l'ozone dans le cadre de mon stage de DEA en 1995, aucune étude démontrant que la stratosphère pouvait être une source d'ozone troposphérique n'avait été reportée pour les régions subtropicales. Mon travail de DEA a été d'analyser la base de données sondages de l'époque, ainsi que les données satellitales TOMS, qui n'étaient pas idéales car produisant une colonne totale et avec une résolution assez faible, mais qui étaient parmi les rares données satellitales d'ozone disponibles à l'époque.

Un premier cas d'étude de déferlement d'onde de Rossby ayant eu lieu début Août 1993 dans la région et induisant une forte déformation de la tropopause a donc été identifié (Figure 2.1). Ce cas d'étude a été approfondi ensuite dans le cadre de ma thèse[8], et publié[9].

Entre temps, d'autres cas d'études dans l'Atlantique subtropical avaient été reportés[10,11], confirmant la possibilité de foliation de tropopause induite par le courant-jet subtropical, et son influence sur le bilan de l'ozone troposphérique.

[5] Palmen E., and C. W. Newton, A study of the mean wind and temperature distribution in the vicinity of the polar front in winter, *J. Meteor.*, **5**, 220-226, (1948).
[6] Shapiro M.A., Turbulent Mixing within tropopause folds as a mechanism for the exchange of chemical constituents between the stratosphere and troposphere*, J. Atm. Sci.*, **37**, 994-1004, 1980.
[7] Ancellet G. et al., Ground-based lidar studies of ozone exchange between the stratosphere and the troposphere*, J. Geophys. Res.*, **96**, 22401-22421, 1991.
[8] Baray J.L., Étude des transferts stratosphère-troposphère en bordure sud de la zone tropicale et impact sur le bilan d'ozone troposphérique, Thèse de doctorat de l'université Paris VI, 1999.
[9] Baray, J.L., et al., Subtropical tropopause break as a possible stratospheric source of ozone in the tropical troposphere, *J. Atm. and Sol.-Terr. Phys*., **60**, 27-36, 1998.
[10] Gouget, H., et al., Ozone peaks associated with a subtropical tropopause fold and with the trade wind inversion : A case study from the airborne campaign TROPOZ II over the Caribbean in winter*, J. Geophys. Res.*, **101**, 25979-25993, 1996.
[11] Folkins, I., and C. Appenzeller, Ozone and potential vorticity at the subtropical tropopause break, *J. Geophys. Res*., **101**, 18787-18792, 1996.

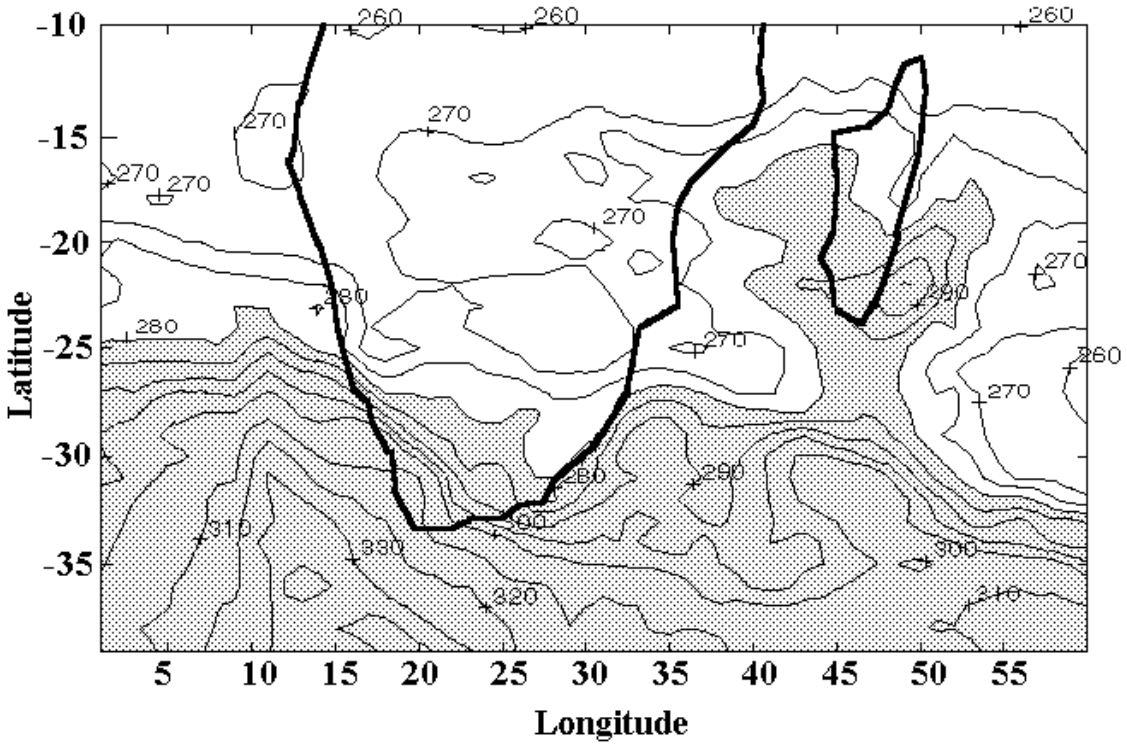

Figure 2.1 Signature du déferlement d'onde de Rossby le 10 Août 1993 sur la carte de colonnes totales d'ozone données par le satellite TOMS (D'après Baray et al., 1998).

Notre cas d'étude étant uniquement basé sur des données satellitales fournissant une colonne totale d'ozone, et sur les données de modèles. Pour en avoir la description dans le plan vertical et avoir un meilleur suivi temporel des événements, nous avons mis en place les voies ozone troposphérique du lidar en 1998 (section 1.2.3 de ce document). Une campagne de mesures d'ozone par radiosondages en supplément des sondages de routine a également été organisée. Coordonné par Gérard Ancellet, le projet TRACAS[12] était une extension du projet THESEO[13] aux régions subtropicales et à la troposphère. Ce projet avait pour objectif la caractérisation des échanges stratosphère-troposphère à proximité du courant-jet subtropical. Une partie du dispositif était déployée dans l'Atlantique de l'hémisphère Nord, avec des mesures par lidar aéroporté embarqué sur avion, et des radiosondages aux îles Canaries, la partie hémisphère sud consistant en les mesures par radiosondages et lidar ozone troposphérique à la Réunion et en Afrique du Sud. L'analyse des profils d'ozone obtenus en juillet 1998 a permis de mettre en évidence un pli de la tropopause à grande échelle, couvrant une grande partie de l'océan indien, et avec une persistance temporelle inattendue (Figure 2.2). Les données ECMWF[14] semblent indiquer l'influence de la branche descendante de la cellule de Hadley associé au flux de retour de la mousson en altitude. Cette étude a fait l'objet d'un article publié aux

[12] Transport of Chemical Species Across the subtropical Tropopause
[13] Third European Stratospheric Experiment on Ozone
[14] European Centre for Medium-Range Weather Forecasts, http://www.ecmwf.int/

Geophysical Research Letters[15]. Bien que le dispositif d'observation de TRACAS n'ait pas été reconduit par la suite, il semble que ce type d'événement dynamique ne s'est pas reproduit de manière aussi prononcée par la suite.

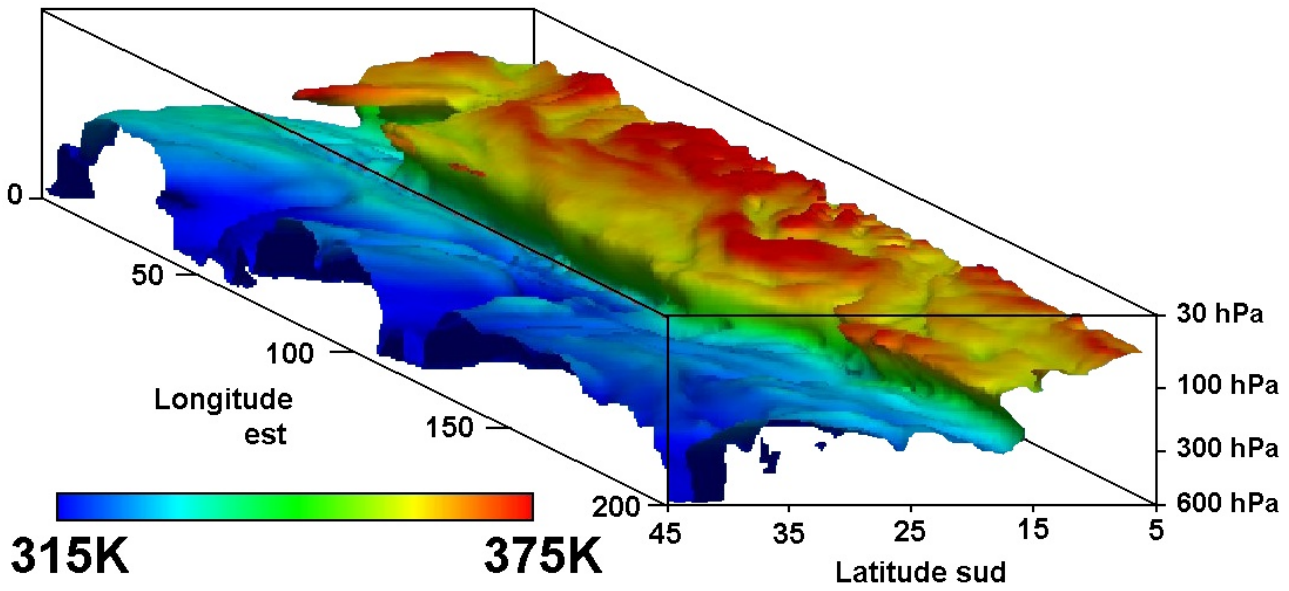

Figure 2.2 Foliation de tropopause ayant eu lieu sur l'Océan Indien en juillet 1998, (d'après Baray et al., 2000).

Dans le cas décrit précédemment, le courant-jet subtropical était avait gardé une forme assez rectiligne et régulière durant le mois qu'avait duré la campagne de mesure. C'est un contexte dynamique relativement rare. La plupart du temps, lorsque la vitesse du vent dans le courant-jet subtropical n'est pas aussi forte, il prend une structure ondulatoire, faisant se succéder des courbures cycloniques et anticycloniques. Une onde de Rossby se forme et peut déferler. Sous certaines conditions dynamiques dans la haute troposphère (Rossby Wave Breaking et blocage), une partie du vortex polaire stratosphérique peut se détacher, former une dépression cyclonique d'altitude et migrer en direction de l'équateur. Un cas d'étude de goutte froide tropicale a été analysé en utilisant les données MOZAIC, radiosondages, satellitales et de modélisation (ECMWF et advection de contours). Ces mécanismes sont bien répertoriés aux latitudes moyennes et polaires, mais les cas de goutte froide se détachant à proximité du courant-jet subtropical, et atteignant les latitudes tropicales sont assez rares. Le cas d'étude que nous avons analysé concerne une goutte froide se détachant d'une ondulation du courant-jet subtropical au-dessus de l'Afrique du sud en octobre 1996, atteignant la latitude 10°S, avec une durée de vie de 2 semaines, et un diamètre d'environ 10°

[15] Baray J.L. et al., Planetary-scale tropopause folds in the southern subtropics, *Geophys. Res. Lett.*, **27**,3, 353-356, 2000.

(1100 km). La particularité de ce cas d'étude, par comparaison aux autres cas observés aux latitudes plus hautes, outre son temps de vie, sa taille, la latitude atteinte, et sa forte concentration en ozone, est que le détachement de la masse d'air s'est produit à la fois dans le plan horizontal, mais aussi vertical. De ce fait, la masse d'air enrichie en ozone ne remonte pas dans la stratosphère au cours de sa dissipation et le transfert stratosphère-troposphère est irréversible. Cette étude a fait l'objet d'un article[16] présenté dans la section 2.2.1.

Un autre mécanisme d'échange stratosphère-troposphère que nous avons abordé est associé à la convection tropicale. La dynamique de la convection est complexe, mettant en jeu des mouvements verticaux ascendants et subsidents. Le lien avec l'ozone troposphérique l'est tout autant, mettant en jeu les transports verticaux et la chimie. Nous avons abordé cette thématique complexe avec un cas d'étude d'enrichissement d'ozone troposphérique d'ampleur exceptionnelle à la Réunion en avril 1995 lorsque le Cyclone Marlène était à proximité de la Réunion.

Dans le cadre de ma thèse, nous avons analysé ce cas d'étude avec les données ECMWF. Le mois d'avril n'est pas la période durant laquelle l'influence de la photochimie est significative. Elle n'est pas non plus la période durant laquelle l'influence du courant-jet subtropical est la plus forte. Nous avons donc évoqué l'hypothèse d'échanges stratosphère-troposphère induits par la circulation d'altitude du cyclone qui auraient engendré des mouvements subsidents dans la périphérie du cyclone. Cette étude a fait l'objet d'un article publié au *Journal of Geophysical Research*[17]. Il se trouve que simultanément à notre article, un autre article dans la même thématique et la même région d'étude a été publié dans le même journal par De Laat et al.[18] Cet article était basé sur une série de radiosondages effectués dans l'Océan Indien à partir d'un navire de recherche américain, le Malcolm Baldridge, dans le cadre d'une campagne préparatoire au projet INDOEX[19]. Ayant également observé des valeurs importantes d'ozone dans la troposphère libre, De Laat et al. En attribuaient l'origine à de l'advection à grande échelle de pollution d'Afrique, en se basant principalement sur des données de modèle European Centre Hambourg (ECHAM), et sur une analyse trajectographique. En désaccord sur l'origine de l'ozone troposphérique, nous avons donc publié un court-article commentaire qui montre que les données présentées dans l'article de De Laat et al sont compatible avec notre hypothèse[20].

[16] Baray J.L. et al., Dynamical study of a tropical cut-off low over South Africa, and its impact on tropospheric ozone, *Atmospheric Environment*, **37**, 11, 1475-1488, 2003.
[17] Baray J.L., G. Ancellet, T. Randriambelo, and S. Baldy, Tropical cyclone Marlene and stratosphere-troposphere exchange, *Journal of Geophysical Research*, **104**, D11, 13953-13970, 1999.
[18] De Laat, A. T. J, et al., Tropospheric O3 distribution over the Indian Ocean During Spring 1995 Evaluated with a Chemistry-Climate Model, *J. Geophys. Res*., **104**, 13881-13910, (1999).
[19] INDian Ocean EXperiment
[20] Baray J.L., et al., Comment on 'Tropospheric O_3 distribution over the Indian Ocean during spring 1995 evaluated with

L'origine dynamico-chimique des enrichissements d'ozone troposphérique observés près des zones de convections tropicales restaient une question ouverte et force était de constater que le mécanisme dynamique n'était pas mis clairement en évidence, les signatures des échanges sur les champs de vorticité potentielle n'étant pas flagrantes dans les données ECMWF ERA-40.

Nous avons décidé d'entreprendre un approfondissement de cette thématique. J'ai donc proposé un sujet, puis encadré la thèse de Jimmy Leclair de Bellevue[21].

L'enjeu était d'approfondir notre connaissance sur les mécanismes dynamiques d'échanges stratosphère-troposphère, près des zones de convection profonde. Pour cela, il s'agissait de modéliser à méso-échelle le cas du cyclone Marlène avec le modèle Meso-nh, pour mettre en évidence en expliciter le mécanisme et si possible quantifier l'échange de masse d'air. D'autre part, nous souhaitions aborder l'aspect climatologique.

D'autres cas avaient-ils eu lieu à la Réunion?
Ce type d'échange était-il fréquent ?
Influence-t-il significativement le bilan de l'ozone troposphérique?

La thèse de Jimmy Leclair de Bellevue a permis d'apporter un certain nombre d'éléments de réponse.

La modélisation à meso-échelle du cas du cyclone Marlène, a permis de mettre en évidence un filament d'origine stratosphérique dans la haute troposphère, ainsi que la circulation agéostrophique d'altitude, les zones de divergence associées et la contribution du cisaillement vertical de vent. Le modèle idéalisé de convection tropicale Hurricane développé par Kerry Emanuel[22] a également apporté des compléments dynamiques et a généralisé cette étude de mécanismes reliant cyclones et échanges dynamiques entre les compartiments atmosphériques.

D'autres cas d'étude (Novembre 2000 et Février 2002) ont été reportés et ont fait l'objet d'une approche synoptique basée sur les données ECMWF, Meteosat et in-situ radiosondage et lidar. La diversité des situations météorologiques et des signatures dynamiques et physico-chimiques des échanges stratosphère-troposphère a été mise en évidence, de même que la forte interaction entre les

a chemistry-climate model', by A.T.J. de Laat et al., *J. Geophys. Res*., **106** , D1, 1365-1368, 2001.

[21] Leclair de Bellevue J., Analyse et modélisation des échanges verticaux induits par les systèmes convectifs des latitudes tropicales: effets sur l'ozone troposphérique, thèse de doctorat de l'université de la Réunion, 2006.

[22] http://wind.mit.edu/~emanuel/modella/modella.html

dynamiques de la convection, du système jet-front et des ondes de Rossby. Enfin une approche climatologique a montré que l'influence de l'occurrence fréquente de ces systèmes convectifs sur l'ozone troposphérique est double : des apports d'ozone en moyenne troposphère et une diminution d'ozone en haute troposphère. Deux articles ont pu être publiés, un présentant la climatologie et les cas d'étude (Novembre 2000 et Février 2002)[23] et l'autre sur la modélisation à méso-échelle du cas du cyclone Marlène[24]. Ces deux articles sont présentés respectivement dans les sections 2.2.2 et 2.2.3.

Jusqu'à présent, je m'étais principalement intéressé au bilan de l'ozone troposphérique par le biais des échanges stratosphère-troposphère, mais au niveau du laboratoire, la source photo-chimique constituée par les injections de précurseurs d'ozone émis dans la troposphère par les feux de biomasse et la pollution africaine avait été abordée dans le cadre de l'étude de Serge Baldy et des thèses de Fabienne Taupin et de Tantely Randriambelo. Grâce à ces études, nous savions que l'ozone troposphérique subissait un cycle annuel avec une augmentation pendant la saison des feux de végétation, de Septembre à Novembre. Cependant, les radiosondages étant effectués à une fréquence hebdomadaire, nous n'avions pas d'information sur la variabilité journalière de l'ozone troposphérique pendant la saison des feux, alors que le lidar ozone troposphérique, comme nous l'avons constaté lors de la campagne de juillet 1998, pouvait nous fournir cette information et apporter des éléments de réponse aux questions suivantes :

Quelle est la variabilité journalière de l'ozone troposphérique pendant la saison des feux?

La source photo-chimique est-elle une montée du niveau de background de l'ozone ou bien au contraire une période dans laquelle la variabilité de l'ozone est très grande ?

Pour répondre à ces questions, nous avons profité d'une dizaine de soirs consécutifs de ciel clair en Novembre-Décembre 1999 pour effectuer une campagne de tirs lidar ozone troposphérique. Cette saison correspond à la fin de la saison des feux de végétation en Afrique et à Madagascar, et au début de la saison convective. Les profils d'ozone montrent des caractéristiques très stratifiées, avec une variabilité d'un jour à l'autre très importante, par rapport à ce à quoi l'on aurait pu s'attendre. Cette variabilité peut s'expliquer par l'addition ponctuelle d'apports stratosphériques pour partie, et surtout par une très grande variabilité du contexte dynamique qui advecte (ou non) les masses d'air

[23] Leclair de Bellevue, J., et al., Signatures of stratosphere to troposphere, transport near deep convective events in the southern subtropics, *J. Geophys. Res*., 111, D24107, doi:10.1029/2005JD006947, 2006.
[24] Leclair De Bellevue J., et al., Simulations of a Stratospheric to tropospheric transport during the tropical cyclone Marlene event, *Atmospheric Environment*, 41, 6510-6526, 2007.

enrichies (ou non) en ozone et en précurseurs d'ozone. Cette étude a fait l'objet d'un article[25] présenté dans la section 2.2.4.

La base de données de radiosondages a également été exploitée pour construire une climatologie de la tropopause, et comparer la climatologie obtenue à d'autres climatologies établies pour d'autres sites de mesure[26]. Cela a été fait dans le cadre du séjour post-doctoral de Sivakumar arrivé à mon initiative au laboratoire en Novembre 2002. Trois types de tropopause sont basés sur les profils de température et d'ozone : cold-point tropopause (CPT), lapse rate tropopause (LRT) et ozone tropopause (OT). La distribution statistique et la variabilité mensuelle des trois types de tropopause ont été étudiées. L'application sur la base de donnée de la Réunion de l'algorithme de détermination de la structure de tropopause de Bethan et al. (1996) a montré que la fréquence de tropopause OT définie est plus grande que pour CPT et LRT, et qu'il n'y a pas de cas de tropopause OT indéfinie (avec la définition de Bethan). Une adaptation des seuils de l'algorithme de Bethan a permis de détecter 3 cas de tropopause OT indéfinie. Pour ces trois cas, l'île de la Réunion était dans une zone de divergence d'altitude, en entrée d'un noyau de courant jet subtropical, sur la face anticyclonique. Les calculs de régression linéaire et corrélation entre les distributions entre les différentes hauteurs de tropopause indiquent la plus haute corrélation entre CPT et LRT, puis entre CPT et OT, puis entre LRT et OT. Cette étude a fait l'objet d'un article[27] présenté dans la section 2.2.5.

Les travaux présentés dans la section 2.2 sont des travaux publiés, ceux présentés dans la section 2.3 sont des travaux en cours qui visent au développement et la validation d'un code de trajectoire et d'advection de traceurs, et à la détermination des tendances de l'ozone troposphérique.

Les trajectoires calculées à partir de champs météorologiques sont un outil très utilisé depuis longtemps en physique de l'atmosphère pour la description des processus de transport et la compréhension des écoulements atmosphériques. Elles permettent par exemple d'identifier les origines des masses d'air lorsque l'on veut analyser les différentes contributions sur les distributions d'un traceur par exemple sur un profil vertical. Elles peuvent être à la base de méthodes statistiques de la détermination de l'advection et de la dispersion de traceurs. Nous avons donc, au laboratoire

[25] Randriambelo T. et al, Investigation of the short-time variability of tropical tropospheric ozone, Annales Geophysicae, 21, 9, 2095-2106, 2003.
[26] Bethan S. et al., A comparison of ozone and thermal tropopause heights and the impact of tropopause definition on quantifying the ozone content of the troposphere, Q. J. R. Meteorol., 929–944, 1996.
[27] Sivakumar, V. et al., Tropopause characteristics over a southern subtropical site, Reunion Island (21 S, 55 E): Using radiosonde-ozonesonde data, J. Geophys. Res., 111, D19111, doi:10.1029/2005JD006430, 2006.

LACY, développé un code de trajectoire et de reconstruction RDF[28], LACYTRAJ. Le développement et la validation de ce code est l'objet de la section 2.3.1.

La dernière thématique qui sera développée dans ce chapitre sera l'étude des tendances de l'ozone troposphérique. En effet, les mesures d'ozone ayant débuté en 1992 à la Réunion, nous disposons maintenant d'un jeu de données qui couvre plus de 15 ans. Les études de tendances stratosphériques nécessitent l'utilisation de modèles de tendance prenant en compte les influences cycliques bien établies que subit la stratosphère et qu'il convient de corriger pour l'estimation des tendances (cycle solaire, QBO,... etc.). Ce n'est pas le cas dans la troposphère ou la variabilité de l'ozone est également plus importante. Nous avons donc choisi, comme première approche, d'effectuer une simple régression linéaire sur le jeu de données. Cette approche sera également appliquée par comparaison au jeu de données de la station de Irene en Afrique du sud depuis 1990. Synthétisés dans la section 2.3.2, ces résultats ont été intégrés dans un article détaillant la climatologie de l'ozone troposphérique dans l'océan indien, et basé sur différents jeux de données indépendantes, publié dans la revue *Atmos. Chem. Phys. and Disc.* et en cours de révision à la revue *Atmos. Chem. and Phys.*[29].

[28] Reverse Domain Filling

[29] Clain G. et al., Tropospheric ozone climatology at two southern subtropical sites, (Reunion Island and Irene, South Africa) from ozone sondes, LIDAR, aircraft and in situ measurements, *Atmos. Chem. Phys. Discuss.*, 8, 11063-11101, 2008

2.2 Travaux publiés

2.2.1 Echange stratosphère-troposphère : Déferlement d'onde de Rossby et goutte froide d'altitude

PERGAMON

AE International – Africa & the Middle East

Atmospheric Environment 37 (2003) 1475–1488

ATMOSPHERIC ENVIRONMENT

www.elsevier.com/locate/atmosenv

Dynamical study of a tropical cut-off low over South Africa, and its impact on tropospheric ozone

J.L. Baray[a,b,*], S. Baldy[a], R.D. Diab[c], J.P. Cammas[d]

[a] *Laboratoire de Physique de l'Atmosphère (LPA), CNRS-UMR 8105, Université de la Réunion, 15 Av. René Cassin, BP 7151, 97715 Saint-Denis Messag. Cedex 9, La Réunion 97715, France*

[b] *Institut Pierre Simon Laplace (IPSL), Observatoire de Physique de l'Atmosphère de la Rèunion (OPAR), La Réunion, France*

[c] *School of Life and Environmental Sciences, University of Natal, Dalbridge 4041, South Africa*

[d] *Laboratoire d'Aérologie (LA), CNRS-UMR 5560, Observatoire Midi-Pyrénées, 14 Av. Edouard Belin, 31400 Toulouse, France*

Received 10 July 2002; received in revised form 21 November 2002; accepted 2 December 2002

Abstract

The structure and evolution of an intense tropical cut-off low (COL) occurring over South Africa is documented, by combining meteorological and ozone data from a number of different sources, such as in situ radiosoundings, Measurement of ozone and water vapor by airbus in-service aircraft data, satellite (Meteosat) and modelled European Center for Medium-Range Weather Forecast data. The COL extends to latitude 10°S, with a lifetime of approximately 2 weeks, and a horizontal size of about 10°. A distinguishing feature of this case study is that it becomes detached from the stratospheric reservoir in both the vertical and horizontal planes, in an irreversible way and as such is different in structure to a mid-latitude or a polar COL. Consequently, even though tropical COLs may occur infrequently, it is likely that the tropospheric ozone enhancement induced by this irreversible intrusion could be significant.

Keywords: Tropical tropospheric dynamics; Southern Hemisphere; Stratosphere–troposphere exchange; Tropospheric ozone; Airborne measurements; Radiosounding

1. Introduction

A cut-off low (COL) is an upper tropospheric trough of air coming from the stratosphere, which becomes isolated from its external environment and is advected equatorward of the mid-latitude westerlies. This kind of feature is of dual importance: on the one hand, it plays a significant role in the tropospheric ozone balance through dissipation and mixing of stratospheric ozone; and on the other, it is important in terms of the weather it produces through the disturbance of flow in the upper troposphere, the formation of jet-streams and its role in convective activity which is often triggered by lower static stability under the COL and/or by potential vorticity advection on the down-shear side of the COL.

COLs are well-known mechanisms in the middle and polar latitudes. Many studies of polar and mid-latitude COLs have been published in recent years: for example, modelling of COL case studies and tropopause folds (Ebel et al., 1991; Langford et al., 1996), impact of COLs on tropospheric ozone (Ancellet et al., 1994), and a mesoscale analysis of the decay of a COL (Ravetta and Ancellet, 2000; Gouget et al., 2000). Most of these studies have focused on mid-latitude COLs; however, it has been noted that they may extend quite far towards the equator (Kentarchos et al., 1998, 1999).

In their statistical study of the size and distribution of COL systems, Price and Vaughan (1992) identified three types of COL, depending on the location of the

*Corresponding author. Laboratoire de Physique de l'Atmosphère (LPA), CNRS-UMR 8105, Université de la Réunion, 15 Av. René Cassin, BP 7151, 97715 Saint-Denis Messag. Cedex 9, La Réunion 97715, France. Tel.: +262-262-96-86-64; fax: +262-262-93-86-65.

E-mail address: baray@univ-reunion.fr (J.L. Baray).

1352-2310/03/$ - see front matter
doi:10.1016/S1352-2310(02)00999-8

detachment: polar vortex, polar, and subtropical. Polar COLs, which usually extend to mid-latitude regions, are the most studied systems. According to that study, subtropical COLs are smaller than the two other types, and their lifetime is shorter. The authors concluded that, a priori, subtropical COLs do not play a significant role in the tropospheric ozone budget.

However, Barsby and Diab (1995) analyzed the relationship between ozone and synoptic weather systems, for different situations including a case of a subtropical COL over South Africa. By using the analysis of daily total ozone mapping system (TOMS) and European Center for Medium-Range Weather Forecast (ECMWF) data (geopotential heights and potential vorticity fields), they highlighted the importance and the strength of the link between ozone and day-to-day weather systems in cases of COLs and subtropical anticyclones. The observation of the synoptic weather context of another case study of a COL over Australia has also been reported (Griffiths et al., 1998).

Despite these studies, the literature, which is very rich in case studies of polar COLs, is deficient when it comes to case studies of subtropical COLs. The objective of this paper is to document a case of a tropical COL, which occurred over South Africa during October 1996. By using instrumental data sets (Measurement of OZone and water vapor by Airbus In-service airCraft, MOZAIC, flights from Vienna to Johannesburg and radiosoundings over Reunion Island), satellite (Meteosat and TOMS) and global model data (ECMWF), we shall characterize the manner in which this tropical COL differs from a typical COL based on case studies from the polar latitudes. Aspects such as their dynamics and tropospheric ozone influence will be considered.

2. Synoptic situation before the formation of the COL

In this section, we shall examine the synoptic situation before the formation of the COL and its detachment from the mid-latitude regime using ECMWF analysis (1° grid, 15 vertical pressure levels between 1000 and 10 hPa and 6 h time resolution). A Rossby wave intensified over the southern part of Africa, at the latitude of the subtropical jet-stream, at the end of September 1996. The associated potential vorticity (PV, we use the absolute value in the Southern Hemisphere) disturbance propagated towards the east, and reached Reunion Island (21°S, 55°E) on 1 October (Fig. 1). The subtropical jet-stream intensified in two jet streaks, south of South Africa and south-east of Reunion Island (wind speed in excess of 60 m/s). As the wave breaking process proceeded, a significant irreversible deformation of isentropic PV contours occurred, ending in isolated PV structures over Africa at 15°S in the wake of the wave. This case of Rossby wave breaking (RWB) behaved similarly to the one reported by Scott et al. (2001) over the South Atlantic, ending in the formation

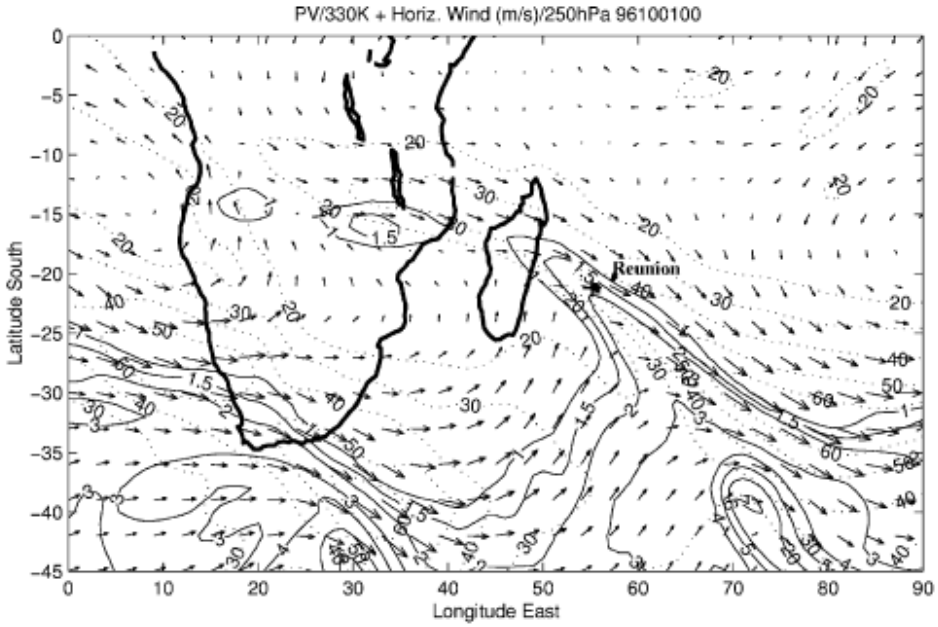

Fig. 1. ECMWF (spherical harmonics T213, 1 degree of resolution in latitude and longitude) horizontal wind field on the isobaric level 250 hPa, and PV on the isentropic level 330 K, on 1 October 1996, 00 GMT (1 PVU = 1 potential vorticity unit = 10^{-6} m^2 s^{-1} K kg^{-1}). Reunion Island (55°E, 21°S) is labelled by a cross.

doi:10.1016/S1352-2310(02)00999-8

of a filament of stratospheric origin, located equatorwards of the mid-latitude regime. The PV structure over Africa that is left behind in the wake of the Rossby wave is called a COL in the following discussion, whilst the PV structure that links the COL to the wave is called the filament.

The vertical perspective of the wave breaking event is further illustrated by an ozone radiosounding performed at Reunion Island (Fig. 2). The values of the ozone mixing ratio in the layer located between 10 and 11 km, are substantially higher (>180 ppbv) than corresponding values in other cases of subtropical tropopause folds reported in the literature (80 ppbv for Gouget et al., 1996 and 70 ppbv for Folkins and Appenzeller, 1996). The large vertical thickness of the filament (almost 3 km from 345 to 360 K) is suggesting more of a barotropic event (RWB), than a baroclinic event, which leads to slanted upper level frontogenesis associated with tropopause folds, that are typically 1–1.5 km deep (Shapiro, 1980). The tropospheric total ozone column derived from the radiosounding is 47.9 DU (tropopause level: 90 hPa); The ozone filament contribution is 27.9 DU (layer 210–310 hPa), which represents 58% of the tropospheric ozone column.

A signature of the RWB event over Reunion Island is also detected in the total column ozone derived from TOMS data which shows an increase of about 14 DU during the event (277.6 DU over Reunion Island on 28 September, before the event; 290.9 DU on 1 October and 291.8 DU on 2 October, during the event; 282.3 DU on 6 October, after the event). The ozone filament at Reunion Island (11 km) is located 4 km below the ozonopause (15 km) and 6 km below the thermal tropopause (17 km). It is very likely that in the following days, tropospheric diffusion processes such as gravity waves, convection, turbulence, will contribute to the final stage of an irreversible exchange from the stratosphere to the troposphere. As no data were available to investigate this issue, we will focus the study on the part of the wave that broke over South Africa for which MOZAIC aircraft data are available.

Studies of RWB in the subtropics, such as those based on ECMWF analyses by Postel and Hitchman (1999) and Scott and Cammas (2002), show that this phenomenon is quite frequent and undergoes a seasonal cycle with substantial interannual variability. It emphasizes the importance of investigating further case studies with ozone measurements from radiosondings, lidar systems or from the MOZAIC program to improve our understanding of the tropospheric ozone budget in the subtropics.

3. Dynamical evolution of the COL and its impact on tropospheric ozone

The temporal evolution of the COL in the horizontal and vertical planes based on ECMWF data is shown in

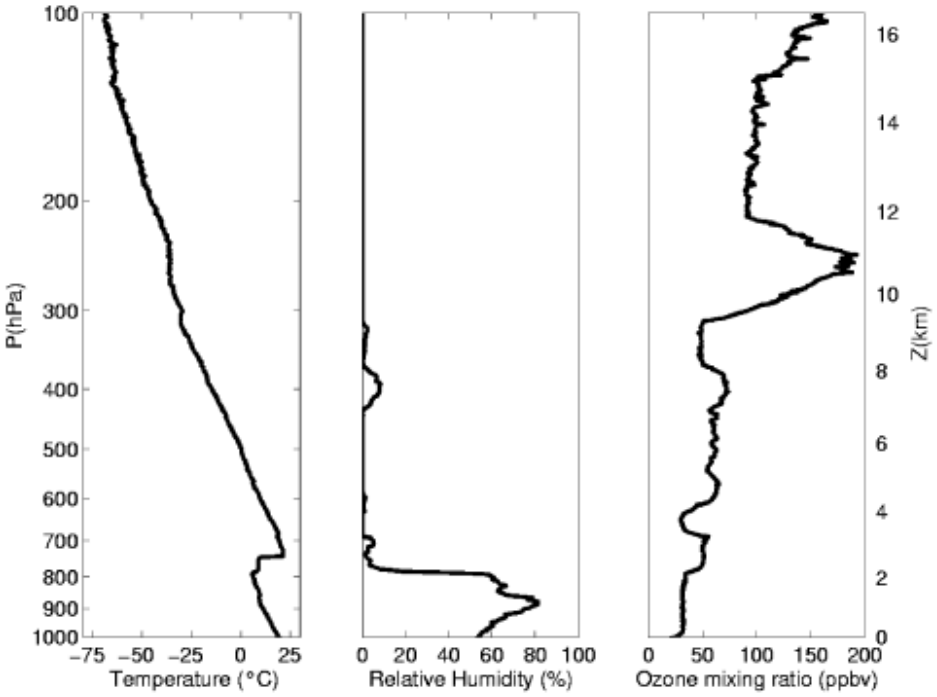

Fig. 2. Temperature (°C), relative humidity (%) and ozone mixing ratio (ppbv) profiles obtained by radiosounding at Reunion Island on the morning of 1 October 1996.

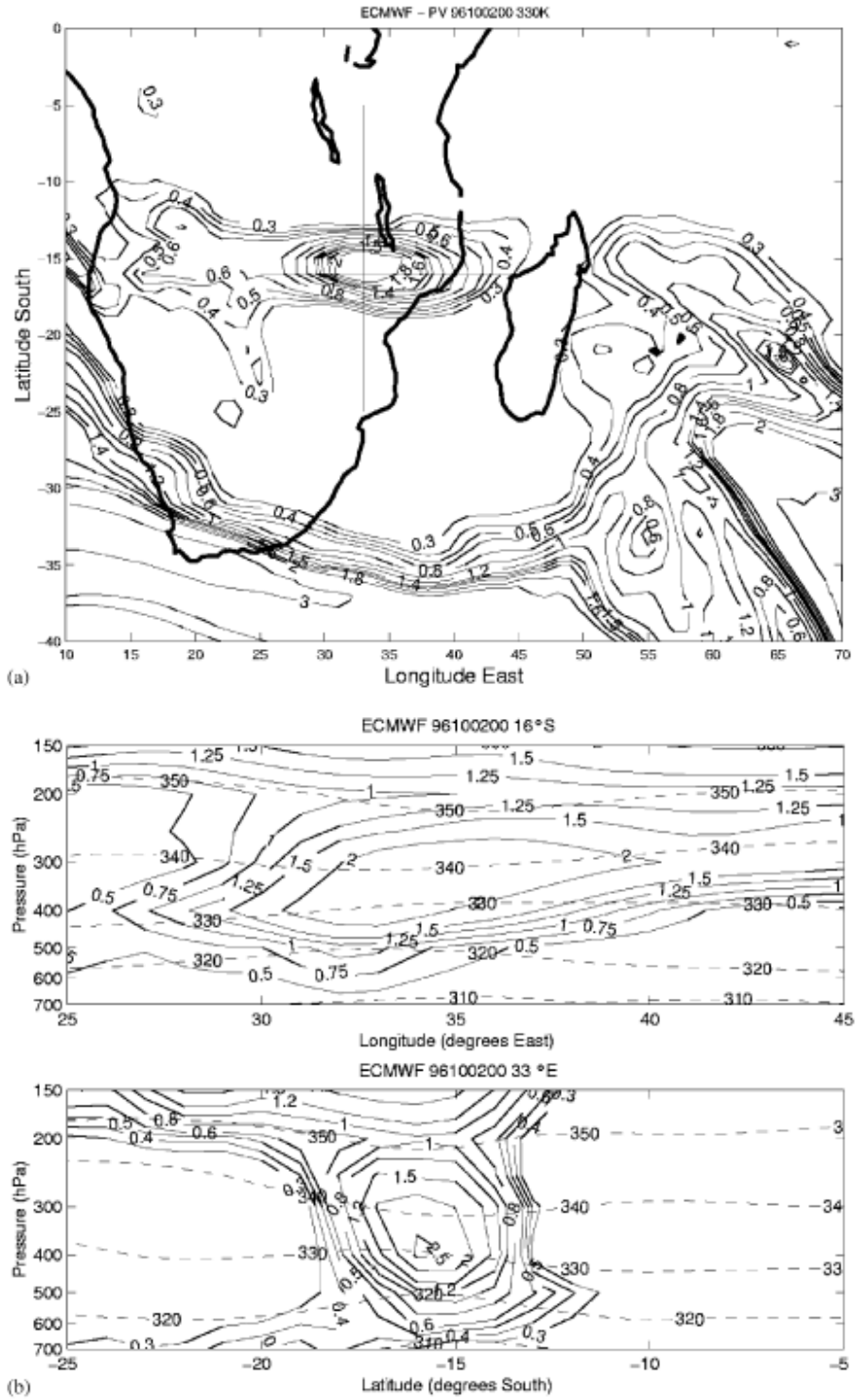

Fig. 3. (a) PV field on the 330 K surface on 2 October 1996, (b) vertical cross-section of PV along 16°S (top) and 33°E (bottom) on 2 October 1996, (c) PV field on the 330 K surface on 7 October 1996, and (d) vertical cross-section of PV along 10°S (top) and 36°E (bottom) on 7 October 1996.

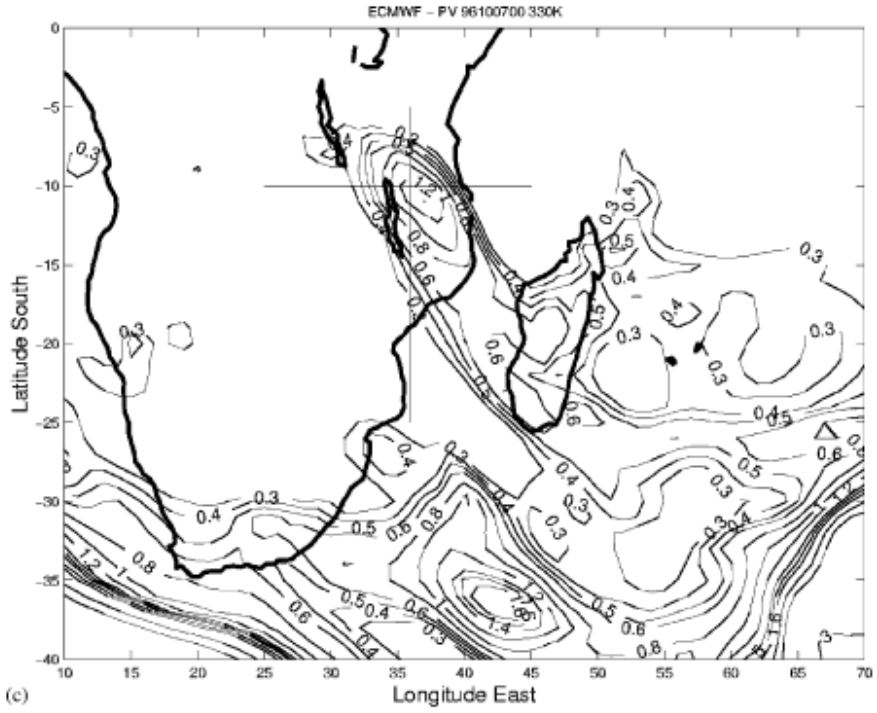

(c)

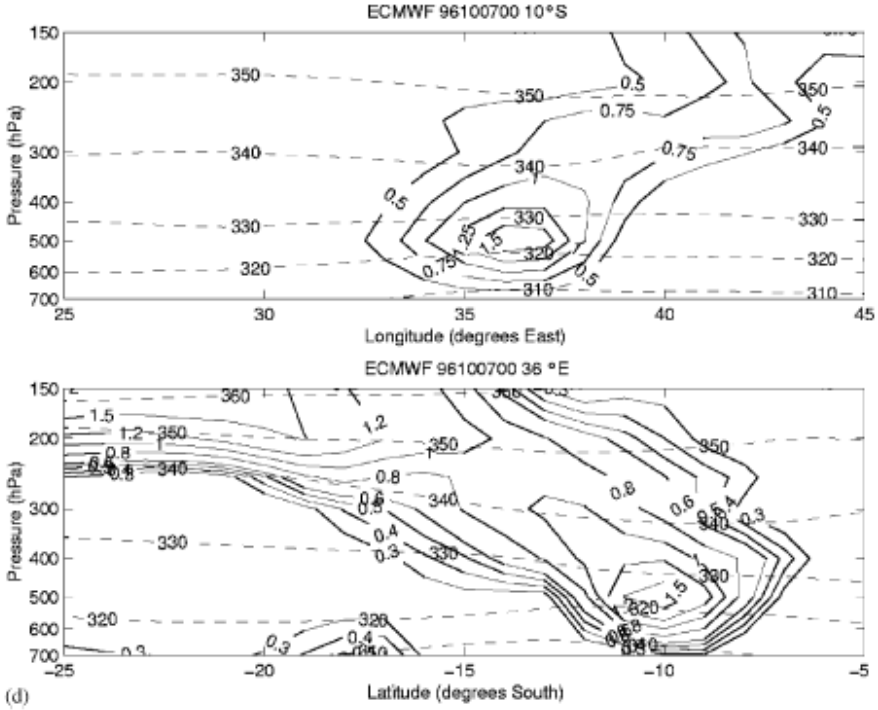

(d)

Fig. 3 (*continued*).

Table 1
Evolution of the center of the COL, and of the PV profile at the center (ECMWF data at 00 GMT)

Day	Center	PV on different pressure levels					
		200 hPa	250 hPa	300 hPa	400 hPa	500 hPa	700 hPa
09/28		Not detached from the stratosphere					
09/29	33°E, 18°S	1.89	**3.40**	1.99	0.18	0.21	0.24
09/30	41°E, 18°S	1.41	2.01	**3.08**	0.48	0.25	0.21
10/01	33°E, 17°S[a]	1.53	2.65	**3.16**	0.82	0.23	0.26
10/02	37°E, 17°S[b]	1.08	2.39	**3.05**	0.96	0.26	0.42
10/03	38°E, 13°S[c]	0.77	0.25	0.72	**2.11**	0.86	0.25
10/04	37°E, 13°S[d]	0.32	0.73	1.02	**1.51**	0.94	0.15
10/05	37°E, 15°S	0.48	1.13	0.92	**1.50**	0.84	0.19
10/06	37°E, 14°S	0.34	0.65	0.85	**1.55**	0.83	0.28
10/07	37°E, 11°S	0.50	0.93	1.03	1.24	**1.78**	0.21
10/08	38°E, 11°S	1.82	1.55	1.39	**1.67**	1.01	0.21
10/09	35°E, 9°S	0.80	1.13	1.17	**1.26**	0.81	0.22
10/10	36°E, 12°S	0.41	0.95	**1.36**	0.81	0.43	0.12
10/11	38°E, 15°S	1.09	1.16	**1.21**	0.56	0.30	0.08
10/12	37°E, 17°S	**1.49**	1.26	1.18	0.74	0.51	0.13
10/13	38°E, 21°S	**1.51**	1.00	0.87	0.99	0.56	0.43
10/14		The COL is no longer visible in the troposphere[e]					

[a] Formation of a secondary PV maximum at 19°E, 14°S, whose intensity is lower (PV = 0.6).
[b] The secondary PV maximum is moving towards the north-east. In the Atlantic Ocean, PV remains under 0.6.
[c] The secondary PV maximum has dissipated. The COL lengthens (longitude > latitude), inducing another secondary maximum at 24°E, 14°S (PV = 0.7).
[d] PV over Africa is quite high (PV = 0.3–0.4), but it is difficult to distinguish any secondary maxima (outside of the principal COL).
[e] After the complete dissipation of the COL, another system appears. It will be completely detached on 17 October, reaching the latitude band 5°S–10°S on 18–19 October, with PV between 0.5 and 1.
The maximum PV value (in PVU) for each profile is indicated in bold type.

Fig. 3. After 2 October, the COL is completely detached from the stratosphere, in both the horizontal (Fig. 3a) and the vertical (Fig. 3b) planes. Its center, where the PV value is at a maximum, is located at 16°S; 33°E in the horizontal, and at 400 hPa in the vertical, which corresponds approximately to the 330 K isentropic level and to an altitude of 8 km. The fact that the air mass is completely cut off from the stratosphere in the vertical plane distinguishes this kind of feature from polar or mid-latitude COLs, in which PV contours on isentropic planes are detached from the general PV field in the horizontal, but not frequently in the vertical plane. The PV fields and the vertical cross-sections on 7 October (Figs. 3c and d) show that the COL is always quite intense (PV > 1.2 PVU in the center of the COL), and continues its northwards and sinking movement. The center is located at 10°S; 36°E, and at the 500 hPa pressure level. It is noted that 6 days after its detachment, the air mass did not return to the stratosphere. Notwithstanding the fact that a tropical COL occurs rarely, it is likely to have a significant impact on tropospheric ozone as the majority of the ozone may dissipate in the troposphere.

The evolution of the COL is summarized in Table 1. Until 8 October, the values of PV remain above 1.5 PVU, whereafter, the PVU values diminish but remain above 1 PVU until 13 October. This COL thus had a very long lifetime, compared to the statistics presented by Price and Vaughan (1992). They claimed that 72% of subtropical COLs have a lifetime less than 3 days, and 98% less than 6 days. Moreover, on 2 October, the horizontal size of the COL is 6° in latitude, and 15° in longitude. This COL thus had a large horizontal extent, compared to the statistics of Price and Vaughan (1992), who stated that 53% of subtropical COLs have a horizontal diameter less than 5°, and 91% less than 10°. However, these figures of Price and Vaughan (1992) need to be treated with caution, since they are based on low-resolution data.

The cloud activity associated with the COL is visible on the Meteosat images (Fig. 4). The infrared and water vapor images for the 1 October (simultaneously with the radiosounding over Reunion Island), 8 and 11 October 1996 (simultaneously with the MOZAIC measurement) are shown in Fig. 4. The streamer of dry air is clearly visible on the water vapor image of 1 October, as a dark filament. The barotropic deformation, which is at the origin of the COL, is associated with an upper level front, visible on the infrared Meteosat images. On 2 October, when the COL is most intense, and when it is

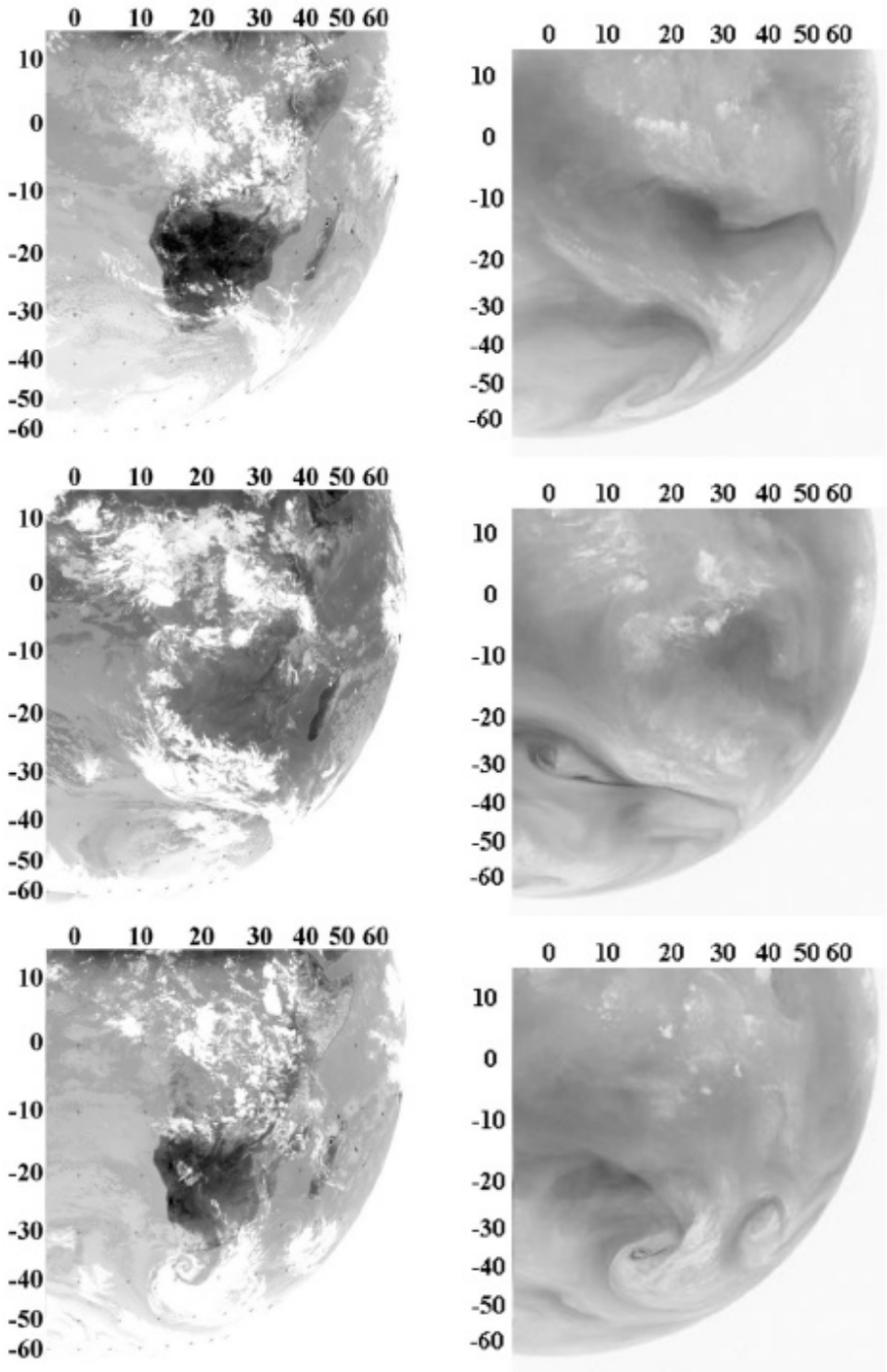

Fig. 4. Meteosat images on 1 October 1996 (top), 8 October (middle), and 11 October (bottom) 12 GMT, in infrared (left) and water vapor (right) channels. Each 10° in latitude and longitude is marked by crosses on the infrared images. Infrared and visible images are available on the web site http://www-grtr.u-strasbg.fr/ and water vapor images on http://www.eumetsat.de/.

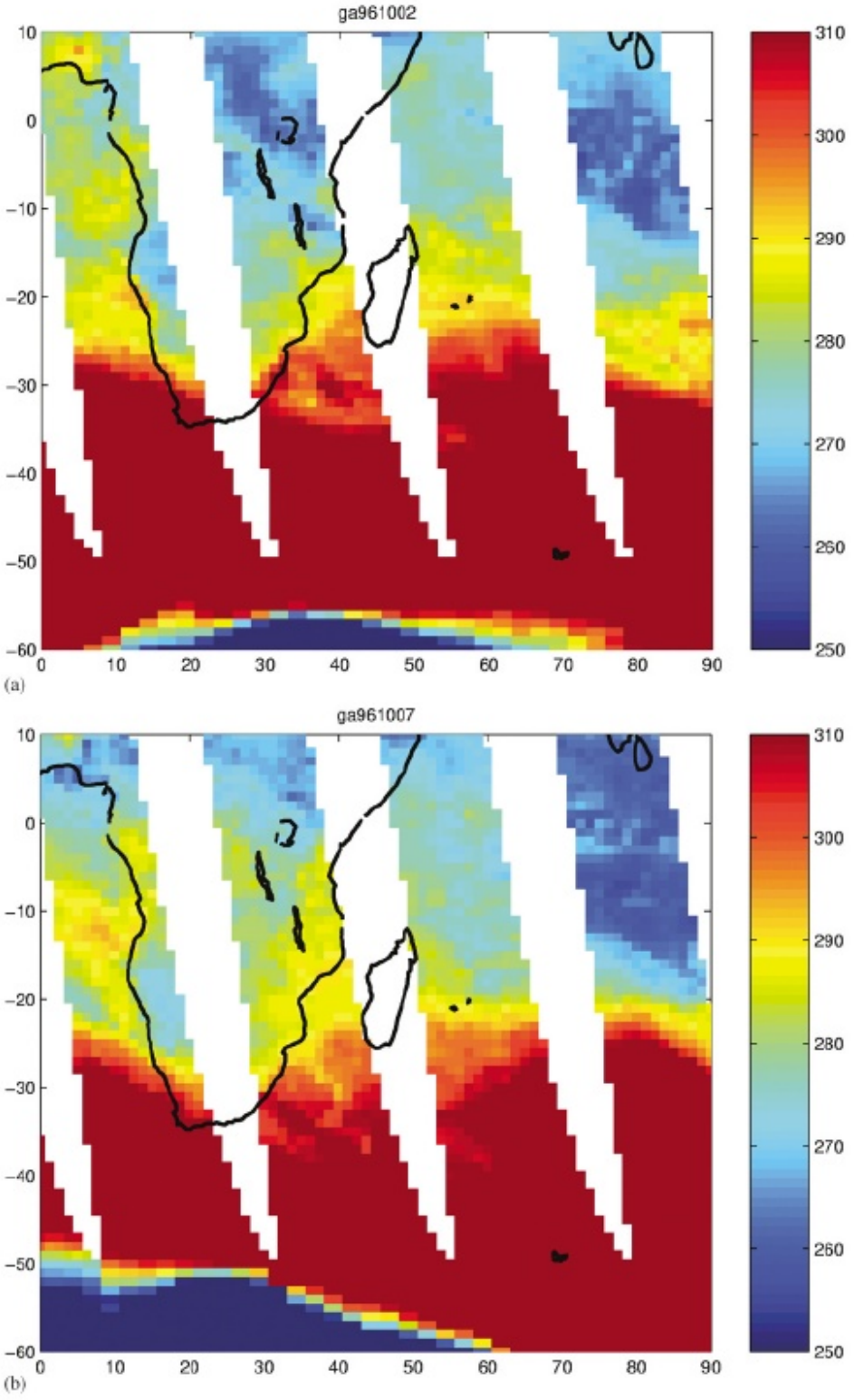

Fig. 5. Distribution of total ozone as measured by the TOMS instrument for 2 October (a) and 7 October 1996 (b).

completely detached, the location of the PV maximum at the center of the COL corresponds to an area without cloud, situated to the south of the cloudy area. Thereafter, this cloudy area seems to enlarge and by 8 October the COL corresponds well with the cloudy zone. Machado et al. (1992) have studied this kind of equatorial deep convective cloud over tropical Africa and showed that cloud heights reach 14.7 km. This cloud activity could take part in the convective dissipation of the COL and the subsequent convective redistribution of ozone and humidity, which decreases the vertical contrasts of PV, ozone and humidity (Table 1). Because of the COL dissipation, the dark zone corresponding to the COL area is no longer visible on the 11 October water vapor image (Fig. 4).

Dynamical elements of the study suggest that this COL could have a significant influence on tropospheric ozone over South Africa. If this is true, it is expected that some signatures on ozone and humidity should be visible in the TOMS and MOZAIC data.

The signature of the COL is weak and could be locally perturbed by upper tropospheric clouds. Moreover, this signature is difficult to distinguish from other processes influencing stratospheric ozone variations. But despite these inconveniences, quite strong values of total ozone content are visible at the location of the COL on 2 October, and the signature is more visible, 290 DU on 7 October (Fig. 5). These strong values could correspond to the influence of the COL on the total ozone column.

The European project MOZAIC consists of airborne observations of humidity, temperature and ozone on in-service aircraft (Marenco et al., 1998). The geographical coverage of MOZAIC data extends over the whole globe, and the route Vienna–Johannesburg cuts Africa transversely and passes close to the area affected by this COL. Fig. 6 indicates the concentration of ozone and humidity along MOZAIC flights, which took place before the formation of the COL (25 and 26 September), and during its dissipation (11 and 12 October). The location of the aircraft (latitude, longitude and altitude, Figs. 6e and f) indicates that the aircraft crossed ozone enriched zones on 12 October at 06 and 20 GMT, both near 27°E. Following the ECMWF analysis (PV map at 330 K on 12 October), the center of the COL is located near 37°E (cf. Table 1), at about 900 km from the trajectories of the MOZAIC flights. The interpolation of PV along the flight paths display tropospheric values (0.3 PVU, Figs 6c and d). However, the signature on the ozone mixing ratio is significant, with values between 80 and 100 ppbv between 8°S and 6°S on 11 October (Fig. 6a). Southward of 8°S and northward of 6°S, the ozone values are lower, 80 ppbv or less. On 12 October, the same enhanced ozone signature is visible, although it is spatially restricted between 7°S and 6°S. It seems that ozone is a better tracer of stratospheric air than PV because of diabatic non-conservation of PV (mixing by filamentation, turbulent diffusivity, convection). The characteristic period of the event, about 12 days from 1 to 12 October, is consistent with the hypothesis of non-conservation of PV and conservation of ozone.

Clustered backtrajectories (Fig. 7) have been calculated starting from the zone enriched in ozone on the MOZAIC flight, and the eastern side of this zone, since the COL is located on this side. Backtrajectories are calculated using three-dimensional ECMWF wind fields. At each running point of the trajectory, wind components (horizontal and vertical) are interpolated in time and space. The trajectory is then determined by iterative advection of the air mass using a 5-min time step. This trajectory model developed at Reunion University has been used in previous studies (Randriambelo et al., 2000). These calculations confirm that the MOZAIC flight has passed just above but within the vicinity of the COL: The black backtrajectories (250 hPa) indicate a southerly movement, after a recirculation near 5°S, 25°E, but no clear subsidence. The red backtrajectories (400 hPa the altitude of the COL), indicate a subsiding southerly movement over 3 days. Most of the green backtrajectories indicate a southerly movement, and a subsidence 3 days earlier. Because of the low resolution of ECMWF data it is difficult to study the dynamics of an air mass thoroughly. It is necessary to initialize backtrajectories with a mesoscale model to provide better evidence of the stratospheric origin of air masses (Kowol-Santen and Ancellet, 2000).

In order to analyze the fine-scale evolution of PV missing in the ECMWF analyses, we use contour advection with Dritschel's algorithm (1989). This algorithm has been recently applied to the evolution of RWB and mixing in the subtropics, with good agreement between advected PV and MOZAIC measurements of ozone (Scott et al., 2001). Fine-scale PV on the 330 K isentropic surface, estimated according to the algorithm, is depicted in Fig. 8, for 12 October, 06 GMT, which coincides with the passage of the first MOZAIC flight. Figs. 8a–d represent fine-scale PV based on initialization for 3, 5, 7, and 9 October, respectively. The COL is well modelled by the initialization on 9 October (Fig. 8d). The center of the COL as identified by the algorithm is located near 12°S, 35°E, slightly to the east of the MOZAIC flight

The simulations initialized on 3, 5, and 7 October display similar results, with the COL not being well reproduced by the advection model for these simulations. This suggests that the most intensive diabatic effect occurs before 9 October. Fig. 8 shows that the COL spins, emitting several filaments in the process. The last filament (created on 8 October) cuts the trajectory of the MOZAIC flight with an intensity more than 1 PVU, near 9°S, 27°E. Although the advection model is a pure isentropic advection model, the results suggest that an air mass could escape from the COL on 8 October and

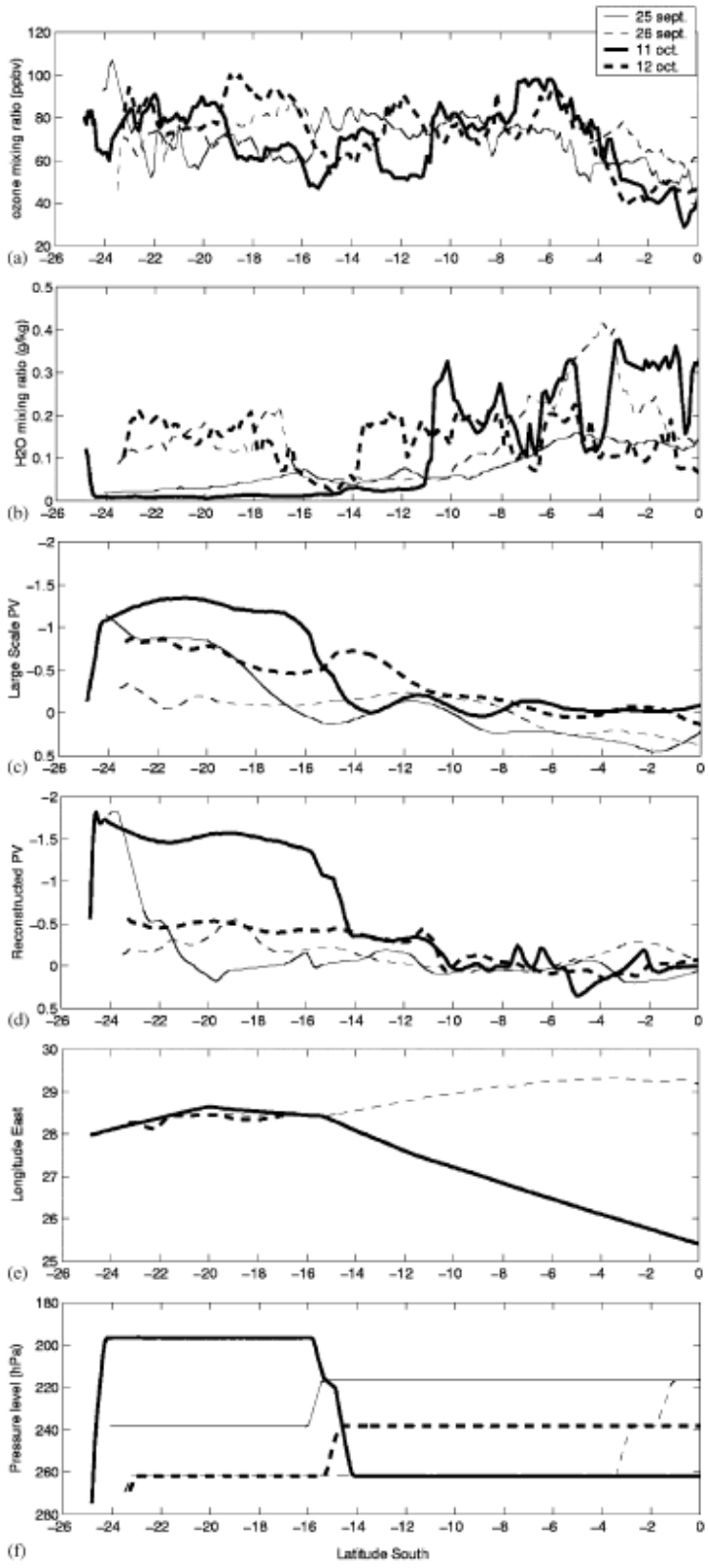
25 sept.
26 sept.
11 oct.
12 oct.
ozone mixing ratio (ppbv)
H2O mixing ratio (g/kg)
Large Scale PV
Reconstructed PV
Longitude East
Pressure level (hPa)
Latitude South
(a)
(b)
(c)
(d)
(e)
(f)

lose PV because of diabatic effects. In short, we then can directly interpret the ozone enhancements on the MOZAIC flights as a net result of the stratosphere–troposphere exchange around the COL in the tropical free troposphere, the dynamical character of the stratospheric origin of the COL, as evidenced by PV, having almost totally disappeared.

October is the beginning of the biomass burning period in South Africa. During this period, an ozone enhancement due to biomass burning influences cannot, a priori, be excluded. Moreover, lightning can produce NO_x and, then, through photochemistry, induce ozone generation (Pickering et al., 1993). This influence can also not be excluded, since convective activity is noted close to the ozone peak. However, in our case, it is noted in the MOZAIC data that the ozone-rich air mass, (between 6°S and 8°S on 11 October) is also very dry, with a very low water vapor mixing ratio at 7°S, and surrounded by relatively higher values. This is consistent with clouds observed by satellite (Fig. 4), with the stratospheric origin of the air mass near 7°S on the trajectory of the aircraft, and with the convective redistribution of 7–8 October. The interpolation of PV along the MOZAIC flight indicates a small maximum in large scale PV at 7°S, and a clearer signature (2 maxima at 6°S and 8°S) in reconstructed PV. These signatures are weak in amplitude (it has been shown previously that the COL is not at its maximum and that its dissipation started on 7–8 October, and that the MOZAIC flight did not pass through the center, but around and over the COL), but these stratospheric signs are persistent over longer time periods than those considered in the statistical study of Price and Vaughan (1992).

4. Conclusion

In this study, we have investigated a tropical COL occurring in October 1996 over South Africa, and have studied its impact on tropospheric ozone. This tropical COL differs in structure from the polar and mid-latitude COLs reported in previous studies. In the case presented in this study, there is a complete detachment of the mass of air from its external surroundings, in both the horizontal and vertical planes, and it has a lifetime of about 2 weeks. This is not always true of mid-latitude and polar COLs, where the detachment is sometimes only in the horizontal, and in the vertical the COL consists of an upper level depression where the tropopause is lower than its usual level, but without a clear vertical detachment. There have been a few studies of Northern Hemisphere COLs that show a similar behavior, but in such cases the lifetimes are smaller (less than 5 days for the studies of Ebel et al., 1991; Appenzeller et al., 1996; Langford et al., 1996, and less than 8 days for the studies of Ravetta and Ancellet, 2000 and Gouget et al., 2000). If this kind of structure is not unique to our case study, but is more generally reproduced for other cases of tropical COL, then this characteristic could imply that the mass of air contained in the tropical COL has a potentially more significant impact on tropospheric ozone than other COLs, due to a reduced tendency to return to the stratosphere. Moreover, the lifetime (about 2 weeks) and the size of this event (more than 15°) are very significant, and several dynamical elements of the study suggest that the stratospheric air introduced into the troposphere did not return to the stratosphere during the event. Previous studies have suggested that the impact of subtropical COLs on tropospheric ozone is minor. Our study suggests that this impact could be larger than previously thought.

Acknowledgements

The authors acknowledge the MOZAIC project that is funded by the European Communities, CNRS, Forschungszentrum Jülich, University of Cambridge, and Météo-France and supported by EADS Airbus and the Airlines: Air France, Deutsche Lufthansa, Sabena, and Austrian Airlines who carry free of charge the MOZAIC instruments. Alain Marenco is particularly acknowledged for the major role he played in the creation and development of the MOZAIC project. We thank ECMWF for providing the meteorological analysis, GRTR (University of Strasbourg, France) and Eumetsat for providing the Meteosat data, and NASA for providing TOMS data. The radiosoundings of Reunion Island are funded by the French institute CNRS/IPSL, under the local assistance of Françoise Posny and Jean-Marc Metzger. Jean-Luc Baray gratefully acknowledges Gérard Ancellet, Gérard Mégie, Yves Pointin and Tantely Randriambelo for helpful discussions.

Fig. 6. MOZAIC flights Vienna–Johannesburg and Johannesburg–Vienna on 25 and 26 September 1996, and on 11 and 12 October 1996. Plots of ozone (a) and water vapor mixing ratios (b) as a function of latitude; Calculations of large scale (c) and reconstructed PV (d) interpolated along the flights; Position of the aircraft (longitude (e) and pressure level (f) as a function of latitude). The reconstructed PV data have been calculated by interpolation of meteorological ECMWF data along the aircraft trajectory using the reverse domain filling technique (the MOZAIC III report is available on the MOZAIC web site http://www.aero.obs-mip.fr/mozaic/).

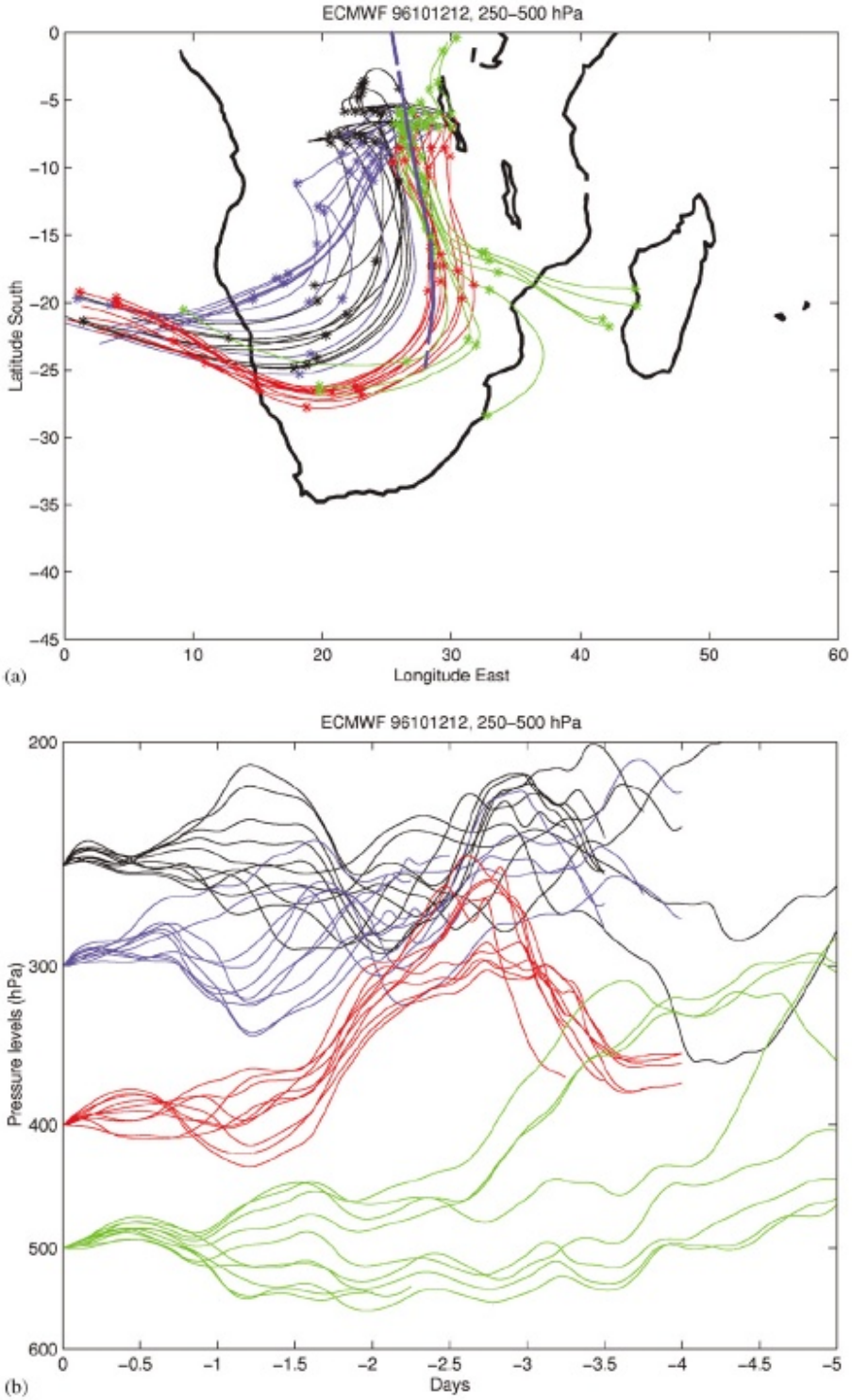

Fig. 7. (a) Cluster backtrajectories (10 ending points between 6–7°S and 26–30°E with a 1° interval between each point) ending on 12 October 1996, 12 GMT for different levels (black: 250 hPa, the approximative level of the MOZAIC flight, blue: 300 hPa, red: 400 hPa, the level of the COL as seen by the ECMWF analysis and green, 500 hPa). Each star corresponds to one day backward movement. (b) Altitude corresponding to these transports.

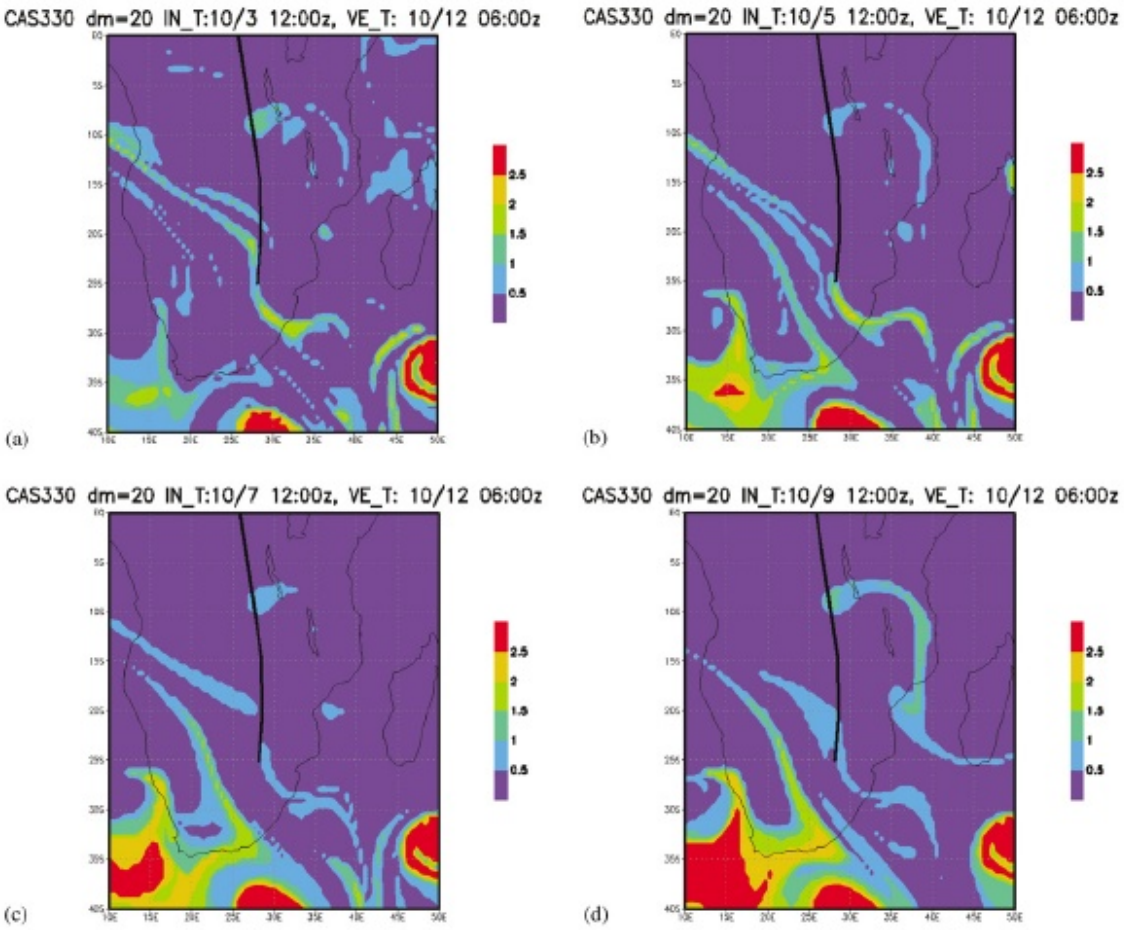

Fig. 8. PV on the 330 K isentropic surface from a contour advection simulation initialized on 3 (a), 5 (b) 7 (c) and 9 October (d) 1996 at 12 GMT, and ending on 12 October, 06 GMT, coinciding with the first MOZAIC flight.

References

Ancellet, G., Beekmann, M., Papayannis, A., 1994. Impact of a cutoff low's development on downward transport of ozone in the free troposphere. Journal of Geophysical Research 99, 3451–3468.

Appenzeller, C., Davies, H.C., Norton, W.A., 1996. Fragmentation of stratospheric intrusions. Journal of Geophysical Research 101, 1435–1456.

Barsby, J., Diab, R.D., 1995. Total ozone and synoptic weather relationships over southern Africa and surrounding oceans. Journal of Geophysical Research 100, 3023–3032.

Dritschel, D.G., 1989. Contour dynamics and contour surgery: numerical algorithms for extended, high-resolution modelling of vortex dynamics in two-dimensional, inviscid, incompressible flows. Computer Physics Reports 10, 77–146.

Ebel, A., Hass, H., Jakobs, H.J., Laube, M., Memmesheimer, M., Oberreuter, A., 1991. Simulation of ozone intrusion caused by a tropopause fold and COL. Atmospheric Environment 25A, 2131–2144.

Folkins, I., Appenzeller, C., 1996. Ozone and potential vorticity at the subtropical tropopause break. Journal of Geophysical Research 101, 18787–18792.

Gouget, H., Cammas, J.P., Marenco, A., Rosset, R., Jonquières, I., 1996. Ozone peaks associated with a subtropical tropopause fold and with the trade wind inversion: a case study from the airborne campaign TROPOZ II over the Caribbean in winter. Journal of Geophysical Research 101, 25979–25993.

Gouget, H., Vaughan, G., Marenco, A., Smit, H.G.J., 2000. Decay of a cut-off low and contribution to stratosphere–troposphere exchange. Quarterly Journal of the Royal Meteorological Society 126, 1117–1141.

Griffiths, M., Reeder, M.J., Low, D.J., Vincent, R.A., 1998. Observations of a cut-off low over southern Australia. Quarterly Journal of the Royal Meteorological Society 124, 1109–1132.

Kentarchos, A.S., Davies, T.D., Zerefos, C.S.A., 1998. Low latitude stratospheric intrusion associated with a cut-off low. Geophysical Research Letters 25, 67–70.

Kentarchos, A.S., Roelofs, G.J., Lelieveld, J., 1999. Model study of a stratospheric intrusion event at lower midlatitude associated with the development of a cut-off low. Journal of Geophysical Research 104, 1717–1727.

Kowol-Santen, J., Ancellet, G., 2000. Mesoscale analysis of transport across the subtropical tropopause. Geophysical Research Letters 27, 3345–3348.

Langford, A., Masters, C., Proffitt, M., Hsie, E., Tuck, A., 1996. Ozone measurements in a tropopause fold associated with a cut-off low system. Geophysical Research Letters 23, 2501–2504 (and correction in, Geophysical Research Letters 24, 109–110).

Machado, L.T.A., Desbois, M., Duvel, J.-PH., 1992. Structural characteristics of deep convective systems over tropical Africa and Atlantic Ocean. Monthly Weather Review 120, 392–406.

Marenco, A., Thouret, V., Nédélec, P., Smit, H.G., Helten, M., Kley, D., Karcher, F., Simon, P., Law, K., Pyle, J., Poshmann, G., Von Wrede, R., Hume, C., Cook, T., 1998. Measurement of ozone and water vapor by Airbus In service aircraft: the MOZAIC airborne programme, an overview. Journal of Geophysical Research 103, 25631–25642.

Pickering, K.E., Thompson, A.M., Tao, W.K., Kucsera, T.L., 1993. Upper tropospheric ozone production following mesoscale convection during STEP/EMEX. Journal of Geophysical Research 98, 8737–8749.

Postel, G.A., Hitchman, M.H., 1999. A climatology of Rossby wave breaking along the subtropical tropopause. Journal of the Atmospheric Sciences 56, 359–373.

Price, J.D., Vaughan, G., 1992. Statistical studies of cut-off-low systems. Annales Geophysicae 10, 96–102.

Randriambelo, T., Baray, J.L., Baldy, S., 2000. The effect of biomass burning, convective venting and transport on tropospheric ozone over the indian ocean: Reunion Island field observations. Journal of Geophysical Research 105, 11813–11832.

Ravetta, F., Ancellet, G., 2000. Identification of dynamical processes at the tropopause during the decay of a cut-off low using high resolution airborne lidar ozone measurements. Monthly Weather Review 128, 3252–3267.

Scott, R.K., Cammas, J.P., 2002. Wave breaking and mixing at the subtropical tropopause. Journal of the Atmospheric Sciences 59, 2347–2361.

Scott, R.K., Cammas, J.P., Mascart, P., Stolle, C., 2001. Stratospheric filamentation into the upper tropical troposphere. Journal of Geophysical Research 106, 11835–11848.

Shapiro, M.A., 1980. Turbulent mixing within tropopause folds as a mechanism for the exchange of chemical constituents between the stratosphere and the troposphere. Journal of the Atmospheric Sciences 37, 994–1004.

2.2.2 Echanges stratosphère-troposphère et convection tropicale : Modélisation à méso-échelle du cyclone Marlène

ELSEVIER

Available online at www.sciencedirect.com
ScienceDirect

Atmospheric Environment 41 (2007) 6510–6526

ATMOSPHERIC ENVIRONMENT

www.elsevier.com/locate/atmosenv

Simulations of stratospheric to tropospheric transport during the tropical cyclone Marlene event

J. Leclair De Bellevue[a,*], J.L. Baray[a], S. Baldy[a], G. Ancellet[b], R. Diab[c], F. Ravetta[b]

[a]*Laboratoire de l'Atmosphère et des Cyclones (LACy), CNRS-UMR 8105, Université de La Réunion, 15 Av. René Cassin, BP 7151, 97715 Saint-Denis Messag Cedex 9, La Réunion, France*
[b]*Service d'Aéronomie (SA), CNRS-UMR 7620, Boite 102, Université Pierre et Marie Curie, 4 Place Jussieu, 75252 Paris Cedex 05, France*
[c]*School of Environmental Sciences, University of KwaZulu-Natal, Room 365, Memorial Tower Building, Howard College Campus, Durban 4041, South Africa*

Received 20 June 2006; received in revised form 15 April 2007; accepted 16 April 2007

Abstract

Enhanced ozone values observed in the upper troposphere near intense tropical cyclones have raised the question of the role of stratospheric–tropospheric exchange. The dynamical mechanisms involved in the enhanced ozone values of 6 April 1995 observed at Reunion and associated with the tropical cyclone Marlene could not be explained by ECMWF meteorological analysis with 1.125° horizontal resolution. A previous study based on the ECHAM model has demonstrated the impact of biomass burning, but of limited amplitude (<60–80 ppbv max). In this paper, the upper tropospheric ozone enhancement on the periphery of Marlene has been studied with a mesoscale model (MESO-NH). This model is able to reproduce a stratospheric PV filament into the troposphere, crossing the isentropes to the 350 K level. The ageostrophic circulation associated with divergence zones that have induced vertical movements has been shown. Further, the influence of vertical wind shear, evident in both the mesoscale analysis and in the idealized HURRICANE tropical cyclone model, also contributes to our understanding of this downward transport process.

Keywords: Stratospheric–tropopsheric exchange; Tropospheric ozone; Tropical cyclone; Mesoscale modelling

1. Introduction

Dynamical exchange of air masses from the stratosphere to the troposphere is known to be a source of tropospheric ozone. Several dynamical mechanisms able to induce this kind of exchange in (sub) tropical regions have been recently identified: tropopause folds near the subtropical jet stream following dynamical mechanisms similar to polar jet stream-induced tropopause folds (Gouget et al., 1996; Folkins and Appenzeller, 1996; Baray et al., 1998), filamentation (Scott et al., 2001), Rossby wave breaking (Postel and Hitchman, 1999), and subtropical cut-off lows (Baray et al., 2003; Kentarchos et al., 1999).

A case study of record high contamination of tropospheric ozone has been recently reported (Baray et al., 1999). These authors put forward the hypothesis that the subsidence around intense

*Corresponding author. Fax: +262 262 93 82 54.
E-mail address: j.ldb@univ-reunion.fr (J. Leclair De Bellevue).

1352-2310/$ - see front matter © 2007 Elsevier Ltd. All rights reserved.
doi:10.1016/j.atmosenv.2007.04.040

tropical cyclones (TC) could induce stratospheric–tropospheric exchange (STE).

In the case study of TC Marlene, since potential vorticity (PV) signatures in the ECMWF analysis were not clear (Baray et al., 1999), the objective of this paper is to present a mesoscale simulation, in order to confirm the stratospheric origin of the tropospheric ozone enhancement, and to detail the dynamical mechanism. Further, the use of the two-dimensional model HURRICANE for idealized TC modeling will provide additional dynamical insights. The effect of vertical wind shear, in particular, on STE will be discussed.

A summary of previous findings relating to tropical cyclone Marlene is given, followed by a description of the MESO-NH model and of the associated simulation results. Finally, description of the HURRICANE model and simulations through it will presented and discussed.

2. Synthesis of earlier studies of tropical cyclone Marlene

This section summarizes previously published results on the TC Marlene event.

The track of TC Marlene is depicted in Fig. 1. Tropical depression Marlene formed on 30 March 1995, at about 2000 km north-east of Reunion. On 1 April, it became a TC, the strongest of the 1994–1995 cyclonic season in the Indian Ocean (Lander and Angove, 1998). Between 3 and 4 April, TC Marlene reached maximum intensity, with gusts of 82 $m\,s^{-1}$ and sustained winds of 67 $m\,s^{-1}$. On 6 April, it was located closest to Reunion, at about 1000 km east. Then, TC Marlene moved away in an east-southeasterly direction, weakening at he same time.

Ozone profile measurements have been done over the south-western part of the Indian Ocean during the period of early April 1995 included airborne MOZAIC data at Johannesburg, and ozone soundings performed at Reunion (20.8°S; 55.5°E) and Irene (25.9°S; 28.2°E) (Baray et al., 1999) and from the Malcolm/Baldridge ship within the framework of the pre-Indian Ocean Experiment (pre-INDOEX) campaign (De Laat et al., 1999). The measurement locations are shown in Fig. 1.

The ozonesonde launched from Reunion on 6 April 1995 (Fig. 2a) showed record high ozone values in the entire free troposphere, higher than 100 ppbv between 800 and 100 hPa. These values are largely above those of the mean April profile for the period 1998–2006. In addition to the very high mean values of this ozone profile, two peaks are apparent, one in excess of 300 ppbv at 10.5 km (260 hPa), and a secondary peak of lower intensity (200 ppbv) at 9 km (350 hPa). The humidity profile is characterized by high values in the low layers

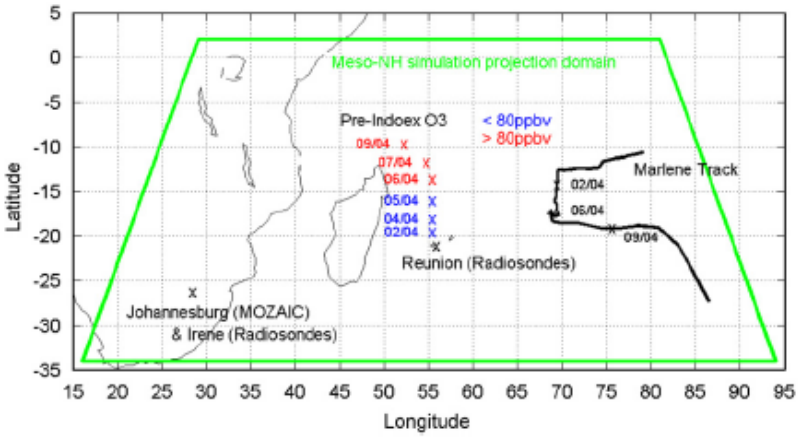

Fig. 1. Location of the in-situ measurements used in the 6 April 1995 case study. The horizontal projection of the domain used in the MESO-NH simulation is visible (green). In red and blue are the dates and locations of the sondes launched from the R.V. *Malcolm Baldridge* ship during Pre-Indoex. The ozone values indicated are mid-tropospheric and are from the profiles visible on Fig. 7 in De Laat et al. (1999). Track of the tropical cyclone Marlene and locations of the Irene radiosonde launch and MOZAIC measurements above Johannesburg are also depicted.

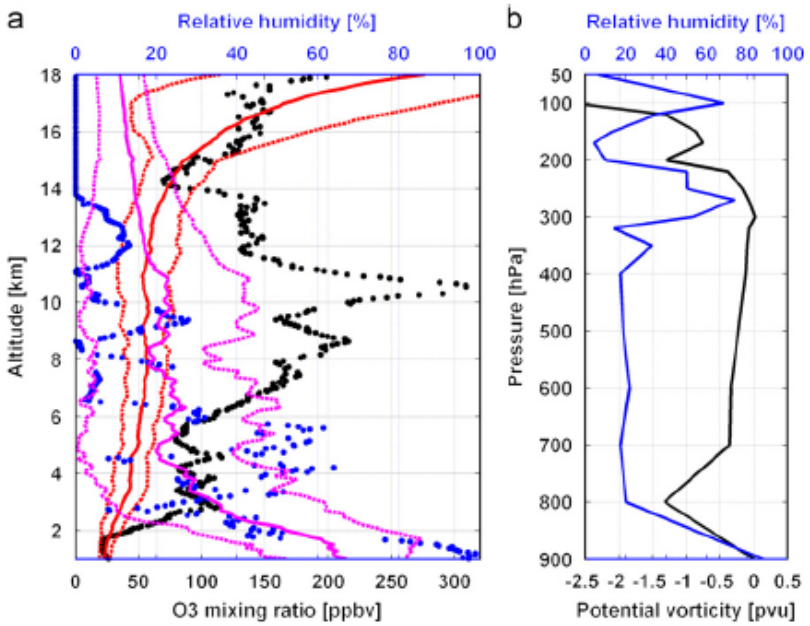

Fig. 2. (a) Vertical profiles of ozone mixing ratio (black) and relative humidity (blue) obtained by radiosounding over Reunion on 6 April 1995 at 06 UT, superimposed with a climatological profile of ozone (red line) and relative humidity (magenta) for April (based on 25 profiles from 1998 to 2006). The standard deviation associated to the average profiles are in dashed lines. (b) Vertical profiles of relative humidity and PV modeled by MESO-NH over Reunion on 6 April at 00UT.

(60% below 6 km), yet the two ozone peaks are strongly anticorrelated with humidity (see Fig. 4 in Baray et al. (1999) for more details about anticorrelation calculations; the difference between the 6 April profile and the climatological background profile from MOZAIC data and from Irene and Reunion radiosondes corresponding to the March–May period is plotted). At these two altitudes, humidity values are also largely below the climatological profile. Baray et al., (1999) hypothesized that a TC could induce STE in its peripheral zone. ECMWF analysis enabled them to detect zones of instability and subsidence above Reunion, but explicit determination based on PV fields was not clear in the global model.

De Laat et al. (1999) have presented a large dataset obtained in the Indian Ocean during pre-INDOEX. Ozonesondes released as part of this campaign (see Fig. 7 in De Laat et al., 1999), close in time and space to the cyclone, also showed ozone enhancements relative to climatological values, with a structure similar to that observed above Reunion. However, ozone values were significantly lower than those of Reunion, with less than 80 ppbv around 400 hPa on 2, 4 and 5 April (in blue on Fig. 1), and between 80 and 100 ppbv in the 400–200 hPa pressure range on 6, 7 and 9 April (in red on Fig. 1). The dynamical role of upward motions in TC Marlene and of the tropopause fold of a subtropical jet were analyzed using ECHAM, a chemistry–climate model developed at the Max Planck Institute for Meteorology in Hamburg and based on the ECMWF data. The authors inferred that the enrichment of ozone observed in the upper troposphere during this campaign came mostly from the transport of polluted African air.

The differences between the two hypotheses provoked a debate in the literature. De Laat and Lelieveld (2001) argued that a chemical origin of the ozone enhancement was most likely based on simulated high CO values (e.g. sonde 10 of de Laat and Lelieveld, 2001). The relatively good agreement between modeled and observed ozone, demonstrates unambiguously the impact of biomass burning, but it is shown to be of limited amplitude (<60–80 ppbv max). In response, Baray et al. (2001) noted that MOZAIC data recorded on the Johannesburg to Vienna flight during this period (31 March, and on 5 and 12 April 1995) indicated very low ozone values above South Africa (see Fig. 1 in Baray et al., 2001).

Moreover, the month of April falls outside the biomass burning season in Africa, as evidenced in NOAA AVHRR satellite images, and there are also ozone layers not captured by the ECHAM model (particularly sonde 9 of de Laat and Lelieveld, 2001 on the day of Reunion sonde), attributed by the authors to a deficiency in the model that prevented it from capturing mesoscale dynamical phenomena. But since there is no indication of CO enhancement (or even the opposite), the biomass origin is difficult to support.

Following on from these studies and debate, it appears that the tropospheric ozone enhancement observed in this case study is still an open question and deserving of further investigation.

3. Mesoscale simulation

3.1. Description of MESO-NH

The MESO-NH model (Lafore et al., 1998) is used in the present study. This three-dimensional and non-hydrostatic mesoscale numerical model is the result of a joint effort by Centre National de recherches Météorologiques (CNRM, Meteo-France) and Laboratoire d'Aérologie (Centre National de la Recherche Scientifique). It is based on the Lipps and Hemler (1982) modified anelastic system to avoid problems due to the fast propagation of acoustic waves and to allow a correct representation of the gravity wave momentum flux in the upper atmosphere. The basic atmospheric variables are temperature, pressure, and density of dry and moist air. The prognostic variables are the three Cartesian components of velocity, dry potential temperature and the different water mixing ratios. The MESO-NH system of equations includes (i) the anelastic approximation for air mass conservation, (ii) the conservation of momentum for dry air, including the Coriolis force due to the Earth's rotation and subgrid-scale turbulent diffusion, (iii) the thermodynamic equation including diabatic effects (latent heat release, radiation, diffusion), (iv) the conservation of water quantities.

For the present study, the horizontal mesh consists of 150×100 grid points with a uniform grid spacing of 45 km and is centered at 20.8°S and 55.5°E. This large domain has been chosen to cover the in situ measurement sites, the cyclone track and the location of the subtropical jet. In our simulation, the vertical Gal-Chen and Sommerville (1975) coordinate grid spacing varies continuously with altitude, from 150 m close to the surface to 500 m at an altitude of 30 km. The turbulence scheme of Bougeault and Lacarrère (1989) has been used with a mixing length, that takes into account possible anisotropies of the grid. Air-sea fluxes of sensible and latent heat are calculated through aerodynamic formulae with wind-dependent exchange coefficients (Dupuis et al., 1997). The radiation scheme calculates the radiative fluxes, considering absorption-emission of long-wave radiation and reflection, scattering and absorption of solar radiation by the Earth's atmosphere and surfaces (Morcrette, 1989). Convective parameterization is based on the Kain and Fritsch (1993) scheme, with closure based on static stability, parameterization of moist downdrafts, detrainment of hydrometeors and realistic computation of entrainment through a buoyancy mechanism.

The MESO-NH model (MASDEV4_4, bugfix2) was initialized with large-scale fields provided by ECMWF analysis for the boundary conditions. In this version of MESO-NH, the "Wave-radiation open boundary" variant of open boundary conditions is used, described in Xue and Thorpe (1991) and Klemp and Wilhelmson (1978). In order to simulate the mesoscale dynamical processes before the radiosounding and to examine their temporal evolution, the simulation started at 12 UT on 4 April 1995 and continued for 54 h.

3.2. Results of simulations and comparison to ECMWF analysis

On 6 April 1995, TC Marlene had already started to weaken. Its central pressure is estimated at 975 hPa and its intensity about 3.5 on Dvorak scale. The wind profile above Reunion simulated by the MESO-NH model showed moderate southeasterly winds (5–10 m s^{-1}) in the lower levels, and a higher intensity westerly component (10–20 m s^{-1}) in the upper levels. This is consistent with in situ observed winds (Fig. 3). The simulated profile is consistent with the presence of a TC east of Reunion. The cyclonic circulation reinforces the southeasterly trade winds in the lower levels. The trade wind inversion usually observed at the 4–5 km altitude is replaced by a regular rotation of the wind resulting in a westerly wind, reinforced by the divergent circulation aloft. The primary circulation in TC's is an axisymmetric, cyclonic flow in the horizontal. Superimposed on the primary circulation are weaker asymmetric horizontal motions and a secondary

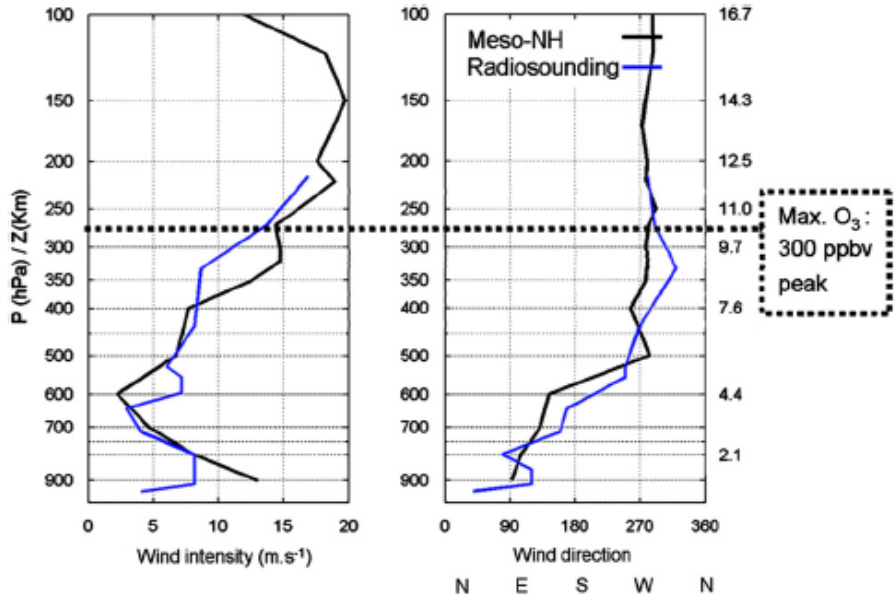

Fig. 3. Wind profiles (intensity and direction) above Reunion at 06 UT on 6 April 1995 from a Meteo—France radiosounding, and a simulated profile from the MESO-NH model. The level of the tropospheric ozone maximum observed at this time is indicated.

circulation in a radius-height plane (Willoughby, 1988). In its simplest form, the secondary circulation consists of lower-tropospheric air that flows inward and converges toward the convectively active parts of the eyewall and rain bands, mid-tropospheric air that rises in the deep convection, and upper-tropospheric air that diverges outward or converges inward and subsides in the eye. The cyclonic and anticyclonic circulations and also the dynamic context surrounding Marlene, including the jet stream described hereafter are depicted in Fig. 4. The MESO-NH wind pattern on the 200 hPa isobaric level on 6 April 1995 (Fig. 4b) shows a local maximum intensity ($>40\,m\,s^{-1}$) between grid points (60; 40) and (120; 30). This jet streak, located south of Reunion, could induce secondary downward motion. However, Reunion is located near the entrance zone of the jet streak and, on the anticyclonic side, hence the probability of a tropopause fold is theoretically weak, and exchanges on this side occur mainly by turbulent flux (Bertin et al., 1995). Moreover, this jet streak is rectilinear, so there is no curvature to amplify an eventual tropopause fold. The TC center is located at grid point (102; 60), i.e. 1250 km north–east of Reunion. Horizontal winds associated with the cyclonic circulation at 700 hPa reach about $20\,m\,s^{-1}$ (Fig. 4a). Simulated winds of $20\,m\,s^{-1}$ correspond approximately with observed winds of $30\,m\,s^{-1}$ winds noted by Baray et al. (1999).

The anticyclonic circulation at 200 hPa centered at grid point (102; 58), is shifted approximately 90 km south from the TC center. Because of this horizontal shift in the vertical plane and the anticyclonic circulation assymetry, as the TC's low and mid-tropospheric cyclonic circulations develop, the storm becomes more inertially stable, and less permeable to environmental forcing at these levels. However, at the outflow level, we may suppose that the anticyclonic asymmetry is more inertially unstable and more responsive to upper-level environmental forcing (Holland and Merrill, 1984).

Reunion (grid points 78; 47) is under the influence of the north-western component of this anticyclonic circulation. Moreover, this anticyclonic flow enters an area where there is shear in the mean flow due to the jet streak. This structure is the result of the interaction (horizontal shear) between the divergent circulation of the cyclone and the mean westerly flow and also the subtropical jet-stream more to the south. Thus, the jet stream may play a role in secondary circulation by inducing such horizontal wind shear.

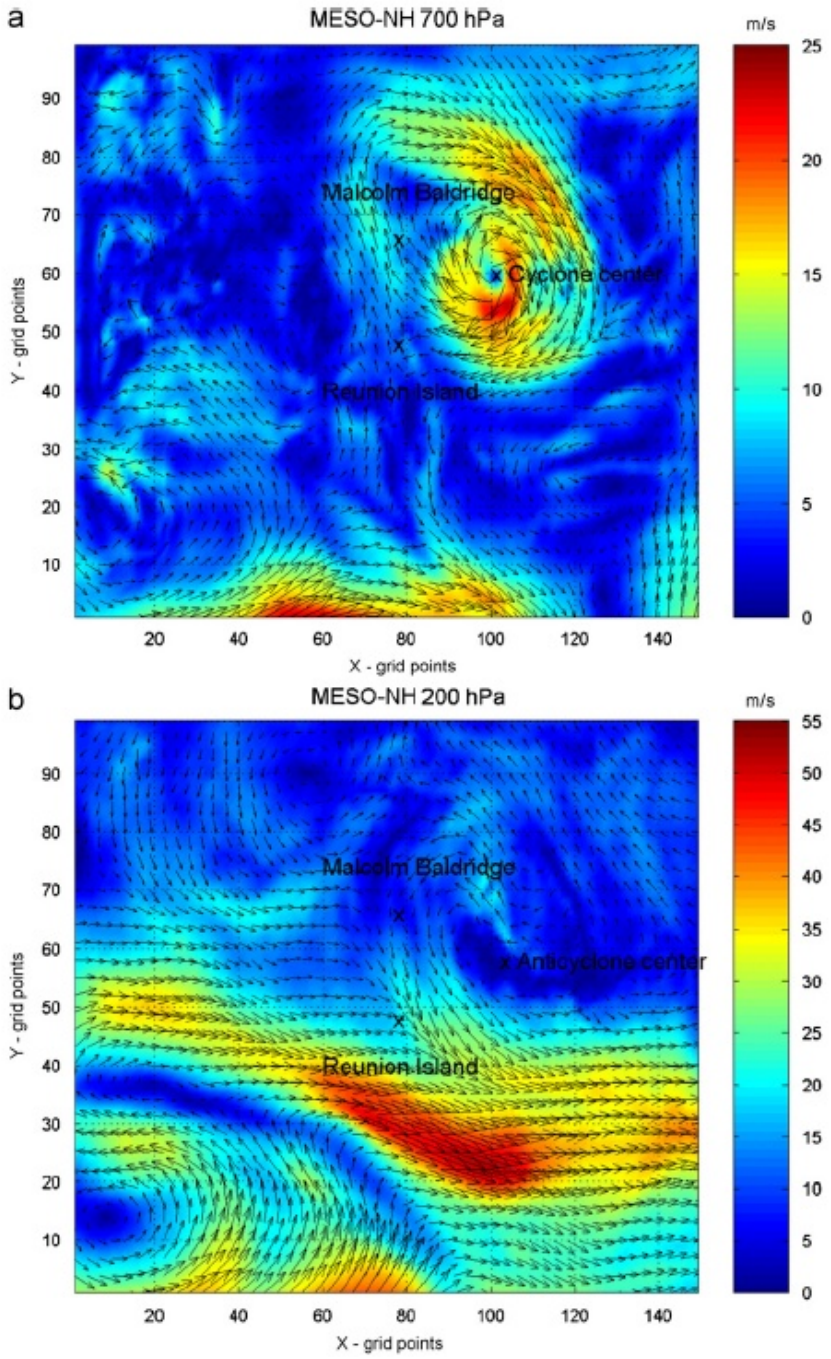

Fig. 4. MESO-NH horizontal wind patterns on the (a) 700 hPa and (b) 200 hPa isobaric surfaces at 06 UT 6 April 1995. The color scale represent the horizontal wind intensity ($m s^{-1}$).

Potential vorticity (PV), used as a dynamical tracer, which is a criterion of stability, is conserved in the atmosphere in the absence of vertical gradients of diabatic heating and frictional forces (Hoskins et al., 1985). In TC's, the generation of PV due to latent heating may become important and the

PV may not be conserved. However, at the 200 hPa outflow level where the latent heating is negligible, the PV may still be a good indicator of general rising and sinking motions, especially outside of the inner convective region. Indeed, studying the interaction between a synoptic scale trough and a mesoscale TC, Molinari et al. (1995) argued that a rather complex mix of shear and diabatic heating influences can make the control of this scale interaction in real numerical simulations complicated. The result is that the interpretation of PV fields is not easy in the lower layers but PV is an appropriate indicator in the outflow layer where latent heating is negligible.

To further illustrate that the secondary circulation is a persistent feature associated with the outflow structure, we now discuss the distribution of PV and relative humidity at the outflow level.

Fig. 5 depicts the PV fields obtained by both MESO-NH and ECMWF analysis. The ECMWF analysis with 1.125° horizontal resolution does not show any particular anomaly in the peripheral part of the cyclone. In contrast, a 1.2 PVU PV filament between the (80; 80) and (100; 40) grid point pairs is clearly visible on the 200 hPa isobaric surface of the MESO-NH simulation. The dynamical tropopause is usually characterized by PV values ranging between 1 and 2 PVU at tropical latitudes, according to a number of authors. This 1.2 PVU PV filament at 200 hPa would correspond therefore to an air mass that is characteristic of the tropopause region. We can also observe a strong PV filament (2 PVU) south of the jet streak depicting subtropical stratospheric air masses.

The relative humidity fields visible in Fig. 6 highlight the contribution of the mesoscale simulation compared to the 1.125° horizontal resolution ECMWF analysis. In the latter, due to the weaker resolution, the TC is more coarsely represented. Nevertheless, one finds the finger print of the PV filament which is associated with low relative humidity values, between grid points pairs (80; 80) and (100; 40) (Fig. 6a). This spatial agreement between the PV filament on the western periphery of the cyclone and the low values of relative humidity is clearer on the MESO-NH simulated fields. Strong values of humidity (100%) are visible in Fig. 6a and confirm the deep convection areas of the cyclone. There is no significant condensation at the outflow level, and so, the relative humidity field at the 200 hPa level is mainly a manifestation of the transport process, reflecting several important features. This is also valid for low relative humidity values associated with the PV filament surrounding the cyclone. Fig. 2b depicts the relative humidity and PV modeled profiles above Reunion and shows the consistency between the −1.2 PVU and the 10% relative humidity peaks at 200 hPa.

Based on Figs. 5a and 6a, a good agreement between humidity and PV fields simulated by MESO-NH is observed. The two strong PV areas (i.e. the filament west of the cyclone and the large zone south of the jet stream) are very dry, with less than 10% relative humidity. Thus, the signatures of PV and humidity correspond well to a dynamical situation of STE.

The location of Reunion is exactly under the PV filament on 6 April 1995 whereas the Malcolm/Baldridge ship in the framework of pre-INDOEX campaign was at 55°E; −14°S (grid point 78; 66), i.e. 800 km north of Reunion. Due to this geographical shift, the signatures of this STE event were stronger on the ozone profile observed above Reunion than that from the ship. Indeed, the ozone values recorded in the ship's profile were much lower because of the position of the ship east of the filament.

Accepting that the PV and humidity anomalies point towards stratosphere to troposphere transport as the origin of the enhanced ozone values, the mesoscale model simulation allows us to study the dynamics at the origin of these signatures. The following part will focus on the transversal ageostrophic circulation and induced vertical movements.

3.3. Discussion about the dynamics at the origin of the signatures

In Fig. 7, a strong ageostrophic component of the wind can be viewed, with intensities reaching 20 m s^{-1}. We considered only a part of the simulation domain which is indicated by a black rectangle in Fig. 5a. The horizontal wind divergence field has been superimposed on the ageostrophic wind field. The positive (negative) values of divergence (convergence) appear in red (blue). Subsidence above altitude divergence zones and below convergence zones is induced by mass conservation. The ageostrophic circulation is radial and directed outward and participates in the evacuation of air masses on the southwestern face of the cyclone. This situation is different from the case of jet-stream curvature, in which the ageostrophic circulation is longitudinal. Indeed, considering a uniform jet-stream

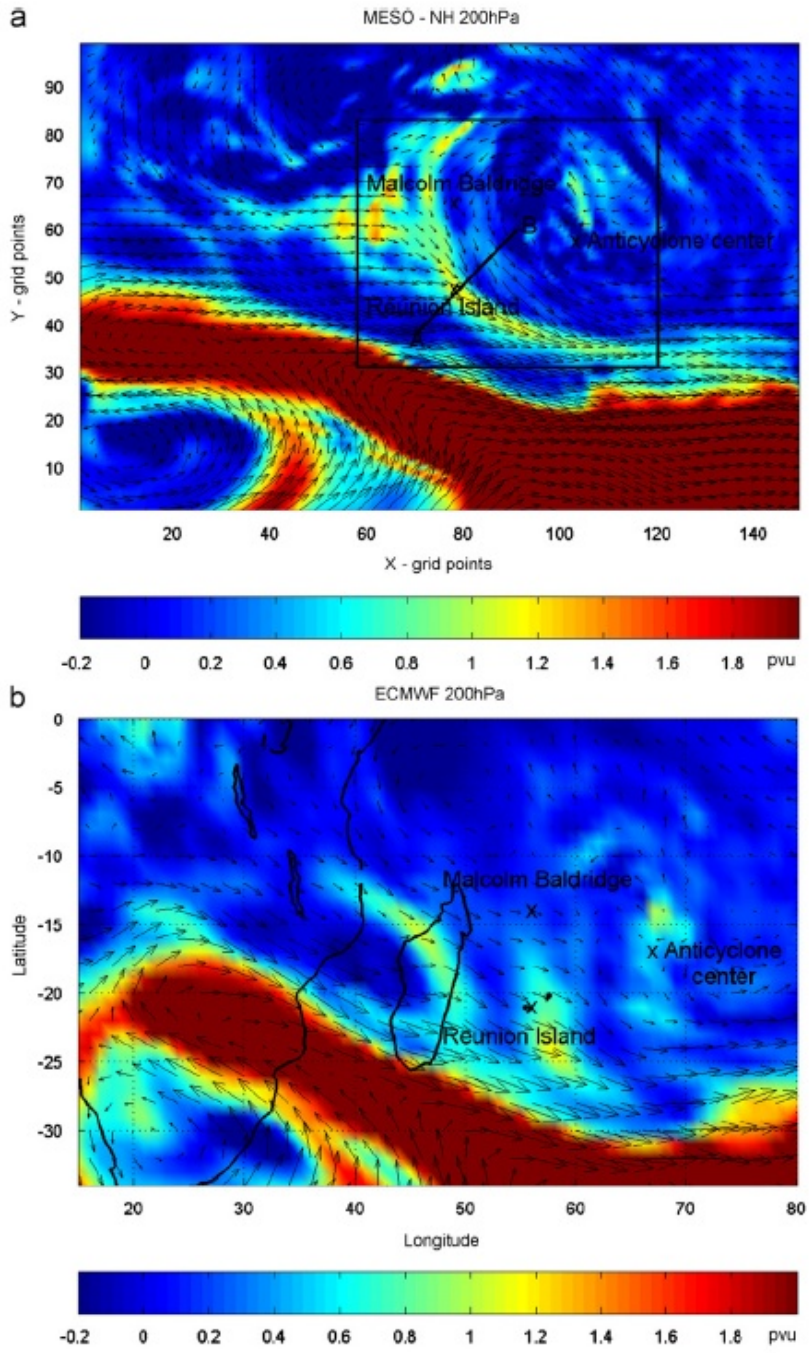

Fig. 5. PV at 00 UT 6 April 1995 on the (a) 200 hPa isobaric surface (MESO-NH). Also shown is the horizontal wind direction. Locations of the R.V. *Malcolm Baldridge* and of the anticyclone center at this time and of Reunion are indicated. The straight line AB across the PV filament marks the location of the cross-section used in Fig. 8 and the black rectangle is the domain of Fig. 7. The color scale represents the PV intensity [PVU]. (b) Equivalent 1.125° horizontal resolution ECWMF PV field.

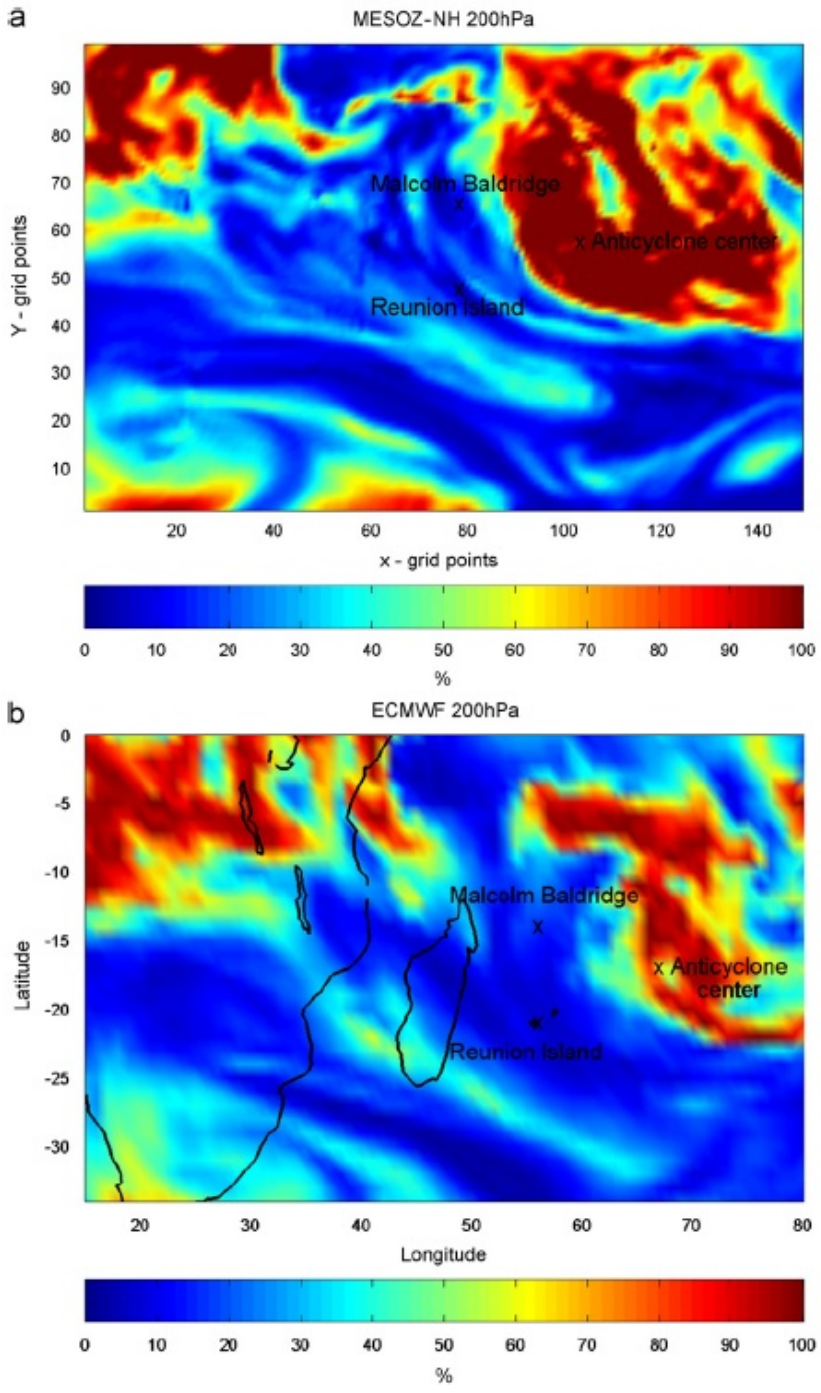

Fig. 6. Relative humidity (%) at 00 UT 6 April 1995 on the (a) 200 hPa isobaric surface (MESO-NH) and (b) 1.125° horizontal resolution equivalent ECWMF relative humidity field. Locations of the R.V. *Malcolm Baldridge* and of the anticyclone center at this time and of Reunion are indicated. The color scale represents the relative humidity values (%).

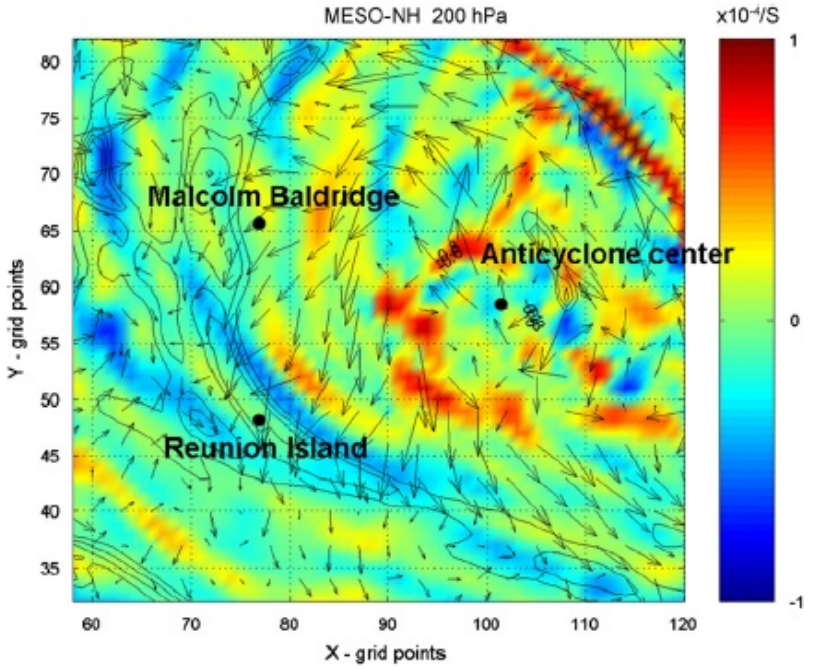

Fig. 7. Horizontal ageostrophic wind vectors on the 200 hPa isobaric surface at 00 UT 6 April 1995. The maximum intensity reached is 20 m s^{-1} and corresponds to the longest vector. Divergence of the horizontal wind has been superimposed and its intensity is represented by The horizontal domain of Fig. 7 is the color scale (s^{-1}). marked by the black rectangle in Fig. 5.

following a curvilinear trajectory, centripetal accelerations, due to the curvature of the jet-stream, induce longitudinal ageostrophic circulations and modifications of the field of divergence at the level of the jet-stream (Shapiro and Kennedy, 1981). In the present study, the ageostrophic component of the wind is transverse to the anticyclonic circulation. A succession of distinct divergence/convergence zones can be observed from the center to the periphery of the cyclone, organized in the shape of rings. The signatures of PV described in the previous section are located on the right side of the ageostrophic wind maximum facing downstream. The interaction between the cyclone dynamics and surrounding flow (westerly mean flow and jet-stream) is non-stationary. It is the prime reason for the localization of the maximum of the ageostrophic component of the wind (confluence effect). The curvature of the anticyclonic circulation is the second reason (curvature effect).

The situation in the vertical plane is described by Fig. 8. The vertical component of the wind is presented in a vertical cross-section transverse to the PV filament. This PV filament comes from the stratosphere and penetrates into the troposphere as far as the 350 K isentropic surface, crossing the isentropes diabatically. White contours represent positive values of the vertical wind component (reaching 10 cm s^{-1}) and thus ascending movements, in the eyewall between grid points 57 and 60. The tropopause forcing due to the strong ascending motion at the top of the eyewall can be seen through the dynamical tropopause deformation at this location. Negative values of the vertical wind component in black contours are visible under the stratospheric PV filament and also between this filament and the positive vertical wind core described above.

The persistence of the PV anomaly in the vicinity of the cyclone above Reunion is presented in Fig. 9a. High simulated PV values compared to those of the background are visible between 100 hPa (tropopause) and 220 hPa between 15 UT on 5 April and 09 UT on 6 April. The vertical wind shear (VWS) has been calculated between 400 and 150 hPa above Reunion over the same period (Fig. 9b).

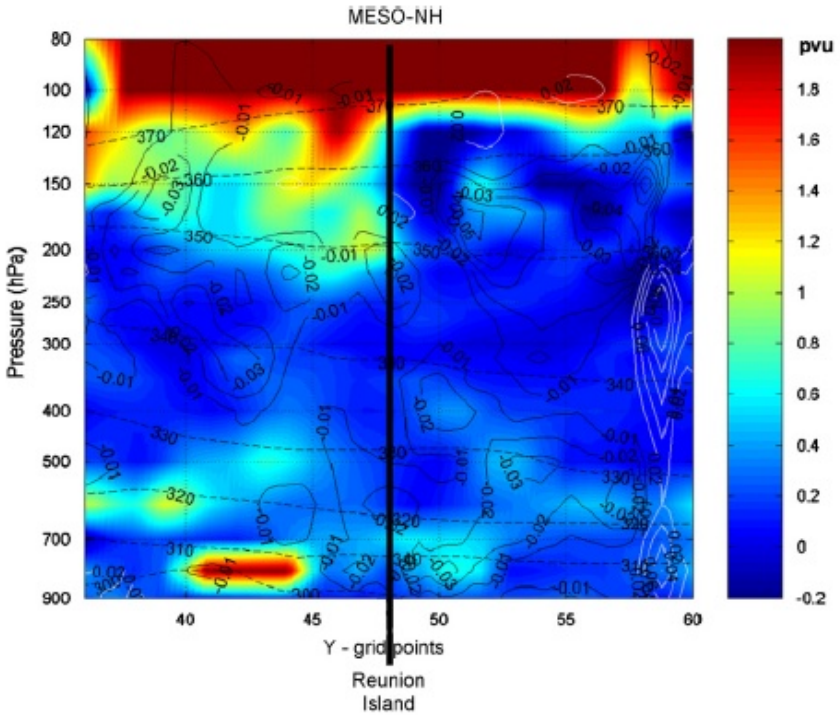

Fig. 8. PV on a vertical cross-section AB marked in Fig. 5 at 00 UT 6 April 1995. Also shown are the vertical wind isotachs (white solid lines for positive values and black for negative in ms^{-1}) and the isentropes (K) (dashed). The color scale represents the PV values [PVU]. The vertical straight line indicates the position of Reunion in this cross-section.

It represents the difference, in terms of intensity and direction, of the MESO-NH horizontal wind between these two levels. From Figs. 9a and b it is noted that the events of high PV correspond to the highest VWS values.

In Section 4, we propose an approach that addresses the influence of VWS intensity on the vertical movements in the eye and in the periphery of an idealized tropical cyclone.

4. Impact of wind shear. HURRICANE model simulations

4.1. The HURRICANE idealized tropical cyclone model

Except for the convective parameterization and a few minor changes, the hurricane model used here is identical to that of Emanuel (1989). Recent work on the interaction of convection with large-scale flow suggests that a closure based on a presumed equilibrium between surface enthalpy fluxes and input of low-entropy air into the subcloud layer by convective downdrafts works well in models of the tropical atmosphere. Such a convective representation is used in the HURRICANE model and further simplifies the model, while in many respects improving its performance. The model is axisymmetric and phrased in angular momentum coordinates, using the potential radius R (Schubert and Hack, 1983). The model consists of two parts: a subcloud layer and the rest of the troposphere. The latter is assumed to be in hydrostatic and gradient wind balance, and to be neutral to slantwise moist convection. The primary dynamic variables of the model are: the radius of R at the sea surface, the radius of R at the tropopause, the mean mass streamfunction in the middle troposphere, the mass streamfunction at the top of the boundary layer, the convective updraft mass flux at the top of the boundary layer and the convective downdraft mass flux at the top of the boundary layer. More details can be found at http://wind.mit.edu/~emanuel/modella/modella.html.

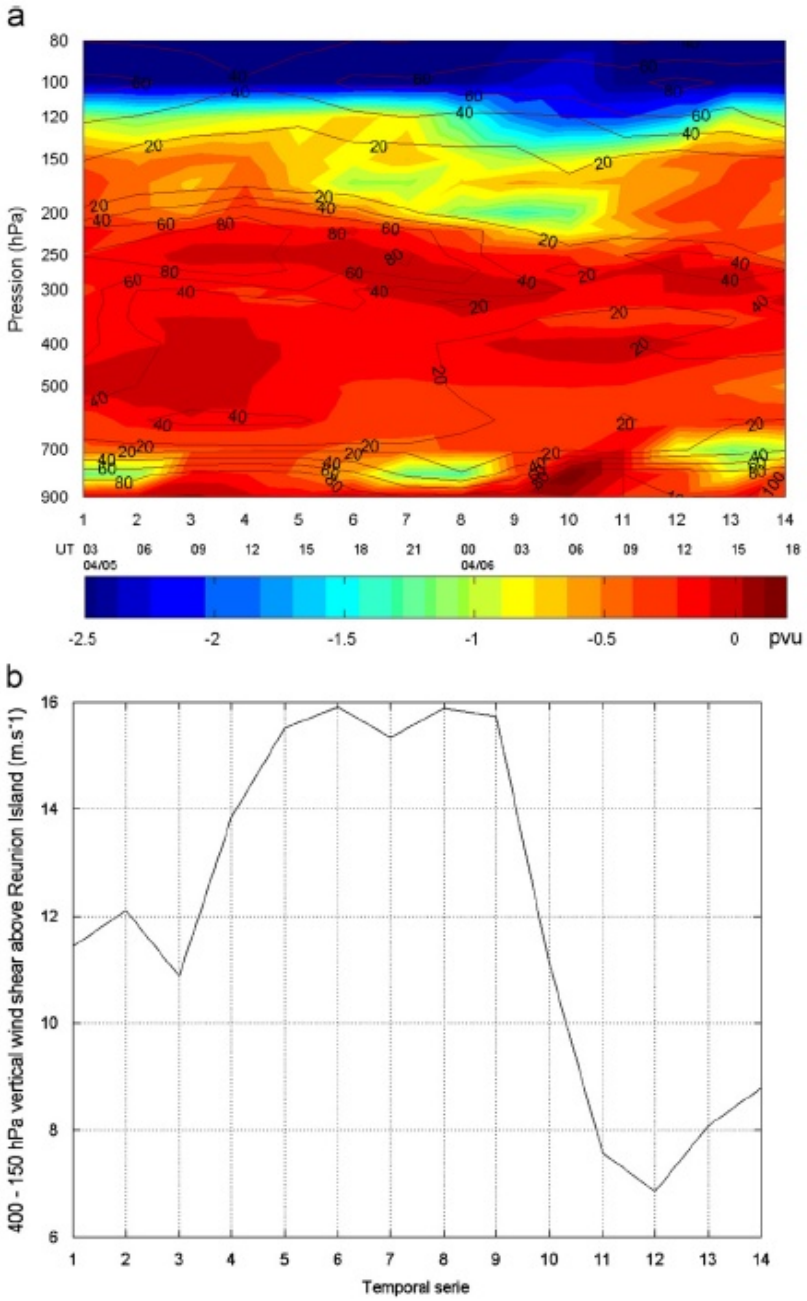

Fig. 9. (a) PV [PVU] represented by the color scale and relative humidity contours (%) over Reunion between 03 UT 5 April and 18 UT 6 April (MESO-NH); (b) vertical wind shear between 400 and 150hPa over Reunion during the same time series (MESO-NH).

The HURRICANE model will be useful in this study to identify the updrafts and downdrafts occurring in the eye and in the outer part of the cyclone. This will allow the simplification of the interaction of the cyclone circulation with the subtropical jet to a single parameter, namely the vertical wind shear.

4.2. Contribution of the HURRICANE model in an idealized tropical cyclone simulation: effects of the vertical wind shear

The HURRICANE model allowed us to consider the interactions between a cyclone and its environment to the presence of a VWS.

Simulations in which a VWS of different magnitude was applied during the evolution of the cyclone were undertaken. The magnitude is calculated as the difference in the wind speed between two surfaces, viz. the top and bottom of the model. From Fig. 10, it is observed that the greater this difference in wind speed surrounding the cyclone, the weaker the surface winds. A VWS was applied on day 13 and its effects were felt on day 15. A $6\,m\,s^{-1}$ VWS intensity causes a decrease in surface wind speed of $20\,m\,s^{-1}$ compared to a simulation where flow surrounding the cyclone is uniform, i.e. without VWS (VWS $= 0\,m\,s^{-1}$). A stronger VWS ($15\,m\,s^{-1}$) tends to decrease the value of the maximum surface wind speed back to its cyclogenesis value.

Fig. 11 presents the vertical component of the wind in an r–z cross-section of a mature cyclone under the influence of VWS of different intensities. In Fig. 11a, where there is no VWS, we have a structure with three major characteristics: strong ascent in the convective tower with positive vertical wind speeds up to $0.5\,m\,s^{-1}$; weak subsidence in the eye; and significant subsidence in the outer part of the eye wall. On the other hand, when a relatively low amplitude VWS ($6\,m\,s^{-1}$) is applied (Fig. 11b), vertical winds weaken in the eye and in the outer part of the eye wall, but stronger subsidence is observed in the periphery of the cyclone (900 km from the center). This area is located where low level cyclonic and upper level anticyclonic circulations are sheared with the surrounding flow of the cyclone. With a stronger amplitude VWS ($15\,m\,s^{-1}$), it is observed that a reinforcement of the secondary circulation occurs simultaneously in the eye and in close proximity to the cyclone (Fig. 11c).

In summary, the VWS has two obvious effects on the tropical cyclone. The surface winds are weakened and the subsidence in the periphery of the cyclone is reinforced.

4.3. Discussion

In the real atmosphere, VWS must be accompanied by a horizontal temperature gradient. Strong convection associated with the TC leads to a large amount of latent heat release, which will modify the

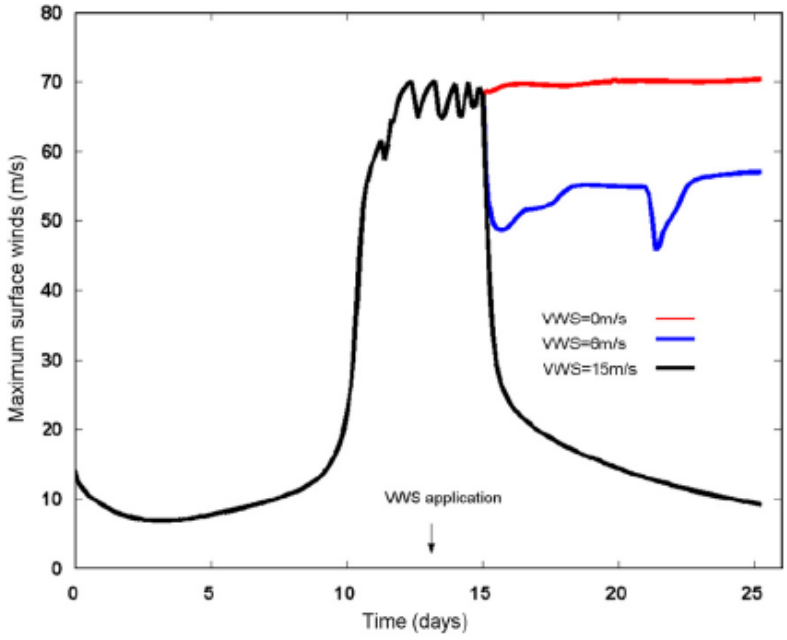

Fig. 10. Evolution of the maximum surface wind ($m\,s^{-1}$) during a HURRICANE simulation of an idealized tropical cyclone with three different intensities of the vertical wind shear applied (0, 6 and $15\,m\,s^{-1}$).

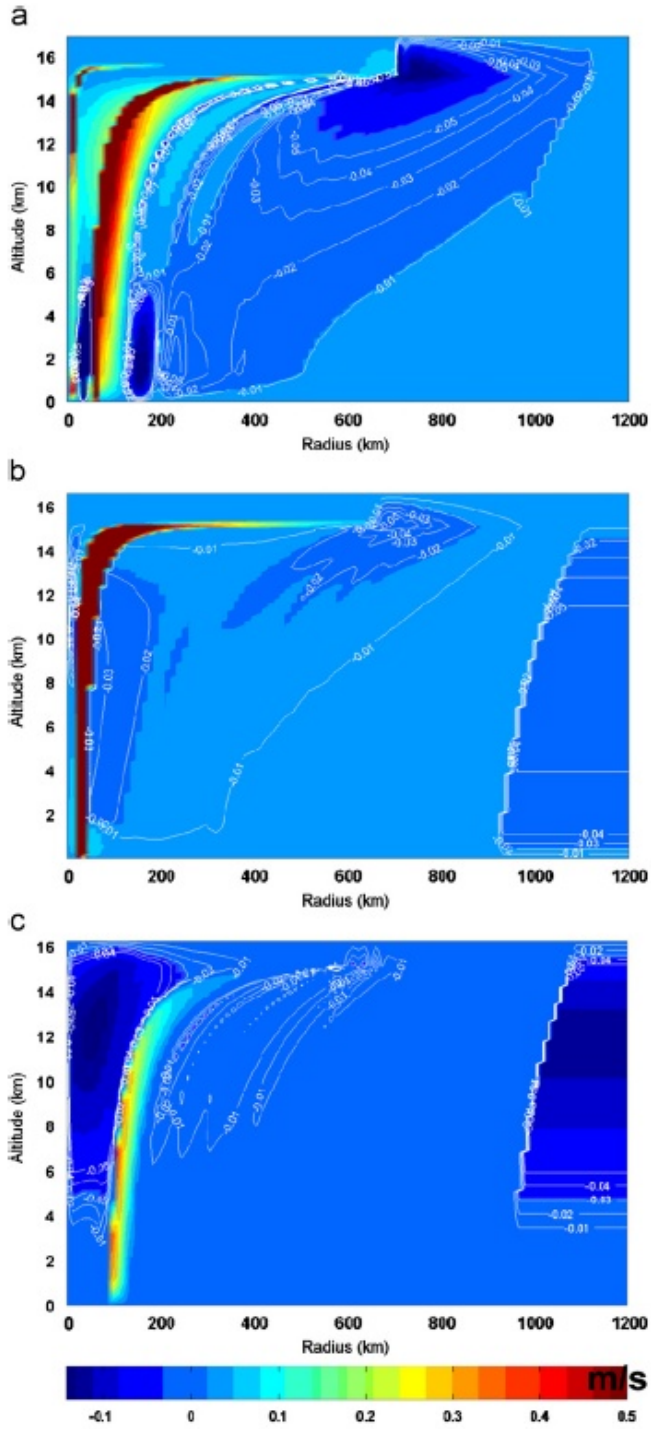

Fig. 11. Vertical r–z cross-section of the vertical wind with a vertical wind shear of (a) 0 m s^{-1} intensity, (b) 6 m s^{-1} and (c) 15 m s^{-1} (HURRICANE). The color scale represents the vertical wind intensity (m s^{-1}) and the white solid lines represent particularly negative vertical wind isotachs.

temperature structure, and in turn, the VWS. So, a vertical shear modifies the temperature structure of the atmosphere, which results in a change in the distribution of PV Even under adiabatic conditions, the presence of a VWS will result in a horizontal gradient of PV, as first pointed out by Kasahara and Platzman (1963). The vertical shear also tilts the vortex such that the upper level anticyclone will be downstream of the shear relative to the low-level cyclone. Wu and Emanuel (1993) suggested that conservation of PV would cause a downward (upward) penetration of the upper level anticyclone (low level cyclone). Only a few observational studies on TC motion related to non-barotropic processes have been made and all were based on case studies (e.g. Wu and Emanuel, 1995a, b; Wu and Kurihara, 1996; Shapiro and Franklin, 1999). The general conclusion from these studies is that PV at the upper levels appears to be an important contributor, apparently through the downward penetration process.

In the Marlene case study, at 200 hPa, the stratospheric PV filament signature is located where the horizontal shear between the mean westerlies and the anticyclonic circulation takes place. The non-stationarity caused by this interaction involves the development of an ageostrophic component of the wind which will be reinforced by the curvature of the anticyclonic circulation. Regarding the agreement between the relative PV and VWS maxima, the reinforcement of the negative vertical wind core in close proximity to the HURRICANE simulated cyclone underscores the hypothesis that VWS has played a role in the downward penetration of PV.

5. Conclusions

The tropospheric ozone budget over Reunion in the Southwestern part of the Indian Ocean is mainly controlled by photochemical production based on released pollutants coming from the African subcontinent and Madagascar, and by dynamical transport events from the upper-troposphere lower-stratosphere. In this last contribution, one possibility is the influence of tropical lows which was the purpose of the present study.

The dynamical mechanisms involved in the high ozone values of 6 April 1995 observed at Reunion were not previously detailed mainly due to the absence of signatures in the global model PV fields. Based on the results of a mesoscale simulation carried out using MESO-NH, we have highlighted some of the characteristic dynamic elements of this stratospheric ozone intrusion on the periphery of tropical cyclone Marlene, in addition to the limited amplitude contribution of biomass burning detailed by de Laat et al. (1999, 2001).

ECMWF analysis with 1.125° horizontal resolution did not reveal any particular anomaly of PV, whereas a filament was clearly visible in MESO-NH fields. Moreover, a good agreement in space between the PV filament and low relative humidity values was observed. The 1.2 PVU value for this filament could be consistent with a stratospheric origin. The model reproduces a penetration of the filament into the troposphere to the 350 K isentropic level, crossing the isentropes diabatically. It is located in the vicinity of the cyclone, directed inwards and has a centripetal form.

The radial ageostrophic circulation is directed outwards from the cyclone and is associated with divergence/convergence annular rings that have induced vertical movements. Two origins can be proposed. The first one is a confluence of the anticyclonic circulation with the subtropical jet-stream and the mean westerlies. The second one is the curvature of the anticyclonic circulation. This component of the wind is transversal to the anticyclonic circulation. Thus, the present situation is different from jet-stream curvature, where the ageostrophic circulation is found to be longitudinal.

Moreover, the reinforcement of the negative vertical wind core in close proximity to the HURRICANE simulated cyclone underscores the hypothesis that the VWS may have played a role in the downward penetration of PV.

The agreement of the dynamical and chemical signatures, which were not visible in ECMWF global model data, the description of the upper level ageostrophic circulation and associated divergent zones, and the influence of the VWS which has been discussed through the mesoscale analysis and via the idealized HURRICANE tropical cyclone model, all support the role of stratospheric to tropospheric transport in this event.

Acknowledgments

Our first acknowledgment is to Pr. Kerry Emanuel from MIT, MA for very useful discussions and for providing the HURRICANE model. The authors are also thankful to the Centre National de Recherches Météorologiques (CNRM)

and Laboratoire d'Aérologie (LA) for providing the MESO-NH model. We acknowledge the Institut du Développement et des Ressources en Informatique Scientifique (IDRIS—CNRS) for facilitating computational time. The Laboratoire de l'Atmosphère et des Cyclones (LACy) is supported by the Centre National de la Recherche Scientifique (CNRS)/Institut National des Sciences de l'Univers (INSU) and the Conseil Régional de La Réunion.

References

Baray, J.-L., Ancellet, G., Taupin, F., Bessati, M., Baldy, S., Keckhut, P., 1998. Subtropical tropopause break as a possible stratospheric source of ozone in the tropical troposphere. Journal of Atmospheric and Terrestrial Physics 60, 27–36.

Baray, J.L., Ancellet, G., Randriambelo, T., Baldy, S., 1999. Tropical cyclone Marlene and stratosphere-troposphere exchange. Journal of Geophysical Research 104, 13953–13970.

Baray, J.L., Randriambelo, T., Baldy, S., Ancellet, G., 2001. Comment on "Tropospheric O3 distribution over the Indian Ocean during spring 1995 evaluated with a chemistry–climate model," by A.T.J. De Laat et al. Journal of Geophysical Research 106, 1365–1368.

Baray, J.L., Baldy, S., Diab, R.D., Cammas, J.P., 2003. Dynamical study of a tropical cut-off low over South Africa, and its impact on tropospheric ozone. Atmospheric Environment 37, 1475–1488.

Bertin, F., Van Velthoven, P., Cremieu, A., Ney, R., Beugin, R., 1995. UHF radar observation of strato-tropospheric transfers on the anticyclonic side of a jet-streak. Annales de Geophysique 13, 1229–1236.

Bougeault, P., Lacarrère, P., 1989. Parametrisation of orography-induced turbulence in a meso-beta scale model. Monthly Weather Review 117, 1872–1890.

De Laat, J., Lelieveld, J., 2001. Reply. Journal of Geophysical Research 106, 1369–1371.

De Laat, J., Zachariasse, M., Roelofs, G.J., van Velthoven, P., Dickerson, R.R., Rhoads, K.P., Oltmans, S.J., Lelieveld, J., 1999. Tropospheric O3 distribution over the Indian Ocean during spring 1995 evaluated with a chemistry–climate model. Journal of Geophysical Research 104, 13881–13894.

Dupuis, H., Taylor, P.K., Weill, A., Katsaros, K., 1997. Inertial dissipation method applied to derive turbulent fluxes over the ocean during the surface of the ocean, fluxes and interactions with the atmosphere/atlantic stratocumulus transition experiment (SOFIA/ASTEX) and structure des echanges mer-atmosphere, proprietes des heterogeneities oceaniques. Journal of Geophysical Research 102, 21115–21129.

Emanuel, K.A., 1989. The finite-amplitude nature of tropical cyclogenesis. Journal of Atmospheric Science 46, 3431–3456.

Folkins, I., Appenzeller, C., 1996. Ozone and potential vorticity at the subtropical tropopause break. Journal of Geophysical Research 101, 18787–18792.

Gal-Chen, T., Sommerville, R.C.J., 1975. On the use of coordinate transformation for the solution of the Navier–Stokes equations. Journal of Computational Physics 17, 209–228.

Gouget, H., Cammas, J.P., Marenco, A., Rosset, R., Jonquières, I., 1996. Ozone peaks associated with a subtropical tropopause fold and with the trade wind inversion: a case study from the airborne campaign TROPOZ II over the Caribbean in winter. Journal of Geophysical Research 101, 25979–25993.

Holland, G.J., Merrill, R.T., 1984. On the dynamics of tropical cyclones structural changes. Quarterly Journal of the Royal Meteorological Society 110, 723–745.

Hoskins, B.J., McIntyre, M.E., Robertson, A.W., 1985. On the use and significance of isentropic potential vorticity maps. Quarterly Journal of the Royal Meteorological Society 111, 877–946.

Kain, J.S., Fritsch, J.M., 1993. Convective parametrizations for mesoscale models: the Kain–Fritsch scheme. Meteorological Monographs 46, 165–170.

Kasahara, A., Platzman, G.W., 1963. Interaction of a hurricane with the steering flow and its effect upon the hurricane trajectory. Tellus 15, 321–335.

Kentarchos, A.S., Roelofs, G.J., Lelieveld, J., 1999. Model study of a stratospheric intrusion event at lower midlatitudes associated with the development of a cutoff low. Journal of Geophysical Research 104, 1717–1727.

Klemp, J.B., Wilhelmson, R.B., 1978. The simulation of three-dimensional convective storm dynamics. Journal of Atmospheric Science 35, 1070–1096.

Lafore, J.P., Stein, J., Ascencio, N., Bougeault, P., Ducrocq, V.D., Duron, J., Fisher, C., Hereil, P., Mascart, P., Pinty, J.P., Redelsperger, J.L., Richard, E., Vila-Guerau de Arellano, J., 1998. The MesoNH atmospheric simulation system. Part I: adiabatic formulation and control simulations. Annales de Geophysique 16, 90–109.

Lander, M.A., Angove, M.D., 1998. Eastern Hemisphere tropical cyclones of 1995. Monthly Weather Review 126, 257–280.

Lipps, F.B., Hemler, R.S., 1982. A scale analysis of deep moist convection and some related numerical calculations. Journal of Atmospheric Science 39, 2192–2210.

Molinari, J., Skubis, S., Vollaro, D., 1995. External influences on hurricane intensity: part III. Potential vorticity structure. Journal of Atmospheric Science 52, 3593–3606.

Morcrette, J.-J., 1989. Description of the radiation scheme in the ECMWF model. ECMWF Tech. Memo., No. 165, European Centre for Medium-Range Weather Forecasts, Reading, England, 26pp.

Postel, G.A., Hitchman, M.H., 1999. A climatology of Rossby wave breaking along the subtropical tropopause. Journal of Atmospheric Science 56, 359–373.

Schubert, W.H., Hack, J.J., 1983. Transformed Eliassen balanced vortex model. Journal of Atmospheric Science 40, 1561–1583.

Scott, R.K., Cammas, J.P., Mascart, P., Stolle, C., 2001. Stratospheric filamentation into the upper tropical troposphere. Journal of Geophysical Research 106, 11835–11848.

Shapiro, M.A., Kennedy, P.J., 1981. Research aircraft measurements of jet stream geostrophic and ageostrophic winds. Journal of Atmospheric Science 38, 2642–2652.

Shapiro, L.J., Franklin, J.L., 1999. Potential vorticity asymmetries and tropical cyclone motion. Monthly Weather Review 127, 124–131.

Willoughby, H.E., 1988. Linear motion of a shallow-water barotropic vortex. Journal of Atmospheric Science 45, 1906–1928.

Wu, C.C., Emanuel, K.A., 1993. Interaction of a baroclinic vortex with background shear: application to hurricane movement. Journal of Atmospheric Science 50 (1), 62–76.

Wu, C.C., Emanuel, K.A., 1995a. Potential vorticity diagnosis of hurricane movement. Part I: a case study of hurricane Bob (1991). Monthly Weather Review 123, 69–92.

Wu, C.C., Emanuel, K.A., 1995b. Potential vorticity diagnosis of hurricane movement. Part II: tropical storm Ana (1991) and hurricane Andrew (1992). Monthly Weather Review 123, 93–109.

Wu, C.C., Kurihara, Y., 1996. A numerical study of the feedback mechanisms of hurricane–environment interaction on hurricane movement from the potential vorticity perspective. Journal of Atmospheric Science 53, 2264–2282.

Xue, M., Thorpe, A.J., 1991. A mesoscale numerical model using nonhydrostatic pressure-based sigma coordinate equations: model experiments with dry mountain flows. Quarterly Journal of the Royal Meteorological Society 119, 1168–1185.

2.2.3 Echanges stratosphère-troposphère et convection tropicale : D'autres événements et leur influence sur la climatologie de l'ozone troposphérique

JOURNAL OF GEOPHYSICAL RESEARCH, VOL. 111, D24107, doi:10.1029/2005JD006947, 2006

Signatures of stratosphere to troposphere transport near deep convective events in the southern subtropics

J. Leclair De Bellevue,[1] A. Réchou,[1] J. L. Baray,[1] G. Ancellet,[2] and R. D. Diab[3]

Received 5 December 2005; revised 20 June 2006; accepted 25 August 2006; published 20 December 2006.

[1] A climatology of tropospheric ozone profiles associated with tropical convection in the southwestern part of the Indian Ocean and over South Africa is presented. Then case studies of stratospheric-tropospheric exchange are documented using radiosoundings, ozone lidar, satellite and ECMWF global model data. In three distinct cases of varying tropical convection intensity (depression and cyclone Guillaume near Reunion in February 2002 and convection near Irene in November 2000), strong interaction between convection-induced upper level circulation, jet front systems and Rossby Wave Breaking induces stratosphere to troposphere exchanges. Stratospheric filaments in the upper troposphere evident in the ECMWF analyses are in good agreement with ozone, humidity and temperature vertical profile observations. For the Guillaume case study near Reunion, filaments and subsidence occur in both cases (depression on 15 February and cyclone on 19 February 2002). On 15 February, a moderate enhancement of ozone in the free troposphere is observed and on 19 February, a 100 ppbv ozone peak is recorded. In the Irene case study, a large upper level depression coming from the stratosphere, fed by a filament wrapped around the convective area in the Mozambican channel, induces an ozone peak of larger magnitude (170 ppbv). Secondary ozone sources (jet front system in the Atlantic and biomass burning in South America) could further amplify this ozone enhancement. The radiosounding indicates a strong ozone enhancement in the upper troposphere, without a signature of pumping from the lower layers, in contrast to the Guillaume case.

Citation: Leclair De Bellevue, J., A. Réchou, J. L. Baray, G. Ancellet, and R. D. Diab (2006), Signatures of stratosphere to troposphere transport near deep convective events in the southern subtropics, *J. Geophys. Res.*, *111*, D24107, doi:10.1029/2005JD006947.

1. Introduction

[2] The understanding of the transport of trace chemical species between the stratosphere and the troposphere is necessary for global change prediction. Tropospheric ozone is a minor component of the atmosphere which plays an important part in the photochemical balance of the troposphere, because of its high oxidizing potential with other chemical species. Moreover, changes in the vertical distribution of ozone, a greenhouse gas, influence the atmospheric radiative balance. Two main mechanisms explain high ozone concentration in the upper levels of the troposphere: photochemistry (pollution, biomass burning) and stratospheric-tropospheric exchange (STE).

[3] In the tropics, earlier studies of tropospheric ozone suggested that the ozone budget is controlled primarily by biomass burning which injects ozone precursors into the troposphere [*Fishman et al.*, 1990; *Browell et al.*, 1996; *Fujiwara et al.*, 1999; *Randriambelo et al.*, 2000; *Thompson et al.*, 2003].

[4] More recent studies indicate that STE, induced by the subtropical jet stream or by Rossby Wave Breakings (RWB), could also contribute significantly to tropospheric ozone enhancement [*Scott et al.*, 2001; *Gouget et al.*, 1996; *Folkins and Appenzeller*, 1996].

[5] Indeed, tropospheric ozone inputs could also result from convection induced downdraughts. Apart from its role in upward transport and diffusion of chemical species produced by biomass burning, the influence of convection on tropospheric ozone is complex and includes both dynamical and chemical components. Owing to mass conservation, convection-induced dynamical influences are not likely to be limited to upward lifting of ozone-poor air from lower layers of the troposphere. Detrainment of air is expected to play some part in the tropospheric ozone budget [*Chatfield and Crutzen*, 1984; *Dickerson et al.*, 1987; *Thompson et al.*, 1996]. Ozone measurements have been performed regularly at Reunion (20.8°S, 55.5°E) since 1992 [*Baldy et al.*, 1996]. At Irene (25.9°S, 28.2°E), located in South Africa [*Diab et al.*, 1996, 2004], soundings were taken in 1990–1993 and again from 1998 to the present. A first case study of convection-induced downdraughts injecting a high concentration of ozone in the troposphere has

[1]Laboratoire de l'Atmosphère et des Cyclones, CNRS-UMR 8105, Université de La Réunion, La Réunion, France.
[2]Service d'Aéronomie, CNRS-UMR 7620, Université Pierre et Marie Curie, Paris, France.
[3]School of Environmental Sciences, Howard College Campus, University of KwaZulu-Natal, Durban, South Africa.

0148-0227/06/2005JD006947$09.00

Table 1. Number of Tropospheric Ozone DIAL Nighttime Measurements and Radiosounding Performed by Year Since 1995

Year	Lidar Acquisitions	Ozonesondes
1995	...	18
1996	...	17
1997	...	25
1998	35	35
1999	32	49
2000	17	39
2001	4	28
2002	30	30
2003	23	18
2004	51	41

been presented by *Baray et al.* [1999a]. This high ozone enhancement attributed to tropical cyclone Marlene has also been observed in the pre-INDOEX (Indian Ocean Experiment) campaign [*De Laat et al.*, 1999; *Baray et al.*, 2001].

[6] In this paper, in order to improve our understanding of deep convection- or tropical cyclone- induced downdraughts and STE, we first demonstrate that STE induced by cyclones is quite frequent and propose an approach to assess its impact on ozone profiles. Then, the variability of STE signatures, observed on O_3, H_2O, and potential vorticity (PV) for two case studies will be analyzed in relation to the upper troposphere circulation induced by tropical convection.

[7] In section 2, we describe the data set used in the paper. The influence of cyclonic systems on ozone climatology is presented in section 3. Section 4 focuses on case study analyses and the concluding discussion is given in section 5.

2. Data Set

2.1. In Situ Data

[8] This paper is based on two types of in situ data. The first type is combined PTU-ozone soundings (PTU is from the radiosonde and attached to it during flight is the separate ozonesonde) performed at Irene and Reunion. The second in situ data come from a tropospheric ozone lidar operating at Reunion.

[9] The soundings provide vertical profiles of ozone, relative humidity and temperature from the ground to around 30 km. The balloon-borne device used at Irene was a Science Pump ECC (electrochemical concentration cell) Type 6A ozonesonde with a Vaisala radiosonde. At Reunion both Science Pump Type 6A and EnSci Z-type ozonesondes have been used [*Thompson et al.*, 2003]. The accuracy of these devices has been evaluated in field and chamber tests [*Barnes et al.*, 1985; H. J. G. Smit et al., Assessment of the performance of ECC-ozonesondes under quasi-flight conditions in the environmental simulation chamber: Insights from the Julich Ozone Sonde Intercomparison Experiment (JOSIE), submitted to *Journal of Geophysical Research*, 2006]. The vertical resolution of the data is around 50 meters. Irene and Reunion are part of the SHADOZ (Southern Hemisphere Additional Ozonesondes) network [*Thompson et al.*, 2003] and the sonde data used here are available at http://croc.gsfc.nasa.gov/shadoz.

[10] The measurements of tropospheric ozone by the lidar system are made by differential absorption in the ultraviolet wavelength band (289–316 nm). These wavelengths are obtained by stimulated Raman scattering of the fourth harmonic of the Nd-Yag laser beam in deuterium. The lidar altitude range is typically from 3 km to around 15 km, the upper limit depending on the meteorological conditions and ozone amount. The altitude resolution of the final ozone profiles is 15 m for the analog signal (from 3 to 6–7 km), and 150 m for the photon counting signal (from 6–7 km to the upper limit). Technical details of the system and validation are given by *Baray et al.* [1999b].

[11] Both types of measurements are currently operational and the number of profiles recorded by each system is given in Table 1.

2.2. Satellite Data

[12] Geostationary satellite images from METEOSAT are used in this study. Currently, EUMETSAT (Europe's Meteorological Satellite Organization) is operating Meteosat satellites at positions of 63°E (Meteosat 5) and 0° longitude (Meteosat 7). For the Zero Degree Service browse images are available every 6 hours (0000, 0600, 1200 and 1800 UT). For the Indian Ocean Data Coverage Service (IODC) (images from 63°E) images are available every 3 hours. These are provided in three different channels: visible, thermal infrared and water vapor infrared (http://www.eumetsat.de).

2.3. Global Model Data and Back Trajectories

[13] The meteorological data (wind, humidity and PV) used in the present study are 6-hourly (0000, 0600, 1200 and 1800 UTC), on 60 vertical levels from routine analysis of the European Centre for Medium-Range Weather Forecasts (ECMWF). We used data with a horizontal resolution of 0.5°.

[14] Back trajectories were calculated by the Lagrangian particle dispersion model FLEXPART version 4.3 [*Stohl et al.*, 1998], which was used in several studies of long-range transport of trace substances [e.g., *Stohl and Trickl*, 1999]. The model uses ECMWF input fields with a horizontal resolution of 1°, at all 60 vertical model levels, and with a time resolution of 3 hours. Advection and turbulent dispersion are taken into account by calculating the trajectories of a multitude of parcels. Solving Langevin equations, stochastic fluctuations of the three wind components are superimposed on the grid-scale winds to represent transport by turbulent eddies. The convection scheme used in FLEXPART was developed by *Emanuel and Zivkovic-Rothman* [1999].

3. Tropospheric Ozone Climatology During the Cyclonic Season

[15] *Rodgers et al.* [1990], studying the undulatory adjustments near to tropical cyclones from simulations and TOMS data, observed a significant descent of the tropopause height in the eye and the peripheral areas of the cyclone.

[16] Links between ozone and tropical convection have been investigated in CEPEX (Central Equatorial Pacific Experiment): *Wang et al.* [1995], modeling a deep convective storm showed considerable stratosphere to troposphere

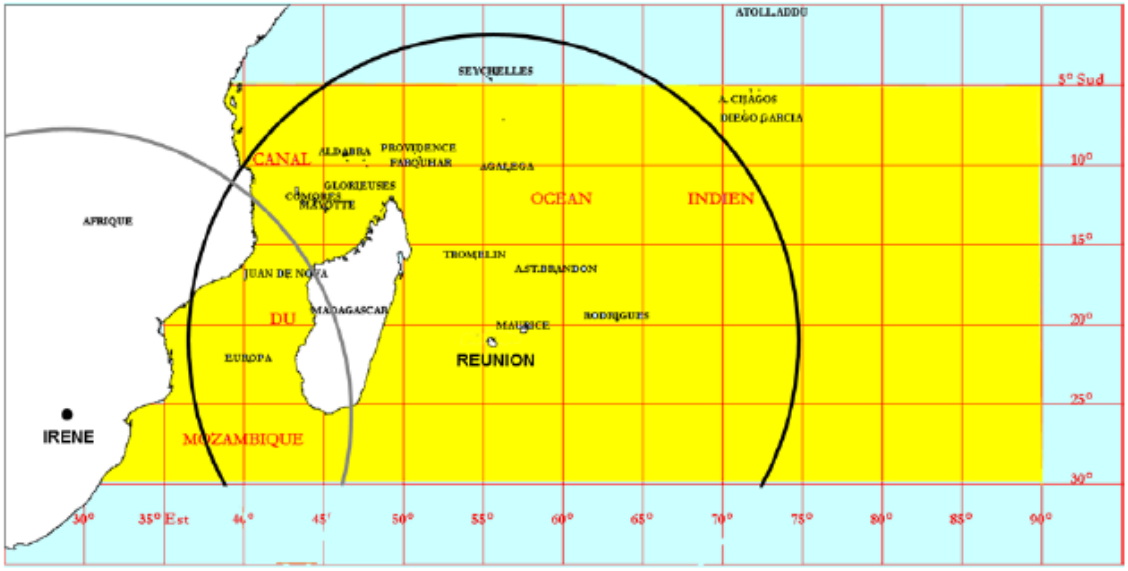

Figure 1. Cyclonic area of the southwestern Indian Ocean, depicted in yellow. The sampling of cyclonic systems for the climatological study is taken inside the geographical zones defined by a 2000 km radius around Reunion and Irene.

exchanges compared to upward exchanges in the convective tower.

[17] Analyzing data in the framework of TRACE-A, and carrying out statistical analysis of back trajectories, *Loring et al.* [1996] drew similar conclusions to those of *Rodgers et al.* [1990], published 6 years earlier.

[18] Other analyses showed that the vertical speeds induced by mesoscale convective clouds of the midlatitudes [*Stenchikov et al.*, 1996; *Poulida et al.*, 1996], during tropical convection events linked to the Inter Tropical Convergence Zone (ITCZ) [*Crutzen et al.*, 1979], and cumulonimbus clouds [*Mitra*, 1996] could play a role in the tropospheric ozone budget, by stratospheric-tropospheric exchange. Further, although large differences exist between tropical and midlatitudes cyclones, stratospheric ozone advection signatures into the troposphere are also found to accompany midlatitude cyclones [*Cooper et al.*, 2002].

[19] These recent studies showed that important subsidence could induce stratosphere to troposphere exchanges in the tropics, and that a dynamical link could exist between the cyclonic systems of tropical latitudes and tropospheric ozone distribution.

[20] According to the statistics available over 20 years, a global mean of 80–85 cyclonic events occur each year [*McBride*, 1995]. They are all localized at latitudes higher than 5°, and 87% of them occur within the tropics. The number of cyclones fluctuates from year to year, with a 10% standard deviation. However, strong interannual variability (15 to 70%) is observed when separate cyclonic regions are considered individually. Cyclonic activity fluctuates more in the northern Indian, the southwestern Pacific and the Atlantic Oceans than over the northwestern Pacific and the southwestern Indian Oceans. (The last one is our particular region of interest). Phenomena, such as the ENSO (El Nino Southern Oscillation) for the ocean and tropical troposphere and the QBO (Quasi Biennial Oscillation) for the low stratosphere, also influence the frequency of cyclones [*Gray*, 1979; *McBride*, 1995].

3.1. Cyclonic Activity in the Southwestern Indian Ocean

[21] The climatological study presented hereafter concerns the cyclonic area of the southwestern Indian Ocean using data from the Centre des Cyclones Tropicaux de La Réunion (CCTR). CCTR is a research center based at Reunion and keeps cyclonic data records. Figure 1 depicts the geographical delimitation of this area. The interannual variability of the cyclonic activity in the southwestern Indian Ocean region is illustrated in Figures 2 and 3.

[22] Figure 2 displays the temporal variation of cyclogenesis events (number of storms, depressions and tropical cyclones) by cyclonic season from 1992/1993 to 2003/2004, each season defined from 1 August to 31 July of the following year. The 1992/1993, 1993/1994 and 1996/1997 seasons have experienced greatest activity over this last decade, with 14, 15 and 14 cyclogenesis events respectively. In 1997/1998, 1998/1999 and 2000/2001, only 8 systems were observed in the region. It also appears that several consecutive active seasons are followed by seasons of reduced activity, as was the case between 1992/1993 and 1996/1997, when the number of events was equal to or greater than 11 systems per cyclonic season. Further, the seasons from 1997/1998 to 2001/2002 had an equivalent or lower activity than the mean over the period 1992 to 2004.

[23] The choice of seasonal period for the sampling of the cyclonic systems for the ozone climatology is an important criterion. Figure 3 shows monthly frequencies of systems based on the observations of 136 events (61 cyclones and 75 storms and depressions) between 1992 and 2004. The most common months for cyclones are from November to April (89% of the cyclonic activity), and hence examples for

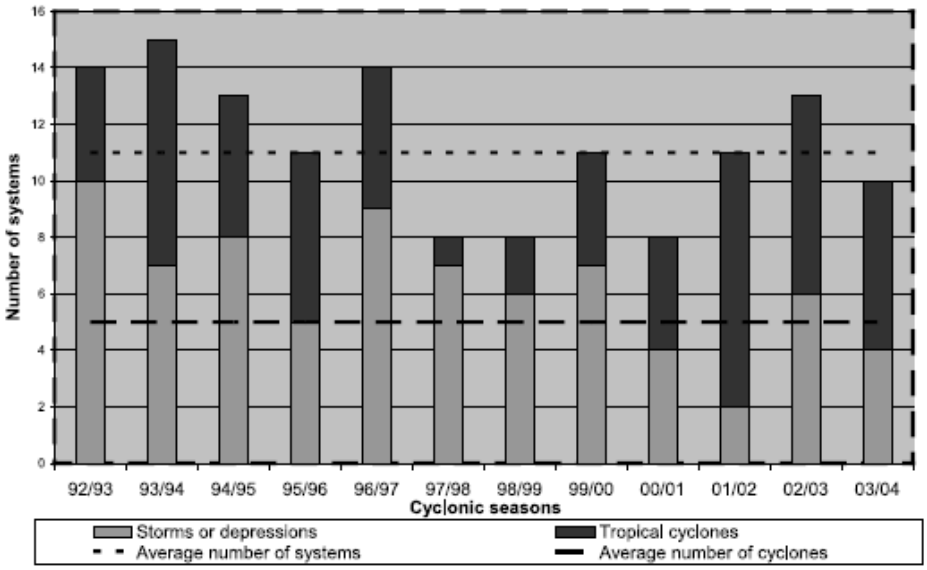

Figure 2. Interannual variability of storms, depressions and cyclones in the southwestern Indian Ocean during the 1992/1993 to 2003/2004 cyclonic seasons. The average is 11 systems and 5 cyclones per cyclonic season.

analysis are taken from this period. January and February experience 52% of the cyclonic activity. The sampling of systems in the ozone climatological study presented in section 3.2 relates to the period November to April.

3.2. Tropical Cyclonic Systems: Effects on the Mean Ozone Profiles

3.2.1. Methodology

[24] Two measurement sites, Reunion and Irene, are compared through the climatology based on radiosounding data from each station and the archives of CCTR. Reunion, located on the southern edge of the tropical zone, is well located for the study of exchanges related to tropical convection in summer, and the southerly movement of the ITCZ. Irene, in South Africa, which is more in the subtropics at 25.5°S, is less influenced by the ITCZ, and has a different geographical situation, being located 700 km from the coast, and at an altitude of 1523 m.

[25] The choice of the geographical area of radius 2000 km around each site is based on the assumption that the influence of convective systems beyond this threshold is not very significant. This dimension is higher than the

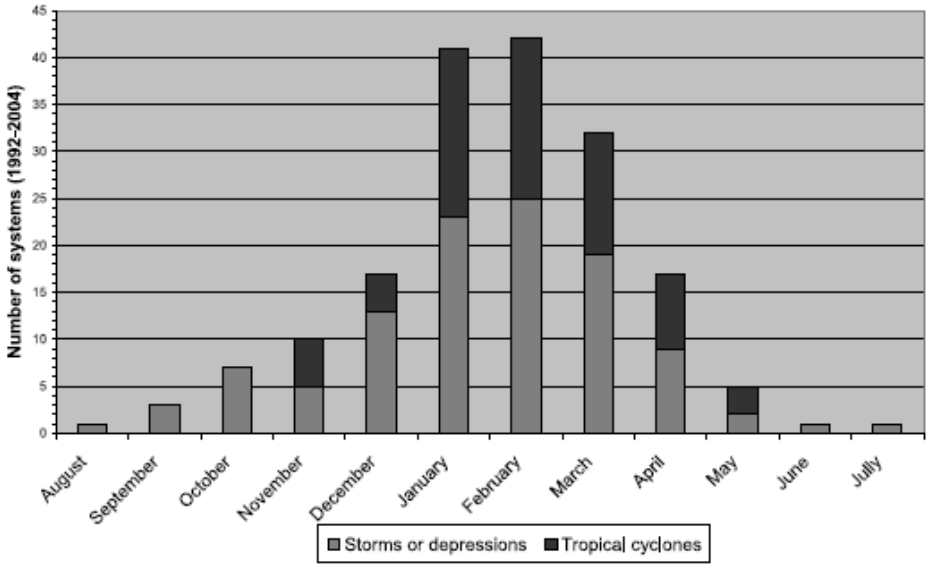

Figure 3. Seasonal frequency of cyclogenesis events in the southwestern Indian Ocean during 1992/1993 to 2003/2004 cyclonic seasons.

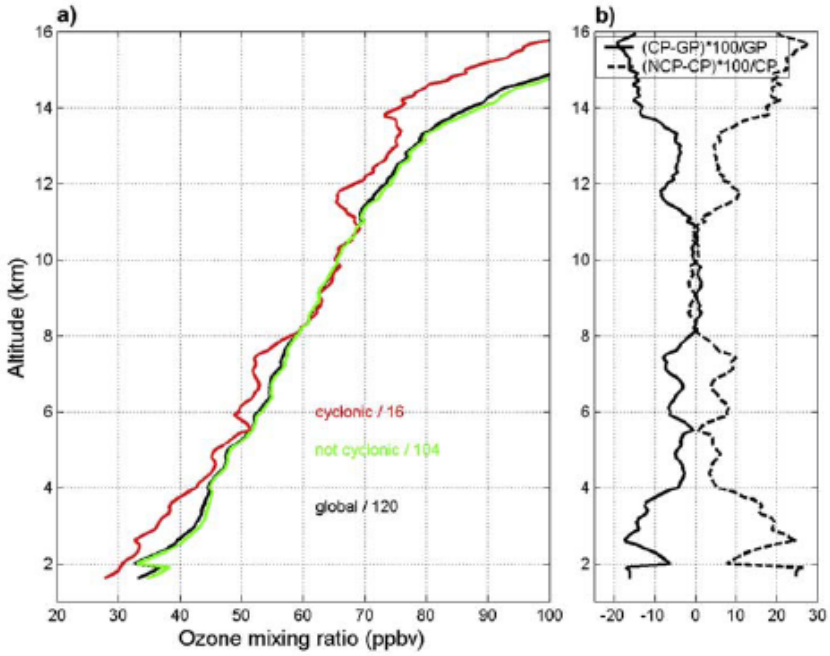

Figure 4. (a) Mean ozone mixing ratio profiles during November to April from 1998 to 2004, over Irene: "cyclonic" mean profile (red), "noncyclonic" profile (green) and global mean profile (black). The number of profiles used to calculate the mean profiles is indicated on the figure. (b) Relative deviation between cyclonic and global profiles (solid line) and between noncyclonic and cyclonic profiles (dashed line).

dimension of the most intense events. The number of systems of each cyclonic season is thus reduced by this criterion, from 136 to 112 around Reunion. Over the periods 1990 to 1993, and 1998 to 2003, 30 disturbances were observed in the geographical area of radius 2000 km around Irene. Most were over the southern part of the Mozambique Channel, with seven penetrating over the African subcontinent.

[26] The climatology of ozone profiles was first based on all ozone profiles measured for the months from November to April, for the period 1992 to 2004 at Reunion and 1990–1993, and 1998–2003 at Irene. On the basis of these data, a mean profile (GP) at each station for the cyclonic season was determined. Two classes of profiles were then distinguished: cyclonic (CP) and noncyclonic (NCP). The mean CP profile was calculated by using radiosoundings released during the active period of a cyclonic system and inside the 2000 km radius around the two sites. The mean NCP profile was calculated by using radiosoundings released without any cyclonic system in the 2000 km radius zone. A total of 94 profiles were obtained at Reunion during the cyclonic season; 59 of these profiles were cyclonic and 35 were noncyclonic. At Irene, 120 profiles were obtained during the cyclonic season, 16 being cyclonic and 104 noncyclonic.

3.2.2. Results

[27] Figure 4 depicts the three mean profiles above Irene. The relative difference between the cyclonic and noncyclonic profiles varies between 0 and +30% between 1 and 8 km altitude, whereas the relative difference between the cyclonic and global profiles varies between 0 and −20% over the same height interval. The cyclonic influence thus tends to decrease the mean ozone values, whereas the noncyclonic ozone values are higher than the mean global profile in the first 8 km of the troposphere. Between 8 and 11 km, the influence of the cyclonic systems on the mean ozone profile is not clearly discernible, and above 11 km, the cyclonic influence again tends to decrease the mean global ozone values.

[28] Figure 5a presents the three profiles for Reunion. The relative differences between the cyclonic and global profiles, and between the cyclonic and noncyclonic profiles are depicted in Figure 5b. The mean cyclonic profile exhibits a 0 to 5% enhancement over the mean global profile in the 3.5 km to 11.5 km altitude range, and up to a 5% reduction above 11.5 km. Compared with the mean noncyclonic profile, the differences are 0–20% and −15% to 0% between 3.5 km and 11.5 km respectively.

[29] It is clearly evident that the influence of cyclonic events on tropospheric ozone is much less structured and perceptible for Irene than for Reunion. This is due to the fact that, between 1998 and 2004, only 12 tropical cyclones occurred in the Mozambique Channel. Irene, which is situated far inland is less subject to the influence of these systems. In contrast, 112 systems were recorded in the 2000 km radial zone around Reunion. This oceanic site is thus potentially under the direct influence of these systems.

[30] The different geographical positions of Reunion and Irene thus explain the less visible influence at Irene. Moreover, the global mean ozone profile above Irene is

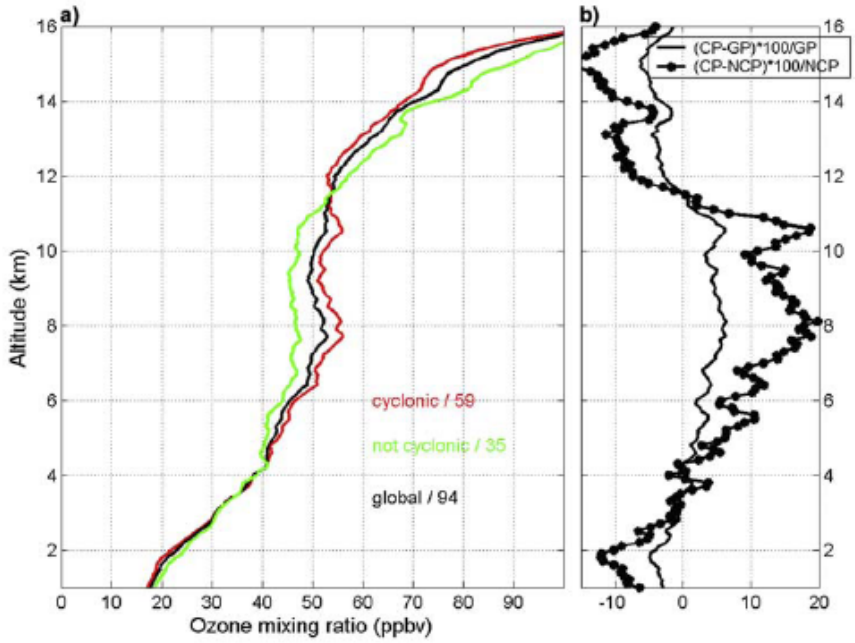

Figure 5. (a) Mean ozone mixing ratio profiles during November to April from 1992 to 2004, over Reunion: "cyclonic" mean profile (red), "noncyclonic" profile (green) and global mean profile (black). The number of profiles used to calculate the mean profiles is indicated on the figure. (b) Relative deviation between cyclonic and global profiles (solid line) and between cyclonic and noncyclonic profiles (dashed line).

close to typical midlatitude profiles. The climatological approach that we carried out by distinguishing the cyclonic from noncyclonic profiles underlines two effects of cyclonic systems on the ozone profiles, viz. an ozone enhancement in the midtroposphere and an ozone decrease in the upper troposphere. An hypothesis to explain this vertical ozone distribution would be the dual influence of convective systems (tropical storms, depressions and cyclones) on the climatology of tropospheric ozone: transfer of ozone from the stratosphere to the midtroposphere and a pumping of ozone-poor air masses from the boundary layer to the upper troposphere.

[31] An important outstanding question relates to the dynamical influences on the structure of the climatological ozone profiles during the cyclonic season.

[32] To further document exchanges near convective events, specific measurement campaigns have been undertaken [*Réchou et al.*, 2002], in addition to weekly routine ozone measurements. In the next section we present two case studies which can be considered as representative of the southern part of Africa and the southwestern Indian Ocean.

4. Case Studies of Stratospheric-Tropospheric Exchange Near Convective Events

4.1. Guillaume Event, February 2002

4.1.1. Observations

[33] Figure 6 depicts ozone, temperature and relative humidity profiles obtained on 15 and 19 February 2002, during the development of tropical cyclone Guillaume. The ozone profiles have been superimposed on the mean ozone profile and its associated variability calculated from 19 radiosoundings recorded at Reunion during the month of February since 1992.

[34] The 15 February ozone profile presents no strong ozone peak, but a large concentration of ozone in the entire upper troposphere (600 to 220 hPa). Between 350 and 150 hPa, the ozone mixing ratio is constant at ~70 ppbv, about 20 ppbv above the climatological profile, corresponding to the upper limit of ozone variability in February. The ozonopause is at a low altitude (around 150 hPa, 15 km), indicated by a very sharp ozone increase (around 25 ppbv/km at 15 km). It is about 2 km below the thermal tropopause (−80°C at 17 km) depicted in Figure 6b. The fact that the ozonopause is below the thermal tropopause (the height where the vertical temperature gradient changes from a tropospheric value of about −6°C/km, to a stratospheric value of about +3°C/km) means that there is ozone in the upper tropical troposphere, under the tropopause. This feature is sometimes observed at midlatitude sites in the Northern Hemisphere [*Bethan et al.*, 1996], and has been described by the concept of the Tropical Tropopause Layer (TTL) where the maximum altitude of deep convection does not reach the coldest temperature level [*Gettelman and Forster*, 2002].

[35] The profiles of relative humidity present large values in the lower layers (more than 80% between 0 and 3.5 km). The free troposphere is very dry (less than 20% until

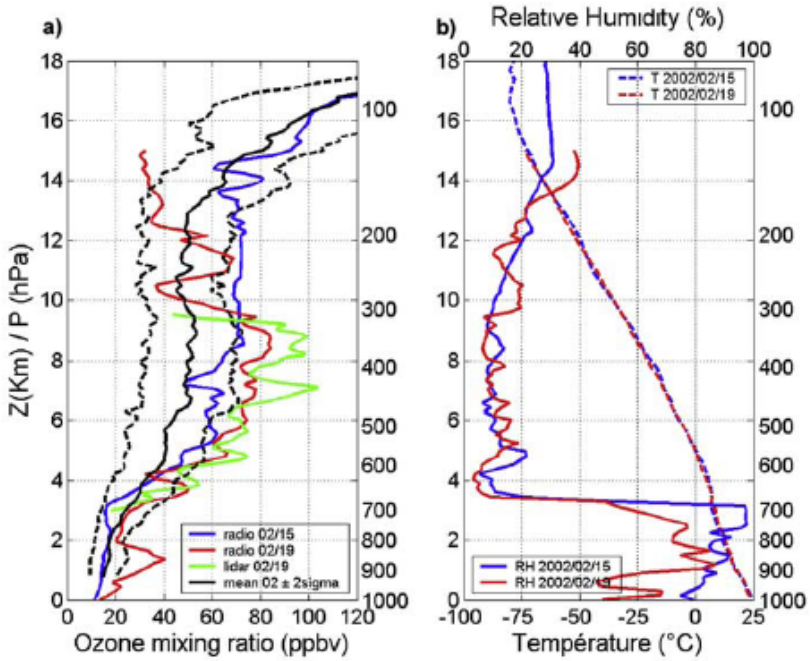

Figure 6. (a) Vertical profiles of ozone mixing ratio obtained by radiosounding over Reunion on 15 February 2002 at 1530 UT (blue), 19 February 2002 at 1300 UT (red) and by lidar profile between 1615 and 1650 UT (green), superimposed with a climatological profile of ozone for February (19 profiles from 1992 to 2002) (black line) and its standard deviation (black dashed lines). (b) Vertical profiles of relative humidity and temperature.

12.5 km). Nevertheless, because of the decreasing accuracy of the radiosounding sensor with altitude, humidity measurements in the upper troposphere can only be indicative.

[36] The two 19 February ozone profiles present an ozone peak at 350 hPa (83 ppbv for the radiosounding and 100 ppbv for the lidar). This peak is part of a larger ozone-enriched layer between 600 and 350 hPa. A negative ozone anomaly is observed in the upper levels (less than 40 ppbv at 275 hPa). The ozonopause is at a higher altitude than for the 15 February profile. This configuration has previously been observed when upper vertical motions affect the TTL by an overshoot of the deep convection.

[37] The 19 February ozone lidar profile was acquired three hours after the radiosounding. The upper limit of the profile was only 10 km, limited by the poor sky conditions during the cyclonic season (frequent clouds and high humidity). In the altitude range of the lidar (3–10 km), radiosounding and lidar profiles display the same structure, with peaks being more pronounced in the lidar profile. The 19 February relative humidity profile is very close to that recorded on 15 February, with a slightly less moist boundary layer (50 to 85% between 0 and 3.5 km).

4.1.2. Synoptic Situation

[38] We now highlight the synoptic context of this case study using Meteosat images (Figure 7). During the second half of February 2002, the Indian Ocean was affected by the convective system Guillaume. On 15 February, Guillaume was a convective zone without an apparent eye, and was detached from the ITCZ. The center was located near 16°S; 52°E, 750 km northwest of Reunion. On 19 February, the ITCZ moved northward. The convective depression Guillaume strengthened and became a cyclone. It was located near 18°S; 59°E, 350 km northeast of Reunion.

[39] Further, an upper level front was visible on the Meteosat image, about 2000 km southwest of Reunion. Two dry zones are evident on the water vapor images on 15 and 19 February, one located west of the front and the other located on the edge of Guillaume.

4.1.3. Temporal Evolution of the Air Masses

[40] Back trajectories ending over Reunion between 9.5 and 10.5 km on 15 and 19 February, 2002 display the history of the ozone-enriched air parcels (Figure 8). 120 hours before arriving over Reunion, the air mass was over the equatorial Atlantic Ocean. The air mass went southward, with subsidence occurring on 12 February, around 1200 UT (−75 hours) from altitudes of between 12.5 km and 13.5 km. This first subsidence was located in a northwesterly air stream over South Africa. An upward movement then occurred between −45 and −40 hours, and the trajectory moved northward, in the direction of Reunion. A second subsidence occurred on 14 February, around 0600 UTC (−30 hours) from a level of around 12.5 km (Figures 8a and 8b).

[41] In order to understand the origin of the air parcels, we used ECMWF wind and PV fields observed during this period (Figure 9). PV is a dynamical tracer frequently used in STE studies [*Hoskins*, 1991]. Despite some well known limitations of this tracer (diabatic production of PV in cyclones, its equatorial limit, and ECMWF data resolution

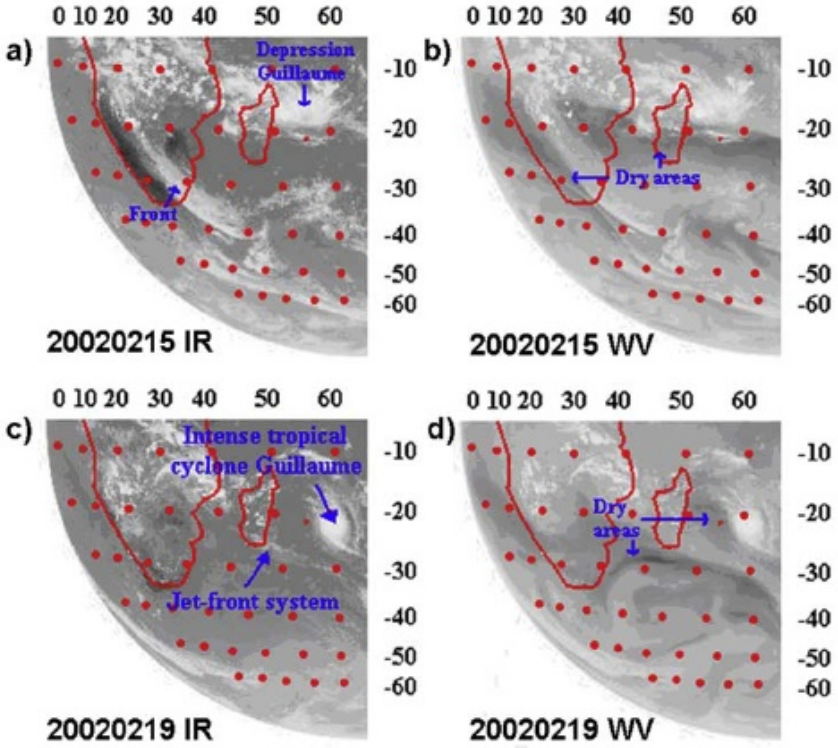

Figure 7. Meteosat-5 images on (a and b) 15 February and (c and d) 19 February at 1200 UT in the infrared (Figures 7a and 7c) and water vapor channels (Figures 7b and 7d).

mesoscale dynamics), we show hereafter that some significant characteristics are present.

[42] The first subsidence corresponds to the passage of the parcels in the jet front system above the Southern Atlantic on 12 February. The intense upward movement corresponds to the passage of the parcels in a strong anticyclonic curve of the jet stream over the southeastern coast of South Africa (Figure 8a), associated with a strong Rossby wave breaking (RWB hereafter) development in this region.

[43] RWB along the tropopause occurs preferentially during summer over the oceans, in relative proximity to the planetary-scale high-pressure systems in the subtropics [*Postel and Hitchman*, 1999]. These authors showed, using synoptic maps of RWB, that an acute tropopause folding in the meridional plane typically accompanies RWB. Some cases reveal the rich interaction between the tropical flow and the extratropical westerly current. The Guillaume case study showed a low-latitude penetration of the jet stream with the RWB, and a possible interaction between the RWB and the upper level circulation of Guillaume system.

[44] Just before arriving over Reunion, the trajectory indicates a second subsidence (Figures 8a and 8b). This second subsidence corresponds to the passage of the parcels in a high PV filament developing around the Guillaume system, and identified on the water vapor Meteosat image by a dry zone (Figure 7b). The trajectories arriving over Reunion between 8 and 9 km on 19 February 2002 have been calculated over 150 hours, i.e., beginning on 15 February (Figures 8c and 8d). Parcels present subsidence on 17 February around 0000 UT (−60 hours), linked to an almost southerly air stream. The long-term origin of some of the parcels (−150 hours) displays an important dispersion of the air masses, with a lower-tropospheric origin over Africa (between 10°E and 30°E and between 15°S and 20°S) for some parcels. The geographic area of this subsidence is the western and southwestern edge of the tropical cyclone area and corresponds to a cloudless and dry area on Meteosat images.

[45] Wind and absolute values of PV fields have been calculated at 340 K (275 hPa to 10 km) when the trajectories show clear subsidence, on 12, 14 and 17 February (Figure 9).

[46] The third subsidence described above seems to have the same dynamical origin as the first subsidence. However, on 17 February, no strong wind shear nor RWB occurred in the Mozambican channel, which explains why no strong upward movement has been observed.

[47] The parcels coming from the boundary layer could contribute to limit the magnitude of ozone peaks on 19 February, and induce some perturbations on the ozone profile of 19 February (Figure 6a), which presented some ozone-rich layers (at 7 and 9 km) and some ozone-poor layers (at 6.5, 7.5 and 10.5 km).

[48] When the Rossby wave moves eastward, the tongue of PV separates from the cyclone and the filament in the

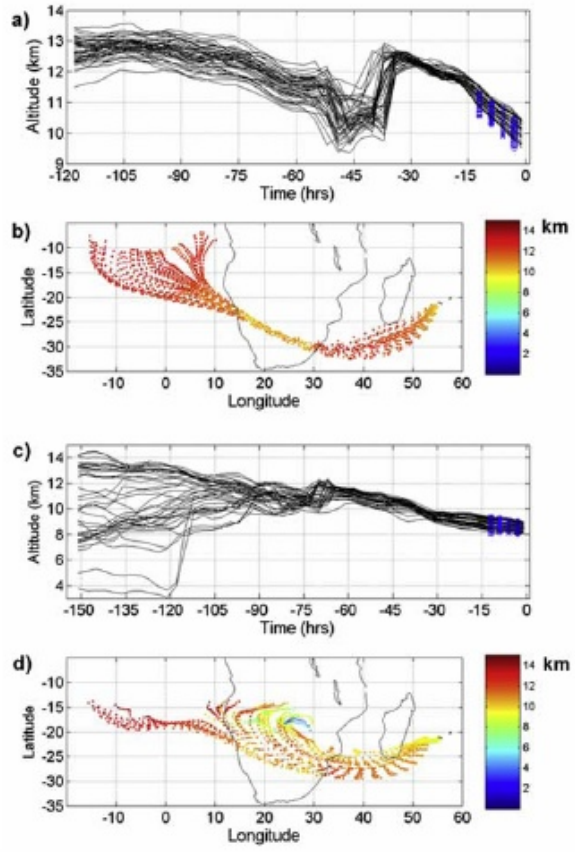

Figure 8. Cluster back trajectories using 2000 parcels ending on (a and b) 15 February 2002 at Reunion, between 9.5 and 10.5 km, and (c and d) 19 February between 8 and 9 km at 1200 UT. Corresponding latitude-longitude positions and their altitude are given by the color scale on the right.

western vicinity of the cyclone (not shown) persists until 19 February (0000 UT), suggesting a PV destruction on 19 February. The signature of ozone intrusions from the stratosphere into the troposphere is still visible on the ozone profile, although the PV filament disappeared 12 hours before. The persistence of a dry air filament on the 19 February Meteosat image (Figure 7d) corroborates this intrusion. Furthermore, stratospheric air observed in the troposphere can retain its original chemical signature for longer than its thermodynamic signature [*Bithell et al.*, 2000].

[49] Vertical PV cross sections have been plotted (Figure 10) to detect the level to which stratospheric PV filaments penetrate: 330 K on 14 February (Figure 10a), 350 K on 17 February (Figures 10b and 10c). On 17 February the convective tower is clearly identified by high values of PV, produced by diabatic heating and frictional forces occurring around the eye of Guillaume (Figure 10c). In Figure 10c, the stratospheric PV filament is visible on the western edge of Guillaume.

[50] Biomass burning is a possible chemical source of ozone precursors in the tropical troposphere [*Randriambelo et al.*, 2000]. The ESA publishes monthly global fire maps on the Web and the February 2002 map is available on http://dup.esrin.esa.int/ionia/wfa/products/0202ESA02.gif. Most of fires during February 2002 occurred north of the equator in Africa, Central America and Asia. Back trajectories calculated in this case study do not indicate their origins. Very few fires occur in the Southern Hemisphere over South Africa [*Randriambelo et al.*, 1998]. This result is in agreement with previous studies of the biomass burning climatological influence, and we can conclude that in this case study, the photochemical origin of ozone played a minor role, in comparison with dynamical mechanisms.

4.2. Irene Event, November 2000

4.2.1. Observations

[51] Figure 11 depicts ozone, temperature and relative humidity profiles obtained by radiosoundings at Irene on

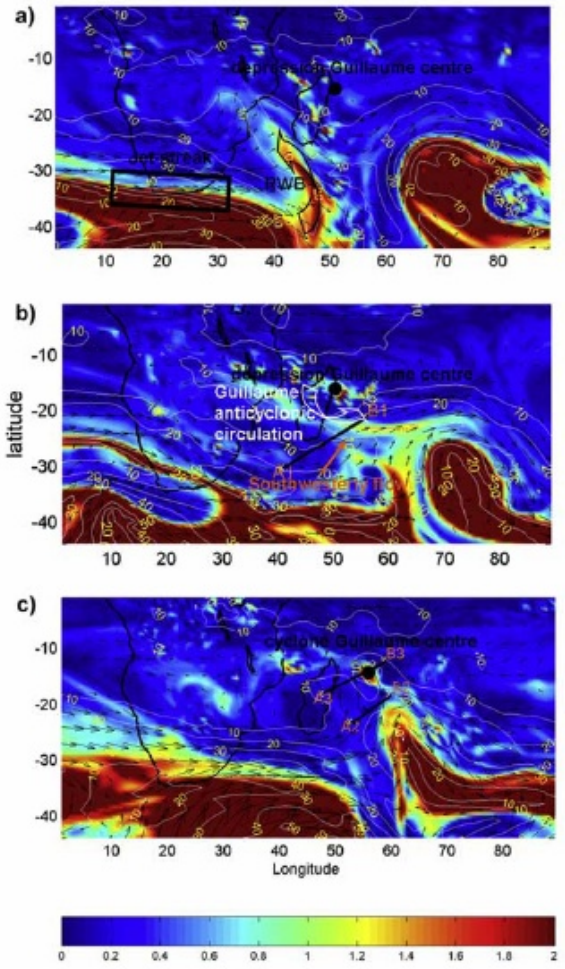

Figure 9. ECMWF potential vorticity (absolute value) on the 340 K isentropic surface on (a) 12 February 2002, (b) 14 February 2002 at 1200 UT, and (c) 17 February 2002 at 0600 UT. Horizontal wind direction and intensity (m s^{-1}) have been superimposed. The lines A and B indicate the limits of the vertical cross sections shown in Figure 10.

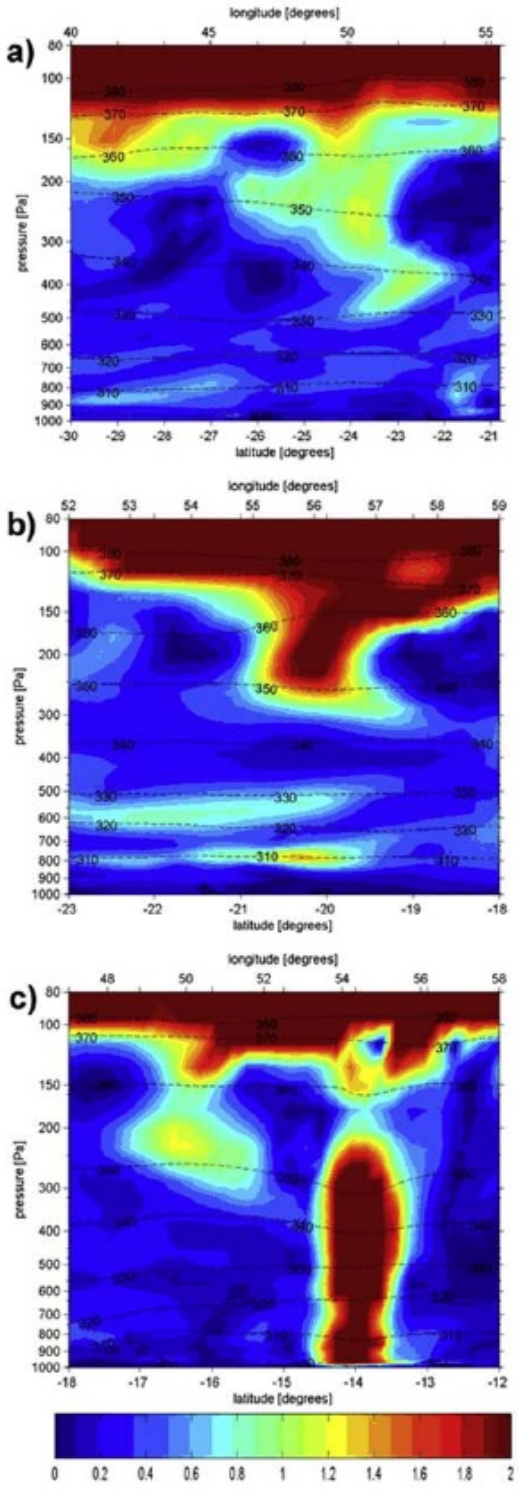

Figure 10. Potential vorticity (absolute value) vertical cross section whose trace is marked on Figure 9. (a) A1B1, (b) A2B2, and (c) A3B3. The potential temperature contours have been superimposed.

11 November 2000. The ozone profile is superimposed on the November climatological profile at Irene.

[52] The ozone profile presents very different characteristics from those obtained for the Guillaume case study. Between the ground and 8 km, ozone values are between 40 and 70 ppbv, within the climatological variability. Between 9 and 14 km (330 K to 370 K), extremely high ozone values (more than 100 ppbv) are observed, with two peaks reaching 170 ppbv. One, located at 10.5 km is a very thin enriched ozone layer and the other is larger, between 12 km and 12.5 km. These values are considerably higher than the climatological mean. The enriched ozone layer is capped by a temperature inversion based at ~13 km (Figure 11b). Another slight variation is visible on the temperature profile near an altitude of 11.5 km. It could be caused by the warming of the atmosphere by ozone. The thermal tropopause is very high (18 km), which is unusual for a site at this latitude (25°S).

[53] The humidity profile is characterized by large values in the lower part of the profile, reaching 90% at 3 km, and above this a layer with 40% relative humidity between 3 and 4 km is observed. The air is dry above 4 km (10–20% RH between 4 and 12 km), exhibiting a rather noisy profile in the free troposphere. A wetter layer (40% between 12 and 14 km) caps the ozone enriched layer observed between 10 and 13 km. Above 15 km, the air is dry again.

4.2.2. Synoptic Situation

[54] As in the Guillaume case study, a convective zone and a jet front system are in the region, but the situation is different (Figure 12). The convective zone is in the Mozambique Channel, and the jet front system is situated to the southwest in the South Atlantic Ocean. The ITCZ is well developed over the central African continent, but far from the measurement point. A large area between 0 and 40°E, and north of 10°S is very cloudy and wet.

[55] On the water vapor Meteosat image (Figure 12b), two dry areas appear: one is close to the upper level front, at 0°E longitude, and 20 to 40°S; the other is larger, near 20°S, 20°E, in the vicinity of the convective area. The second area is larger and drier (darker on the water vapor Meteosat image) than the former area near the front, and also drier than the area near Guillaume, seen in the preceding case study.

4.2.3. Temporal Evolution of the Air Masses

[56] Back trajectories (Figure 13) indicate the short-term origin of the enriched ozone layer: the parcels come from the southwest, and then the west. They have passed through the two dry areas identified on Meteosat images. The long-term origin of the parcels is South America. We note the greater speed of the air parcels, in comparison with the Guillaume case study, due to the influence of the subtropical jet stream.

[57] In the vertical plane, two areas of subsidence are identified, one at −80 hours, which corresponds to the passage of the air parcels over South America (Chili). Many strong vertical perturbations occur in this area, perhaps induced by the mountain chain Cordillere des Andes and by convection. Another area of subsidence is observed between −45 hours and the end point of the trajectories, when the air parcels are between the eastern part of the South Atlantic Ocean and Irene.

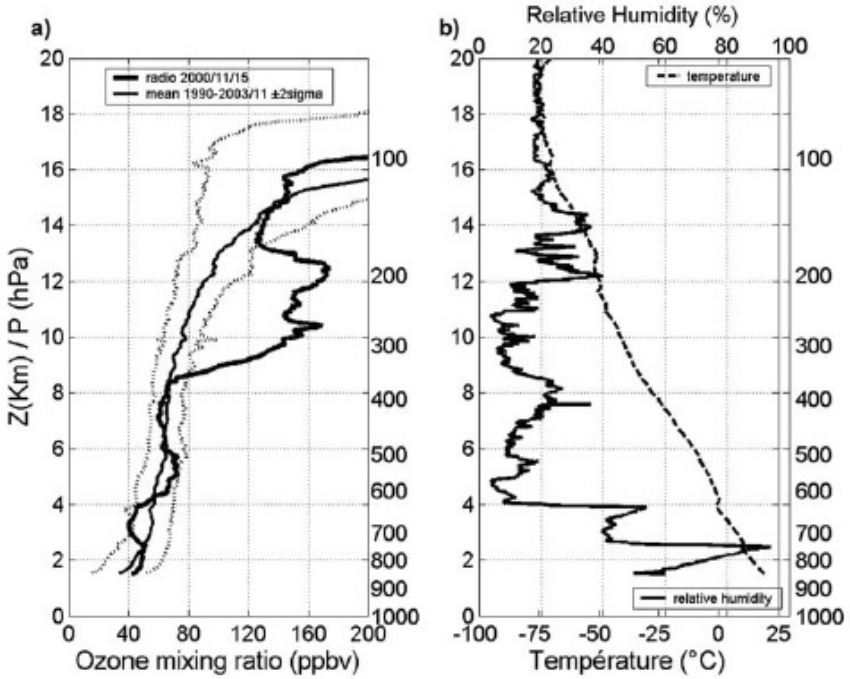

Figure 11. (a) Vertical profiles of ozone mixing ratio obtained by radiosounding over Irene on 15 November 2000 at 0600 UT, superimposed with a climatological profile of ozone for November (24 profiles between 1990 and 2003) and its standard deviation (dashed lines). (b) Vertical profiles of relative humidity and temperature.

[58] PV cross-sectional fields (Figure 14) confirm the stratospheric origin of the dry area near Irene, and the other near the upper level front, visible between 0 and 15°E on 15 November, and which was situated between 25°W and 0° longitude on 13 November (not shown).

[59] If we compare this case study to the preceding one (Guillaume), we find here evidence of important STE signatures (very high ozone and PV values).

[60] In fact, the dry area observed near the convective area is an upper level depression containing stratospheric air, fed by the filament around the convective area in the Mozambique Channel. This case shows some similarities to a previous study of a cutoff low (COL) over South Africa [*Baray et al.*, 2003]. The radiosounding performed on 1 October 1996 in Reunion presents an ozone peak with magnitude and height comparable to the present case study. The main difference between the synoptic situations of the two cases is the role of the convective system (not present in October 1996, present in November 2000) in the stratospheric filamentation and COL formation.

[61] The vertical cross section (Figure 15) shows that the deformation of the PV field reaches the level 330 K. Near

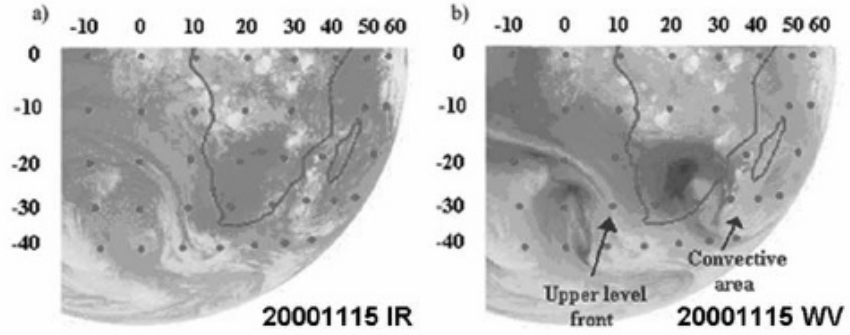

Figure 12. Meteosat-7 image on 15 November 2000 at 0600 UT in the (a) infrared and (b) water vapor channels.

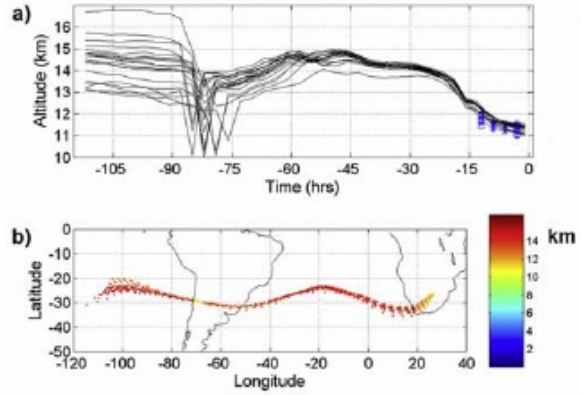

Figure 13. Cluster back trajectories using 2000 parcels ending on 15 November 2000 at 0600 UT over Irene (South Africa) between 11 and 13 km. Corresponding latitude-longitude positions and their altitude are given by the color scale on the right.

the PV anomaly, the isentropic surface 330 K presents important slopes, suggesting frontogenesis mechanisms near the COL. The detachment of the COL in the vertical plan is in progress, but not completed on 15 November 2000.

[62] In November, biomass burning is a possible source for tropospheric ozone in the Southern hemisphere [*Randriambelo et al.*, 1998]. The ESA fire map for November 2000 (available at http://dup.esrin.esa.int/ionia/wfa/products/0011ESA02.gif) shows that few fires occur in South Africa, but some fires occur in South America, where some strong vertical perturbations have been observed on back trajectories. In addition to dynamical sources of ozone (STE), they could contribute to the ozone peak.

[63] In summary, dynamical and chemical mechanisms have both had a role to play in this case study. Moreover, the dynamical mechanism is different to the Guillaume case study. The stratospheric filament which developed around the convective zone in the Mozambican channel fed an upper level depression of stratospheric air in the upper troposphere. The size of this depression and its high concentration of ozone produced a strong ozone peak, amplified by two other sources (fires in South America and an upper level front in the Atlantic Ocean).

5. Conclusion

[64] In this study, in order to improve our understanding of the influence of deep convection and tropical cyclones on the vertical distribution of tropospheric ozone, we have presented a statistical overview and dynamical case studies.

[65] The case studies include three distinct situations (depression Guillaume, cyclone Guillaume, and convection at Irene) of STE occurring in the vicinity of deep tropical convection. In each case, a strong interaction between the dynamics of convection, the jet front system and RWB induces the stratosphere to troposphere exchanges. Stratospheric filaments in the upper troposphere have been detected in ECMWF analyses, and are in good agreement with ozone, humidity and temperature observations. This shows that the STE observed in association with tropical cyclone Marlene was not an isolated event, and that the synoptic context is an important influence on the variability of tropospheric ozone signatures.

[66] In the Guillaume case study, filamentation and subsidence occurred in the two configurations: without an ozone peak but a moderate enhancement of ozone in the major part of the free troposphere on 15 February 2002

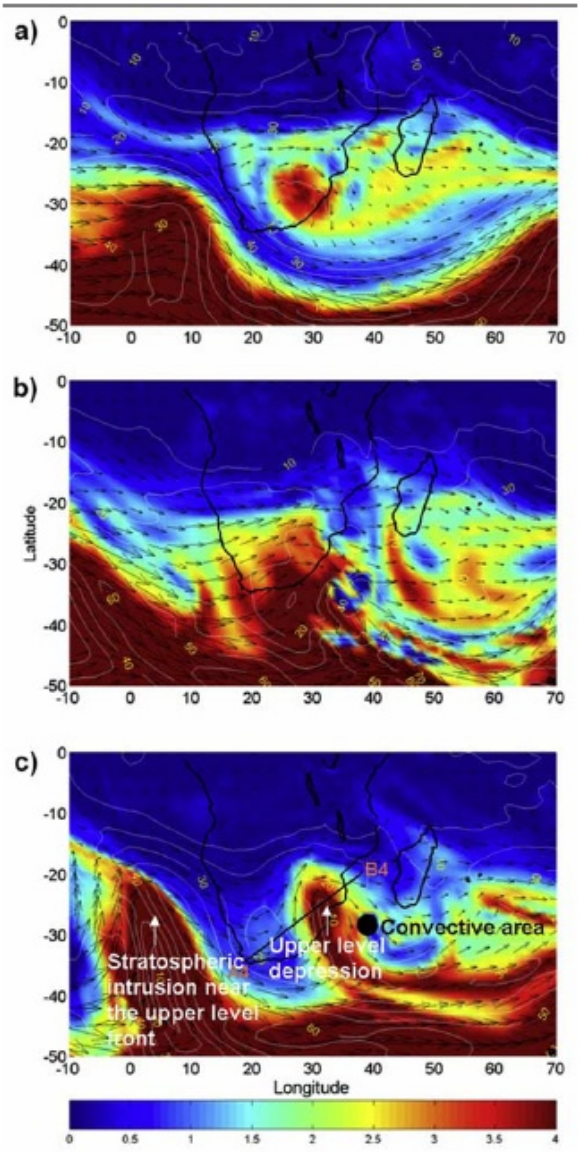

Figure 14. ECMWF potential vorticity (absolute value) on the 350 K isentropic surface on (a) 11 November 2000, (b) 13 November 2000, and (c) 15 November 2000 at 1200 UT. Horizontal wind and geopotential height have been superimposed. A-B indicates the limits of the vertical cross section shown in Figure 15.

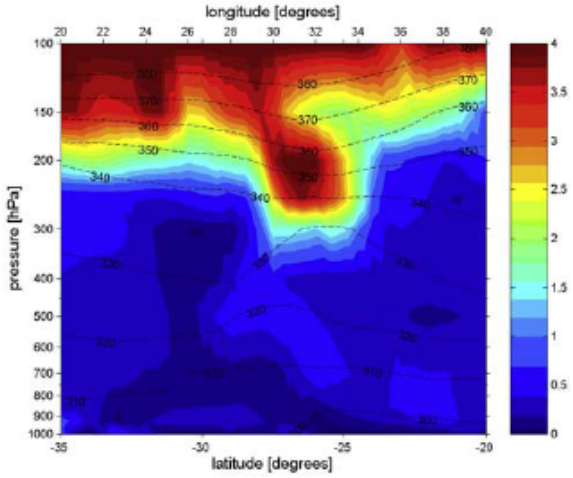

Figure 15. Potential vorticity (absolute) vertical cross section whose trace is marked on Figure 14. The potential temperature (K) contours have been superimposed.

(depression), and with a 100 ppbv ozone peak on 19 February 2002 (cyclone).

[67] In the Irene case study, a large upper level depression coming from the stratosphere, fed by a filament around the divergent zone above the convective area in the Mozambican channel, induced an ozone peak of larger magnitude (170 ppbv) on 15 November 2000. Moreover, secondary ozone sources (a jet front system above the Atlantic and biomass burning in South America) could amplify this ozone enhancement. The radiosounding showed strong ozone enrichment in the upper troposphere, without a signature of pumping from the lower layers, in contrast to the Guillaume case study.

[68] Present observations show that not only cyclones but also cases of deep convection are likely to induce exchanges of air masses between the lower stratosphere and the upper troposphere, especially when deep convection interacts with the subtropical jet stream. Moreover, we have observed that the respective contributions of dynamical components of the interaction at the origin of the ozone intrusion can vary considerably.

[69] The climatological analysis from the Reunion database suggests that the cyclonic mean ozone profile, formed from profiles influenced by cyclones, is characterized by above average ozone values in the mean troposphere. In the upper troposphere the reverse behavior is observed.

[70] This climatological result, with regard to the dynamical elements shown in the case studies, is consistent with the hypothesis put forward at the end of section 3: a dual influence of the convective systems (tropical storms, depressions and cyclones) on the climatology of tropospheric ozone: transfer of ozone from the stratosphere to the midtroposphere and a pumping of ozone-poor air masses from the boundary layer to the upper troposphere.

[71] To further diagnose the fine structure of the upper level interactions associated with convection-induced STE, mesoscale model studies are necessary. Owing to a better resolution, model analyses are actually expected to lead to an improved evaluation of STE induced by deep convection.

[72] **Acknowledgments.** The Laboratoire de Physique de l'Atmosphère is supported by the Centre National de la Recherche Scientifique (CNRS)/Institut National des Sciences de l'Univers (INSU) and the Conseil Régional de La Réunion. Authors are thankful to the ECMWF center for making access to the archived data, to Andreas Stohl for providing the FLEXPART model and Eumetsat for providing the Meteosat data. We thank Françoise Posny and Jean-Marc Metzger for the two balloon launches during the Guillaume event, which were supported by the Programme National de Chimie Atmosphérique (PNCA). We acknowledge Thierry Lin-Chan for his preliminary work on the Irene case study and also Serge Baldy for helpful discussions and suggestions.

References

Baldy, S., G. Ancellet, M. Bessafi, A. Badr, and D. L. S. Luk (1996), Field observation of the vertical distribution of tropospheric ozone at the island of Reunion (southern tropics), *J. Geophys. Res.*, *101*, 23,835–23,849.

Baray, J. L., G. Ancellet, T. Randriambelo, and S. Baldy (1999a), Tropical cyclone Marlene and stratosphere-troposphere exchange, *J. Geophys. Res.*, *104*, 13,953–13,970.

Baray, J. L., J. Leveau, J. Porteneuve, G. Ancellet, P. Keckhut, F. Posny, and S. Baldy (1999b), Description and evaluation of a tropospheric ozone lidar implemented on an existing lidar in the southern subtropics, *Appl. Opt.*, *38*, 3817–6808.

Baray, J. L., T. Randriambelo, S. Baldy, and G. Ancellet (2001), Comment on "Tropospheric O_3 distribution over the Indian Ocean during spring 1995 evaluated with a chemistry-climate model" by A. T. J. de Laat et al., *J. Geophys. Res.*, *106*, 1365–1368.

Baray, J. L., S. Baldy, R. D. Diab, and J. P. Cammas (2003), Dynamical study of a tropical cut-off low over South Africa, and its impact on tropospheric ozone, *Atmos. Environ.*, *37*, 1475–1488.

Barnes, R. A., A. R. Bandy, and A. L. Torres (1985), Electrochemical concentration cell ozonesonde accuracy and precision, *J. Geophys. Res.*, *90*, 7881–7887.

Bethan, S., G. Vaughan, and S. J. Reid (1996), A comparison of ozone and thermal tropopause heights and the impact of tropopause definition on quantifying the ozone content of the troposphere, *Q. J. R. Meteorol. Soc.*, *122*, 928–944.

Bithell, M., G. Vaughan, and L. J. Gray (2000), Persistence of stratospheric ozone layers in the troposphere, *Atmos. Environ.*, *34*, 2563–2570.

Browell, E. V., et al. (1996), Ozone and aerosol distributions and air mass characteristics over the South Atlantic Basin during the burning season, *J. Geophys. Res.*, *101*, 24,043–24,068.

Chatfield, R. B., and P. J. Crutzen (1984), Sulfur dioxide in remote oceanic air: Cloud transport of reactive precursors, *J. Geophys. Res.*, *89*, 7111–7132.

Cooper, O. R., J. L. Moody, D. D. Parrish, M. Trainer, J. S. Holloway, G. Hübler, F. C. Fehsenfeld, and A. Stohl (2002), Trace gas composition of midlatitude cyclones over the western North Atlantic Ocean: A seasonal comparison of O_3 and CO, *J. Geophys. Res.*, *107*(D7), 4057, doi:10.1029/2001JD000902.

Crutzen, P. J., L. E. Heidt, J. P. Krasnec, W. H. Pollock, and W. Seiler (1979), Biomass burning as a source of atmospheric gases CO, H_2, N_2O, NO, CH_3Cl, and COS, *Nature*, *282*, 253–256.

De Laat, A. T. J., M. Zachariasse, G. J. Roelofs, P. van Velthoven, R. R. Dickerson, K. P. Rhoads, S. J. Oltmans, and J. Lelieveld (1999), Tropospheric O_3 distribution over the Indian Ocean during spring 1995 evaluated with a chemistry-climate model, *J. Geophys. Res.*, *104*, 13,881–13,893.

Diab, R. D., et al. (1996), Vertical ozone distribution over southern Africa and adjacent oceans during SAFARI-92, *J. Geophys. Res.*, *101*(D19), 23,823–23,834.

Diab, R. D., A. M. Thompson, K. Mari, L. Ramsay, and G. J. R. Coetzee (2004), Tropospheric ozone climatology over Irene, South Africa, from 1990 to 1994 and 1998 to 2002, *J. Geophys. Res.*, *109*, D20301, doi:10.1029/2004JD004793.

Dickerson, R. R., et al. (1987), Thunderstorms: An important mechanism in the transport of air pollutants, *Science*, *235*, 460–465.

Emanuel, K. A., and M. Zivkovic-Rothman (1999), Development and evaluation of a convection scheme for use in climate models, *J. Atmos. Sci.*, *56*, 1766–1782.

Fishman, J., C. E. Watson, J. C. Larsen, and J. A. Logan (1990), Distribution of tropospheric ozone determined from satellite data, *J. Geophys. Res.*, *95*, 33,599–36,117.

Folkins, I., and C. Appenzeller (1996), Ozone and potential vorticity at the subtropical tropopause break, *J. Geophys. Res.*, *101*, 18,787–18,792.

Fujiwara, M., K. Kita, S. Kawakami, T. Ogawa, N. Komala, S. Saraspriya, and A. Suripto (1999), Tropospheric ozone enhancements during the Indonesian forest fire events in 1994 and in 1997 as revealed by ground-based observations, *Geophys. Res. Lett.*, *26*, 2417–2420.

Gettelman, A., and P. M. De F. Forster (2002), Climatology of the tropical tropopause layer, *J. Meteorol. Soc. Jpn.*, *80*, 911–924.

Gouget, H., J. P. Cammas, A. Marenco, R. Rosset, and I. Jonquières (1996), Ozone peaks associated with a subtropical tropopause fold and with the trade wind inversion: A case study from the airborne campaign TROPOZ II over the Caribbean in winter, *J. Geophys. Res.*, *101*, 25,979–25,993.

Gray, W. M. (1979), Hurricanes: Their formation, structure and likely role in tropical circulation, in *Meteorology Over the Tropical Oceans*, pp. 155–218, R. Meteorol. Soc., Reading, U. K.

Hoskins, B. J. (1991), Towards a PV-θ view of the general circulation, *Tellus*, *43*, 27–35.

Loring, R. O., Jr., H. E. Fuelberg, J. Fishman, M. V. Watson, and E. V. Browell (1996), Influence of a midlatitude cyclone on tropospheric ozone distributions during a period of TRACE A, *J. Geophys. Res.*, *101*, 23,941–23,956.

McBride, J. (1995), Global perspectives on tropical cyclones, *TD 693 TCP 38*, pp. 63–105, World Meteorol. Organ., Geneva, Switzerland.

Mitra, A. P. (1996), Troposphere-stratosphere coupling and exchange at low latitude, *Adv. Space Phys.*, *17*, 1189–1197.

Postel, G. A., and M. H. Hitchman (1999), A climatology of Rossby wave breaking along the subtropical tropopause, *J. Atmos. Sci.*, *56*, 359–373.

Poulida, O., R. R. Dickerson, and A. Heymsfield (1996), Stratosphere-troposphere exchange in a midlatitude mesoscale convective complex: 1. Observations, *J. Geophys. Res.*, *101*, 6823–6836.

Randriambelo, T., S. Baldy, M. Bessafi, M. Petit, and M. Despinoy (1998), An improved detection and characterization of active fires and smoke plumes in south-eastern Africa and Madagascar, *Int. J. Remote Sens.*, *19*(14), 2623–2638.

Randriambelo, T., J. L. Baray, and S. Baldy (2000), Effect of biomass burning, convective venting, and transport on tropospheric ozone over the Indian Ocean: Reunion Island fields observations, *J. Geophys. Res.*, *105*, 11,813–11,832.

Réchou, A., J. L. Baray, S. Baldy, and T. Portafaix (2002), Influence of deep convection on the injection of ozone into the troposphere (stratosphere-troposphere exchange), paper presented at 21st International Laser Radar Conference, Int. Assoc. of Meteorol. and Atmos. Phys., Quebec City, Que., Canada.

Rodgers, E. B., J. Stout, J. Steranka, and S. Chang (1990), Tropical cyclone-upper atmospheric interaction as inferred from satellite total ozone observations, *J. Appl. Meteorol.*, *29*, 934–954.

Scott, R. K., J. P. Cammas, P. Mascart, and C. Stolle (2001), Stratospheric filamentation into the upper tropical troposphere, *J. Geophys. Res.*, *106*, 11,835–11,848.

Stenchikov, G., R. R. Dickerson, K. Pickering, W. Ellis, B. Doddridge, S. Kondragunta, O. Poulida, J. Scala, and W. K. Tao (1996), Stratosphere-troposphere exchange in a midlatitude mesoscale convective complex: 2. Numerical simulations, *J. Geophys. Res.*, *101*, 6837–6851.

Stohl, A., and T. Trickl (1999), A text example of long-range transport: Simultaneous observation of ozone maxima of stratospheric and North American origin in the free troposphere over Europe, *J. Geophys. Res.*, *104*, 30,445–30,462.

Stohl, A., M. Hittenberger, and G. Wotawa (1998), Validation of the Lagrangian particle dispersion model FLEXPART against large scale tracer experiment data, *Atmos. Environ.*, *32*, 4245–4264.

Thompson, A. M., K. E. Pickering, D. P. McNamara, M. R. Schoeberl, R. D. Hudson, J. H. Kim, E. V. Browell, V. W. J. H. Kirchhoff, and D. Nganga (1996), Where did tropospheric ozone over southern Africa and the tropical Atlantic come from in October 1992? Insights from TOMS, GTE/TRACE-A and SAFARI-92, *J. Geophys. Res.*, *101*, 24,251–24,278.

Thompson, A. M., et al. (2003), Southern Hemisphere Additional Ozonesondes (SHADOZ) 1998–2000 tropical ozone climatology: 1. Comparison with Total Ozone Mapping Spectrometer (TOMS) and ground-based measurements, *J. Geophys. Res.*, *108*(D2), 8238, doi:10.1029/2001JD000967.

Wang, C., P. J. Crutzen, and V. Ramanathan (1995), The role of a deep convective storm over the tropical pacific ocean in the redistribution of atmospheric chemical species, *J. Geophys. Res.*, *100*, 11,509–11,516.

G. Ancellet, Service d'Aéronomie, CNRS-UMR 7620, Boite 102, Université Pierre et Marie Curie, 4 Place Jussieu, F-75252 Paris Cedex 05, France.

J. L. Baray, J. Leclair De Bellevue, and A. Réchou, Laboratoire de l'Atmosphère et des Cyclones, CNRS-UMR 8105, Université de La Réunion, 15 Av. René Cassin, BP 7151, F-97715 Saint-Denis Messag Cedex 9, La Réunion, France. (j.ldb@univ-reunion.fr)

R. D. Diab, School of Environmental Sciences, Howard College Campus, University of KwaZulu-Natal, Durban 4041, South Africa.

2.2.4 Variabilité de l'ozone troposphérique pendant la saison des feux de biomasse

Annales Geophysicae (2003) 21: 2095–2106 © European Geosciences Union 2003

Annales Geophysicae

Investigation of the short-time variability of tropical tropospheric ozone

T. Randriambelo[1], J.-L. Baray[1], S. Baldy[1], A. M. Thompson[2], S. Oltmans[3], and P. Keckhut[4]

[1]Laboratoire de Physique de l'Atmosphere, UMR-CNRS 8105,15 Avenue René Cassin, Reunion Island 97715, France
[2]NASA Goddard Laboratory for Atmosphere, GSFC, Greenbelt, MD, USA
[3]NOAA, Climate Monitoring and Diagnostics Laboratory, Boulder, Colorado, 325 Broadway, Boulder, Colorado, USA
[4]Service d'Aeronomie, BP 3, 91371 Verriéres-le-Buisson Cedex Paris, France

Received: 10 July 2002 – Revised: 10 February 2003 – Accepted: 28 February 2003

Abstract. Since 1998, a ground-based tropospheric ozone lidar has been running at Reunion Island and has been involved with a daily measurement campaign that was performed in the latter part of the biomass burning season, during November–December 1999. The averaged ozone profile obtained during November–December 1999 agrees well with the averaged ozone profile obtained from the ozonesondes launch at Reunion during November–December (1992–2001). Comparing weekly sonde launches (part of the Southern Hemisphere Additional Ozonesondes: SHADOZ program) with the daily ground-based lidar observations shows that some striking features of the day-to-day variability profiles are not observed in the sonde measurements. Ozone profiles respond to the nature of disturbances which vary from one day to the next.

The vertical ozone distribution at Reunion is examined as a function of prevailing atmospheric circulation. Back trajectories show that most of the enhanced ozone crossed over biomass burning and convectively active regions in Madagascar and the southern African continent. The analyses of the meteorological data show that ozone stratification profiles are in agreement with the movement of the synoptic situations in November–December 1999. Three different sequences of transport are explained using wind fields. The first sequence from 23 to 25 November is characterized by northerly transport; during the second sequence from 26 to 30 November, the air masses are influenced by meridional transport. The third sequence from 2 to 6 December is characterized by westerly transport associated with the subtropical jet stream. The large, standard deviations of lidar profiles in the middle and upper troposphere are in agreement with the upper wind variabilities which evidence passing ridge and trough disturbances. During the transition period between the dry season and the wet season, multiple ozone sources including stratosphere-troposphere exchanges, convection and biomass burning contribute to tropospheric ozone at Reunion Island through sporadic events characterized by a large spatial and temporal variability.

Key words. Atmospheric composition and structure (troposphere-composition and chemistry) – Meteorology and atmospheric dynamics (climatology; tropical meteorology)

Correspondence to: T. Randriambelo
(randriam@univ-reunion.fr)

1 Introduction

In the southern tropics, photochemical formation from biomass burning emissions is an important source of ozone. International measurement programs like SAFARI (Southern African Fire-Atmosphere Research Initiative) and TRACE A (Transport and Atmospheric Chemistry near Equator Atlantic) (Andreae et al., 1996), TROPOZ (TROPospheric OZone) (Marenco et al., 1990), and DECAFE (Dynamique Et Chimie de l'Atmosphère en Forêt Equatoriale) (Lacaux et al., 1995) have characterised the role of pollutant emissions over Africa, one of the principal regions of biomass burning in the Southern Hemisphere. One of the objectives of these campaigns was to study atmospheric photochemistry and tropospheric circulation patterns in relation to the enhanced ozone concentration observed over the southern Africa continent and the adjacent oceans (Fishman et al., 1990; Thompson et al., 1996). The contribution of the stratospheric air is also observed in the southern Africa during meteorological disturbances, such as westerly waves, cut-off low and frontal zones (Bachmeier and Fuelberg, 1996; Diab et al., 1996a, b; Fuelberg et al., 1996; and Garstang et al., 1996). Meteorological analysis demonstrates that a large part of the flow from the African continent, evaluated on trajectory statistics, could be advected towards the Indian Ocean (Garstang et al., 1996). Consequently, Reunion Island (21° S, 55° E) should be a well-suited location for the study of the transport of aerosols and trace gases in plumes from southern Africa.

Since 1992, the ozone profiles observed at Reunion Island support these findings. Analyses of ozonesondes showed

the influence of different contamination mechanisms from biomass burning by-products (Baldy et al., 1996; Taupin et al., 1999, 2001) and stratosphere troposphere exchange (Baray et al., 1998). The climatology using ozonesondes and satellite observations of fire and convective areas pinpoint the impact of different mechanisms (Randriambelo et al., 2000). A case study of extremely high ozone mixing ratio, where stratosphere-troposphere exchange and anthropogenic emissions work together, has been reported (Randriambelo et al., 1999).

In the southern Africa, meteorological conditions exert a major influence on the horizontal and vertical distributions of aerosols and trace gases (Fuelberg et al., 1996; Garstang et al., 1996). Daily measurements at Namibia give evidence of the influence of anticyclones and troughs on the vertical distribution of ozone (Diab et al., 1996a). Over the Pacific persistent layers of high ozone from biomass burning are evident in MOZAIC (Measurement of Ozone and Water Vapor by Airbus In-Service Aircraft) data and also in soundings (Newell et al., 1999; Stoller et al., 1999). Thus, it is of special interest to study the influence of meteorological conditions on vertical ozone distributions in the Indian Ocean. Because of the low frequency of in situ measurements (weekly or less), it has been hard to characterize the day-to-day variability of tropospheric ozone. Several studies based on INDOEX measurements (De Laat et al., 1999; Zachariasse et al., 2000) have dealt with short-term variability of ozone though mainly north of the equator and in the Indian Ocean, when the convective activity is maximum, and biomass burning in Southern Africa is minimum (February-April) (Cahoon et al., 1992; Barbosa et al., 1999; Arino et al., 2001).

From these studies, and with the SHADOZ program providing regular ozone profiles for ten stations in the Southern Hemisphere (Thompson et al., 2003a), the climatological impact of biomass burning, including its horizontal extent and timing has been documented. The "curtain figures" of the ozone mixing ratio show that week-to-week variability is intense at most SHADOZ stations (Thompson et al., 2003b). In particular, alternation of clean and polluted layers is observed during the biomass burning season. Since Reunion Island is both influenced by stratosphere troposphere exchanges and biomass burning, Reunion station data is expected to be characteristic of SHADOZ data set variability. The question still to be answered is whether biomass burning leads to an enhancement of the background ozone or to sporadic enhancements of ozone, with a large variability on a day-to-day time scale. This day-to-day monitoring could be achieved by complementing SHADOZ data by lidar measurement campaigns.

Since 1998, a ground-based tropospheric ozone lidar has been running at Reunion Island University. A first intensive measurement campaign performed during austral winter (July 1998) was used to study planetary scale tropopause folds (Baray et al., 2000). The objective of the present paper is to analyze a second lidar campaign (one lidar sounding per night) performed in November–December 1999. This period corresponds to the transition between the dry season and the rainy season, where traditional intensive forest fires from shifting cultivation are the practice in Madagascar (Randriambelo et al., 1998). This new data set is used to investigate the day-to-day variability of tropospheric ozone in the context of meteorological conditions.

2 Data

This study is principally based on remotely sensed data obtained by a ground-based tropospheric ozone lidar at Reunion Island. Measurements of tropospheric ozone are made by differential absorption in the ultraviolet (289–316 nm). These wavelengths are obtained by stimulated Raman scattering of the fourth harmonic of the Nd-Yag laser beam in a high-pressure deuterium cell. The reception system includes a mosaic of 4 parabolic mirrors, which collect the backscattered signal. The signal is then transmitted by optical fibers. Spectral separation of the 289 and 316 beams is obtained with a spectrometer that includes a Czerny-Turner holographic grating of 3600 lines/mm. Then each beam is redirected toward non-cooled Hamamatsu R1527P PMTs (Photomultiplier tubes) by concave mirrors. The signal processing electronic chain and data processing are similar to those used at the Observatoire de Haute Provence ozone lidar station (Ancellet et al., 1991). Technical details of the system and validation measurements (comparisons with electrochemical concentration cell ozone soundings) are given in Baray et al. (1999).

The lidar altitude ranges from 3 km to around 15 km, with the upper limit depending on the meteorological conditions and ozone amount, and on the alignment of the reception system. The altitude resolution of the final ozone profiles is 15 m for the analog signal (from 3 to 6–7 km), and 150 m for the photon-counting signal (from 6–7 km to the upper limit). Lidar measurements were made on almost all the days from 23 November to 6 December 1999. The acquisition time is from 30 to 45 min for each profile, generally beginning at night under clear sky conditions (near 16:00–17:00 UT which corresponds to 20:00–21:00 LT). One profile per night corresponding to the averaged acquisition is considered.

One ozone sounding was performed during this intensive campaign (on 2 December 1999), providing a profile of ozone mixing ratio (measured by electro-chemical concentration cell ozone), temperature and relative humidity (measured by a Vaisala RS 80-15 radiosonde). The vertical resolution of the ozonesonde is around 50 m and launches are generally made early in the morning, (near 07:00 UT). The characteristics of the ozonesonde are detailed elsewhere (Baldy et al., 1996).

These in situ data are augmented by the global product of satellite TOMS data (Total Ozone Mapping Spectrometer), and by ECMWF analysis data (European Centre for Meteorological Weather Forecast). In 1999, the TOMS spectrometer was on board the Earth Probe observation satellite, providing a global coverage of the total ozone column with a

resolution of 1.25 degree in longitude and 1 degree in latitude. ECMWF data used are T213 spherical harmonics, interpolated to a horizontal resolution of 1 degree in longitude and latitude, and 15 vertical levels between 1000 and 10 hPa. Back trajectories calculated from ECMWF data are used. The validation of kinematic back trajectories has been addressed elsewhere (Baldy et al., 1996; Randriambelo et al., 2000).

3 Atmospheric circulation during November – December

3.1 Dynamical context

Southern Africa and adjacent Atlantic and Indian Oceans are located in the region of large-scale subsidence occurring between the Hadley and Ferrel cells of the Southern Hemisphere general circulation. Subsidence is the dominant features of the circulation. The circulation patterns in the southern Africa and the adjacent oceans are described by Preston-Whyte and Tyson (1988). The main elements affecting the day-to-day weather in southern Africa and the Indian ocean owe their origin to subtropical, tropical and temperate features of the general circulation. The subtropical control is effected through the semi-permanent south Indian anticyclone, the continental high and the south Atlantic anticyclone. The south Atlantic and Indian anticyclones vary significantly in position throughout the year in their latitudinal and zonal position. On the scale of days, the south Atlantic high may ridge eastward and to the south continent. Extended ridging leads to breaking of a separate high, which drifts eastward into the Indian Ocean before being subsumed into the South Indian high. The tropical control is effected through tropical easterly flow in the southern Africa and the low level easterly jet stream equatorward of Reunion Island. The temperate control is exerted through travelling perturbations in the westerlies.

3.2 Circulation at surface level

The wind fields at 925 hPa show that several prominent circulation features are present in the study region from 23 November to 6 December 1999 (Fig. 1). The south Atlantic anticyclone position varies during the period. Two ridging south Atlantic anticyclones are observed near 40 S, 22 E for the 24 November (Fig. 1a) and near 37 S, 35 E for the 30 November (Fig. 1c). They moved eastward to reach the south Indian anticyclone after around two days. The westerly waves associated with a trough are regularly observed in the edge of the southern Africa and move towards the Indian Ocean. These westerly waves are associated with a cold front that passes over South Africa. During the period November–December 1999, the frontal zone does not reach Reunion Island.

Reunion Island is under the influence of the south Indian anticyclone and the easterly low-level jet stream (Fig. 1). Table 1 shows that the position of the south Indian anticyclone

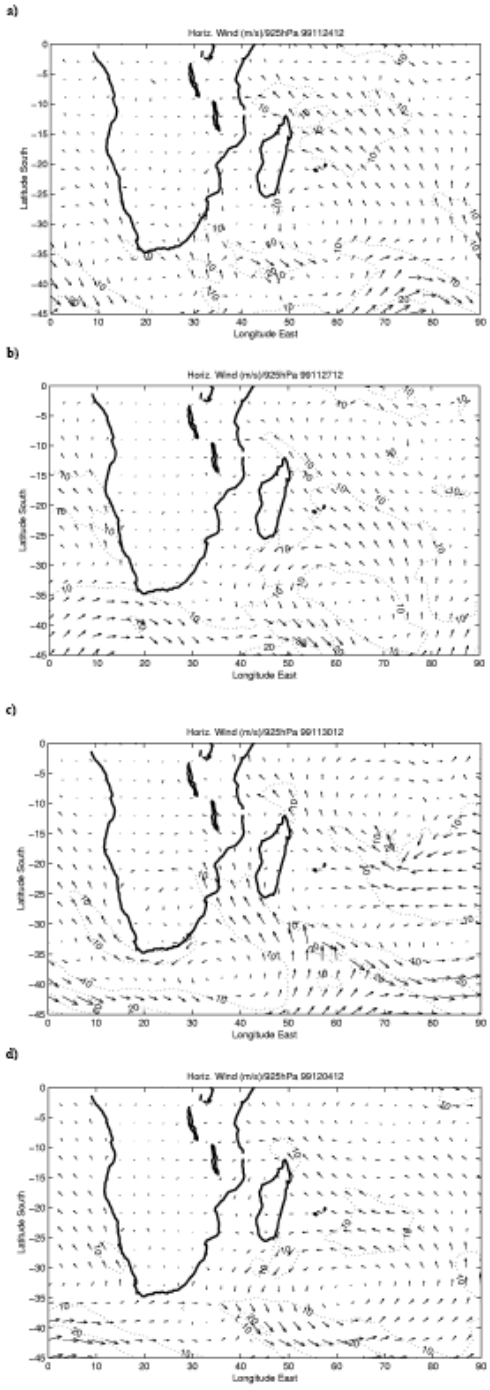

Fig. 1. Wind fields at 925 hPa from ECMWF data showing the circulation patterns at low level in the southern Africa and the adjacent oceans for (**a**) 24 November, (**b**) 27 November, (**c**) 30 November, and (**d**) 4 December.

Table 1. Location of the center of the south Indian anticyclone and the zonal winds as function of the day at 925 hPa and at 250 hPa

Day	latitude	longitude	925 hPa (m/s)	250 hPa (m/s)
23	28	58	3,40	14,83
24	28	55	5,03	17,9
25	25	43	5,10	8,86
26	42	52	5,55	5,77
27	37	66	6,56	10,34
28	32,5	64	6,40	8,52
29	34	73	4,98	7,47
30	31	85	1,13	1,69
1	37	45	2,94	16,43
2	37	48	4,19	22,72
3	37	48	3,66	24,5
4	36	61	3,62	24,13
5	35	67	2,08	15,91
6	35	72	2,61	14,49

varies along latitudinal and longitudinal positions. The south Indian anticyclone moves towards the east, pushed by the passage of the regular frontal zones. The Indian Ocean anticyclone is displaced in its maximum eastward position for 30 November and 6 December (Fig. 1c, Table 1). The daily wind fields at surface level show three different sequences of circulation. First, from 23 to 25 November, the latitudinal variation is weak and corresponds to the end of the addition of the ridging south Atlantic anticyclone and the south Indian anticyclone. For the second period from 26–30 November, the latitudinal variation of the south Indian anticyclone is strong. For the third period from 1 to 6 December, the south Indian anticyclone is stronger than the first period and its latitudinal variation is weak.

3.3 Circulation at high altitude

The wind fields at 250 hPa show that the upper level anticyclone and the westerly waves are observed in the southern Africa and the adjacent oceans (Fig. 2). In the Indian Ocean, as at surface level, the winds fields present three different sequences of circulation. First, from 23–25 November, the winds come from the north (Fig. 2a). The second period of 26–30 November is under the influence of a strong curvature of the westerly waves and the winds come from the south (Fig. 2b). The third period from 1 to 6 December is associated with a weak curvature of the jet stream (Fig. 2d). The beginning of this period is influenced by the northerly winds and ends with the displacement of the jet stream towards the east.

The upper wind fields observed at Reunion Island also give evidence of an important variability (Fig. 3). At ground level, the trade-wind regime appears regular. Above 800 hPa, the variability depends on location of the subtropical jet stream, and the influence of the tropical convection. The upper wind variabilities are in agreement with the different sequences of

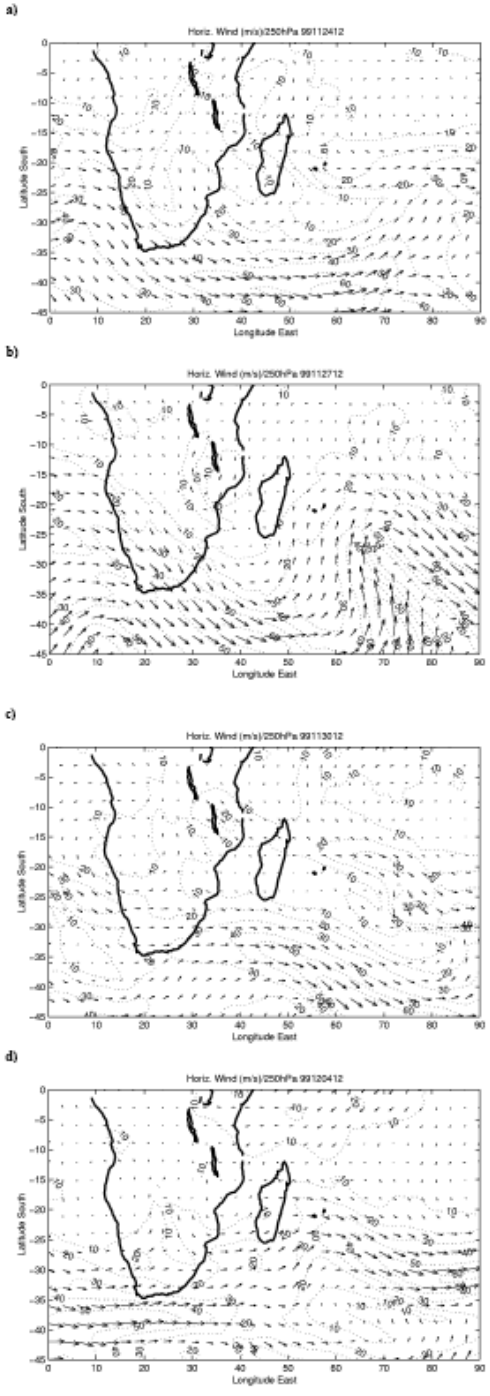

Fig. 2. Wind fields at 250 hPa from ECMWF data showing the circulation patterns at the upper troposphere in the southern Africa and the adjacent for (**a**) 24 November, (**b**) 27 November, (**c**) 30 November, and (**d**) 4 December.

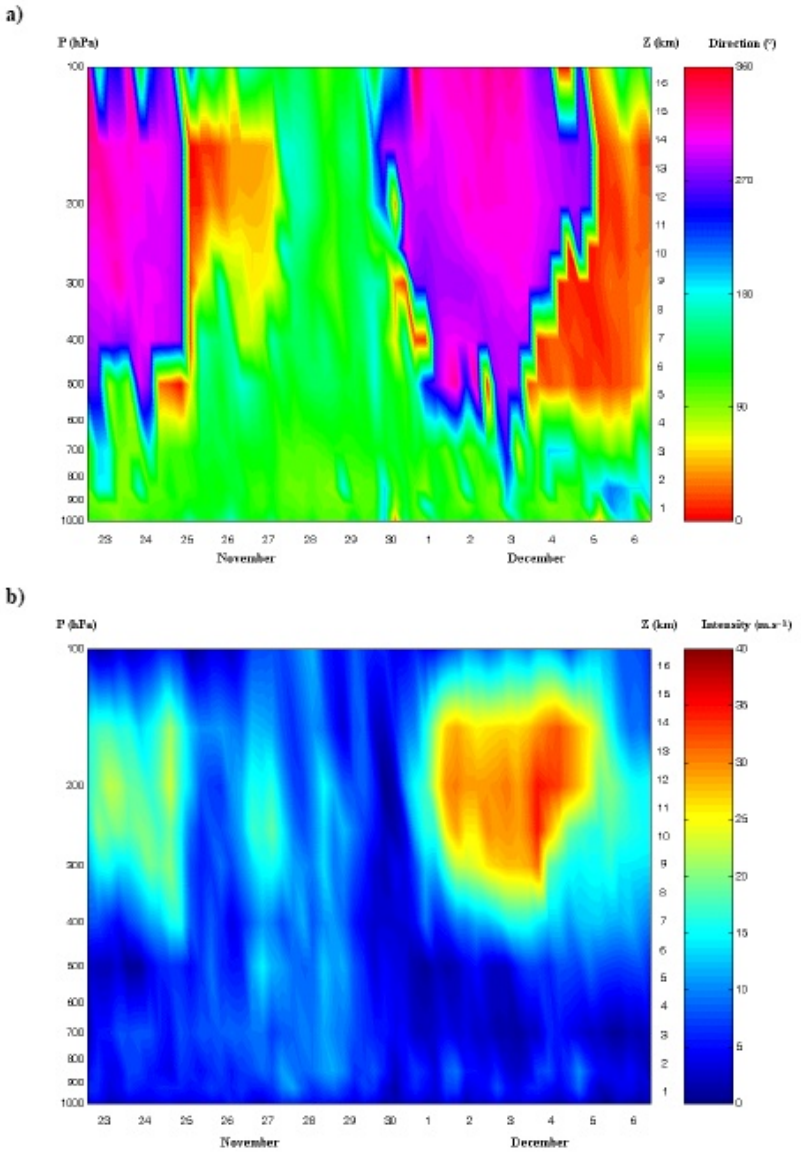

Fig. 3. (a) Horizontal wind direction (in degrees), and (b) intensity (in $m.s^{-1}$) over Reunion Island from 23 November to 6 December 1999. The direction 0° means a wind direction toward east, 90° toward north, 180° toward west and 270° toward south. The figure has been built from ECMWF with every 6 h outputs.

circulation which show passing ridge and trough sequences.

The meteorological data from ECMWF show that both wind fields at the surface level and at the high altitude show three different sequences of circulation. These results are in agreement with those obtained elsewhere (Preston-Whyte and Tyson, 1988; Garstang et al., 1996). These meteorological patterns can induce considerable day-to-day variability on the atmospheric circulation in southern Africa and the adjacent oceans, and consequently could affect the redistribution and transport of aerosols and trace gases.

4 Tropospheric ozone at the end of the biomass burning season: measurements and analysis

4.1 Vertical ozone distribution

In order to study the day-to-day ozone variation during the end of the biomass burning period, a continuous survey of ozone was undertaken during the period from 23 November to 6 December 1999. The ozone profiles from lidar measurements, presented in Fig. 4, show that daily con-

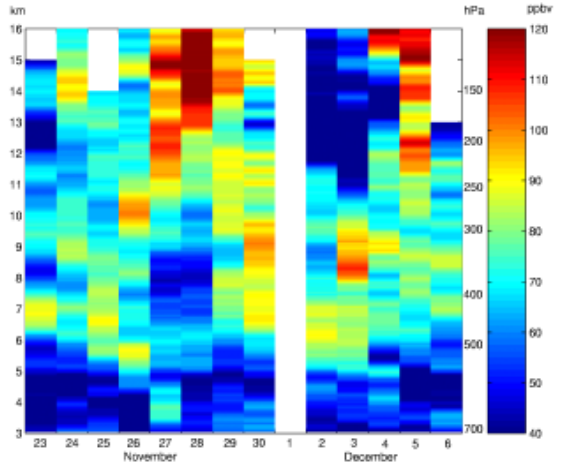

Fig. 4. Evolution of ozone mixing ratio (as a function of altitude in km) over Reunion Island measured by lidar from 23 November to 6 December 1999. The color scale on the right gives values in ppbv.

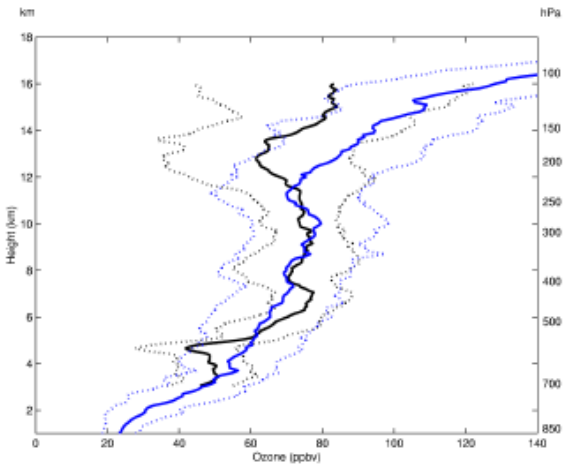

Fig. 5. Comparison of ozonesondes (bi-monthly or less 1992–1998, and weekly or less SHADOZ 1999–2001) (blue) and lidar (black) mean ozone profiles and the corresponding standard deviations.

centrations are in accordance with climatological profiles corresponding to the November–December period including bi-monthly (or less) ozonesondes (1992–1998) and weekly (or less) ozonesondes recorded from SHADOZ (1999–2001) (Fig. 5). Hence, the November–December 1999 campaign period corresponds to typical months.

Actually, the comparison of the averaged ozonesondes and lidar averaged ozone profiles show that both profiles present the same features with five distinct layers. Below 5 km, the ozonesonde mixing ratios are larger than lidar. Above 5 km, both profiles display an ozone increase, but lidar ozone mixing ratios are larger than the ozonesondes until 7 km. Above 7 km, there is a coincidence of diminution of ozone (7.5–8.5 km) followed by an augmentation of ozone (8.5–11 km) for both profiles. Above, the two profiles decrease, and reach the minimum at different altitudes from 10 to 11 km for the ozonesondes and from 12 to 13 km for the lidar. Indeed, the decrease around 12 km was observed by the ozonesondes and lidar on 2 December.

During this period, the ozonesonde of 2 December (Fig. 6) displays the same ozone enhancement (80 ppbv between 6 and 11 km) as the lidar profile obtained in the nighttime. The relative humidity profile shows high values below 3 km, with moderately large values in the free troposphere. Humidity values observed within the free troposphere, between 3 and 10 km are concordant with the climatological profiles obtained during austral summer for Reunion station, presented in Baray et al. (1998).

The comparison of the seasonal picture based on ozonesonde observations and the continuous ground-based lidar observations shows large, standard deviation values (Fig. 5). Thus, high values of the lidar standard deviation show that the day-to-day variability is intense. It is to be noted further that the weekly SHADOZ measurements display a strong variation of ozone mixing ratios (Thompson et al., 2003b), but some daily striking features are not observed during weekly measurements. Consequently, the day-to-day variability of ozone needs to be considered.

The lidar ozone mixing ratios show that ozone enhancements are observed in the whole free troposphere from 5 km (Fig. 4). The maximum enhancement (> 100 ppbv) is observed on 3 December 1999, where ozone enhancements are observed regularly in the free troposphere from 5 to about 11 km. These ozone enhanced layers do not persist from one day to the following day, and display a high day-to-day variability of ozone mixing ratios. Ozone layers are very stratified on many days (especially 23 November, 26 November and 3 December), with thin layers (1 to 2 km thick) of very enhanced ozone mixing ratio (more than 30–40 ppbv, by comparison with adjacent ozone layers).

The stratification was not observed in the austral winter 1998 measurements from ozonesounding and lidar (Baray et al., 2000). Hence, it is interesting to compare the results of the austral summer of 1999 to the austral winter month July of 1998. During this period, an intensive measurement campaign was performed at Reunion Island and at Irene in South Africa.

Dynamical analysis showed the influence of planetary scale tropopause folds over the whole Indian Ocean (Baray et al., 2000). Figure 1 of Baray (2000) shows that, compared to the ozone enhancement during November–December 1999, the ozone enhancement induced by these planetary tropopause folds during July 1998 appears to have almost the same intensity (about 70 ppbv) but is more confined in height, between 6 and 9 km height. The ozone increase observed during November–December is less localized at different heights in the free troposphere.

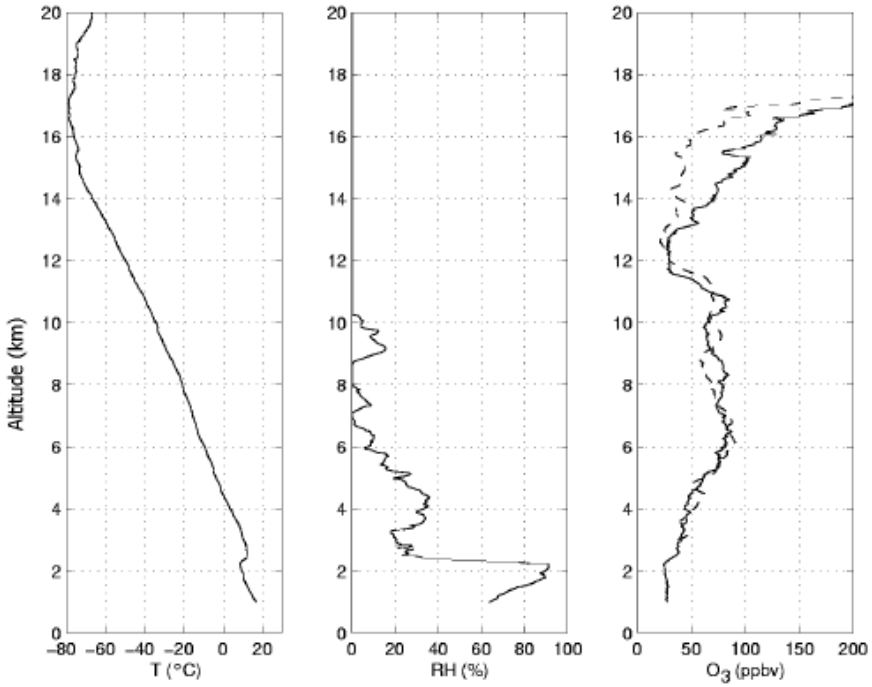

Fig. 6. Temperature (left), relative humidity (middle) and ozone mixing ratio (right) profiles obtained by ozonesounding on 2 December 1999, in the morning (continuous lines), and ozone mixing ratio profile obtained the same day at the end of the evening by lidar (dashed lines).

4.2 Comparison between the synoptic situations and vertical ozone distribution

The ozone profiles display three sequences in agreement with synoptic situations near source region and over Reunion Island. First, the 23–25 November period corresponds to the enhancement of ozone in the middle troposphere, which is in accordance to the winds that come from the northwest in the middle and upper troposphere. Second, the 26–30 November period corresponds to the enhancement of the upper tropospheric ozone and coincides with the strong westerly waves. The low ozone values (<50 ppbv) during 27–28 November in the middle and low altitude correspond to ozone-poor mid-latitude air masses, and the strong ozone values observed in the upper troposphere correspond to a stratospheric intrusion along the strong westerly wave. The ozone increase observed in the whole free troposphere on 30 November corresponds to a transition period for the middle latitude and the tropical influences in the middle troposphere. The third period from 2 to 6 December corresponds to the stronger values of ozone in the middle troposphere (>100 ppbv) and coincides with the shifting of the jet streak and the northerly winds. The ozone maximum observed on 3 December coincides with the presence of the jet streak over Reunion Island and the low ozone is associated with the northerly winds (<50 ppbv) in the upper troposphere (Fig. 7). For 4–5 December, the ozone peak and the decreased ozone tend to disappear, and the ozone profiles display a regular ozone enhancement with altitude resulting from the shifting of the northerly winds and the jet stream influences. During this period, tropospheric ozone amounts remain large (more than 110 ppbv at 12 km height on 5 December).

4.3 Biomass burning influence

To determine the origin of the sampled air masses, back trajectories ending at Reunion were used. Back trajectories show that most of the enhanced ozone crossed over biomass burning regions of Madagascar and the southern African continent. The analysis of back trajectories during the study period found three different sequences of transports which are in agreement with the movement of synoptic situations. The 23 to 25 November period corresponds to air masses that cross over the north of Madagascar and the southern part of Africa (data not shown). The 26–30 November period corresponds to air masses coming from southern Africa and crossing over the mid-latitude regions (Fig. 8). From 2 to 6 December air masses cross over Madagascar and the southern part of Africa (Fig. 9). These results are corroborated by trade winds recorded at Reunion, indicating that northerly winds are predominant for the first period, southerly winds for the second period and westerly winds for the third period

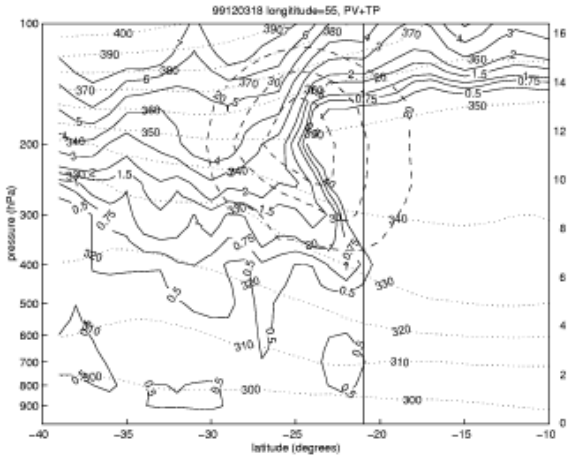

Fig. 7. Vertical longitudinal cross section of potential vorticity (in PVU, 1 PVU = 10^{-6} $m^2.s^1.kg^{-1}$, solid lines), potential temperature (in K, dashed lines) and horizontal wind (in $m.s^{-1}$, dotted lines) on 3 December 1999 at the longitude 55° East. The latitude of Reunion Island (21°S) is marked by a vertical black line (from ECMWF data).

in the middle and upper troposphere (Fig. 3).

The end of November corresponds to the end of the dry season and, hence, to the termination of traditional forest fires that generate extended smoke plumes visible over Madagascar more than 500 km downstream (Cahoon et al., 1992; Justice and al., 1996; Goldammer et al., 1996; Brivio and Grégoire, 1997; Randriambelo et al., 1998; and Arino et al., 2001). Large quantities of aerosols associated with biomass burning have also been observed in the Polder satellite data over the Indian Ocean near the Mozambique channel and Madagascar during the end of November (Deuzé et al., 1999).

During the period November–December 1999, total ozone from TOMS images indicates quite large ozone values in the study region (>295 DU) (Fig. 10). TOMS also evidences the interseasonal variability corresponding to a decrease in the TOMS data during December. Indeed, TOMS is influenced by the contribution of anthropogenic source in the tropics (Fishman et al., 1990). Hence, these observations further suggest that the observed ozone enhancement is likely to result from biomass burning emissions.

Moreover, during the interseasonal period in the latter part of biomass burning, deep convection is intensive, and through venting of ozone precursors, is likely to contribute to an ozone increase. Actually, during this period lightning is intense due to the presence of ITCZ over the southern Africa continent and Madagascar (Fig. 11). In addition, lightning could further enrich the upper troposphere in NO_x (Pickering et al., 1996).

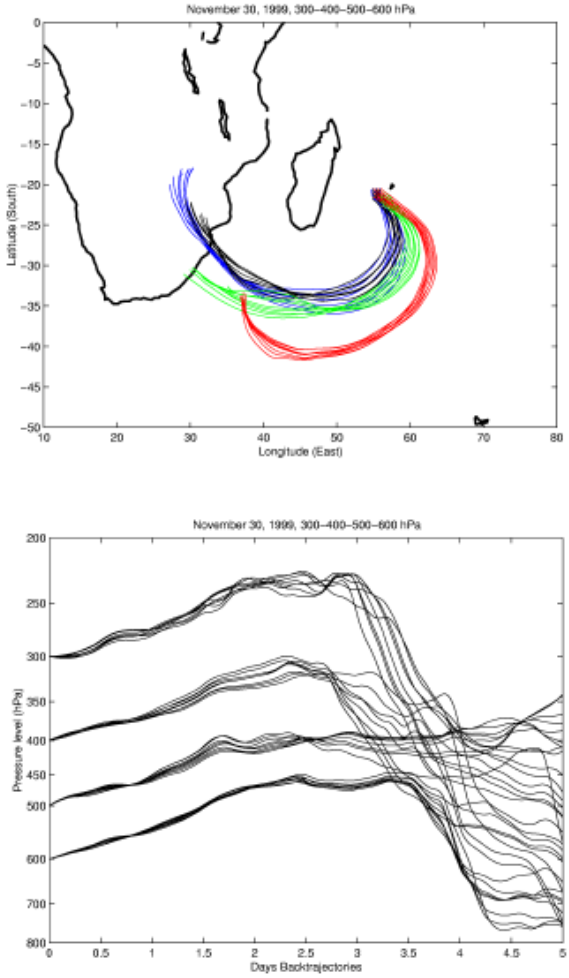

Fig. 8. Cluster back trajectories for 5 days (latitude range 20.5 to 21.5° S, longitude range from 55 to 56° E, ending on 30 November 1999, over Reunion Island (**a**) for different levels: 300 hPa (blue), 400 hPa (black), 500 hPa (green) and 600 hPa (red), and (**b**) altitude corresponding to these transports.

4.4 Stratospheric influence

Westerly disturbances are still observed in the end of the dry season and stratospheric contributions should be considered at Reunion Island. The evolution of potential vorticity (PV) (Fig. 12) calculated from ECMWF data show low PV values in the middle troposphere. Higher PV values in the upper troposphere suggests a stratospheric intrusion. A comparison between Fig. 4 and Fig. 12 suggests that stratospheric and anthropogenic influences coexist during this period. Indeed, Beekmann et al. (1994) showed, from a mid-latitude European data base, that a good correlation between PV and ozone mixing ratio in the free troposphere is a good indication of recent stratospheric intrusion into the troposphere.

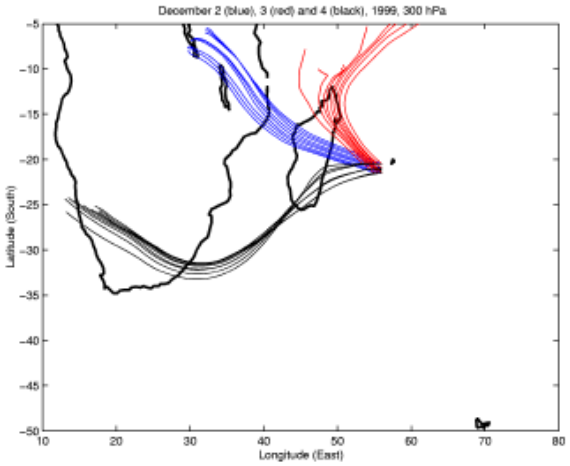

Fig. 9. As Fig. 8, cluster back trajectories for 3 days ending on 2 December (blue), 3 (red) and 4 (black) 1999, over Reunion Island, at 300 hPa level, corresponding approximately to 9 km altitude.

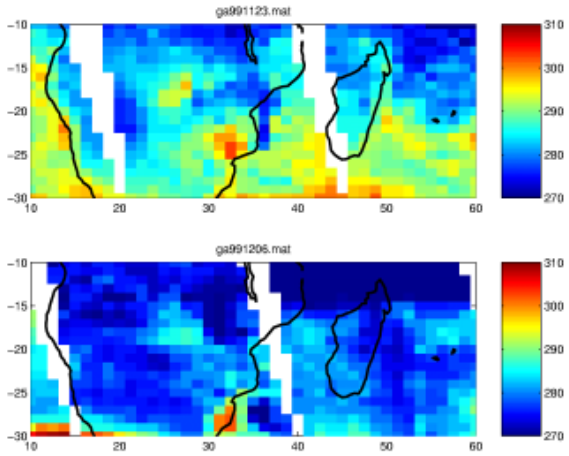

Fig. 10. Distribution of total ozone as measured by the TOMS instrument for 23 November 1999 (top) and 6 December 1999 (bottom). Data provided by web site at http//www.toms.gsfc.nasa.gov.

Air masses characterized by high ozone concentrations, and weak PV values, are more likely to be influenced by anthropogenic sources like biomass burning, or other pollution.

On 30 November, the upper tropospheric (300 hPa) ozone mixing ratio values are also consistent with higher potential vorticity, and the corresponding ozone profile could be influenced by a stratospheric intrusion. But this stratosphere troposphere exchange is not expected to be induced by the subtropical jet stream, which is very far from Reunion Island (Fig. 2c). In addition, winds are very low in the upper troposphere. It is further to be noted that back trajectories (above 500 hPa) indicate that air masses are coming from the southern African continent and cross over the mid-latitude regions (Fig. 8). After cloud venting near the source region, air masses undergo subsidence before reaching Reunion Island. Biomass burning and deep convection near source regions contribute to the ozone enhancement and westerly waves that enhance transport which exits the subcontinent to the east into the Indian Ocean (Garstang et al., 1996). Below 600 hPa, back trajectories show that air masses are coming from ozone poor regions to the mid-latitudes.

On 3 December, strong ozone values were observed (110 ppbv at 8 km, more than 80 ppbv between 5 and 10 km). Since the subtropical jet stream is localised at Reunion Island stratospheric intrusions are possible (Fig. 7). Strong ozone values observed over Reunion are not associated with high potential vorticity values, but we cannot exclude a stratospheric influence for this date. However, potential vorticity remains very weak over Reunion, compared to values for a typical subtropical fold (Baray et al., 2000). Since ozone values observed on 3 December 1999 are close to those observed on 16 July 1998, and since potential vorticity values are much lower than July 1998 records, stratosphere-troposphere exchange is not likely to be the only source of tropospheric ozone on 3 December 1999. Indeed, potential vorticity measured during July 1998 reached up to 1.25 PVU (Baray et al., 2000). To better determine the different contributions, the analysis of ozone profiles around 3 December is of special interest.

Around 9 km altitude, ozone values on 2, 3, and 4 December are, respectively, 59 ppbv, 108 ppbv and 97 ppbv. Corresponding cluster back-trajectories starting from Reunion Island at 300 hPa pressure level, approximately 9 km altitude, are given in Fig. 9. It is first to be noted that every cluster-trajectory crosses a potential source zone of ozone precursors (Madagascar, eastern and southeastern Africa) and also a deep convection zone able to induce vertical transports of these precursors. Moreover, from one day to another, the source areas are expected to greatly vary. On 2 December, air masses cross over the centre of Madagascar and eastern Africa, then influenced by biomass burning. On 3 December, 4 December air masses are influenced by biomass burning, respectively, in the North of Madagascar and in the south of Madagascar and the southern Africa. During this sequence, the jet stream induces a strong enhancement of ozone in the middle troposphere on 3 December. After a few days, due to the displacement of the jet stream far from Reunion, the ozone peak disappears and conversely ozone in the upper troposphere increases. Hence, the influence of tropical convection is observed on 5 December which corresponds to a regular ozone profile enhancement. These results show that during one week from 30 November to 5 December, different contributions influence the ozone vertical distributions.

5 Concluding discussion

Since 1998, a ground-based tropospheric ozone lidar has operated at Reunion Island (Baray et al., 1999). A sec-

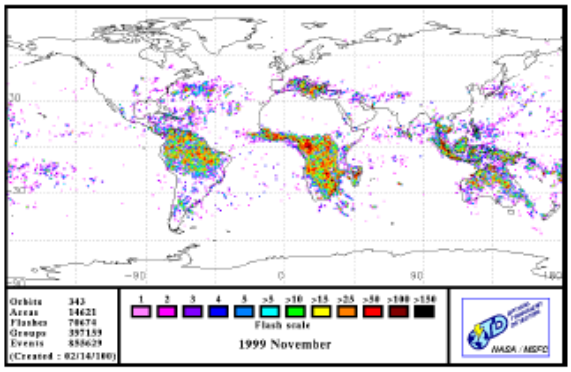

Fig. 11. Lightning data for November 1999 detected by the Optical Transient Detector. Data provided by web site at http://thunder.nsstc.nasa.gov/data.

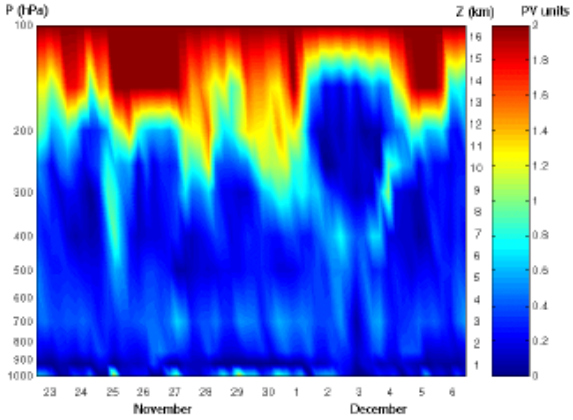

Fig. 12. Evolution of the profiles of potential vorticity as a function of pressure level, over Reunion Island from 23 November to 6 December 1999 from ECMWF data. The right scale shows the approximate correspondence between pressure levels and altitudes.

ond lidar campaign has been performed during the end of the biomass burning season in November–December 1999. The averaged lidar ozone profile obtained during November–December 1999 is consistent with the averaged ozonesonde profile obtained during November–December from 1992 to 2001. Both the seasonal picture based on ozonesonde observations and the continuous ground-based from lidar observations show large standard deviations values. Although the week-to-week variability is intense, weekly measurement is not sufficient to characterize the day-to-day variability of ozone profile. The ozone profile responds to the nature of disturbances which vary from one day to the next.

The comparison of each daily ozone profile appeared very stratified compared to austral winter 1998 daily profiles; ozone maxima are observed at different heights within the whole free troposphere (from 5 to 16 km). The dynamical context is different compared to July where the effect of the subtropical jet stream is predominant. The period of November-December coincides with the end of the dry season where biomass burning from forest fires is intense at Madagascar and with the onset of the rainy season characterized by numerous deep convective clouds. Back trajectories show that most of the enhanced ozone crossed over biomass burning and convection regions at Madagascar and the southern Africa continent.

Vertical ozone distributions during the observing period displays three sequences in agreement with the synoptic situations. First, the 23–25 November period corresponds to the enhancement of ozone in the middle troposphere, which is in accordance with winds that come from the northwest in the middle and upper troposphere. Second, the 26-30 November period corresponds to an enhancement of upper tropospheric ozone and coincides with the strong westerly waves. The 2–6 December period corresponds to stronger values of ozone in the middle troposphere, associated with the shifting of the subtropical jet stream and the northerly winds.

The vertical ozone distributions show daily stratification in agreement with disturbances that can vary greatly during a single week. For example, from 30 November to 5 December, ozone profiles display stratospheric intrusion, northerly influence, jet stream influences and convection, including passing ridge and trough disturbances. This study shows that because of the dynamical context and the frequent superposition of multiple ozone sources, the transport of aerosols and trace gases in the troposphere over southern Africa, Madagascar and adjacent oceans is conditioned by interacting planetary and synoptic-scale features of the general circulation of the Southern Hemisphere. Consequently, the impact of biomass burning over tropospheric ozone at Reunion Island, located far way from source regions, is actually not a steady ozone enhancement, but at the opposite, is composed of sporadic events with a large variability.

Acknowledgements. The lidar development at Reunion Island has been supported by CNRS/INSU and by the Conseil Régional de la Réunion. The technical implantation of the ozone lidar at Reunion Island has been supervised by Jacques Porteneuve and Gérard Ancellet (SA/CNRS), and we gratefully acknowledge the assistance of all the SA technical staff. Reunion ozonesoundings are supported by CNRS/INSU and NASA, under the responsibility of Françoise Posny and Jean-Marc Metzger. We are indebted to the ECMWF for providing model analyses, to the NASA/GSFC TOMS Ozone Processing Team (OPT) for providing satellite data, to the Global Hydrology and Climate Center at NASA for providing lightning data, and to the two reviewers for their comments which have improved the manuscript.

Topical Editor O. Boucher thanks two referees for their help in evaluating this paper.

References

Ancellet, G., Pelon, J., Beekmann, M., Papayannis, A., and Mégie, G.: Ground-based lidar studies of ozone exchange between the

stratosphere and the troposphere, J. Geophys. Res., 96, 22 401–22 421, 1991.

Andreae, M. O., Fishman, J., and Lindesay, J.: The Southern Tropical Atlantic Experiment (STARE): Transport and Atmospheric Chemistry near the Equator-Atlantic (TRACE A) and Southern African Fire-Atmosphere Research Initiative (SAFARI): An introduction, J. Geophys. Res., 101, 23 519–23 520, 1996.

Arino, O., Simon, M., Piccolini, I., and Rosaz, J. M.: The ERS-2 ATSR-2 World Fire Atlas and the ERS-2 ATSR-2 World Burnt Surface Atlas projects, Proceedings of the 8th ISPRS conference on Physical Measurement and Signatures in Remote Sens., 2001.

Bachmeier, A. S. and Fuelberg, H. E.: A meteorological overview of the TRACE-A period, J. Geophys. Res., 101, 23 881–23 888, 1996.

Baldy, S., Ancellet, G., Bessafi, M., Badr, A., and Lan Sun Luk, D.: Field observation of the vertical distribution of tropospheric ozone at the island of Reunion (Southern Tropics), J. Geophys. Res., 96, 23 835–23 849, 1996.

Baray, J. L., Ancellet, G., Taupin, F., Bessafi, M., Baldy, S., and Keckhut, P.: Subtropical tropopause break as a possible stratospheric source of ozone in the tropical troposphere, J. Atmos. Sol. Terr. Phys., 60, 27–36, 1998.

Baray, J. L., Leveau, J., Porteneuve, J., Ancellet, G., Keckhut, P., Posny, F., and Baldy, S.: Description and evaluation of a tropospheric ozone lidar implemented on an existing lidar in the southern subtropics, Appl. Opt., 38, 6808–6817, 1999.

Baray, J. L., Daniel, V., Ancellet, G., and Legras, B.: Planetary-scale tropopause folds in the southern subtropics, Geophys. Res. Lett., 27, 353–356, 2000.

Barbosa, P. M., Grégoire, J. M., and Pereira, J. M. C.: An algorithm for extracting burned areas from time series from AVHRR GAC data applied at a continental scale. Remote Sens. of Environment, 69, 253–263, 1999.

Beekmann, M., Ancellet, G., and Mégie, G.: Climatology of tropospheric ozone in southern Europe and its relation to potential vorticity, J. Geophys. Res., 99, 12 841–12 853, 1994.

Brivio, P. A. and Grégoire, J. M.: Spatial analysis of vegetation fire patterns : A multiannual rose diagram atlas fire for Africa, in Fire in Global Resource and Environmental Monitoring, Joint Research Center, Ispra, Italy, 1997.

Cahoon Jr., D. C. B., Stockst, J., Levine, J. S., Coffer III, W. R., and O'Neill, K. P.: Seasonal distribution of African savanna fire, Nature, 359, 812–815, 1992.

De Laat, A. T. J., Zachariasse, M., Roelofs, G. J., Van Velthoven, P., Dickerson, R. R., Rhoads, K. P., Oltmans, S. J., and Lelieveld, J.: Tropospheric O_3 distribution over the Indian Ocean during spring 1995 evaluated with a chemistry-climate model, J. Geophys. Res., 104, 13 881–13 893, 1999. (Comments by Baray, J. L., Randriambelo, T., Baldy, S., and Ancellet, G., and reply by De Laat, A. T. J., and Lelieveld, J., J. Geophys. Res., 106, 1365–1370, 2001).

Diab, R. D., Jury, M. R., Combrik, J., and Sokolic, F.: A comparison of anticyclone and trough influences on the vertical distribution of ozone and meteorological conditions during SAFARI-92, J. Geophys. Res., 102, 23 809–23 821, 1996a.

Diab, R. D., Thompson, A. M., Zunckel, M., Coetzee, G. J. R., Combrik, J., Bodeker, G. E., Fishman, J., Sokolic, F., McNamara, D. P., Archer, C. B., and Nganga, D.: Vertical ozone distribution over southern Africa and adjacent oceans during SAFARI-92, J. Geophys. Res., 102, 23 823–23 833, 1996b.

Deuzé, J. L., Herman, M., Goloub, P., Tanré, D., and Marchand, A.: Characterization of aerosols over ocean from POLDER/ADEOS-1, Geophys. Res. Lett., 26, 1421–1424, 1999.

Fishman, J., Watson, C. E., Larsen, J. C., and Logan, J. A.: Distribution of tropospheric ozone determined from satellite data, J. Geophys. Res., 95, 33 599–33 617, 1990.

Fuelberg, H., Van Ausdall, J., Browell, E., and Longmore, S.: Meteorological conditions associated with vertical distributions of aerosols off the west coast of Africa, J. Geophys. Res., 101, 24 105–24 116, 1996.

Garstang, M., Tyson, P. D., Swap, R., Edwards, M., Kallberg, P., and Lindesay, J. A.: Horizontal and vertical transport of air over southern Africa, J. Geophys. Res., 101, 23 721–2 736, 1996.

Goldammer, J. G., Pfund, J. L., Helfert, M. R., Lulla, K. P., and STS-61 Mission Crew: Use of the Earth observation system in the space shuttle program for research and documentation of global vegetation fires: A case study from Madagascar, in: Biomass Burning and Global Change, vol. 1, edited by Levine, J. S., MIT Press, Cambridge Mass, 236–240, 1996.

Justice, C. O., Kendall, J. D., Dowty, P. R., and Scholes, R. J.: Satellite remote sensing of fires during the SAFARI campaign using NOAA advanced very high resolution radiometer data, J. Geophys. Res., 101, 23 851–23 863, 1996.

Lacaux, J. P., Brustet, J. M., Delmas, R., Menault, J. C., Abbadie, L., Bonsang, B., Cachier, H., Baudet, J., Andreae, M. O., and Helas, G.: Biomass burning in the tropical savannas of Ivory coast: An overview of the field experiment fire of savannas (FOS/DECAFE'91), J. Atmos. Chem., 22, 195–216, 1995.

Marenco, A., Medale, J. C., and Prieur, S.: Study of tropospheric ozone in the tropical belt (Africa, America) from STRATOZ and TROPOZ campaigns, Atmospheric Environment, 24(A) 2823–2834, 1990.

Newell R. E., Thouret, V., Cho, J. Y. N., Stoller, P., Marenco, A., and Smit, H. G.: Ubiquity of quasi-horizontal layers in the troposphere, Nature, 98, 316–319, 1999.

Pickering, K. E., Thompson, A. M., Wang, Y., Tao, W. K., Mc Namara, D. P., Kirchhoff, V. W. J. H., Heikes, B. G., Sachse, G. W., Bradshaw, J. D., Gregory, G. L., and Blake, D. R.: Convective transport of biomass burning emissions over Brazil during TRACE-A, J. Geophys. Res., 101, 23 993–24 012, 1996.

Preston-Whyte, R. A., and Tyson, P. D.: The atmosphere and weather of Southern Africa, 374 pp., OXFORD University press Cape Town, 1988.

Randriambelo, T., Baldy, S., Bessafi, M., Petit, M., and Despinoy, M.: An improved detection and characterization of active fires and smoke plumes in south-eastern Africa and Madagascar, Int. J. Remote Sens., 19, 2623–2638, 1998.

Randriambelo, T., Baray, J. L., Baldy, S., Bremaud, P., and Cautenet, S.: A case study of extreme tropospheric ozone contamination in the tropics using in situ, satellite and meteorological data, Geophys. Res. Lett., 26, 1287–1290, 1999.

Randriambelo, T., Baray, J. L., and Baldy, S.: The effect of biomass burning, convective venting and transport on tropospheric ozone over the Indian Ocean: Reunion island field observations, J. Geophys. Res., 105, 11 813–11 832, 2000.

Stoller, P., Cho, J. Y. N., Newell, R. E., V. Thouret, Carroll, M. A., Albercook, G. M., Anderson, B. E., Barrick, J. D. W., Browell, E. V., Gregory, G. L., Sachse, G. W., Vay, S., Bradshaw, J. D., and Sandholm, S.: Measurements of atmospheric layers from the NASA DC-8 and P-3B aircraft during PEM-Tropics A, J. Geophys. Res., 104, 5745–5764, 1999.

Taupin, F. G., Bessafi, M., Baldy, S., and Bremaud, P. J.: Tropospheric ozone above the southwestern Indian Ocean is strongly linked to dynamical conditions prevailing in the tropics, J. Geo-

phys. Res., 104, 8057–8066, 1999.

Taupin, F. G., Beekmann, M., Brémaud, P. J., and Randriambelo, T.: Ozone generation over the Indian Ocean during the South African biomass-burning period: case study of October 1992, Ann. Geophysicae, 19, 1–11, 2001.

Thompson, A. M., Pickering, K. E., McNamara, D. P., Schoelberl, M. R., Hudson, R. D., Kim, J.-H., Browell, E. V., Kirchoff, J. H., and Nganga, D.: Where did tropospheric ozone over Southern Africa and the tropical Atlantic come from in October 1992? Insights from TOMS, GTE/TRACE-A and SAFARI-92, J. Geophys. Res., 101, 24 251–24 278, 1996.

Thompson, A. M., Witte, J. C., McPeters, R. D., Oltmans, S. J., Schmidlin, F. J., Logan, J. A., Fujiwara, M., Kirchhoff, V. W. J. H., Posny, F., Coetzee, G. J. R., Hoegger, B., Kawakami, S., Ogawa, T., Johnson, B. J., Vömel, H., and Labow, G.: Southern Hemisphere Additional Ozonesondes (SHADOZ) 1998–2000 tropical ozone climatology 1. Comparison with Total Ozone Mapping Spectrometer (TOMS) and ground-based measurements, J. Geophys. Res., 108, 8238, doi: 10.1029/2001JD000967, 2003a.

Thompson, A. M., Witte, J. C., Oltmans, S. J., Schmidlin, F. J., Logan, J. A., Fujiwara, M., Kirchhoff, V. W. J. H., Posny, F., Coetzee, G. J. R., Hoegger, B., Kawakami, S., Ogawa, T., Fortuin, J. P. F., and Kelder, H. M.: Southern Hemisphere Additional Ozonesondes (SHADOZ) 1998–2000 tropical ozone climatology 2. Tropospheric variability and the zonal wave-one, J. Geophys. Res., 108, 8241, doi: 10.1029/2002JD002241, 2003b.

Zachariasse, M., Van Velthoven, P. F. J., Smit, H. G. J., Lelieveld, J., Mandal, T. K., and Kelder, H.: Influence of stratosphere-troposphere exchange on tropospheric ozone over the tropical Indian Ocean during the winter monsoon, J. Geophys. Res., 105, 15 403–15 416, 2000.

2.2.5 Climatologie de la tropopause

JOURNAL OF GEOPHYSICAL RESEARCH, VOL. 111, D19111, doi:10.1029/2005JD006430, 2006

Tropopause characteristics over a southern subtropical site, Reunion Island (21°S, 55°E): Using radiosonde-ozonesonde data

V. Sivakumar,[1] J.-L. Baray,[1,2] S. Baldy,[1] and H. Bencherif[1]

Received 28 June 2005; revised 5 June 2006; accepted 28 June 2006; published 13 October 2006.

[1] In this paper, we present tropopause characteristics using in situ radiosonde-ozonesonde observations carried out over the past 13 years (September 1992 to February 2005) from a southern subtropical site, Reunion Island (21°S, 55°E). Three kinds of tropopause definitions, namely, cold-point tropopause (CPT), lapse rate tropopause (LRT), and ozone tropopause (OT), are characterized. The ozone tropopause for Reunion is appropriately defined as the height at which the vertical gradient of the ozone mixing ratio exceeds 55 ppbv/km and the ozone mixing ratio is over 75 ppbv. The overall height distribution of the three kinds of tropopause ranges in between 12.5 and 18.5 km. Of the three definitions, CPT follows higher heights of distribution, followed by LRT and then OT. The sharpness of tropopause height detection for LRT and OT has been examined, and it has been found that the detection frequency of a definite OT is larger than that for LRT. The results also showed no indefinite OT for a subtropical station in comparison to the results obtained for Northern Hemisphere midlatitude and high-latitude stations. After adopting a few modifications in the sharpness of ozone tropopause detection, the result remains the same, with a single indefinite case. The indefinite ozone tropopause case was identified when Reunion Island was located nearer to the divergence zone of wind as well as in the anticyclonic region of jet stream entrance. The LRT sharpness results are found to be in good agreement with the other published definition.

Citation: Sivakumar, V., J.-L. Baray, S. Baldy, and H. Bencherif (2006), Tropopause characteristics over a southern subtropical site, Reunion Island (21°S, 55°E): Using radiosonde-ozonesonde data, *J. Geophys. Res.*, *111*, D19111, doi:10.1029/2005JD006430.

1. Introduction

[2] The tropopause plays an important role in trace gas exchange and wave dynamics between the troposphere and lower stratosphere (e.g., stratosphere-troposphere exchange (STE), gravity wave dynamics or planetary/Rossby wave interactions, etc.). Further, the studies on tropopause characteristics are expected to provide a better understanding of stratospheric/tropospheric chemical constituents (mainly water vapor and ozone). Globally, temperature measurements from radiosonde data have been used to characterize tropopause and to study the temperature variability between the troposphere and lower stratosphere [*Atticks and Robinson*, 1983; *Parker*, 1985; *Gaffen*, 1993, 1996; *Reid*, 1994; *Finger et al.*, 1995; *Parker and Cox*, 1995; *Parker et al.*, 1997; *Highwood and Hoskins*, 1998; *Seidel et al.*, 2001].

[3] At present, five different definitions are accepted and widely used for identifying the tropopause, namely, the cold-point tropopause (CPT), the lapse rate tropopause (LRT), the ozone tropopause (OT), the isentropic potential vorticity (IPV) tropopause and the 100-hPa pressure level (PLT). *Selkirk* [1993] and *Highwood and Hoskins* [1998] suggested that the cold-point tropopause height (the height where the temperature inversion takes place) plays an important role in stratosphere-troposphere exchange (STE). Later, *Highwood and Hoskins* [1998] used three different definitions to locate tropopause and characterized the significance of each definition. The World Meteorological Organization (WMO) defines the thermal tropopause as the lowest level where the lapse rate exceeds 2 K/km, provided that it remains above this threshold within this level and 2 km above, this definition has operational use but limited physical relevance, especially over equatorial latitude where there is a possible link between the convective processes and LRT [*Highwood and Hoskins*, 1998]. The IPV tropopause definition of the tropopause is useful for higher latitudes, but not close to the equator. The 100-hPa pressure surface has been considered for the tropopause as available directly from models, such as climate change models or simple radiative convective models. Over a subtropical site, Pan Chiao, (25°N; 121°E), Taiwan, *Thulasiraman et al.* [1999] presented the temperature structure for 0.5–30 km region and found that the CPT follows the annual variation with height around 16.5 km and temperature about 192.6 K. *Shimizu and Tsuda* [2000] also used the CPT definition to characterize the tropical tropopause at Bandung (6.9°S, 107.6°E) and found that the tropopause height is distributed between 16.6 and 17.4 km with a minimum temperature in the range from 188 K to

[1]Laboratoire de l'Atmosphère et des Cyclones, UMR 8105, CNRS, Université de La Réunion, La Réunion, France.
[2]Also at Institut Pierre-Simon Laplace, Observatoire de Physique de l'Atmosphère de la Réunion, La Réunion, France.

0148-0227/06/2005JD006430$09.00

191 K. Their results are also in agreement with *Reid and Gage* [1996] for Truk (7.47°N; 151.85°E). Recently, *Seidel et al.* [2001] used radiosonde data from 83 stations around the globe during the period from 1961 to 1990 and studied the tropopause climatological statistics. The study indicated an increase in height of about 20 m/decade, a decrease in pressure of about 0.5 hPa/decade, a cooling of about 0.5 K/decade, a small change in potential temperature, and a decrease in saturation volume mixing ratio of about 0.3 ppmv/decade.

[4] On the other hand, the tropopause sharpness depends on the method of detection and it quantifies the separation between troposphere and stratosphere [*Zängl and Hoinka*, 2001; *Birner et al.*, 2002; *Pan et al.*, 2004; *Zahn et al.*, 2004a, 2004b; *Schmidt et al.*, 2005]. Further, the failure or low accuracy of tropopause height detection is due to the background atmospheric conditions, such as STE, cyclonic events, Intertropical Convective Zone (ITCZ) passage and strong jet streams. Few results are published in connection with this, and many of them are focused on the lapse rate tropopause (or thermal tropopause) detection. *Kyro et al.* [1992] suggested that the ozone concentration and its gradient provide a more accurate and appropriate measure of tropopause height than the temperature lapse rate. However, the ozone tropopause identification is difficult when there are interleaved layers of low and high ozone concentrations in the upper tropospheric heights (as in the case of STE). *Bethan et al.* [1996] compared the ozone and thermal tropopause heights for the northern extratropical region and found that the ozone tropopause is just below the thermal tropopause. They reported that ozone tropopause could provide a more accurate position of tropopause height than thermal tropopause. *Zängl and Hoinka* [2001] used radiosonde and ERA Reanalysis data to characterize tropopause in the polar regions. They also provided details on the sharpness of the thermal tropopause defined by a change in the vertical temperature gradient across the tropopause and found high and low value in summer and winter, respectively. Using 10 years of radiosonde data for two midlatitude stations, *Birner et al.* [2002] illustrated a strong inversion at the lapse rate tropopause with a vertical extension of 2 km and a temperature increase of 4 K. Similarly, *Bethan et al.* [1996], *Pan et al.* [2004], and *Zahn et al.* [2004a] have also addressed the sharpness of tropopause using the relationship between stratospheric tracer (O_3) and tropospheric tracer (CO) and they proposed a "chemical tropopause" definition based on sudden changes in correlation between O_3 and CO concentrations. The result also documented that the uncertainty in chemical tropopause height determination was ~150–200 m. More recently, *Schmidt et al.* [2005] used Global Positioning System (GPS) radio occultation (RO) and studied lapse rate tropopause variations and their sharpness. They quantified the sharpness of tropopause with changes in the vertical temperature gradient across the tropopause and documented that the sharpness is high for the tropics and less for the polar regions.

[5] Tropopause height varies with latitude and is generally higher at the equator and decreasing toward the poles. It is also highly variable from day to day and from season to season [*Hoerling et al.*, 1993; *Hoinka et al.*, 1993]. Over the subtropics, very few studies are available for characterizing the tropopause and the sharpness of its detection. In this paper, we present the detailed characteristics of the tropopause and their sharpness of detection using 13 years of radiosonde-ozonesonde data from a subtropical site, Reunion (21°S, 55°E). The paper is organized as follows: the next section provides a brief sketch on data used and the analysis pursued. Section 3 presents results obtained from 13 years of in situ radiosonde-ozonesonde data. It includes the detection of ozone tropopause height and the sensitivity of detection, different tropopause characteristics and sharpness variation. Subsequently, the results are discussed and compared with the earlier reported results. The summary and conclusion are given in section 4.

2. Radiosonde-Ozonesonde Data

[6] We have used standard radiosonde-ozonesonde data to study the tropopause characteristics. The radiosonde includes different atmospheric sensors that provide information on temperature, humidity and pressure. The radiosonde is of Vaisala RS 80 type with ascent rate of 5 m/s. The raw data correspond to a ~35 m height resolution in the tropospheric height region and extend to ~90 m in the tropopause region. Further details on the explanation and accuracy of ozonesonde measurements are available elsewhere [*Baldy et al.*, 1996; *Randriambelo et al.*, 2000]. Balloons were launched bimonthly from September 1992 to December 1999 and once a week since January 1999. The registered data at a fixed time interval are linearly interpolated to fit for 150 m vertical resolution in the height range of 0.5–30 km. The radiosonde is accompanied by an Electrochemical Concentration Cell (ECC) to provide height profile of ozone mixing ratio (in terms of partial pressure in nanobars). Then the ozone mixing ratio is converted to parts per billion volume (ppbv) and used for the present study. The data have been collected regularly in the framework of two different programs: the Southern Hemisphere Additional Ozonesonde (SHADOZ) and the Network for Detection of Atmospheric Composition and Change (NDACC, previously NDSC). More details on the SHADOZ program are available from *Thompson et al.* [2003a, 2003b] and for NDACC from *Kunylo and Solomon* [1990].

[7] The present study uses 293 radiosonde-ozonesonde flights data collected for the period from September 1992 to February 2005. The available data distributions for each month are of ~25–30 flights. In case of tropopause characterization, the radiosonde-ozonesonde flights that reached a height range of at least 20 km have been used. Out of 293 observations, 275 cases (94%) are considered for tropopause characteristics, irrespective of year and month.

2.1. Tropopause Definitions

[8] Following *Bethan et al.* [1996], *Reid and Gage* [1996], *Highwood and Hoskins* [1998], and *Seidel et al.* [2001], we have used the existing three kinds of tropopause definitions with minor modifications: (1) The lapse rate tropopause (LRT) is the lowest height at which the temperature gradient is greater than or equal to −2 K/km, provided that the averaged temperature gradient between this level and all the higher levels within 2 km does not exceed −2 K/km. (2) The cold-point tropopause (CPT) is the height

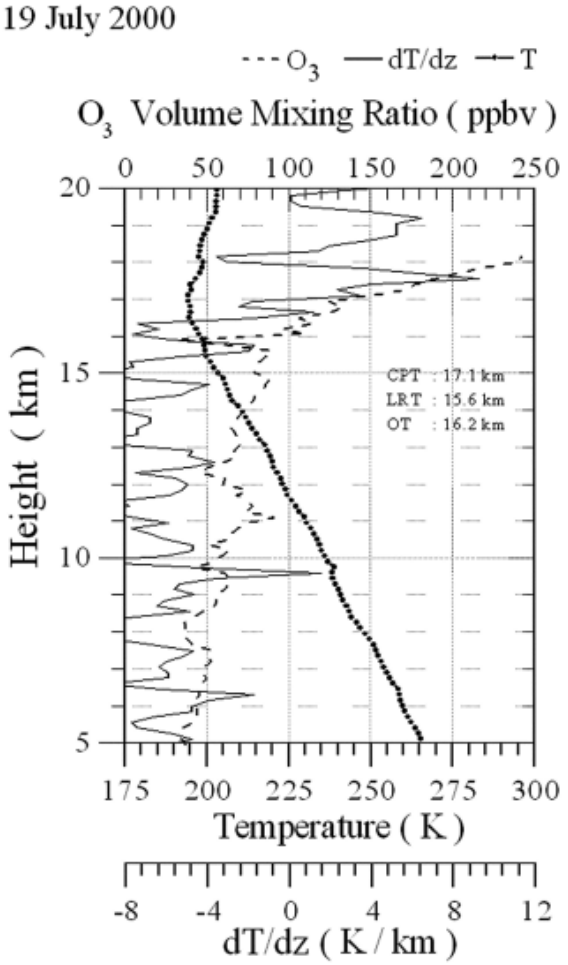

Figure 1. Height profile of temperature, temperature gradient, and ozone obtained for 19 July 2000.

where the minimum temperature is found below 20 km. (3) The ozone tropopause (OT) is the height at which the vertical gradient of ozone mixing ratio exceeds 55 ppbv/km and ozone mixing ratio is over 75 ppbv (at and above this height).

[9] The above mentioned methods of identification of tropopause height are illustrated in Figure 1, which shows the height profiles of temperature and ozone as observed on 19 July 2000. It is noted that the actual measurements of temperature and ozone are obtained for the height region from ground to 30 km. By applying the above definitions to this profile, the tropopause heights are found to be at 16.2 km, 15.6 km and 17.1 km, which correspond to OT, LRT and CPT.

2.2. Sharpness Criteria

[10] The accuracy of detecting tropopause is sometimes questionable and needs to be examined. Few studies on tropopause detection found the existence of more than one tropopause and tropopause folding [e.g., *Selkirk*, 1993; *Bethan et al.*, 1996; *Folkins et al.*, 1999; *Baray et al.*, 2000]. *Bethan et al.* [1996] reported on the sharpness of LRT and OT detection for midlatitude regions. There is no study on sharpness for tropical tropopause detection though the tropics are highly influenced by ITCZ, convections, cyclones, etc. Here, we examine the sharpness of detected LRT and OT. Initially, we have examined the *Bethan et al.* [1996] criteria for OT and LRT definition by adopting the sharpness height h as definite when $h \leq 0.6$ km, intermediate when 1.2 km $\geq h > 0.6$ km and indefinite when $h > 1.2$ km. The results obtained are tabulated in Table 1. This leads to a large number of indefinite LRT cases and very few definite LRT cases, whereas most OT are reported as definite with a few indefinite cases. This distribution is likely to result from a lower interval of sharpness height region (0.6 km) used and a lower height resolution of data than given by *Bethan et al.* [1996]. To optimize h for our data sets, we have used various permutation level of h for classifying the tropopause sharpness and optimized by finding the lower frequency of occurrence of indefinite tropopause for both LRT and OT. We proceeded in step of 0.3 km, i.e., h with an interval of 0.9 km, 1.2 km and 1.5 km. When we used the sharpness interval (h) of 0.9 km, we found almost the similar result as before (i.e., more number of indefinite LRT cases). Whereas when 1.2 km sharpness height interval was utilized, we found that the LRT show more intermediate cases than indefinite. At the same time, we have not found any significant difference in OT distribution between h as 0.9 km, 1.2 km and 1.5 km. Thereby we modified the *Bethan et al.* [1996] criteria with h interval as 1.2 km, which uniformly fit for the LRT and OT definitions. The criteria used are as follows: (1) For the lapse rate tropopause, the sharpness of LRT has been classified into three categories: definite, ($h \leq 1.2$ km), intermediate, (2.4 km $\geq h > 1.2$ km) and Indefinite, ($h > 2.4$ km). Here, h stands for the height region from the lapse rate tropopause height to the height where the temperature gradient is less than −5 K/km (upper troposphere lapse rate). (2) For the ozone tropopause, the sharpness is defined as above, with h given by the distance from the ozone tropopause to the level where the ozone mixing ratio falls to within 5 ppbv of the mean free tropospheric ozone value. The free troposphere is defined as the region between 3 km and OT.

3. Results and Discussion

3.1. Sensitivity of Ozone Tropopause Definition

[11] The ozone tropopause definition is not widely used and the threshold adopted by *Bethan et al.* [1996] (i.e., OT as the height at which the vertical gradient of ozone mixing ratio exceeds 60 ppbv/km and ozone mixing ratio is over 80 ppbv) might be applicable for the northern extratropics. Hence we performed a sensitivity study on the above

Table 1. Percentage of Detected LRT and OT Sharpness Following the *Bethan et al.* [1996] Criteria

Criteria	LRT, %	OT, %
Definite, $h \leq 0.6$	5.5	95.7
Intermediate, $1.2 \leq h > 0.6$	7.3	2.6
Indefinite, $h > 1.2$	87.2	1.7

Table 2. Sensitivity of the Ozone Tropopause Height Detection Using Different Thresholds

Criteria Parameters				
Referential Threshold		Modified Threshold		Tropopause Height Within ±0.15 km by Change in Criteria, %
O_3, ppbv	dO_3/dz, ppbv/km	O_3, ppbv	dO_3/dz, ppbv/km	
80	60	80	55	86.2
80	60	75	55	70.5
75	60	75	55	88.0
80	60	75	60	82.2
80	55	75	55	81.4

defined definition (refer to section 2.1) to optimize the threshold value of ozone vertical gradient and the ozone mixing ratio for identifying the ozone tropopause height over Reunion (southern subtropics). The study was conducted by decreasing the threshold value of vertical gradient of ozone mixing ratio and ozone mixing ratio in steps of 5. The result obtained from different kinds of threshold variations and the number of cases (in terms of percentage) where OT remains within ±0.15 km is listed in Table 2. Finally, we ascertained that the OT defined by the vertical gradient of ozone mixing ratio exceeds 55 ppbv/km and ozone mixing ratio over 75 ppbv is found to be 88% of cases in agreement with OT differences within ±0.15 km by the one defined with the vertical gradient of 60 ppbv/km.

3.2. Tropopause Characteristics: Frequency of Distribution

[12] The radiosonde-ozonesonde balloon flights that reached up to a minimum height of 20 km and above are used for a statistical study (275 observations). The three different tropopause heights are determined for each case using the definitions given in section 2.1. Thereby the frequency distributions based on three different kinds of tropopause height, such as cold-point tropopause (CPT), lapse rate tropopause (LRT) and ozone tropopause (OT), are obtained and shown in Figures 2a–2c. The distributions of all kinds of tropopause height (CPT, LRT and OT) are in the height range from 14 to 18 km with small differences in the maximum number of occurrences and also roughly depict a Gaussian shape. The CPT, LRT and OT show the maximum number of occurrences at 17.2 km, 16.0 km and 15.5 km, respectively. Relatively, it is noted that the highest tropopause corresponds to CPT followed by LRT and then by OT. The above obtained tropopause height characteristics are analogous to the results presented by *Seidel et al.* [2001], on tropical tropopause climatology by employing the radiosonde data from 83 stations located in the tropical belt from 30°N to 30°S. The result documented that the LRT varies from ~16.5 km in the equatorial zone to less than 16 km in the subtropics. Similarly, the CPT is found to be resided at ~16.9 km with very little north-south hemisphere variability. *Highwood and Hoskins* [1998] also found that the mean occurrence of CPT and LRT are 16 km and 13 km over tropics. They suggested that CPT is a reliable tropopause definition when the lower stratosphere is not close to being isothermal, i.e., within the deep tropics.

[13] Figures 3a–3c illustrate the frequency of occurrence of the differences between CPT, LRT and OT. The differences in distribution between CPT-LRT, CPT-OT and LRT-OT are respectively within −0.3 km to +4.8 km, −1.5 km to +6.0 km and −3.3 km to +6.0 km ranges. The maximum number of occurrence differences of CPT versus LRT, CPT versus OT and LRT versus OT correspond to positive values with mean differences at 1.1 km, 1.9 km and 0.4 km. The result again evidenced that OT is observed at lower height than LRT and CPT. The distribution is also highly weighted toward the positive sign and further verifies the tropopause height distribution, i.e., highest tropopause recorded for CPT followed by LRT and OT.

[14] The presented result shows that the differences between CPT and LRT are from −0.3 km to +3.0 km with 0.3 km differences for maximum number of times. Similarly, *Seidel et al.* [2001] reported in their study that the differences between CPT and LRT up to ~1 km. They also proposed that the LRT and CPT are likely to meet at the same height, if the coldest point of a sounding is located at the base of an inversion layer deep enough (2 km) and it could be the case when there is a deep convection. *Folkins et al.* [1999] also argued that the difference between ozone tropopause and LRT or CPT is due to the convective detrainment of ozone-depleted marine boundary layer air above 14 km where the Hadley circulation occurs and convective penetration above this altitude is rare.

3.3. Sharpness of Detected Tropopause Height

[15] In this section, we present the result obtained on sharpness of detected LRT and OT heights. As explained in section 2.2, the sharpness determines the separation between troposphere and stratosphere region. So far, very few studies have been published for extratropics, and there are no results on sharpness of detection for tropics/subtropics using radiosonde data. Here, the tropopause sharpness is classified into three different categories: definite, intermediate and indefinite (refer to section 2.2). Table 3a shows the occurrence frequencies of LRT and OT based on the classified categories. It substantiates that the ozone tropopause of definite category is found to occur for a larger number of cases (98.2%) in comparison with LRT (24.7%). Next to the definite tropopause, the indefinite tropopause is more numerous for LRT than OT.

[16] The above results of more definite ozone tropopause detection are consistent with the earlier reported result revealing that the OT provides a definite one [*Kyro et al.*, 1992; *Bethan et al.*, 1996; *Pan et al.*, 2004]. They suggested that the ozone concentration and its gradient provide a more accurate and appropriate measure of tropopause height than the temperature lapse rate. Yet the ozone tropopause fails when there are interleaved layers of low and high ozone concentration in the upper troposphere (as in the case of STE). Earlier reports from Reunion suggest that there could be many occurrences of STE, tropopause folds induced by

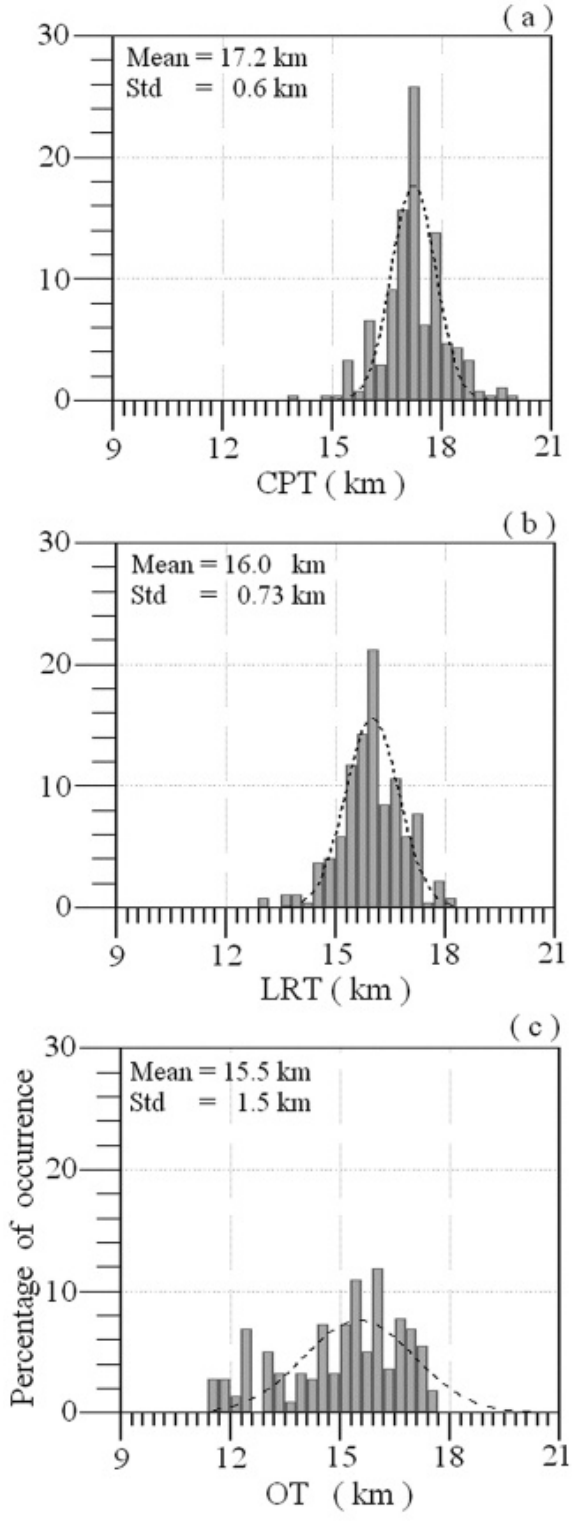

Figure 2. Percentage of occurrence of three different kinds of tropopause height obtained from the radiosonde-ozonesonde data.

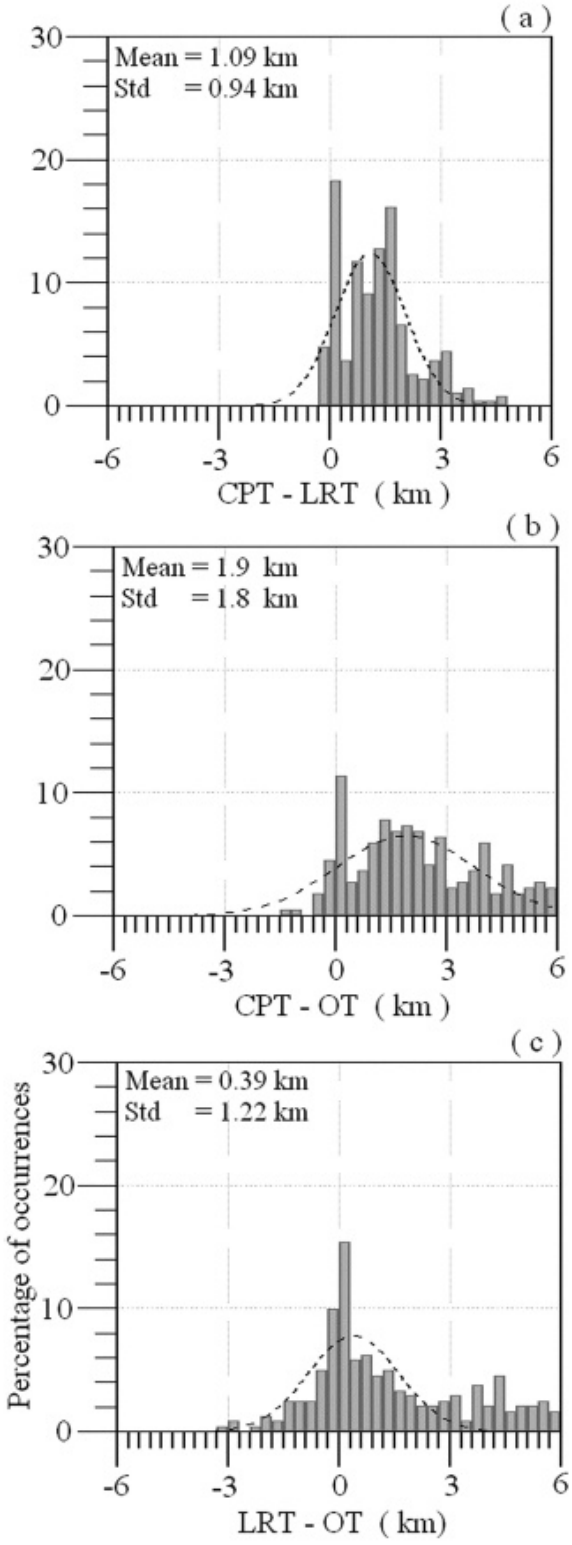

Figure 3. Percentage of occurrence of mutual differences in the tropopause height by the definition used.

Table 3a. Sharpness of Detected Tropopause Height: Occurrence

	LRT	OT
Definite	68 (24.7%)	270 (98.2%)
Intermediate	148 (53.8%)	5 (1.8%)
Indefinite	59 (21.5%)	

subtropical jet streams [*Baray et al.*, 2000], tropical cyclones [*Baray et al.*, 1999] and cutoff lows [*Baray et al.*, 2003]. The changes in the LRT height may be due to prevailing different atmospheric conditions, due to convective activity, atmospheric waves and also due to the presence of high-level cirrus clouds. An earlier study [*Cadet et al.*, 2003] on climatological aspect of subvisible cirrus at Reunion Island, reports that the occurrence frequency is relatively high in December and less during July and August. The occurrence height is predominantly positioned within 11–14 km range, with maximum level during January. This also further elucidates that the detected cold-point tropopause is at higher height than the cirrus used to occur.

[17] Table 3b presents the mean tropopause height and its standard deviation obtained for the LRT and OT definitions and for the three categories (definite, intermediate and indefinite). The definite tropopause heights show the highest height (16.8 km) of occurrence for LRT than OT and a larger standard deviation for OT than LRT. The intermediate tropopause height reveals a high value with standard deviation for the cases of LRT than OT. The indefinite cases were found to be zero for OT in comparison with more in number for the LRT.

[18] More recently, *Schmidt et al.* [2005] studied the sharpness of LRT detection using the equation

$$S = \frac{\Gamma_+ - \Gamma_-}{\Gamma_{uppertrop} - \Gamma_{strat}} = \frac{\left(\delta T/\delta z\right)_+ - \left(\delta T/\delta z\right)_-}{6.5} \qquad (1)$$

where $(\delta T/\delta z)_+$ and $(\delta T/\delta z)_-$ are the mean temperature gradient above and below the detected tropopause height for the height region of about 1 km.

[19] They considered that the parameter (S) quantifies the order of separation between troposphere and stratosphere. The value 6.5 in the denominator is the difference between the lapse rate assuming that Γ_{strat} is 0 K/km and the upper troposphere Γ_{trop} as −6.5 K/km. Here, we compare the obtained LRT sharpness result by applying the above equation. Since we have used −5.0 K/km as the upper troposphere lapse rate and the sharpness height "h," interval as 1.2 km (see section 2.2), we therefore use the same value here too. Values greater than 1 refer to high sharpness, or, in other words, it is a definite tropopause. The parameter S is computed for all 275 cases and it was found that ~38.5% of cases had values greater than one. This is in agreement with the LRT sharpness result presented by using the criteria ($h \leq 1.2$) and found for 24.7% as definite (see Table 3a). Further, it confirms that the threshold used is highly coherent and appropriate for the subtropical site.

Table 3b. Sharpness of Detected Tropopause Height: Mean Height and Its Standard Deviation

	LRT, km	OT, km
Definite	16.8 ± 0.7	14.0 ± 2.6
Intermediate	16.1 ± 0.7	10.2 ± 2.1
Indefinite	15.4 ± 1.2	

Table 3c. Modified Distribution of OT

	Frequency and Percentage of Occurrence	Mean Height Distribution, km
Definite	260 (94.6%)	14.2 ± 2.5
Intermediate	14 (5.0%)	10.2 ± 1.6
Indefinite	1 (0.4%)	11.9

[20] Our classification of OT sharpness reveals no indefinite case. Hence we modified the sharpness of tropopause definition followed by *Bethan et al.* [1996] for middle/high latitudes, which may not suit for subtropical stations, like Reunion (21°S, 55°E). To conform and get a clear view, we have introduced modification on the sharpness criteria for ozone tropopause height, i.e., we changed the fall of ozone mixing ratio of free troposphere ozone regions from 5 ppbv to 10 ppbv. The results obtained are presented in Table 3c. They exhibit again a similar distribution with very little variation in comparison with the earlier results. The mean height distributions for the definite and intermediate cases are almost the same except variation in standard deviation and now an indefinite case found at 11.9 km. Yet the modified distribution for indefinite ozone tropopause detected only one case, which further ascertains that the OT provides the exact location of tropopause for a subtropical station.

[21] The identified indefinite ozone tropopause case corresponds to the observation made on 3 January 2001. The height profile of ozone mixing ratio, temperature and the temperature gradient for the above day is shown in Figure 4. It is evident from the temperature gradient profile that a large perturbations just above and below to the tropopause. The ozone profile shows a significant perturbation in the ozone value. Though the figure illustrates the location of ozone tropopause just near to the LRT at ~16 km, the method identifies the OT at ~11.9 km. The figure displays a peak in the ozone values ~60 ppbv just above ~11.85; thereby the method pointed the OT at 11.9 km. This could be the reason for the detected indefinite ozone tropopause. The LRT sharpness definition followed by *Schmidt et al.* [2005] also illustrates the value of 0.22, which is again less than 1 and illustrating low sharpness. To examine the background synoptic situations on this day, we used wind and potential vorticity data from the European Centre for Medium-Range Weather Forecasts (ECMWF) Reanalysis. It is found that Reunion is located nearer to the entrance zone of a strong jet stream (in the anticyclone side) and the calculated potential vorticity (PV) at 350 K isentropic surface is greater than 1.5 PVU (data not shown). The high PV value suggests that there is a possibility of STE and of stratospheric ozone transfers into the troposphere heights. This background meteorological condition could probably be the reason for the detected indefinite tropopause. The theoretical interpretation by *Shapiro and Kennedy* [1981] suggested that zones of horizontal convergence and divergence appear at the entrance and exit zones of jet stream, and vertical ageostrophic winds are induced over and under these convergence and divergence zones. Hence the ob-

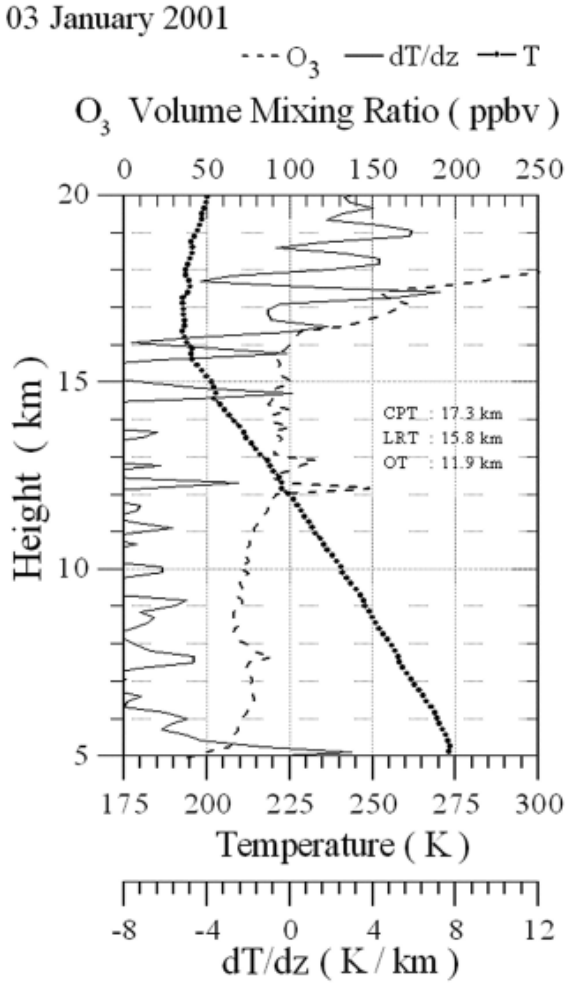

Figure 4. Height profile of temperature, temperature gradient, and ozone obtained for 3 January 2001.

served indefinite case is influenced by the passage of jet stream and STE, which makes the proposed method, fails to identify the location of ozone tropopause.

[22] During summer, other mechanisms are known to influence the upper tropospheric and tropopause dynamics (severe convection, cyclones and ITCZ). Several cases of stratosphere-troposphere exchange near convection have been reported, over Reunion Island [*Baray et al.*, 1999], and over other locations [*Poulida et al.*, 1996; *Stenchikov et al.*, 1996; *Folkins et al.*, 1999]. However, the method has not detected many indefinite cases (except the one presented in Figure 4) during summer (December–February), when there are possibilities of severe convection, cyclone, or ITCZ over Reunion. This implies that a more sophisticated method is required to detect the tropopause height exactly, during convection, cyclone or ITCZ. Further, few results are published on chemical tropopause definition based on the O_3 and CO relationship and stated that the chemical tropopause provide a better result than one defined using single traces gas (ozone) [*Pan et al.*, 2004; *Zahn et al.*, 2004a, 2004b].

4. Summary and Conclusion

[23] In this paper, the tropopause characteristics using 13 years of in situ radiosonde-ozonesonde measurements from a subtropical site (Reunion; 21°S, 55°E) are presented. The following salient features are noted:

[24] 1. The performed sensitivity study on threshold to define the ozone tropopause has proven that the vertical gradient of ozone mixing ratio exceeds 55 ppbv/km and that the ozone mixing ratio over 75 ppbv is an appropriate for the site.

[25] 2. Three different kinds of tropopause height definitions, i.e., LRT, CPT and OT, have been investigated. The distribution of CPT is found to be at higher heights than LRT and OT with the maximum number of occurrences at 17.2 km, 16.0 km and 15.5 km, respectively.

[26] 3. Differences between the tropopause heights indicate that OT is found to be 1.9 km below the CPT and 0.4 km below the LRT for most of the cases. Mostly, the differences between CPT and LRT are within the height difference of ~1 km.

[27] 4. The performed analysis on sharpness of tropopause height evidenced that the OT acts as the more highly sensitive one (98%), even at the subtropical stations in comparison with LRT (24.7%). Also, the frequency of occurrence of indefinite tropopause height for OT is found to be lower (one case) for the subtropical site, Reunion (21°S, 55°E), in comparison with the midlatitude and high-latitude observations reported by *Bethan et al.* [1996]. The result suggests that the ozone tropopause also locates the tropopause height accurately for the subtropical site.

[28] 5. The LRT sharpness results are also found to be concurrent with the definition followed by *Schmidt et al.* [2005].

[29] 6. It was ascertained that the occurrence of the indefinite ozone tropopause is due to the occurrence of STE and divergence zone of the jet stream near the site location.

[30] Though the method of identification of tropopause sharpness detection is well suited for a subtropical site, like Reunion, it fails to reproduce the indefinite cases during the presence of a cyclone or ITCZ passage. Further improvements in the method are planned in future studies. The identification of tropopause height by isentropic potential vorticity and its comparison with other definitions may provide a better understanding of tropopause characteristics. The examination of tropopause identification failure with the help of classic/dynamic models is in perspective.

[31] **Acknowledgments.** Laboratoire de l'Atmosphère et des Cyclones (LACy) is supported by the French Centre National de la Recherche Scientifique (CNRS)/Institut National des Sciences de l'Univers (INSU) and Conseil Régional de la Réunion. INSU/CNRS and SHADOZ/NASA programs financially support the Radiosonde launching. One of the authors, V.S.K., acknowledges the CNRS, the European Community (FEDER), and the Reunion Regional Council (Conseil Régional de la Réunion) for financial support under a postdoctoral fellowship scheme. We are also grateful to the LACy radiosounding team (especially Françoise Posny, Jean-Marc Metzger, and Guy Bain) for their constant cooperation in radiosonde launching. We thank Amith Sharma for language correction in the manuscript. Authors are thankful to the anonymous reviewers for their valuable comments and suggestions.

References

Atticks, M. G., and G. D. Robinson (1983), Some features of the structure of the tropical tropopause, *Q. J. R. Meteorol. Soc.*, *109*, 295–308.

Baldy, S., G. Ancellet, M. Bessafi, A. Badr, and D. Lan Sun Luk (1996), Field observations of the vertical distributions of tropospheric ozone at the island of la Reunion (southern tropics), *J. Geophys. Res.*, *101*, 23,835–23,849.

Baray, J. L., G. Ancellet, T. Randriambelo, and S. Baldy (1999), Tropical cyclone Marlene and stratosphere-troposphere exchange, *J. Geophys. Res.*, *104*, 13,953–13,970.

Baray, J. L., V. Daniel, G. Ancellet, and B. Legras (2000), Planetary-scale tropopause folds in the southern subtropics, *Geophys. Res. Lett.*, *27*, 353–356.

Baray, J. L., S. Baldy, R. D. Diab, and J. P. Cammas (2003), Dynamical study of a tropical cut-off low over South Africa and its impact on tropospheric ozone, *Atmos. Environ.*, *37*, 1475–1488.

Bethan, S., G. Vaughan, and S. J. Reid (1996), A comparison of ozone and thermal tropopause heights and the impact of tropopause definition on quantifying the ozone content of the troposphere, *Q. J. R. Meteorol.*, 929–944.

Birner, T., A. Dörnbrack, and U. Schumann (2002), How sharp is the tropopause at mid latitudes?, *Geophys. Res. Lett.*, *29*(14), 1700, doi:10.1029/2002GL015142.

Cadet, B., L. Goldfarb, D. Faduilhe, S. Baldy, V. Giraud, P. Keckhut, and A. Rechou (2003), A sub-tropical cirrus clouds climatology from Reunion Island (21°S, 55°E) lidar data set, *Geophys. Res. Lett.*, *30*(3), 1130, doi:10.1029/2002GL016342.

Finger, F. G., R. M. Nagatani, M. E. Gelman, C. S. Long, and A. J. Miller (1995), Consistency between variations of ozone and temperature in the stratosphere, *Geophys. Res. Lett.*, *22*, 3477–3480.

Folkins, I., M. Loewenstein, J. Podolske, S. J. Oltmans, and M. Proffitt (1999), A barrier to vertical mixing at 14 km in the tropics: Evidence from ozonesondes and aircraft measurements, *J. Geophys. Res.*, *104*, 22,095–22,102.

Gaffen, D. J. (1993), Historical changes in radiosonde instruments and practices, *WMO/TD 541, Instrum. Obs. Methods Rep. 50*, 123 pp., World Meteorol. Organ., Geneva.

Gaffen, D. J. (1996), A digitized metadata set of global upper-air station histories, *NOAA Tech. Memo. ERL-ARL 211*, 38 pp., Natl. Oceanic and Atmos. Admin., Silver Spring, Md.

Highwood, E. J., and B. J. Hoskins (1998), The tropical tropopause, *Q. J. R. Meteorol. Soc.*, *124*, 1579–1604.

Hoerling, M. P., T. K. Schaack, and A. J. Lenzen (1993), A global analysis of stratospheric-tropospheric exchange during northern winter, *Mon. Weather Rev.*, *121*, 162–172.

Hoinka, K. P., M. E. Reinhardt, and W. Metz (1993), North Atlantic air traffic within the lower stratosphere: Cruising times and corresponding emissions, *J. Geophys. Res.*, *98*, 23,113–23,131.

Kunylo, M. J., and S. Solomon (1990), Network for the detection of stratospheric change: A status and implementation report, NASA Upper Atmos. Res. Program and NOAA Clim. and Global Change Program, Natl. Aeronaut. and Space Admin., Washington, D. C.

Kyro, E., et al. (1992), Analysis of the ozone soundings made during the first quarter of 1989 in the Arctic, *J. Geophys. Res.*, *97*, 8083–8091.

Pan, L. L., W. J. Randel, B. L. Gary, M. J. Mahoney, and E. J. Hintsa (2004), Definitions and sharpness of the extratropical tropopause: A trace gas perspective, *J. Geophys. Res.*, *109*, D23103, doi.10.1029/2004JD004982.

Parker, D. E. (1985), On the detection of temperature changes induced by increasing atmospheric carbon dioxide, *Q. J. R. Meteorol. Soc.*, *111*, 587–601.

Parker, D. E., and D. I. Cox (1995), Towards a consistent global climatological rawinsonde database, *Int. J. Climatol.*, *15*, 473–496.

Parker, D. E., M. Gordan, D. P. N. Cullum, D. M. H. Sexton, C. K. Folland, and N. Rayner (1997), A new global gridded radiosonde temperature database and recent temperature trends, *Geophys. Res. Lett.*, *24*, 1499–1502.

Poulida, O., R. R. Dickerson, and A. Heymsfield (1996), Stratosphere-troposphere exchange in a midlatitude mesoscale convective complex: 1. Observations, *J. Geophys. Res.*, *101*, 6823–6836.

Randriambelo, T., J. L. Baray, and S. Baldy (2000), Effect of biomass burning, convective venting and transport on tropospheric ozone over the Indian Ocean: Reunion Island field observations, *J. Geophys. Res.*, *105*, 11,813–11,832.

Reid, G. C. (1994), Seasonal and interannual temperature variations in the tropical stratosphere, *J. Geophys. Res.*, *99*, 18,923–18,932.

Reid, G. C., and K. S. Gage (1996), The tropical tropopause over the western Pacific: Wave driving, convection, and the annual cycle, *J. Geophys. Res.*, *101*, 21,233–21,241.

Schmidt, T., S. Heise, J. Wickert, G. Beyerle, and C. Reigber (2005), GPS radio occultation with CHAMP and SAC-C: Global monitoring of thermal tropopause parameters, *Atmos. Chem. Phys.*, *5*, 1473–1488.

Seidel, D. J., R. J. Ross, J. K. Angell, and G. C. Reid (2001), Climatological characteristics of the tropical tropopause as revealed by radiosondes, *J. Geophys. Res.*, *106*, 7857–7878.

Selkirk, H. B. (1993), The tropopause cold trap in the Australian monsoon during STEP/AMEX 1987, *J. Geophys. Res.*, *98*, 8591–8610.

Shapiro, M. A., and P. J. Kennedy (1981), Research aircraft measurements of jet stream geostrophic and ageostrophic winds, *J. Atmos. Sci.*, *38*, 2642–2652.

Shimizu, A., and T. Tsuda (2000), Variations in tropical tropopause observed with radiosondes in Indonesia, *Geophys. Res. Lett.*, *27*, 2541–2544.

Stenchikov, G., R. Dickerson, K. Pickering, W. Ellis Jr., B. Doddridge, S. Kondragunta, O. Poulida, J. Scala, and W. K. Tao (1996), Stratosphere-troposphere exchange in a midlatitude mesoscale convective complex: 2. Numerical simulations, *J. Geophys. Res.*, *101*, 6837–6851.

Thompson, A. M., et al. (2003a), Southern Hemisphere Additional Ozonesondes (SHADOZ) 1998–2000 tropical ozone climatology: 1. Comparison with Total Ozone Mapping Spectrometer (TOMS) and ground-based measurements, *J. Geophys. Res.*, *108*(D2), 8238, doi:10.1029/2001JD000967.

Thompson, A. M., et al. (2003b), Southern Hemisphere Additional Ozonesondes (SHADOZ) 1998–2000 tropical ozone climatology: 2. Tropospheric variability and the zonal wave-one, *J. Geophys. Res.*, *108*(D2), 8241, doi:10.1029/2002JD002241.

Thulasiraman, S. J. B. Nee, W. N. Chen, and J. H. Chen (1999), Temporal characteristics of tropopause and lower stratosphere over Taiwan during 1990–1995, *J. Atmos. Terr. Phys.*, *61*, 1299–1306.

Zahn, A., C. A. M. Brenninkmeijer, and P. F. J. van Velthoven (2004a), Passenger aircraft project CARIBIC 1997–2002, Part I: The extratropical chemical tropopause, *Atmos. Chem. Phys. Discuss.*, *4*, 1091–1117.

Zahn, A., C. A. M. Brenninkmeijer, and P. F. J. van Velthoven (2004b), Passenger aircraft project CARIBIC 1997–2002, Part II: The ventilation of the lowermost stratosphere, *Atmos. Chem. Phys. Discuss.*, *4*, 1119–1150.

Zängl, G., and K. P. Hoinka (2001), The tropopause in the polar regions, *J. Clim.*, *14*, 3117–3139.

S. Baldy, J.-L. Baray, H. Bencherif, and V. Sivakumar, Laboratoire de l'Atmosphère et des Cyclones, UMR 8105, CNRS, Université de La Réunion, 15 Avenue René Cassin, BP 7151, F-97715 Saint-Denis Messag Cedex 9, La Réunion, France. (venkataraman.sivakumar@univ-reunion.fr)

2.3 Travaux en cours

2.3.1 LACYTRAJ : un code de trajectoires-RDF développé au LACY

2.3.1.1 Contexte

Historiquement, l'origine de LACYTRAJ est un code de trajectoire cinétique développé dans le cadre de ma thèse et codé en langage Matlab. Le code fonctionnait convenablement, mais présentait deux défauts. Tout d'abord il était très lent car basé sur des boucles d'interpolation qui n'étaient pas optimisées. Pour remédier à ce problème, une solution était de réduire la taille des matrices de champs initiaux à la région dans laquelle restaient localisées les trajectoires. Mais cela faisait apparaître un deuxième défaut du code, les conditions aux limites n'étaient pas gérées. Lorsqu'une trajectoire du faisceau sortait du domaine couvert par les matrices contenant les paramètres ECMWF (qui avait été optimisé pour réduire le temps de calcul), celui-ci s'arrêtait et il fallait reprendre le calcul en agrandissant la matrice ECMWF. C'était donc un code qu'il était possible d'utiliser pour des cas d'étude, et il a été utilisé sous cette forme pour plusieurs articles[30,31,32,,33]. Mais lancer un grand nombre de calculs, par exemple pour une étude climatologique ou statistique n'était pas envisageable avec le code sous cette forme. Or, tel était notre objectif lorsque j'ai proposé le sujet de thèse de Gaëlle Clain en 2005.

Pour les études de l'ozone troposphérique menées jusqu'alors, l'approche de l'influence des différentes sources a été abordée au moyen de cas d'études. Des climatologies de l'ozone troposphérique avaient permis d'établir la variation saisonnière de l'influence des feux de végétation, mais nous avions alors comme objectif de franchir un pas supplémentaire, avec la quantification climatologique des sources sur l'ozone troposphérique. Pour cela, il fallait disposer d'un outil trajectographique qui puisse être lancé sur un grand nombre de calculs pour pouvoir déterminer l'origine des masses d'air pour chaque profil d'ozone lidar et radiosondage de la base de données ozone de l'OPAR. L'outil trajectographique le plus élaboré est actuellement FLEXPART[34]. C'est un code d'advection-dispersion lagrangien qui est couramment utilisé pour les études de dynamique troposphérique. Cependant, s'il est parfaitement judicieux d'utiliser FLEXPART pour approfondir un cas d'étude, ce code étant relativement lourd à installer et utiliser, il n'est pas très

[30] Roumeau S. et al., Tropical cirrus clouds: a possible sink for ozone, *Geophys. Res. Lett.*, 27, 15, 2233-2236, 2000.
[31] Randriambelo T., et al., The effect of biomass burning, convective venting and transport on tropospheric ozone over the Indian ocean : Reunion island field observations, *J. Geophys . Res.*, 105, D9, 11813-11832, 2000.
[32] Baray J.L. et al., Dynamical study of a tropical cut-off low over South Africa, and its impact on tropospheric ozone, *Atmos. Environ.*, 37, 11, 1475-1488, 2003.
[33] Randriambelo T., et al., Investigation of the short-time variability of tropical tropospheric ozone, *Annales Geophys.*, 21, 9, 2095-2106, 2003.
[34] Stohl, A., et al., Validation of the Lagrangian particle dispersion model FLEXPART against large scale tracer experiments. *Atmos. Environ*. 32, 4245-4264., 1998.

bien adapté pour une application en bloc sur 500 profils d'ozone à la Réunion. Deux autres codes ont été envisagés, MIMOSA, un code d'advection de vorticité potentielle développé initialement pour les études de dynamique stratosphérique[35], et LAGRANTO, un code de trajectoires tri-dimentionnelles développé à l'école polytechnique de Zurich[36]. L'application de MIMOSA à la troposphère n'est pas sans poser quelques problèmes par rapport aux conditions aux limites basses par exemple, et il n'est également pas possible de calculer simplement des coupes verticales de vorticité potentielle advectée avec MIMOSA, celui-ci étant basé sur le principe d'advection sur surfaces isentropes. Ce code pourra donc être utilisé pour des inter-comparaisons, ou pour des cas d'études, mais il n'est pas très bien adapté pour détecter les masses d'air d'origine stratosphériques sur toute une base de données de profils d'ozone troposphérique. Quant à LAGRANTO, des problèmes de compilations de librairies se sont révélés insurmontables lors de son installation sur titan, le centre de calcul de l'université de la Réunion.

Pour les raisons indiquées précédemment, le code de trajectoire codé pendant ma thèse n'était pas adapté à ce travail non plus. Cependant, grâce au travail de Franck Gabarrot, ingénieur informaticien arrivé au LACY en 2007, mon programme de trajectoires a été recodé en C++, optimisé et les conditions aux limites gérées. Devenu LACYTRAJ, ce code a été appliqué à la base de données de la Réunion par Gaëlle Clain dans le cadre de sa thèse, ce qui a permis de quantifier l'influence des échanges stratosphère-troposphère sur la climatologie de l'ozone troposphérique de la Réunion. Les résultats sont en cours de finalisation et seront présentés par Gaëlle dans le cadre de sa thèse et d'un article en cours de rédaction.

D'autre part, l'objet du chapitre 1 de ce document était la présentation du parc instrumental qui s'est développé à la Réunion. L'analyse géophysique des données qui y sont faites, et particulièrement pour les études troposphériques, nécessite de pouvoir identifier sur un profil vertical les contributions des origines des masses d'air et leur mélange, pour comprendre les contributions des différents mécanismes. Cela peut être fait pour des études de cas. Cela peut aussi être étendu à la dimension climatologique et tendances à long terme. Les analyses de modèles globaux tels que ECMWF peuvent fournir des informations sur la compréhension des mesures, et c'est pour cela que la base de données des reanalyses ERA-40 est archivée sur les serveurs de l'OPAR.

[35] Hauchecorne, A., et al., Quantification of the transport of chemical constituents from the polar vortex to midlatitudes in the lower stratosphere using the high-resolution advection model MIMOSA and effective diffusivity, J. Geophys. Res., 107 (D20), 8289, doi :10.1029/2001JD000491, 2002.

[36] Wernli, H. and Davies, H. C.: A Lagrangian-based analysis of extratropical cyclones. Part I: The method and some applications, Quart. J. Roy. Meteorol. Soc., 123, 467–489, 1997.

Au-delà se son exploitation dans le cadre de la thèse de Gaëlle Clain, un autre intérêt de LACYTRAJ pourra donc être, en liaison avec les données de l'OPAR, de le faire fonctionner en routine sur toutes les données produites par la station et ainsi fournir une information additionnelle sur l'origine des masses d'air.

En aval du calcul des trajectoires LACYTRAJ, nous avons également développé un module RDF[37,38] utilisant les trajectoires calculées avec LACYTRAJ. RDF est une technique d'advection de traceurs conservatifs qui, à partir d'un champ donné, permet de retrouver des informations supplémentaires sous-grille par rapport aux champs d'assimilation. Ce type d'outil peut être utilisé pour la caractérisation de l'influence des feux de biomasse ou des échanges stratosphère-troposphère.

L'algorithme du code de calcul de trajectoire, ses performances et des comparaisons avec FLEXPART seront présentés dans la section 2.6.2. La vorticité potentielle est un traceur stratosphérique dont la durée de vie dans la troposphère est de l'ordre d'une semaine. Des exemples de reconstructions RDF de vorticité potentielle et leur utilisation pour l'étude climatologique qui est faite dans le cadre de la thèse de Gaëlle Clain seront présentés dans la section 2.6.3. Le rapport de mélange de vapeur d'eau peut également être utilisé comme traceur des masses d'air, puisque ce traceur présente des distributions très contrastées, avec de fortes valeurs dans les plus basses couches de la troposphère et des faibles valeurs dans la haute troposphère et la stratosphère. Néanmoins, l'utilisation de la technique RDF sur les rapports de mélange de vapeur d'eau n'est pas aussi simple que sur la vorticité potentielle, du fait du caractère peu conservatif de la vapeur d'eau dans la troposphère. Les premiers tests de reconstructions de profils et de champs de vapeur d'eau seront présentés dans la section 2.6.4, ainsi que les pistes prospectives que nous proposons pour améliorer la méthode.

2.3.1.2 Trajectoires : Algorithme de LACYTRAJ et comparaisons avec FLEXPART

[37] Dritschel, D. G., Contour Surgery: A topological reconnection scheme for extended integrations using contour dynamics, *J. Comput. Phys.*, 77, 240-266, 1988.
[38] Sutton, R. T, et al., High-Resolution Stratospheric Tracer Fields Estimated from Satellite Observations using Lagrangian Trajectory Calculations, *J. Atmos. Sci.*, 51, 2995-3005, 1994.

LACYTRAJ est un code de trajectoires cinétiques codé en C++ utilisant les réanalyses ECMWF ERA-40 archivées localement et en format wgrib. Les données ont une résolution horizontale de 1.125 degrés, 21 ou 23 niveaux de pression et une résolution temporelle de 6 heures (analyses à 0, 6, 12, 18 UTC). Il est possible de lancer LACYTRAJ sur des données ayant une meilleure résolution. Il peut également être lancé sur d'autres types de données en format wgrib (d'autres types de reanalyses, données de forecast... etc).

L'utilisateur définit une grille de départ en 3 dimensions (une pour un profil ou 2 pour une coupe verticale ou un champ horizontal), et chaque point de grille est advecté par interpolation bi-linéaire du champ de vent horizontal et du temps. L'altitude de chaque point est calculée par interpolation du vent vertical ECMWF par interpolation logarithmique sur le niveau de pression. Cette opération est faite sur un pas de temps défini par l'utilisateur, typiquement entre 15 minutes pour un calcul de trajectoire de l'ordre de quelques jours. Après le calcul, un fichier de sortie binaire contenant les points de toutes les trajectoires est écrit, il est possible de ne sauvegarder qu'une partie des points (uniquement les points d'origine, 25 ou 50% des points).

LACYTRAJ fonctionne actuellement sur un PC-linux équipé d'un double processeur Intel, 4MB Cache, 1.60GHz, 1066MHz FSB, 4GB FB 533MHz Memory (4x1GB dual rank DIMMs). Sur cette machine, un calcul LACYTRAJ de 40000 trajectoires de 6 jours avec un pas de temps de 15 minutes ne dure que 2'52.

LACYTRAJ ne fonctionne actuellement qu'en mode retro-trajectoire, mais un mode de trajectoires avant est à l'étude. Dans le futur, compte tenu de la vitesse de calcul et de la facilité d'utilisation de LACYTRAJ, ce mode pourrait être utilisé en quasi-temps réel pour optimiser les stratégies d'observations lors de campagnes multi-instrumentales.

Dans l'étude présentée dans la section 2.3.2 (Leclair de Bellevue et al., 2006) des trajectoires ont été calculées avec le modèle de dispersion FLEXPART dans sa version 4.3. FLEXPART était initialisé avec les réanalyses ECMWF avec une résolution horizontale de 1 degré, 60 niveaux verticaux de modèle et une résolution temporelle de 3 heures. Les trajectoires LACYTRAJ présentées dans la figure 2.3 correspondent aux trajectoires FLEXPART de la situation synoptique du cyclone Guillaume en Février 2002, (figure 8 de Leclair de Bellevue et al., 2006, section 2.3.2).

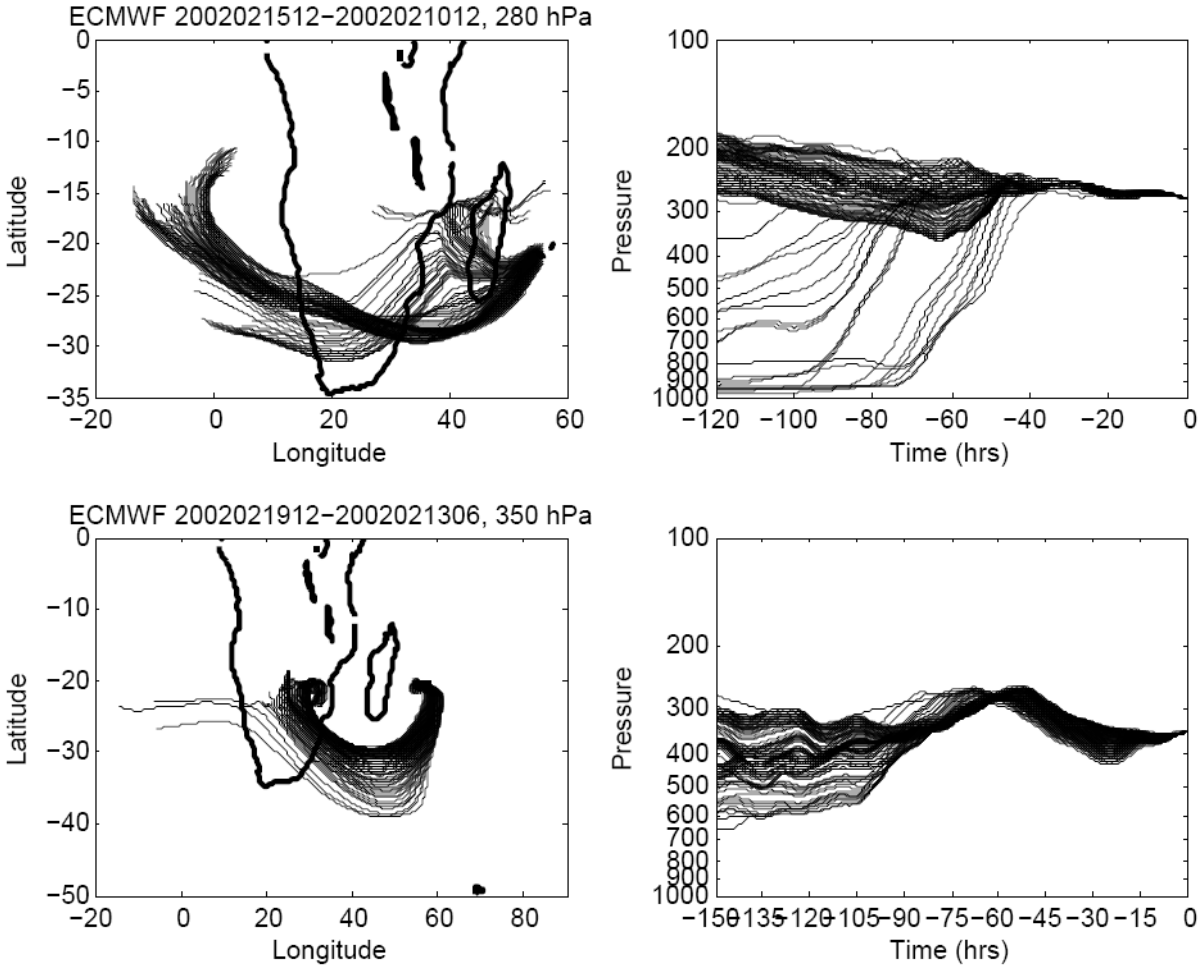

Figure 2.3 Faisceau de rétrotrajectoires arrivant au-dessus de la Réunion le 19 et le 15 Février 2002, coïncidant aux trajectoires Flexpart présentés dans la figure 8 de l'article présenté dans la section 2.3.2 (Leclair de Bellevue et al., 2006).

Calculer des trajectoires à proximité d'un cyclone tropical n'est pas un exercice simple, car les champs de vent présentent des gradients localement forts et un petit écart de trajectoire à un instant donné peut très vite induire des écarts beaucoup plus grands sur une trajectoire de quelques jours, d'autant plus lorsque l'on veut comparer des modèles de nature différente. FLEXPART est un code de dispersion recalculant les niveaux verticaux avec son propre schéma convectif, ce que ne fait pas LACYTRAJ. Ceci étant précisé, les comparaisons FLEXPART-LACYTRAJ pour le cas de Guillaume montrent que :

–Pour les trajectoires arrivant au-dessus de la Réunion le 15 Février 2002, les deux modèles sont en accord pour voir deux subsidences, séparées par une ascension des masses d'air entre -60 et -30

heures.

–Une partie du faisceau de trajectoire LACYTRAJ provient de la basse troposphère dans le canal de Mozambique, ou des zones convectives associées à Guillaume sont visibles sur les images Meteosat. Cette origine n'est pas vu par FLEXPART. Le reste du faisceau LACYTRAJ est en accord avec FLEXPART, avec une origine dans l'océan Atlantique pour les deux modèles.

–Pour les trajectoires arrivant au-dessus de la Réunion le 19 Février 2002, les trajectoires sont très similaires pour les deux modèles.

On peut donc constater qu'en dépit de la différence de nature des deux codes, et de la différence de résolution des données d'initialisation, les deux modèles sont en relativement bon accord pour les comparaisons de Février 2002.

2.3.1.3 Advection RDF de vorticité potentielle

Après le calcul des trajectoires, il est possible d'advecter un traceur le long de chaque trajectoire, et ainsi reconstruire un profil ou un champ du paramètre advecté. Cette méthode appelée RDF permet d'obtenir de l'information qui ne figure plus dans le champ d'initialisation, y compris à une échelle sous-grille sur la distribution de traceur.

La vorticité potentielle (PV) peut être considérée comme un traceur des masses d'air d'origine stratosphérique, conservatif dans la troposphère à une échelle temporelle de quelques jours. Deux profils d'ozone avaient été obtenus par lidar le 3 et le 4 décembre 1999, 18 heures TU à la Réunion, à l'occasion de l'étude qui est présentée dans la section 2.4. La figure 2.4 la comparaison entre les deux profils d'ozone et les profils de vorticité potentielle directement obtenus avec les analyses ERA-40 de ECMWF, et les profils advectés avec LACYTRAJ sur 24 et 48 heures le 4 décembre 1999, 0 heure TU. Dans les deux profils, on peut observer une couche présentant des fortes valeurs d'ozone entre 5 et 11 km le 3 décembre, et entre 6 et 12 km le 4 décembre, avec des valeurs maximales de 108 ppbv à 8.3 km le 3 décembre et 94 ppbv à 8.8 km le 4 décembre. La reconstruction de PV montre un pic important, 2.5 PVU avec un temps de trajectoire de 48 h, et également un pic de 1 PVU avec un temps de trajectoire de 24 heures. L'altitude du pic de PV est entre les niveaux isobares 500 et 350 hPa, correspondant à la partie basse de la couche enrichie en ozone observée sur les radiosondages, environ 2 km en dessous du pic d'ozone. L'origine stratosphérique suggérée par les reconstructions RDF n'était pas bien capturée par les analyses ERA-40 sans advection RDF. On peut supposer que dans le cas étudié, des échanges stratosphère-

troposphère ont partiellement contribué à l'enrichissement d'ozone troposphérique observé par le lidar, en plus de l'influence des feux de biomasse, début Décembre étant la fin de la saison des feux d'Afrique et de Madagascar. Cet exemple montre que pour la PV, une advection de 48 heures est préférable que 24 heures pour la détection des masses d'air stratosphériques. Dans le cadre de sa thèse, Gaëlle Clain va utiliser LACYTRAJ avec une combinaison de trajectoires de 48 heures et de 120 heures pour détecter les masses d'air d'origine stratosphérique sur les profils d'ozone obtenus par lidar et radiosondage à la Réunion.

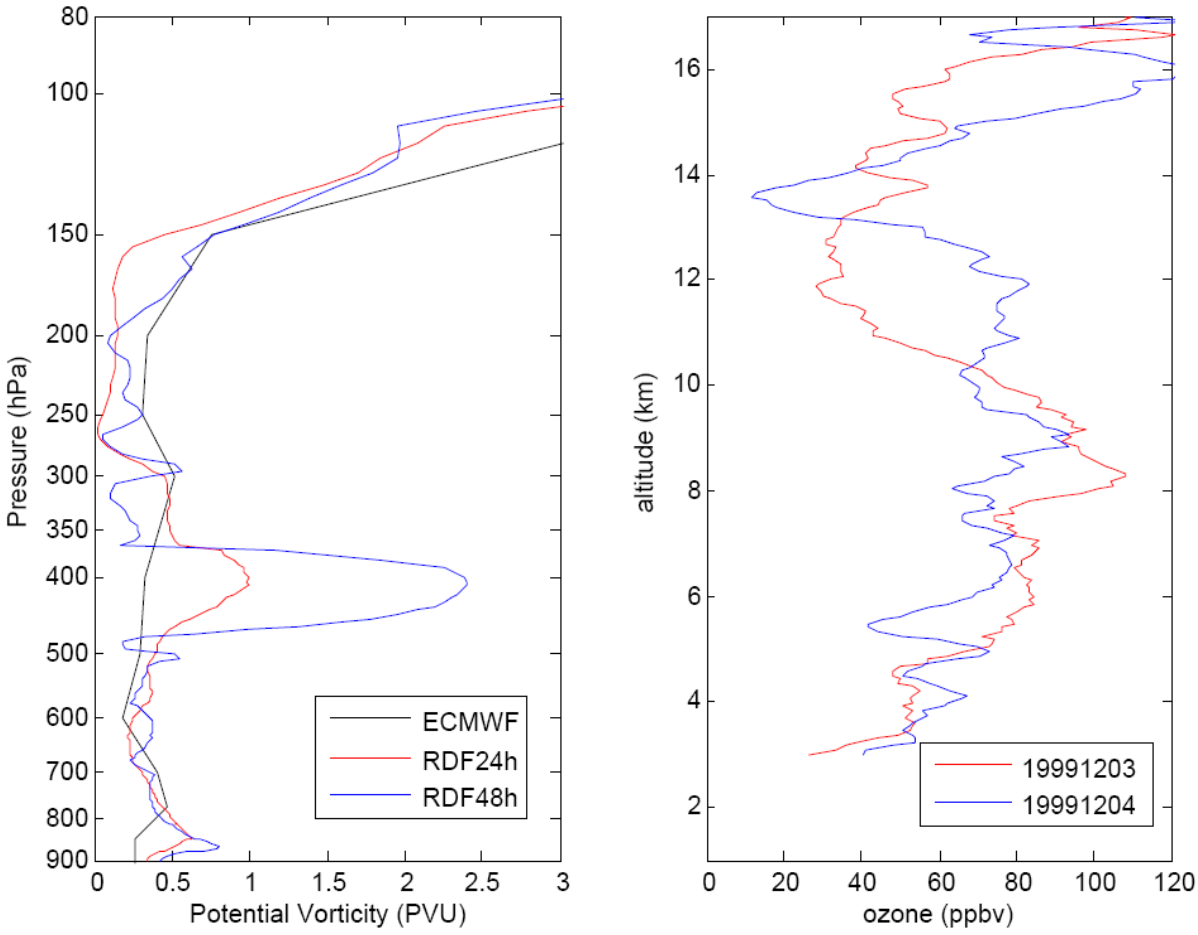

Figure 2.4 Profils de vorticité potentielle (en valeur absolue) le 4 décembre 1999, 0 hTU (gauche) et d'ozone (droite) obtenus par mesure lidar.

Le code ne permet pas uniquement de calculer un profil de traceur advecté, mais sur un domaine tridimensionnel, et donc sur une coupe verticale ou un champ isobare. La figure 2.5 présente la section verticale méridienne de PV à la longitude de la Réunion le 3 et le 4 Décembre 1999, en

comparaison avec les analyses ERA-40. On observe que la reconstruction RDF amplifie le filament stratosphérique d'une foliation de tropopause, la Réunion étant localisée en entrée d'un noyau de courant-jet. L'analyse ERA-40 voyait une déformation de la tropopause d'amplitude trop limitée pour qu'elle concerne la latitude de Réunion. Le 4 Décembre, on observe une dilution du filament qui reste toutefois visible avec la reconstruction RDF.

Nous avons également effectué une comparaison avec un calcul de vorticité potentielle advectée par le code MIMOSA dans le cadre de la thèse de Nadège Montoux[39]. L'advection de la vorticité potentielle avec LACYTRAJ permet de faire apparaître des filamentations très proches de celles obtenues avec le code MIMOSA (Figure 2.6).

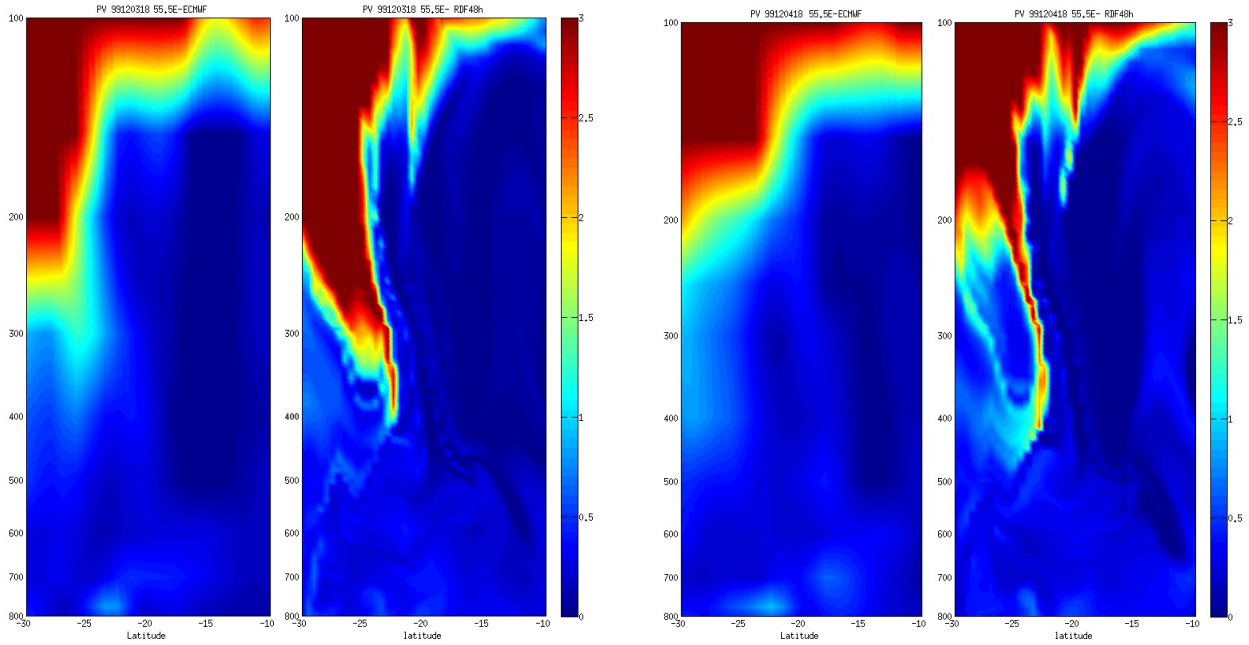

Figure 2.5 Coupes de vorticité potentielle (en valeur absolue) à la longitude 55°E , de gauche à droite respectivement : ECMWF et RDF, le 3 et le 4 Décembre 1999.

[39] Montoux N., Etude du transport isentrope de la vapeur d'eau dans la haute troposphère et la basse stratosphère, thèse de doctorat de l'université Pierre et Marie Curie, 2008.

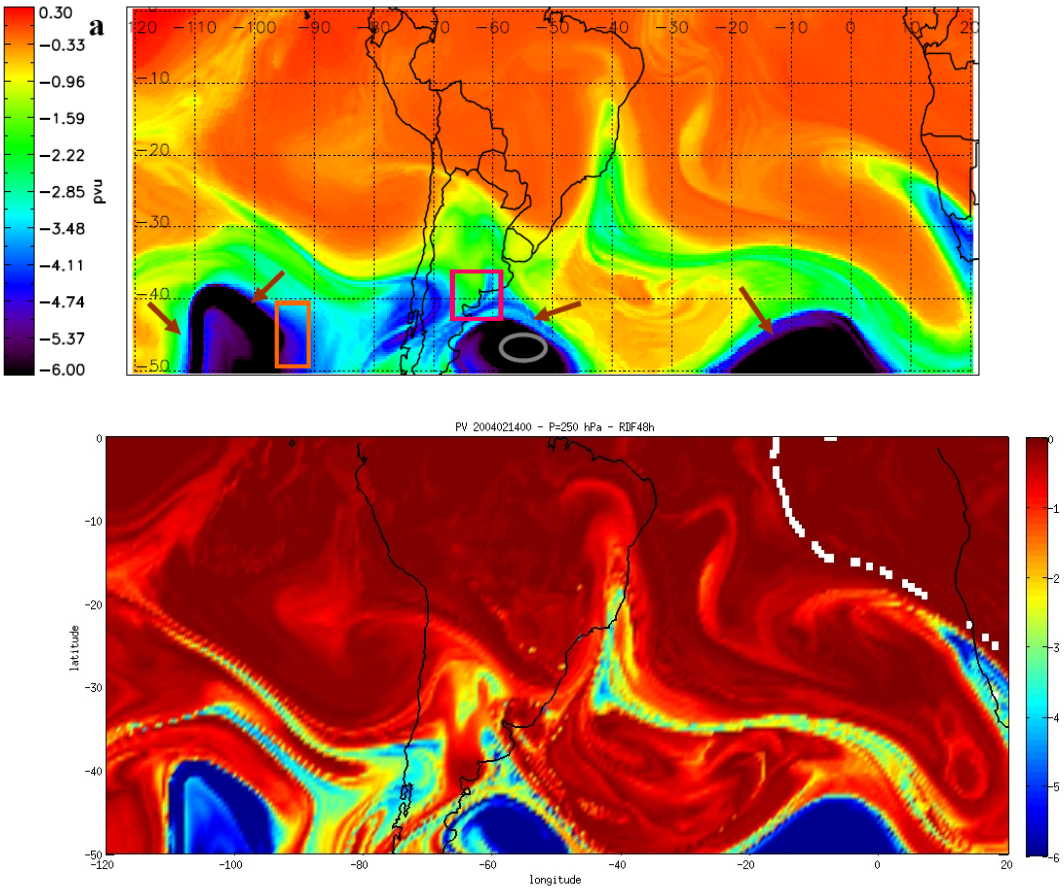

Figure 2.6 Champs horizontaux de vorticité potentielle advectée sur le niveau 250 hPa le 14 Février 2004, en haut avec MIMOSA (figure4.4 de la page 82 de la thèse de Nadège Montoux), et en bas avec LACYTRAJ.

2.3.1.4 Advection RDF de vapeur d'eau

Nous avons vu que l'advection RDF de la vorticité potentielle avec 48 heures de temps de trajectoire permet d'apporter une information additionnelle par rapport aux champs d'initialisation, et en accord avec d'autres codes validés tels que MIMOSA. Un autre traceur utilisable pour la détection de l'origine des masses d'air est le rapport de mélange de vapeur d'eau. Le rapport de mélange est calculé à partir de l'humidité relative en utilisant la formule de Hyland et Wexler[40]. Le problème de l'utilisation de ce traceur avec la méthode RDF est la non-conservation de ce traceur dans la troposphère à l'échelle de quelques jours. Nous avons donc effectué les premiers tests en limitant les temps de trajectoire à 6 ou 12 heures.

Sur la figure 2.7 nous présentons une comparaison entre le profil de vapeur d'eau obtenu à la

[40] Hyland, R. W. and A. Wexler, Formulations for the Thermodynamic Properties of the saturated Phases of H2O from 173.15K to 473.15K, ASHRAE Trans, 89(2A), 500-519, 1983.

Réunion par lidar Raman le 5 avril 2002. Le profil lidar est comparé avec les profils de vapeur d'eau ECMWF et RDF.

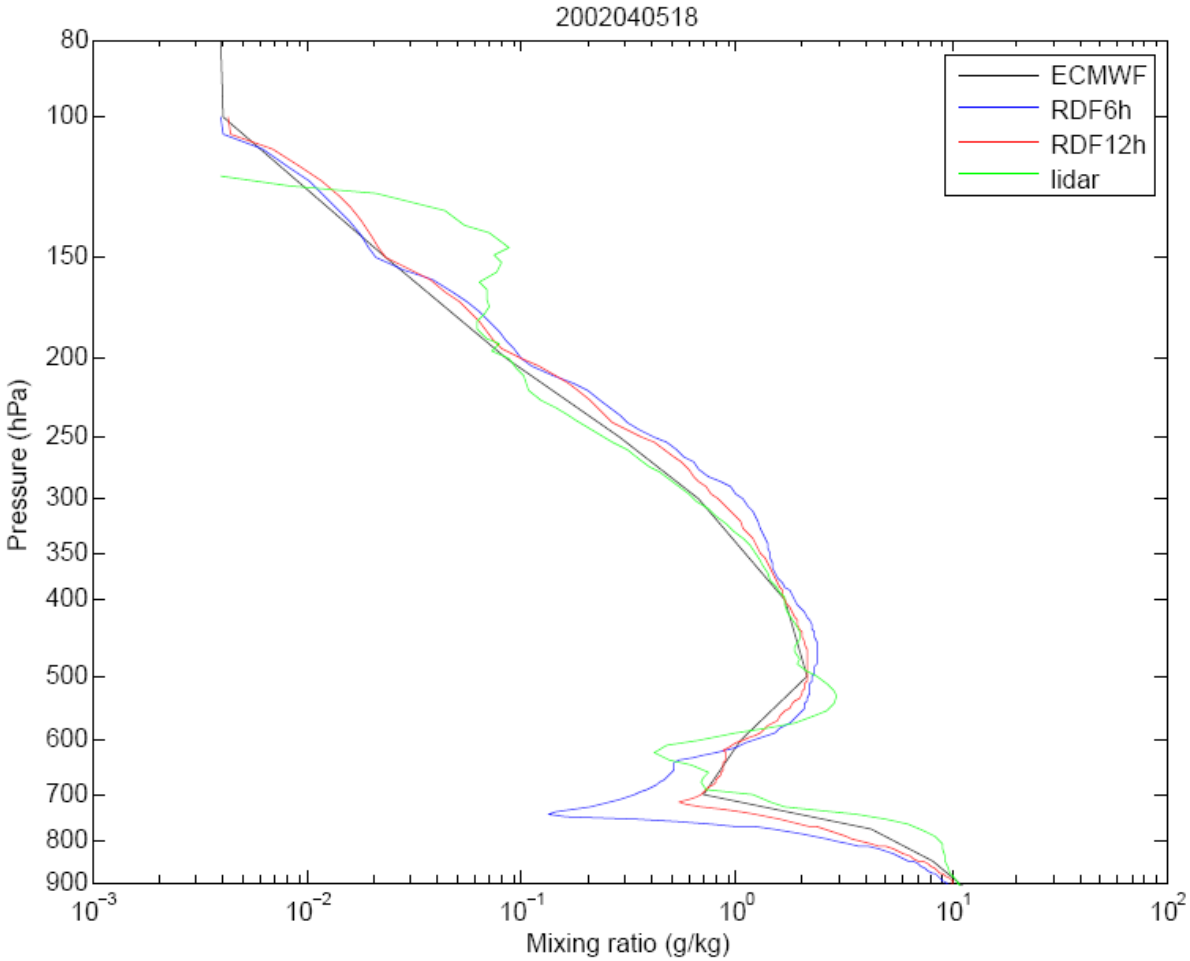

Figure 2.7 Profils de vapeur d'eau obtenus le 5 avril 2002 par lidar Raman, en comparaison des profils ECMWF et RDF sur 6 et 12 heures. Développement instrumental et acquisition lidar : Laurent Robert ; Traitement : Christophe Hoareau.

Le profil lidar Raman a été calibré avec le profil ECMWF entre 3 et 8 km. Le profil ECMWF présente une couche sèche sur deux points : 700 et 600 hPa. Le profil RDF confirme cette couche sèche, particulièrement avec 6 heures de trajectoires. L'accord entre les profils de vapeur d'eau est bon jusqu'à 180 hPa. Le profil ECMWF sous-estime la vapeur d'eau au-dessus de 180 hPa, en comparaison avec le lidar Raman, l'advection RDF n'améliorant pas l'accord avec le profil Raman.

Des profils de reconstruction RDF ont été calculés sur d'autres profils lidar Raman, ainsi que sur la

campagne de mesure par sondes CFH[41] effectuée en juin-juillet 2006. Ces inter-comparaisons ne présentent pas un meilleur résultat que celle présentée dans la figure 2.7.

La reconstruction RDF de profils de vapeur d'eau avec 6 heures de trajectoire n'éloigne donc pas le profil ECMWF des données in-situ. Par contre, les exemples calculés jusqu'alors ne permettent pas non plus d'affirmer qu'ils apportent une information additionnelle significative par rapport aux champs d'initialisation, contrairement à l'advection de PV sur 48 heures.

De la même façon que pour la PV, il est possible de reconstruire des coupes verticales de rapport de mélange de vapeur d'eau, ce qui a été fait pour le 3 et le 4 décembre 1999 (figure 2.8). On peut voir que les filaments qui avaient été identifiés comme d'origine stratosphérique sur la vorticité potentielle (figure 2.5) correspondent effectivement à des zones sèches. Les gradients des structures sèches semblent mieux marquées avec la reconstruction RDF avec 6 heures de trajectoires que sur les champs ECMWF.

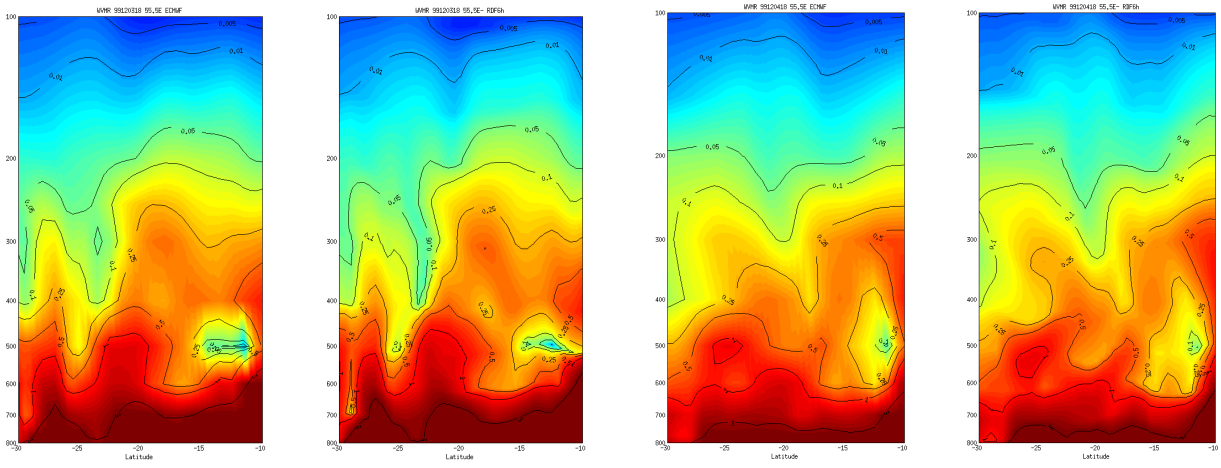

Figure 2.8 Coupes verticales de rapport de mélange de vapeur d'eau (en valeur absolue) à la longitude 55°E , de gauche à droite respectivement : ECMWF et RDF (6 heures), le 3 et le 4 décembre 1999. Les échelles de couleur sont logarithmiques entre 0.001 (bleu) et 3 g/kg (rouge).

[41] Vömel H. et al., Accuracy of tropospheric and stratospheric water vapor measurements by the cryogenic frost point hygrometer: Instrumental details and observations, J. Geophys. Res., 112, D08305, doi:10.1029/2006JD007224, 2007.

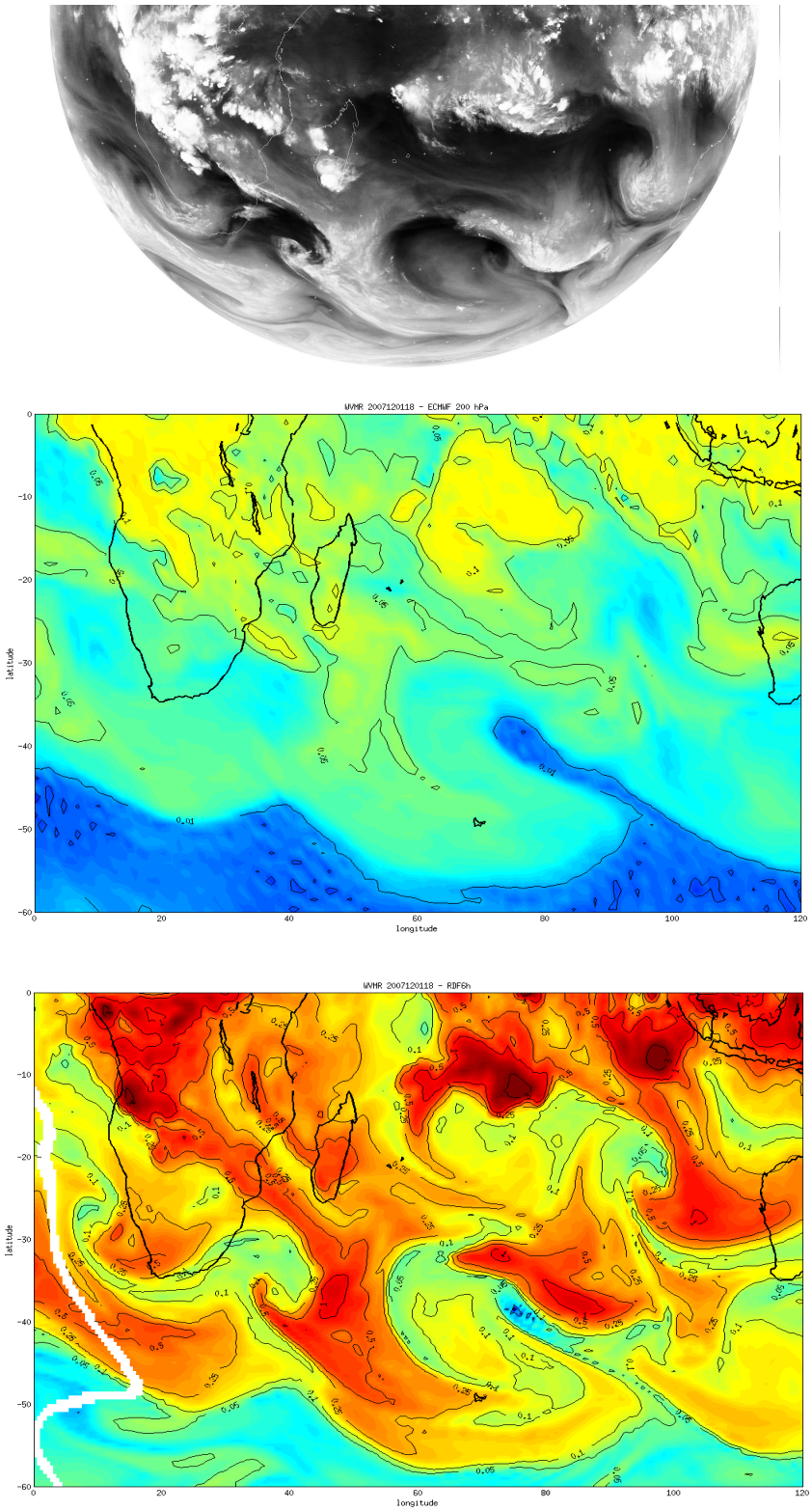

Figure 2.9 Comparaison entre le canal vapeur d'eau de Meteosat 7 le 12 Janvier 2007 (haut), avec le champ ECMWF-ERA 40 (milieu), et la reconstruction RDF-LACYTRAJ. Les échelles de couleur sont logarithmiques entre 0.001 (bleu) et 3 g/kg (rouge).

Pour la vapeur d'eau, les inter-comparaisons les plus convaincantes sont celles qui ont été calculées sur des champs horizontaux dans la haute troposphère. La figure 2.9 présente une comparaison de

RDF-LACYTRAJ avec le canal vapeur d'eau de Meteosat 7 le 12 janvier 2007, et la figure 2.10 avec une simulation MIMOSA présentée dans la thèse de Nadège Montoux.

MIMOSA est un code d'advection isentrope, un module microphysique a été développé pour modéliser les changements de phase de l'eau et la sédimentation des particules de glace. Cela permet de modéliser la coexistence dans le modèle des 3 phases de l'eau, et les interactions entre ces trois réservoirs en fonction de la température et de la pression. L'utilisation de trajectoires plus longues (6 jours) devient donc possible et réaliste.

Les inter-comparaisons entre les champs de vapeur d'eau LACYTRAJ et les images Meteosat (figure 2.9) et les modélisations MIMOSA (Figure 2.10), tout en restant dans le domaine qualitatif, sont satisfaisantes par rapport aux petites structures sèches et humides.

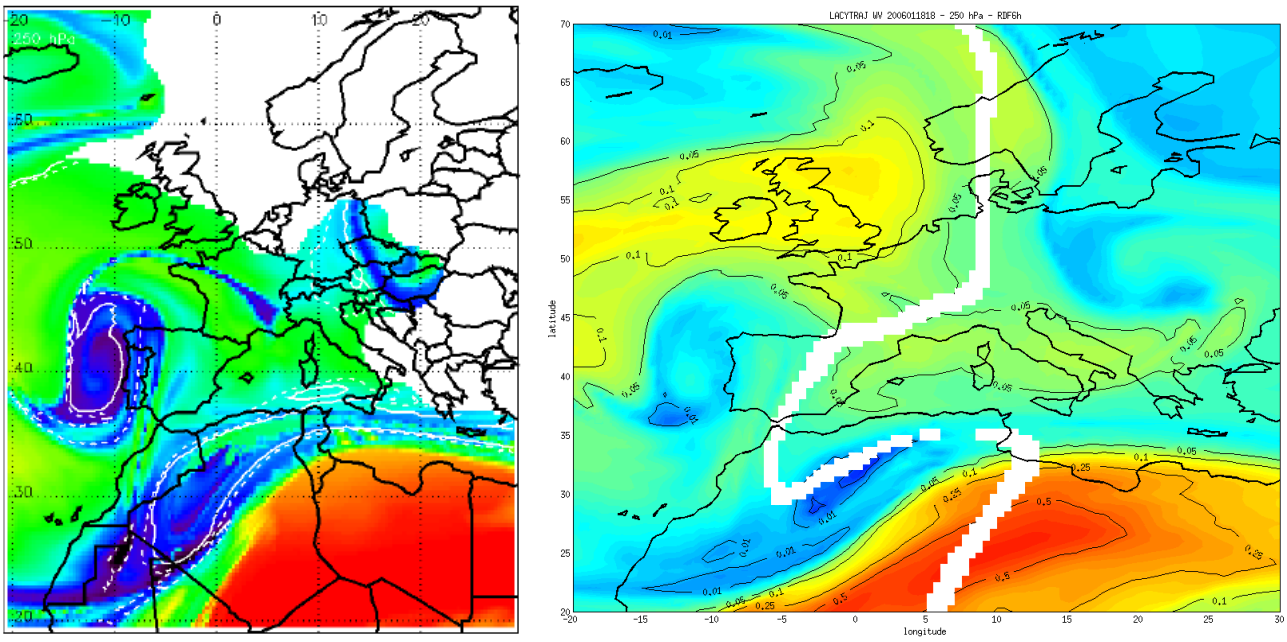

Figure 2.10 Comparaison entre le champ de vapeur d'eau obtenu au-dessus de l'Europe à l'altitude 250 hPa par simulation mimosa (à gauche, en ppmv, l'échelle de couleur allant de 0-bleu à 100–rouge) et avec LACYTRAJ à droite (en g/kg, même échelle de couleurs que la figure 2.9). La simulation MIMOSA est extraite de la thèse de Nadège Montoux (figure 5.7, page 125).

Toutefois, deux problèmes subsistent :

- La durée de vie de la vapeur d'eau dans la troposphère est court. A cause des changements de

phase de l'eau, en particulier dans les masses d'air influences par la convection tropicale, le rapport de mélange de vapeur d'eau est un traceur peu conservatif, ce qui nous a amené à réduire le temps des trajectoires à 6 heures. Nous prévoyons d'améliorer ce point en allongeant le temps des trajectoires et en appliquant le code micro-physique qui a été développé pour le code MIMOSA dans le cadre de la thèse de Nadège Montoux.

- Les calculs RDF sont initialisés avec les données ECMWF-ERA40 qui, pour l'humidité et la vapeur d'eau, sont bonnes pour la basse et moyenne troposphère, mais qui sous-estiment la vapeur d'eau dans l'UTLS. Pour améliorer ce point, une possibilité serait de n'utiliser les données ECMWF que pour les calculs de trajectoires, et d'utiliser d'autres données pour l'initialisation de la vapeur d'eau pour les calculs RDF. Nous prévoyons de tester dans un premier temps les nouveaux produits ECMWF tels que les analyses ERA-INTERIM. Les données satellites telles que AIRS/AMSU, SAGE-II, HALOE, MIPAS ou GOMOS pourront également être utilisées dans le futur.

2.3.2 Etude des tendances de l'ozone troposphérique par régression linéaire

2.3.2.1 Méthodologie

Les mesures d'ozone ayant débuté en 1992 à la Réunion, nous disposons d'un jeu de données qui couvre plus de 15 ans. La base de données de Irene en Afrique du sud a commencé en 1990, mais avec une interruption des données entre 1994 et 1998. La temporalité de ces jeux de données étant suffisante pour effectuer une estimation des tendances, nous avons donc choisi, comme première approche, d'effectuer une simple régression linéaire sur le jeu de données.

La droite de régression linéaire liant l'ozone et le temps est donnée par la formule suivante :

(1) $$y = a \cdot x + b$$

où x est la colonne d'ozone, y le temps (en années), a est le coefficient directeur de la droite de régression linéaire et b la valeur à l'origine.

Le jeu de données x des colonnes d'ozone (en DU) comporte n valeurs, chacune d'entre elles étant associée à une date (en années + jours juliens). Le coefficient directeur a représente donc la tendance de l'ozone que l'on cherche à estimer. Nous devons également déterminer l'erreur

statistique sur a. Pour cela, nous avons besoin d'un certain nombre de calculs intermédiaires.

La moyenne, la variance et l'écart-type de l'ozone :

(2) $$\overline{x} = \frac{1}{n}\sum_{i=1}^{n} x_i \quad V(x) = \frac{1}{n}\sum_{i=1}^{n}(x_i - \overline{x})^2 = \overline{x^2} - \overline{x}^2 \qquad \sigma_x = \sqrt{V(x)}$$

La moyenne, la variance et l'écart-type du temps :

(3) $$\overline{y} = \frac{1}{n}\sum_{i=1}^{n} y_i \qquad V(y) = \frac{1}{n}\sum_{i=1}^{n}(y_i - \overline{y})^2 = \overline{y^2} - \overline{y}^2 \qquad \sigma_y = \sqrt{V(y)}$$

La covariance de la matrice (ozone, temps) est donné par la formule :

(4) $$cov(x,y) = \frac{1}{n}\sum_{i=1}^{n}(x_i - \overline{x})(y_i - \overline{y}) = \overline{x \cdot y} - \overline{x} \cdot \overline{y}$$

On obtient finalement les coefficients de la droite de régression :

(5) $$a = \frac{cov(x,y)}{V(x)} \qquad\qquad b = \overline{y} - \frac{\overline{x} \cdot cov(x,y)}{V(x)} = \overline{y} - a \cdot \overline{x}$$

Pour calculer l'erreur statistique sur la tendance, due à la variabilité des données d'ozone, nous devons calculer la différence entre les valeurs observées et la valeur données par le modèle de régression, avec la formule suivante :

(6) $$\varepsilon_i = y_i - a x_i - b$$

L'estimateur de la variance résiduelle et de la variance de a sont données respectivement par :

(7) $$\hat{\sigma}_\varepsilon^2 = \frac{1}{n-2} \cdot \sum_{i=1}^{n} \varepsilon_i^2 \qquad\qquad \hat{\sigma}_a^2 = \frac{\hat{\sigma}_\varepsilon^2}{n \cdot V(x)}$$

On est dans le cadre d'un test de Student sur l'espérance avec écart-type inconnu. L'erreur statistique sur a est donc donné par la formule suivante:

(8) $$\Delta a = \hat{\sigma}_a \cdot t^{n-2}_{(1-\alpha)/2}$$

Dans laquelle $t^{n-2}_{(1-\alpha)/2}$ est le quantile de la loi de Student, dont les valeurs sont données dans la table 1.

Table 1. Valeurs des quantiles de la loi de Student, en fonction du nombre de données n et du niveau de confiance. D'après Spiegel M.R et al.[42].

n	***75%***	***85%***	***95%***	***97.5%***	***99%***
5	0.727	1.156	2.015	2.571	3.365
20	0.687	1.064	1.725	2.086	2.528
100	0.677	1.042	1.660	1.984	2.364
120	0.677	1.041	1.658	1.980	2.358
∞	0.674	1.036	1.645	1.960	2.326

Nous prendrons comme valeur de quantile 1,645 , correspondant au niveau de confiance 95% pour un échantillon infini, le nombre de points étant supérieur à 120.

La tendance et l'erreur statistique ainsi calculées sont en DU/an. Par la suite nous multiplierons par 10 pour les obtenir en DU/décade.

2.3.2.2 Résultats

Les tendances de l'ozone troposphérique calculées pour les sites de Irene et de la Réunion sont présentées dans la figure 2.11.

[42] Spiegel, et al., Statistique. Cours et problemes, Paris : McGraw-Hill ed., Série Schaum, 432 p., 1993.

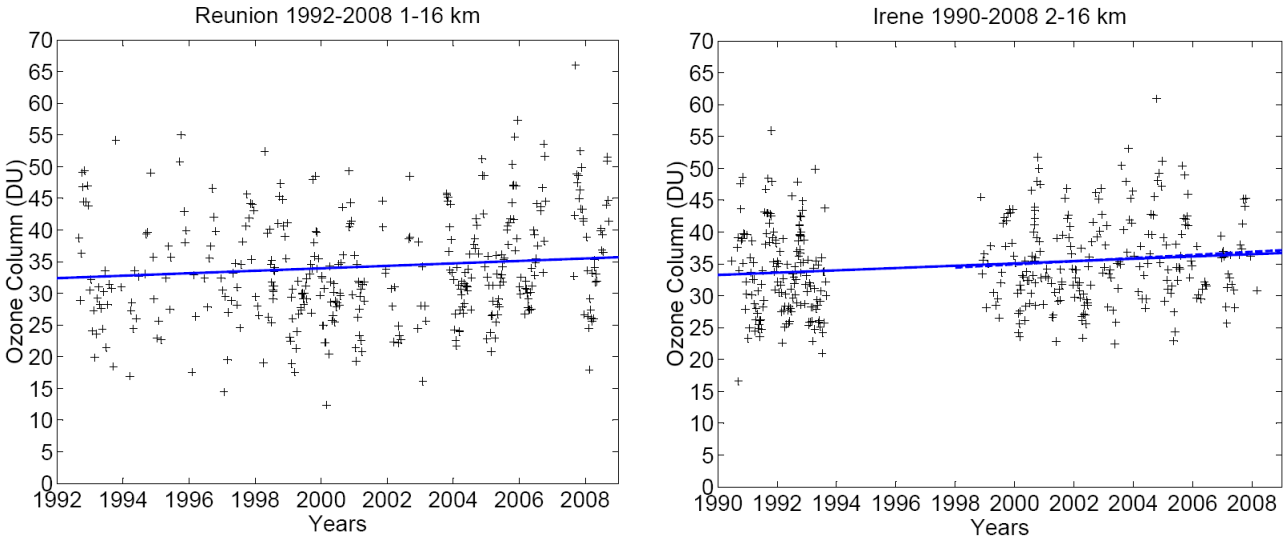

Figure 2.11 Tendances de l'ozone troposphérique à la Réunion (à gauche) et Irene (à droite). La ligne pointillées indique la tendance pour la période 1998-2008 à Irene.

La limite inférieure de la colonne troposphérique est fixée à 1 km pour la Réunion et 2 km pour Irene, de fait de l'altitude des sites de mesure. La limite supérieure est fixée à 16 km, ce qui se situe en dessous de la hauteur de tropopause des deux sites[43]. La tendance observée pour la colonne troposphérique est positive (1.94 +/- 1.81 DU/décade) pour la Réunion, ainsi que pour (1.81 +/- 0.97 DU/décade). Ces deux valeurs sont supérieures à l'erreur statistique calculée pour les deux sites.

Dans le but d'étudier l'influence potentielle des deux principales source de l'ozone troposphérique (anthropiques-feux et dynamiques-STE) sur les tendances observées, la troposphère a été séparée en trois couches. Une en dessous de 4 km, l'altitude ou l'on observe généralement l'inversion des alizés[44], et la troposphère libre qui est séparée en 2 couches d'égale épaisseur : la moyenne troposphère entre 4 et 10 km et la haute troposphère entre 10 et 16 km.

Certaines différences entre les deux sites apparaissent (Fig. 2.12):

–La tendance pour basse troposphère à Irene est clairement positive (0.93 +/- 0.26 DU/décade), alors qu'à la Réunion, aucune tendance significative n'est observée (0.01 +/- 0.37 DU/décade).

–La tendance pour la moyenne troposphère à Irene est positive (0.63 +/- 0.53 DU/décade), mais plus faible que la tendance pour la basse troposphère (0.92 +/- 0.26 DU/décade). La tendance la plus faible est obtenue pour la haute troposphère (0.24 +/- 0.43 DU/décade).

[43] Sivakumar, V. et al., Tropopause characteristics over a southern subtropical site, Reunion Island (21 S, 55 E): Using radiosonde-ozonesonde data, J. Geophys. Res., 111, D19111, doi:10.1029/2005JD006430, 2006.
[44] Taupin F.G. et al., tropospheric ozone above southwestern Indian ocean is strongly linked to dynamical conditions prevailing in the tropics, J. Geophys. Res., 104, 8057-8066, 1999.

–Pour la Réunion, on observe le comportement opposé. La tendance pour la moyenne troposphère est supérieure à celle pour la basse troposphère, mais n'est pas significative (0.70 +/- 0.93 DU/décade). La tendance la plus forte est obtenue pour la haute troposphère (1.31 +/- 0.62 DU/décade).

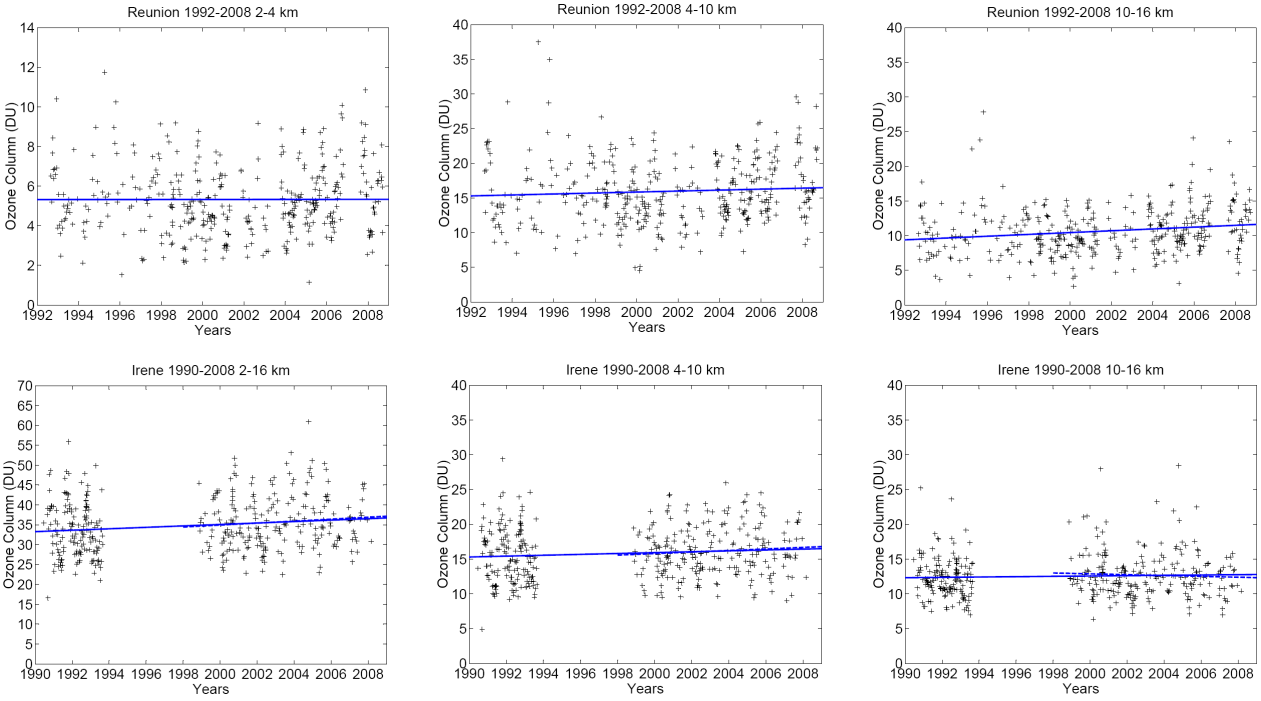

Figure 2.12 Tendances troposphériques par couches, à la Réunion (en haut) et à Irene (en bas), entre 2 et 4 km (à gauche), entre 4 et 10 km (au centre) et entre 10 et 16 km (à droite). La ligne pointillées indique la tendance pour la période 1998-2008 à Irene.

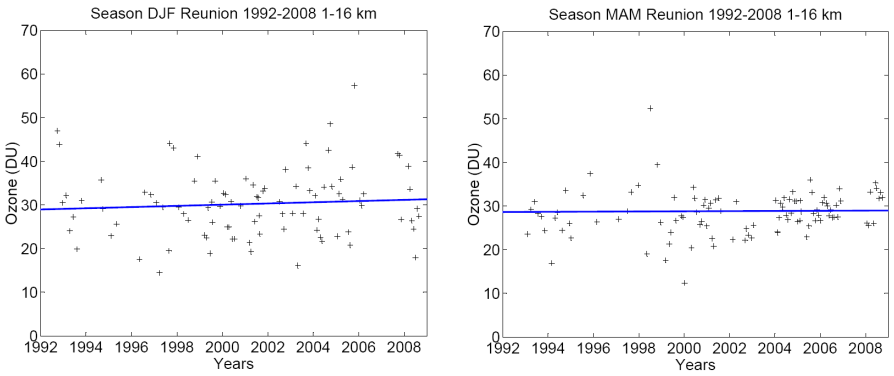

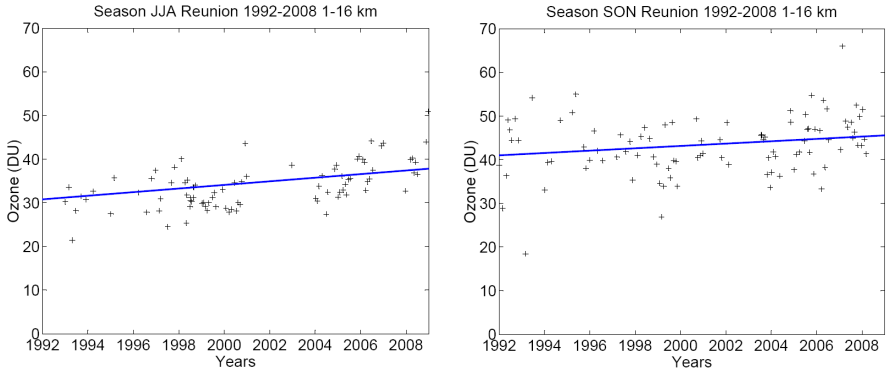

Figure 2.13 Tendances saisonnières troposphériques à la Réunion.

Pour approfondir d'avantage l'étude de l'influence des différents mécanismes sur les tendances, nous avons séparé le jeu de données en saisons pour les deux sites, La Réunion (Figure 2.13) et Irene (Figure 2.14).

–Pour les deux sites, aucune tendance significative n'est observée pour Mars-Avril-Mai.

–Pour la Réunion, une la tendance est importante en Septembre-Octobre-Novembre (2.69+/-2.47 DU/décade) et maximale en Juin-Juillet-Août (4.14 +/- 3.70 DU/décade). La tendance la plus forte de la saison Septembre-Octobre-Novembre est observée en haute troposphère, et en Juin-Juillet-Août, dans toute la troposphère libre (moyenne et haute).

–Pour Irene, la tendance est forte en Septembre-Octobre-Novembre (2.70 +/- 1.66 DU/décade), mais également en Décembre-Janvier-Février (2.41 +/- 1.95 DU/décade), les deux avec des fortes valeurs dans la basse troposphère. La tendance est maximale en Juin-Juillet-Août (3.12 +/- 1.74 DU/décade) dans la moyenne troposphère, entre 4 et 10 km.

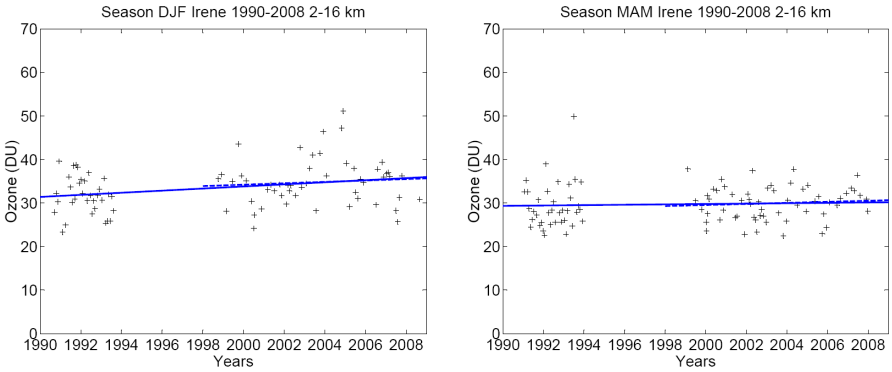

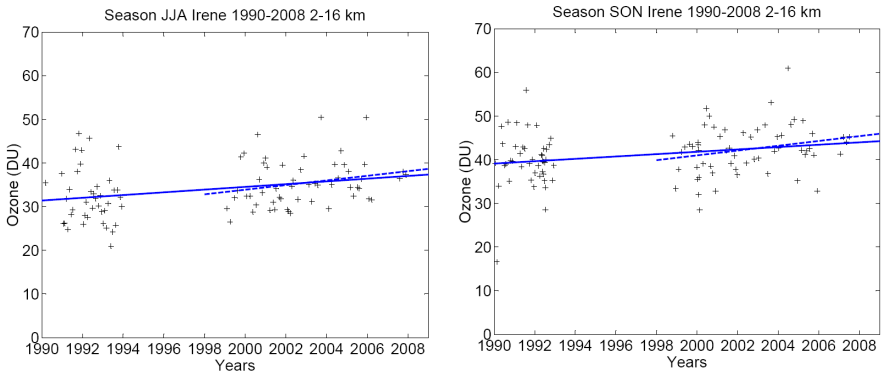

Figure 2.14 Tendances saisonnières troposphériques à Irene. La ligne pointillées indique la tendance pour la période 1998-2008 à Irene.

2.3.2.3 Discussions

Si la troposphère libre est potentiellement sous l'influence des feux de biomasse africains, les plus basses couches ne le sont pas directement à cause du régime d'est des vents d'alizés. On suppose que la plus basse couche n'est également pas directement influencée par les échanges stratosphère-troposphère, mais indirectement, des échanges avec la troposphère libre peuvent avoir lieu. A Irene, les sources locales de pollution sont importantes, en plus des feux de biomasse. Pour les deux sites, les deux couches 4-10 km et 10-16 km peuvent être influencées par les feux de biomasse et par les échanges stratosphère-troposphère.

Irene a une tendance positive pour la plus basse couche, ce qui n'est pas le cas de la Réunion. L'hypothèse d'une augmentation des feux de biomasse et/ou de la pollution en Afrique du Sud serait cohérente avec une tendance positive des plus basses couche à Irene, du fait des recirculations qui ont lieu en Afrique du Sud dans les basses couches[45] (Tyson and Preston-Whyte, 1988). Ce n'est pas le cas pour la Réunion ou les plus basses couches subissent le régime d'alizés, une injection des polluants suffisamment haute pour atteindre les régimes d'ouest est nécessaire pour que ceux-ci contaminent la Réunion.

Au regard des trois couches troposphériques, on observe que la tendance à Irene diminue avec l'altitude, ce qui suggère également que cette tendance est gouvernée par les plus basses couches, et donc par une éventuelle augmentation des sources anthropiques.

A la Réunion, la tendance est maximum entre 10 et 16 km. Deux explications pour cette tendance positive dans la plus haute couche troposphérique sont possibles : L'influence de l'augmentation des sources Anthropiques en Afrique du sud qui, du fait du contexte dynamique, peuvent influencer la troposphère libre de la Réunion après transport. La seconde explication serait une augmentation des

[45] Tyson, P. D. and Preston-Whyte, R. A.: the weather and Climate of Southern Africa, Oxford Univ. Press, 2000.

échanges stratosphère-troposphère induit par le changement climatique.

La séparation saisonnière du jeu de données de la Réunion et Irene est basée sur les résultats des travaux développé dans le cadre des thèses de Fabienne Taupin, Tantely Randriambelo, Jimmy Leclair de Bellevue et la mienne :

–L'influence des feux de biomasse est maximale en Septembre-Octobre-Novembre.

–La position en latitude du courant-jet subtropical est la plus haute, et son intensité est maximale en Juin-Juillet-Août. La Réunion étant localisée au nord de la position moyenne du courant-jet, en théorie, on peut supposer que l'influence maximale du courant-jet est donc maximale pendant cette saison.

–La saison cyclonique de la Réunion est Décembre-Janvier-Février. L'influence des échanges stratosphère-troposphère associés à la convection tropicale est donc maximale pendant cette saison.

–La saison Mars-Avril-Mai est représentation du niveau de fond de l'ozone troposphérique, puisque ses deux sources sont relativement faibles.

En regard de ces considérations, les résultats sur les tendances saisonnières montrent que :

–Les deux sites montrent effectivement des tendances faibles en Mars-Avril-Mai.

–Pour la Réunion, la tendance est maximale en Juin-Juillet-Août, ce qui suggère que la tendance à la Réunion est principalement influencée par les échanges stratosphère-troposphère, la source d'ozone la plus importante à cette saison.

–A Irene, la tendance est forte en Septembre-Octobre-Novembre, Décembre-Janvier-Février et Juin-Juillet-Août. Les intrusions stratosphériques et les mécanismes photo-chimiques ont donc probablement joué un rôle important sur les tendances observées.

Récemment, une étude des tendances à long terme de l'ozone troposphérique a été publiée[46]. L'étude de Oltmans et al. était basée sur un réseau global d'observation, avec plusieurs stations des régions subtropicales de l'hémisphère sud : les îles Samoa, Nouvelle Zélande, Australie et Afrique du Sud. Pour Cape Grimm (Australie) et Lauder (Nouvelle Zélande), Oltmans et al. n'observent pas de tendance en été, mais ils observent une tendance positive et significative à la fin de l'hiver et au printemps austral. Pour Lauder, ils montrent une structure verticale pour les tendances, positive en dessous de 500 hPa, légèrement négative (non significativement) au-dessus de 500 hPa pour Lauder, ce qui est assez similaire à ce que nous avons observé pour le site de Irene. Pour Cape Point (Afrique du Sud) des tendances positives sont observées tout au long de l'année, mais les plus fortes augmentations sont également reportées pour la fin de l'hiver et le printemps. Pour tous les sites de

[46] Oltmans, S.J., et al., Long-term changes in tropospheric ozone, Atmos. Environ., 40, 3156–3173, 2006

l'hémisphère sud, ils signalent que les tendances positives saisonnières coïncident avec les saisons ou les feux de biomasse sont les plus actifs.

En conclusion, cette étude des tendances de l'ozone troposphérique met en évidence un comportement légèrement différent entre les deux sites étudiés, et donc des influences sur l'ozone troposphérique et son évolution à long terme dans la région. Ce travail peut être poursuivi et étendu. Il ouvre des perspectives importantes dans plusieurs directions :

–Utiliser d'un modèle de tendances plus complexe et élaboré, utilisant par exemple des régressions multiples ou des réseaux de neurones[47].

–Calculer des tendances à la TTL (hauteur de tropopause, tendances sur les quantités d'ozone à la tropopause...etc.), certains modèles climatiques prévoient une diminution de la hauteur de tropopause de plusieurs hPa/décade[48].

–Calculer des tendances d'ozone troposphérique en utilisant la détermination lagrangienne des échanges stratosphère-troposphère qui est actuellement en cours de finalisation dans le cadre de la thèse de Gaëlle Clain.

[47] Lu C.S and Chang T.S., Meteorologically adjusted trends of daily maximum ozone concentrations in Tapei, Taiwan, Atmos. Environ., 39, 6491-6501, 2005

[48] Gettelman A., et al., The tropical tropopause layer 1960-2100, Atmos. Chem. Phys. Discuss., 8, 1367-1413, 2008.

Conclusion et prospective

Comme indiqué dans le préambule de ce document, nous avons commencé à réfléchir sur les échanges stratosphère-troposphère à la Réunion dans les années 1995. Pour les régions subtropicales, l'influence de ces mécanismes sur l'ozone troposphérique était alors hypothétique et non démontrée.

Je me suis impliqué depuis plus de douze ans sur l'étude de l'ozone troposphérique, qui est devenu une thématique importante du LACY et dans le développement de l'OPAR qui est devenu une station importante de la zone tropicale de l'hémisphère sud. Une étape supplémentaire sera franchie avec la station d'altitude du Maïdo prévue en 2010.

Sur le plan de la thématique de l'ozone troposphérique, nous avons pu détailler et expliciter de nombreux mécanismes dynamiques d'échange stratosphère-troposphère et leur influence sur l'ozone troposphérique : foliation de tropopause, déferlement d'onde de Rossby, goutte froide d'altitude, filamentation de la tropopause en relation avec les mécanismes de convection tropicale.

Une climatologie de la tropopause a été établie par Sivakumar avec qui j'ai collaboré dans le cadre de son séjour post-doctoral. Une première estimation des tendances de l'ozone troposphérique a été établie.

J'ai été associé également à des études sur l'influence de la photo-chimie effectuée dans le cadre d'études menées par Tantely Randriambelo.

J'encadre actuellement deux étudiants en thèse, Gaëlle Clain qui est en phase de rédaction et Valentin Duflot qui débute.

Gaëlle a établi une climatologie de l'ozone comparative entre divers instruments (lidar, sondes, données avions MOZAIC) et divers site de mesure dans la région (Réunion et Afrique du Sud). Elle a pu mettre en particulier en évidence certaines différences entre les climatologies lidar et radiosondage, qui sont dues au fait que contrairement aux radiosondages, l'acquisition des mesures lidar est dépendante du temps, ce qui peut influencer significativement la climatologie de l'ozone, particulièrement en été austral. D'autre part, la gamme d'altitude couverte par le lidar est variable et dépend de plusieurs facteurs, dont la

quantité d'ozone troposphérique mesurée, ce qui peut également induire des biais sur les climatologies dans la partie haute des profils. Elle a également participé aux travaux de développement de LACYTRAJ, et appliqué cet outil dynamique sur toute la base de données ozone de la Réunion (radiosondages et lidar) pour déterminer l'influence climatologique des échanges stratosphère-troposphère. Les résultats sont en cours d'analyse, et plusieurs articles basés sur son travail sont en cours de rédaction.

Après avoir participé à l'encadrement du stage de master de Valentin Duflot qui portait sur le traitement et l'analyse des données de la campagne FTIR de 2007, je lui ai proposé un sujet sur l'étude du transport et de la dispersion des polluants à la Réunion. L'objectif de ce sujet est d'avoir une approche multi-instrumentale de la thématique de l'influence des feux de biomasse et de la pollution sur la troposphère dans l'océan indien, et de combiner l'exploitation des données instrumentales (FTIR, lidar), satellitales (MOPITT) et en utilisant aussi la modélisation de type MOCAGE[1] en s'appuyant sur des collaborations extérieures, principalement avec le laboratoire d'aérologie. Ces études seront menées dans un cadre régional et seront intégrées dans le Groupement de Recherche International ARSAIO[2]. Une étude des distributions de monoxyde de carbone basée sur les campagnes FTIR de 2004 et de 2007 et sur les données MOPITT dans l'hémisphère sud sur la période 2000-2007 est déjà en cours de formalisation pour un article.

D'un point de vue instrumental, la station de la Réunion était au tout début de son développement avec des sondages effectués à une fréquence bi-hebdomadaire depuis 3 ans et un système lidar fournissant ses premiers profils de température. Comme cela a été développé dans le chapitre 1, la station a connu une évolution instrumentale importante constituée par les mesures de constituants trace par radiométrie (FTIR), l'augmentation de la fréquence des mesures d'ozone grâce aux radiosondages hebdomadaires complétés par les mesures lidar ozone, les mesures d'aérosols par lidar et la mesure du vent par sonde GPS et lidar doppler. Cette évolution instrumentale nous a permis de bien appréhender la dynamique atmosphérique à l'échelle locale et régionale.

[1] Teyssèdre, H., et al.: A new tropospheric and stratospheric Chemistry and Transport Model MOCAGE-Climat for multi-year studies: evaluation of the present-day climatology and sensitivity to surface processes, Atmos. Chem. Phys., 7, 5815-5860, 2007.

D'autres projets instrumentaux tels que les mesures par radar UHF et le développement des mesures de vapeur d'eau par lidar et radiométrie viendront compléter cet essor instrumental. Nous franchirons une nouvelle étape du développement avec la construction de la station d'observation du Maïdo et son intégration dans une structure fédérative, l'Observatoire des Sciences de l'Univers de la Réunion.

La perspective de la station d'altitude permet d'envisager un nouveau cadre de travail et de dégager un développement de l'activité scientifique autour du projet thématique dynamique et physico-chimie de la troposphère du LACY dont je vais prendre la responsabilité et qui va s'intégrer dans l'organigramme fonctionnel qui a été proposé dans le document prospectif du LACY pour la période 2009-2013

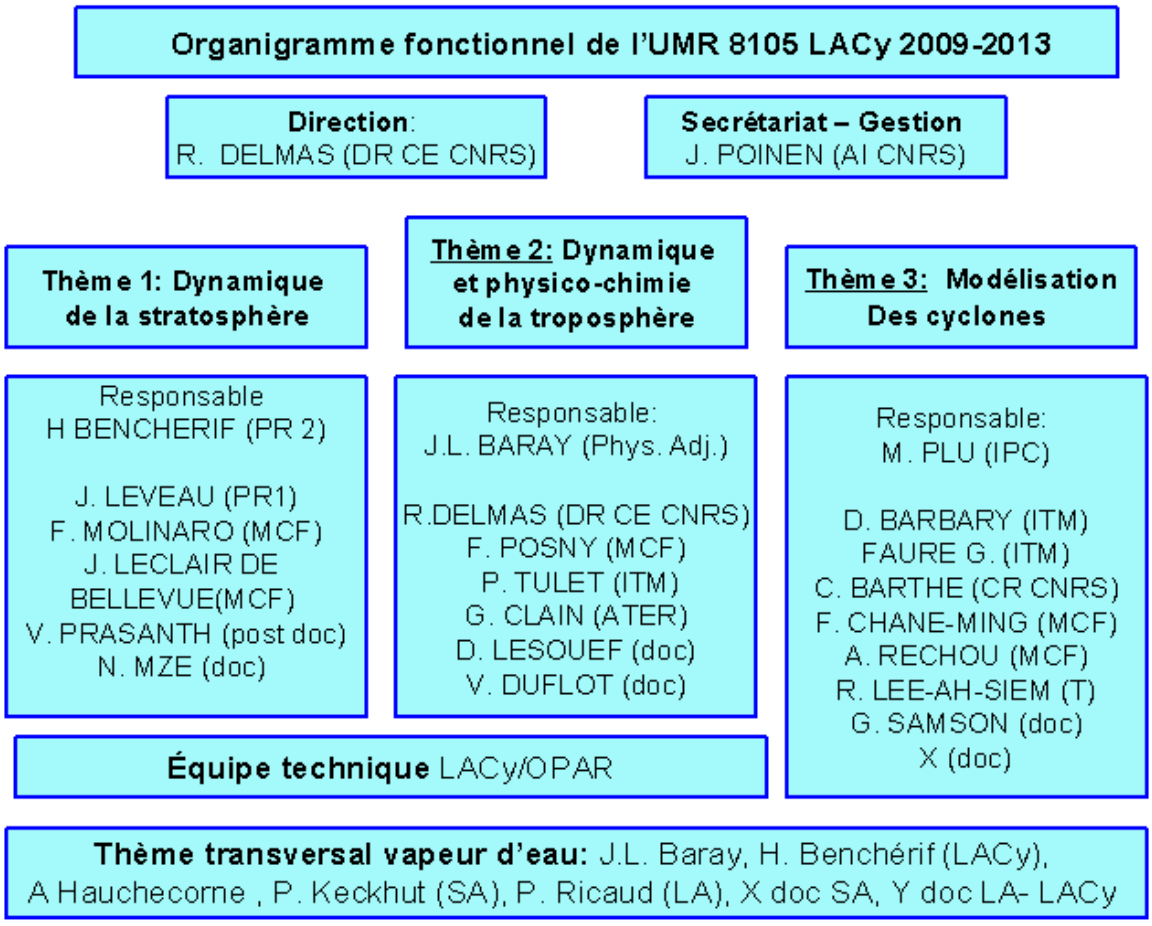

Le domaine d'activité de ce projet thématique, auquel va contribuer de manière importante Pierre Tulet dont l'arrivée au laboratoire est prévue dès 2009, va englober la poursuite des études des échanges stratosphère-troposphère, et la quantification et l'étude du transport des

[2] Atmospheric Research in Southern Africa and Indian Ocean

espèces polluantes (ozone, CO, CO_2…etc, et aérosols) dans toute la troposphère et aux différentes échelles d'espace et de temps. Il va également englober l'analyse des mesures effectuées dans le cadre du programme de surveillance des gaz à effet de serre puisque que, comme indiqué dans la partie 1.4 du chapitre .1, il est envisagé de faire de l'OPAR, après son installation dans le bâtiment du Maïdo, une station globale du programme GAW. La compréhension des mesures in situ en altitude à l'observatoire du Maïdo nécessite cependant un une bonne connaissance des échanges verticaux à petite échelle au niveau de la l'île de la Réunion pour être capable de discriminer d'éventuelle pollutions par les sources locales à la fois sur les gaz à effet de serre et sur les aérosols. C'est la raison pour laquelle il est important de mener a terme les études entreprises dans le cadre de la thèse de Dorothée Lesouef de modélisation numérique à haute résolution en les enrichissant d'une approche expérimentale basée sur l'exploitation du lidar mobile aérosols et des radiosondages GPS effectués dans le cadre de l'expérience ECLAIR. L'arrivée de Pierre Tulet et les données acquises par les nouveaux systèmes lidar aérosol nous permettront de documenter de façon précise l'étude de la distribution des aérosols à la Réunion et leur impact sur le changement climatique. Au niveau de l'océan Indien, l'Afrique Australe ainsi que Madagascar sont des zones sources d'aérosols significatives à l'échelle globale et représentant des mélanges de particules que l'on ne rencontre que dans peu de région du monde. Il est aujourd'hui largement admis que les aérosols atmosphériques ont un fort impact sur les bilans thermodynamique et radiatif de la Terre[3],[4]. Les aérosols ont une large palette d'effets climatiques que l'on peut, de façon simplifiée, classifier entre effet radiatif direct (i.e., les effet basés sur l'interaction des particules avec le rayonnement solaire ou tellurique) et les effets radiatifs indirects (i.e., les effets radiatifs qui résultent de l'influence des aérosols sur l'abondance et propriétés des nuages). Les aérosols influent aussi sur les processus de formation des précipitations et les aérosols d'origine anthropique sont susceptibles de modifier ces processus[5],[6]. Ces effets sont une des principales causes d'incertitudes sur le forçage anthropique et ses répercussions dans les modèles climatiques et dans leurs projections de l'évolution du climat sur les décennies à venir[7],[8].

[3] Houghton J.T et al, Climate Change 2001: The scientific basis. Contribution of working group I to the first assessment report of the International Panel on Climate Change, Cambridge University Press, UK 881p, 2001
[4] Andreae M.O., Climatic effects of changing atmospheric aerosol levels, in Henderson-SellersA. (ed), World survey of climatology, Future climates of the world, 16, Elsevier Amsterdam, 341-292, 1995.
[5] Charlson R.J. and Heitzenberg J;, (eds) Aerosol forcing on climate, Wile Chichester, NewYork, 416pp, 1995.
[6] Lohmann U., Feitcher J., Global indirect aerosol effect: a review, Atmos. Chem. Phys. 5, 715-737, 2005.
[7] IPCC 2007, The physical science basis, summary for policy makers, 2007.
[8] IAPSAG, 2007WMO/IUGG International Aerosol Precipitation Science Assessment Group (IAPSAG° report: Aerosol pollution impact on precipitation, a scientific review. WMO, Geneva, 2007.

Pour ce qui me concerne plus personnellement, je vais m'impliquer dans l'étude des échanges stratosphère-troposphère dont les perspectives se dégagent de la thèse de Gaëlle Clain, et dans l'étude des mécanismes de contamination et de la dynamique des polluants dans le cadre de la thèse de Valentin Duflot.

En effet, les résultats obtenus par Gaëlle dans le cadre de sa thèse permettent de dégager un certain nombre de perspectives que nous avons détaillées dans le cadre du projet ANR TOST[9].

- Effectuer l'analyse statistique de l'occurrence des intrusions stratosphériques sur le site de Irene en Afrique du Sud, ainsi que sur d'autres sites du réseau SHADOZ pour analyser d'éventuelles différences entre les sites.
- Combiner différents outils diagnostiques tels que LACYTRAJ, FLEXPART ou MIMOSA pour produire une meilleure description du transport autour de la TTL[10].
- Développer une méthodologie pour analyser la réversibilité des transports verticaux lors de la mise en évidence climatologique des intrusions stratosphériques.

Pour ce qui concerne les perspectives pour la caractérisation de la dynamique et la physico-chimie de la troposphère tropicale, un certain nombre de nouveaux instruments, détaillés dans le paragraphe 1.4 de ce document, seront disponibles dans le proche futur.
Le lidar vent, le radar UHF, les radiomètres tels que le FTIR permettront de produire des profils résolus de vent et de traceurs et documenteront de manière originale les études troposphériques, et particulièrement dans le cadre de la thèse de Valentin Duflot.

Un autre aspect sur lequel je compte m'impliquer dans l'avenir est le domaine de la vapeur d'eau dans l'UTLS[11] qui, comme l'indique l'organigramme fonctionnel du LACY, constitue un thème transversal du LACY.

En effet, l'eau dans l'UTLS, aussi bien sous forme de vapeur d'eau que de glace (cirrus) joue un rôle important sur le climat du fait de sa contribution majeure dans le bilan radiatif. La distribution de l'eau et sa variabilité au voisinage de la tropopause n'est pas parfaitement

[9] Transport de l'Ozone dans la Stratosphère Tropicale
[10] Tropical transition layer
[11] Haute troposphère et basse stratosphère

comprise du fait des nombreux processus mis en œuvre et de leurs échelles spatio-temporelles variées. Les mesures à long terme de sa variabilité aussi bien dans la haute troposphère que la basse stratosphère restent, encore à l'heure actuelle, inexpliquées. En effet, ni la tendance positive du méthane (source stratosphérique) ni la tendance négative de la température à la tropopause (injection directe de la troposphère dans la stratosphère) ne permettent d'expliquer la tendance positive de la vapeur d'eau stratosphérique jusque dans les années 2000[12], et sa stagnation depuis. Cette augmentation pourrait être reliée soit à des changements dans les échanges verticaux entre troposphère et stratosphère, soit à des changements dans les échanges isentropiques (quasi-horizontaux) entre les tropiques et les moyennes latitudes.

Le site de la Réunion, en région tropicale, est particulièrement adapté à l'étude du cycle de l'eau dans l'UTLS, car c'est la région ou se produit le transport d'air de la troposphère vers la stratosphère et où la tropopause est suffisamment froide pour le dessécher et l'amener à de très faibles concentrations en vapeur d'eau. Comme indiqué dans le paragraphe 1.4 de ce document, des outils d'observations de la vapeur d'eau sont donc en cours de développement à la Réunion, par lidar (projet d'utiliser le télescope de 1.20 m de diamètre à la station du Maïdo) et radiomètre (en collaboration avec l'équipe de Philippe Ricaud, Laboratoire d'aérologie, Toulouse).

Mon implication dans cette thématique portera à la fois sur le plan de la modélisation et de l'observation.

Sur le plan de l'observation, le lidar permet de sonder les cirrus et la vapeur d'eau (technique Raman) avec une grande sensibilité, et une bonne résolution verticale. Des mesures systématiques ont été réalisées à la Réunion de nuit et en continu par un système lidar Raman vapeur d'eau. Une base de données couvre la période 2001-2005.

Dans le cadre de la thèse de Christophe Hoareau qui a débuté récemment au service d'aéronomie et dont l'encadrement principal est assuré par Philippe Keckhut, il est prévu de :
- Traiter et valider la base de données lidar Raman H_20 pour la période 2001-2005.

[12] SPARC Assessment of Upper Tropospheric and Stratospheric Water Vapour, Prepared by the SPARC Water Vapour Working Group under the auspices of the SPARC Scientific Streering Group, Edited by D. Kley, J.M. Russell III and C. Phillips, December 2000

- Exploiter cette base de données pour la caractérisation de la variabilité aux différentes échelles de la vapeur d'eau dans la troposphère tropicale, et sa climatologie.

Si les profils de vapeur d'eau acquis durant la période 2001-2005 s'avèrent de bonne qualité, nous envisageons de poursuivre les mesures en utilisant cette voie du système lidar de la Réunion et d'assurer une activité de surveillance régulière de ce paramètre atmosphérique.

Sur le plan de la modélisation, nous avons vu dans le paragraphe 2.6 de ce document que le modèle LACYTRAJ permettait la reconstruction RDF de champs de vorticité potentielle avec un accord satisfaisant avec les données in-situ (profils d'ozone) et les autres modèles disponibles. Pour l'advection de vapeur d'eau, il reste à améliorer le code pour pouvoir prendre en compte les changements de phase de l'eau et produire des champs pertinents dans toutes les situations.
L'intégration dans LACYTRAJ du code micro physique développé pour MIMOSA devrait nous permettre d'atteindre cet objectif.

Grâce au parc instrumental unique pour l'étude de la vapeur d'eau en cours d'installation à l'OPAR, le LACY pourra développer un projet transverse particulièrement original sur la vapeur d'eau dans l'UTLS tropicale. Ceci contribuera à améliorer la compréhension des processus qui interviennent dans le transport et la transformation de l'eau sous ses différentes phases et de contribuer ainsi à mieux représenter la vapeur d'eau et des cirrus dans les modèles climatiques.

D'un point de vue général, le couplage vapeur d'eau – ozone – CO - vent, la mise en synergie des moyens d'étude, des données satellitale, en complément des observations et des outils de modélisation, et le développement de mesures dans un cadre régional nous permettront d'aborder les études dynamiques de manière beaucoup plus globale et complète, que ce soit pour la caractérisation des échanges stratosphère-troposphère, ou des transports de polluants.

Les perspectives générales à long terme s'articulent autour de l'implication des études de caractérisation des échanges dynamiques entre les principaux compartiments atmosphérique et de l'évolution des sources de polluants sur le réchauffement climatique planétaire. La complexité des mécanismes implique à la fois la chimie et la dynamique, et à des échelles de temps et d'espaces très variables et les couplages dynamiques devraient être directement

influencés par ces évolutions différentielles et, en retour, devraient avoir une rétroaction sur les forçages primaires. Une étude préliminaire des tendances de l'ozone troposphérique a été présentée dans la partie 2.7 du chapitre 2. Elle pourra être poursuivi et étendu dans l'avenir. A terme, je serai donc amené à m'impliquer d'avantage sur la détermination des tendance à long terme de l'évolution des compositions atmosphériques en ozone, vapeur d'eau, humidité et des différents polluants émis et diffusés dans la troposphère, et à analyser les couplages dynamiques des différents compartiments atmosphériques dans l'optique de leur évolution à long terme.

Annexes

Annexe 1 Activités d'enseignement et d'encadrement, niveau maîtrise et master

Au cours de la période 1996-2001, j'ai eu des activités d'enseignement en premier cycle universitaire au département de physique de l'université de la Réunion, sous le statut de moniteur (3 ans, 64 heures par an) puis ATER (1 an, 96 heures). Mon service était composé de travaux dirigés et de travaux pratiques de physique en premier cycle universitaire (optique, mécanique, électromagnétisme).

J'ai été recruté comme physicien-adjoint en 2001. J'ai été affecté à l'université Versailles St Quentin, l'établissement de tutelle de l'Institut Pierre Simon Laplace, et détaché à l'université de la Réunion pour mon service d'observation à l'OPAR. Du fait de l'éloignement, il m'était difficile d'effectuer un service d'enseignement classique (TP, TD, cours) au sein de mon université d'affectation (Université Versailles St Quentin). Pour compenser ce manque de contact avec les étudiants, j'ai proposé des sujets de stages aux étudiants de la maîtrise de physique et applications du département de physique de l'université de la Réunion.

L'année 2006 a vu l'application de la réforme L.M.D au sein du département de physique de l'université de la Réunion. J'ai saisi cette opportunité de retrouver une activité d'enseignement en proposant de faire un cours sur l'instrumentation géophysique au niveau M1 et un autre sur les réseaux d'observation au niveau M2. Je dispense donc une quinzaine d'heures de cours au master géosphère depuis 2006. J'ai d'autre part continué à proposer des sujets de stage aux étudiants de niveau master 1 et 2.

Encadrement de stages de maîtrise de Physique et Applications

Année	***Etudiant***	***Sujet***	***Co-encadrant***
2002	Ulrich Frontin	Développement de codes de trajectoires	
2002	Shaick Akbaraly	Modèle HYSPLIT	
2003	Laurent Lasour	Classification des profils d'ozone troposphérique	Roseane Diab
2003	Thierry Lin Chan	Influence de l'ITCZ sur l'ozone troposphérique	
2004	Olivier Payet	Données Meteosat	
2005	Raphaël Huet	Modèle HURRICANE	Jimmy Leclair de Bellevue

Encadrement de stages de master

Année	***Etudiant***	***Sujet***	***Niveau***	***Co-encadrant***
2007	Joannie Payet	Climatologie des cirrus tropicaux	Master 1	Bertrand Cadet
2008	Valentin Duflot	Mesures FTIR	Master 2	Martine De Mazière
2008	Stefan Bourge	Exploitation des sondages vent GPS	Master 2	
2009	Elodie Felds	Etude dynamique d'une dépression de mousson	Master 2	Gaëlle Clain

Annexe 2 Encadrement de thèses

Depuis mon recrutement en tant que physicien-adjoint, j'ai proposé trois sujets de thèse et donc participé à l'encadrement de trois étudiants en thèse. La direction de thèse a été assurée par Serge Baldy jusqu'à son départ à la retraite, puis ensuite par Robert Delmas. Le sujet de Jimmy Leclair de Bellevue consistait à approfondir notre connaissance des échanges stratosphère-troposphère induits par la convection tropicale, sujet qu'il a mené à bien de façon remarquable puisqu'il a soutenu durant sa quatrième année de thèse, que deux articles ont été publiés (section 2.3 de ce document d'H.D.R.), qu'il a obtenu sa qualification CNU dès la première candidature et qu'il a été recruté comme maître de conférences au sein de l'équipe stratosphère du LACY.

Alors que Jimmy était en fin de thèse, j'ai eu l'opportunité de proposer un nouveau sujet à Gaëlle Clain. L'objectif de ce nouveau sujet est d'avoir une approche climatologique des échanges stratosphère-troposphère, pour exploiter la base de données ozone lidar et radiosondages acquis à la Réunion depuis maintenant plus de 10 ans. Gaëlle a effectué un travail important dans l'exploitation de LACYTRAJ sur la base de données de l'OPAR, et obtenu des résultats intéressants, qui ne sont pas pour l'essentiel présentés dans ce document d'HDR puisque Gaëlle est actuellement en cours de rédaction de thèse. Enfin, ayant eu l'opportunité de travailler avec Valentin Duflot un étudiant particulièrement brillant en master, je lui ai proposé un nouveau sujet sur l'étude du transport des espèces polluantes à la Réunion. L'objectif de ce sujet est d'avoir une approche multi-instrumentale de la thématique de l'influence des feux de biomasse et de la pollution sur la troposphère dans l'océan indien, et de combiner l'exploitation des données instrumentales (FTIR, lidar), satellitales (MOPITT) et en utilisant aussi la modélisation de type MOCAGE.

Etudiant	*Sujet*	*Début*	*Soutenance*	*Co-directeur*
Jimmy Leclair de Bellevue	Analyse et modélisation des échanges verticaux induits par les systèmes convectifs des latitudes tropicales : effets sur l'ozone troposphérique	Octobre 2002	Mars 2006	Serge Baldy
Gaëlle Clain	Climatologie de l'ozone troposphérique par approche lagrangienne	Octobre 2005	Prévue début 2009	Serge Baldy puis Robert Delmas
Valentin Duflot	Quantification et étude du transport des espèces polluantes dans la troposphère tropicale (Ile de la Réunion)	Octobre 2008	2011-2012	Robert Delmas

Annexe 3 Responsabilités instrumentales, administratives et extra-universitaires

A/ Responsabilités instrumentales

1996-2008 : Suivi de campagnes de mesure et accueil d'instruments pour l'OPAR

1998-2008 : Responsable scientifique du lidar ozone troposphérique de l'OPAR

2001-2008 : Coordination scientifique de l'instrumentation de l'OPAR et participation à l'élaboration des demandes de financement et des comptes-rendu d'activité pour l'OPAR

2002-2008 : Responsable scientifique du lidar ozone stratosphérique de l'OPAR

Depuis 2008 : Responsable scientifique du lidar vapeur d'eau de l'OPAR

B/ Responsabilités administratives

1999-2008 : Reviewer de 17 publications pour des journaux de rang A

2001-2008 : Accueil de visiteurs et présentation des installations lidar lors des visites de l'OPAR

2001-2008 : Participation à l'élaboration des demandes de financement pour le laboratoire de physique de l'atmosphère (LPA) puis le laboratoire de l'atmosphère et des cyclones (LACY)

2002 à 2005 : Responsable de la thématique « Echanges Stratosphère / Troposphère et bilan de l'ozone troposphérique» du LPA

2003-2008 : Membre du comité de pilotage de l'OPAR

2003-2007 : Responsable de plan de Formation du laboratoire LPA puis LACY (UMR 8105)

2006-2008 : Membre du bureau NDACC-France

2007 : Membre du comité d'organisation de RIIS (Reunion Island International Symposium)

2007-2008 : Participation aux opérations de présentation et de vulgarisation de l'instrumentation (participation à l'émission « les nouveaux défis » sur RFO en 2007, tournage d'un DVD en 2008

Depuis 2008 : Responsable de la thématique « Dynamique et physico-chimie de la troposphère » du LACY

Depuis 2008 : Membre du comité AGACC (Advanced exploitation of Ground-based measurements for Atmospheric Chemistry and Climate applications)

C/ Responsabilités extra-universitaires

Depuis 2004 : Membre du comité directeur de la ligue réunionnaise de tennis de table

Depuis 2004 : Membre de la commission informatique et classement de la ligue réunionnaise de tennis de table (président de cette commission de 2004 à 2006 et depuis 2008).

Depuis 2005 : Secrétaire du club Sainte Marie Tennis de Table.

Depuis 2006 : Membre de la commission sportive de la ligue réunionnaise de tennis de table

2008 : Médaille de bronze du mérite fédéral de la fédération française de tennis de table.

Depuis 2008 : Membre du bureau et secrétaire du Comité Régional des Médaillés de la Jeunesse et des Sports de la Réunion

Annexe 4 Références bibliographiques

A/ Publications dans des revues internationales à comité de lecture (rang A)

1/ Baray J.L., G. Ancellet, F. G. Taupin, M. Bessafi, S. Baldy, P. Keckhut, Subtropical tropopause break as a possible stratospheric source of ozone in the tropical troposphere, *Journal of Atmospheric and Solar-Terrestrial Physics*, **60**, 1, 27-36, 1998.

2/ Baray J.L., G. Ancellet, T. Randriambelo, S. Baldy, Tropical cyclone Marlene and stratosphere-troposphere exchange, *Journal of Geophysical Research*, **104**, D11, 13953-13970, 1999.

3/ Randriambelo T., **J.L. Baray**, S. Baldy, P. Bremaud, and S. Cautenet, A case study of extreme tropospheric ozone contamination in the tropics using in-situ, satellite and meteorological data, *Geophysical Research Letters* , **26**, 9, 1287-1290, 1999.

4/ Baray J.L., J. Leveau, J. Porteneuve, G. Ancellet, P. Keckhut, F. Posny, and S. Baldy, Description and evaluation of a tropospheric ozone lidar implemented on an existing lidar in the southern subtropics, *Applied Optics*, **38**, 33, 6808-6817, 1999.

5/ Baray J.L., V. Daniel, G. Ancellet, B. Legras, Planetary-scale tropopause folds in the southern subtropics, *Geophysical Research Letters*, **27**, 3, 353-356, 2000.

6/ Randriambelo T., **J.L. Baray**, S. Baldy, The effect of biomass burning, convective venting and transport on tropospheric ozone over the Indian ocean : Reunion island field observations, *Journal of Geophysical Research*, **105**, D9, 11813-11832, 2000.

7/ Roumeau S., P. Brémaud, E. Rivière, S. Baldy, **J.L. Baray**, Tropical cirrus clouds: a possible sink for ozone, *Geophysical Research Letters*, **27**, 15, 2233-2236, 2000.

8/ Baray J.L., T. Randriambelo, S. Baldy, G. Ancellet, Comment on 'Tropospheric O_3 distribution over the Indian Ocean during spring 1995 evaluated with a chemistry-climate model', by A.T.J. de Laat et al., *Journal of Geophysical Research*, **106** , D1, 1365-1368, 2001.

9/ Baray J.L., S. Baldy, R.D. Diab, J.P. Cammas, Dynamical study of a tropical cut-off low over South Africa, and its impact on tropospheric ozone, *Atmospheric Environment*, **37**, 11, 1475-1488, 2003.

10/ Bencherif H. , T. Portafaix,, **J.L. Baray,** B. Morel, S. Baldy, J. Leveau, A. Hauchecorne, P. Keckhut, A. Moorgawa, M.M. Michaelis, R. Diab, LIDAR observations of lower stratospheric aerosols over South Africa linked to large scale transport across the southern subtropical barrier, *Journal of Atmospheric and Solar-Terrestrial Physics*, **65**, 6, 707-715, 2003.

11/ Randriambelo T., **J.L. Baray**, S. Baldy, A.M. Thompson, S. Oltmans, P. Keckhut, Investigation of the short-time variability of tropical tropospheric ozone, *Annales Geophysicae*, **21**, 9, 2095-2106, 2003.

12/ Keckhut P., S. McDermid, D. Swart, T. McGee, S. Godin-Beekmann, A. Adriani, J. Barnes, **J.L. Baray,** H. Bencherif , H. Claude , A. G. di Sarra , G. Fiocco , G. Hansen , A. Hauchecorne , T. Leblanc , C. Hie Lee , S. Pal , G. Megie , H. Nakane , R. Neuber , W. Steinbrecht, J. Thayer, Review of ozone and temperature lidar validations performed within the framework of the Network for the Detection of Stratospheric Change, *Journal of Environmental Monitoring*, 6, 721-733, 2004.

13/ Sivakumar V., B. Morel, H. Bencherif, **J.L. Baray**, S. Baldy, A. Hauchecorne, and P.B. Rao Rayleigh lidar observation of a warm stratopause over a tropical site, Gadanki (13.5N; 79.2E), *Atmospheric Chemistry and Physics*, **4**, *1989-1996*, 2004.

14/ Sivakumar, V., **J.L. Baray**, S. Baldy, H. Bencherif, Tropopause characteristics over a southern subtropical site, Reunion Island (21 S, 55 E): Using radiosonde-ozonesonde data, *Journal of Geophysical Research*, **111**, D19111, doi:10.1029/2005JD006430, 2006.

15/ Leclair De Bellevue, J., A. Réchou, **J.L. Baray**, G. Ancellet, R. D. Diab, Signatures of stratosphere to troposphere, transport near deep convective events in the southern subtropics, *Journal of Geophysical Research*, **111**, D24107, doi:10.1029/2005JD006947, 2006.

16/ Baray J.L., J. Leveau, S. Baldy, J. Jouzel, P. Keckhut, G. Bergametti, G. Ancellet, H. Bencherif, B. Cadet, M. Carleer, C. David, M. De Mazière, D. Faduilhe, S. Godin Beekmann, P. Goloub, F. Goutail, J.M. Metzger, B. Morel, J.P. Pommereau, J. Porteneuve, T. Portafaix, F. Posny, L. Robert, M. Van Roozendael, An instrumented station for the survey of ozone and climate change in the southern tropics: Scientific motivation, technical description and future plans**,** *Journal of Environmental Monitoring***,** DOI**:** 10.1039/b607762e, 2006.

17/ Leclair De Bellevue J., **J.L. Baray,** S. Baldy, G. Ancellet, R. D. Diab, F. Ravetta, Simulations of a Stratospheric to tropospheric transport during the tropical cyclone Marlene event, *Atmospheric Environment*, **41**, 6510-6526, 2007.

18/ Theys N., M. Van Roozendael, F. Hendrick, C. Fayt, C. Hermans, **J.L. Baray**, F. Goutail, J.-P. Pommereau, M. De Mazière, Retrieval of stratospheric and tropospheric BrO columns from multi-axis DOAS measurements at Reunion Island (21° S, 56° E), *Atmospheric Chemistry and Physics*, **7**, 4733-4749, 2007

19/ Senten C., M. De Mazière, B. Dils, C. Hermans, M. Kruglanski, E. Neefs, F. Scolas, A. C. Vandaele, G. Vanhaelewyn, C. Vigouroux, M. Carleer, P. F. Coheur, S. Fally, B. Barret, **J.L. Baray**, R. Delmas, J. Leveau, J. M. Metzger, E. Mahieu, C. Boone, K. A. Walker, P. F. Bernath, K. Strong, New ground-based FTIR measurements at Ile de La Réunion: observations, error analysis, and comparisons with independent data, *Atmospheric Chemistry and Physics*, **8**, 3483-3508, 2008

20/ Clain G. , **J.L. Baray**, R. Delmas, R. Diab, J. Leclair de Bellevue, P. Keckhut, F. Posny, J. M. Metzger, and J. P. Cammas, Tropospheric ozone climatology at two southern subtropical sites, (Reunion Island and Irene, South Africa) from ozone sondes, LIDAR, aircraft and in situ measurements, *Atmospheric Chemistry and Physics*, en révision, 2008

21/ van Gijsel J.A.E., D.P.J. Swart, **J.L**. **Baray,** , H. Claude, T. Fehr, P. von der Gathen, S. Godin-Beekmann, G. Hansen, T. Leblanc, T., I.S. McDermid, Y.J. Meijer, H. Nakane, E. Quel, W. Steinbrecht, K. Strawbridge, B. Tatarov, E. Wolfram, Global validation of ENVISAT ozone profiles using lidar measurements, *International Journal of Remote Sensing*, accepté 2008

B/ Autres revues, publications nationales, actes de colloques et conférences

1/ Baray J.L., P. Keckhut, F. G. Taupin, G. Ancellet, S. Baldy, M. Bessafi, "Tropical stratosphere-troposphere exchange over Reunion island", *IAMAS-IAPSO, Melbourne, Australie*, 1997.

2/ Baray J.L., S. Baldy, M. Bessafi, F. G. Taupin, G. Ancellet, P. Keckhut, "Tropical stratosphere-troposphere exchange over Reunion island, proceedings of the advanced study course on tropospheric chemistry and space observation", *European commission air pollution research report* N° 65, pp. 239, 1997.

3/ Ancellet G., **J.L. Baray**, "Analysis of La Réunion data", *1st Meeting of the European TRACAS project., Paris, France*, 1998.

4/ Baray J.L., "Etude d'un cas de pénétration d'air stratosphérique dans la troposphère en région tropicale", *bulletin NDSC-France* N°3, pp. 4, 1998.

5/ Ancellet G., **J.L. Baray**, S. Baldy, "Présentation des instruments de la station d'observation de La Réunion pour l'étude de la stratosphère : Lidar ozone troposphérique", *bulletin NDSC-France* N°4, pp. 6-7, 1998.

6/ Baray J.L., S. Baldy G. Ancellet, "Ozone DIAL measurements and stratosphere-troposphere exchange studies", *NDSC steering commitee, La Réunion, France*, 1998.

7/ Baray J.L., J. Leveau, J. Porteneuve, G. Ancellet, S. Baldy, P. Keckhut, "Mesures d'ozone tropospherique par sondage lidar à l'île de la Réunion (Océan indien, tropiques sud)", *Atelier expérimentation et instrumentation, INSU-Météo-France, Toulouse, France*, 1998.

8/ Ancellet G., **J.L. Baray**, "TRACAS field experiment in the southern hemisphere", campaign report, 1998.

9/ Baray J.L., G. Ancellet, S. Baldy, "TRACAS measurements in the southern hemisphere in July 1998", *2nd Meeting of the European TRACAS project., Tenerife, Espagne*, 1999.

10/ Daniel V., **J.L. Baray**, B. Legras, G. Ancellet, "Large scale tropopause folding and exchanges across the subtropical jet in the southern hemisphere", *22nd general assembly of the IUGG, Birmingham, Angleterre*, 1999.

11/ Baray J.L., J. Leveau, J. Porteneuve, G. Ancellet, P. Keckhut, F. Posny, S. Baldy, "Description of a tropospheric ozone lidar implemented on an existing lidar in the southern subtropics", *5th Stratospheric Ozone Workshop*, St-Jean-de-Luz, France, poster European Commission in Air Pollution Report N° 73, pp. 667-670, 1999.

12/ Randriambelo T., **J.L. Baray**, S. Baldy, P. Bremaud, S. Cautenet, "Tropospheric ozone maximum in the tropics: the role of the stratosphere-troposphere exchange and biomass burning", *5th Stratospheric Ozone Workshop*, St-Jean-de-Luz, France, poster European Commission in Air Pollution Report N° 73, pp. 649-652, 1999.

13/ Baray J.L., B. Legras, "Ozone data of Reunion Island : Comparison of 1998 and 1999 austral winters", *3rd Meeting of the European TRACAS project, Utrecht*, 2000.

14/ Réchou A., S. Baldy, **J.L. Baray**, R. Dupuy, "Cyclone contribution to stratosphere-troposphere exchange (STE) and ozone incomes in the tropical troposphere", *EGS XXV General Assembly, Nice*,

France, 2000.

15/ Ancellet G., **J.L. Baray**, E. Cuevas, "Transport of ozone across the southern and northern subtropical tropopause", *EGS XXV General Assembly, Nice, France*, 2000.

16/ Baray J.L., V. Daniel, G. Ancellet, B. Legras, "Planetary-scale tropopause folds in the southern hemisphere", CEC Env. Res. Prog., TRACAS Final report, G. Ancellet Ed., chapitre 7, pp. 79-85, 2000.

17/ Legras B., V. Daniel, **J.L. Baray**, G. Ancellet, "Planetary-scale tropopause folds in the southern subtropics (Solicited Paper)", *EGS XXV General Assembly, Nice, France*, 2000.

18/ Randriambelo T., **J.L. Baray**, S. Baldy, "Analyses of 8 years ozone measurements in the tropics Reunion island field observations", *AGU Session meeting, Washington*, 2000.

19/ Randriambelo T., **J.L. Baray**, S. Baldy, "Analyses of the seasonal variability of the tropospheric ozone in the tropics : using in-situ, satellite and meteorological data", *Quadriennal ozone symposium, Sapporo, Japon*, 2000.

20/ Baray J.L., S. Baldy , G. Ancellet, V. Daniel, B. Legras, "Stratosphere-troposphere exchanges at the southern edge of the tropical zone and impact on the tropospheric ozone balance", *Quadriennal ozone symposium, Sapporo, Japon*, 2000.

21/ Posny F., T. Portafaix, **J.L. Baray**, S. Baldy, J. Leveau, "Vertical ozone distributions measured at La Réunion island (Southern tropics) between 1992 and 1999", *Quadriennal ozone symposium, Sapporo, Japon*, 2000.

22/ Baray J.L., T. Randriambelo, S. Baldy, G. Ancellet, "Tropospheric ozone lidar at Reunion island (southern tropics): insight to stratosphere-troposphere exchanges and African biomass burning contaminations, *XXth International Laser Radar Conference, Vichy, France*, 2000.

23/ Baray J.L., T. Randriambelo, G. Ancellet, "Seasonal evolution of the cross tropopause transport observed in the Southern subtropics using the La Réunion data set", CEC Env. Res. Prog., TRACAS Final report, G. Ancellet Ed., chapitre 6, pp. 73-78, 2000.

24/ Bencherif, H., T. Portafaix, B. Morel, **J.L. Baray**, S. Baldy, J. Leveau, A. Hauchecorne, A. Moorgawa, M. Michaelis, "Meridional transport in the lower stratosphere across the southern subtropical barrier : a case study", 16th annual assembly of the South African Society of Atmospheric Sciences (SASAS), *Pretoria, Afrique du Sud*, 2000.

25/ Bencherif H., T. Portafaix, B. Morel, **J.L. Baray**, S. Baldy, J. Leveau, A. Hauchecorne, A. Moorgawa, M. Michaelis, "A case study of sporadic transport across the southern boundary of the tropical stratospheric reservoir", *Stratospheric processes and their role in climate (SPARC), Mar del Plata - Argentine*, 2000.

26/ T. Randriambelo, **J.L. Baray,** S. Baldy, A. Thompson, S. Oltmans, P. Keckhut, “ozone LIDAR insight to the short term variability of the tropical troposphere, *Network for the Detection of Stratospheric Change 2001 symposium, Arcachon - France*, 2001.

27/ Baray, J.L., S. Baldy, R.D. Diab, J.P. Cammas, A. Marenco, Upper tropospheric Rossby wave breaking, filamentation and tropical cut-off low over South Africa, *EGS XXVII General Assembly, Nice, France*, 2002.

28/ A. Rechou, **J.L. Baray**, S. Baldy, Influence of deep convection on the introduction of ozone into the troposphere (Stratosphere- Troposphere Exchange), *EGS XXVII General Assembly, Nice, France*, 2002.

29/ A. Réchou, **J.L Baray**, S. Baldy, T. Portafaix, Influence of deep convection on the injection of ozone into the troposphere (stratosphere-troposphere exchange), 21st ILRC - Quebec city, Canada, 2002.

30/ P. Keckhut, G. Ancellet, L. Goldfarb, A. Hauchecorne, E. Riedinger **J.L. Baray**, B. Cadet, J. Leveau, T. Randriambelo, A. Rechou, L. Robert, « Climatology of the upper troposphere with lidar », SPIE's Third International Asia-Pacific Symposium on Remote Sensing of the Atmosphere, Ocean, Environment, and Space, Hangzhou, China, 2002

31/ Keckhut P., S. Marchand, A. Hauchecorne, S. Godin, S. McDermid, T. Leblanc, G. Hansen, **J.L. Baray**, H. Bencherif, D. Swart, Y. Meijer, S. Pal, C. Vialle, F. Posny, F. Goutail, « Validation of GOMOS ozone profiles using NDSC LIDAR : statistical comparisons », ENVISAT meeting, Italy, 2002

32/ V. Sivakumar, B. Morel, H. Bencherif, **J.L. Baray**, P.B. Rao, « Rayleigh lidar observations of sudden stratopause warming over a low latitude », *EGS XXVIII General Assembly, Nice, France*, 2003.

33/ V. Sivakumar, **J.L. Baray**, S. Baldy, « troposphere-lower stratosphere temperature variability over Reunion (21°S, 55°E) : special attention to tropopause variations in conjunction with ozone concentration », *EGS XXVIII General Assembly, Nice, France*, 2003.

34/ T. Portafaix, S. Baldy, H. Bencherif, **J.L. Baray**, S. Godin, B. Morel, « Climatology of the southern stratospheric subtropical barrier since 1992 over the southern indian ocean », *EGS XXVIII General Assembly, Nice, France*, 2003.

35/ J.L. Baray, T. Portafaix, V. Sivakumar, S. Baldy, « Detection of tropopause as a dynamical barrier during a large scale subtropical tropopause fold », *EGS XXVIII General Assembly, Nice, France*, 2003.

36/ T. Randriambelo, **J.L. Baray**, S. Baldy, A.M. Thompson, S. Oltmans, P. Keckhut, "LIDAR measurements of tropospheric ozone over Reunion Island : influence of the synoptic situations", Toulouse, France, IGARSS, 2003.

37/ A. Réchou, J. Leclair de Bellevue, **J.L. Baray**, S. Baldy, "Campagnes de mesures par radiosondages à l'île de la Réunion à proximité de systèmes convectifs : Résultats et perspectives", St Jean De Luz, France, colloque du PNCA, 2003

38/ V. Sivakumar, J. Leclair de Bellevue, **J.L. Baray**, S. Baldy, H. Bencherif, « Climatological characteristics of the jet streams over southern hemisphere », SIVOM Conference, Munar, Inde, 2003

39/ V. Sivakumar, **J.L. Baray,** H. Bencherif, S. Baldy, « Troposphere and lower stratosphere temperature variability over northern and southern hemisphere stations. », INTROMET-2003, International Symposium on Natural Hazards Hyderabad Inde, 2003

40/ V. Sivakumar, **J.L. Baray**, S. Baldy, « Tropopause characteristics over Northern and Southern

hemisphere stations. », INTROMET-2003, International Symposium on Natural Hazards Hyderabad Inde, poster, 2003.

41/ J. Leclair de Bellevue, **J.L. Baray**, S. Baldy, G. Ancellet, « Cyclone tropical intense Marlène et échanges stratosphere-troposphere : Simulation à meso-echelle », ateliers de modélisation de l'atmosphère (AMA 2003), Toulouse, France, 2003.

42/ J.L. Baray, G. Ancellet, G. Bain, S. Baldy, B. Johnson, J. Leclair de Bellevue, J. Leveau, J.M. Metzger, J. Porteneuve, F. Posny, T. Randriambelo, V. Sivakumar, S. Richard, C. Vialle., Regional Status Report on tropospheric ozone : Reunion Island Tropospheric ozone workshop, Durban, 2003.

43/ Baray J.L., G. Ancellet, S. Baldy, J. P. Cammas, V. Daniel, R. Diab, B. Legras, T. Randriambelo, Dynamics : stratosphere-troposphere exchanges and subtropical jet, Tropospheric ozone workshop, Durban, 2003

44/ Baray, J.L.; Posny, F.; Metzger, J.M.; Sivakumar, V.; Leclair de Bellevue, J.; Baldy, S.; Ancellet, G.; Porteneuve, J.; Thompson, A.M., Tropospheric ozone profiles over Reunion island : Influences of biomass burning and STE induced by jet stream and convection; EGU - 1st General Assembly, Nice, France, 2004.

45/ Sivakumar, V; Leclair De Bellevue, J; **Baray, J.L**; Baldy, S; Bencherif, H. ; Jet stream characteristics over southern hemisphere region EGU - 1st General Assembly, Nice, France, 2004.

46/ Diab R.D., A.M. Thompson, R. Chatfield, V. Thouret, B. Sauvage, S. Piketh, **J.L. Baray** and G Coetzee, Synthesis of Recent Research on Tropospheric Ozone over Africa
quadriennal ozone symposium, Kos, Grece, 2004

47/ Leblanc T., I. S. McDermid, P. von der Gathen, O. Schrems, R. Neuber, M. Muller, F. Immler, K. Stebel, G. Hansen, W. Steinbrecht, H. Claude, A. Pazmino, S. Godin-Beekmann, G. Ancellet, **J.L. Baray**, H. Bencherif, Y. Meijer, D. Swart, L. Twigg, T. McGee, J. Thayer, J. Livingston, P. Kekchut, A. Hauchecorne, J.E. Barnes. The NDSC ozone and temperature lidar algorithm initiative (A2I) : Project overview 22nd International Laser Radar Conference (ILRC22) Matera City, Basilicata, Italy, 2004.

48/ Leclair De Bellevue J., **J.L. Baray**, S. Baldy, G. Ancellet, Stratosphere-Troposphere exchange near tropical convection : observations, mesoscale and global analyses. SPARC Conference, Victoria, Canada, 2004

49/ Sivakumar V., **J.L. Baray**, S. Baldy, H. Bencherif, Climatological characteristics of troposphere-stratosphere ozone from Reunion Island (21°S 55°E): using insitu (Ozonesonde and Lidar) and Satellite (HALOE and TOMS) measurements SPARC Conference, Victoria, Canada, 2004.

50/ Baray J.L., J. Leclair De Bellevue,S. Baldy, G. Ancellet, J.P. Cammas, Etude des échanges stratosphère-troposphère à l'île de la Réunion.3ème réunion des utilisateurs de Méso-NH Toulouse, 2005

51/ Leclair De Bellevue J., **J.L. Baray**, G. Ancellet, A. Rechou, S. Baldy, Mesoscale characteristics of stratosphere-troposphere exchange in the vicinity of tropical cyclone, EGU General Assembly 2005, Vienne, 2005.

52/ Meijer Y.J., **J.L. Baray**, G.E. Bodeker, H. Claude, K.H. Fricke, P. von der Gathen, S. Godin-

Beekmann, G. Hansen, P. Keckhut, T. Leblanc, D.E. Lolkema, I.S. McDermid, H. Nakane, S. Pal, P. Snoeij, D.P.J. Swart., Envisat Quality Assessment with Lidar (EQUAL): a project to support the long-term validation of ozone and temperature profiles, EGU General Assembly 2005, Vienne, 2005.

53/ Baray J.L., Atmospheric measurements at Reunion Island, SPIE Newsroom, DOI: 10.1117/2.1200606.0254**,** 2006.

54/ Senten,C., M. De Mazière, C. Hermans, B. Dils, A. Merlaud, M. Kruglanski, E. Neefs, F. Scolas, A.C. Vandaele, C. Vigouroux, K. Janssens, B. Barret, M. Carleer, P.-F. Coheur, S. Fally, **J.L. Baray**, J. Leveau, J.M. Metzger, E. Mahieu., Ground-based FTIR measurements at Ile de La Réunion: Observations, error analysis and comparisons with satellite data, European Geosciences Union General Assembly, Vienna (Austria), 15-20 April 2007, Vienna, Austria, [Geophysical Research Abstracts, Vol. 9, 08640], 2007.

55/ Baray J.L., Delmas R., Clain G., Leclair de Bellevue J., Posny F., Keckhut P., Diab R**.,** Long-term tropospheric ozone behaviour at Reunion Island and Irene based on linear trends calculations, RIIS Symposium, La Réunion, 2007.

56/ Clain G., **J.L. Baray**, R. Delmas, J. Leclair de Bellevue, R. Diab**,** Tropospheric ozone climatology at two southern subtropical sites, (Reunion island and Irene, South Africa) from ozone sondes, LIDAR, aircraft and in situ measurements, RIIS Symposium, La Réunion, 2007.

57/ Fally S., H. Herbin, P.-F. Coheur, C. Clerbaux, M. Carleer, D. Hurtmans, C. Senten , M. De Mazière, C. Hermans, B. Dils, M. Kruglanski, A. Merlaud, F. Scolas, C. Vigouroux, **J.L. Baray**, J. Leveau, J.-M. Metzger, Ground-based and IASI satellite FTIR measurements of water vapour isotopologues above Ile de la Réunion, RIIS Symposium, La Réunion, 2007.

58/ Senten, C., M. De Mazière, C. Hermans, B. Dils, M. Kruglanski, E. Neefs, F. Scolas, A.C. Vandaele, C. Vigouroux, K. Janssens, B. Barret, M. Carleer, P.F. Coheur, S. Fally, **J.L. Baray**, R. Delmas, J.M. Metzger, E. Mahieu, Ground-based FTIR measurement campaigns at Ile de La Réunion: Campaign specifications, retrieval method and results, RIIS Symposium, La Réunion, 2007.

59/ Vigouroux, C., M. De Mazière, M. Van Roozendael, I. De Smedt, B. Dils, F. Hendrick, C. Hermans, M. Kruglanski, A. Merlaud, E. Neefs, F. Scolas, C. Senten, S. Fally, M. Carleer, P.F. Coheur, J.M. Metzger, **J.L. Baray**, R. Delmas, P. Duchatelet, Observations of CH4, CH3D and H2CO at Ile de La Réunion from ground-based FTIR and MAXDOAS campaign measurements, RIIS Symposium, La Réunion, 2007.

60/ Baray J.L., Courcoux Y., Bencherif H., Leveau J., Delmas R., Porteneuve J., Ancellet G., Godin Beekmann S., Keckhut P., Overview of lidar measurements at Reunion Island, South Africa – French LiDAR workshop, Pretoria, 2007**.**

61/ De Mazière, M., C. Vigouroux, F. Hendrick, G. Vanhaelewyn, I. De Smedt, M. Van Roozendael, B. Dils, C. Hermans, M. Kruglanski, A. Merlaud, F. Scolas, C. Senten, M. Carleer, S. Fally, V. Duflot, J.M. Metzger, **J.L. Baray**, R. Delmas, P. Duchatelet, Observations of halogens, CO, CH_4, and H_2CO at Ile de La Réunion from ground-based FTIR and MAXDOAS campaign measurements, poster presented at the "*4th general Assembly of SCOUT-O3*", 21-24 April 2008, Alfred Wegener Institute, Potsdam, Germany, 2008.

62/ Baray J.L., Delmas R., Courcoux Y., Metzger J.M., Ferré H., Gabarrot F. , Keckhut P., Porteneuve J., L'OPAR (Observatoire de Physique de l'Atmosphère de la Réunion), un site

privilégié pour l'étude de l'atmosphère tropicale : parc instrumental, résultats scientifiques et projets, Atelier Instrumentation et Expérimentation, Toulouse, 2008

63/ Baray J.L., R. Delmas, G. Clain, F. Gabarrot, J.P. Cammas, P. Keckhut, Stratosphere-troposphere exchange study in the Southern subtropics using experimental data, trajectory and Reverse Domain Filling calculations, SPARC, Bologne, 2008

64/ Clain G., **J. L. Baray**, R. Delmas, R. Diab, J. Leclair de Bellevue, F. Posny, and J.P. Cammas, Ozone climatology in the southern subtropics, SPARC, Bologne, 2008

65/ Baray J.L., Robert Delmas, Gaëlle Clain, Jimmy Leclair de Bellevue, Françoise Posny, Jean-Marc Metzger, Philippe Keckhut , and Roseanne Diab, Tropospheric ozone trends in the southern subtropics (Reunion Island and South Africa) based on radiosondes linear regression analysis, IGAC, Annecy, 2008

66/ Clain G., **J.L. Baray**, R. Delmas, Detection of stratospheric intrusions in the troposphere with a lagrangian approach at Reunion Island (Southern Subtropics, Indian Ocean), IGAC, Annecy, 2008